Engineering Porous Electrodes for Redox Flow Batteries

Modeling, Diagnostics, and Manufacturing

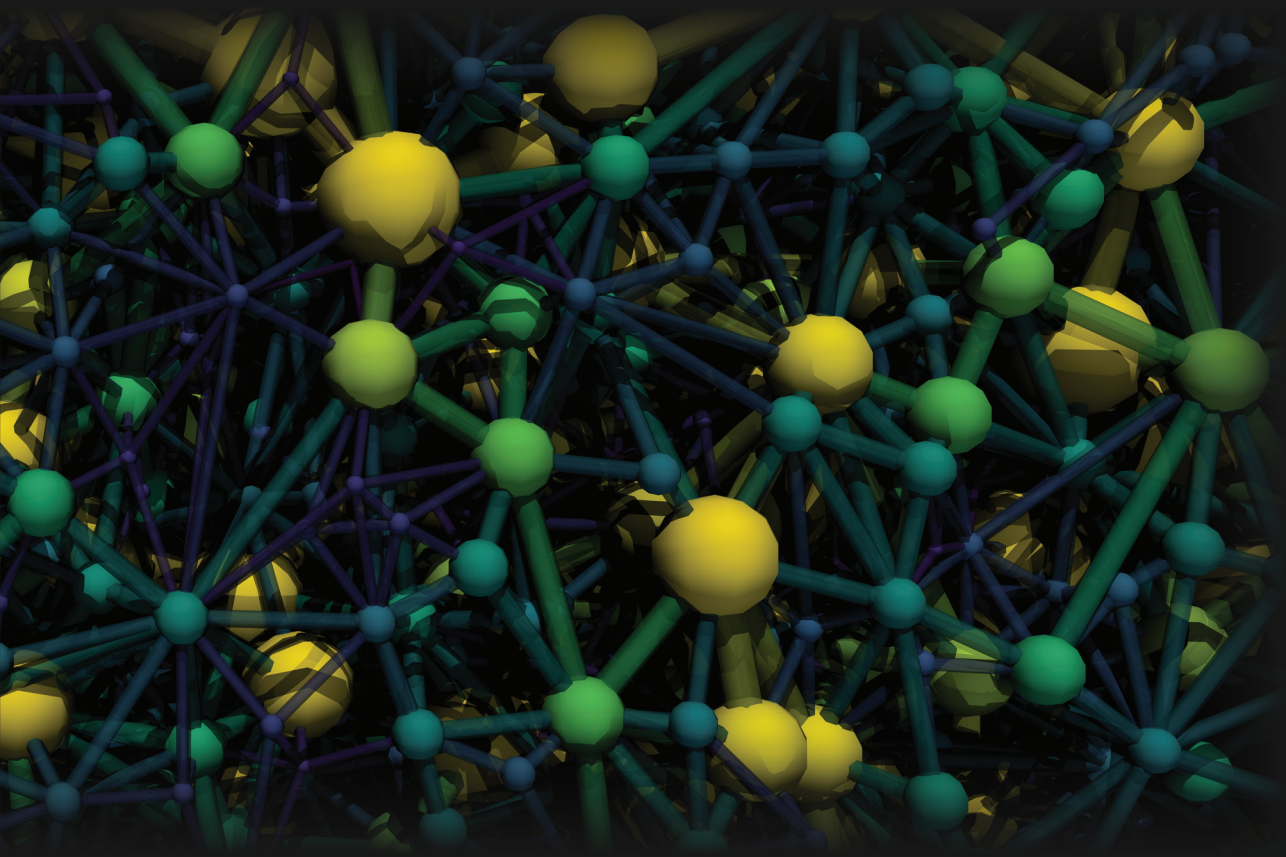

Maxime van der Heijden

Engineering Porous Electrodes for Redox Flow Batteries

Modeling, Diagnostics, and Manufacturing

PROEFSCHRIFT

ter verkrijging van de graad van doctor aan de Technische Universiteit Eindhoven, op gezag van de rector magnificus prof.dr. S.K. Lenaerts, voor een commissie aangewezen door het College voor Promoties, in het openbaar te verdedigen op woensdag 6 december 2023 om 16:00 uur

door

Maxime van der Heijden

geboren te Valkenswaard

Dit proefschrift is goedgekeurd door de promotoren en de samenstelling van de promotiecommissie is als volgt:

voorzitter:	prof.dr.ir. D.C. Nijmeijer
1e promotor:	dr. A. Forner-Cuenca
Copromotor:	dr.ing. Z. Borneman
leden:	prof.dr.ir. J.A.M. Kuipers
	prof.dr.ir. M. van Sint Annaland
	prof.dr.ing. T. Breugelmans (Universiteit Antwerpen)
	dr. Y. Gonzalez Garcia (Universiteit Delft)

Het onderzoek of ontwerp dat in dit proefschrift wordt beschreven is uitgevoerd in overeenstemming met de TU/e Gedragscode Wetenschapsbeoefening.

"My problem is that I want to do too much"

Maxime van der Heijden

A catalogue record is available from the Eindhoven University of Technology Library

ISBN: 978-90-386-5878-0

Cover design by Maxime van der Heijden

Printing: Proefschrift specialist | www.proefschrifspecialist.nl

The research in this thesis was conducted in the Electrochemical Materials and Systems group and the Membrane Materials and Processes group at Eindhoven University of Technology, The Netherlands.

This research is part of the project *"Bottom up fabrication of hierarchically-organized porous electrodes for electrochemical reactors"* with project number 17324 of the Talent Research Program Veni which is financed by the Dutch Research Council (NWO).

Summary

Advanced electrochemical systems, such as redox flow batteries, rely on porous electrodes, which determine the system performance and costs. Conventional porous electrodes currently used in convection-enhanced technologies are fibrous carbonaceous materials developed for low-temperature fuel cells; as such, their microstructure and surface chemistry are not suited for redox flow batteries. Thus, there is a need for targeted synthesis and engineering of porous electrodes with tailored properties to meet the requirements of liquid-phase electrochemistry. Specifically, the three-dimensional structure of the electrode is critical as it determines the available surface area for electrochemical reactions, electrolyte transport, fluid pressure drop, and electronic and thermal conductivity. However, the role of the electrode microstructure and, consequently, the optimal design for specific flow battery chemistries remains unknown. Hence, a multi-variable optimization problem at different length scales must be solved with highly coupled transport phenomena and kinetics. In this doctoral dissertation, a novel framework is developed to design and synthesize electrode structures from the bottom up, tailored to emerging electrochemical technologies with a focus on redox flow batteries. In this thesis, fundamental structure-function-performance relationships are elucidated by imaging and modeling commercial electrodes, which are used to design hierarchically organized porous electrodes through topology optimization and to manufacture model grid structures with 3D printing.

In **Chapter 1**, redox flow batteries are introduced as a technology that is promising for large-scale energy storage to bridge the temporal and geographical gaps between energy demand and supply. Thereafter, the transport phenomena and cell overpotentials in redox flow batteries are discussed in detail. Furthermore, experimental diagnostics, electrode manufacturing, multiphysics simulations, and computational electrode optimization strategies are introduced to aid the theoretical understanding and design of advanced electrode structures, as the empirical design process alone is time- and resource-intensive, limiting exploration of the wider design space. Finally, the scope of the doctoral dissertation is presented based on four objectives.

In **Chapter 2**, the developed pore network model is explained, which is a simulation framework for flow batteries that is microstructure-informed and electrolyte-agnostic, constructed using an open-access platform (OpenPNM), and validated with experimental data. The model utilizes a network-in-series approach to account for species depletion over the entire length of the electrode, enabling the simulation of large electrode sizes. To validate the robustness of the modeling framework, single-electrolyte flow cell experiments were performed for two distinct electrolytes – aqueous and non-aqueous – and two types of porous electrodes – carbon paper and -cloth, extracted using X-ray computed tomography and converted into a pore network. The electrochemical model solves the electrolyte fluid transport and couples both half-cells by iteratively solving the

species and charge transport at a low computational cost. The electrochemical performance of the non-aqueous electrolyte is well captured by the model without fitting parameters, allowing rapid benchmarking of porous electrode microstructures. For the aqueous electrolyte, it is found that incomplete wetting of the electrode results in overprediction of the electrochemical performance. Finally, a parametric sweep is discussed for the identification of operation envelopes.

In **Chapter 3**, the pore network model of **Chapter 2** is used, together with experimental techniques, to investigate the effect of stacking electrode layers for two prevailing commercial electrodes and flow fields. To this end, the pore network model is extended to simulate an interdigitated flow field design, and thickness-structure-performance relationships are obtained for specific electrode-flow field configurations. By stacking commercial electrodes, for example, two carbon paper electrodes with a flow-through configuration, the overall reactor efficiency can be enhanced. Furthermore, both the electrochemical power and pressure drop are improved, providing a facile strategy to enhance the performance of flow batteries.

In **Chapters 4** and **5**, a genetic algorithm is developed and coupled with the pore network model of **Chapter 2** for the bottom-up design of electrode structures. Using this approach, the electrode microstructure evolves driven by a fitness function that minimizes the pumping power and maximizes the electrochemical power, requiring only the electrolyte chemistry, initial electrode morphology, and flow field geometry as inputs. Thus, making it a versatile framework that can be applied to other electrochemical systems. In **Chapter 4,** the principle of the genetic algorithm is introduced, where a flow-through cubic lattice structure with fixed pore positions is analyzed and shows significant improvement in the fitness function over 1000 generations. The evolution results in a structure with a bimodal pore size distribution containing longitudinal electrolyte flow pathways of large pores, significantly reducing the pumping requirements. Additionally, an increase in surface area at the membrane-electrode interface is found, resulting in an enhancement of the electrochemical performance.

In **Chapter 5**, the genetic algorithm is extended to allow for more evolutionary freedom during the optimization process by evolving structures beyond fixed flow-through cubic lattice designs. To this end, pore merging and splitting are incorporated to allow larger geometrical flexibility. In addition, the optimization of complex structures is investigated by the implementation of Voronoi networks and X-ray tomography extracted off-the-shelf fibrous electrodes as starting networks. Subsequently, the effect of operational conditions is analyzed by evaluating two chemistries and two prevailing flow field geometries. Furthermore, optimization definitions (fitness function and geometrical definitions) are elaborated upon to inform about their importance and to show the flexibility of the algorithm.

In **Chapter 6**, a new neutron radiography approach is introduced to quantify concentration distributions in *operando* redox flow cells, providing a new diagnostic tool to better understand reactive transport phenomena in electrochemical reactors. The presented approach is developed for a non-aqueous model redox system where the attenuation comes from the hydrogen or boron atoms that compose redox active molecules or supporting ions in non-aqueous electrolytes. Concentration profiles are resolved across the electrode thickness by employing in-plane imaging and are correlated to the cell performance with polarization measurements under various operating

conditions. Two neutron imaging methods are used, where first the combined attenuation of the active species and supporting salt is examined over the electrode thickness. Thereafter, a time-of-flight neutron imaging approach is used to analyze deconvoluted active species and supporting ion transport over time. With this approach, the transport of species in the reactor under a voltage bias is revealed, gaining insights into reactive transport phenomena within an operating flow cell.

In **Chapter 7**, the neutron radiography approach of **Chapter 6** is utilized to study local transport properties and concentration distributions in the porous electrode for three distinct electrode structures and with two flow field designs. By tracking the cumulative active species movement, it is found that, for electrolytes with facile kinetics and low ionic conductivity, an electrode structure with a bimodal pore size distribution with large through-plane voids is favorable combined with parallel flow fields because of the high through-plane hydraulic conductance and effective diffusivity, enhancing the current output. Comparably, interdigitated flow fields feature higher reaction rates and current output compared to parallel designs because of forced convection. Moreover, neutron radiography is proven useful in the detection of system secondary phenomena including salt precipitation and underutilization of flow field channels.

In **Chapter 8**, the manufacturing of porous electrodes using 3D printing is presented. Model grid structures were manufactured with stereolithography followed by carbonization to tune the physicochemical properties of electrodes. A suite of microscopy, tomography, spectroscopy, fluid dynamics, and electrochemical diagnostics was employed to evaluate the thermal behavior, manufacturing fidelity, and fluid and mass transport performance of ordered lattice structures in non-aqueous redox flow cells. The influence of the pillar geometry, printing orientation regarding the printing platform, and flow field design on the electrode performance is investigated. It is found that although commercial electrodes feature a greater internal surface area and therefore better performance, the area-normalized mass transfer coefficient is improved and the pressure drop is reduced by utilizing 3D-printed electrodes.

Finally, the main findings of this work are summarized in **Chapter 9**, and future research directions to accelerate and broaden the design and fabrication processes of advanced electrode structures are provided.

Samenvatting

Geavanceerde elektrochemische systemen, zoals redox flowbatterijen, maken gebruik van poreuze elektroden, die bepalend zijn voor de kosten en systeemprestaties. Conventionele poreuze elektroden die vandaag de dag worden gebruikt in convectie-gedreven technologieën zijn koolstofvezel materialen die oorspronkelijk zijn ontwikkeld voor brandstofcellen bij lage temperaturen. Als zodanig zijn in de huidige vorm de microstructuur en oppervlaktechemie niet geschikt voor redox flowbatterijen. Er is dus behoefte aan gerichte synthese en ontwikkeling van poreuze elektrodes met op maat gemaakte eigenschappen om te voldoen aan de vereisten van elektrochemie in de vloeistoffase. Met name de driedimensionale structuur van de elektrode is van cruciaal belang omdat deze het beschikbare oppervlak voor elektrochemische reacties, elektrolyttransport, vloeistofdrukval en elektronische- en thermische geleidbaarheid bepaalt. Het optimale ontwerp voor specifieke flowbatterijchemie en de rol van de elektrodemicrostructuur is echter nog onbekend. Hiervoor moet een multivariabel optimalisatieprobleem op verschillende lengteschalen worden opgelost met sterk gekoppelde transportverschijnselen en kinetiek. In dit proefschrift wordt een nieuw kader ontwikkeld om elektrodestructuren te ontwerpen en te synthetiseren van de bottom-up, gebruik makend van opkomende elektrochemische technologieën met een focus op redox flowbatterijen. Daarnaast worden fundamentele structuur-functie-prestatierelaties in kaart gebracht door commerciële elektrodes te visualiseren en te modelleren. Deze relaties worden vervolgens gebruikt om hiërarchisch georganiseerde poreuze elektrodes te ontwerpen door middel van topologie-optimalisatie en om modelrasterstructuren te vervaardigen met 3D-printen.

In **hoofdstuk 1** worden redox flowbatterijen geïntroduceerd als een veelbelovende technologie voor grootschalige energieopslag om de variatie in energieaanbod en -vraag, zowel op verschillende tijdstippen als op verschillende locaties, te overbruggen. Daarna worden de transportverschijnselen en celoverpotentialen in redox flowbatterijen in detail besproken. In aanvulling hierop worden verschillende benaderingen geïntroduceerd om het begrip van geavanceerde elektrodestructuren te verbreden en het ontwerp te optimaliseren, omdat het traditionele empirische ontwerpproces veel tijd en middelen kost en de mogelijkheid om de volledige ontwerpruimte te verkennen beperkt. Dit omvat het gebruik van experimentele methoden, elektrodefabricage, multifysische simulaties en computationele strategieën. Tot slot wordt de strekking van het proefschrift gepresenteerd op basis van vier doelstellingen.

In **hoofdstuk 2** wordt het ontwikkelde poriënnetwerkmodel toegelicht; een simulatiekader voor flowbatterijen dat microstructuurinformatie bevat en elektrolyt agnostisch is, gebouwd met behulp van een open-access platform (OpenPNM) en gevalideerd met experimentele data. Het model maakt gebruik van een netwerk-in-series benadering om rekening te houden met de reacties die plaatsvinden over de gehele lengte van de elektrode, wat het simuleren van grote elektroden mogelijk maakt. Om de

robuustheid van het model te valideren, zijn experimenten uitgevoerd met flowcellen waarbij twee verschillende soorten elektrolyten werden gebruikt, namelijk waterige en organische elektrolyten. Deze experimenten werden uitgevoerd met twee typen poreuze elektroden, koolstofpapier en -doek, geëxtraheerd met behulp van röntgencomputertomografie en omgezet in een poriënnetwerk. Het elektrochemische model lost het transport van elektrolytvloeistof op en verbindt beide helften van de cel door het soorten- en ladingstransport efficiënt op te lossen met lage rekenkosten. Het model vertoont een nauwkeurige voorspelling van de elektrochemische prestaties voor het organische elektrolyt, zonder de noodzaak van fittingsparameters, waardoor snelle benchmarking van poreuze elektrodemicrostructuren met experimentele data mogelijk is. Voor de elektrolyt op waterbasis blijkt dat onvolledige bevochtiging van de elektrode resulteert in een te hoge voorspelling van de elektrochemische prestaties. Tot slot worden verschillende parameters getest voor de identificatie van de operatie-enveloppen.

In **hoofdstuk 3** wordt het poriënnetwerkmodel uit **hoofdstuk 2** samen met experimentele technieken gebruikt om het effect van het stapelen van elektrodelagen te onderzoeken voor twee gangbare commerciële elektrodes en stromingsveldontwerpen. Hiervoor wordt het poriënnetwerkmodel uitgebreid om een interdigitated stromingsveld te simuleren en om de prestatie in relatie tot de dikte en structuur van de elektrode te onderzoeken voor specifieke stromingsveldconfiguraties. Door het stapelen van commerciële elektrodes, bijvoorbeeld twee koolstofpapierelektrodes met een flow-through configuratie, kan de algehele reactorefficiëntie worden verhoogd. Bovendien worden zowel het elektrochemisch vermogen als de drukval verbeterd, wat een eenvoudige strategie biedt om de prestaties van flowbatterijen te vergroten.

In de **hoofdstukken 4** en **5** wordt een genetisch algoritme ontwikkeld en gekoppeld aan het poriënnetwerkmodel uit **hoofdstuk 2** voor het bottom-up ontwerpen van elektrodestructuren. Met deze aanpak evolueert de elektrodemicrostructuur op basis van een fitnessfunctie die het pompvermogen minimaliseert en het elektrochemische vermogen maximaliseert, waarbij alleen de elektrolytchemie, de initiële elektrodemorfologie en de geometrie van het stromingsveld als invoergegevens nodig zijn. Dit maakt het algoritme veelzijdig en zorgt ervoor dat het kan worden toegepast op andere elektrochemische systemen. In **hoofdstuk 4** wordt het principe van het genetische algoritme geïntroduceerd, waarbij een kubusvormige roosterstructuur met vaste porieposities wordt geanalyseerd in een flow-through configuratie en een significante verbetering laat zien in de fitnessfunctie over 1000 generaties. De evolutie resulteert in een structuur met een bimodale poriegrootteverdeling die longitudinale elektrolytstroompaden van grote poriën bevat, wat leidt tot aanzienlijk minder energieverlies door verminderde pompvereisten. Bovendien is er een toename van het elektrodereactieoppervlak aan de membraankant, wat resulteert in een verbetering van de elektrochemische prestaties.

In **hoofdstuk 5** wordt het genetisch algoritme uitgebreid om meer evolutionaire vrijheid toe te staan tijdens het optimalisatieproces, door structuren te laten evolueren die meer geavanceerd zijn dan kubusvormige roosterstructuren met vaste porieposities in een flow-through configuratie. Hiertoe worden poriën samengevoegd en gesplitst om een grotere geometrische flexibiliteit te verstrekken. Daarnaast wordt de optimalisatie van complexe structuren onderzocht door de implementatie van Voronoi-netwerken en röntgentomografie-geëxtraheerde commerciële elektroden als startnetwerken. Vervolgens wordt het effect van operationele omstandigheden geanalyseerd door twee

elektrolytsoorten en twee stromingsveldgeometrieën te evalueren. Verder worden optimalisatiedefinities (fitnessfunctie en geometrische definities) nader toegelicht om hun belang te benadrukken en om de flexibiliteit van het algoritme te laten zien.

In **hoofdstuk 6** wordt een nieuwe neutronenradiografiebenadering geïntroduceerd om concentratiedistributies in *operando* redox flowcellen te kwantificeren, wat een nieuw diagnostisch hulpmiddel biedt om reactieve transportfenomenen in elektrochemische reactoren beter te begrijpen. De gepresenteerde benadering is ontwikkeld voor een organisch model redoxsysteem waarbij de attenuatie afkomstig is van de waterstof- of booratomen waaruit redox-actieve moleculen of ondersteunende ionen in organische elektrolyten zijn opgebouwd. Concentratieprofielen worden over de elektrodedikte verkregen en worden gecorreleerd aan de celprestaties met polarisatiemetingen onder verschillende operationele omstandigheden. Er worden twee neutronenbeeldvormingsmethoden gebruikt, waarbij eerst de gecombineerde attenuatie van de redox-actieve moleculen en ondersteunende ionen wordt onderzocht over de elektrodedikte. Daarna wordt een time-of-flight neutronenbeeldvormingsmethode gebruikt om het transport van de gedeconvolueerde redox-actieve moleculen en ondersteunende ionen in de tijd te analyseren. Met deze benadering wordt het transport in de reactor onder een stroomveld onthuld, waardoor inzicht wordt verkregen in reactieve transportverschijnselen in een werkende flowcel.

In **hoofdstuk 7** wordt de neutronenradiografiebenadering uit **hoofdstuk 6** gebruikt om de lokale transporteigenschappen en concentratieverdeling in de poreuze elektrode te bestuderen voor drie verschillende elektrodestructuren en twee stroomveldontwerpen. Door de cumulatieve beweging van redox-actieve moleculen te volgen kunnen we vaststellen dat voor elektrolyten met een snelle kinetiek en een lage ionengeleidbaarheid, een elektrodestructuur met een bimodale poriegrootteverdeling met grote poriën in het doorlaatvlak gunstig is in combinatie met parallelle stromingsvelden. Dit komt door de hoge hydraulische geleiding in het doorlaatvlak en de effectieve diffusie, waardoor de stroomopbrengst toeneemt. Op vergelijkbare wijze vertonen interdigitated stromingsvelden hogere reactiesnelheden en stroomopbrengst vergeleken met parallelle ontwerpen vanwege de geforceerde convectie. Bovendien is neutronenradiografie nuttig gebleken bij het detecteren van secundaire fenomenen in de reactor, zoals zoutneerslag en onderbenutting van stromingsveldkanalen.

In **hoofdstuk 8** wordt de productie van poreuze elektroden met behulp van 3D-printen gepresenteerd. Modelroosterstructuren werden vervaardigd met stereolithografie gevolgd door carbonisatie om de fysicochemische eigenschappen van elektroden te verfijnen. Een reeks van microscopie, tomografie, spectroscopie, vloeistofdynamica en elektrochemische experimenten werd gebruikt om het thermische gedrag, de productiegetrouwheid en de vloeistof- en massatransportprestaties van geordende roosterstructuren in organische redox flowcellen te evalueren. De invloed van de pijlergeometrie, de printoriëntatie ten opzichte van het printplatform en het ontwerp van het stromingsveld op de elektrodeprestaties wordt onderzocht. Het blijkt dat hoewel commerciële elektroden een groter elektrodereactieoppervlak hebben en daardoor beter presteren, de reactieoppervlakte-genormaliseerde massaoverdrachtscoëfficiënt wordt verbeterd en de drukval wordt verminderd door gebruik te maken van 3D-geprinte elektroden.

Tot slot worden de belangrijkste bevindingen van dit werk samengevat in **hoofdstuk 9** en worden toekomstige onderzoeksrichtingen besproken om het ontwerp en de fabricageprocessen van geavanceerde elektrodestructuren te versnellen en te verbreden.

Table of contents

Chapter 1
Introduction

Abstract

Redox flow batteries are a promising technological option for large-scale energy storage, but their deployment is hampered by suboptimal performance and elevated costs. The reactor performance is determined by the mass, charge, momentum, and heat transport rates coupled with electrochemical reactions. Understanding, measuring, and simulating these metrics is thus necessary for device optimization. In this chapter, first, the need for large-scale energy storage and the working principles of redox flow batteries are described. Second, the main components of a redox flow battery, the primary physics of reactive transport phenomena in redox flow batteries, and the three types of overpotentials with basic formulas to compute them are introduced. Third, the predominant redox chemistries are discussed, and key experimental techniques are reviewed that enable the quantification of overpotentials based on macro-homogenous approaches and locally resolved diagnostics. Subsequently, electrode manufacturing strategies and the most promising modeling approaches to support experimental efforts are briefly elaborated upon, followed by an overview of computational electrode optimization methods. Finally, the scope of this doctoral dissertation is described by four main objectives.

This chapter is partially published as:

M. van der Heijden, A. Forner-Cuenca, Transport Phenomena and Cell Overpotentials in Redox Flow Batteries, *in Encyclopedia of Energy Storage*, L. F. Cabeza, Ed. (Elsevier Inc., Oxford, ed. 2, 2022), pp. 480–499. doi:10.1016/B978-0-12-819723-3.00132-3

1.1. Large-scale energy storage

Since the industrial revolution in 1760, global energy consumption is rising yearly because of an increasing population and economic and technological developments (**Figure 1.1**). The primary sources of energy are fossil fuels (coal, oil, and natural gas, **Figure 1.1**); however, they are natural sources with limited availability and are rapidly depleting. Moreover, the use of fossil fuels as an energy source is accompanied by the emission of greenhouse gasses, resulting in climate change by global warming (i.e., 1.1 °C increase in 2022 since 1880, with a rapid increase since 1975 of 0.15 - 0.2 °C per decade) [1]. The energy sector, including energy in the form of electricity, heat, transport, or industrial processes, accounted for 73 % of the total greenhouse gas emissions in 2016 [2]. The urgent need to reduce greenhouse emissions to combat climate change has motivated the development of low-carbon emitting renewable energy technologies, such as solar photovoltaics and wind power, with the goal of net-zero greenhouse gas emissions by 2050, as stated by the Paris Agreement [3]. Renewable energy technologies include solar, wind, geothermal, biomass, tidal, wave, hydrokinetic, and hydropotential [4].

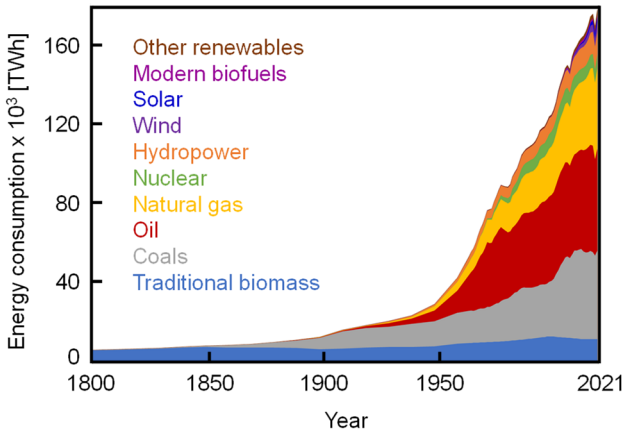

Figure 1.1: Global energy consumption from various sources over the past two centuries. Graph adapted from [5].

Most renewable energy sources are irregular (both daily and seasonal) and non-dispatchable, causing a partial incompatibility with the traditional electricity grid, where the generated electricity must be used instantly. The varying daily energy needs amplify this mismatch between energy demand and supply [4], increasing the stress on the stable operation of the current electrical grid, potentially resulting in negative energy prices or disconnection of the renewable sources from the grid. Moreover, the generated electricity must be transported, as some renewable energy sources have geographical restrictions, resulting in increased costs and loss of energy. Therefore, more energy must be generated than consumed to meet the varying demand. This could be minimized by using long- and short-term energy storage by decoupling energy generation from consumption, improving the implementation of renewable energy sources [4, 6–8]. Energy storage systems (ESS) play a crucial role in the efficient integration of renewable energy technologies by systematic adjustment of charging and discharging periods by storing and converting the electrical energy into another form of energy, providing optimal power system

management [4, 7]. Electrical energy can be stored in several forms including chemical, electrical, electrochemical, mechanical, and thermal storage, where their working principle defines their application in terms of capacity, power density, or geographical location [4]. The ESSs can be divided based on several properties (e.g., discharge time, energy density, power density, power rating, lifetime, and efficiency [9]), including low-power applications, medium-power applications, network connection applications with peak leveling, and power-quality control applications [7]. The low- and medium-power applications are for small-scale ESSs which include compressed air energy storage (CAES), flywheel energy storage (FES), superconducting magnetic energy storage (SMES), and supercapacitors (SCES). Whereas the network connection and power-quality control applications are for large-scale systems including pumped hydro storage (PHS), CAES, and redox flow batteries (RFBs) [7], see **Figure 1.2**. As a result of the high energy demand, spanning multiple time scales, both small- and large-scale ESSs are necessary. Grid-scale utilization of ESSs for reliable grid operation requires both a quick response time, ensuring power quality in the short term, and a high-power rating over a long discharge period, bridging power gaps in the long term.

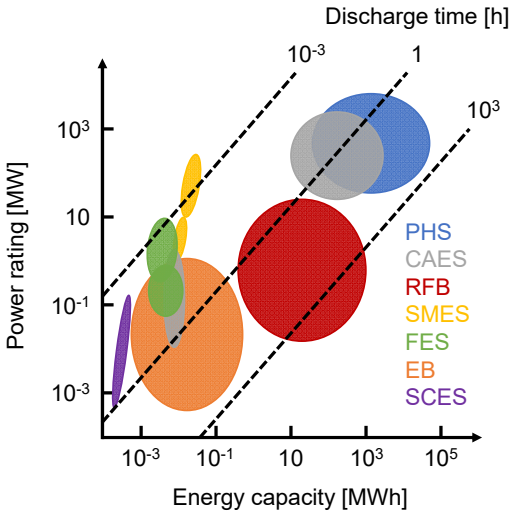

Figure 1.2: Comparison between energy storage systems based on their energy capacity, power rating, and discharge time, for: pumped hydro storage (PHS), compressed air energy storage (CAES), redox flow batteries (RFBs), superconducting magnetic energy storage (SMES), flywheel energy storage (FES), electrochemical batteries (EB), and supercapacitors (SCES). Modified from [7].

Electrical ESSs include capacitors, SCES, and SMES systems, which are used in the case of high currents and short durations, for high capacitance in a small volume, or to stabilize power plant outputs, respectively [4]. These systems cannot operate at large power rates for a longer period, but they can provide great discharging power rates over a short period (for example, capacitors have a power density of 10^5 W kg^{-1} but an energy density of 0.05 – 5 Wh kg^{-1} [9]) and are thus promising for electrical devices. *Chemical ESSs* store the electrical energy in chemical bonds upon chemical reactions and focus on hydrogen, biofuels, and synthetic natural gas storage [4]. Hydrogen-related systems are clean, abundant, and can discharge at great power rates for a long period (power density of 5 - 800 W kg^{-1} and energy density of 600 - 1200 Wh kg^{-1} [9]), though they are inefficient

[9] and have high investment costs. *Mechanical ESSs* include CAES, PHS, and FES storage technologies and store the electrical energy as pressurized gas, potential, or kinetic energy, respectively [6]. These technologies are environmentally friendly and can possess great energy capacities and delivery powers (**Figure 1.2**); however, their application is often geographically bound [7], limiting global implementation. *Thermal ESSs* store energy in the form of heat or cold and include latent heat systems, phase change reactions and sensible heat systems, which use various solid and/or liquid materials to store energy [6]. Thermal ESSs are useful for a more adaptable and steady energy supply. *Electrochemical ESSs* convert electrical energy into chemical energy through reversible redox reactions under the application of a current at a certain potential and time and include electrochemical batteries such as RFBs and lithium-ion batteries [4]. Electrochemical ESSs cover a wide application range (**Figure 1.2**, EB and RFB), ranging from energy storage for small-scale electronic devices with lithium-ion batteries, to large-scale long-duration energy storage using RFBs, but the investment and/or material costs are generally high [3].

PHS is the most widely deployed grid-scale energy storage technology with a total installed capacity of 160 GW in 2021 and a global capability of 8500 GWh in 2020, which is 90 % of the total global energy storage capacity in 2021 [10]. Grid-scale battery implementation is growing, with 10 GW in 2020 and 28 GW in 2022, led by lithium-ion batteries. By the net-zero scenario, grid-scale battery storage needs to grow significantly to 970 GW in 2030 [10]. Alongside lithium-ion batteries, RFBs have the potential for stationary energy storage as they have long operation lifetimes, can be sized according to energy needs by the decoupling of energy (tanks) and power (reactor), have discharge durations ranging from hours to days with a quick response time (seconds), and can be manufactured without rare earth elements [3, 10].

1.2. Redox flow batteries

The first flow battery was invented by John Doyle who filed a patent for a zinc/bromine battery in 1879. Nevertheless, till the oil crisis in the 1970s, the research on RFBs was on hold. Motivated by the ongoing transition towards renewable energy technologies, the interest in flow batteries was renewed and the research output is rapidly growing ever since [11, 12]. To date, vanadium RFBs are the most mature and widely deployed systems, developed in 1985 by Sum, Rychcik, and Skyllas-Kazacos [13, 14]. The major advantage of vanadium RFBs are the four distinct oxidation states of vanadium ions, limiting the capacity fade losses as active species crossover is not detrimental and can be recovered reversibly [11, 15]. Currently, vanadium RFBs are employed worldwide (estimated capacity of 1.5 GWh in 2022 [16]) with the largest installation featuring 100 MW / 400 MWh in Dalian, China in 2022 [11].

RFBs are reversible electrochemical energy storage systems that interconvert chemical and electrical energy by leveraging redox couples dissolved or suspended in liquid electrolytes, housed in external tanks. In RFBs, the electrolyte solution is pumped through the electrochemical stack (**Figure 1.3a**), consisting of an anodic and cathodic compartment, separated by a membrane or separator, where the active species undergo redox reactions to charge and discharge the battery (**Figure 1.3b**), where the general redox reactions can be written as [17]:

$$A^{n+} + xe^- \underset{discharge}{\overset{charge}{\rightleftharpoons}} A^{(n-x)+} \quad (1.1)$$

$$B^{m+} \underset{discharge}{\overset{charge}{\rightleftharpoons}} B^{(m+y)+} + ye^- \quad (1.2)$$

for the anode and the cathode, respectively. The anolyte and catholyte are pumped through the flow fields into the porous electrodes, **Figure 1.3a**, where the active redox molecules undergo charge transfer reactions. The electrons flow through the external circuit to the other half-cell where they are used for other redox reactions, and the charge-carrying species are transported through the separator (typically an ion-exchange membrane) that electrically isolates both compartments but ensures electroneutrality through ion transport.

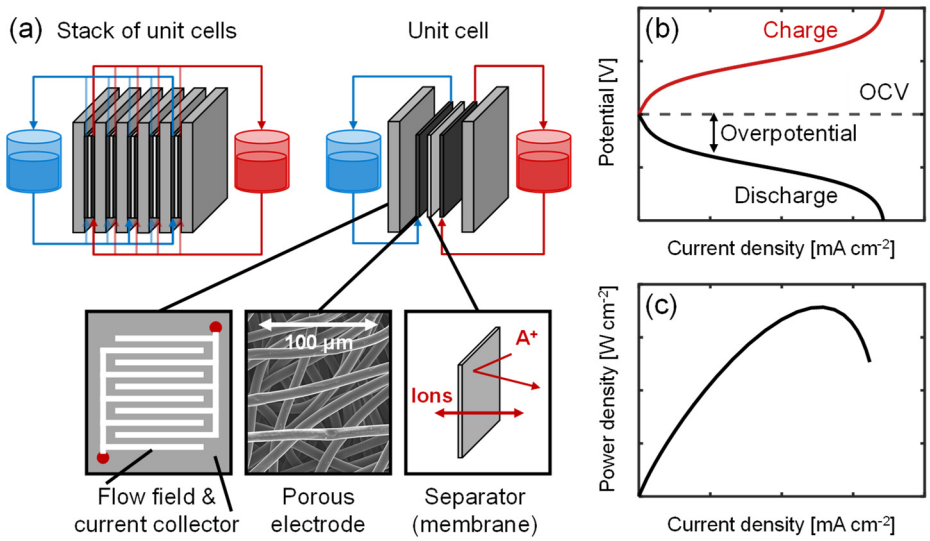

Figure 1.3: (a) Schematic representation of the reactor core of a stack of unit cells and a unit cell with the exploded view of the components: the flow field (with interdigitated design) and current collector, porous electrode, and separator. **(b)** Polarization curve where the potential is plotted over the current density in charge (red) and discharge mode (black). **(c)** Power density curve where the power density is plotted over the current density in discharge mode.

As compared to sealed batteries (e.g., lithium-ion), RFBs offer increased safety, easy manufacturing, and the ability to decouple energy and power, providing economic opportunities for modular scale-up [17]. However, current RFBs remain too costly for widespread deployment, motivating research into new electrolyte formulations and alternative reactor concepts [15]. The target for 2030 set by the European Strategic Energy Technology Plan for vanadium flow batteries is a system cost of < €100 kWh^{-1} (for a 100 kW system) and a power cost of < €150 kW^{-1} with a lifetime of >50000 cycles. State-of-the-art all-vanadium RFBs however currently do not meet this goal, as they have a system cost of €400 kWh^{-1} and a power cost of €600 kW^{-1} [3]. Decreasing the cost of the electrolyte (i.e., energy costs) is needed to enable long-duration discharge applications

while lowering the stack costs and increasing power density (i.e., power costs) can facilitate economically feasible short- to mid-discharge duration applications [18].

Drawing inspiration from other electrochemical technologies such as low-temperature fuel cells, RFB stacks leverage multiple piled unit cells to boost the potential or current needed to obtain the desired power [19]. Optimization of flow battery stacks poses unique challenges, which has motivated recent efforts to develop *in-situ* diagnostics using impedance spectroscopy [20] and improved flow field designs to minimize pressure drops and increase electrochemical performance [21]. At the core of the stack, individual cells feature a planar arrangement of a cathodic electrode, a separator, and an anodic electrode, sandwiched between current collectors with an embedded flow field (**Figure 1.3a**). At the stack level, the performance is highly convoluted by complex phenomena including electrochemical reactive transport, hydraulic losses, and inhomogeneous properties arising from non-uniform compression, shunt currents, and reactant depletion. Consequently, while developing optimal stacks is critical for commercialization, their use in research can complicate analysis and limit the fundamental learnings of transport phenomena and resulting overpotentials. Furthermore, characterizing novel materials (e.g., electrodes, separators, electrolytes) using technical stacks is resource- and time-intensive. Thus, simplified cell designs, which are the focus of this doctoral dissertation, are well-suited platforms to accelerate research progress in discovering new materials and reactor concepts by enabling straightforward analysis of individual cell components in well-controlled conditions.

Under the application of an electrical current, RFBs experience efficiency losses, called overpotentials, which can be assessed with the polarization curves, where the potential (V) is plotted versus the current density (i), also known as iV curves (**Figure 1.3b**). These overpotentials can be classified into activation, ohmic, and mass-transfer overpotentials, which are related to the reaction kinetics, ionic and electronic resistances, and transport of species to the reaction sites, respectively. Reducing these overpotentials is critical for increasing the power density of the stack (**Figure 1.3c**) and enabling smaller reactors for a given power output with reduced system footprints. However, unambiguous quantification of these overpotentials is not straightforward due to the intrinsic coupling between transport phenomena and kinetics. The performance of the flow cell is typically evaluated by charge-discharge curves at a fixed current, where the total capacity is evaluated as a function of time for a given potential. And, while this method is functional to evaluate performance under representative operating conditions, the quantification of overpotentials remains challenging, motivating the development of systematic methodologies to assess cell overpotentials under well-controlled conditions that enable meaningful comparison between material sets and reactor configurations.

Minimizing these overpotentials requires a detailed understanding of reactive transport processes in the various cell components, including momentum, species, charge, and heat transfer. These transport processes are highly coupled, which, combined with the lack of sophisticated diagnostic tools, complicates the analysis and frustrates design strategies. Thus, there is a need to develop rigorous and systematic methodologies that enable the isolation of individual transport processes. In this context, locally resolved diagnostics and advanced modeling techniques have recently been developed on various lengths and timescales to visualize and understand the individual transport processes.

1.3. Transport phenomena

The performance of RFBs is determined by complex multi-physics occurring at various time- and length scales, including electrochemical reactions at the porous electrode surfaces, electrolyte distribution through the electrode architecture, and hydraulic resistances throughout the system. Understanding the transport processes within the cell is thus critical in engineering RFBs with enhanced power outputs and efficiencies. These transport processes include momentum, species, charge, and heat transfer, and are schematically illustrated in **Figure 1.4**. In this doctoral dissertation, the focus is on all-liquid RFBs given their commercial maturity. The accurate description of other emerging systems, e.g., metal-air, gas-liquid, or suspension-based, introduces additional physics that are beyond the scope of this work. First, the main components of the RFB single cell will be described before going into detail about the four main transport mechanisms within the electrochemical cell.

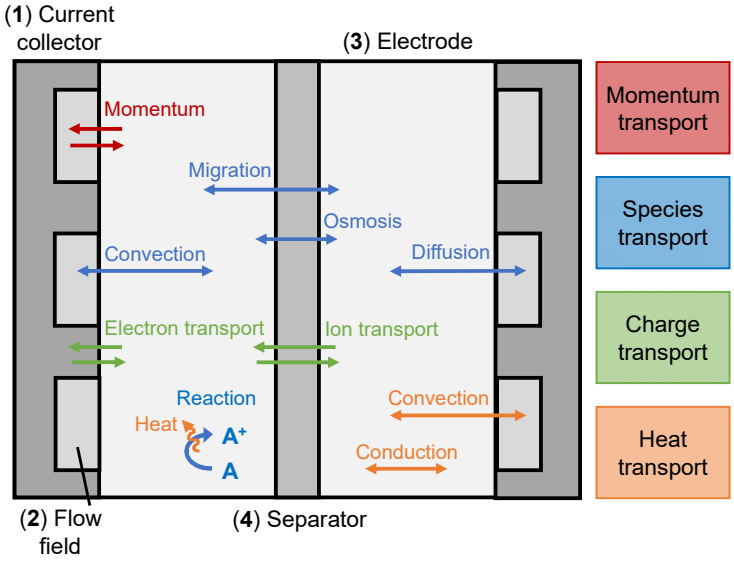

Figure 1.4: Schematic representation of the various transport mechanisms in the current collector, flow field, electrode, and separator within a unit cell of an RFB. For clarity, the respective transport mechanisms are shown in the dominant cell components, but they are relevant throughout the cell. The colors depict the distinct transport mechanisms, where the red color represents the momentum transport, blue the reactive species transport, green the charge transport, and orange the heat transport. The cell components are numbered in the order they will be discussed in (**Section 1.3.1**).

1.3.1. Transport domains

The main components of the battery responsible for the transport mechanisms are the current collector, flow field, electrode, and separator, shown in **Figure 1.4**. The performance of components (**2-4**) are highly coupled and dictate the overall battery operation. Hence, they should be precisely chosen and designed, keeping in mind the trade-off between electrochemical performance and pumping power output. The current collector (**1**) is a bridging component between the electrode and external circuit,

collecting electrical current generated at the electrodes by the redox reactions, and transporting the generated electrons to the external load, or vice versa. The current collector must therefore be made of an adequate electrical conductor (e.g., from a wide choice of metals or graphite) and offer good corrosion resistance.

The flow field (**2**), which is typically embedded in the current collector, largely defines the distribution of the electrolyte and the pressure drop within the electrochemical reactor [22, 23]. Several flow field designs exist (**Figure 1.5a-d**) and can be divided into two general configurations: 'flow-through' and 'flow-by'. In 'flow-through' designs, the electrolyte is forced through the electrode by convection; whereas in 'flow-by' designs, the electrolyte is forced to flow through the flow channels and over the electrode where the electrolyte only partially penetrates the porous electrode driven by diffusion [24]. Thus, in flow-through flow fields, higher mass transfer rates are achieved in the electrode due to the convective nature of this flow field [25]. Yet, a higher pressure drop is sustained through the reactor, increasing the pumping requirements. In the parallel flow field on the other hand, which is a 'flow-by' design, low pressure drops are maintained but the mass transport in the electrode is limited resulting in a low current output [26–28]. Moreover, hybrid designs drawing from fuel cell literature, including interdigitated and serpentine, have been investigated [29]. In the interdigitated flow field, the electrolyte is distributed over the channels where it is forced into the porous electrode over a small rib, generally resulting in a lower pressure drop compared to the flow-through flow field because of the shorter distance through the electrode [22, 26, 30, 31]. Whereas, in the serpentine flow field, only a small fraction of the electrolyte penetrates the porous electrode. Hence, the selection of the flow field design strongly depends on the operating conditions (i.e., flow rate, viscosity) and the electrode structure (e.g., bimodal or unimodal pore size distribution). Besides the above-mentioned flow fields, other designs have been investigated in the literature, including the spiral flow field, tubular flow field, circular flow field, and bioinspired flow field designs [24, 32]. Furthermore, novel concepts leverage topology optimization to engineer advanced geometries providing facile electrolyte distribution, low pressure drop [33, 34], and facile mass transport [35].

Porous electrodes (**3**) are performance-defining components as they must facilitate mass transport, provide the surfaces for electrochemical reactions, and conduct electrons and heat. Moreover, fast kinetics and high selectivity towards desired redox reactions must go in tandem with the mechanical, physical, and chemical stability of the electrode [23, 36]. The ideal electrode has a high electrochemically active surface area, high electrical conductivity, high stability, the ability to operate at a wide range of current densities, a reasonable cost, oxidation resistance, and an optimized pathway for the mass transport of ions [37]. State-of-the-art electrodes are inspired by polymer electrolyte fuel cell gas diffusion layers but, while there is an overlap in desired properties (e.g., high permeability and electronic conductivity), these materials have not been optimized for RFB application. Specifically, the fundamental challenge remains to provide seemingly contradictory requirements, i.e., high electrochemically active surface area, facile mass transport, and low pressure drop. Depending on their manufacturing process (e.g., papermaking, weaving, hydroentangling), the resulting electrodes (papers, cloths, felts (**Figure 1.5e-h**)) feature a unique three-dimensional structure that defines the performance of the cell [38]. Carbon papers are non-woven fibrous materials with a random in-plane orientation, held together by a binder (e.g., SGL, Toray) or by other means (Freudenberg). Within this class of electrodes, the binder content, pore size distribution,

thickness, and orientation degree vary significantly, resulting in distinct microstructures. In contrast, carbon cloths are interwoven materials with a particular weave pattern, similar to textile manufacturing, enabling a broad array of materials by varying the weave characteristics. As a result of its structure, carbon cloths are highly aligned structures with two pore sets. Finally, carbon felts are thicker electrodes that are loosely aligned in two preferential directions [38]. Thick felts are often used in traditional RFBs because of their higher surface area; though, they require high volumetric flow rates at constant electrolyte velocities resulting in increased pumping losses [38]. The above-mentioned carbon fiber electrodes are the current state-of-the-art with high electrolyte permeability, electronic conductivity, and (electro)chemical stability [39], but are not optimized to sustain the requirements of RFBs. Hence, in addition to the conventional electrodes, a significant amount of research is conducted on designing porous electrodes tailored for the application in RFBs [31, 40–48].

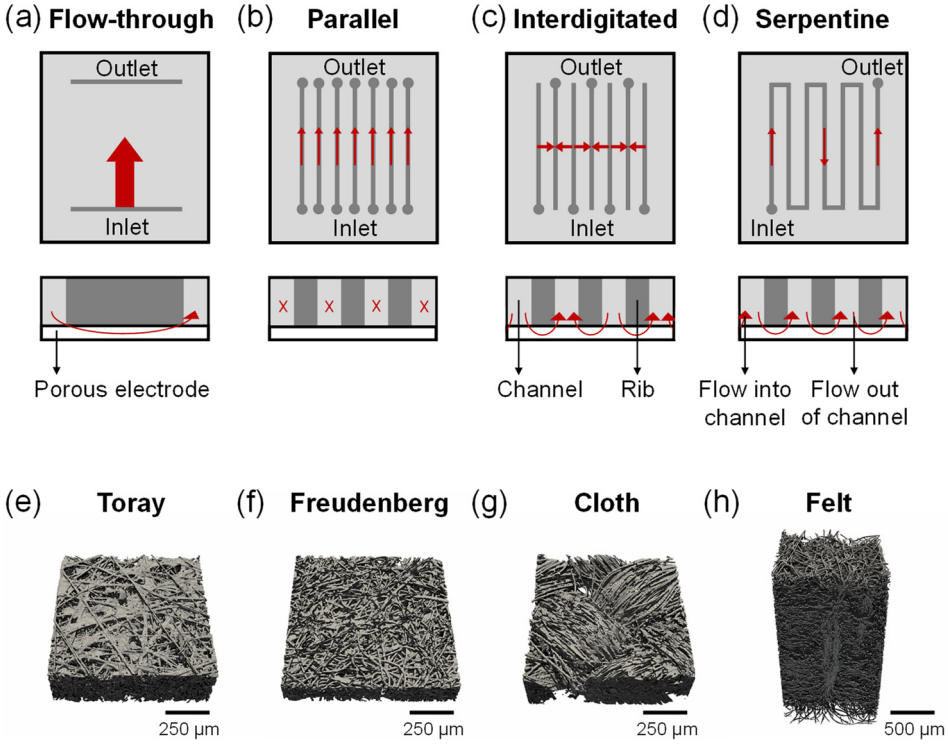

Figure 1.5: Current state-of-the-art flow field geometries and electrode structures used in RFBs. **(a-d)** The flow-through, parallel, interdigitated, and serpentine flow field designs, with their inlet and outlet and main flow path through the flow field channels and electrode structure. **(e-h)** The Toray paper, Freudenberg paper, woven cloth, and felt electrodes, extracted using X-ray tomographic microscopy using the method described in [49].

Finally, the membrane or separator (**4**) is a physical barrier between cell compartments impacting the cell resistance, which is responsible for ion transport, preventing active species crossover, and suppressing electronic conduction. Two types generally can be used, namely porous, size-selective separators or ion-exchange membranes (IEM). While porous separators are economically attractive, commercial

RFBs typically leverage IEMs, where research is conducted to optimize ion conductivity, ion selectivity, permeability, chemical stability, and mechanical stability [17]. Both anion- and cation-exchange membranes, the difference lies in the fixed charged groups within the membrane, have been explored for RFBs operating over a wide pH range. Nafion, a cation-exchange membrane, is the most frequently used.

1.3.2. Momentum transport

Momentum transport facilitates the replenishment of fresh electrolyte from the electrolyte tanks through the flow field to the porous electrode in both half-cells. The replenishment is crucial as it provides the reactants for the electrochemical reactions occurring on the porous electrode to charge or discharge the battery. Furthermore, the design of the cell, flow fields, and electrodes, as well as the operating parameters (e.g., flow rate), determine the pressure drop throughout the reactor, which is an important metric to minimize to ensure low pumping costs.

The conservation equations describing the electrolyte flow comprise mass and momentum balances. As most RFB systems consist of only one phase (liquid), complicated expressions for multiphase flow are omitted. Emerging flow battery architectures relying on multiphase flow would require more sophisticated models and are not discussed in this work. The mass conservation is derived by determining the velocity profile through the flow fields, electrode, and separator, which specifies that the rate of mass change in a unit volume is equal to the summation of the net rate of all species entering and exiting the volume in a given period by convection, defined as

$$\frac{\partial(\varepsilon\rho)}{\partial t} = -\nabla \cdot (\varepsilon\rho\boldsymbol{v}). \tag{1.3}$$

The mass change is defined by the density (ρ) and the porosity (ε) over time (t), whereas the mass change by convection also depends on the electrolyte velocity vector ($\boldsymbol{v}$). The porosity is implemented in the mass conservation equation to account for different porosities in the flow field, electrode, and separator as it defines the fraction of the volume occupied by electrolyte in each domain [50]. Typical porosity values are $\varepsilon = 1$ for the flow channels in flow fields, $\varepsilon = 0.8$ for the porous fibrous electrodes, and $\varepsilon = 0.57$ for Daramic porous separators [51]. For clarity, in this work convection is used (instead of advection) to describe the movement of the electrolyte through the different domains by the velocity field.

On the other hand, the momentum conservation for electrolyte flow through the different domains is defined by the Navier-Stokes equation

$$\frac{\partial(\varepsilon\rho\boldsymbol{v})}{\partial t} + \nabla \cdot (\varepsilon\rho\boldsymbol{v}\boldsymbol{v}) = -\varepsilon\nabla p + \varepsilon\mu\nabla^2\boldsymbol{v} + \frac{\varepsilon^2\mu\boldsymbol{v}}{\kappa}, \tag{1.4}$$

where the first term captures the rate of momentum change per unit volume, the second term the convection, the third term the net rate of momentum change per unit volume by pressure (p), the fourth term the viscous friction as a function of the shear stress, dependent on the electrolyte viscosity (μ) and the velocity vector, and the fifth term accounts for the porous structure, dependent on the permeability (κ) [50, 52]. **Equation (1.4)** can be simplified for electrolyte flow in the porous electrode by only considering the third and fifth terms. These two terms are dominant in the porous electrode as steady-state

uniform flow (neglecting the first term), low Reynolds numbers (neglecting the second term), and a low viscous term (neglecting the fourth term) can be assumed, resulting in Darcy's law [53], defining the viscous drag of fluids in porous media

$$\boldsymbol{v}|_e = -\frac{\kappa_{p,e}}{\mu}\nabla p, \tag{1.5}$$

where the permeability ($\kappa_{p,e}$) is the hydraulic permeability of the electrode. The permeability quantifies the strength of the viscous drag interaction in the pore structure and can be estimated by the Carman-Kozeny equation, modified for fibrous carbon electrodes

$$\kappa_{p,e} = \frac{d_f^2 \varepsilon^3}{K_{ck}(1-\varepsilon)^2}, \tag{1.6}$$

depending on the fiber diameter (d_f) and the Carman-Kozeny constant (K_{ck}), where the latter is a fitting parameter characterizing the shape and orientation of the fibrous material [54]. For systems evaluated at high electrolyte velocities, deviations from Darcy's law can be observed as inertial forces (second term in **equation (1.4)**) start to influence the fluid behavior, which can be described by the Darcy-Forchheimer coefficient [38].

Additionally, the electrolyte flow through porous separators can be simplified to **equation (1.5)**; however, an additional term is required for charged membranes as the electrolyte flow in IEMs is not only driven by the pressure gradient but also by the ionic potential gradient [55], defining the electrolyte velocity in charged membranes by Schlogl's equation

$$\boldsymbol{v}|_m = -\frac{\kappa_{p,m}}{\mu}\nabla p - \frac{\kappa_{\emptyset,m}}{\mu} C_f \mathrm{F} \nabla \emptyset_l, \tag{1.7}$$

where $\kappa_{p,m}$ is the hydraulic permeability of the membrane, $\kappa_{\emptyset,m}$ is the electro-kinetic permeability of the membrane, C_f is the concentration of the fixed charges in the membrane, F is Faraday's constant, and $\nabla\emptyset_l$ is the ionic potential in the electrolyte. Where the first term represents the viscous drag of fluids through the membrane as a result of the pressure difference between the half-cells, and the second term is the electro-osmotic convection caused by viscous interactions between the fluid and mobile ions [56]. It must be noted that the hydraulic and electro-kinetic permeabilities of the IEM ($\kappa_{p,m}$ = 1.58 x 10^{-18} m^2 and $\kappa_{\emptyset,m}$= 3.95 x 10^{-19} m^2 for Nafion IEMs [55]) are negligible compared to the hydraulic permeability of the electrode (for carbon fibers $\kappa_{p,e}$ = 6.0 x 10^{-11} m^2 [55]). Finally, the flow field can be described by the third and fourth terms of **equation (1.4)** as the shear stress cannot be neglected in flow field channels [34].

1.3.3. Reactive species transport

Species transport occurs at various length scales in all cell components, including the electrolyte transport from the electrolyte tanks through the flow field to the electrode, the transport of ions through the separator, the active species transport to and from the porous electrode surface, and the electrochemical reactions occurring on the electrode surface. The initial species present in the electrolyte and the species generated by redox reactions are transported through the cell domains by diffusion, migration, and convection.

The conservation of mass for each active species is based on the material balance for the concentration flux in each domain. In the limit of an infinitely small control volume, this translates to the following differential material balance of species i, describing the transport of species in the electrolyte

$$\frac{\partial \varepsilon C_i}{\partial t} = -\nabla \cdot \boldsymbol{N}_i + S_i. \tag{1.8}$$

This equation relates the rate of accumulation in the control volume over time, dependent on the porosity and the concentration of species i (C_i), to the net rate of material entering the control volume in all directions ($-\nabla \cdot \boldsymbol{N}_i$) and the source term ($S_i$).

The second term in **equation (1.8)** is defined by the concentration flux of the active species ($\boldsymbol{N}_i$), describing the active species transport within the flow field, porous electrode, and separator using the Nernst-Planck equation, assuming the dilute-solution theory holds

$$\boldsymbol{N}_i = -D_i^{eff} \nabla C_i - z_i u_i{}^{eff} F C_i \nabla \emptyset_l + C_i \boldsymbol{v}, \tag{1.9}$$

where D_i^{eff} is the effective diffusion coefficient, z_i the charge number, and $u_i{}^{eff}$ the effective ion mobility. The effective diffusion coefficient in **equation (1.9)** accounts for diffusion within porous media, dependent on the porosity and the tortuosity (τ) of the electrode or separator

$$D_i^{eff} = D_i \frac{\varepsilon}{\tau} = D_i \varepsilon^b. \tag{1.10}$$

When experimental data of the electrode tortuosity is absent, the Bruggeman correlation is adopted to calculate the effective diffusivity, where the Bruggeman coefficient (b) is assumed to be 1.5 for carbon fiber electrodes, originating from a derivation suggesting that tortuosity scales with porosity to the -0.5 [57, 58].

Equation (1.9) consists of three species transport terms: diffusion, migration, and convection, respectively.

- *Diffusion:* The first term relates the flux to the concentration gradient by the effective diffusion coefficient, capturing the transport of material by diffusion due to the random thermal movement of molecules described by Fick's law. The gradients in concentration diffuse the active species from high to low concentration to and from the surface of the electrode where the electrochemical reaction takes place. For the electrolyte in the porous electrode, the electroneutrality condition applies

  $$\sum_i z_i C_i \varepsilon = 0. \tag{1.11}$$

  Whereas for charged membranes, the valence charge (z_f) and concentration of the fixed charges in the membrane additionally need to be taken into consideration [56]

  $$z_f C_f + \sum_i z_i C_i^m \varepsilon = 0. \tag{1.12}$$

- *Migration:* The second term depends on the force experienced by charged species as a result of the electric field (equal to $-z_i F \nabla \emptyset$) dependent on the potential gradient and the charge number, where the charge of species i can be

either positive or negative and the positive ions migrate from high to low potential. Migration additionally depends on the concentration of active species i and the effective ion mobility, where the latter can be calculated from the Nernst-Einstein equation, describing the motion of charged species by the relation between the effective mobility and effective diffusivity of ions at infinite dilution

$$u_i^{eff} = \frac{D_i^{eff}}{RT}, \tag{1.13}$$

where R is the molar gas constant and T the absolute temperature. In separators, migration can have a substantial influence on the species crossover at high current densities [59, 60]. However, for non-charged reactants and products, the Nernst-Planck equation can be implemented without the migration term, resulting in the convection-diffusion equation [17].

- *Convection*: The final term in **equation (1.9)** is the convective term, representing the motion of active species from the bulk movement of the electrolyte. The contribution of this term to the electrolyte transport from the flow field to the electrode and vice versa strongly depends on the flow field geometry and dominates at high velocities for 'flow-through' flow field designs [61]. Whereas the contribution of this term in separators is marginal due to small pressure differences across separators [55].

For transport through separators, **equation (1.9)** can be extended with an osmotic term capturing the flux from an osmotic pressure gradient depending on the osmotic pressure ($\Pi = i_\Pi RTC_i$, with i_Π the van 't Hoff index) and the osmotic transport coefficient of species i. This osmotic transport coefficient has a positive sign as the solvent (e.g., water), convecting species i along, moves up its osmotic pressure gradient [62]. Additionally, the convection term can be extended for charged membranes to incorporate the electroosmotic drag using **equation (1.7)**. This term refers to the movement of electroneutral fluid through the membrane associated with the movement of ions caused by the electric field [63], depending on the liquid potential difference across the membrane [56, 62]. Therefore, the contribution to species crossover increases with increasing current densities [59, 60].

Assuming dilute-solution theory, the Nernst-Planck equation (**equation (1.9)**) only considers the interactions between ions and solvent and not the ion-ion interactions. To expand this equation for more concentrated solutions, ion-ion interactions need to be taken into account [64].

Looking back at the material balance (**equation (1.8)**), the third term is the source term, which includes the reaction rate (R_i) and self-discharge rate (R_d) of the active species, capturing the local consumption or generation of species i by

$$S_i = R_i \pm R_d \tag{1.14}$$

$$S_i = \frac{\lambda_i i_{c/a}}{nF} \pm (n_i k_s C_i \pm n_j k_s C_j \pm \cdots), \tag{1.15}$$

where the reaction rate defines the formation or consumption of the active species by Faraday's law and is a function of the current density ($i_{c/a}$) in the cathodic and anodic half-cells, the number of electrons transferred when an electrochemical reaction occurs

(n), and a dimensionless stoichiometric coefficient (λ_i) defining the formation or consumption of active species i. Subsequently, the self-discharge rate defines the self-discharge reactions induced by the crossover of active species through the separator and is defined by the self-discharge reaction rate constant (k_s), the number of ions involved in the crossover (n_i), and the species concentration of active species present in the self-discharge reactions of species i [65]. Finally, the dissociation rate could be included in the source term, describing the dissociation of electrolyte species, depending on the equilibrium constant of the reaction and the reaction rate constant. Moreover, the dissociation of electrolyte species could be suppressed within charged membranes as a result of the presence of fixed charges [55, 66]. The source term (**equation (1.15)**) is defined for electrochemical reactions in the electrodes, whereas in the flow field, no reaction or self-discharge is assumed to take place.

The local reaction current density (in **equation (1.15)**) characterizes the desired electrochemical reactions occurring on the electrochemically active surface of the porous electrode, in the cathodic and anodic compartments. The current density can be described by one of the most fundamental relationships in electrochemical kinetics, the Butler-Volmer equation, depicting the dependency of electrical current through an electrode on the potential difference between the electrode and the bulk electrolyte [50, 64], derived from the electronic energy change as a result of occurring reactions

$$i_{c/a} = i_{o,c/a}\left[\frac{C_j^s}{C_j}\mathrm{e}^{\frac{-\alpha_{c,c/a}nF\eta_{c/a}}{RT}} - \frac{C_i^s}{C_i}\mathrm{e}^{\frac{\alpha_{a,c/a}nF\eta_{c/a}}{RT}}\right], \tag{1.16}$$

where $C_{i/j}^s$ is the surface concentration at the electrolyte-electrode interface of species i or species j, where species j has a greater oxidation number than species i, α_a and α_c are the charge transfer coefficients of each redox reaction taking place at the anodic and cathodic half-cells defined as the fraction of the total energy change that impacts the activation energy, η is the surface overpotential which is the driving force of the reaction, and $i_{o,c/a}$ is the exchange current density in the cathodic or anodic compartment and is defined at the equilibrium potential where the net current is zero, given by

$$i_{o,c/a} = A_v F k_{0,c/a} C_i^{\alpha_{c,c/a}} C_j^{\alpha_{a,c/a}}, \tag{1.17}$$

where A_v is the specific internal electrochemically active surface area of the positive or negative electrodes (surface area of the porous structure per unit volume of the total porous electrode) and $k_{0,c/a}$ the standard rate constant for the reactions in the cathodic or anodic compartment.

The Butler-Volmer equation is dependent on two types of concentrations, the surface and bulk concentration of active species i; these can be related to one another by the local mass transport between the surface and the bulk electrolyte by a mass transfer coefficient (k_m). A simplified expression for the mass transfer coefficient can be used in the presence of supporting electrolyte [64]. Where at steady state, the rate of mass transfer of the reactant to the surface must be equal to the reaction rate at the surface, approximated by the following equation, assuming a linear diffusion layer

$$k_m(C_i - C_i^s) = -\frac{\lambda_i i_{c/a}}{nFA_v}. \tag{1.18}$$

The mass transfer coefficient is connected to the transport within the system and could therefore be related to the velocity vector in a non-linear fashion by

$$k_m = b|\boldsymbol{v}|^a, \tag{1.19}$$

where a and b are empirical constants depending on the electrode microstructure, electrolyte properties, flow field design, and reactor architecture [27].

1.3.4. Charge transport

Charge transport is crucial to facilitate the electrochemical reactions taking place in the RFB. Both electrons and ions must be transported through the battery, where electrons are conducted between both half cells through the current collector and external circuit, and ions through the liquid electrolyte and separator.

The conservation of charge defines that the total current is conserved throughout the electrodes, separator, and channels of the flow field. The current flux vector ($\boldsymbol{i}$) is defined by the two types of charges that are present in the system – electrons and ions – and obeys the charge neutrality principle

$$\nabla \cdot \boldsymbol{i} = \nabla \cdot (\boldsymbol{i_s} + \boldsymbol{i_l}) = 0, \tag{1.20}$$

where $\boldsymbol{i_s}$ is the electronic current through an electron conducting phase, such as the porous electrode and current collector, and $\boldsymbol{i_l}$ the ionic current through an ion-conducting phase, such as the liquid electrolyte in the flow channels, porous electrode, or separator. These currents can be related to the local reaction current density [59, 65], by

$$\nabla \cdot \boldsymbol{i_s} = -\nabla \cdot \boldsymbol{i_l} = i_{c/a}. \tag{1.21}$$

The electronic current density is described by Ohm's law, specifying that the current through a conductor between two points is directly proportional to the potential difference in the solid phase across the two points ($\nabla \emptyset_s$) with the electronic conductivity of the solid phase (σ_s) as the proportionality constant

$$\boldsymbol{i_s} = -\sigma_s^{\text{eff}} \nabla \emptyset_s, \tag{1.22}$$

where the conductivity is the effective conductivity (σ_s^{eff}) depending on the porosity and tortuosity of the solid phase obtained by the Bruggeman correction (**equation (1.10)**):

$$\sigma_s^{\text{eff}} = \sigma_s(1-\varepsilon)^b. \tag{1.23}$$

The ionic current density relates the charge to the species transport in the cell, as this term is proportional to the concentration flux defined by **equation (1.9)**, by

$$\boldsymbol{i_l} = F \sum_i z_i \boldsymbol{N}_i. \tag{1.24}$$

Equation (1.21) can be universally applied to all domains by setting proper values for the electronic conductivity and species flux, for example, ionic conduction is neglected in the current collector, whereas electronic conduction can be neglected in the separator [56].

1.3.5. Heat transport and generation

Thermal management within the RFB is crucial for commercial usage, as the temperature rise inside the RFB stack may exceed its safety limit at high charge and discharge currents, leading to thermal precipitation [67]. The flow field design and the electrolyte flow rate can be tailored to control the cell temperature by managing the distribution of the electrolyte through the system. The energy conservation equation describes the thermal balance within all domains in the RFB by taking into account heat conduction, convective heat transport, and heat generation by reaction and ohmic resistance [59, 68] and is given by

$$\frac{\partial}{\partial t}\left(\varepsilon\overline{\rho C_p}T\right) + \nabla\cdot\left(\varepsilon\boldsymbol{v}(\rho C_p)_l T\right) = \nabla\cdot\left(\overline{k^{eff}}\nabla T\right) + S_T. \tag{1.25}$$

The first term is the rate of energy change per unit volume and is dependent on the volume-averaged thermal capacitance ($\overline{\rho C_p}$), whereas the second term represents convective heat transport and depends on the density and specific heat capacity of the liquid ($(\rho C_p)_l$). The third term accounts for the rate of energy change as a result of thermal conduction and is dependent on the volume-averaged thermal conductivity ($\overline{k^{eff}}$) which accounts for heat conduction through porous domains [50]. The volume-averaged thermal capacitance and thermal conductivity are different for each domain, depending on the corresponding specific heat capacities and thermal conductivities of individual phases [69].

The final term in the energy conservation equation (**equation (1.25)**) is the source term (S_T) which differs for each domain (electrode, separator, and current collector). In the electrode, the source term is defined as

$$S_T|_e = \eta_{c/a} i_{c/a} - \Delta S_{0,j} T i_{c/a}/F + \frac{i_l^2}{\sigma_l^{eff}} + \frac{i_s^2}{\sigma_s{}^{eff}}. \tag{1.26}$$

The first term accounts for activation and concentration losses and is dependent on the current density and overpotential within each half-cell. The second term captures the electrochemical reaction and is dependent on the standard entropy associated with the reactions in both half-cells ($\Delta S_{0,j}$), the current density, and the temperature [50, 69]. Whereas the final two terms capture the Joule heating due to ohmic losses [50], dependent on the generated current and conductivity of the electrolyte and the electrode, respectively. In the separator and the current collector, the only form of heat transport is conduction as there are no activation and concentration losses or reactions present in these domains.

The energy conservation equation assumes that the liquid and solid phases are at the same temperature, which is equivalent to assuming an infinite rate of heat transfer between the two phases resulting in instant relaxation to the same temperature [69]. Additionally, the rate of energy change due to mechanical work in the fluids is ignored since little pressure-volume work is done [50].

1.4. Cell overpotentials

Overpotentials are voltaic performance losses arising in the electrochemical cell under the application of an electrical current. The operating potential of the electrochemical cell is defined by the open circuit voltage (OCV, E_{OCV}) and the cell overpotentials (**Figures 1.3b** and **1.6a**). The E_{OCV} represents the potential without electrons flowing through the cell and it is proportional to the thermodynamic potential (E_{th}). The E_{th} can be calculated from the equilibrium potentials in the cathodic ($E_{th,c}$) and anodic ($E_{th,a}$) compartments at their specific conditions (concentration, temperature, and pressure):

$$E_{th} = E_{th,c} - E_{th,a}, \tag{1.27}$$

where the thermodynamic potentials in each half-cell can be calculated by the modified Nernst equation [50, 64], assuming that the activity coefficients can be approximated to unity as a result of the dilute-solution assumption (**Section 1.3.3**)

$$E_{th,c/a} = E^0_{c/a} - \frac{RT}{nF}\ln\left(\frac{\prod_{j=1}^{N}[C_j]^{\nu_j}}{\prod_{i=1}^{N}[C_i]^{\nu_i}}\right), \tag{1.28}$$

with $E^0_{c/a}$ the standard equilibrium potential for the respective reactions occurring in the half cells and $\nu_{i/j}$ the stoichiometric coefficient of the active species in the reaction. In practical operation, the E_{OCV} deviates from the thermodynamic potential due to ionic activities and Donnan potentials, which requires experimental measurements of this parameter as it remains challenging to provide accurate predictions [70].

When applying (charge) or drawing (discharge) electrical current, the cell potential deviates from the E_{OCV} because of the overpotential losses that arise. The practical cell potential (E_{cell}) is subsequently defined for the charge (**equation (1.29)**) and discharge modes (**equation (1.30)**), by:

$$E_{cell} = E_{OCV} + |\eta_c| + |\eta_a| \tag{1.29}$$

$$E_{cell} = E_{OCV} - |\eta_c| - |\eta_a|, \tag{1.30}$$

with η_c and η_a the overpotentials in the cathodic and anodic half-cells, respectively.

Reducing the overpotentials is crucial for improving the power density of the stack and decreasing the power costs, as they capture the total potential losses in the electrochemical cell under operation, converted to heat. More generally, the overpotential can be classified by three contributors: the activation (η_{act}), ohmic (η_{ohm}), and mass transfer overpotential (η_{mt}), according to

$$\eta_{c/a} = \eta_{act,c/a} + \eta_{ohm,c/a} + \eta_{mt,c/a}. \tag{1.31}$$

The contributions of these three overpotentials to the polarization curve are conceptualized in a discharge operation mode in **Figure 1.6a** and discussed in more detail in the following sections.

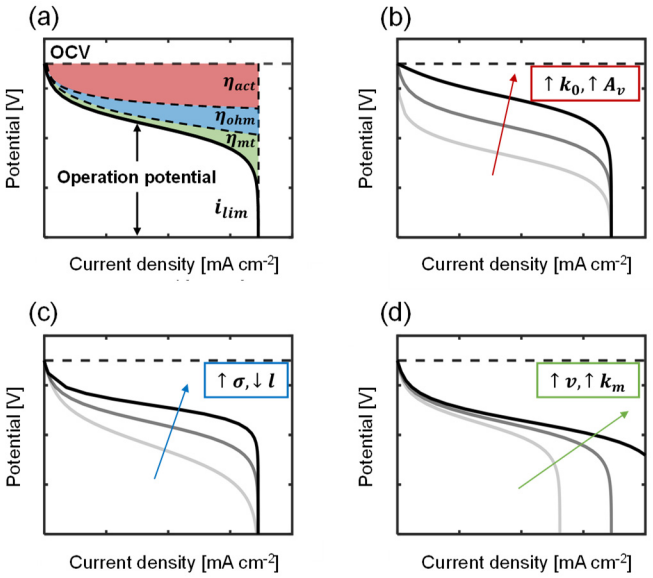

Figure 1.6: Discharge polarization curves for RFB systems. **(a)** Breakdown of the three overpotentials affecting the system performance, where the red area depicts the activation overpotential, the blue the ohmic overpotential, and the green the mass transfer overpotential. **(b-d)** Illustrates the contribution of various parameters to the shape of the polarization curve, affecting: **(b)** the activation overpotential by the kinetic rate constant (k_0) or the specific internal electrochemically active surface area (A_v), **(c)** the ohmic overpotential by the electrolyte conductivity (σ) or the electrode thickness (l), and **(d)** the mass transfer overpotential by the velocity (v) or the mass transfer coefficient (k_m).

1.4.1. Activation overpotential

The activation overpotential is dominant primarily at low current densities (**Figure 1.6b**) as a result of the charge transfer to and from the electrode surface to drive electrochemical reactions as the activation barrier must be overcome. This contributor is defined as the potential difference above the equilibrium potential required to produce the achieved current, neglecting the effect of surface concentration in the Butler-Volmer equation (**equation (1.16)**), resulting in the following equation for the ideal current in both compartments

$$i_{c/a,ideal} = i_{o,c/a}\left[\frac{C_j^0}{C_j}e^{\frac{-\alpha_{c,c/a}nF\eta_{act,c/a}}{RT}} - \frac{C_i^0}{C_i}e^{\frac{\alpha_{a,c/a}nF\eta_{act,c/a}}{RT}}\right], \quad (1.32)$$

where ${C_{i/j}}^0$ is the initial concentration of active species i or j.

The main parameter influencing the activation overpotential is the exchange current density (**equation (1.17)**), defined by the standard rate constant of the electrolyte, which is a measure of the reaction rate of the redox reactions and was described in **Section 1.3.3**. The activation overpotential is strongly dependent on the type of active species as the standard rate constant is reaction-specific [71]. Kinetically sluggish electrolytes (i.e., inner-sphere redox) such as vanadium species (k_0 = 6.8 x 10^{-7} m s^{-1} [14, 72]), feature low

rate constants and result in large activation overpotentials, motivating research on electrode functionalization to accelerate reaction rates or surface engineering to increase the available surface area. On the contrary, kinetically facile active species (i.e., outer-sphere redox), such as 2,2,6,6-tetramethylpiperidin-1-oxyl (TEMPO) (k_0 = 2.0 x 10^{-4} m s^{-1} [73, 74]) are only minimally affected by activation overpotentials.

1.4.2. Ohmic overpotential

The losses from resistance to electron and ion transport within the cell are classified as ohmic losses as they obey Ohm's law, resulting in a linear increase of the overpotentials with current (**Figure 1.6c**). The loss is the result of different compounding contributions, including the resistance of the flow of ions in the electrolyte at both cell compartments (R_c, R_a), resistance through the separator (R_m), circuit resistances ($R_{circuit}$), the electronic resistance of the electrode (R_e), and contact resistance ($R_{contact}$). Accordingly, the ohmic overpotential can be represented by the following equation

$$\eta_{ohm} = IR_c + IR_a + IR_m + IR_{circuit} + IR_e + IR_{contact}, \tag{1.33}$$

where I is the current and R represent the various resistances. The ionic conductivity of the electrolyte and the membrane resistance are the main contributors to the ohmic overpotential. Aqueous electrolytes containing sulfuric acid (σ = 80 S m^{-1} at 1 M [75]) are highly conductive, resulting in low ohmic overpotentials; whereas organic electrolytes such as tetraethylammonium tetrafluoroborate in acetonitrile (σ = 6 S m^{-1} at 1 M [75]) feature low conductivities and thus a significant ohmic overpotential. The resistance through the separator is strongly dependent on its type, thickness, and ability to conduct ions, as well as the separator-electrolyte interaction. The electrical conductivity of the electrode, on the other hand, is typically not a limiting factor in terms of ohmic overpotential as the solid phase is significantly more conductive ($\sigma \approx$ 300 S m^{-1} [26]) than the liquid phase. Finally, the contact resistances can be reduced by ensuring proper contact between the flow field, electrode, and separator by applying compressive force to the system.

1.4.3. Mass transfer overpotential

At high current densities, the mass transfer – or concentration – overpotential is the dominant loss (**Figure 1.6d**), which originates as a result of concentration gradients near the electrode surface and along the reactor length due to the consumption of active species. When the current increases, the concentration at the surface is reduced until the reactants are depleted, and a limiting current density is reached (**Figure 1.6a**). This limiting current density (i_{lim}) is derived from **equation (1.18)** by assuming that the surface concentrations are zero [64] and that there are no electromigration contributions (i.e., excess supporting salt), resulting in the following relation

$$i_{lim} = nA_vFC_0k_m. \tag{1.34}$$

The limiting current density defines the ultimate battery mass transport limit, but mass transfer losses also occur at lower current densities, as concentration differences between the electrode surface and bulk affect the cell performance in two ways: by

decreasing the Nernst potential ($\eta_{conc,Nernst}$) and by increasing the activation losses ($\eta_{conc,BV}$) [50]

$$\eta_{mt} = \eta_{mt,Nernst} + \eta_{mt,BV}. \tag{1.35}$$

The first term quantifies the variations in the thermodynamic potential, following the Nernst equation (**equation (1.28)**), due to concentration variations at the electrode surface (${E_{th,c/a}}^{s}$) with respect to the initial bulk concentration (${E_{th,c/a}}^{b}$)

$$\eta_{mt,Nernst} = {E_{th,c/a}}^{b} - {E_{th,c/a}}^{s}. \tag{1.36}$$

The second contribution in **equation (1.35)** is defined by the change in activation overpotential when using surface (η_{BV}, **equation (1.16)**) or bulk concentrations (η_{act}, **equation (1.32)**)

$$\eta_{mt,BV} = \eta_{BV} - \eta_{act}. \tag{1.37}$$

Substituting **equations (1.36)** and **(1.37)** into **equation (1.35)**, leveraging the definition of the limiting current density from **equation (1.34)**, and using a relation for the mass transfer coefficient to couple the bulk and surface concentrations (**equation (1.18)**), a compact form to compute the mass transfer overpotential is obtained

$$\eta_{mt} = c \ln\left(\frac{i_{lim}}{i_{lim}-i}\right), \tag{1.38}$$

where c is a constant ($c = \frac{RT}{nF}(1 + \frac{1}{\alpha})$) [50].

Accordingly, the parameters affecting the mass transfer overpotential are the electrolyte properties, concentration, electrolyte velocity and distribution, electrode microstructure, and reactor design. For example, as compared to 'flow-through' flow fields, 'flow-by' flow fields feature lower mass transfer coefficients with a weak flow rate dependency as they do not promote forced convection through the porous electrode [27], which is unfavorable for RFB implementation. The electrode microstructure also affects the mass transfer overpotential by the pore size distribution, fiber alignment, and internal surface area of the electrode [38].

1.5. Redox flow battery electrolytes

The RFB electrolyte is typically composed of a solvent, redox-active species, and a supporting salt where their composition governs the overall performance and price of the storage system. The electrolyte composition determines the energy density (i.e., solubility, redox potential), and impacts the activation (redox kinetics), ohmic (electrolyte conductivity), and mass transfer overpotentials (species concentration) as illustrated in **Figure 1.6**. Thus, electrolyte engineering is crucial to enhance battery efficiency and increase energy storage capacity. RFBs are classified according to two main groups, classical (all-liquid systems) and hybrid systems (e.g., hydrogen-bromide, iron-air, zinc/bromine [17]), which are further divided by the type of redox-active species and the solvent used to dissolve the active species [37]. This work focuses on classical RFBs using single-phase flow, which can be further divided into aqueous and non-aqueous systems (**Figure 1.7**) as the solvent governs the electrochemical stability window, solubility, viscosity, dielectric constant, and temperature operation range, dictating the transport rate

of ions in the electrolyte [17, 37, 76]. Other important factors to consider for the choice of electrolyte are the reaction kinetics, energy density, concentration, cost, and availability of the components [37].

The first-generation RFBs have been based on aqueous electrolytes, utilizing an aqueous solution of active species, combined with strong acids or bases as supporting salts. Water is an attractive solvent as it is cheap, not toxic, and has a high ionic conductivity. On the other hand, the main disadvantages of using water as a solvent are the lower temperature range and the electrochemical stability window of water [77]. Water electrolysis takes place at 1.23 V (in standard conditions), limiting the operation potential of aqueous systems and the suitable redox chemistries [78]. Traditional aqueous RFBs employ inorganic transition metals with high energy densities (**Figure 1.7**), such as the all-vanadium, iron/chromium, bromine/polysulfide, vanadium/bromine, and all-iron batteries [17]. Furthermore, organic redox molecules can be used which could provide a cheaper option to scarce metallic salts with good reversibility and reaction rates. Examples of redox-active species used in aqueous RFBs include quinones, viologens, or TEMPO-derivates [76]. However, these molecules generally suffer from capacity fade by chemical decomposition [79].

To overcome the limitation of water electrolysis at high operating potentials, non-aqueous RFBs can be deployed. A broad range of solvents can be used (e.g., acetonitrile, propylene carbonate [80]), providing a wide range of electrochemical operating windows, dielectric constants, viscosities, and temperature operating windows [76, 78]. The main drawback is their limited conductivity and poor solubility, increasing the ohmic overpotential and limiting the volumetric capacity [17, 77]. Redox chemistries that can be used for non-aqueous RFBs include coordinated metal complexes, metallocene, conjugated hydrocarbons, and nitroxyl radicals [76, 81].

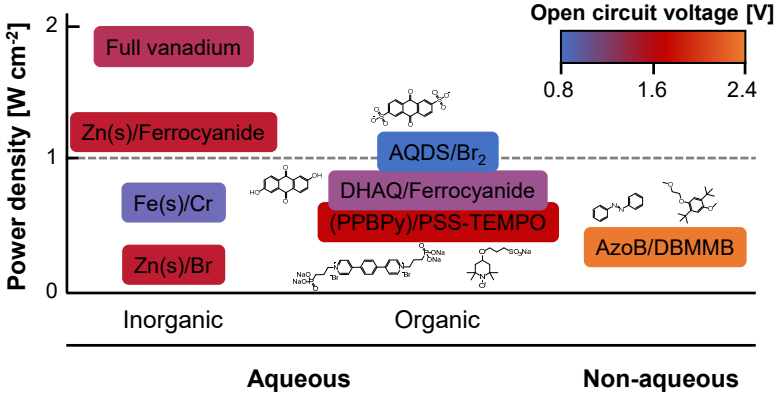

Figure 1.7: Power density and open-circuit-voltage values of several electrolyte types (aqueous inorganic, aqueous organic, and non-aqueous), based on [82].

1.6. Experimental methods

Engineering next-generation RFBs necessitates a fundamental understanding of the coupled transport phenomena and resulting overpotentials in the electrochemical cell. To this end, it is paramount to develop diagnostic tools that enable the isolation and quantification of performance-limiting phenomena that can aid the design of advanced materials and novel reactor concepts. Traditional characterization of RFBs involves charge-discharge cycling at a fixed current density to quantify energy, voltage, and current efficiencies as a function of time for a commercial battery design [83]. While this technique enables characterization at conditions close to actual operation, it does not enable deconvolution of individual cell overpotentials and transport phenomena and frustrates analysis of structure-function-performance relationships. Over the last years, several experimental methods have been developed to facilitate systematic analysis of cell losses using a combination of diagnostic platforms, model active species, and imaging techniques. In this section, a suite of experimental methods is described used to, first, quantify averaged properties over the entire flow cell, and second, quantify spatially dependent properties using locally resolved diagnostics.

1.6.1. Macrohomogeneous cell characterization

Cell-averaged characterization methods enable the quantification of averaged properties over the entire flow cell. These properties range from measuring the overall cell performance (e.g., by polarization and impedance measurements) to parameter identification (kinetic rate constant, conductivities, internal surface area) and can be measured using *in-situ* and *ex-situ* methodologies. In this work, *in-situ* techniques are defined as methods that can be applied during cell operation with electrochemical reactions. With *in-situ* characterization techniques, the system performance can be evaluated; however, quantitative comparisons between different studies are challenged by highly coupled phenomena in full battery designs [45]. Accordingly, various cell configurations can be employed to extract distinct information about the system performance **(Figure 1.8)**, namely the single-electrolyte cell, symmetric cell, and full cell configuration.

In the single-electrolyte configuration (**Figure 1.8a**), both compartments are connected to the same electrolyte tank, ensuring a constant state-of-charge (SOC). Accordingly, the OCV is near 0 V and the opposite redox reactions take place in the half-cells. Therefore, this setup offers simple cell-level analysis of a wide variety of cell components including the electrode and flow field configuration over a broad range of operating conditions [26]. The symmetric flow cell configuration (**Figure 1.8b**) is similar to the single-electrolyte configuration, as they both employ one single redox species in two oxidation states but leverage two electrolyte tanks to enable charge and discharge with small electrical and chemical potential gradients. This is a result of the SOC in the electrolyte tanks (0 and 100%), resulting in an OCV $\neq$ 0 V according to the Nernst equation (**equation (1.28)**). The symmetric cell configuration can be employed for electrolyte stability measurements and membrane performance experiments. These two configurations enable a simple and quick assessment of different cell components and operating conditions by *in-situ* characterization techniques such as polarization and impedance measurements. Additionally, model electrolytes (e.g., TEMPO/TEMPO$^+$ in

non-aqueous electrolytes), which are inherently stable, kinetically facile, and show good wetting behavior, can be leveraged to extract relevant performance metrics by deconvoluting kinetics and mass transport properties [38].

In the full cell configuration (**Figure 1.8c**), both compartments are connected to two separate electrolyte tanks with distinct redox couples of disparate potentials, resulting in an OCV ≠ 0 V for reversible processes (**equation (1.28)**). If suitable redox couples are not identified, electrochemical analyses are complicated by the poor performance of the cell, related to materials degradation (instability of the redox couples) or shortcomings in cell design (e.g., active species crossover). In addition to the characterization methods for the single-electrolyte and symmetric cell configurations, charge-discharge cycling is typically used for full cell configurations to analyze flow battery performance over time.

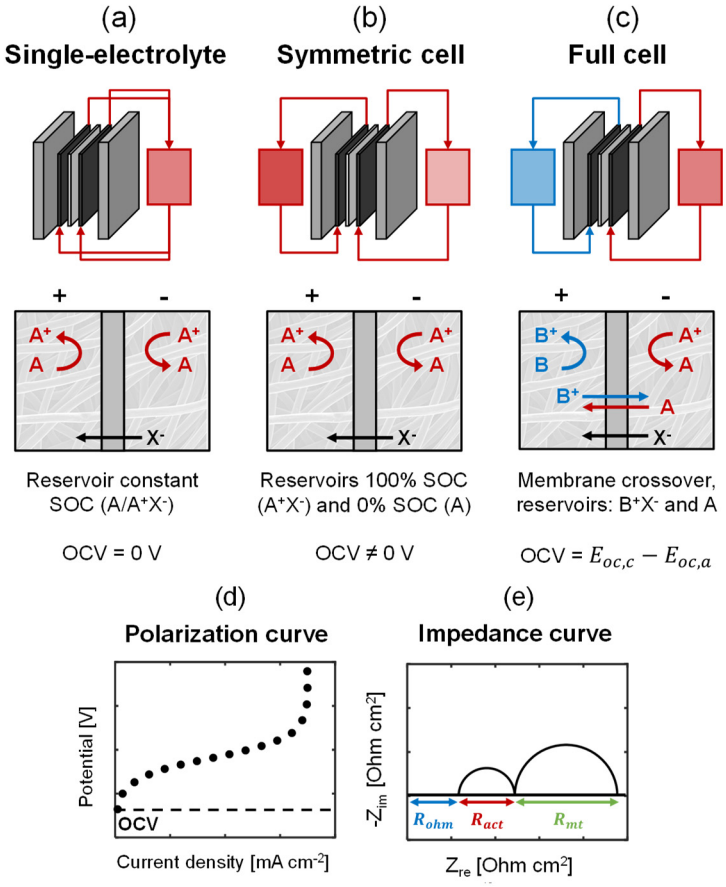

Figure 1.8: Schematic representation of three different RFB cell designs: **(a)** single-electrolyte, **(b)** symmetric cell, and **(c)** full cell design, with the redox reactions in the half-cell compartments shown below. **(d)** Typical polarization curve in charge mode applicable to all cell designs shown, depending on the OCV of the cell. **(e)** Typical impedance curve schematically showing the three overpotentials: activation, ohmic, and mass transfer overpotentials.

The two main *in-situ* techniques to analyze cell performance and related overpotentials are polarization and electrochemical impedance spectroscopy (EIS) measurements. In polarization measurements (**Figure 1.8d**), a potential or current is applied and the response is measured in terms of current or potential, respectively. As mentioned in **Section 1.4**, the polarization curve shows three distinct regions related to the three overpotentials present in the battery. These can be quantified using complementary EIS measurements, which is a multifrequency measurement technique in which a small sinusoidal perturbation (potential or current) is applied to the cell to measure the response. In EIS, the electrical resistance (impedance) of the cell is measured over a wide range of applied frequencies. For RFBs, a representative but schematic EIS spectrum is shown in **Figure 1.8e**, which provides a performance footprint that can be deconvoluted using two approaches: fitting to an equivalent circuit model, or by using physical models to extract relevant parameters [84]. Roughly, phenomena like ion and electron conduction are revealed at high frequency, charge transfer processes at the high to medium frequency range, while mass transport is revealed at lower frequencies. The relative contribution of each transport mode and reaction rate influences the magnitude and shape of the spectra [85].

In combination, *in-situ* polarization and EIS enable the quantification of overpotentials and cell resistances. Furthermore, alternative *ex-situ* characterization methods have been deployed to measure relevant cell-averaged transport and kinetic properties that complement the observations in flow cell testing and can enable faster research progress. Here, examples of relevant *ex-situ* cell-averaged characterization methods are highlighted and divided based on their relation to the different overpotentials.

- *Rotating disk electrode - kinetic overpotential:* The traditional method in electrochemistry to obtain kinetic information is using a rotating disk electrode (RDE) setup. Here, an electrode, which is typically a smooth surface (e.g., glassy carbon), is embedded in a rotating cylinder submerged in electrolyte [64]. At conditions below the limiting current regime, where the current is still high for mass transfer to be important, RDE can be used to measure kinetic parameters (k_i, D_i). An example of such an analysis is that of Koutecký-Levich, which can be used for first-order reactions at the surface. The RDE measurements are performed at different potentials or currents and rotation rates, where at low rotation rates mass transfer limitations are dominant, and at high rotation rates kinetic limitations. The relation between the measured electric current at the electrode from an electrochemical reaction (i_m) and the kinetic activity and mass transport of reactants, is given by the Koutecký-Levich equation [64]

$$\frac{1}{i_m} = \frac{1}{i_k} + \frac{1}{i_l}, \tag{1.39}$$

where the kinetic current (i_k) is the current when no mass-transfer limitations are present, i.e., the surface and bulk concentrations are equal, and the limiting current (i_l) is the current when the surface concentration is zero, given by

$$i_k = k_0(\eta) n F C_i^b \tag{1.40}$$

$$i_l = 0.62 n F D_i^{2/3} \omega^{1/2} \upsilon^{-1/6} C_i^b, \tag{1.41}$$

where $k_0(\eta)$ is the reaction rate constant at a specific potential, C_i^b is the bulk concentration, ω the angular rotation rate, and υ the kinematic viscosity.

Although RDE with a smooth model electrode (e.g., glassy carbon) works well for redox couples that are not affected by the surface chemistry of the electrode (outer-sphere), it might fail to accurately capture electrokinetic phenomena in inner-sphere systems. One challenge is that glassy carbon is not representative of existing carbon fiber electrodes due to its composition and morphology, which motivates research on developing accurate electrochemical measurements with single fiber electrodes [86].

- *Electrochemically active surface area measurements – kinetic overpotential:* The electrochemically active surface area (ECSA) of porous electrodes is an important parameter affecting the kinetic overpotential. The ECSA can be obtained using various methods including physical adsorption of gas molecules on a solid surface (Brunauer-Emmett-Teller method) and mercury intrusion porosimetry; however, both techniques might result in an overestimation of the ECSA that can be accessed by the molecules dissolved in the electrolyte [87]. Another approach to estimate the ECSA is to measure the electrochemical double layer capacitance (EDLC), determined by performing cyclic voltammetry in a single cell using a blank electrolyte solution, e.g., KCl or H_2SO_4 [38, 88]. From cyclic voltammetry measurements, the capacitance can be obtained using a linear fit of the scan rate dependent capacitive current

$$I = EDLC\frac{dV}{dt}, \tag{1.42}$$

where I is the average capacitive current obtained from the negative and positive non-Faradaic currents extracted at 0 V, and dV/dt the scan rate. Subsequently, the ECSA can be obtained from the following relationship:

$$ECSA = \frac{EDLC}{C_s m_e}, \tag{1.43}$$

where C_s is the specific capacitance and m_e the mass of the porous electrode [38]. While the method is functional, it may underestimate the surface area available for electrochemical reactions in an operating flow cell due to the nature of the current distribution and the reaction-transport balance within porous electrodes. Furthermore, obtaining exact values of specific capacitance remains challenging as this parameter is highly dependent on the composition and morphology of the electrode surface, which is typically heterogeneous [89]. Existing limitations in the characterization of ECSA motivate further research into more accurate techniques.

- *Conductivity measurements - ohmic overpotential:* The main ohmic contributors in RFBs are the electrolyte conductivity and the separator resistance, which can be obtained with a two-electrode cylindrical conductivity cell employing graphite current collectors [27]. For the electrolyte conductivity, the compartment of the conductivity cell is flooded and sealed shut, whereas, for the separator resistance, the separator is cut to size and sealed in the compartment with a drop of the electrolyte using an additional graphite connector to ensure proper contact. The resistance is subsequently obtained from the high-frequency intercept obtained with EIS measurements, from which the conductivity can be obtained. To account for the cylindrical cell resistance, a calibration curve must be

obtained for both the conductivity of the electrolyte and the separator resistance using known conductivity standards.

- *Limiting current density - mass transfer overpotential:* Limiting current density experiments can be performed to estimate chemistry and electrode-specific mass transfer coefficients at distinct velocities defined by the flow field geometry. The limiting current can be obtained in a single-electrolyte cell configuration to control the SOC in the system. To achieve limiting current conditions at the applied potentials, the concentration of active species is reduced (to e.g., 3 mM [87]) and subsequently, a chronoamperometry measurement (potential is induced in a stepwise fashion and the resulting current is monitored) is performed from which the limiting current density can be obtained at the current plateau [90]. By performing the experiment at distinct electrolyte velocities, a velocity *vs.* mass transfer coefficient relationship can be obtained, generally described by **equation (1.19)**.

1.6.2. Locally resolved diagnostics

In addition to cell-averaged characterization methods, locally resolved diagnostics provide information about the local properties within the cell, otherwise impossible to obtain or visualize by *in-situ* or *ex-situ* cell-averaged measurements. Properties ranging from local velocity and concentration profiles through the cell, to extracting the porous electrode three-dimensional structure, provide relevant information regarding transport processes within the electrochemical cell.

Several imaging techniques have been used to reconstruct digital 2D and 3D microstructures of RFB components at high spatial resolutions [91]. For example, X-ray tomographic microscopy (XTM) is frequently used in the battery community for obtaining the three-dimensional structure of porous electrodes (**Figure 1.9**) [40], both *ex-situ* [92] and *operando* [93] characterization of structural changes occurring in electrodes during operation, *operando* visualization of gas formation in the electrode [94–97], and investigating the electrolyte-gas diffusion layer interface [98, 99]. Additionally, XTM can be combined with microstructure-informed models to model transport processes within the electrochemical cell at the cell- or pore-level [100]. XTM can be used to obtain quantitative morphological information in the micrometer range; however, high X-ray doses are generally needed to obtain a high spatial and temporal resolution, resulting in a trade-off between high resolution and exposure time [101, 102].

Besides these microstructure-resolved imaging diagnostics, other techniques can be used to gain insight into the electrolyte distribution through the cell. Two *operando* examples are fluorescence microscopy and neutron imaging (**Figure 1.9**). Fluorescence imaging is a non-invasive imaging technique that can visualize velocity and concentration profiles within a transparent cell design with a high spatial resolution. Some examples include visualization of reactant distribution and mass transport in various flow field designs by injecting luminol solutions [103], and visualization of electrochemical reactions and heterogeneous transport of redox-active species in porous electrodes leveraging the natural fluorescence of quinones (**Figure 1.9**) [104]. Nonetheless, fluorescent species are required for operation, the technique is restricted to a limited penetration depth through porous electrodes, and it requires cell modifications. Alternatively, neutron imaging is a

non-invasive imaging technique that has been deployed to visualize multiphase flows in polymer electrolyte fuel cells [105], bubble generation in vanadium RFBs [106], and most recently, to map concentration distributions in non-aqueous flow cells (**Figure 1.9**) [107]. Neutron imaging is a well-suited technique for steady-state imaging (relatively low temporal resolution) of electrochemical cells as it is non-invasive and minimal cell modifications are required [105]. The reason is that neutrons, as opposed to X-rays, feature high penetration depths even through high atomic weight elements which are used as engineering housing materials (e.g., aluminum, carbon, steel), and greatly attenuate with lighter elements such as hydrogen, lithium, and boron which are contained in redox active molecules, making neutron imaging an attractive method with unique properties. All things considered; *operando* imaging of electrochemical systems combined with complementary electrochemical diagnostics is particularly powerful to obtain microstructure-informed information through the battery.

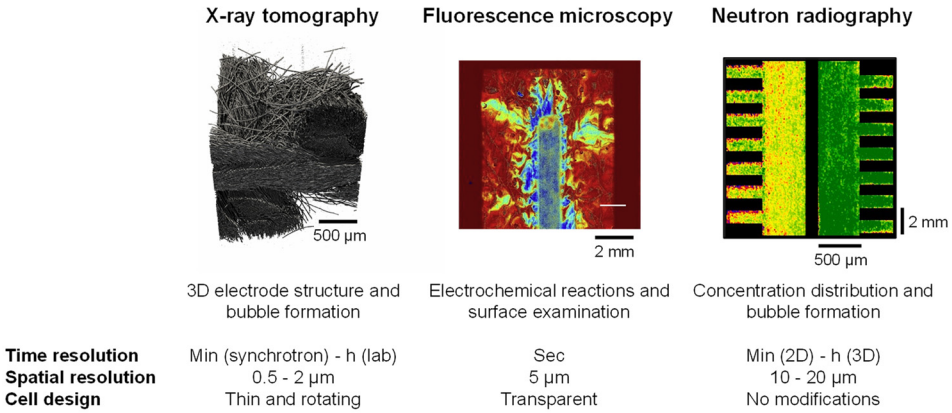

Figure 1.9: Locally resolved diagnostic techniques (X-ray tomographic microscopy, fluorescence imaging, and neutron radiography) with their measured property, time resolution, spatial resolution, and required cell modifications. The fluorescence microscopy image was adapted from [104].

1.7. Electrode additive manufacturing

The performance of porous electrodes in RFBs is defined by their microstructure and surface chemical composition. The microstructure determines the available open space for the transport of species, electronic conductivity, permeability, and the available area for reactions. Whereas the surface chemical composition determines the kinetic rate constant, wettability, and selectivity. Conventional porous electrodes used in RFBs are papers, cloths, and felts (**Figure 1.5e-h**), which are fibrous mats assembled in coherent structures fabricated by the carbonization of polymeric fiber precursors. The manufacturing processes used, e.g., weaving, compacting, hydroentangling, and electrospinning, define the arrangement of the carbon fibers and thus impact the electrode structure and resulting thickness [43, 45]. However, these commercial electrodes are repurposed from polymer electrolyte fuel cell gas diffusion layers and are not optimized for all-liquid RFBs [40, 45]. Moreover, conventional electrodes feature limited morphological diversity as a result of the manufacturing techniques used, motivating the development of new manufacturing techniques with high control on the material

properties and structure, e.g., electrospinning [108], post-synthetic modifications [45, 109], non-solvent induced phase-separation [39, 40], metal foams [110], etching [111], and additive manufacturing (3D printing) methods [31, 112, 113].

Additive manufacturing has recently been employed to manufacture customized electrodes with high control over the structure through computer-aided design, enabling the tuning of the permeability and internal surface area. The manufacturing method and choice of precursor (plastics, metals, composites, inorganics [114]) dictate the electrode properties including the size, geometry, feature size, conductivity, kinetic activity, porosity, mechanical stability, and surface roughness, but additionally the manufacturing time [115]. Several additive manufacturing techniques have been used to manufacture electrodes for electrochemical devices including VAT photopolymerization (stereolithography [46, 116, 117] and digital light processing [118, 119]), two-photon polymerization [120], powder bed fusion [44, 121], and direct ink writing [43, 122, 123], see **Figure 1.10**.

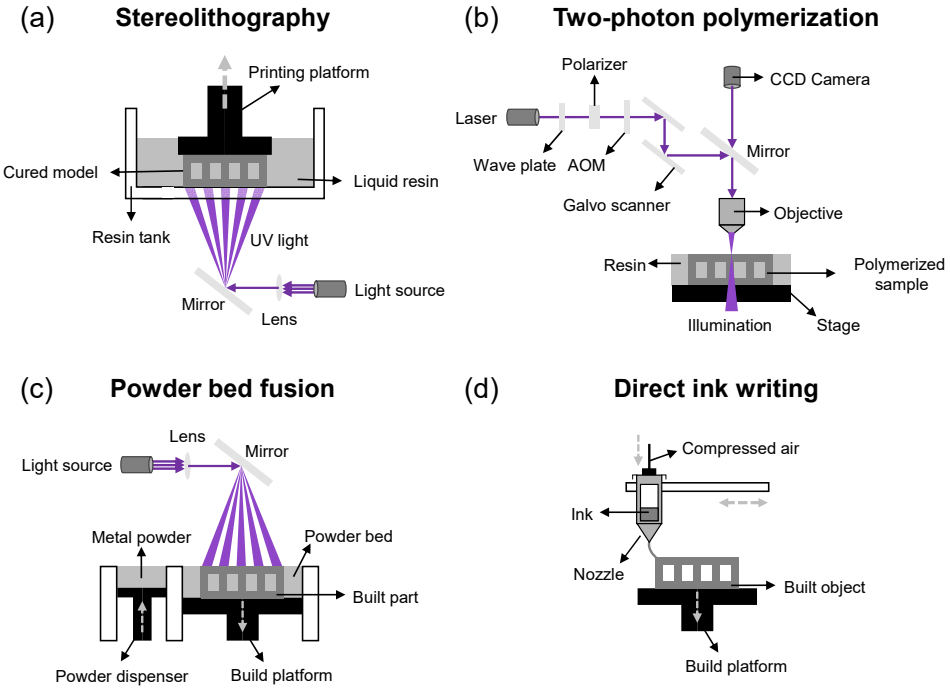

Figure 1.10: Additive manufacturing techniques that can be used to manufacture porous electrodes for redox flow batteries: **(a)** stereolithography, **(b)** two-photon polymerization, **(c)** powder bed fusion, and **(d)** direct ink writing.

Stereolithography and two-photon polymerization are both photopolymerization techniques in which a liquid resin is polymerized by a light source. In stereolithography (**Figure 1.10a**), the resin, stored in a tank, is polymerized in a layer-by-layer fashion with a UV laser [31]. Two-photon polymerization on the other hand is based on the simultaneous absorption of two photons by a photosensitive material (**Figure 1.10b**). Stereolithography is generally fast and allows large objects to be printed, but with a limited feature size of approximately 50 µm, whereas two-photon polymerization provides excellent nanometer

resolution (≤ 200 nm) depending on the objective used [124], but at the cost of the sample size and printing time. Both techniques provide high accuracy, can produce complex features, and have a smooth surface finish, but the resulting material is a non-conductive plastic that requires post-treatment, such as pyrolysis, to be converted into a conductive carbon electrode [31, 116]. The powder bed fusion process includes several printing techniques, such as selective laser sintering and electron beam melting, and uses either a laser or electron beam to melt and fuse material powder in a layer-by-layer approach, where fresh material is supplied by a reservoir alongside the bed (**Figure 1.10c**). Powder bed fusion allows a layer thickness of 100 μm, is scalable, and produces conductive metals, but is relatively slow [124]. Finally, direct ink writing is also a layer-by-layer technique in which the material, often a ceramic/metallic slurry, is extruded from a nozzle (**Figure 1.10d**). The slurry is a highly viscous liquid that retains its shape after printing, is conductive, and produces features of 50 μm, though the final product undergoes an additional sintering step to achieve mechanical strength [124].

Although most of the additive manufacturing techniques described above do not reach sub-micrometer feature sizes, the increased interest and developing rate of additive manufacturing techniques make it a promising strategy to investigate and implement in electrochemical devices. Owing to the great structural design flexibility, additive manufacturing can be combined with topology optimization strategies to realize the manufacturing of computationally optimized electrode structures for RFBs. Furthermore, the manufacturing process can be parallelized and combined with electrochemical reactor design through for example multi-material 3D printing (i.e., using multiple materials at the same time), showing the upscaling potential of this technology [114, 125].

1.8. Modeling across length-scales

With recent progress in computing power and theoretical approaches to simulate electrochemical phenomena, computational modeling has the potential to enable the bottom-up design of materials and electrochemical reactors at an unprecedented rate. Modeling and simulations can therefore be used as predictive tools, and to provide insights often impossible or impractical to discover theoretically or experimentally. Promising examples include the discovery of redox molecules with machine learning, understanding the role of electrode microstructure, and predicting optimal flow field geometries with topology optimization. In this dissertation, when referring to models we refer to computational models, unless stated otherwise.

Models for RFBs vary widely in level of detail, accuracy, and computational complexity. A range of modeling approaches have been reported for the analysis and optimization of RFB systems, ranging from continuum models to quantum mechanical methods, describing the physical processes occurring in the system on a range of length scales from macroscopic to atomic scale. These models can be applied to solve complete cells or stacks, flow transport within porous electrodes, or even interactions or orientations of active molecules. Generally, there is a trade-off between the length scale of interest and the computational complexity (**Figure 1.11**), and thus choosing the right model is paramount. Accordingly, the most frequently used models are briefly discussed in this section.

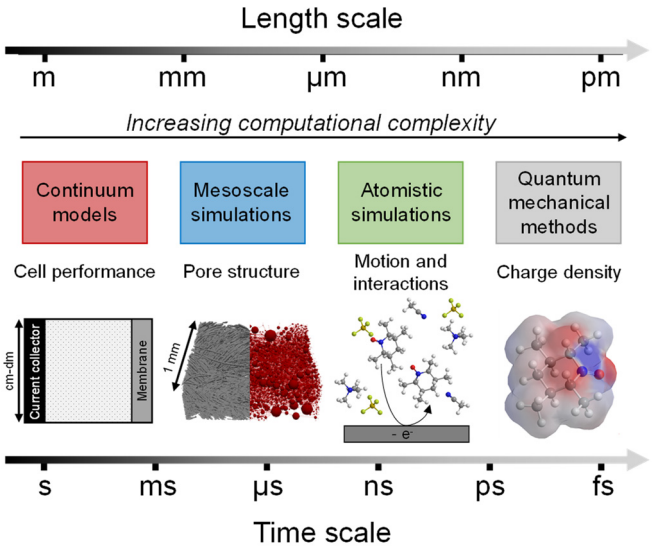

Figure 1.11: Typical time and length scales of various simulation techniques applied to study electrochemical processes.

1.8.1. Macro-scale continuum models

Macroscopic models for RFBs have been extensively studied and are used to address engineering problems at large length and time scales where the continuum approximation holds [91]. These models can therefore be used to predict the cell performance for multiple charge-discharge cycles for all cell designs (from single cell to stacked cell designs) [58], and cell-averaged properties such as the overpotential and limiting current density [126].

Macroscopic models are volume-averaged continuum models, where spatial homogenization within the control volume is performed [127], categorized into two groups: 1) lumped models, and 2) distributed models. Lumped models (zero-dimensional models) mainly serve as control and monitoring tools on the system level. Some examples include the prediction of the SOC, flow rate, and system efficiency using global energy and mass balances and equivalent circuit models to represent the characteristics of the battery [28]. These lumped models do not consider the structure of the battery, whereas distributed models do describe the physical and chemical processes occurring within the cell to model the performance of the flow fields, electrodes, and separators. Distributed models are therefore used for cell design and optimization by capturing spatial variations of field variables within the electrochemical cell by including the mathematical descriptions to model pressure and flow within the cell [72], distribution of chemical species [55], and distribution of the electric field and current density [126]. Distributed models can be further classified by their order as 1D, 2D, and 3D models, with increasing accuracy of the physical domain but at the cost of increased computational times [28].

1.8.2. Meso-scale simulations

Mesoscopic models, as opposed to macroscopic models, provide local information in RFBs from which information such as local transport profiles (velocity, concentration, current) [73], overpotential contributions (activation, ohmic, and mass transfer), and parameter studies (permeabilities, mass transfer coefficients, standard rate constant) [128] can be obtained or predicted. These models can be divided into continuum and particle-based models [127] and are designed to address problems at mesoscopic length scales to evaluate the local effects of the material's nano- and micro-structure on the battery performance.

In continuum-based mesoscale models, a representative region is determined as the computational domain with a discretized mesh in which the non-linear governing equations are discretized and solved using initial and boundary conditions [91]. Examples of continuum-based mesoscale models are pore-scale models including pore network, finite element, and finite volume methods. In pore network models (PNM), the void space within the porous domain is represented by pores that are interconnected by throats, where the pores are assumed well-mixed entities [128]. In PNMs, the complexity of the model equations is reduced as the transport through the network is modeled using finite volume or finite difference discretized 1D analytical solutions, while the underlying physics is retained. This results in a strong reduction in computational time with only a limited loss in computational accuracy [129, 130]. Therefore, PNMs can be leveraged to study complex flow problems in relatively large domains, which makes them suitable for electrode microstructure optimization studies. In finite element and finite volume methods, partial differential equations are solved by subdividing the system into smaller simpler finite-sized parts [131]. These models are geometry-resolved where information about the microstructure of porous media is included in the model, and specialized for structural and transport analysis within the cell on the pore level. Therefore, these models are often coupled with locally resolved imaging techniques, e.g., XTM, to directly model the transport within the microstructure of the porous media [100]. Relevant information that can be extracted from these models includes velocity, concentration, and current distributions as well as extracting microstructure-property-performance relationships and distinct overpotential contributions.

Often, the available properties for electrochemical reactions are not based on the geometry of the actual materials. Thus, to evaluate the local effects of the material's nano- and micro-structure on the battery performance, continuum models implementing surface or volume averaging at the cell level cannot be employed [28]. On the other hand, particle-based models at the mesoscale describe the transport processes for a single or a cluster of molecules, which makes them limited to the sub-micron scale and often smaller. These types of models can again be classified as non-first principle-based models, including kinetic Monte-Carlo models, and first principle-based models, such as Lattice Boltzmann models. The non-first principle methods simulate the microstructure formation of porous media and the process of aggregation for particles suspending in the colloid phase, by considering interactions among forces using methodologies similar to particle dynamics [127]. Therefore, kinetic Monte-Carlo models can for example be used to simulate semisolid RFBs [132]. On the contrary, first principle, or *ab initio,* methods follow established laws of physics without the use of ad hoc assumptions and fitting parameters [127], where the Lattice Boltzmann model is especially successful in describing interface dynamics, such as complex geometries like porous electrodes and multiphase flow [133].

Both methods provide detailed information about the transport processes at the pore level [73], and the reaction rates [134] or bubble formation [133] at the interface of the carbon fibers of the porous electrode. Accordingly, these modeling approaches could be used to complement locally resolved diagnostics such as XTM [73, 134], fluorescence microscopy, and neutron imaging to provide more detailed information about the local transport processes within the porous domains.

1.8.3. Atomistic models

Atomic-scale models involve modeling the physical behavior of porous energy materials at the scale of atoms. These models are also part of the first-principle, particle-based models, as the Lattice Boltzmann model, but provide information at a smaller length scale. Therefore, to gain more information regarding the electrochemical reactions at the electrode interface, the combination of meso- and atomistic-scale models could be powerful, as the former provides information regarding the porous structure and the latter about motion and interactions among molecules. An example of a particle-based first-principle atomic scale model is the molecular dynamics method. This method explicitly solves the motion of molecules and interactions among them [135], where the atoms are considered solid spheres, and the motion of molecules is described by Newton's second law [127]. Molecular dynamics provide useful information about the complex mechanisms at the molecular scale, providing a tool to model interactions among thousands of molecules. Examples include the development of methods for simulating reactive force fields for simulating bond formation and breaking, the modeling of interfacial electron transfer events [136], simulating the hydration shells of distinct active species in aqueous RFBs [137], and interactions between active species and counter ions or additives [135]. Molecular dynamics is a powerful tool to understand and extract electrokinetic parameters and redox potentials [138].

1.8.4. Quantum mechanical methods

Quantum mechanical models involve the modeling of the physical behavior of energy materials at a subatomic scale. It is a powerful tool to calculate the dissociation energy barriers, activation energy, adsorption geometry, reversible potential, and potential-dependent properties for elementary electron transfer steps [127]. Density functional theory is an example of a quantum mechanical modeling method that is specialized to model subatomic scales (electrons), involving quantum-mechanical theories for various molecular interactions, revealing complex physical behaviors [91]. The properties evaluated with the density functional theory models include chemical, structural, and electronic properties of RFBs [139], including the electronic charge density, total energy, magnetic configuration, and electronic band structure of the electrode [91]. Density functional theory can be coupled to (*in-situ*) experimental work to for example obtain insight into the fundamentals of the hydrogen evolution reaction [140], which is a side reaction in RFBs resulting in a decrease in coulombic efficiency, the reactivity of the electrode towards active species [141], or the effect of additives on active species solvation structures [142]. Accordingly, density functional theory can be a powerful tool to explain experimental results and in revealing reaction mechanisms to facilitate the development of new electrolytes and the improvement of surface functionalities of the electrode.

1.9. Computational optimization strategies for electrode design

As briefly mentioned in **Section 1.8**, modeling strategies have the potential to enable the bottom-up design of reactor components through optimization strategies. The rapid rise in computational power has driven the increasing interest in optimization methods for a wide range of applications, including electrochemical technologies. The optimization of the electrode structure is of special interest because of a range of contracting requirements that motivate computational work, i.e., high electrochemical surface area, facile mass transport, and low pressure drop.

An example of a taxonomy of optimization methods is provided in **Figure 1.12**, showing a wide variety of optimization classifications. The optimization method of choice depends on the optimization problem, as no optimization method is a clear winner to all kinds of problems, and depends on the complexity of the problem, the objective function, the constraints, and the number of variables and unknowns [143]. To define which optimization category is suited for the application, the problem type needs to be defined. In **Figure 1.12** an example is provided of a workflow that can be followed to determine the appropriate optimization method. First, it needs to be determined whether the problem is discrete or continuous. In discrete optimization problems, the problem variables adopt values of a discrete set, often a subset of integers, and can be further divided into exact (often used to provide optimal solutions for smaller problems [143]) and approximate methods, of which the latter is used to find close-to-optimal solutions for complex optimization problems in a short time period [144]. In continuous optimization problems, the values can have any real value and can be subdivided into nonlinear and linear programming [145]. The nonlinear programming branch can be further divided into global and local search methods, of which the global method can be split into heuristic, random search, and meta-heuristic methods. In heuristic methods, the optimization determines an optimal solution by iteratively improving the candidate solutions concerning a given problem. In random search methods, the gradient of the problem does not need to be optimized and thus relies solely on random sampling of solutions near the problem. Meta-heuristic methods are similar to heuristic methods; however, the algorithm used is generic and can deal with multiple problems [146]. The meta-heuristic methods comprise single-solution or population-based optimizations, in which the latter is divided into evolutionary and swarm intelligence algorithms. Swarm intelligence algorithms are based on studied interactions by living organisms (e.g., birds, fish, ants) by enhancing the objective function, or fitness function, by self-organization with a limited number of restrictions towards a global optimum [144]. Evolutionary algorithms, on the other hand, are based on the principle of natural evolution of a solution set over generations using operators based on diversity and selection. They can handle complex optimization problems with many variables and constraints, making evolutionary algorithms promising for the optimization of electrodes for electrochemical devices with complex performance trade-offs.

Artificial intelligence emerged in the mid-1950s inspired by Alan Turing and is gaining an increased interest in battery research to solve complex multivariable problems. Especially the machine learning branch is of interest which is capable to evaluate multidimensional datasets, discover data patterns, and can unlock applications that are difficult to exploit otherwise [147]. Both population-based algorithms mentioned above are unsupervised search-based machine learning algorithms that optimize for the global maxima and do not require training data, which for example is necessary when using

neural networks as a machine learning strategy. Though, these population-based algorithms do not guarantee an optimal solution [148]. Evolutionary algorithms are a rapidly growing area of artificial intelligence, whereas swarm intelligence has only recently been applied and is thus still in the beginning stage [148].

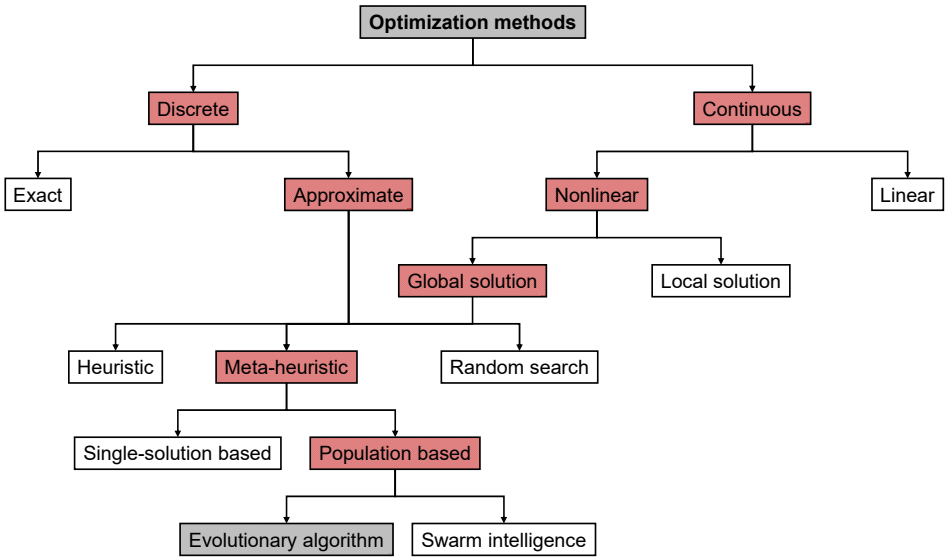

Figure 1.12: Taxonomy of optimization methods, with the evolutionary algorithm optimization method highlighted, modified from [143].

1.10. Thesis scope and outline

Conventional porous electrodes currently used in convection-enhanced electrochemical technologies are fibrous carbonaceous materials developed for low-temperature fuel cells; as such, their microstructure and surface chemistry are not suited for the requirements of redox flow batteries. Thus, there is a need for targeted synthesis and engineering of porous electrodes with tailored properties to meet the stringent requirements of liquid-phase electrochemistry with great control over the morphology, which is challenging as it requires solving a multivariable optimization problem at different length scales with highly coupled transport and kinetics. ***In this dissertation, I aim to develop a novel framework to design and synthesize electrode architectures from the bottom-up resulting in highly controlled microstructures, tailored to emerging electrochemical technologies with a focus on redox flow batteries***. Therefore, fundamental structure-function relationships must be elucidated by experimentally-validated modeling (**Objective 1**) and reactor-level imaging (**Objective 3**) of state-of-the-art electrodes and reactors. These relationships can subsequently be used to develop methods to design hierarchically organized porous electrodes through topology optimization (**Objective 2**) and fabricate them using advanced manufacturing techniques (**Objective 4**), as illustrated in **Figure 1.13**.

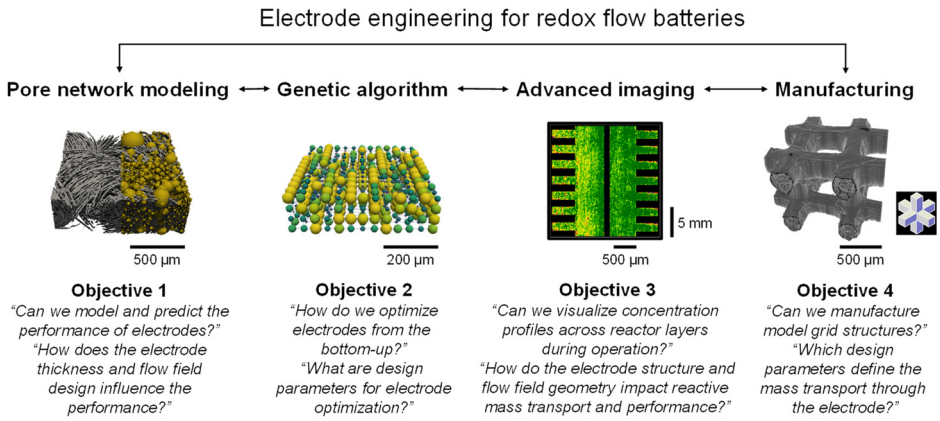

Figure 1.13: Schematic representation of the aim of this dissertation with the four main objectives: **(1)** modeling of porous electrodes, **(2)** electrode optimization, **(3)** advanced imaging of porous electrodes, and **(4)** electrode manufacturing. By coupling experimental and modeling approaches, structure-function-performance relations in electrode microstructures can be understood to aid the bottom-up design and manufacturing of optimized electrode microstructures.

Objective 1 is to develop a pore network modeling framework to investigate the impact of the porous electrode microstructure on the flow battery performance. The objective is to model and predict the performance of porous electrodes and as a case study investigates the influence of the electrode thickness and flow field design on the electrode performance. Therefore, in **Chapter 2**, the developed pore network model is presented including a systematic and rigorous validation with two electrode structures and two redox electrolytes. Moreover, an extensive study into the electrode performance is provided in terms of the overpotentials, current distribution, concentration profile, pressure drop, and overall performance trade-off, to ultimately elucidate structure-performance relationships for improved electrode design. Finally, a parametric sweep is performed to identify operation envelopes for efficient flow cell operation. In **Chapter 3**, the validated pore network model is used to study the effect of the electrode thickness on the cell performance for four distinct flow cell architectures, by stacking electrode layers. The pore network model is extended to include an interdigitated flow field design and is used to elucidate thickness-structure-performance relationships. Combined with pressure drop, polarization, and electrochemical impedance spectroscopy measurements, it is found that the co-design of the electrode (i.e., thickness and microstructure) and flow field geometry is necessary to obtain efficient system operation.

Objective 2 focuses on the optimization of the electrode structure from the bottom-up using a genetic algorithm based on the theory of evolution, combined with the pore network model developed in **Chapter 2**. The goal is to explore the optimization of the electrodes and to investigate important design parameters. In **Chapter 4**, the development of the genetic algorithm is described for flow-through model grid structures with fixed pore positions. The evolution is driven by a fitness function that optimizes for both the electrochemical power output and the pumping power and results in electrodes with a bimodal pore size distribution containing longitudinal electrolyte flow pathways of larger pores. In addition, a parametric study is performed, showing the dependency of the electrode optimization on the operating and electrolyte conditions. In **Chapter 5**, the developed algorithm is expanded to include more evolutionary freedom during the

optimization process by evolving the electrodes beyond fixed flow-through cubic lattice structures. The concept of merging and splitting is introduced together with the optimization of complex structures. Moreover, the electrode-flow field interdependency is analyzed as well as the effect of the redox chemistry on the electrode optimization.

In **Objective 3** a novel neutron radiography approach is introduced to quantify concentration distributions in *operando* flow cells using non-aqueous electrolytes. The approach provides a new diagnostic tool to improve the understanding of reactive transport phenomena in electrochemical systems and includes a study on the electrode-flow field interactions. In **Chapter 6**, the approach is introduced where concentration profiles are resolved across the reactor for two electrolyte configurations and under various operating conditions. Two neutron imaging approaches are developed, one in which the concentration distributions are resolved across the electrode thickness, and one in which a time-of-flight approach is used to deconvolute the concentration of active species and supporting ions. In **Chapter 7**, the developed approach is used to study the influence of the electrode and flow field on the cell performance by coupling the concentration profiles through the reactor to the current-voltage output and capacity. Here, again, the electrode-flow field interdependency is shown and correlated to local concentration distributions to aid the understanding of their coupled effect on cell performance.

Finally, **Objective 4** is focused on the advanced manufacturing of porous electrodes. The aim is to manufacture controlled model grid structures to study mass transport through model electrodes. In **Chapter 8**, a 3D printing methodology is developed to manufacture model grid structures using stereolithography followed by carbonization to tune the physiochemical properties of electrodes. The influence of the pillar geometry, printing orientation regarding the printing platform, and flow field design on the electrode performance is systematically investigated using electrochemical diagnostics, fluid dynamics, microscopy, tomography, and spectroscopy. Finally, a comparison to off-the-shelf commercial electrodes is performed, showing the potential of 3D printed electrodes to enhance the mass transport through porous electrodes.

1.11. References

[1] P. Przyborski, R. Levy, “World of Change: Global Temperatures” (2022), (available at https://earthobservatory.nasa.gov/world-of-change/global-temperatures).

[2] H. Ritchie, M. Roser, P. Rosado, *Our World In Data* (2020) (available at https://ourworldindata.org/co2-and-greenhouse-gas-emissions).

[3] EASE, EERA, “European Energy Storage Technology Development Roadmap” (2017), (available at https://www.eera-set.eu/component/attachments/?task=download&id=312).

[4] M. S. Guney, Y. Tepe, *Renew. Sustain. Energy Rev.* **75**, 1187–1197 (2017).

[5] H. Ritchie, *Our World Data* (2021) (available at https://ourworldindata.org/global-energy-200-years).

[6] R. A. Huggins, *Energy Storage* (Springer, Stanford, ed. 2, 2016).

[7] H. Ibrahim, A. Ilinca, J. Perron, *Renew. Sustain. Energy Rev.* **12**, 1221–1250 (2008).

[8] S. Sumathi, L. Ashok Kumar, P. Surekha, *Solar PV and Wind Energy Conversion Systems* (2015; http://link.springer.com/10.1007/978-3-319-14941-7).

[9] J. Mitali, S. Dhinakaran, A. A. Mohamad, *Energy Storage Sav.* **1**, 166–216 (2022).

[10] IEA, “Grid-Scale Storage” (Paris), (available at https://www.iea.org/reports/grid-scale-storage).

[11] Y. V Tolmachev, *J. Electrochem. Soc.* **170**, 030505 (2023).

[12] M. Bartolozzi, *J. Power Sources*. **27**, 219–234 (1989).

[13] E. Sum, M. Rychcik, M. Skyllas-kazacos, *J. Power Sources*. **16**, 85–95 (1985).

[14] E. Sum, M. Skyllas-Kazacos, *J. Power Sources*. **15**, 179–190 (1985).

[15] E. Sánchez-Díez *et al.*, *J. Power Sources*. **481**, 228804 (2021).

[16] P. Gunjan, M. Chavez, D. Power, “Guidehouse Insights: Vanadium Redox Flow Batteries” (2022).

[17] A. Z. Weber *et al.*, *J. Appl. Electrochem.* **41**, 1137–1164 (2011).

[18] Z. Li *et al.*, *Joule*. **1**, 306–327 (2017).

[19] M. Guarnieri, A. Trovò, A. D’Anzi, P. Alotto, *Appl. Energy*. **230**, 1425–1434 (2018).

[20] A. Trovò, W. Zamboni, M. Guarnieri, *J. Power Sources*. **493**, 229703 (2021).

[21] R. Gundlapalli, S. Jayanti, *J. Power Sources*. **487**, 229409 (2021).

[22] V. Muñoz-Perales *et al.*, *ChemRxiv* (2023), doi:10.26434/chemrxiv-2023-2zthc.

[23] M. van der Heijden, A. Forner-cuenca, in *Encyclopedia of Energy Storage*, L. F. Cabeza, Ed. (Elsevier Inc., Oxford, ed. 2, 2022), pp. 480–499.

[24] X. Ke *et al.*, *Chem. Soc. Rev.* **47**, 8721–8743 (2018).

[25] J. D. Milshtein *et al.*, *J. Electrochem. Soc.* **164**, E3265–E3275 (2017).

[26] R. M. Darling, M. L. Perry, *J. Electrochem. Soc.* **161**, A1381–A1387 (2014).

[27] J. D. Milshtein *et al.*, *J. Electrochem. Soc.* **164**, E3265–E3275 (2017).

[28] B. K. Chakrabarti *et al.*, *Sustain. Energy Fuels*. **4**, 5433–5468 (2020).

[29] M. Macdonald, R. M. Darling, *AIChE J.* **65**, 1–11 (2019).

[30] V. Muñoz-Perales *et al.*, *ChemRxiv* (2023), doi:10.26434/chemrxiv-2023-n2mmd.

[31] M. van der Heijden, M. Kroese, Z. Borneman, A. Forner-Cuenca, *Adv. Mater. Technol.*, 2300611 (2023).

[32] V. Muñoz-Perales, M. van der Heijden, P. Á. García-Salaberri, M. Vera, A. Forner-Cuenca, *ACS Sustain. Chem. Eng.* (2023).

[33] R. Behrou, A. Pizzolato, A. Forner-Cuenca, *Int. J. Heat Mass Transf.* **135**, 72–92 (2019).

[34] C. H. Chen, K. Yaji, S. Yamasaki, S. Tsushima, K. Fujita, *J. Energy Storage*. **26**, 100990 (2019).

[35] K. Yaji, S. Yamasaki, S. Tsushima, T. Suzuki, K. Fujita, *Struct. Multidiscip. Optim.* **57**, 535–546 (2018).

[36] M. H. Chakrabarti *et al.*, *J. Power Sources*. **253**, 150–166 (2014).

[37] L. F. Arenas, C. Ponce de León, F. C. Walsh, *J. Energy Storage*. **11**, 119–153 (2017).

[38] A. Forner-Cuenca, E. E. Penn, A. M. Oliveira, F. R. Brushett, *J. Electrochem. Soc.* **166**, A2230–A2241 (2019).

[39] R. R. Jacquemond *et al.*, *Cell Reports Phys. Sci.* **3**, 100943 (2022).

[40] C. T. Wan *et al.*, *Adv. Mater.* **33**, 2006716 (2021).
[41] T. Roy, M. A. S. de Troya, M. A. Worsley, V. A. Beck, *Struct. Multidiscip. Optim.* **65**, 171 (2022).
[42] R. van Gorp, M. van der Heijden, M. A. Sadeghi, J. Gostick, A. Forner-Cuenca, *Chem. Eng. J.* **455**, 139947 (2023).
[43] V. A. Beck *et al.*, *Proc. Natl. Acad. Sci. U. S. A.* **118**, 1–10 (2021).
[44] L. F. Arenas, C. Ponce de León, F. C. Walsh, *Electrochem. commun.* **77**, 133–137 (2017).
[45] A. Forner-Cuenca, F. R. Brushett, *Curr. Opin. Electrochem.* **18**, 113–122 (2019).
[46] P. Wang *et al.*, *Adv. Mater. Technol.* **5**, 1901030 (2020).
[47] S. Wan *et al.*, *Appl. Energy*. **298**, 117177 (2021).
[48] V. A. Beck *et al.*, *J. Power Sources*. **512**, 230453 (2021).
[49] M. van der Heijden, R. van Gorp, M. A. Sadeghi, J. Gostick, A. Forner-Cuenca, *J. Electrochem. Soc.* **169**, 040505 (2022).
[50] R. P. O 'Hayre, S.-W. Cha, W. G. Colella, B. Prinz, Frits, *Fuel Cell Fundamentals* (Wiley, Third Edit., 2016).
[51] X. Wei *et al.*, *J. Power Sources*. **218**, 39–45 (2012).
[52] Q. Ma *et al.*, *Chem. Eng. J.* **393**, 124753 (2020).
[53] H. Darcy, "Les fontaines publiques de la ville de Dijon" (Dalmont, 1856).
[54] M. D. R. Kok, A. Khalifa, J. T. Gostick, *J. Electrochem. Soc.* **163**, A1408–A1419 (2016).
[55] X. G. Yang, Q. Ye, P. Cheng, T. S. Zhao, *Appl. Energy*. **145**, 306–319 (2015).
[56] K. W. Knehr, E. Agar, C. R. Dennison, A. R. Kalidindi, E. C. Kumbur, *J. Electrochem. Soc.* **159**, A1446–A1459 (2012).
[57] B. Tjaden, S. J. Cooper, D. J. Brett, D. Kramer, P. R. Shearing, *Curr. Opin. Chem. Eng.* **12**, 44–51 (2016).
[58] J. L. Barton, F. R. Brushett, *Batteries*. **5**, 25 (2019).
[59] K. Oh, S. Won, H. Ju, *Electrochim. Acta*. **181**, 238–247 (2015).
[60] L. Gubler, *Curr. Opin. Electrochem.* **18**, 31–36 (2019).
[61] G. Qiu, C. R. Dennison, K. W. Knehr, E. C. Kumbur, Y. Sun, *J. Power Sources*. **219**, 223–234 (2012).
[62] D. I. Kushner, A. R. Crothers, A. Kusoglu, A. Z. Weber, *Curr. Opin. Electrochem.* **21**, 132–139 (2020).
[63] D. Wiley, G. F. Weihs, *Encycl. Membr.*, 3 (2015).
[64] R. C. Alkire, *Electrochemical engineering* (1983), vol. 60.
[65] X. L. Zhou, T. S. Zhao, L. An, Y. K. Zeng, L. Wei, *J. Power Sources*. **327**, 67–76 (2016).
[66] G. Pourcelly, A. Lindheimer, C. Gavach, H. D. Hurwitz, *J. Electroanal. Chem.* **305**, 97–113 (1991).
[67] A. Bhattacharjee, H. Saha, *Appl. Energy*. **230**, 1182–1192 (2018).
[68] A. Z. Weber *et al.*, *J. Electrochem. Soc.* **161**, F1254–F1299 (2014).
[69] A. A. Shah, F. C. Walsh, *Electrochem. Acta*. **55**, 78–89 (2009).
[70] K. W. Knehr, E. C. Kumbur, *Electrochem. commun.* **13**, 342–345 (2011).
[71] S. Petrovic, *Basic Electrochemistry Concepts* (Springer, 2021).
[72] Z. Cheng *et al.*, *Appl. Energy*. **279**, 115530 (2020).
[73] D. Zhang *et al.*, *J. Power Sources*. **447**, 227249 (2020).
[74] T. Suga, Y. J. Pu, K. Oyaizu, H. Nishide, *Bull. Chem. Soc. Jpn.* **77**, 2203–2204 (2004).
[75] C. Zhong *et al.*, *Chem. Soc. Rev.* **44**, 7484–7539 (2015).
[76] H. Chen, G. Cong, Y. C. Lu, *J. Energy Chem.* **27**, 1304–1325 (2018).
[77] G. L. Soloveichik, *Chem. Rev.* **115**, 11533–11558 (2015).
[78] K. Gong, Q. Fang, S. Gu, S. F. Y. Li, Y. Yan, *Energy Environ. Sci.* **8**, 3515–3530 (2015).
[79] S. V. Modak *et al.*, *Nat. Commun.* **14**, 3602 (2023).
[80] P. Leung *et al.*, *J. Power Sources*. **360**, 243–283 (2017).
[81] J. A. Kowalski, L. Su, J. D. Milshtein, F. R. Brushett, *Curr. Opin. Chem. Eng.* **13**, 45–52

(2016).
[82] K. Amini, A. N. Shocron, M. E. Suss, M. J. Aziz, *ACS Ener*. **8**, 3526–3535 (2023).
[83] Y. Yao, J. Lei, Y. Shi, F. Ai, Y. C. Lu, *Nat. Energy*. **6**, 582–588 (2021).
[84] A. M. Pezeshki, R. L. Sacci, F. M. Delnick, D. S. Aaron, M. M. Mench, *Electrochim. Acta*. **229**, 261–270 (2017).
[85] J. Zhang, H. Zhang, J. Wu, J. Zhang, *High-Temperature PEM Fuel Cells* (2013).
[86] I. Kroner, M. Becker, T. Turek, *ChemElectroChem*. **7**, 4314–4325 (2020).
[87] K. M. Tenny, A. Forner-Cuenca, Y.-M. Chiang, F. R. Brushett, *J. Electrochem. Energy Convers. Storage*. **17**, 041010 (2020).
[88] K. V. Greco, A. Forner-Cuenca, A. Mularczyk, J. Eller, F. R. Brushett, *ACS Appl. Mater. Interfaces*. **10**, 44430–44442 (2018).
[89] T. J. Rabbow, A. H. Whitehead, *Carbon N. Y.* **111**, 782–788 (2017).
[90] L. F. Arenas, C. P. de León, F. C. Walsh, *Electrochim. Acta*. **221**, 154–166 (2016).
[91] Z. Niu *et al.*, *Energy Environ. Sci.* **14**, 2549–2576 (2021).
[92] P. Trogadas *et al.*, *Electrochem. commun.* **48**, 155–159 (2014).
[93] X. Lu *et al.*, *Nat. Commun.* **11**, 1–13 (2020).
[94] R. Jervis *et al.*, *J. Phys. D. Appl. Phys.* **49**, 434002 (2016).
[95] F. Tariq *et al.*, *Sustain. Energy Fuels*. **2**, 2068–2080 (2018).
[96] K. Köble *et al.*, *J. Power Sources*. **492**, 229660 (2021).
[97] L. Eifert *et al.*, *ChemSusChem*. **13**, 3154–3165 (2020).
[98] J. Eller *et al.*, *J. Electrochem. Soc.* **158**, B963 (2011).
[99] A. Mularczyk *et al.*, *J. Electrochem. Soc.* **167**, 084506 (2020).
[100] A. G. Lombardo, B. A. Simon, O. Taiwo, S. J. Neethling, N. P. Brandon, *J. Energy Storage*. **24**, 100736 (2019).
[101] J. Roth, J. Eller, F. N. Büchi, *J. Electrochem. Soc.* **159**, F449–F455 (2012).
[102] Y. A. Gandomi *et al.*, *J. Electrochem. Soc.* **165**, A970–A1010 (2018).
[103] J. Rubio-Garcia, A. Kucernak, A. Charleson, *Electrochem. commun.* **93**, 128–132 (2018).
[104] A. A. Wong, S. M. Rubinstein, M. J. Aziz, *Cell Reports Phys. Sci.* **2**, 100388 (2021).
[105] P. Boillat, E. H. Lehmann, P. Trtik, M. Cochet, *Curr. Opin. Electrochem.* **5**, 3–10 (2017).
[106] J. T. Clement, PhD thesis, University of Tennessee (2016).
[107] A. Forner-Cuenca, K. V. Greco, J. A. Kowalski, P. Boillat, F. R. Brushett, in *ECS Meeting Abstracts* (The Electrochemical Society, 2019).
[108] J. Sun, H. R. Jiang, B. W. Zhang, C. Y. H. Chao, T. S. Zhao, *Appl. Energy*. **259**, 114198 (2020).
[109] E. B. Boz, P. Boillat, A. Forner-Cuenca, *ACS Appl. Mater. Interfaces*. **14**, 41883–41895 (2022).
[110] M. S. Park *et al.*, *ACS Appl. Mater. Interfaces*. **6**, 10729–10735 (2014).
[111] C. Ding *et al.*, *Appl. Surf. Sci.* **569**, 151057 (2021).
[112] V. A. Beck *et al.*, *Proc. Natl. Acad. Sci.* **118**, 1–10 (2021).
[113] J. Hereijgers, J. Schalck, T. Breugelmans, *Chem. Eng. J.* **384**, 123283 (2020).
[114] V. Egorov, U. Gulzar, Y. Zhang, S. Breen, C. O'Dwyer, *Adv. Mater.* **32**, 1–27 (2020).
[115] M. P. Browne, E. Redondo, M. Pumera, *Chem. Rev.* **120**, 2783–2810 (2020).
[116] D. Niblett, Z. Guo, S. Holmes, V. Niasar, R. Prosser, *Int. J. Hydrogen Energy*. **47**, 23393–23410 (2022).
[117] J. Wicks *et al.*, *Adv. Mater.* **33**, 2003855 (2021).
[118] B. Bian *et al.*, *Nano Energy*. **44**, 174–180 (2018).
[119] M. A. Saccone, R. A. Gallivan, K. Narita, D. W. Yee, J. R. Greer, *Nature*. **612**, 685–690 (2022).
[120] J. Bauer, A. Schroer, R. Schwaiger, O. Kraft, *Nat. Mater.* **15**, 438–443 (2016).
[121] J. Lölsberg *et al.*, *ChemElectroChem*. **4**, 3309–3313 (2017).
[122] C. Zhu *et al.*, *Nano Lett.* **16**, 3448–3456 (2016).
[123] Q. Li *et al.*, *J. Power Sources*. **542**, 231810 (2022).

[124] I. Gibson, D. Rosen, B. Stucker, M. Khorasani, *Additive Manufacturing Technologies* (Springer, Twente, the Netherlands, ed. 3, 2021).
[125] X. Tian *et al.*, *Adv. Energy Mater.* **7**, 1–17 (2017).
[126] J. Wlodarczyk, Master thesis, Zurich University of Applied Sciences (2019).
[127] P.-C. Sui, X. Zhu, N. Djilali, *Electrochem. Energy Rev.* **2**, 428–466 (2019).
[128] R. Banerjee, N. Bevilacqua, L. Eifert, R. Zeis, *J. Energy Storage*. **21**, 163–171 (2019).
[129] X. Yang *et al.*, *Adv. Water Resour.* **95**, 176–189 (2016).
[130] M. Agnaou, M. A. Sadeghi, T. G. Tranter, J. Gostick, *Comput. Geosci.* **140**, 104505 (2020).
[131] M. Li *et al.*, *J. Energy Storage*. **32**, 101782 (2020).
[132] G. Shukla, A. A. Franco, *J. Phys. Chem. C*. **122**, 23867–23877 (2018).
[133] L. Chen *et al.*, *Electrochim. Acta*. **248**, 425–439 (2017).
[134] D. Maggiolo *et al.*, *Energy Storage Mater.* **16**, 91–96 (2019).
[135] S. Gupta, T. M. Lim, S. H. Mushrif, *Electrochim. Acta*. **270**, 471–479 (2018).
[136] K. A. Dwelle, PhD thesis, Massachusetts Institute of Technology (2020).
[137] C. Choi *et al.*, *J. Energy Storage*. **21**, 321–327 (2019).
[138] J. Yu, T. S. Zhao, D. Pan, *J. Phys. Chem. Lett.* **11**, 10433–10438 (2020).
[139] J. F. Kucharyson, L. Cheng, S. O. Tung, L. A. Curtiss, L. T. Thompson, *J. Mater. Chem. A*. **5**, 13700–13709 (2017).
[140] M. Chen *et al.*, *J. Mater. Chem. A*. **8**, 8783–8812 (2020).
[141] M. Meskinfam Langroudi *et al.*, *J. Power Sources*. **420**, 134–142 (2019).
[142] F. J. Oldenburg *et al.*, *Phys. Chem. Chem. Phys.* **20**, 23664–23673 (2018).
[143] M. Janga Reddy, D. Nagesh Kumar, *H2Open J.* **3**, 135–188 (2020).
[144] M. Koopialipoor, A. Noorbakhsh, in *Emerging Trends in Mechatronics*, A. Azizi, Ed. (IntechOpen, 2020), p. 30.
[145] S. Wright, *Found. Comput. Process Des.*, 1–14 (1999).
[146] Vinicius Fulber-Garcia, Heuristics vs. Meta-Heuristics vs. Probabilistic Algorithms. *Baeldung* (2023), (available at https://www.baeldung.com/cs/heuristics-vs-meta-heuristics-vs-probabilistic-algorithms).
[147] T. Lombardo *et al.*, *Chem. Rev.* **122**, 10899–10969 (2022).
[148] K. Thoiba Meetei, *Int. J. Sci. Res.* **3**, 231–235 (2014).

1.12. Appendix 1

Abbreviations

Symbol	Description
CAES	Compressed air energy storage
EB	Electrochemical battery
ECSA	Electrochemically active surface area
EDLC	Electrochemical double-layer capacitance
EIS	Electrochemical impedance spectroscopy
ESS	Energy storage systems
FES	Flywheel energy storage
IEM	Ion-exchange membrane
OCV	Open-circuit voltage
PHS	Pumped hydro storage
PNM	Pore network model
RDE	Rotating disk electrode
RFB	Redox flow battery
SCES	Supercapacitors
SMES	Superconducting magnetic energy storage
SOC	State-of-charge
XTM	X-ray tomographic microscopy

List of symbols

Symbol	Description	Units
a	Empirical constant	-
A_v	Specific internal electrochemically active surface area	$m^2\ m^{-3}$
b	Bruggeman coefficient, or empirical constant	-
c	Constant	V
C	Concentration	$mol\ m^{-3}$
C_p	Specific heat capacity	$J\ kg^{-1}\ K^{-1}$
C_s	Specific capacitance	$F\ m^{-2}$
d_f	Fiber diameter	m
D	Diffusion coefficient	$m^2\ s^{-1}$
dV/dt	Scan rate	$V\ s^{-1}$
$ECSA$	Electrochemically active surface area	$m^2\ kg^{-1}$
$EDLC$	Electrochemical double-layer capacitance	F
E_{OCV}	Open-circuit voltage potential	V
F	Faradaic constant, 96,485 C mol^{-1}	$C\ mol^{-1}$
i	Current density	$A\ m^{-3}$
$\boldsymbol{i}$	Current flux vector	$A\ m^{-2}$
I	Current, average capacitive current	A
i_Π	Van ‘t Hoff index	-
i_k	Kinetic current	$A\ m^{-2}$
i_l	Limiting current	$A\ m^{-2}$
i_{lim}	Limiting current	$A\ m^{-3}$
i_m	Measured electric current	$A\ m^{-2}$
i_o	Exchange current density	$A\ m^{-3}$
k_0	Standard rate constant	$m\ s^{-1}$
k	Thermal conductivity	$W\ m^{-1}\ K^{-1}$
K_{ck}	Carman-Kozeny constant	-

k_m	Mass transfer coefficient	m s^{-1}
k_s	Self-discharge reaction rate constant	s^{-1}
m	Mass	kg
n	Number of electrons transferred	-
n_i	Number of ions	-
$\boldsymbol{N}$	Concentration flux	mol m^{-2} s^{-1}
p	Pressure	Pa
R	(a) Molar gas constant, 8.314 J mol^{-1} K^{-1}	J mol^{-1} K^{-1}
	(b) Resistance	Ω
R_d	Self-discharge rate	mol m^{-3} s^{-1}
R_i	Reaction rate	mol m^{-3} s^{-1}
S_i	Source term	mol m^{-3} s^{-1}
S_T	Thermal source term	kg m^{-1} s^{-3}
S_o	Standard entropy	J mol^{-1} K^{-1}
t	Time	s
T	Temperature	K
u	Ion mobility	m^2 mol J^{-1} s^{-1}
$\boldsymbol{v}$	Electrolyte velocity vector	m s^{-1}
z	Charge number	-

Greek

α	Charge transfer coefficient	-
ε	Porosity	-
η	Overpotential	V
κ	Permeability	m^2
λ	Stoichiometric coefficient	-
μ	Electrolyte viscosity	Pa s
Π	Osmotic pressure	Pa
ν	Stoichiometric coefficient	-
ρ	Density	kg m^{-3}
σ	Conductivity	S m^{-1}
τ	Tortuosity	-
υ	Kinematic viscosity	m^2 s^{-1}
$\emptyset$	Potential	V
ω	Angular rotation rate	rad s^{-1}

Superscripts

‾	Volume-averaged
0	Initial, inlet, standard
b	Bulk
eff	Effective
m	Membrane
s	Surface

Subscripts

$\emptyset$	Electro-kinetic
0	Initial
a	Anodic or anode
act	Activation
BV	Butler Volmer
c	Cathodic or cathode
$cell$	Battery or cell
$circuit$	Circuit

$contact$	Contact
e	Electrode
f	Fixed charges
i	Species
$ideal$	Ideal
j	Species
k	Kinetic
l	Ionic or liquid
lim	Limiting
m	Separator, membrane
mt	Mass transfer or concentration
oc	Open-circuit or equilibrium
$Nernst$	Nernst
ohm	Ohmic
p	Hydraulic
s	Electronic or solid
th	Thermodynamic

Chapter 2

Assessing the versatility and robustness of pore network modeling to simulate redox flow battery electrode performance

Abstract

Porous electrodes are core components that determine the performance of redox flow batteries. Thus, optimizing their microstructure is a powerful approach to reducing system costs. Here we present a pore network modeling framework that is microstructure and chemistry agnostic, iteratively solves transport equations in both half-cells, and utilizes a network-in-series approach to simulate the local transport phenomena within porous electrodes at a low computational cost. In this study, we critically assess the versatility and robustness of pore network models to enable the modeling of different electrode geometries and redox chemistries. To do so, the proposed model was validated with two commonly used carbon fiber-based electrodes (a paper and a cloth), by extracting topologically equivalent networks from X-ray tomograms and evaluated for two model redox chemistries (an aqueous iron-based and a non-aqueous TEMPO-based electrolyte). We find that the modeling framework successfully captures the experimental performance of the non-aqueous electrolyte but is less accurate for the aqueous electrolyte which was attributed to incomplete wetting of the electrode surfaces in the conducted experiments. Furthermore, the validation reveals that care must be taken when extracting networks from the tomogram of the woven cloth electrode, which features a multiscale microstructure with threated fiber bundles. Employing this pore network model, we elucidate structure-performance relationships by leveraging the performance profiles and the simulated local distributions of physical properties, and finally, we deploy simulations to identify efficient operation envelopes.

This chapter is published as:

M. van der Heijden*, R. van Gorp*, M.A. Sadeghi, J. Gostick, and A. Forner-Cuenca, Assessing the versatility and robustness of pore network modeling to simulate redox flow battery electrode performance, *Journal of the Electrochemical Society*, **169** (2022), pp. 040505, doi:10.1149/1945-7111/ac5e46.

*Co-first authors

This paper is part of the JES Focus Issue on Women in Electrochemistry

2.1. Introduction

Large-scale, stationary energy storage technologies, such as redox flow batteries (RFBs), are attracting widespread interest due to their ability to compensate for the intermittent nature of renewable energy sources (i.e., solar photovoltaics and wind power) [1–3]. RFBs are rechargeable electrochemical systems that interconvert chemical and electrical energy by leveraging redox couples, dissolved in liquid electrolytes, that are pumped through an electrochemical stack to charge and discharge the battery [4]. Their most appealing features are the ability to decouple power and energy capacity which is not possible with sealed batteries (e.g., lithium-ion), high round-trip efficiency, extended durability, fast response times, low environmental impact, and geographic independence [5, 6]. Despite their promise, RFBs have so far seen limited market penetration due to their current elevated costs and suboptimal performance, motivating substantial research efforts on alternative redox chemistries and novel reactor architectures [7–12]. As a core component of the flow battery stack, the porous electrode largely determines the battery performance by providing both the active surface area for electrochemical reactions, the solid architecture for electron conduction, and the open porosity for electrolyte flow and mass transport. Hence, optimizing the electrode microstructure and surface chemistry is an effective approach to decreasing reactor and system costs.

Electrode engineering has been driven primarily by empirical approaches, targeting increases in available surface area, kinetic activity, and wettability for the most studied systems (e.g., all-vanadium) [7, 13, 14], but this approach is time- and resource-consuming. Furthermore, each redox chemistry and reactor concept necessitates a unique set of electrode properties, which results in a very broad design space. Recent advances in computational sciences enable the simulation of complex electrochemical flows within porous electrodes, which can be leveraged to understand the role of the porous electrodes and ultimately to accelerate their design pipeline. In this context, simulations have been deployed for RFBs at multiple length scales [15, 16]. For example, cell-level macroscopic continuum models have been employed [17–24], aided in investigations of cell-averaged properties [18], and proved to be effective for predicting the cell performance for multiple charge-discharge cycles for all cell designs [21]. However, these models build on volume-averaged grids and fail to capture the complex effects of the electrode three-dimensional structure (e.g., local variations in porosity or surface area, inhomogeneous pore size distributions) which results in inaccurate predictions of the reactor performance. Therefore, to accurately describe the three-dimensional structure of the material, microstructure-informed simulations have been deployed.

Highly detailed models using finite element and Lattice Boltzmann methods have been employed to gain insight into the transport within porous materials [25–27]. These models solve the velocity field of the electrolyte using the voxels of a tomogram as the mesh, and can therefore deal with highly complex geometries, such as carbon fiber-based electrodes. Qiu *et al.* employed a multiphysics Lattice Boltzmann method to obtain the local velocity field at the pore scale [26] and investigated the effect of the electrode porosity and electrolyte flow rate on overall RFB performance, quantifying the effect of fuel starvation within vanadium systems [27]. The authors found that low porosity electrode structures result in a more uniform current density and lower absolute overpotential distributions at the expense of increased pumping requirements. Recently, Bao *et al.* coupled a multi-scale model with a deep neural network to optimize a time-varying electrolyte inlet velocity for an all-vanadium RFB leading to a 74 % reduction in the

pumping power consumption [28]. Additionally, Yoon *et al.* investigated the effect of the electrode's local porosity on battery efficiency, showing that lower porosity at the electrolyte inlet regions resulted in superior energy efficiency as it provides a larger active area where the reactant concentration is highest [29]. These studies demonstrate the potential of three-dimensional modeling to inform electrode and reactor design; however, they require large computational power to solve the defined set of equations [30]. The large number of nodes required to model even a few pores and the non-linearity of the physics limits the application of these models to a small subdomain of the electrode. Thus, to accurately describe reactor performance at larger sizes, modeling approaches that can simultaneously capture electrode microstructures and simulate varying phenomena at the reactor level need to be developed.

In recent years, pore network modeling (PNM) has been employed as an alternative modeling technique that can capture microstructural effects at the mesoscale at a reasonable computational cost by invoking geometrical simplifications on the porous network [9, 10, 31]. In PNM, the complex porous space is approximated by a network of spheres (pores) connected by cylinders (throats), and one-dimensional analytical solutions are leveraged to compute the transport of mass and charge within the network. Agnaou *et al.* demonstrated that this simplification of the model equations results in a computational time reduction of up to 10^4 times compared to finite element simulations within the same geometry, with a limited loss in computational accuracy [30]. PNM has been employed in the simulation of multiphase flows of fuel cell gas diffusion layers [32-34] and has been recently applied to porous electrodes in RFBs. Sadeghi *et al.* built a PNM framework to study the liquid side of the hydrogen-bromine flow battery [10]. The authors investigated the effect of the electrode porosity on the performance of a simulated SGL 25AA electrode and computed a relationship between electrode permeability and voltage efficiency [10]. Lombardo *et al.* presented a framework for transient PNM to simulate the coupled flow, species, and charge transport within a vanadium flow battery using an extracted Toray 090 electrode [9]. They displayed the existence of mass-transport limited areas that significantly contribute to performance losses. Finally, other groups have employed PNM as a tool to compute the permeabilities and parasitic losses in carbon papers and cloths from tomographic reconstructions of dry electrodes [35, 36].

These previous studies offer an optimistic prospect for the use of PNM as a platform for electrochemical simulations of porous electrodes in RFBs. However, there are notable knowledge gaps that must be addressed to deploy PNM broadly. First, methods that can reliably represent complex electrode geometries while affording larger sample sizes (i.e., cell level) are lacking as most research has focused on a small domain of the electrode [9, 10, 35, 36]. Second, the investigation of geometrical algorithms that afford large versatility and robustness across microstructures and redox chemistries has not been performed. Inspired by these knowledge gaps and previous work in the field, we seek to answer the following questions: "*Can we build a framework that is robust and versatile to accurately describe different electrode structures and electrolytes?*" and "*What is the minimum number of fitting parameters required to accurately describe the cell performance with PNM?*". Furthermore, we aim to leverage this framework to theoretically investigate and understand the performance differences between cloths and papers under different electrolyte systems, which has recently triggered significant attention from experimentalists [7, 37–39].

Here, we introduce a computationally inexpensive, chemistry-agnostic, and microstructure-informed PNM framework using the open-source software OpenPNM [31]. An iterative algorithm enables the coupling of both half-cells and utilizes a network-in-series approach to account for species depletion over the length of the electrode. We study two fibrous electrodes – a Freudenberg paper and an ELAT Cloth – and two electrolytes – a Fe^{2+}/Fe^{3+} couple in aqueous media and a TEMPO/$TEMPO^{+}$ couple in a non-aqueous media – to screen a broad property space and, in turn, assess the versatility of the modeling framework. First, X-ray tomographic microscopy is performed to obtain dry microstructures. The network extraction is evaluated by comparing the pore size distributions of the extracted pore networks with mercury intrusion porosimetry. Second, the model is validated against experiments, using single-electrolyte flow cells to enable precise quantification of the cell performance, for both electrodes with the non-aqueous electrolyte. Third, we compare simulations to flow cell experiments using an aqueous electrolyte and assess the versatility and robustness of the model, revealing that incomplete wetting of the porous structure impacts physical descriptors used for single-phase flows. Fourth, a systematic analysis of the electrochemical performance in tandem with local properties (i.e., pressure drop, current density, reactant depletion, and overpotentials) is performed to elucidate microstructure-performance relationships. Finally, a parametric study was performed to identify efficient operation envelopes.

2.2. Model development

The present study offers a numerical platform that can be leveraged to simulate the local transport within porous electrodes for different RFB chemistries at a low computational cost. The modeled domain (**Figure 2.1**) consists of two symmetric, mirrored 1 mm long by 1 mm wide porous electrodes, extracted using X-ray tomographic microscopy (XTM). Single-electrolyte flow cell simulations were conducted with the co-current operation of the anodic and cathodic half-cells. In this setup, the oxidation reaction of the redox couple occurs in the anodic half-cell and the reduction reaction of the same redox couple takes place in the cathodic half-cell. Local transport equations are solved within the porous electrodes, while the location of the flow channels, current collector, and membrane are dictated by the boundary conditions. Coupling of the two half-cells is achieved using the boundary conditions of the membrane, which is treated as a macro continuum entity and thus only the overall macroscopic ionic resistance of the membrane is considered.

Pore networks (PNs) are an idealization of real tomographic extracted porous structures. In PNMs, it is assumed that the void space within the porous structure can be approximated by spherical pores and cylindrical throats. The bulk solution in each pore is assumed to be well-mixed within the pore body and transport in the PN occurs via the throats. This idealization of the void space allows for the reduction of complexity of the considered model equations, while still retaining information about the microporous structure and topology of the porous electrode [31]. Consequently, the computational time to run one network with the network-in-series approach, for applied potentials of -1 - 0 V (to simulate the consumption of reactant species, we run the model in discharge mode) using -0.05 V step intervals, was only ~100 minutes for a 1.7 cm long electrode using a single Intel® Core™ i7-8750H CPU, depending on the electrolyte chemistry and velocity.

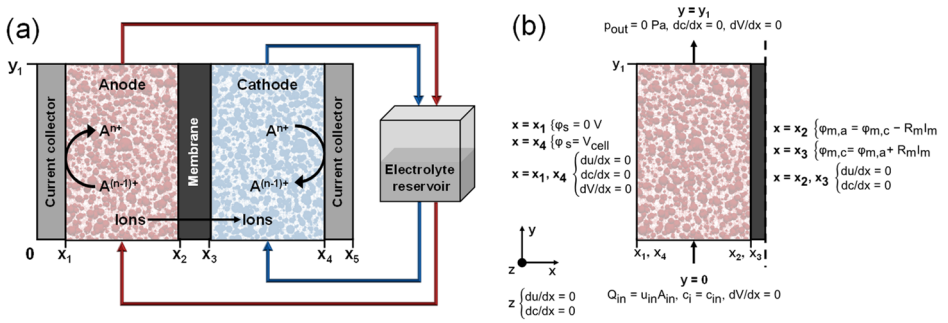

Figure 2.1: Schematic representations of: **(a)** a single-electrolyte redox flow cell in discharge mode with the electrodes represented by the extracted pore networks of a carbon paper electrode, showing the computational domain with 0-x_5 the x-coordinates of the different interfaces and 0-y_1 the y-coordinates, and **(b)** the corresponding boundary conditions for one of the half cells in the single-electrolyte cell.

2.2.1. Model equations

The considered physics within the three-dimensional porous electrode and electrolyte account for fluid transport, species transport, reaction kinetics, and conservation of charge. The flow fields, electrodes, and membrane are coupled by the applied boundary conditions. The governing equations and the formulated boundary conditions within the electrochemical cell are described for the case of cell discharge and are based on the convention of describing the flux of positive charges. To simplify the complexity of the model, the following assumptions are made:

1. The electrochemical cell operates at steady-state, iso-thermal conditions.
2. The dilute-solution theory is applied and only the active species are included.
3. The crossover of active species through the membrane is neglected.
4. The electric potential of the solid electrode phase is assumed to be constant due to its high electronic conductivity [32].
5. The flow within the porous structure is classified as a creeping flow, due to the small flow dimensions and low Reynolds numbers, thus inertial effects were neglected when computing the pressure drop.
6. The charge flux within the liquid phase is approximated using the bulk conductivity of the electrolyte, neglecting migration effects.
7. The half-cell reaction is described as a single-step reaction mechanism and neglects the formation of intermediates that are adsorbed on the electrode surface and side reactions.
8. The electrochemically active surface area of a pore is equal to the extracted area obtained with the SNOW algorithm, which utilizes the marching cubes algorithm to obtain areas of smoothed surfaces from the voxelated image.
9. The electrochemical reaction is only occurring in the pores and not throughout the connecting throats, though the area of the throats was assigned to the pores during the network extraction.

The fluid transport within the porous electrode is described by the steady-state Navier-Stokes equations. The total mass balance for the electrolyte phase around pore i

in the network is defined as

$$-\sum_{j=1}^{N_T} \rho u_{ij} S_{ij} = 0, \tag{2.1}$$

where ρ is the electrolyte density, u_{ij} the fluid velocity from pore i to pore j, S_{ij} the cross-sectional area of the throat connecting pore i and j, and N_T the number of throats connected to pore i. By treating the throats as cylindrical tubes, the Hagen-Poiseuille equation can be used to express the velocity field based on the pore pressures as described by

$$u_{ij} = \alpha_{ij}(p_i - p_j), \tag{2.2}$$

where p is the pressure in pore i or j, and α_{ij} is the hydraulic conductance of the throat connecting pore i and j

$$\alpha_{ij} = \frac{S_{ij}}{8\pi\mu L_{ij}}, \tag{2.3}$$

where μ is the dynamic viscosity of the electrolyte, and L_{ij} the conduit length of the connecting throat.

The mass transport of chemical species in the porous electrode is described by the advection-diffusion-reaction equation. The conservation equation around each pore for the active species that is consumed is described by

$$-\sum_{j=1}^{N_T} m_{ij} S_{ij} = R_i = \frac{\lambda_i I_i}{nF}, \tag{2.4}$$

where m_{ij} is the mole flux of the active species between pore i and j which contains both advective and diffusive terms, R_i the net reaction rate of the active species, λ_i the dimensionless stoichiometric coefficient in the corresponding half-reactions, I_i the applied current in pore i, n the number of electrons participating in the half-reaction, and F the Faradaic constant. The mole flux is derived from the exact solution for the one-dimensional advection-diffusion equation, based on the exponential approach described by Sadeghi *et al.* [40], defined as

$$m_{ij} = u_{ij}\left(c_i + \frac{c_i - c_j}{\exp(Pe) - 1}\right), \tag{2.5}$$

where c is the concentration of the reacting species in pore i or j, and $Pe = u_{ij} L_{ij} / D$ the local Peclet number at the considered throat, with D the diffusion coefficient of the active species in the electrolyte.

The applied current in both the anodic and cathodic compartments is described by the Butler-Volmer equation defined as

$$I_{i,a} = j_0^a A_i \left(\frac{c_{i,s}^{red}}{c_{ref}^{red}}\right)\left[\exp(-\frac{\alpha_a F \eta_a}{RT}) - \exp(\frac{\alpha_c F \eta_a}{RT})\right] \tag{2.6}$$

$$I_{i,c} = j_0^c A_i \left(\frac{c_{i,s}^{ox}}{c_{ref}^{ox}}\right)\left[\exp(\frac{\alpha_a F \eta_c}{RT}) - \exp(-\frac{\alpha_c F \eta_c}{RT})\right], \tag{2.7}$$

where I_i is the applied current in the anodic or cathodic compartment, j_0 the exchange current density in the anodic or cathodic compartment, A_i the electrochemically active internal surface area of pore i, $c_{i,s}$ the concentration of the reduced or oxidized form at the electrode surface, c_{ref} the reference concentration of the reduced or oxidized form at which the exchange current density was measured, η the overpotential in the cathodic or anodic compartment, R the universal gas constant, T the operating temperature, and α the anodic or cathodic reaction transfer coefficient, where $\alpha_a + \alpha_c = n$ with n the number of electrons transferred in the electrochemical reaction (for all tested chemistries in this study $n = 1$). The overpotentials in both half cells are given by

$$\eta_c = \varphi_s - \varphi_e - E_{oc} \tag{2.8}$$
$$\eta_a = \varphi_s - \varphi_e, \tag{2.9}$$

where φ_s is the solid phase potential, φ_e the liquid phase potential, and E_{oc} the equilibrium potential, defined against the same reference electrode. The concentration of the active species at the electrode surface is estimated from the corresponding bulk concentrations through the mass transfer of the active species toward the electrode surface

$$I_{i,a} = Fk_m^{red}A_i\left(c_{i,b}^{red} - c_{i,s}^{red}\right) \tag{2.10}$$
$$I_{i,c} = -Fk_m^{ox}A_i\left(c_{i,b}^{ox} - c_{i,s}^{ox}\right), \tag{2.11}$$

where k_m is the mass transfer coefficient of the considered species, and $c_{i,b}$ the bulk concentration of the active species. Combining **equations (2.6)** and **(2.10)**, and **(2.7)** and **(2.11)** by substituting for the surface concentrations, the Butler-Volmer equation for a one-electron electrochemical reaction including mass transfer limitations is obtained. It may be verified that the resulting equations reduce to the case without mass transfer limitations (**equations (2.10)** and **(2.11)**) when the mass transfer terms approach infinity ($k_m \to \infty$). An estimation of the mass transfer coefficient towards the porous electrode was obtained by neglecting inertia effects and applying the film theory, assuming that the film layer is equal to the pore radius of every pore

$$k_m = 2\frac{D}{d_p}, \tag{2.12}$$

where d_p is the pore diameter.

The conservation of charge around each pore is coupled to the species transport in the electrochemical cell by the current and the potential field described by

$$-\sum_{j=1}^{N_T} I_{ij}S_{ij} = I_i, \tag{2.13}$$

where I_i is the applied current defined by the Butler-Volmer equation, and I_{ij} the charge flux from pore i to j, which is proportional to the potential field in the liquid phase

$$I_{ij} = \beta_{ij}\left(\varphi_i - \varphi_j\right), \tag{2.14}$$

where $\beta_{ij} = \sigma_l/L_{ij}$ is the electrical conductance of the connecting throat, σ_l the bulk electrolyte conductivity, and φ the liquid potential in pore i or j.

2.2.2. Boundary conditions

For the fluid transport boundary conditions (**Figure 2.1b**), the inlet pressure boundary condition is determined by setting a target inlet velocity. From the target inlet velocity, the target flow rate is calculated by

$$Q_{in} = u_{in}A_{in}, \qquad y = 0 \tag{2.15}$$

where Q_{in} is the flow rate of the electrolyte, u_{in} the inlet velocity of the electrolyte, and A_{in} the geometrical inlet area of the electrode. Subsequently, the inlet pressure at the bottom boundary pores is computed such that the total flow rate entering the network matches the target flow rate. The discharge pressure was set to zero. Furthermore, no-flux boundary conditions were imposed at the width and thickness of the electrode

$$p_{out} = 0\ Pa \qquad y = y_1 \tag{2.16}$$

$$du/dx = 0. \qquad x = x_1, x_2, x_3, x_4, \text{ and } z \tag{2.17}$$

For the species transport, a constant concentration of species i, c_{in}, is imposed at the inlet. At the other boundaries, no-flux boundary conditions are applied

$$c_i = c_{in} \qquad y = 0 \tag{2.18}$$

$$dc/dx = 0. \qquad x = x_1, x_2, x_3, x_4, y_1 \text{ and } z \tag{2.19}$$

At the current collector-electrode interface in the cathodic compartment, the boundary condition for the solid potential is equal to the given cell voltage, while in the anodic compartment, the solid potential is equal to zero as a result of the symmetry of the modeled domain

$$\varphi_s = \begin{cases} 0\ V & x = x_1 \text{ (a)} \\ V_{cell}, & x = x_4 \text{ (b)} \end{cases} \tag{2.20}$$

where V_{cell} is the given cell potential. The boundary condition for the electrolyte potential at the membrane in a specific half-cell is iteratively calculated from the electrolyte potential at the membrane in the other half-cell, using Ohm's law to include the average voltage loss across the membrane interface

$$\Delta\varphi_m = R_m I_m \tag{2.21}$$

$$\varphi_{m,a} = \varphi_{m,c} - \Delta\varphi_m \qquad x = x_2 \text{ (a)} \tag{2.22}$$

$$\varphi_{m,c} = \varphi_{m,a} + \Delta\varphi_m, \qquad x = x_3 \text{ (b)}$$

where $\Delta\varphi_m$ is the average voltage loss across the membrane interface, R_m the resistance of the membrane, I_m the current passing the membrane, and φ_m the electrolyte potential at the membrane in the anodic or cathodic compartment. At the other boundaries, the boundary condition of the voltage was defined as

$$dV/dx = 0. \qquad \text{on } x = x_1, x_4 \text{ and } y = 0, y_1 \tag{2.23}$$

2.2.3. Iterative algorithm

The utilized numerical algorithm consists of the coupled mass and charge transport within the porous electrode. In the developed algorithm, the individual transport equations within the anodic and cathodic compartments are updated sequentially within an iterative algorithm. The detailed flowchart of this algorithm is illustrated in **Figure 2.2**.

Due to the assumption of a dilute electrolyte, the viscosity and density of the fluid are assumed constant so fluid transport within the porous electrode is considered to be independent of the other transport processes. Therefore it can be directly solved to obtain the velocity and pressure fields with **equations (2.1)** and **(2.2)**. The velocity field of the liquid electrolyte is provided to the iterative algorithm to solve the species and charge transport equations, which consist of two nonlinear systems of equations (**equations (2.4)** and **(2.13)**) that are coupled by the Butler-Volmer equation (**equations (2.6)** and **(2.7)**). The iterative scheme consecutively solves the advection-diffusion-reaction equation (**equation (2.4)**) and the potential field (**equation (2.14)**). Both half-cells are coupled, using the found solution for the electrolyte potential at the membrane in one-half cell to calculate the electrolyte potential at the other side of the membrane in the other half-cell. In this step, Ohm's law was used to account for the membrane resistance (**equation (2.21)**). The calculated electrolyte potential is subsequently used as a boundary condition for the charge transport equation in the second half cell.

The numerical model solves the coupled transport equations over a given voltage range starting from the open-circuit voltage (0 V for the performed simulations), with an initial guess for the overpotential in the first iteration of 0 V. The initial concentration within all pores was set to the inlet concentration of the active species. While progressing to higher absolute cell potentials, the initial guesses for the concentration, potential field, and overpotential are based on the solution of the previous cell potential.

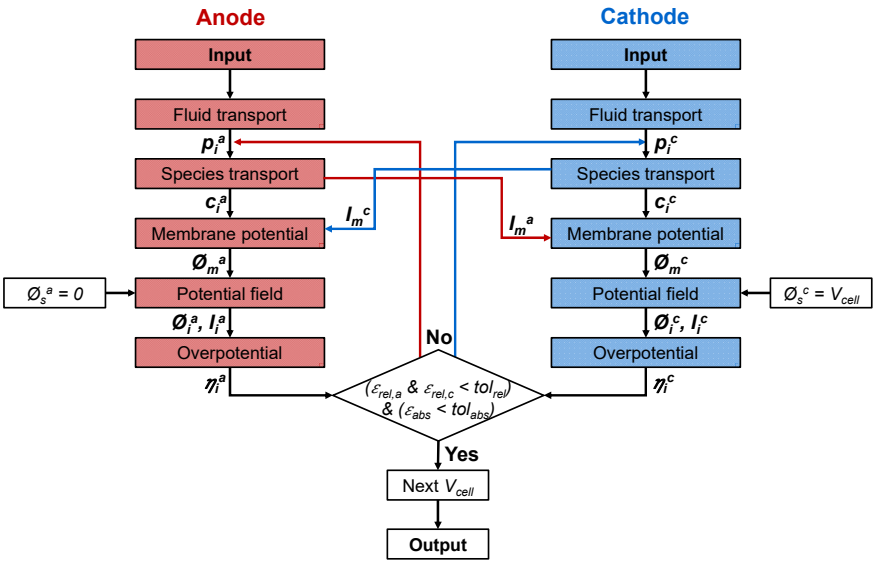

Figure 2.2: Flowchart of the iterative algorithm illustrating the coupling of the potential field between the anodic and cathodic half-cells.

Numerical convergence is achieved when the specified relative and absolute tolerances are met. These tolerances are based on the total current generated or consumed in a half-cell defined as

$$I_{tot} = \sum_{j=1}^{N_p} I_{loc,i}, \tag{2.24}$$

where I_{tot} is the total current generated or consumed in a half-cell, I_{loc} the (local) current generated in each pore, and N_p the number of pores. The relative error can be calculated for both compartments by

$$\epsilon_{rel} = \frac{I_{tot}^{n} - I_{tot}^{n-1}}{I_{tot}^{n-1}}, \tag{2.25}$$

where ϵ_{rel} is the relative error, and n the iteration number, with a maximum of 5 x 10^4 iterations. The absolute error, ϵ_{abs}, consists of the difference in total current between both half-cells and is defined as

$$\epsilon_{abs} = I_{tot}^{a} - I_{tot}^{c}. \tag{2.26}$$

The tolerances for the relative and absolute errors were set to 5 x 10^{-5} and 6 x 10^{-4} A cm^{-2}, respectively. To counteract the divergence of the solution due to the highly nonlinear nature of the system, two numerical strategies were employed. The first strategy consists of under-relaxation during the updating of the concentration and potential fields [10]. In under-relaxation, a relaxation factor is used to dampen the obtained solution

$$X_i^{n+1} \longleftarrow X_i^{n+1}\omega + X_i^{n}(1-\omega), \tag{2.27}$$

where X is the concentration or the potential of species i, and ω is the relaxation factor, set to 0.1. The second strategy consists of linearization of the charge transport source term. When the considered active species has facile kinetics, the mass and charge transport equations become strongly coupled. In this case, linearization of the current generation term can mitigate divergence. The derivation of the source term is further elaborated on in **Section A2.3.1**.

2.2.4. Network-in-series model

To account for species depletion, the numerical framework was modified to match the entire length of the laboratory electrode (1.7 cm) using a network-in-series approach. In this approach, multiple PNs are placed behind one another, where the concentration at the end of the previous network is considered the inlet concentration of the next PN. To map the concentration between the boundary pores of the two networks, each network was manipulated to become a mirrored copy (mirrored in the flow dimension) of the previous network (see **Figure A2.1**). The mass and charge transport algorithms are solved independently for each anode-cathode couple in the series.

2.3. Experimental

2.3.1. Electrode materials

Two different commercial carbon fiber-based electrodes were investigated in this work. A carbon paper, Freudenberg H23 (Fuel Cell Store), and a woven carbon cloth, ELAT Cloth electrode (Fuel Cell Store). Freudenberg H23 has an uncompressed thickness of 210 µm and a porosity of 80 %, and the ELAT Cloth has an uncompressed thickness of 380 µm and a porosity of 82 % [7]. Electrode density measurements were performed for six different electrode pieces for both electrode types (1.7 cm x 1.5 cm x 210 µm or

375 µm) using a Sartorius ED224S analytical balance (± 0.1 mg uncertainty). The electrodes were used as received. In addition, three ELAT Cloth electrodes were functionalized with electrografted taurine (2-aminoethane-1-sulfonic acid) to investigate the impact of electrode hydrophilization on the performance and model validation.

2.3.2. Electrolyte preparation

An electrolyte solution of 0.1 M ferrous chloride hydrate ($FeCl_2 \cdot 4H_2O$, 98 %, Sigma-Aldrich), 0.1 M ferric chloride hydrate ($FeCl_3 \cdot 6H_2O$, 97 %, Sigma-Aldrich), and 1.0 M sodium chloride (NaCl, ≥99.0 %, AkzoNobel), dissolved in deionized water was prepared for the flow cell experiments with the aqueous Fe^{2+}/Fe^{3+} electrolyte.

For the non-aqueous electrolyte, the oxidized form of the redox couple, 2,2,6,6-tetramethyl-1-piperidinyloxy-oxo ($TEMPO^+$) hexafluorophosphate, was synthesized in-house inside a nitrogen-filled glove box (MBraun, LABstar, O_2 <1 ppm, H_2O <1 ppm). $TEMPO^+$ was prepared by chemical oxidation of 2,2,6,6-Tetramethylpiperidin-1-yl)oxyl (TEMPO, Sigma Aldrich 98 %, 12.52 g) dissolved in acetonitrile (MeCN, Acros Organics 99.9+ %). 1.1 molar equivalents of nitrosonium hexafluorophosphate ($NOPF_6$, Thermo Scientific, 95 %, 15.42 g) dissolved in MeCN were slowly added for 2 hours to prevent NO_x build-up [7]. Thereafter, a rotary evaporator (40 °C, gradual decrease from atmospheric pressure to vacuum) was used to remove the solvent and to recover the $TEMPO^+$. An electrolyte solution of 20 mL was prepared before each experiment consisting of 0.1 M TEMPO, 0.1 M $TEMPO^+$ (stored in the glove box), and 1 M tetrabutylammonium hexafluorophosphate ($TBAPF_6$, Sigma Aldrich >99 %) dissolved in MeCN.

2.3.3. Flow cell experiments

Single-electrolyte flow cell experiments were conducted in a laboratory-scale flow cell platform for both the aqueous and non-aqueous electrolytes (see **Figure 2.1a** for a schematic representation of the cell). The corresponding redox reactions are

$$Fe^{2+} \underset{red}{\overset{ox}{\rightleftharpoons}} Fe^{3+} + e^- \qquad E^0 = 0.77\ \text{V vs. RHE}\ [5] \qquad (2.28)$$

$$TEMPO\cdot \underset{red}{\overset{ox}{\rightleftharpoons}} TEMPO^+ + e^- \qquad E^0 = 0.73\ \text{V vs. NHE}\ [41] \qquad (2.29)$$

where E^0 is the standard reduction potential. Separate tubing was used to connect the single solution reservoir to the cell in and outlets to ensure a constant state of charge at the cell inlets. Graphite current collectors milled with a flow-through flow field were employed to force convective electrolyte flow through the porous electrode, resulting in a near unidirectional flow parallel to the membrane. This simplified design is well suited to perform fundamental investigations on the role of the electrode microstructure and electrolyte properties without the complexities of spatially varying flow fields (e.g., interdigitated, serpentine). One electrode with an external area of 2.55 cm^2 (1.7 cm x 1.5 cm) was placed on top of each current collector using incompressible polytetrafluoroethylene gaskets with a total thickness of 210 µm or 375 µm, respectively

for the Freudenberg H23 and the ELAT Cloth, ensuring minimal compression of only a few microns. Here, unless otherwise stated, we elected to study flow cell performance relationships without compressive effects. Thus, both the tomograms and the electrochemical tests were performed using the same, uncompressed, conditions to enable representative comparisons. We acknowledge that practical systems employ compressive forces (20 - 50 %) to minimize contact resistances, which are accounted and corrected for in our study, and that the electrode microstructure changes as a result of compression [42]. However, dedicated investigations on compressive strengths are beyond the scope of this study and have been recently treated elsewhere [43, 44]. Given the small area of the cell and the relative thickness of the endplates, this minimal compression was sufficient to maintain reliable operation. A cation-exchange Nafion 211 membrane (Fuel Cell Store, 25.4 µm), was used for the Fe^{2+}/Fe^{3+} system, and a porous separator, Daramic 175 (SLI Flatsheet Membrane, 175 µm), was used for the TEMPO/$TEMPO^{+}$ system. Subsequently, the cell was tightened with a torque-controlled screwdriver to 2.2 N m. To account for differences in electrode thickness, the performance was compared at the same inlet velocities of 1.5, 5.0, and 20 cm s^{-1}, calculated by dividing the volumetric flow rate set by the pump by the geometrical inlet area of the flow-through flow field (thickness multiplied by the width of the electrode). The electrolyte was pumped through the cell using a Masterflex L/S® Easy-Load® II pump and LS-14 tubing in the co-current operation of the half cells to promote the wetting of the porous carbon electrodes. Electrochemical experiments were conducted in charge mode, performed inside a nitrogen-filled glove box for the non-aqueous electrolyte, and outside the glove box for the aqueous electrolyte. Polarization curves were obtained by employing constant voltage steps of 0.05 V for 1 minute and measuring the steady-state current for a lead-corrected voltage range of 0 - 1 V. For the Fe^{2+}/Fe^{3+} system, an Ivium (Ivium-n-Stat) potentiostat was used and for the TEMPO/$TEMPO^{+}$ system a Biologic VMP-300 potentiostat. The polarization curves were repeated three times for new assemblies and new electrolyte solutions for each flow rate in descending flow rate order.

2.3.4. Electrolyte density, viscosity, and conductivity measurements

Electrolyte density measurements were performed *in triplo* for the two electrolytes using a Sartorius ED224S analytical balance and an electrolyte volume of 10 mL. The electrolyte viscosity was assumed equal to the viscosity of the solvent. Conductivity measurements were performed using a two-electrode custom conductivity cell, similar to the setup used in Milshtein *et al*. [45]. The compartment of the conductivity cell was flooded with electrolyte and sealed shut. Electrochemical impedance spectroscopy (EIS) was conducted using the Biologic VMP-300 potentiostat at open-circuit voltage and room temperature (20 °C) with an amplitude of 10 mV and a frequency range of 1 kHz - 100 kHz, 8 points per decade, 6 measurements per frequency, and a waiting time of 0.10 period before each frequency. The high-frequency intercept was identified as the value of the total resistance (cell, lead, and electrolyte resistance). EIS measurements were performed *in triplo* and were repeated five times for new assemblies and new electrolytes. A calibration curve was obtained using aqueous conductivity standards (0.01 M, 0.1 M, and 1.0 M aqueous potassium chloride) and an empty cell was measured to obtain the combined cell and lead-resistances.

2.3.5. Resistance measurements

EIS measurements were performed at open-circuit voltage where the high-frequency intercept was identified as the value of the flow cell resistance capturing e.g., the membrane resistance and electronic contact resistances. The flow cell resistance (high-frequency intercept corrected for the contact and lead-resistance) for the Fe^{2+}/Fe^{3+} chemistry with the Nafion 211 membrane and NaCl supporting electrolyte was determined to be 0.39 ± 0.02 Ω, while it was 0.77 ± 0.01 Ω for the TEMPO/$TEMPO^{+}$ chemistry with the Daramic 175 membrane and $TBAPF_6$ electrolyte. The obtained values were used in the model as membrane resistivity values, by multiplying the high-frequency intercept resistance by the external area of the electrode (2.55 cm^2).

2.3.6. Exchange current density extraction

The exchange current density (j_0) was extracted from the experimental data by fitting the low current density region (< 100 mA cm^{-2}) of the polarization curve to the Butler-Volmer equation (**equation (2.6)** or **(2.7)**):

$$i = j_0 \left(\frac{c_{i,s}}{c_{ref}}\right)\left[\exp(-\frac{\alpha F \eta_{act}}{RT}) - \exp(\frac{\alpha F \eta_{act}}{RT})\right], \tag{2.30}$$

where i is the measured current density, and η_{act} the activation overpotential obtained after iR_Ω-correction of the experimental data and assuming mass transfer overpotentials to be negligible, resulting in $c_{i,s}$ being equal to c_{ref}. The exchange current densities were obtained for each electrolyte at all inlet velocities and for both electrodes.

2.3.7. X-ray tomography and image processing

Electrode materials were scanned in an uncompressed state using a laboratory micro-CT (Scanco Medical µCT 100 cabinet microCT scanner, holder type U50822 with a diameter of 9 mm and a height of 78 mm) at an isotropic resolution of 3.3 µm/voxel. The scans were carried out using a peak potential of 55 kVp, a current of 72 µA, 4 W, and a 0.1 mm aluminum filter to acquire 312 projection images over 360 degrees.

Gray-scale images produced using XTM contain a certain degree of noise that has to be reduced. Care was taken to preserve phase edges while applying noise reduction filters to limit losses of features in the virtual model. In this work, a two-dimensional median filter with a radius of 2.0 pixels was used to reduce the noise in the gray-scaled image. Subsequently, each voxel in the gray-scale image has been assigned to either the solid or void phase using a K-means cluster segmentation filter [46]. The reported median filter and K-means cluster segmentation filter were imported as plug-ins in the image processing software ImageJ [47, 48]. To prevent boundary effects from sample cutting, a 1.0 mm high and wide sample selection was selected from the center of the processed image, where the thickness of the electrode was reduced by the removal of the first and last few image layers in this dimension to prevent artifacts during the pore network generation.

The electrode geometry used in the PNM was generated by the extraction of the physical electrode structure from XTM images, in combination with image processing

steps consisting of smoothing, segmenting, and network extraction by the SNOW algorithm, using the equivalent diameter [49]. This open-source algorithm was developed for the extraction of porous networks from tomographic images and was validated for porous media with a wide range of porosities (20 - 85 %) [49]. The network extraction operation was performed using a single Intel® Core™ i7-8750H CPU. For the extracted networks, a standard deviation value of the applied convolution mask of 0.4 and a value for the radius of the spherical structure element of 5 voxels were used [49].

2.4. Results and discussion

2.4.1. Network extraction

The reliability of the modeling framework largely depends on the ability of the simplified porous network geometries to represent the complex microstructure of fibrous electrodes. Thus, before validating the simulated electrochemical performance, we first assess the accuracy of the network extraction procedure by comparing relevant microstructural parameters to conventional methods and literature values.

The extracted networks are represented graphically in **Figure 2.3a-b**, including an overlay of the spherical pores over the original tomograms. As a result of the organized fiber bundles of the woven electrode, a bimodal pore size distribution (PSD) is observed consisting of small pores in between the fibers and larger pores at the intersection of the fiber bundles (**Figure 2.3b**). On the contrary, the non-woven material contains a unimodal distribution. To quantify this, we compute the PSDs of the networks and compare them with mercury intrusion porosimetry (MIP) data (**Figure 2.3c-d**) obtained in a previous study [7]. The exact steps taken to evaluate the intrusion data can be found in **Section A2.4.1**. It should be noted that MIP relies on intruding mercury onto the electrode pores and assuming a perfect cylindrical shape. Hence, the resulting comparisons are qualitative but give a good indication of the quality of the extraction procedure.

The pore size distributions represented in **Figure 2.3c-d** reveal a stark microstructural difference. A good agreement was observed for the PSD of the paper electrode obtained by both methods (**Figure 2.3c**), which features an average pore diameter of ~15 µm. However, pores larger than 60 µm are absent in the extracted network as a result of both the presence of artificial bigger pores between stacked electrodes in the MIP measurements and the required image-trimming steps taken in the extraction procedure (the surface layer of conventional fibrous electrodes is characterized by a higher porosity and a lower fiber density packing than the bulk electrode [49]). The extracted PSD of the cloth electrode, on the other hand, differs from the MIP data (**Figure 2.3d**). First of all, the distribution is shifted towards larger pore sizes, as the void space between the individual continuous fibers in the threads of the cloth cannot be accurately represented by pores and throats. Secondly, similar to the paper electrode, the SNOW extraction of the cloth results in the construction of a network with a maximum pore size of 260 µm for the larger pore segments, while the intrusion data displays bigger pores. To investigate whether inhomogeneities in the larger pore segment of the extracted network also play a role, a bigger network (170 % of the original size) was extracted (**Figure A2.2**), which better matches the larger pores observed with MIP. Nonetheless, an investigation into the performance of this bigger extracted network showed only a slightly

better match with the experimental data, but similar curvature offsets were observed for the smaller extracted network (**Figure A2.3**, **Figure 2.4b**, and **Figure 2.5b**).

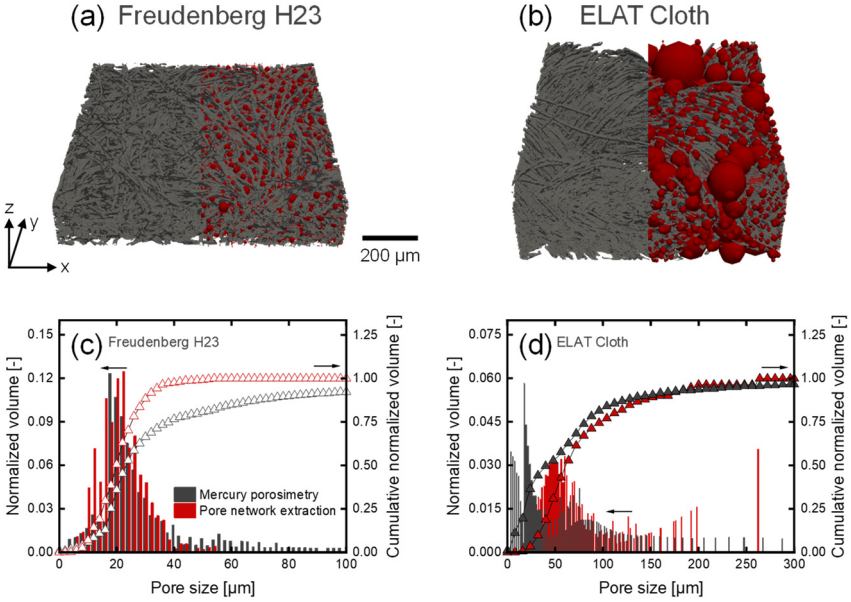

Figure 2.3: Visual representation of the processed X-ray tomography images overlaid with the extracted pore networks, where: **(a)** is the paper electrode, and **(b)** the cloth electrode. Combined with the PSDs of the electrodes obtained with MIP and the SNOW pore network extraction algorithm. The normalized pore size distributions and the cumulative normalized volumes are shown for: **(c)** the paper electrode, and **(d)** the cloth electrode. The normalized volume is defined as the fraction of the total pore volume occupied by all pores within a 2 µm pore size range.

The geometrical surface area, bulk electrode porosity, in-plane and through-plane permeability, anisotropy ratio, and thickness of the extracted PNs are compared to the literature values in **Table 2.1**. The in-plane permeability is defined as the average permeability in the direction parallel to the membrane (x and y-directions), while the through-plane permeability is defined as the permeability perpendicular to the membrane (z-direction). The anisotropy ratio is defined as the ratio between the in-plane and through-plane permeabilities and provides information about the pore alignment. A slightly reduced permeability, thickness, and porosity were observed for all the extracted networks compared to the experimental values. A larger deviation is observed between the extracted networks' internal surface area and the literature-obtained value, with an increase in the surface area of 2.2 x for the paper network and 9.5 x for the cloth network compared to the literature. The higher internal surface area for the extracted networks is a result of assumptions taken in the experimental determination of the electrochemically active surface area (ECSA) through analysis of the electrochemical double-layer capacitance, such as the assumed specific conductance of the electrode, as they can lead to underestimations in the experimentally obtained ECSA [8, 50]. Tenny *et al.* investigated four volume-specific surface area techniques (MIP, Brunauer-Emmett-Teller, electrochemical double-layer capacitance, and morphological methods) for woven electrodes and found that the ECSA value estimated from the electrochemical double-layer capacitance (0.05 - 0.08 x 10^5 m^2 m^{-3}) was several magnitudes lower than estimated

by the other methods (1.1 - 2.6 x 10^5 m^2 m^{-3}), which are in-line with our obtained pore network ECSA [37]. Therefore, the surface area was additionally obtained from the tomograms using the open-source image analysis package PoreSpy, which only relies on the geometrical surface area instead of the ECSA, and the surface roughness is only partially captured as a result of the XTM resolution. Nevertheless, the extracted networks differ by a factor of 1.5 with this estimation of the surface area as a result of the translation of the void space to pores and throats in the pore network. Despite these intrinsic challenges with surface area determinations, we remain confident about the extracted values since we determine the kinetics of the electrode-electrolyte couples from the experimental data in terms of the exchange current density, which corrects any errors in the surface area.

Table 2.1: Network properties of the extracted pore networks and the experimental data, *estimated from data found in [51, 52], **obtained using the open-source image analysis package PoreSpy. It must be noted that some materials from the literature might contain small amounts of polytetrafluorethylene.

Electrode	Parameter	Experiment	Network
Freudenberg	In-plane permeability x 10^{-12} [m^2]	4.2 [51]	2.5
	Through-plane permeability x 10^{-12} [m^2]	1.2 [51, 52]*	1.0
	Anisotropy ratio [-]	3.4	2.5
	Internal surface area [m^2 m^{-3}]	7.2 x 10^4 [7] , 1.0 x 10^5**	1.6 x 10^5
	Porosity [-]	0.8 [7], 0.66**	0.66
	Apparent density [kg m^{-3}]	480	
	Thickness [µm]	210	198
ELAT Cloth	In-plane permeability x 10^{-12} [m^2]	44 [39, 53]	36
	Through-plane permeability x 10^{-12} [m^2]	21 [39]	17
	Anisotropy ratio [-]	2.1	2.1
	Internal surface area [m^2 m^{-3}]	1.4 x 10^4 [54], 8.6 x 10^4**	1.4 x 10^5
	Porosity [-]	0.82 [7], 0.73**	0.73
	Apparent density [kg m^{-3}]	289	
	Thickness [µm]	380-406 [7]	375

2.4.2. Model validation

We then assess the accuracy of the electrochemical model with experimental data for the non-aqueous electrolyte (the electrolyte properties are listed in **Table 2.2**) and both electrode microstructures, by evaluating the single electrolyte cell polarization curves (**Figure 2.4**). Importantly, the data presented in **Figure 2.4** only uses the obtained exchange current density, extracted from the experimental measurements (**Table A2.2**) to obtain the electrolyte-electrode kinetics, as an electrode-dependent parameter. Kinetic information needs to be provided to the PNM as the model is focused on the mesoscale, missing the capability to extract kinetic phenomena taking place at the molecular scale. Therefore, we elect to extract the kinetic information from experimental data, which is a common practice in electrochemical engineering modeling [55, 56]. The exchange current densities obtained from the experimental data range from 1870 - 460 A m^{-2} for the non-aqueous chemistry and are in the same range as reported in the literature, using other electrode structures (375 A m^{-2} for the TEMPO/$TEMPO^+$ chemistry [57]). The extracted exchange current densities are depending on the electrolyte flow rate as within the

timeframe of the experiments, it is likely that (fully wetted) steady-state conditions were not reached and that therefore the accessible surface area varies with different flow rates, resulting in velocity-dependent exchange current densities.

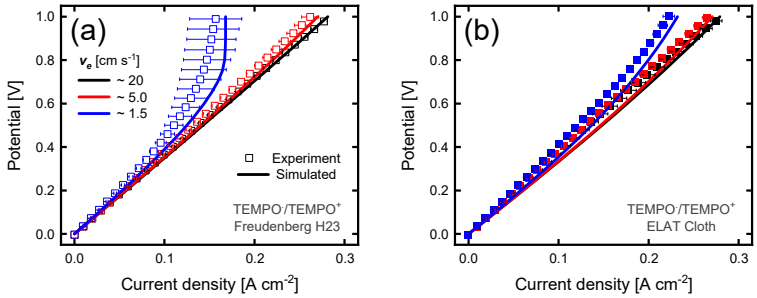

Figure 2.4: Comparison of the polarization curves of the simulated and corresponding experimental data by plotting the current density versus the potential for the non-aqueous electrolyte and the two electrodes at inlet velocities of 20, 5.0, and 1.5 cm s^{-1}, for: **(a)** the paper electrode, and **(b)** the cloth electrode. The experimental data of the three experiments per system (**Figure A2.5**) was averaged and shown with error bars indicating the standard deviation of the current density.

Table 2.2: Electrolyte properties for both the non-aqueous and aqueous electrolytes. The properties are the same in both half-cells. *Diffusion coefficient in the electrode.

Chemistry	Parameter	Symbol	Value	Unit
TEMPO	Electrolyte density	ρ_l	852	kg m^{-3}
	Electrolyte viscosity	μ	3.4 x 10^{-4}	Pa s
	Bulk electrolyte conductivity	σ_l	1.99	S m^{-1}
	Cathodic transfer coefficient	α_c	0.5	-
	Anodic transfer coefficient	α_a	0.5	-
	TEMPO diffusion coefficient* [57]	D_{TEMPO}	1.3 x 10^{-9}	m^2 s^{-1}
	TEMPO$^+$ diffusion coefficient* [57]	D_{TEMPO+}	1.3 x 10^{-9}	m^2 s^{-1}
	Inlet TEMPO concentration	$c_{TEMPO,in}$	100	mol m^{-3}
	Inlet TEMPO$^+$ concentration	$c_{TEMPO+,in}$	100	mol m^{-3}
	Reference concentrations of active species	c_{ref}	100	mol m^{-3}
	Supporting electrolyte concentration	c_{TBAPF6}	1000	mol m^{-3}
Iron	Electrolyte density	ρ_l	1015	kg m^{-3}
	Electrolyte viscosity	μ	8.9 x 10^{-4}	Pa s
	Bulk electrolyte conductivity	σ_l	7.65	S m^{-1}
	Cathodic transfer coefficient	α_c	0.5	-
	Anodic transfer coefficient	α_a	0.5	-
	Fe^{2+} diffusion coefficient* [58]	D_{F2+}	5.7 x 10^{-10}	m^2 s^{-1}
	Fe^{3+} diffusion coefficient* [58]	D_{F3+}	4.8 x 10^{-10}	m^2 s^{-1}
	Inlet Fe^{2+} concentration	$c_{F2+,in}$	100	mol m^{-3}
	Inlet Fe^{3+} concentration	$c_{F3+,in}$	100	mol m^{-3}
	Reference concentrations of active species	c_{ref}	100	mol m^{-3}
	Supporting electrolyte concentration	c_{NaCl}	1000	mol m^{-3}

The PNM framework can predict the electrochemical response of a kinetically facile fully wetted system (non-aqueous) without the use of model-fitting parameters. This can be observed as the comparison between the model and experimental response for the non-aqueous electrolyte for both electrode structures, shown in **Figure 2.4**,

together with the root-mean-square error and the mean relative error (**Table A2.3**), revealed a good match. The extracted exchange current densities provide a more accurate representation of the kinetics of the specific electrode-electrolyte systems; however, when running the simulations with the literature value (375 A m^{-2}), the model was still able to capture the experimental response (**Figure A2.4**). Thus, the proposed modeling framework was validated for the fully wetted non-aqueous electrolyte system with a single-electrolyte cell design.

2.4.3. Incomplete wetting and parameter adaptation

After the model validation with the non-aqueous electrolyte, the versatility and robustness of the PNM is evaluated by comparing the simulated performance with experimental data for an aqueous electrolyte (the electrolyte properties are listed in **Table 2.2**). The exchange current densities obtained from the experimental data range from 652 - 98.7 A m^{-2} for the aqueous chemistry and are in the same range as reported in the literature (23.0 A m^{-2} for the Fe^{2+}/Fe^{3+} chemistry [58]).

Whereas the behavior of the non-aqueous electrolyte is well-captured by the model, the simulated performance of the aqueous electrolyte shows significant deviations from the experimental data (**Figure 2.5a** and **b**, **Table A2.3**) which is hypothesized to be a result of incomplete wetting of the internal porous structure in the experimental measurements. The developed modeling framework assumes that the electrode is fully wetted, meaning that the entire electrode's geometric surface area is electrochemically active and that fluid transport in the open space of the porous structure can be characterized as single-phase flow. However, it has been shown that during the operation of RFBs, unfavorable interactions between aqueous electrolytes and carbon electrodes can result in gas hold-up within the porous structure [8, 59–62]. Especially at lower velocities, this may lead to liquid channeling, which in turn leads to incomplete electrode utilization and hence decreased cell performance compared to the simulated performance assuming fully wetted electrodes. Due to their lower surface tension, organic electrolytes (e.g., acetonitrile-based electrolytes) have been demonstrated to fully wet carbon fibrous electrodes [7]. It is hypothesized that for this reason, the experimental performance of the TEMPO/$TEMPO^+$ electrolyte is well-captured by the model, in contrast to the aqueous electrolyte.

The wetting behavior within RFB operation involves a complex interplay of concentration depletion, surface area utilization, and preferential pathway channeling. However, in this framework, the impact of these phenomena is not individually accounted for but encapsulated within the mass transfer coefficient, k_m. The inability to capture the effect of these individual phenomena is an important limitation of the PNM compared to higher detailed computation models, such as Lattice Boltzmann methods [62, 63]. To account for the sub-optimal wetting in aqueous systems, we propose a fitting procedure for k_m using SciPy's least squares method to minimize the error between the data points obtained from the experimental dataset and the model [64].

The electrochemical response of the corrected paper electrode system (**Figure 2.5c**) yields a good agreement with the experimental data. It is observed that a greater k_m correction factor was required (diverting from unity, factors fluctuate between 0.11 - 1, **Table A2.4**) when operating with a lower hydraulic driving force (i.e., lower electrolyte

velocity), as higher electrolyte velocities favor greater pressure drops, and thus a higher electrode saturation. This result supports the claim that the aqueous electrolyte, with a contact angle around 80° - 90° with carbon fiber electrodes [8], incompletely wets the carbon fibrous electrode in the experimental measurements, leading to limited utilization of the available electrode geometric surface area.

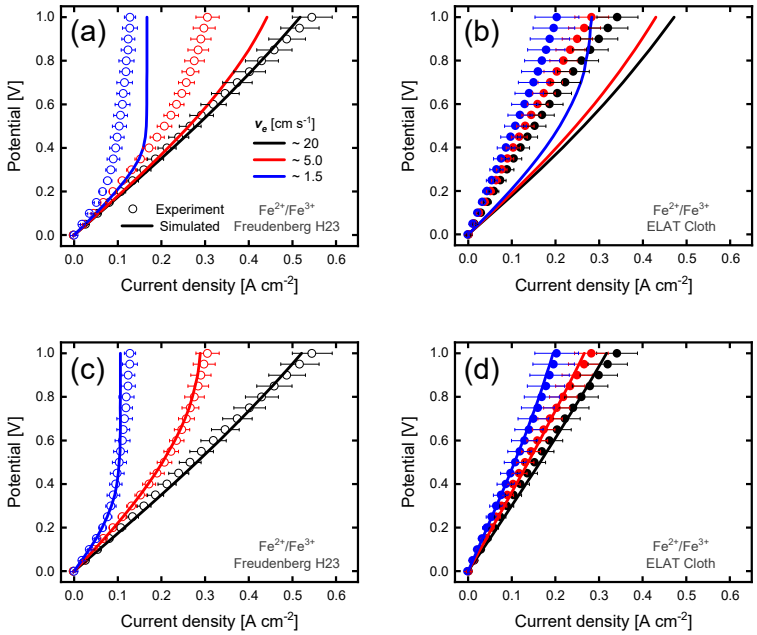

Figure 2.5: Comparison of the polarization curves of the simulated data and the corresponding experimental data by plotting the current density versus the potential at inlet velocities of 20, 5.0, and 1.5 cm s^{-1}, for: **(a)** the paper electrode with the aqueous electrolyte, **(b)** the cloth electrode with the aqueous electrolyte, **(c)** the paper electrode with the aqueous electrolyte with an adapted mass transfer coefficient, and **(d)** the cloth electrode with the aqueous electrolyte with a combined adapted mass transfer coefficient and resistance factor. The experimental data of the three experiments per system (**Figure A2.5**) was averaged and shown with error bars indicating the standard deviation of the current density.

The corrected k_m value for the cloth electrode however does not result in as good of a fit between the simulated and experimental data (**Figure A2.6**), although better than the uncorrected data. The cloth electrode is more likely to suffer from contact resistances at minimal compressions compared to the flat paper electrode, as the inhomogeneous weave pattern of the cloth reduces the contact between the current collector and the electrode. At normal cell assembly conditions, the electrode is compressed to a certain degree, generally, 20 - 30 % [65] to minimize contact resistances, without compressing the electrode microstructure too much to prevent an increased pressure drop [44]. Therefore, impedance measurements were conducted to evaluate the medium frequency ranged arc, roughly translated to the charge transfer overpotential in the electrochemical cell [18]. The medium frequency arc of the uncompressed electrode displays a significant velocity dependency (**Figure A2.7a**). This indicates that, in addition to small changes in activation overpotential with electrolyte velocity affecting the concentration of active species, the geometric surface area is utilized to different degrees.

We hypothesize that, under minimal compression, the electrolyte could flow by the woven electrode, affected by the electrolyte velocity, inducing different pressure drops and electrode utilization. To further investigate this hypothesis, we perform measurements with a 48 % compressed woven electrode (**Figure A2.7b**) and find that the medium frequency arc does not show a significant velocity dependency as the electrolyte is now more likely to be forced through the electrode. Nevertheless, both uncompressed (~ 0.8 - 1.4 Ω for all tested velocities) and compressed (~1.1 - 1.3 Ω for all tested velocities) cells feature a pronounced medium frequency arc in the EIS data as a result of the incomplete wetting causing partial access of the geometrical surface area. To further study the influence of wettability, a super hydrophilic taurine-electrografted cloth electrode was tested and found to result in a smaller medium frequency arc in the EIS data (~0.4 Ω for all tested velocities, **Figure A2.7c**), which validates our hypothesis of incomplete wetting for the studied electrodes. Nonetheless, even the performance of this super hydrophilic electrode (**Figure A2.8**) cannot be completely captured with the model, which further reveals the complexity of simulating woven microstructures using simplified networks.

It is noted that an additional ohmic contribution is present in the system, as the experimental response can be captured using a correction procedure of k_m and a resistance factor (**Figure 2.5d**). This can be explained in light of two factors: the network extraction and the distributed ohmic resistance within the system. As shown in the network extraction section, the inhomogeneous weave pattern of the cloth electrode cannot be precisely captured by pores and throats showing the limitation of the SNOW algorithm for woven materials. Furthermore, distributed ohmic resistance was proven by Pezeshki *et al.* to play a significant role in thick electrode structures [18]. This ohmic contribution is a result of the parallel combination of ionic and electronic resistances that occur in the liquid electrolyte and carbon fibers, respectively. This resistance is not captured by the high-frequency intercept in the EIS data, but by a distributed feature in the high to medium frequency range.

Despite the limitations of the SNOW algorithm to match the structural properties of the cloth electrode with complete accuracy, the modeling framework provides a versatile platform to analyze the impact of the computed network's structural properties on the overall cell performance from first principles. Further research should be conducted on using various geometrical shapes (e.g., Voronoi and Delaunay tessellations [66]) to better represent the pores and throats in complex electrode geometries to increase the robustness of PNMs, as current network extraction methods are not optimal for multiscale images [67]. In addition, going forward, it will be important to ensure fully wetted electrodes in the experimental setup by performing e.g., thermal treatment, chemical etching, and chemical doping, to enhance the performance of the cells. Thus, the modeling of fully wetted systems is relevant, as incomplete wetting is undesired and should be overcome for practical applications. Nonetheless, incorporating the physics of multiphase flows to track gas pockets within the partially wetted porous structure is of interest and could be subjected to further research to increase the versatility and robustness of PNMs.

2.4.4. Porous electrode performance

Pore network modeling can be used to understand the impact of the electrode microstructure on the performance of RFBs for distinct electrolytes, as local distributions of relevant properties (e.g., pressure, concentration, current) through the porous electrode can be obtained. This is an important advantage over experimental methods and macroscopic continuum models, as it enables spatially-resolved analysis of limiting phenomena; and over pore-scale direct numerical simulations, as it reduces computational requirements and affords simulation of larger electrode volumes. This provides valuable insight into the effects of microstructural properties on electrode performance, useful for electrode optimization studies. Here, we compare the performance of both electrodes, assuming fully wetted systems, and demonstrate that the differences in macroscopic performance indicators directly correlate to the unique microstructural properties of both electrodes. To assess the performance on the cell level, the pressure drop, current density fields, concentration depletion effects, and overpotential contributions within both electrodes are discussed in the following subsections.

2.4.4.1. Pressure drop

For efficient system operation, the pumping losses should be minimized compared to the electrical power output. Increased electrolyte flow rate enhances mass transport, improving the electrochemical performance, but simultaneously increasing pumping power requirements as the pumping power loss is defined as

$$P_{pump} = \frac{Q\ \Delta P}{\eta_p}, \tag{2.31}$$

where P_{pump} is the pumping power loss, ΔP the pressure drop, and η_p the pumping efficiency. To keep the pressure drop minimal, the permeability of the electrode should be high, as the pressure drop and permeability are related by Darcy's law

$$-\frac{\Delta P}{L} = \frac{\mu}{\kappa} u, \tag{2.32}$$

where L is the length of the medium and κ the permeability.

The permeabilities of the extracted cloth were observed to be 14.4 (in-plane) and 17 (through-plane) times greater than those of the paper electrode, which resulted in a lower pressure drop (**Figure 2.6a-b**). The superior permeability of the cloth electrode is attributed to the larger pore segments (high porosity transport pathways) within the bimodal PSD (**Figure 2.3d**).

2.4.4.2. Current density profiles

The current distribution over the normalized thickness and length of both electrodes is shown in **Figure 2.6c-f**. Both electrodes show a distinct gradient in their current generation as a function of the electrode thickness, where most of the current is obtained in the region closest to the membrane. This distribution concurs well with the design principle behind zero-gap electrode cells, as the aggregated effect of ohmic losses is the smallest closest to the membrane [68]. This result highlights that the design of through-

plane transport pathways of porous electrodes is not only important to reduce the pressure drop, but also to obtain efficient charge transfer within the porous electrode. Recently, it has been demonstrated that utilizing phase-separated induced porosity gradients in porous electrodes offers a feasible method to trade-off permeability and reactive surface area over the thickness of the electrode [69].

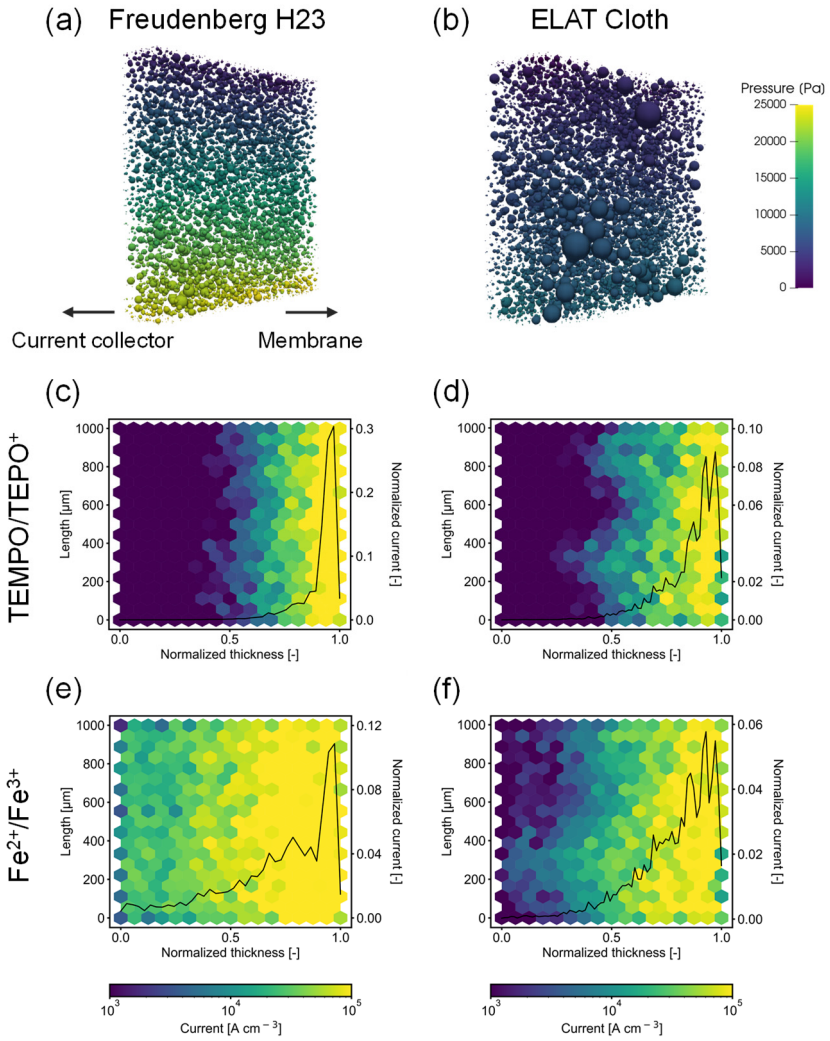

Figure 2.6: Pressure and current profiles of both electrodes at -1 V and 20 cm s^{-1}. The pressure profiles are shown over the length and width of the electrode, for: **(a)** the paper electrode, and **(b)** the cloth electrode. Both for the non-aqueous electrolyte (the profiles are similar for the aqueous electrolyte). The current profiles are shown in 2D with the accumulated current corrected for the volume of the network, for: **(c)** the non-aqueous electrolyte and the paper electrode, **(d)** the non-aqueous electrolyte and the cloth electrode, **(e)** the aqueous electrolyte and the paper electrode, and **(f)** the aqueous electrolyte and the cloth electrode. The 2D electrodes are shown for the last network of the network-in-series model with the membrane side facing the right and with the flow direction from the bottom to the top. The 2D current plots **(c-f)** additionally show a 1D profile of the normalized current (total current normalized to unity) over the thickness of the electrode.

When operating at limiting-current conditions, the current distribution no longer displays a gradient as a function of the electrode thickness but shows a more uniform distribution throughout the electrode (**Figure A2.9**) as all surface area is utilized for the redox reactions. **Figure A2.9** thus shows uniform distributions at 1.5 cm s^{-1} for all systems except the cloth electrode with the non-aqueous electrolyte, which concurs well with **Figure 2.4** (no limiting-current conditions reached). Moreover, the aqueous electrolyte systems **(Figure 2.6e-f)** reveal a flatter drop-off in the current profile as a function of the electrode thickness, which can be explained by the higher ionic conductivity of the aqueous electrolyte (7.65 S m^{-1}) compared to the non-aqueous electrolyte (1.99 S m^{-1}). We anticipate that future work could leverage this systematic analysis to engineer the porous electrode thickness and local distributions of electrochemical surface area for specific chemistries and operating conditions.

2.4.4.3. Reactant depletion

Reactant depletion within the porous structure can be classified by longitudinal depletion and local depletion. The concentration profiles over the electrode length reveal that for both electrodes, the highest degree of reactant starvation occurs in the longitudinal dimension in the flow-through system (**Figure 2.7**, at 1.5 cm s^{-1} for the non-aqueous electrolyte), as the inflow of fresh reactant is outweighed by the electrochemical consumption of reactant. At the end of the 1.7 cm electrode length (**Figure 2.7c, f**), a slightly higher concentration is found for the cloth electrode in comparison with the paper electrode, which is a result of the thickness of the cloth electrode, permitting a larger inlet flow rate at a constant inlet velocity.

The concentration distribution maps in **Figure 2.7** reveal that, while the bimodality of the cloth electrode was found to yield superior permeability, it results in a higher degree of local reactant depletion. Local clusters of smaller pores, with limited convective flow, show a higher degree of reactant depletion than the surrounding larger pore segments. Moreover, the unimodal PSD of the paper electrode results in a more uniform concentration profile.

2.4.4. Overpotential contributions

To compare the electrochemical output of both electrodes in isolation, the performance must be corrected for the membrane resistance (see the calculations in **Section A2.7.2**), as different membranes were used for each electrolyte. The results are shown in **Figure 2.8a-b**, from which several interesting trends can be observed. First, the performance is similar within both microstructures for the non-aqueous electrolyte at high to moderate velocities; however, the cloth electrode outperforms the paper electrode at lower velocities due to its ability to reach higher limiting current densities. Second, the paper electrode outperforms the cloth electrode for the aqueous electrolyte at high to moderate velocities; however, the trend is reversed for lower velocities. Finally, the aqueous electrolyte outperforms the non-aqueous electrolyte, especially at high velocities. These trends can be further analyzed in light of the individual overpotential contributions (i.e., activation, ohmic, and concentration) extracted from the single-electrolyte flow cell simulations by the calculations presented in **Section A2.7.2**.

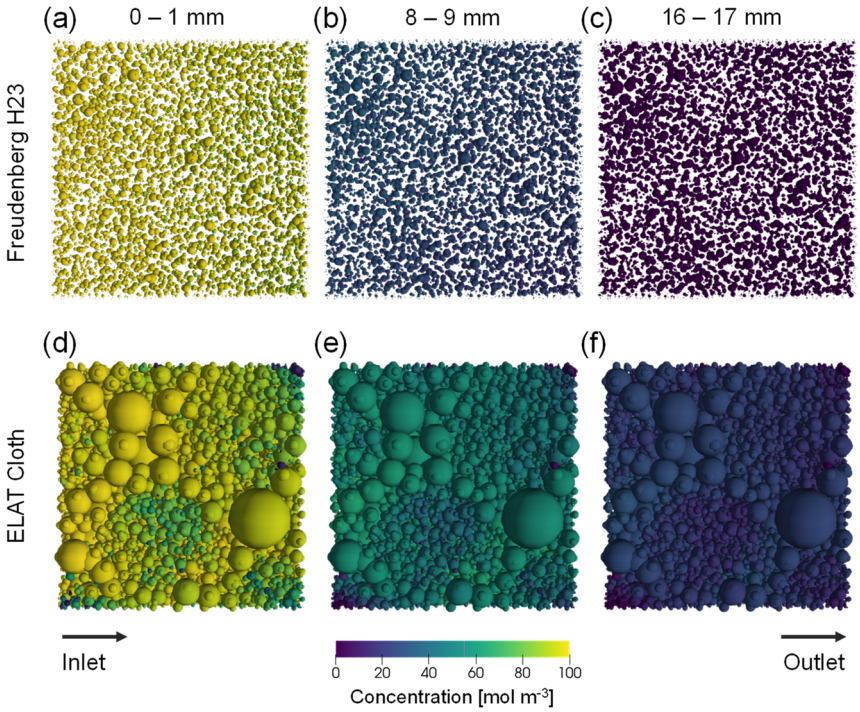

Figure 2.7: Concentration profiles of the non-aqueous electrolyte (the profiles are similar for the aqueous electrolyte) for the paper electrode **(a-c)**, and the cloth electrode **(d-f)** at -1 V for an inlet velocity of 1.5 cm^{-1}, showing the concentration depletion over the electrode length, with: **(a)** and **(d)** the first network, **(b)** and **(e)** the middle network, and **(c)** and **(f)** the last network in the network-in-series model. The electrodes are shown facing the membrane side and with the flow direction from left to right.

Two main trends can be observed in **Figure 2.8c-f**. First, due to the facile kinetics of both systems, the activation overpotential is the smallest contributor to the total overpotential (**Figure 2.8c-d**). The activation overpotential is inversely dependent on the exchange current density and thus the activation overpotential is higher for the aqueous electrolyte in both electrodes. Furthermore, as a consequence of the concentration dependency of the exchange current density, the activation overpotential increases with decreasing electrolyte velocities for all four systems.

Second, the concentration overpotential becomes dominant at low inlet velocities (**Figure 2.8e-f**). When comparing both electrodes, it is observed that the cloth electrode does not reach mass transfer limitations at the same current densities for both electrolytes. As explained in **Section 2.4.4.3.**, care should be taken when attributing this effect to an improved mass transfer induced by the microstructure of the cloth electrode, as the obtained response is mostly a result of comparing the electrodes at the same inlet velocity. However, the pressure drop in the cloth electrode is still lower at similar velocities, indicating that the use of these electrodes is favored when operating in a high conversion regime. When comparing the performance at a velocity of 20 cm s^{-1} and -1 V, only 1 - 10 % of the total overpotential is caused by depletion effects (**Table A2.6**). Notably, the concentration overpotential at 20 cm s^{-1} is slightly higher in the cloth than in the paper electrode, which can be explained by reactant depletion effects in the highly

electrochemically active regions consisting of smaller pores, as observed in **Figure 2.7**. Furthermore, the concentration overpotential is greater for the aqueous electrolyte at a fixed potential, as the higher conductivity of the aqueous electrolyte enables operation at higher current densities, thus increasing the contribution of reactant depletion effects on the overpotential. In addition, the larger diffusivity of active species in the non-aqueous electrolyte, partly explained by the lower viscosity of acetonitrile, can help explain the reduced concentration overpotential for the non-aqueous electrolyte, resulting in a faster rate of mass transfer of active species to the electrode surface.

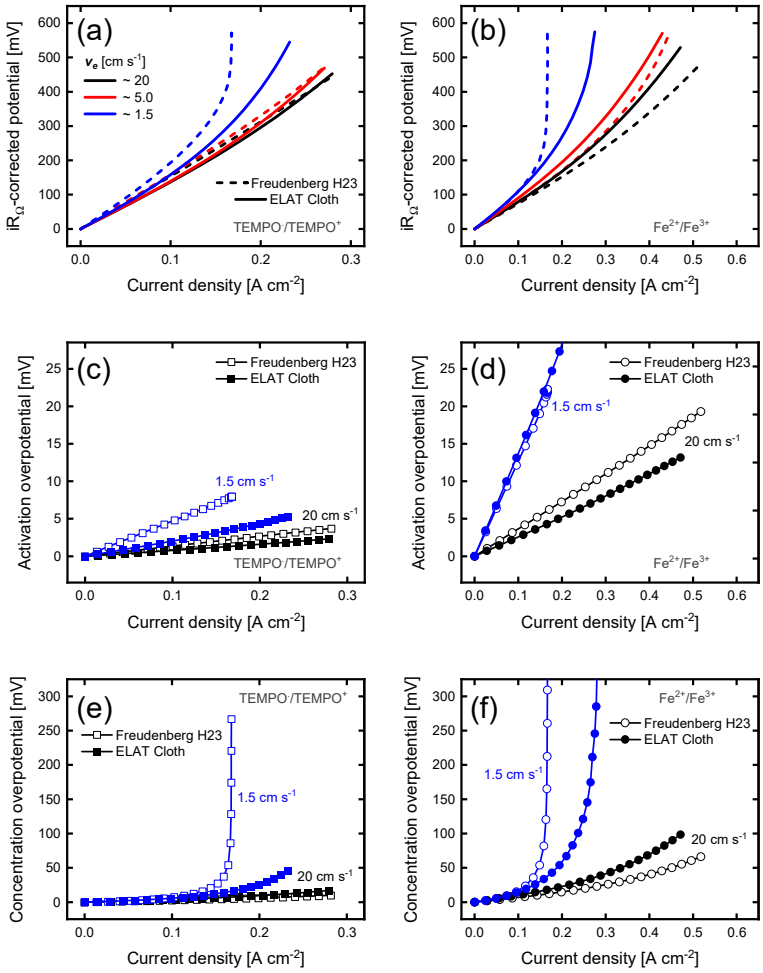

Figure 2.8: (a-b) Comparison of the polarization curves of the simulated data for the paper electrode and the cloth electrode by plotting the iR_Ω-corrected current density versus the potential at inlet velocities of 20, 5.0, and 1.5 cm s^{-1}, for: **(a)** the non-aqueous chemistry, and **(b)** the aqueous chemistry. **(c-f)** Overpotential contributions to the polarization curves at 20 and 1.5 cm s^{-1} inlet velocity for the paper and cloth electrode without fitting parameters, showing: **(c)** the activation overpotential for the non-aqueous chemistry, **(d)** the activation overpotential for the aqueous chemistry, **(e)** the concentration overpotential for the non-aqueous chemistry, and **(f)** the concentration overpotential for the aqueous chemistry. The explanation of how the overpotentials were extracted from the model is given in **Section A2.7.2**.

In addition, for all chosen electrolyte-electrode pairs, the ohmic overpotential is dominant at moderate to high electrolyte velocities (**Figure A2.10** and **Table A2.6**), which can be explained by the facile kinetics, large membrane resistances, and the low effective conductivities of the chosen electrolytes (e.g., dilute conditions). The lower ohmic overpotential of the aqueous system can directly be explained by its higher effective conductivity.

The microstructural analysis showed that the bimodality of the porous cloth electrode had a positive effect on the overall permeation of fluids through porous electrodes, but the bimodal distribution should be engineered carefully to mitigate the effect of reactant depletion in highly electrochemically active regions. Furthermore, the balance between electrode thickness and surface porosity is critical as most of the current is generated near the membrane side of the porous electrode (when not operating at limiting-current conditions). This shows that the power output of the cell depends strongly on the electrode thickness as thicker electrodes will result in increased ohmic losses, but only in an incremental increase in the electrochemical output. To aid in the design of the porous electrode structure, bottom-up electrode optimization studies can be leveraged to balance these contradictory demands.

2.4.5. Operation envelopes

Besides the power of pore network modeling to investigate the impact of existing porous electrode microstructures, it can be leveraged to perform a broad screening of operating conditions and electrolyte chemistries for the identification of efficient operation envelopes. Here, we investigate the effect of the electrolyte velocity and redox chemistry on the cell performance in terms of electrical power output and pumping power losses (**Figure 2.9**).

For efficient flow battery operation, two contradictory requirements must be met: (1) the electrical power output should be maximized, whilst (2) the pumping losses should be minimized. Therefore, we study the correlation between the pumping requirements and achievable current densities using the iR_{Ω}-corrected electrochemical power. In this study, the iR_{Ω}-corrected electrochemical power represents the useful electrical power driven by electrode performance and was calculated by

$$P_{el} = P_{theory} - P_{losses} = I\,(E_{OC} - E_{iR\Omega}), \tag{2.33}$$

where P_{el} is the iR_{Ω}-corrected electrochemical power, P_{theory} is the theoretically achievable electrochemical power calculated by multiplying the open-circuit voltage, E_{OC}, of an iron-chromium battery of 1.18 V, chosen arbitrarily, by the current, I, and P_{losses} are the power losses calculated by multiplying the iR_{Ω}-corrected cell overpotential ($E_{iR\Omega}$) by the generated current. The pumping power was calculated using **equation (2.31)** and assuming a pumping power efficiency of 90 % [70]. In **Figure 2.9**, we plot the electrical power output against the required pumping power to identify operation envelopes that warrant an efficient operation. In this figure, a velocity sweep was performed (at 5, 1, 0.5, 0.2, 0.05, 0.01, 0.005, 0.001, and 0.0005 cm s^{-1}) for the aqueous electrolyte and two hypothetical electrolytes representing relevant systems (e.g., all-vanadium) with sluggish kinetics (exchange current densities of 1 x 10^{-2} A m^{-2} and

1 x 10^{-4} A m^{-2}, using the electrolyte properties of the aqueous electrolyte), for both electrode structures. The figure contains two demarcations indicated by the dashed lines, illustrating a trade-off between the electrochemical power output and pumping power requirements [7] useful in the optimization of next-generation porous electrodes, electrolytes, and system parameters. We find that there is a plateau where higher electrolyte velocities only result in increased pumping requirements without achieving a significantly larger power output. Furthermore, we find that this plateau is reached at lower velocities for kinetically-sluggish electrolytes and the higher permeability of the cloth enables a wider operational range.

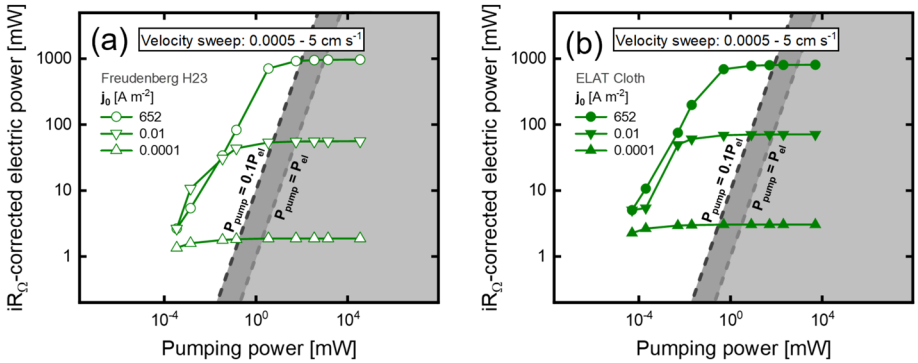

Figure 2.9: The pumping power versus iR_Ω-corrected electric power for the velocity parameter sweep performed at 5.0, 1.0, 0.5, 0.2, 0.05, 0.01, 0.005, 0.001, and 0.0005 m s^{-1}, evaluated at -1 V for three distinct systems with exchange current densities, j_0, of 652, 0.01, and 0.0001 A m^{-2} using the electrolyte properties of the aqueous electrolyte for: **(a)** the paper electrode, and **(b)** the cloth electrode. The dashed lines and shaded regions indicate demarcations of unity and ten [7].

As a more extensive analysis, in **Section A2.8**, the effects of various cell and electrolyte properties on the performance of the cell were further analyzed. We correlate the effect of the exchange current density and the inlet velocity to the overpotential distribution, outlet concentration, limiting current density, and pressure drop in both electrodes to show the potential of this modeling framework for systematic parameter screenings. Altogether, we have developed a pore network modeling framework and critically assessed its versatility and robustness. Based on our findings, and recommendations for further research on topological representations of woven electrodes and partial wetting, we believe this framework can be used as a predictive tool to engineer electrode microstructural properties, perform parameter sweeps, and investigate the effect of individual parameters on the system performance.

2.5. Conclusions

Engineering porous electrode microstructures in redox flow batteries is a promising approach to enhancing stack performance and reducing pumping power requirements. To improve the fundamental understanding of the relationship between electrode microstructure and flow battery performance, we developed an electrolyte agnostic, microstructure-informed, and computationally inexpensive pore network modeling platform that solves for electrochemical kinetics, fluid flow, mass transport, and charge conservation. Compared to fully detailed pore-scale models (e.g., Lattice Boltzmann

simulations), the use of pore network modeling relies on geometrical simplifications which impact accuracy but enables simulation of larger sample sizes. Here, we demonstrated that the model can accurately describe electrochemical performance under a broad range of operating conditions and redox chemistries. Importantly, our systematic and rigorous analysis reveals some scenarios where the current modeling framework lacks accuracy (e.g., aqueous electrolytes with woven electrodes) which motivates further research on three-dimensional modeling of multi-scale microstructures and multi-phase flows.

The model was validated with experimental measurements with single-electrolyte flow cells for the non-aqueous TEMPO/TEMPO$^+$ electrolyte for two different electrode microstructures (Freudenberg H23 paper and the woven ELAT Cloth). We find that the experimental performance is well captured by the numerical model for this non-aqueous electrolyte without the use of fitting parameters. To further investigate the versatility and robustness of the pore network model, the performance of an aqueous Fe^{2+}/Fe^{3+} electrolyte was investigated within both electrodes. For this electrolyte, the simulations only partially describe the experimental performance. We hypothesize that incomplete wetting of the electrode structure with the aqueous electrolyte results in underutilized electrode surface area in the experimental measurements. Thus, we introduced an adaptation of the core physical descriptor of the mass transfer coefficient, resulting in a good fit for the paper electrode. Furthermore, we find that translating the woven electrode microstructure to a network connected by spheres and cylinders with pores spanning several length scales does not result in an accurate description of the electrochemical response. Thus, an additional resistance correction was necessary to obtain a better fit for the woven electrode with the aqueous electrolyte. Multiscale structures like carbon cloths motivate further research into alternative pore network geometries in addition to the investigation of incomplete wetting by experimental and modeling methods. Regardless, the model provides a robust platform to analyze the impact of the structural properties on the overall cell performance from first principles.

Moreover, the ability to simulate the pore-level performance of the electrode microstructure was discussed, showing the strength of using pore network models compared to experimental methods and continuum models, as spatially-resolved analysis of limiting phenomena can be performed, and direct numerical simulations, as larger electrode volumes can be simulated at a low computational cost. Here, it was observed that the presence of a bimodal structure of the woven electrode, with large pores within the threaded bundles, resulted in significantly reduced pumping power requirements in comparison to the unimodal pore size distribution of the paper electrode but also incited a higher degree of local areas with the depleted reactant. The presence of local depletion zones explains the slightly larger concentration overpotential in the cloth compared to the paper electrode at moderate to high electrolyte velocities. Due to the low conductivity of both chosen model electrolytes, the ohmic overpotential was found to be the largest overpotential at velocities of 20 cm s^{-1}; however, at velocities of 1.5 cm s^{-1}, longitudinal reactant depletion effects dominate the electrochemical losses at higher current density operation. Moreover, through-thickness current profiles show that most of the current is generated at the membrane-electrode interface at high electrolyte velocities, which motivates re-engineering electrode thicknesses for flow battery applications. We anticipate that future work could leverage this modeling framework to predict optimal

electrode thickness and microstructure as a function of flow battery chemistry and operating conditions.

Finally, we performed a parametric sweep to study the correlation between useful electrical power and pumping power requirements, hence identifying operation envelopes that warrant an efficient operation. This knowledge can inform technology practitioners in selecting their porous electrodes for specific chemistries and identifying efficient operating conditions. In summary, the developed chemistry and microstructure agnostic pore network model provides a computationally inexpensive framework to investigate porous electrode microstructures and allows for quick parameter screening over the electrode length. The model is well suited for system performance evaluations (electrolyte type, operating conditions), electrode microstructure comparisons, and analysis of flow field geometries in tandem with electrodes. Moreover, semi-quantitative modeling frameworks can enable the optimization of porous electrode structures for multiple system designs (e.g., redox chemistries, reactor architecture).

Going forward, the presented framework should be expanded by including complex flow field geometries, the modeling of the membrane [32] to simulate species crossover, and more detailed physics (e.g., migration [30], ion-ion interactions, partial wetting) to better capture the electrochemical behavior of emerging non-symmetric redox flow battery systems. Coupled with machine learning approaches, the proposed framework can be used as a predictive framework with the potential to accelerate the engineering of porous electrodes for specific electrolyte chemistries from the bottom-up.

2.6. References

[1] L. F. Arenas, C. Ponce de León, F. C. Walsh, *J. Energy Storage*. **11**, 119–153 (2017).
[2] C. Ponce de León, A. Frías-Ferrer, J. González-García, D. A. Szánto, F. C. Walsh, *J. Power Sources*. **160**, 716–732 (2006).
[3] S. Vazquez *et al.*, *IECON Proc.*, 4636–4640 (2011).
[4] P. Alotto, M. Guarnieri, F. Moro, *Renew. Sustain. Energy Rev.* **29**, 325–335 (2014).
[5] A. Z. Weber *et al.*, *J. Appl. Electrochem.* **41**, 1137–1164 (2011).
[6] D. O. Akinyele, R. K. Rayudu, *Sustain. Energy Technol. Assessments*. **8**, 74–91 (2014).
[7] A. Forner-Cuenca, E. E. Penn, A. M. Oliveira, F. R. Brushett, *J. Electrochem. Soc.* **166**, A2230–A2241 (2019).
[8] K. V. Greco, A. Forner-Cuenca, A. Mularczyk, J. Eller, F. R. Brushett, *ACS Appl. Mater. Interfaces*. **10**, 44430–44442 (2018).
[9] A. G. Lombardo, B. A. Simon, O. Taiwo, S. J. Neethling, N. P. Brandon, *J. Energy Storage*. **24**, 100736 (2019).
[10] M. A. Sadeghi *et al.*, *J. Electrochem. Soc.* **166**, A2121–A2130 (2019).
[11] X. Li, H. Zhang, Z. Mai, H. Zhang, I. Vankelecom, *Energy Environ. Sci.* **4**, 1147–1160 (2011).
[12] A. Tang, J. Bao, M. Skyllas-Kazacos, *J. Power Sources*. **248**, 154–162 (2014).
[13] Q. H. Liu *et al.*, *J. Electrochem. Soc.* **159**, A1246–A1252 (2012).
[14] K. T. Cho *et al.*, *J. Electrochem. Soc.* **159**, 1806–1815 (2012).
[15] B. K. Chakrabarti *et al.*, *Sustain. Energy Fuels*. **4**, 5433–5468 (2020).
[16] M. van der Heijden, A. Forner-cuenca, in *Encyclopedia of Energy Storage*, L. F. Cabeza, Ed. (Elsevier Inc., Oxford, ed. 2, 2022), pp. 480–499.
[17] Y. Ashraf Gandomi, D. S. Aaron, M. M. Mench, *Electrochim. Acta*. **218**, 174–190 (2016).
[18] A. M. Pezeshki, R. L. Sacci, F. M. Delnick, D. S. Aaron, M. M. Mench, *Electrochim. Acta*. **229**, 261–270 (2017).
[19] Q. Xu, T. S. Zhao, P. K. Leung, *Appl. Energy*. **105**, 47–56 (2013).
[20] D. K. Kim, S. J. Yoon, J. Lee, S. Kim, *Appl. Energy*. **228**, 891–901 (2018).
[21] J. L. Barton, F. R. Brushett, *Batteries*. **5**, 25 (2019).
[22] C. L. Chen, H. K. Yeoh, M. H. Chakrabarti, *Electrochim. Acta*. **120**, 167–179 (2014).
[23] A. A. Shah, M. J. Watt-Smith, F. C. Walsh, *Electrochim. Acta*. **53**, 8087–8100 (2008).
[24] D. You, H. Zhang, J. Chen, *Electrochim. Acta*. **54**, 6827–6836 (2009).
[25] D. Zhang *et al.*, *J. Power Sources*. **447**, 227249 (2020).
[26] G. Qiu *et al.*, *Electrochim. Acta*. **64**, 46–64 (2012).
[27] G. Qiu, C. R. Dennison, K. W. Knehr, E. C. Kumbur, Y. Sun, *J. Power Sources*. **219**, 223–234 (2012).
[28] J. Bao *et al.*, *Adv. Theory Simulations*. **3**, 1–13 (2020).
[29] S. J. Yoon, S. Kim, D. K. Kim, *Energy*. **172**, 26–35 (2019).
[30] M. Agnaou, M. A. Sadeghi, T. G. Tranter, J. Gostick, *Comput. Geosci.* **140**, 104505 (2020).
[31] J. Gostick *et al.*, *Comput. Sci. Eng.* **18**, 60–74 (2016).
[32] M. Aghighi, M. A. Hoeh, W. Lehnert, G. Merle, J. Gostick, *J. Electrochem. Soc.* **163**, F384–F392 (2016).
[33] R. Wu, Q. Liao, X. Zhu, H. Wang, *Int. J. Hydrogen Energy*. **37**, 11255–11267 (2012).
[34] J. T. Gostick, M. A. Ioannidis, M. W. Fowler, M. D. Pritzker, *J. Power Sources*. **173**, 277–290 (2007).
[35] B. A. Simon *et al.*, *Appl. Energy*. **306**, 117678 (2022).
[36] R. Banerjee, N. Bevilacqua, L. Eifert, R. Zeis, *J. Energy Storage*. **21**, 163–171 (2019).
[37] K. M. Tenny, A. Forner-Cuenca, Y.-M. Chiang, F. R. Brushett, *J. Electrochem. Energy Convers. Storage*. **17**, 041010 (2020).
[38] X. L. Zhou, T. S. Zhao, L. An, Y. K. Zeng, L. Wei, *J. Power Sources*. **339**, 1–12 (2017).
[39] A. A. Wong, M. J. Aziz, *J. Electrochem. Soc.* **167**, 110542 (2020).

[40] M. A. Sadeghi, M. Agnaou, J. Barralet, J. Gostick, *J. Contam. Hydrol.* **228**, 103578 (2020).
[41] J. E. Nutting, M. Rafiee, S. S. Stahl, *Chem. Rev.* **118**, 4834–4885 (2018).
[42] S. Jung *et al.*, *Int. J. Energy Res.* **43**, 2343–2360 (2019).
[43] D. Emmel *et al.*, *ACS Appl. Energy Mater.* **3**, 4384–4393 (2020).
[44] R. Banerjee *et al.*, *J. Energy Storage*. **26**, 100997 (2019).
[45] J. D. Milshtein, J. L. Barton, R. M. Darling, F. R. Brushett, *J. Power Sources*. **327**, 151–159 (2016).
[46] M. L. Porter, D. Wildenschild, *Comput. Geosci.* **14**, 15–30 (2010).
[47] J. Schindelin, C. T. Rueden, M. C. Hiner, K. W. Eliceiri, *Mol. Reprod. Dev.* **82**, 518–529 (2015).
[48] J. Sacha, IJ Plugins, (available at http://ij-plugins.sourceforge.net/).
[49] J. T. Gostick, *Phys. Rev. E*. **96**, 1–15 (2017).
[50] H. Fink, J. Friedl, U. Stimming, *J. Phys. Chem. C*. **120**, 15893–15901 (2016).
[51] Freudenberg Performance Materials, (2019).
[52] S. Hasanpour, M. Hoorfar, A. B. Phillion, *J. Power Sources*. **353**, 221–229 (2017).
[53] J. P. Feser, A. K. Prasad, S. G. Advani, *J. Power Sources*. **162**, 1226–1231 (2006).
[54] A. Forner-Cuenca, F. R. Brushett, *Curr. Opin. Electrochem.* **18**, 113–122 (2019).
[55] J. Gao, H. Li, Z. Luo, L. Gao, P. Li, *Computer Methods in Applied Mechanics and Engineering*, **344**, 451-476 (2019).
[56] K. Zhang, J. Xiong, C. Yan, A. Tang, *Appl. Energy*. **272**, 115093 (2020).
[57] T. Suga, Y. J. Pu, K. Oyaizu, H. Nishide, *Bull. Chem. Soc. Jpn.* **77**, 2203–2204 (2004).
[58] K. L. Hawthorne, J. S. Wainright, R. F. Savinell, *J. Electrochem. Soc.* **161**, A1662–A1671 (2014).
[59] U. Stimming, J. Wang, A. Bund, *ChemPhysChem*. **20**, 3004–3009 (2019).
[60] N. Bevilacqua *et al.*, *J. Power Sources*. **439**, 227071 (2019).
[61] L. Eifert *et al.*, *ChemSusChem*. **13**, 3154–3165 (2020).
[62] D. Zhang *et al.*, *Electrochim. Acta*. **283**, 1806–1819 (2018).
[63] H. Liu *et al.*, *Comput. Geosci.* **20**, 777–805 (2016).
[64] P. Virtanen *et al.*, *Nat. Methods*. **17**, 261–273 (2020).
[65] T. Davies, J. Tummino, *J. Carbon Res.* **4**, 8 (2018).
[66] J. T. Gostick, *J. Electrochem. Soc.* **160**, F731–F743 (2013).
[67] L. C. Ruspini *et al.*, *Transp. Porous Media*. **139**, 301–325 (2021).
[68] V. M. Palakkal *et al.*, *ACS Appl. Energy Mater.* **3**, 4787–4798 (2020).
[69] C. T. Wan *et al.*, *Adv. Mater.* **33**, 2006716 (2021).
[70] Z. Cheng *et al.*, *Appl. Energy*. **279**, 115530 (2020).

2.7. Appendix 2

A2.1. Abbreviations

Symbol	Description
ECSA	Electrochemically active surface area
EIS	Electrochemical impedance spectroscopy
MIP	Mercury intrusion porosimetry
MRE	Mean relative error
PN	Pore network
PNM	Pore network model
PSD	Pore size distribution
RFB	Redox flow battery
RMSE	Root-mean-square error
XTM	X-ray tomography

A2.2. List of symbols

Symbol	Description	Units
ΔP	Pressure drop	Pa
A_i	Electrochemically active internal surface area of pore i	m^2
A_{in}	Geometrical inlet area of the electrode	m^2
c	(a) Concentration	mol m^{-3}
	(b) Constant	A
D	Diffusion coefficient	m^2 s^{-1}
d_p	Pore diameter	m
E	Potential	V
E^0	Standard reduction potential	V
E_{oc}	Open-circuit potential	V
F	Faradaic constant, 96,485 C mol^{-1}	C mol^{-1}
I	Current	A
I_{ij}	Charge flux	A m^{-2}
i	Current density	A m^{-2}
j_0	Exchange current density	A m^{-2}
k_m	Mass transfer coefficient	m s^{-1}
L	Conduit length, length of the medium	m
m	(a) Mole flux	mol m^{-2} s^{-1}
	(b) Constant	V^{-1}
n	Number of electrons, iteration number, or data points	-
N_p	Number of pores	-
N_T	Number of throats	-
P	(a) External pressure	Pa
	(b) Power	W
p	Pressure	Pa
Pe	Peclet number	-
Q	Flow rate	m^3 s^{-1}
R	(a) Molar gas constant, 8.314 J mol^{-1} K^{-1}	J mol^{-1} K^{-1}
	(b) Resistance	Ω
	(c) Net reaction rate	mol s^{-1}
S	Cross-sectional area	m^2
S_{red}	Source term	A
T	Operating temperature	K

u	Fluid velocity	m s^{-1}
V	Voltage	V
V_{cell}	Given cell potential	V
X	Concentration or potential	mol m^{-3} or V
x	Current density	A m^{-2}
	Greek	
α	(a) Transfer coefficient	-
	(b) Hydraulic conductance of the throat	m Pa^{-1} s^{-1}
β	Electrical conductance	S m^{-2}
γ	Surface tension	N m^{-1}
ϵ	Error value	-
η	Overpotential	V
η_p	Pumping energy efficiency	-
θ	Contact angle	°
κ	Permeability	m^2
λ	Stoichiometric coefficient	-
μ	Dynamic viscosity	Pa s
ρ	Electrolyte density	kg m^{-3}
σ_l	Electrical bulk conductivity	S m^{-1}
φ	Potential	V
ω	Relaxation factor	-
	Superscripts	
a	Anode	
$ad-dif$	Advection-diffusion	
c	Cathode	
n	Iteration number	
ox	Oxidized form	
red	Reduced form	
	Subscripts	
$1, 2, 3$	Constants numbers	
a	Anode	
abs	Absolute	
act	Activation	
b	Bulk	
c	Cathode	
$conc$	Concentration	
e	Electrolyte, liquid phase	
el	Electrode, electrochemical	
exp	Experimental	
i	Within pore i, specie i	
$ideal$	Ideal	
ij	Pore i to pore j, throat ij	
in	Inlet	
$iR\Omega$	iR_Ω-corrected	
j	Within pore j, specie j	
loc	Local	
$losses$	Losses	
m	Membrane	
ohm	Ohmic	
out	Outlet	

pnm	Pore network model
$pump$	Pumping
ref	Reference
rel	Relative
s	Solid phase, surface
$theory$	Theoretical
tot	Total

A2.3. Model development

A2.3.1. Linearization of the source term

The charge transport equation is highly nonlinear since the current generation term is exponentially dependent on the overpotential term. When the considered active species has facile kinetics (i.e., a high exchange current density), the mass and charge transport equations are strongly coupled. To mitigate divergence, the charge transport source term is linearized around the current solution for the voltage field. The derivation of the charge transfer source term for the cathodic compartment is shown here. A similar derivation was conducted for the anodic compartment.

The governing cathodic Butler-Volmer equation can be rewritten to

$$I_c = \frac{c_1[\exp(m_1\eta_c) - \exp(-m_2\eta_c)]}{1 + c_2\exp(m_1\eta_c) + c_3\exp(-m_2\eta_c)} \tag{A2.1}$$

using the following terms $c_1 = j_0^c A_i \left(\frac{C_i^{ox}}{C_{ref}^{ox}}\right)$, $c_2 = \frac{j_0^c}{Fk_m^{red}c_{ref}^{red}}$, $c_3 = \frac{j_0^c}{Fk_m^{ox}c_{ref}^{ox}}$, $m_1 = \frac{\alpha_a F}{RT}$ and $m_2 = \frac{\alpha_c F}{RT}$.
Furthermore, the overpotential term can be rewritten to

$$\varphi_e = \varphi_s - \eta_c - E_{oc}. \tag{A2.2}$$

When taking the derivative with respect to the electrolyte potential, the following relation is obtained

$$\frac{dI_c}{d\varphi_e} = \frac{\begin{pmatrix} c_1\begin{pmatrix} -c_3m_2\exp(m1\eta_c - m_2\eta_c) - c_2m_2\exp(m1\eta_c - m_2\eta_c) \\ -c_2m_1\exp(m1\eta_c - m_2\eta_c) - c_3m_1\exp(m1\eta_c - m_2\eta_c) \\ -m_2\exp((-m_2\eta_c) - m1\exp(m_1\eta_c) \end{pmatrix} \end{pmatrix}}{(1+c_2\exp(m_1\eta_c) + c_3\exp(-m_2\eta_c))^2}. \tag{A2.3}$$

Subsequently, the source term, S_{red}, can be linearized

$$S_{red} = \frac{dI_c}{d\varphi_e}\varphi_e^n + I_c^{ad-dif} - \frac{dI_c}{d\varphi_e}\varphi_e^{n-1}, \tag{A2.4}$$

with φ_e^n the new potential field to be solved, I_c^{ad-dif} the current field obtained from the mass transport equation, and φ_e^{n-1} the previous estimation of the potential field.

A2.3.2. Network-in-series model

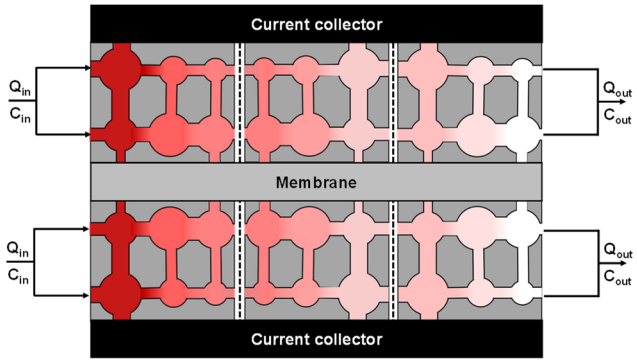

Figure A2.1: Schematic visualization of the network-in-series model, shown for three pore networks separated by dashed lines. Convective transport takes place from the left to the right. Species consumption is depicted by the color in the network, where concentration overpotentials are larger at the end of the porous electrode.

A2.4. Network extraction

A2.4.1. Mercury intrusion porosimetry

In mercury intrusion porosimetry, external pressure is applied to force the intrusion of mercury within a porous substrate. The applied external pressure can be related to the pore diameter by the Washburn equation

$$d_p = -\frac{4\gamma \cos\theta}{\mathrm{P}}, \tag{A2.5}$$

with P the external pressure, d_p the pore diameter, γ the surface tension of mercury, and θ the contact angle between mercury and the wall. Forner-Cuenca *et al.* [1] assumed a constant contact angle of 130° in their measurements to derive the pore size distribution.

A2.4.2. Larger extracted cloth electrode

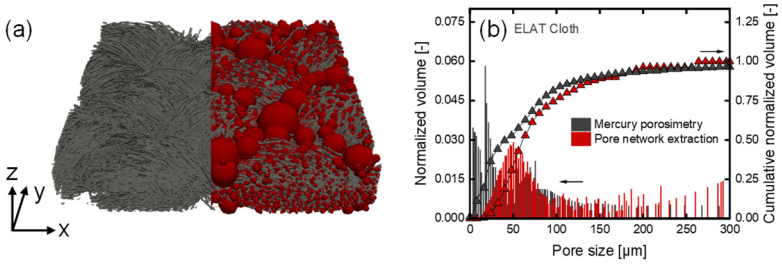

Figure A2.2: The network extraction of the 1.7 mm x 1.7 mm cloth electrode, where: **(a)** is the visual representation of the processed X-ray tomography image overlaid with the extracted pore network, and **(b)** the normalized pore size distribution and the cumulative normalized volume with mercury intrusion porosimetry and the SNOW pore network extraction algorithm, where the normalized volume is defined as the fraction of the total pore volume occupied by all pores within a 2 µm pore size range.

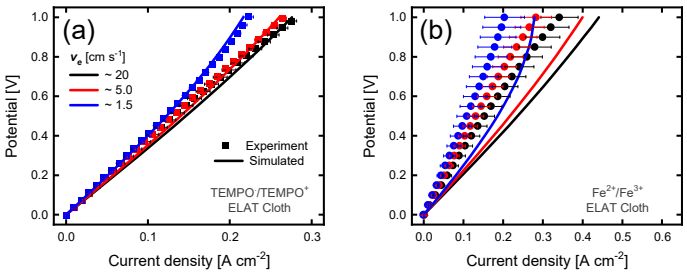

Figure A2.3: Experimental data and the simulations of the larger extracted network (1.7 mm x 1.7 mm), showing the polarization curves by plotting the current density versus the potential for the cloth electrode at inlet velocities of 20, 5.0, and 1.5 cm s^{-1} for the two distinct chemistries: **(a)** the non-aqueous electrolyte, and **(b)** the aqueous electrolyte. The experimental data of the three experiments per system (**Figure A2.5**) was averaged and shown with error bars indicating the standard deviation of the current density.

Table A2.1: Network properties of the 1.7 mm x 1.7 mm extracted pore network, and the experimental data, *estimated from data found in [2, 3], **obtained using the open-source image analysis package PoreSpy. It must be noted that some materials from the literature might contain small amounts of polytetrafluorethylene.

Electrode	Parameter	Experiment	Pore network (1.7 mm x 1.7 mm)
ELAT Cloth	In-plane permeability x 10^{-12} [m^2]	44 [4, 5]	53
	Through-plane permeability x 10^{-12} [m^2]	21 [4]	35
	Anisotropy ratio [-]	2.1	1.5
	Internal surface area [m^2 m^{-3}]	1.4 x 10^4 [6], 8.6 x 10^4**	1.3 x 10^5
	Porosity [-]	0.82 [1], 0.73**	0.74
	Apparent density [kg m^{-3}]	289	
	Thickness [µm]	380-406 [1]	375

A2.5. Model validation

A2.5.1. Exchange current density

Table A2.2: Exchange current density values for both electrodes and electrolyte types.

Electrode	Chemistry	Velocity [cm s^{-1}]	Exchange current density [A m^{-2}]
Freudenberg H23	TEMPO	20	1750
		5.0	1370
		1.5	460
	Iron	20	652
		5.0	478
		1.5	172
ELAT Cloth	TEMPO	20	1680
		5.0	1870
		1.5	606
	Iron	20	625
		5.0	198
		1.5	98.7

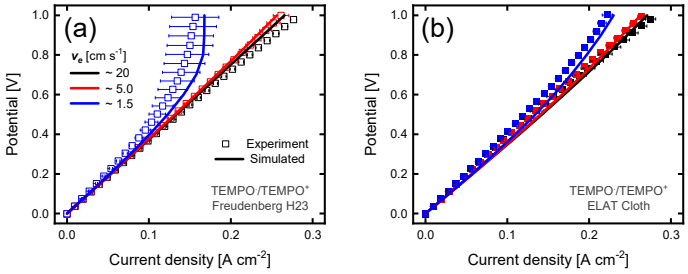

Figure A2.4: Comparison of the polarization curves of the simulated data and the corresponding experimental data by plotting the current density versus the potential at inlet velocities of 20, 5.0, and 1.5 cm s^{-1} for the non-aqueous electrolyte, using the exchange current density value from the literature of 375 A m^{-2} [7], for: **(a)** the paper electrode, and **(b)** the cloth electrode. The experimental data of the three experiments per system (**Figure A2.5**) was averaged and shown with error bars indicating the standard deviation of the current density.

A2.5.2. Experimental data

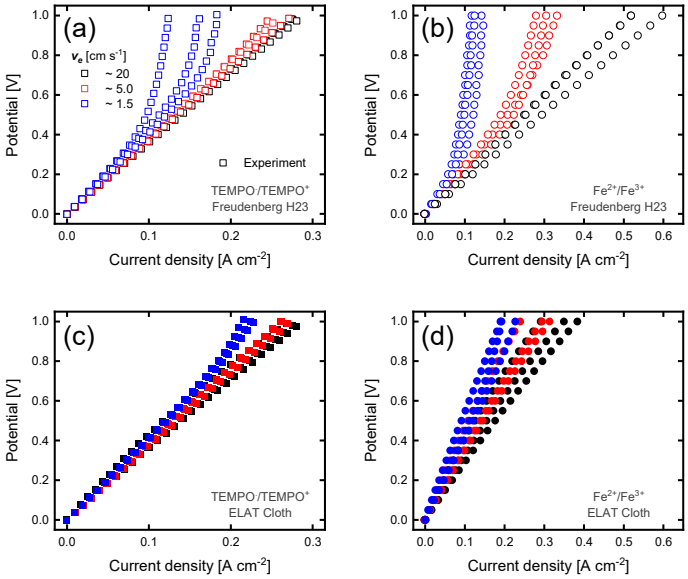

Figure A2.5: Experimental data showing the polarization curves of all three performed experiments by plotting the current density versus the potential for two distinct chemistries and two electrodes at inlet velocities of 20, 5.0, and 1.5 cm s^{-1}, for: **(a)** the paper electrode with a non-aqueous electrolyte, **(b)** the paper electrode with an aqueous electrolyte, **(c)** the cloth electrode with a non-aqueous electrolyte, and **(d)** the cloth electrode with an aqueous electrolyte.

A2.5.3. Model accuracy

To quantify the accuracy of the model, the root-mean-square error (RMSE) and the mean relative error (MRE) were calculated for the different systems, given by:

$$RMSE(x) = \sqrt{1/n * \sum_{i=1}^{n} \left(x_{i,exp} - x_{i,pnm}\right)^2} \tag{A2.6}$$

$$MRE(x) = 1/n * \sum_{i=1}^{n}((x_{i,exp} - x_{i,pnm})/x_{i,pnm}), \quad \text{(A2.7)}$$

where x_i is the current density for n data points [8, 9].

Table A2.3: Root-mean-square error (RMSE) and mean relative error (MRE) values for the model validation with respect to the experimental data for both electrodes and electrolytes.

Electrode	Chemistry	Velocity [cm s^{-1}]	RMSE [A cm^{-2}]	MRE [%]
Freudenberg H23	TEMPO	20	0.005	4.0
		5.0	0.008	6.0
		1.5	0.015	11
	Iron	20	0.012	4.7
		5.0	0.078	24
		1.5	0.047	32
ELAT Cloth	TEMPO	20	0.012	9.8
		5.0	0.013	9.8
		1.5	0.013	11
	Iron	20	0.107	41
		5.0	0.114	46
		1.5	0.086	46

A2.6. Incomplete wetting and parameter adaptation

A2.6.1. Parameter adaptation

Table A2.4: The multiplication factor of the mass transfer coefficient (k_m), together with the root-mean-square error (RMSE) and mean relative error (MRE) values for the corrected data in comparison to the experimental data for the two electrodes and the aqueous chemistry.

Electrode	Velocity [cm s^{-1}]	k_m factor [-]	RMSE [A cm^{-2}]	MRE [%]
Freudenberg H23	20	1.0	0.012	4.8
	5.0	0.27	0.006	2.7
	1.5	0.11	0.010	6.8
ELAT Cloth	20	0.31	0.031	20
	5.0	0.26	0.033	23
	1.5	0.22	0.028	25

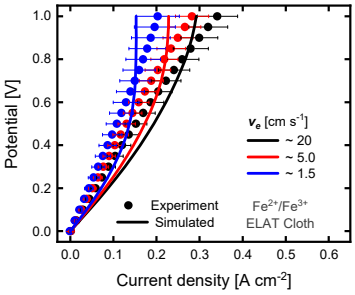

Figure A2.6: Comparison of the polarization curves of the simulated data with corrected mass transfer coefficient, and the corresponding experimental data by plotting the current density versus the potential at inlet velocities of 20, 5.0, and 1.5 cm s^{-1} for the aqueous electrolyte. The experimental data of the three experiments per system (**Figure A2.5**) was averaged and shown with error bars indicating the standard deviation of the current density.

A2.6.2. Electrochemical impedance spectroscopy

Electrochemical impedance spectroscopy measurements were conducted using a Biologic VMP-300 potentiostat at open-circuit voltage and room temperature (20 °C) with an amplitude of 10 mV, a frequency range of 10 kHz - 200 mHz, 8 points per decade, 6 measures per frequency, with a sinus amplitude of 20 mV, and a waiting time of 0.10 period before each frequency. These measurements were performed for the uncompressed, 48% compressed, and taurine-treated cloth electrodes.

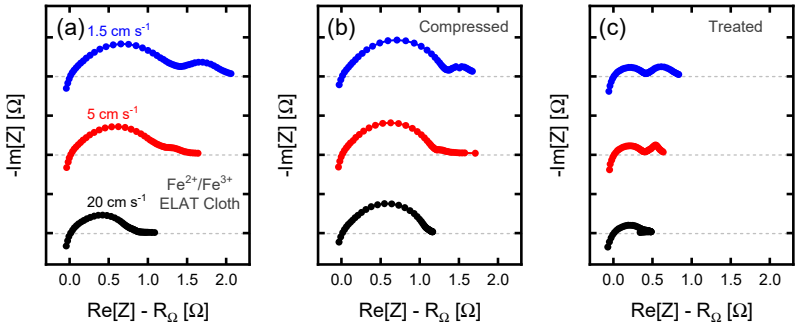

Figure A2.7: Experimentally obtained electrochemical impedance spectroscopy data of the aqueous electrolyte and the cloth electrode at three inlet velocities: 20, 5.0, and 1.5 cm s^{-1} at open-circuit voltage for: **(a)** the uncompressed electrode, **(b)** the 48% compressed electrode, using incompressible polytetrafluoroethylene gaskets of 210 µm, and **(c)** the taurine electrografted electrode.

A2.6.3. Taurine electrografted electrode

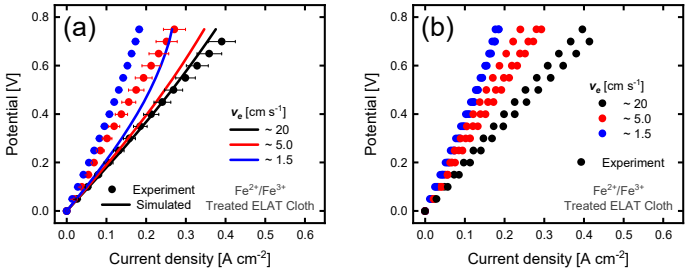

Figure A2.8: (a) Comparison of the polarization curves of the simulated and corresponding experimental data by plotting the current density versus the potential, and **(b)** experimental data showing the polarization curves of all three performed experiments by plotting the current density versus the potential. Both for the aqueous electrolyte and the taurine electrografted cloth electrode at inlet velocities of 20, 5.0, and 1.5 cm s^{-1}. The experimental data of the three experiments per system (**b**) was averaged and shown with error bars indicating the standard deviation of the current density.

A2.6.4. Resistance correction

Table A2.5: The multiplication factor of the mass transfer coefficient (k_m) and the resistance factor, together with the root-mean-square error (RMSE) and mean relative error (MRE) values for the corrected data in comparison to the experimental data for the cloth electrode and the aqueous electrolyte.

Velocity [cm s^{-1}]	k_m factor [-]	Resistance factor [-]	RMSE [A cm^{-2}]	MRE [%]
20	1	2.2	0.011	7.6
5.0	1	2.7	0.007	5.7
1.5	0.50	3.4	0.004	2.8

A2.7. Porous electrode performance

A2.7.1. Current density profiles

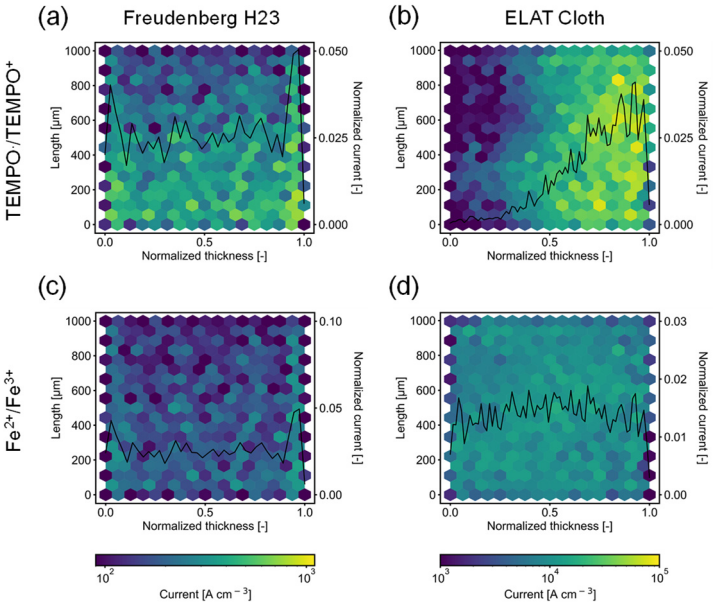

Figure A2.9: 2D current profiles with the accumulated current corrected for the volume of the network, and 1D current profiles of the normalized current (total current normalized to unity), at -1 V and 1.5 cm s^{-1} shown over the length and width of the electrode, for: **(a)** the non-aqueous electrolyte and the paper electrode, **(b)** the non-aqueous electrolyte and the cloth electrode, **(c)** the paper electrode and the aqueous electrolyte, and **(d)** the cloth electrode and the aqueous electrolyte. The plots are shown for the last network in the network-in-series model with the membrane side facing the right and with the flow direction from the bottom to the top.

A2.7.2. Overpotential calculation

The obtained electrode overpotential, which is the applied cell potential in a single-electrolyte cell configuration: $E_{cell} = |\eta_{act}| + |\eta_{conc}| + |\eta_{ohm}|$, can be divided into three overpotential terms: the activation (η_{act}), concentration (η_{conc}), and ohmic overpotential (η_{ohm}). The activation overpotential is defined as the potential difference above the equilibrium potential that is required to produce the achieved current, neglecting the effect of the surface concentration in the Butler-Volmer equation. The activation overpotential term is found for every pore by minimizing the difference between the ideal current and the obtained current (**equations (2.6)** and **(2.7)**), where the ideal current is defined as

$$I_{a,ideal} = j_0^a A_i \left(\frac{c_{in}^{red}}{c_{ref}^{red}}\right)\left[\exp(-\frac{\alpha_a F \eta_{a,act}}{RT}) - \exp(\frac{\alpha_c F \eta_{a,act}}{RT})\right] \quad \text{(A2.8)}$$

$$I_{c,ideal} = j_0^c A_i \left(\frac{c_{in}^{ox}}{c_{ref}^{ox}}\right)\left[\exp(\frac{\alpha_a F \eta_{c,act}}{RT}) - \exp(-\frac{\alpha_c F \eta_{c,act}}{RT})\right], \quad \text{(A2.9)}$$

where c_{in} is the inlet concentration of the active species.

The concentration overpotential, on the other hand, is defined as the summation of mass transfer and depletion effects on the overpotential. The concentration overpotential can be obtained

by subtracting the overpotential found using **equations (2.8)** and **(2.9)** by the activation overpotential from **equations (A2.8)** and **(A2.9)**.

Lastly, the ohmic overpotential within an electrode takes the electrolytic and membrane resistivity into account and can be obtained from the potential field by

$$\eta_{ohm,el} = \varphi_i - \varphi_m, \tag{A2.10}$$

where φ_i is the electrolyte potential in pore i, and φ_m the average potential in the pores closest to the membrane in the considered electrode. The contribution of the membrane can be obtained directly from **equation (2.21)**.

A2.7.3. Overpotential contributions

Table A2.6: The contributions of the activation, concentration, ohmic (without the membrane overpotential), and the membrane overpotential to the overall overpotential loss in the system for both electrodes and chemistries, analyzed at -1 V.

Electrode	Chemistry	Velocity [cm s^{-1}]	Activation [%]	Concentration [%]	Ohmic [%]	Membrane [%]
Freudenberg H23	TEMPO	20	0.4	1.0	43	55
		5.0	0.4	1.5	45	53
		1.5	0.8	27	40	33
	Iron	20	1.9	6.6	40	52
		5.0	2.3	14	39	44
		1.5	2.2	65	16	17
ELAT Cloth	TEMPO	20	0.2	1.7	43	55
		5.0	0.2	2.1	45	53
		1.5	0.5	4.5	49	46
	Iron	20	1.3	9.9	42	47
		5.0	3.4	12	41	43
		1.5	4.4	37	31	28

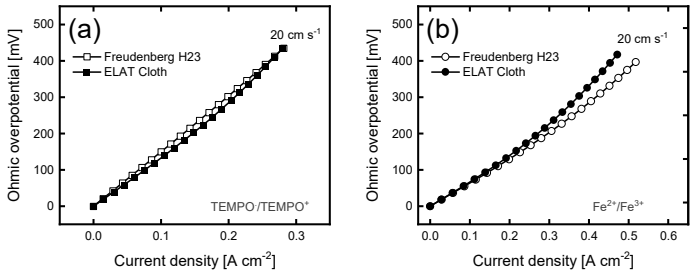

Figure A2.10: Ohmic overpotential contribution to the polarization curves at 20 cm s^{-1} inlet velocity for the paper and cloth electrode without fitting parameters, for: **(a)** the non-aqueous chemistry, and **(b)** the aqueous chemistry. The ohmic overpotential is plotted without the contribution of the membrane. The explanation of how the overpotentials were extracted from the model is given in **Section A2.7.2**.

A2.8. Operation envelopes

For this study, an exchange current density sweep was performed at 1 x 10^{10}, 1 x 10^{5}, 1750, 1, 1 x 10^{-2}, and 1 x 10^{-4} A m^{-2} using the electrolyte parameters of the non-aqueous chemistry, and a velocity sweep at 5, 1, 0.5, 0.2, 0.05, 0.01, 0.005, 0.001, and 0.0005 cm s^{-1} for both chemistries.

The inverse relation between the exchange current density and the activation overpotential is presented in **Figure A2.11a**. Improved kinetics result in increased current densities, a higher reactant consumption, and higher ohmic and concentration overpotentials. The balance between the ohmic and concentration overpotentials is dependent on the specific operating conditions (inlet velocity, inlet concentration), electrolyte properties (effective conductivity, diffusion coefficient), and electrode microstructure (permeability, pore size distribution, thickness). When analyzing the behavior of the two porous electrodes, it is observed that the cloth electrode has lower reactant consumption at the same exchange current densities but on the contrary, shows a higher concentration overpotential than the paper electrode (**Figure A2.11b**). This highlights the relationship between the exchange current density and porous electrode microstructure, showing the potential of this model for a fast parametric sweep providing microstructure-informed information. Furthermore, it is observed that with increasing exchange current densities, a maximum current density is reached, resulting in a constant concentration, concentration overpotential, and ohmic overpotential, highlighting the potential to evaluate parameter or performance regions/envelopes with this model.

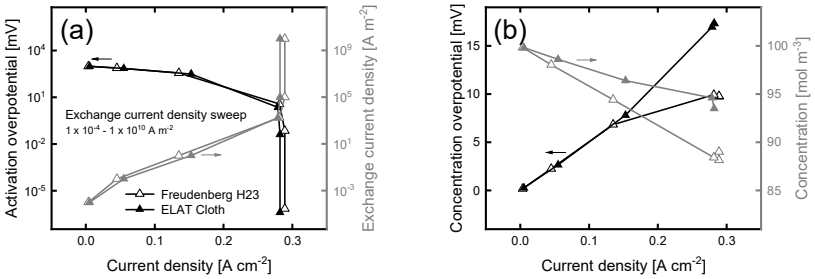

Figure A2.11: The effect of the exchange current density simulated with the PNM with the electrolyte properties of the non-aqueous electrolyte evaluated at 20 cm s^{-1} and -1 V on: **(a)** the activation overpotential and current density, simultaneously showing the exchange current density range used, and **(b)** the concentration overpotential and active species concentration in the last network. The exchange current density sweep was performed at 1 x 10^{10}, 1 x 10^{5}, 1750, 1, 1 x 10^{-2}, and 1 x 10^{-4} A m^{-2}.

The electrolyte velocity affects the performance of the battery differently by strongly affecting the (limiting) current density, concentration, and pressure drop (see **Figure A2.12** and **Table A2.7**). High velocities result in fast electrolyte replenishment, increasing the number of active species that can react, and reaching higher (limiting) current densities. Furthermore, a higher velocity decreases the amount of local reactant depletion zones, thus decreasing the overall concentration overpotential in the system. Care must be taken with increasing velocities, as the pressure drop increases linearly with the velocity, indicating that the velocity is an important cell parameter to optimize concerning the trade-off in pumping requirements and achievable current densities. This trade-off was visualized in **Figure A2.14**, where the iR_{Ω}-corrected electrochemical power (current output multiplied by the iR_{Ω}-corrected applied potential) and pumping power (pressure drop multiplied by the flow rate and corrected for a pumping power efficiency, which was assumed 90 % efficient [9]) are plotted for both performed parameter sweeps. This figure contains demarcations of unity and ten indicated by the dashed lines, showing a possible trade-off between the electrochemical power output and pumping power requirements useful in the optimization of next-generation porous electrodes, electrolytes, and system parameters.

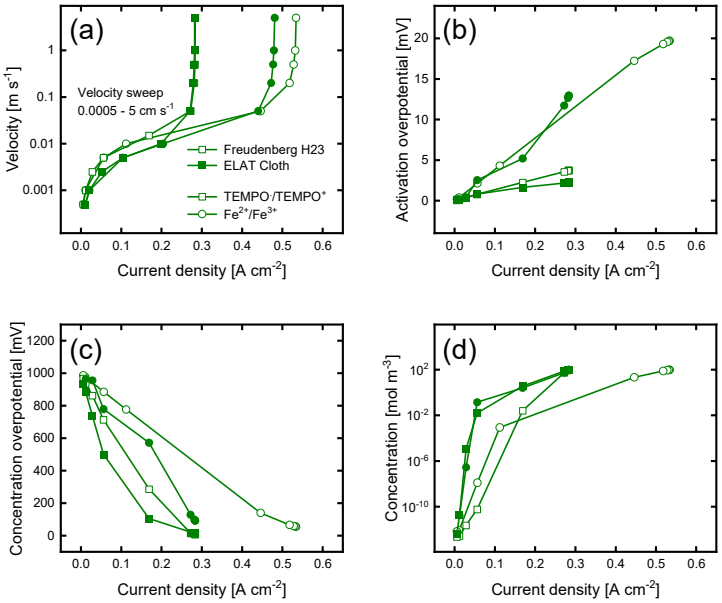

Figure A2.12: The effect of the velocity simulated with the pore network model for both electrodes and electrolytes evaluated at -1 V on: **(a)** the velocity range and current density, **(b)** the activation overpotential, **(c)** the concentration overpotential, and **(d)** the active species concentration in the last network. The velocity sweep was performed at 5.0, 1.0, 0.5, 0.2, 0.05, 0.01, 0.005, 0.001, and 0.0005 m s^{-1}.

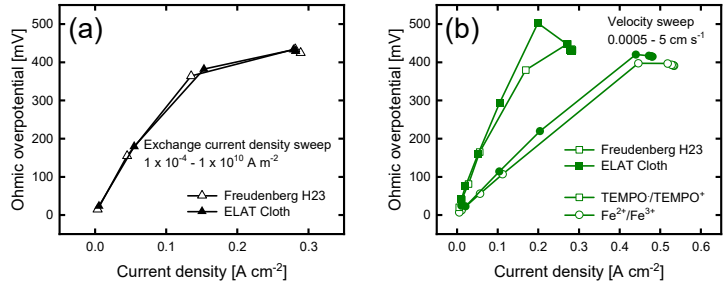

Figure A2.13: The ohmic overpotential over current density for the two parameter sweeps for both electrode types evaluated at -1 V, where: **(a)** shows the exchange current density parameter sweep performed at 1 x 10^{10}, 1 x 10^{5}, 1750, 1, 1 x 10^{-2}, and 1 x 10^{-4} A m^{-2} using the electrolyte properties of the non-aqueous electrolyte, and **(b)** shows the velocity parameter sweep performed at 5.0, 1.0, 0.5, 0.2, 0.05, 0.01, 0.005, 0.001, and 0.0005 m s^{-1} for both electrolytes.

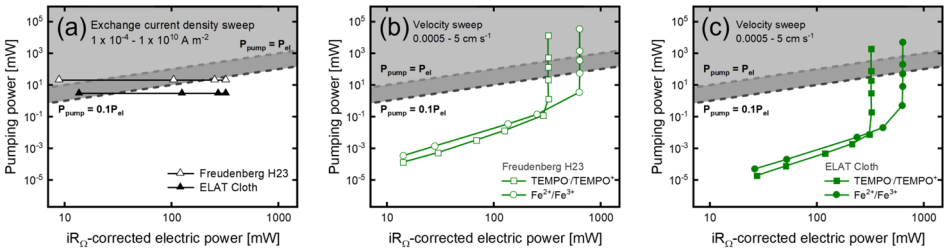

Figure A2.14: The pumping power over iR_Ω-corrected electric power for two parameter sweeps evaluated at -1 V, where: **(a)** shows the exchange current density parameter sweep performed at 1 x 10^{10}, 1 x 10^5, 1750, 1, 1 x 10^{-2}, and 1 x 10^{-4} A m^{-2} using the electrolyte properties of the non-aqueous electrolyte for both electrode types, and **(b)** and **(c)** show the velocity parameter sweep performed at 5.0, 1.0, 0.5, 0.2, 0.05, 0.01, 0.005, 0.001, and 0.0005 m s^{-1} for both electrolytes, for **(b)** the paper electrode and **(c)** the cloth electrode. The dashed lines and shaded regions indicate a demarcation of unity and ten [1].

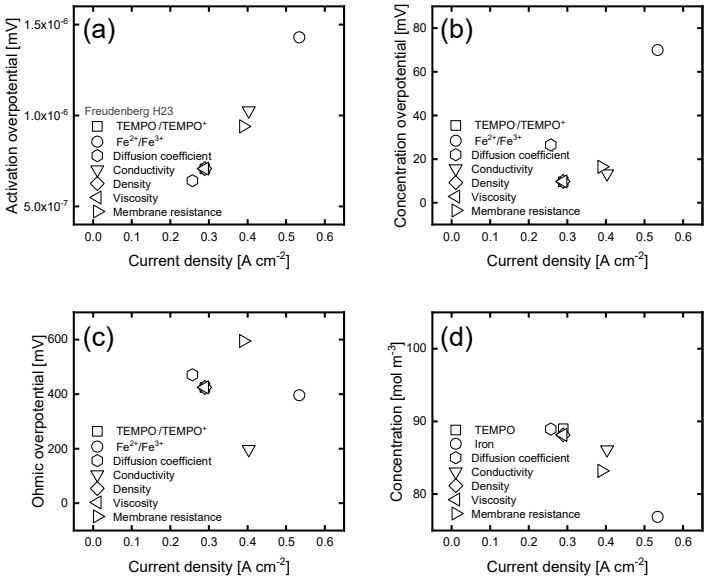

Figure A2.15: The effect of the diffusion coefficient, conductivity, density, viscosity, and membrane resistance of the aqueous chemistry compared to non-aqueous chemistry, simulated with the pore network model, on: **(a)** the activation overpotential, **(b)** concentration overpotential, **(c)** ohmic overpotential without the contribution of the membrane, and **(d)** average concentration in the last network, plotted against the current density at - 1 V, a velocity of 20 cm s^{-1}, and an exchange current density of 1 x 10^{10} A m^{-2} for the paper electrode.

This study enables a way to investigate the effect of different electrolyte parameters individually, e.g., the diffusion coefficient, conductivity, density, viscosity, and membrane resistance. When comparing both chemistries (**Table A2.7**), it is observed that the aqueous chemistry has a greater current density at fixed potential; however, the non-aqueous chemistry has a greater limiting current density and a lower pressure drop. To evaluate which parameters contribute to the different performances, simulations were run to evaluate the effect of one parameter corresponding to the aqueous chemistry compared to the non-aqueous chemistry (see **Figure A2.15** and **Table A2.8**). First, it can be observed that a higher conductivity or a lower membrane resistance enables operation at higher current densities at a fixed potential, thus increasing the contribution of reactant depletion effects in the electrode, additionally affecting the overpotential contributions. Second, the diffusion coefficient influences the limiting current density

and concentration overpotential, which is a direct result of the simplification of how the mass transfer coefficient in the pores was defined in this model (**equation (2.12)**). To evaluate the effect of the diffusion coefficient more precisely, an extended mass conservation equation must be implemented in the model (e.g., the Nernst-Planck [10], or Stefan-Maxwell equation [11]). Finally, the density and viscosity slightly influence the concentration in the system and the viscosity also defines the pressure drop in the system (resistance to flow).

Table A2.7: The current density at -1 V, limiting current density, and the pressure for various exchange current density or velocity values for both electrodes and chemistries.

Electrode	Chemistry	Exchange current density [A m^{-2}]	Velocity [m s^{-1}]	Current density [A cm^{-2}]	Limiting current density [A cm^{-2}]	Pressure [Pa]
Freudenberg	TEMPO	1750	0.2	0.28	1.8	2.7×10^4
		1×10^{10}	0.2	0.29	1.8	2.7×10^4
		1×10^5	0.2	0.29	1.8	2.7×10^4
		1	0.2	0.14	1.8	2.7×10^4
		1×10^{-2}	0.2	0.045	1.8	2.7×10^4
		1×10^{-4}	0.2	0.004	1.8	2.7×10^4
		1750	5.0	0.28	0.34	6.8×10^5
		1750	1.0	0.28	0.30	1.4×10^5
		1750	0.5	0.28	0.26	6.8×10^4
		1750	0.05	0.27	0.056	6.8×10^3
		1750	0.015	0.17	0.017	2.0×10^3
		1750	0.005	0.056	0.056	6.8×10^2
		1750	0.0025	0.028	0.028	3.4×10^2
		1750	0.001	0.012	0.012	1.4×10^2
		1750	0.0005	0.006	0.006	68
	Iron	652	5.0	0.53	1.5	1.8×10^6
		652	1.0	0.53	1.5	3.5×10^5
		652	0.5	0.53	1.4	1.8×10^5
		652	0.2	0.52	1.1	7.0×10^4
		652	0.05	0.45	0.52	1.8×10^4
		652	0.01	0.11	0.11	3.5×10^3
		652	0.005	0.056	0.056	1.8×10^3
		652	0.001	0.011	0.011	3.5×10^2
		652	0.0005	0.006	0.006	1.8×10^2
ELAT Cloth	TEMPO	1750	0.2	0.28	1.7	2.2×10^3
		1×10^{10}	0.2	0.28	1.7	2.2×10^3
		1×10^5	0.2	0.28	1.7	2.2×10^3
		1	0.2	0.15	1.7	2.2×10^3
		1×10^{-2}	0.2	0.055	1.7	2.2×10^3
		1×10^{-4}	0.2	0.005	1.7	2.2×10^3
		1750	5.0	0.28	2.3	5.4×10^4
		1750	1.0	0.28	2.2	1.1×10^4
		1750	0.5	0.28	0.03	5.4×10^3
		1750	0.05	0.27	0.89	5.4×10^2
		1750	0.01	0.20	0.21	1.1×10^2
		1750	0.005	0.11	0.11	54
		1750	0.0025	0.052	0.052	27
		1750	0.001	0.021	0.021	11
		1750	0.0005	0.011	0.011	5.4
	Iron	652	5.0	0.48	1.0	1.4×10^5
		652	1.0	0.48	0.99	2.8×10^4
		652	0.5	0.48	0.96	1.4×10^4
		652	0.2	0.47	0.88	5.6×10^3
		652	0.05	0.44	0.62	1.4×10^3
		652	0.01	0.20	0.20	2.8×10^2
		652	0.005	0.10	0.10	1.4×10^2
		652	0.001	0.021	0.021	28
		652	0.0005	0.010	0.011	14

Table A2.8: The current density at - 1 V, limiting current density, and pressure drop showing the effect of the diffusion coefficient, conductivity, density, viscosity, and membrane resistance of the aqueous chemistry compared to the non-aqueous chemistry.

Chemistry	Exchange current density [A m^{-2}]	Velocity [m s^{-1}]	Current density [A m^{-2}]	Limiting current density [A m^{-2}]	Pressure [Pa]
TEMPO	1 x 10^{10}	0.2	28.9	177	27001
Iron	1 x 10^{10}	0.2	53.4	112	70061
Iron $D_{F2/3}$	1 x 10^{10}	0.2	25.7	112	27001
Iron σ_l	1 x 10^{10}	0.2	40.3	177	27001
Iron ρ_l	1 x 10^{10}	0.2	28.9	177	27001
Iron μ	1 x 10^{10}	0.2	28.9	177	70061
Iron R_m	1 x 10^{10}	0.2	38.9	177	27001

A2.9. References

[1] A. Forner-Cuenca, E. E. Penn, A. M. Oliveira, F. R. Brushett, *J. Electrochem. Soc.* **166**, A2230–A2241 (2019).
[2] Freudenberg Performance Materials, (2019).
[3] S. Hasanpour, M. Hoorfar, A. B. Phillion, *J. Power Sources*. **353**, 221–229 (2017).
[4] A. A. Wong, M. J. Aziz, *J. Electrochem. Soc.* **167**, 110542 (2020).
[5] J. P. Feser, A. K. Prasad, S. G. Advani, *J. Power Sources*. **162**, 1226–1231 (2006).
[6] A. Forner-Cuenca, F. R. Brushett, *Curr. Opin. Electrochem.* **18**, 113–122 (2019).
[7] T. Suga, Y. J. Pu, K. Oyaizu, H. Nishide, *Bull. Chem. Soc. Jpn.* **77**, 2203–2204 (2004).
[8] S. Ressel *et al.*, *J. Power Sources*. **378**, 776–783 (2018).
[9] Z. Cheng *et al.*, *Appl. Energy*. **279**, 115530 (2020).
[10] M. Agnaou, M. A. Sadeghi, T. G. Tranter, J. Gostick, *Comput. Geosci.* **140**, 104505 (2020).
[11] A. Z. Weber *et al.*, *J. Electrochem. Soc.* **161**, F1254–F1299 (2014).

Chapter 3

Understanding the role of electrode thickness on redox flow cell performance

Abstract

The electrode thickness is a critical design parameter to engineer high-performing flow cells by impacting the available surface area for reactions, current and potential distributions, and required pumping power. To date, redox flow cell assemblies employ repurposed off-the-shelf fibrous electrodes that feature a broad range of thicknesses. However, comprehensive guidelines to select the optimal electrode thickness for a given reactor architecture remain elusive. Here, we investigate the effect of the electrode thickness in the range of 200 - 1100 µm on the cell performance by stacking electrode layers in four different flow cell configurations – Freudenberg paper and ELAT cloth electrodes combined with flow-through and interdigitated flow fields. We employ a suite of polarization, electrochemical impedance spectroscopy, and pressure drop measurements together with pore network modeling simulations to correlate the electrode thickness for various reactor designs to the electrochemical and hydraulic performance. We find that thicker electrodes (420 µm paper electrodes and 812 µm cloth electrodes) are beneficial in combination with flow-through flow fields, whereas when using interdigitated flow fields, thinner electrodes (210 µm paper electrodes and 406 µm cloth electrodes) result in a better current density and pressure drop trade-off. We hope our findings will aid researchers and technology practitioners in designing their electrochemical flow cells under convective operation.

This chapter is accepted for publication in *ChemElectroChem*:

V. Muñoz-Perales[*], M. van der Heijden[*], V. de Haas, J. Olinga, M. Vera, and A. Forner-Cuenca, Understanding the role of electrode thickness on redox flow cell performance, *ChemElectroChem* (2023), doi:10.1002/celc.202300380.

[*]Co-first authors

3.1. Introduction

Large-scale and stationary energy storage technologies are poised to play a notable role in the decarbonization of the electrical sector by facilitating the integration of renewable energy sources in the electricity grid [1–3]. Redox flow batteries (RFBs) are a promising electrochemical technology for low-cost, scalable, and long-duration energy storage [4, 5]. RFBs are rechargeable batteries that electrochemically store energy in redox active species dissolved or suspended in electrolyte solutions housed in external tanks. During operation, the solutions are pumped through an electrochemical stack in which the flow field supplies the electrolyte to the porous electrode in two distinct half-cells separated by a membrane, to charge or discharge the battery [6, 7]. Their appealing features of decoupling power and energy, high round-trip efficiency, extended durability, and low environmental impact position them ahead of enclosed batteries (e.g., lithium-ion batteries) for large-scale and stationary applications [4, 8]. Despite the technological maturity and advantages of RFBs, their current elevated costs and limited power and energy density have challenged their market penetration and widespread adoption [9–11]. To increase cost competitiveness and system efficiency, research efforts address technology limitations through the development and engineering of high-performance materials [12–16], alternative flow cell designs [17, 18], new electrolytes [9, 19, 20], and improved operational strategies [21–23].

At the core of the electrochemical flow reactor, the porous electrode and flow field design determine the battery performance as they both impact the mass and charge transport [24]. The porous electrodes provide the active surface area for the electrochemical reactions, distribute the electrolyte (affecting species mass transport and pressure drop), and conduct electrons and heat [21, 25]. The electrodes are defined by their surface chemistry and microstructure, characterized by the pore size distribution (PSD), anisotropy ratio, fiber alignment, and pore morphology [26–32]. As such, authors have studied the role of the electrode microstructure on the electrochemical performance and pressure drop [26, 33–35], while others have designed and synthesized electrode materials with distinct chemical and physical properties [13, 30, 36]. The flow field geometry similarly affects the flow cell performance by controlling the electrolyte distribution and accessibility of the reaction surface area in the porous electrode, electrode compression, and cell pressure drop [27, 37–40]. Conventional geometries – flow-through, interdigitated, parallel, and serpentine – have been investigated by evaluating their pressure drop and electrochemical performance in RFBs and by computational methods [40–45], and have been optimized by changing their geometric parameters (e.g., channel and rib width) [46-48] and patterns [17, 18].

The thickness of the porous electrode plays an integral role in the performance and efficiency of the electrochemical stack. The electrode thickness affects the electrolyte distribution and residence time which impacts the species mass transport, cell overpotentials, electronic contact resistances, electrolyte ionic resistances, and the resulting pressure drop, governing the overall flow cell performance [49–51]. Because of the contradictory nature of some of these requirements, finding the optimal electrode thickness is not trivial and it depends on the balance between high electrochemical performance (e.g., high surface area provided by thicker electrodes) and low pumping requirements (e.g., low flow rates by thinner electrodes to sustain the same electrolyte velocity) which is expected to strongly depend on the specific reactor architecture (electrode type, flow field geometry, electrolyte chemistry, and velocity). To date, two

predominant electrode thickness ranges have been implemented in RFBs. First, thick felts (1-6 mm in thickness) are a common choice in traditional flow battery designs, benefitting from high surface areas but suffering from bulkier reactors and inhomogeneous compression upon assembly [52]. As a consequence, contemporary flow cell reactors leverage thinner electrodes (200-600 µm in thickness) which enable more compact stacks, lower cell resistance, reduced pressure drop, and easier assemblies due to homogeneous cell compression [40, 44, 53, 54]. Among the thin electrodes, commercially available carbon papers and cloths have been primarily repurposed from gas diffusion layers in low-temperature fuel cells [26, 55, 56]. While these materials are functional, they have not been engineered to fulfill the specific requirements of RFBs, leading to untailored properties, microstructures, and macroscopic dimensions (e.g., electrode thickness), which negatively impact performance.

A few groups have explored the role of the electrode thickness on the flow cell performance [53, 54, 57–60]. Aaron *et al*. varied the electrode thickness in each separate half-cell by stacking multiple SGL 10AA carbon paper electrodes (1, 2, or 3 layers) using a serpentine flow field at a constant flow rate of 20 mL min^{-1}. They demonstrated a performance gain in all-vanadium RFBs by stacking electrodes, with an enhanced performance for two electrode layers. While the activation losses were reduced by scaling the available surface area, the ohmic losses conversely affected the system performance [54]. Similarly, Liu *et al*. analyzed the influence of the electrode thickness of SGL 10AA carbon papers, varying from one to nine layers, in combination with a serpentine flow field evaluated at 20 and 90 mL min^{-1}. They found an optimum in three electrode layers, providing simultaneously high electrochemical performance and low pressure drop. Despite the increase in the electrode reaction volume and the limiting current upon increasing the electrode thickness above three layers, they reported that the resulting high area-specific resistance negatively impacts the overall performance [53, 61]. These studies revealed the importance of the electrode thickness by studying the specific combination of SGL 10AA carbon paper electrodes with serpentine flow fields at a certain flow rate and electrolyte chemistry. However, they largely overlook the coupled influence of the electrode microstructure and flow field geometry when evaluating the effects of the electrode thickness on the battery performance. As anticipated by previous literature, the local properties within the cell will be affected by the cell architecture, the operating conditions, and the redox chemistry [7, 24, 25, 35, 62]. In particular, driven by the different penetration depths of the electrolyte through the electrode and the velocity distribution, the influence of the electrode thickness on the cell performance is expected to strongly depend on the unique flow patterns induced by the flow field design used. The available flow pathways in the electrode will correlate to the electrolyte residence time in the electrode, species depletion, surface area utilization, and pressure drop. Although previous studies have shown the dependency of the electrode thickness on the flow cell performance, prior findings show that these correlations are highly dependent on the specific electrode type and flow field geometry. Broad design relationships should be elucidated for prominent electrode morphologies, such as bimodal and unimodal microstructures, and flow field geometries, such as flow-through and interdigitated designs, as they would aid in the understanding of relevant structure-performance relationships in the electrochemical cell and thus assists the research on advanced electrode and flow field designs.

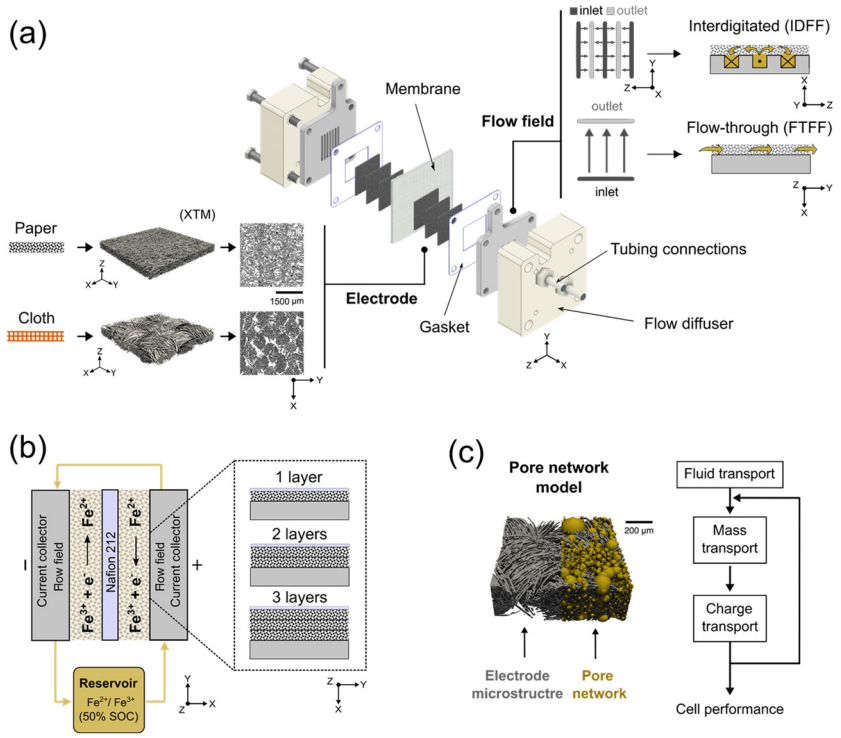

Figure 3.1: Schematic representation of the outline of this work. **(a)** The flow cell configuration with the individual cell components [63], including the two flow field designs (flow-through and interdigitated) and the two electrode structures (carbon paper and cloth) with the 3D renderings and in-plane cross-sections obtained with X-ray tomographic microscopy [24]. **(b)** The single-electrolyte cell configuration with a 0.1 M $FeCl_2$, 0.1 M $FeCl_3$ in 2 M HCl electrolyte solution together with a visualization of the stacked electrode layers used for the electrochemical experiments. **(c)** The electrode microstructure of the cloth electrode (obtained by X-ray tomographic microscopy) overlayed with the resulting pore network, and the simplified iterative flowchart of the model.

In this study, we seek to systematically investigate the correlations between the electrode thickness, electrode microstructure, and flow field geometry for four reactor architectures that cover a representative design space of prevalent material choices. The influence of the electrode thickness on the cell performance is investigated by stacking electrode layers (200 - 1100 µm) of two commercial off-the-shelf porous electrodes – Freudenberg carbon paper and ELAT carbon cloth – in combination with two prevailing flow field geometries – flow-through and interdigitated (**Figure 3.1a**). We use flow cells as analytical platforms for the characterization of the electrochemical and fluid dynamic performance together with a pore network model to gain insight into the local properties to help elucidate thickness-structure-performance relationships. First, we quantify the pressure losses through all electrode-flow field combinations using a custom setup and extract their electrode-flow field apparent permeabilities. Second, we evaluate the electrochemical performance in a single electrolyte flow cell (**Figure 3.1b**) using a kinetically facile redox couple (Fe^{2+}/Fe^{3+}) with electrochemical impedance spectroscopy and polarization measurements. In parallel, pore network model (PNM) simulations (**Figure 3.1c**) are performed to shed light on the local physicochemical profiles sustained under the experimental performance of the battery, capturing fluid dynamics, current

density, and concentration profiles in the porous electrode. The model was previously developed and validated for paper and cloth electrodes with flow-through configurations [35] and is extended in this work to an interdigitated flow field configuration. Finally, we analyze the electrochemical and pressure drop trade-off for stacked electrodes for every electrode-flow field configuration. The current study shows the need for co-designing the electrode thickness, electrode microstructure, and flow field geometry to enhance flow cell performance. While we employ laboratory-scale cells in this study, we anticipate that these results can be used as a guideline to select and design electrodes and flow fields for emerging flow cell reactors.

3.2. Experimental Methods

3.2.1. Materials

Two commercial porous carbon-fiber electrodes were investigated in this work: a Freudenberg H23 carbon paper (Fuel Cell Store) and an ELAT carbon cloth (Fuel Cell Store), hereafter referred to as paper and cloth, respectively. Freudenberg H23 is a non-woven and binder-free paper electrode with an uncompressed thickness of 210 µm and a porosity of 80%, whereas the ELAT cloth is a periodically ordered structure featuring a plain weave pattern with a thickness of 406 µm and a porosity of 82% [26]. Both electrodes were pre-treated by thermal oxidation in air at 450 ºC for 12 h (in a Nabertherm muffle oven, model C290) to increase the hydrophilicity of the electrode to facilitate complete electrode wetting [64]. The geometrical area of the electrodes used in the flow cells was 2.55 cm^2. The two different flow fields used in this work – flow-through and interdigitated – were milled from graphite plates (G347B Plate, MWI). The flow-through flow field (FTFF) had one inlet and one outlet channel of 14 x 1 mm^2, separated by a 16 mm long rib, whereas the interdigitated flow field (IDFF) had 4 inlet channels and 3 outlet channels of 16 x 1 mm^2, alternating with 1 mm wide ribs. A Nafion 212 cation exchange membrane (Fuel Cell Store, 50.8 µm) was used to separate both half-cells and was pre-treated by immersion in 2 M hydrochloric acid (37% w/w HCl diluted in deionized water) for at least 3 days. The electrolyte used for the electrochemical experiments was prepared by dissolving 0.1 M ferrous chloride hydrate ($FeCl_2 \cdot 4H_2O$, 98%, Sigma-Aldrich) and 0.1 M ferric chloride hydrate ($FeCl_3 \cdot 6H_2O$, 97%, Sigma-Aldrich) in 2 M HCl at ambient temperature.

3.2.2. Pressure drop measurements

The pressure drop through the flow cell configurations was measured in a custom flow cell setup (**Figure A3.1**). Water was pumped through the flow cell using a peristaltic pump (Masterflex L/S(R) Easy-Load(R) II) and LS-14 tubing, where only one side of the cell was connected to the solution reservoir. For simplicity, water was used as it has similar density, viscosity, surface tension, and wetting properties as the aqueous electrolyte due to the low species concentration [65]. The flow cell was tightened to 2 N m with a torque-controlled screw-driver and consisted of two flow diffusers, machined from polypropylene (McMaster-Carr), one graphite current collector milled with a flow field design from 3.18 mm thick resin-impregnated graphite plates (G347B graphite, MWI, Inc.) [66] (vide supra), 1-3 electrodes with incompressible polytetrafluoroethylene gaskets

(ERIKS, 210 µm, 105 µm and 55 µm in thickness) that control the electrode thickness by applying compression of ~20 % (where the total gasket thickness depended on the electrode thickness. The exact compression values can be found in **Table A3.1**), and a dense aluminum plate to ensure that the pressure drop was measured over only one flow field and one electrode to avoid secondary effects such as membrane crossover. To account for the different electrode thicknesses throughout the manuscript, we chose to perform the measurements at a constant electrolyte velocity, rather than at a constant flow rate. Using this approach, the electrolyte velocities in the porous electrodes are comparable and allow for a meaningful comparison of mass transport properties between the distinct electrode structures, flow field designs, and number of stacked electrodes. To this end, the electrolyte solution was pumped through the cell at a flow rate calculated based on the desired electrolyte velocity in the electrode (v_e ~0.5 - 8 cm s^{-1}, see **equations A3.1 - A3.2** in **Section A3.4**). For all flow cell experiments, the same pre-conditioning procedure was followed, consisting of a pump calibration step at 5 cm s^{-1} followed by pumping the electrolyte solution through the cell for 30 min at 5 cm s^{-1}. The experiments were performed starting with the highest velocity (8 cm s^{-1}) in descending order to improve the electrode wetting, and the pressure was measured at the inlet and outlet with digital pressure gauges (Stauff SPG-DIGI-USB).

The pressure drop per unit length of the electrode was correlated to the electrolyte velocity using the Darcy-Forchheimer equation:

$$\frac{\Delta P}{L} = \frac{\mu}{k} v_e + \beta \rho v_e^2, \tag{3.1}$$

where ΔP is the pressure drop (Pa), L the length of the electrode (m), v_e the electrolyte velocity (m s^{-1}), and μ and ρ are the electrolyte viscosity (Pa s) and density (kg m^{-3}), respectively. In this study, we refer to k as the apparent permeability (m^2) and to β as the apparent Forchheimer coefficient (m^{-1}) that accounts for inertial effects. Because both the permeability and Forchheimer coefficient are intrinsic properties of the porous material, we refer to them as "apparent" in this work to account for the coupled hydraulic properties of the electrode-flow field combination. All measurements were repeated twice (n=2) for new cell assemblies and solutions.

3.2.3. Electrochemical characterization

The electrochemical performance of every electrode-flow field combination was assessed in a single-electrolyte flow cell (**Figure 3.1b**) [67, 68]. The single-electrolyte configuration has been used in a variety of previous studies [63, 69] and allows us to directly evaluate the ohmic, activation, and mass transfer overpotentials, without convoluted effects such as membrane crossover, secondary reactions, and variations in the state-of-charge over time. A Fe^{2+}/Fe^{3+} electrolyte at 50% state-of-charge was pumped through the cell by a looped tube design, where the outlet of the first half-cell was connected to the inlet of the second half-cell. Once the system reached stationary conditions after cell pre-conditioning, the desired flow rate to sustain a certain velocity was applied and sequential electrochemical impedance spectroscopy (EIS) and polarization measurements were performed using a Biologic VMP-300 potentiostat. EIS was performed at open circuit voltage, with a 10 mV amplitude over a frequency range from 10 kHz - 50 mHz, 6 points per decade, 3 measurements per frequency, and a waiting time of 0.1 period before each frequency. To

deconvolute the ohmic, activation, and mass transfer resistances, an equivalent circuit model [70, 71] was used to fit the averaged experimental values (see **Section A3.5**). The model consists of an inductor (L) capturing the lead resistance, in series with an ohmic resistor (R_Ω), as well as a constant-phase element (CPE_1), representing the non-ideal capacitive effects of porous electrodes [72], in parallel with a charge transfer resistor (R_{CT}), in series with a second constant-phase element (CPE_2), in parallel with a mass transfer resistor (R_{MT}). The second CPE captures inhomogeneities in current and potential distribution, surface reactivity, and porosity common in porous electrodes [73]. Polarization measurements were obtained by applying potentiostatic holds of 1 min at constant voltage steps of 10 mV between 0 - 0.2 V and by recording the steady-state current (one point per second, where only the last 20 seconds were averaged). Because a single-electrolyte configuration was used, the same but opposite reactions occur in both half-cells, resulting in an open circuit voltage of 0 V. Therefore, the applied potential corresponds to the cell overpotential, comprising the ohmic, activation, and mass transfer resistances [26]. All experiments were repeated at least twice ($n \geq 2$) for new cell assemblies and electrolyte solutions.

3.2.4. Electrolyte conductivity and membrane resistance measurements

To improve the accuracy of the pore network model simulations, the electrolyte conductivity and membrane resistance were determined experimentally. Conductivity measurements were performed using a two-electrode custom conductivity cell (similar to the setup used in Milshtein *et al.* [74]), where the open compartment of the conductivity cell was filled with the electrolyte solution and sealed shut. EIS was performed at open-circuit voltage and room temperature with an amplitude of 10 mV and a frequency range of 20 kHz - 200 mHz, 8 points per decade, 6 measurements per frequency, and a waiting time of 0.10 period before each frequency. The high-frequency intercept was identified as the value of the total resistance (cell, lead, and electrolyte resistance) and a calibration curve was obtained using aqueous conductivity standards (0.01 M, 0.1 M, and 1.0 M aqueous potassium chloride) which, together with an empty cell measurement, was used to correct for the combined cell and lead-resistances. EIS measurements were performed three times for the same solution and were repeated five times ($n = 5$) for new assemblies and fresh electrolytes.

To obtain the membrane resistivity, EIS measurements were performed at open-circuit voltage where the high-frequency intercept was identified as the cell resistance including e.g., the membrane resistance and electronic contact resistances. The membrane resistance was obtained by correcting for a cell without a membrane (regular flow cell configuration but without the membrane) and was measured for every electrode-flow field combination with one electrode layer (see **Table A3.6**). Because of the nature of this experiment, the contact resistance contribution to the measured membrane resistance was minimal (both the measurement with and without membrane have a similar electrode-flow field contact resistance and were thus corrected for). EIS measurements were performed for five velocities (20, 10, 5, 3.5, and 1.5 cm s^{-1}) and were repeated two times ($n = 2$) for new membranes, electrodes, and cell assemblies. The obtained values were used in the PNM as membrane resistivity by multiplying the membrane resistance by the geometrical area of the electrode (2.55 cm^2).

3.2.5. Exchange current density extraction

The exchange current density (j_0), used as an input parameter in the pore network simulations, of each electrode and flow field combination was estimated from the polarization experiments by fitting the low current density region (< 100 mA cm^{-2}) of the polarization curve to the Butler-Volmer equation

$$i = j_0 \left(\frac{C_{i,s}}{C_{ref}} \left[exp\left(\frac{\alpha F}{RT} \eta \right) - exp\left(-\frac{\alpha F}{RT} \eta \right) \right] \right), \quad (3.2)$$

where i is the current density, $C_{i,s}$ the surface concentration of species i, C_{ref} the reference concentration of the species at which the exchange current density was measured, α the reaction transfer coefficient which is 0.5 for the Fe^{2+}/Fe^{3+} species, F Faraday's constant (96485 C mol^{-1}), R the universal gas constant (8.314 J mol^{-1} K^{-1}), T the operating temperature (298 K), and η_{act} the activation overpotential obtained after iR_Ω-correction of the applied potential and assuming mass transfer overpotentials to be negligible in the low current density region, resulting in $C_{i,s} = C_{ref}$. The exchange current densities were obtained for each electrode and flow field combination (**Table A3.5**).

3.3. Pore network modeling

Pore network models can be leveraged to simulate the local transport within porous electrodes at a low computational cost by assuming the void space within the porous structure to be approximated by spherical pores and cylindrical throats. Because of the simplification of the pore space and inherent assumptions [35, 67], the PNM should primarily be used to qualitatively obtain and compare property profiles (e.g., concentration, current, velocity, pressure) through the porous electrode while retaining microstructural information. The pore network model used in this study was validated and described in detail in a previous work [35] and the model equations and iterative scheme can be found in **Figure A3.4**. Nevertheless, the model was again validated for all configurations used in this work with experimental data, as the model was extended to simulate the IDFF in this work (**Figure 3.2b**). The validation of all configurations is discussed in detail in **Section A3.10**, where the experimental data is compared with the unfitted model simulations in **Figure A3.7**, the fitted model simulations in **Figure A3.8**, the model parameter fitting data in **Table A3.6**, and a detailed discussion is provided on the model fitting in **Section A3.10**.

The modeled domain consists of two symmetric, mirrored 1 x 1 mm^2 porous electrodes for the FTFF and 1 x 2 mm^2 electrodes for the IDFF simulations, obtained by X-ray tomographic microscopy in previous work [35]. The layer study was performed by stacking the processed uncompressed X-ray tomographic images in the thickness (x) direction in ImageJ to obtain 1, 2, or 3 electrode layers. Subsequently, the pore networks were extracted using the SNOW algorithm, using the inscribed diameter for the paper electrode and the equivalent diameter for the cloth electrode [75], where the network extraction was performed using a single Intel® Core™ i5-12500 CPU. Single-electrolyte flow cell simulations (50% state-of-charge, open circuit voltage of 0 V, see **Table 3.1** for the model parameters) were conducted with applied negative potentials with co-flow operation of the anodic (oxidation reaction) and cathodic (reduction reaction) half-cells. The transport equations were solved at each pore, and the location of the flow channels

and ribs, current collectors, and membrane were defined by boundary conditions (**Figure 3.2**). The single-electrolyte configuration enables the investigation of the electrode performance in isolation without competitive phenomena such as species crossover through the membrane or variations in the state-of-charge [76, 77].

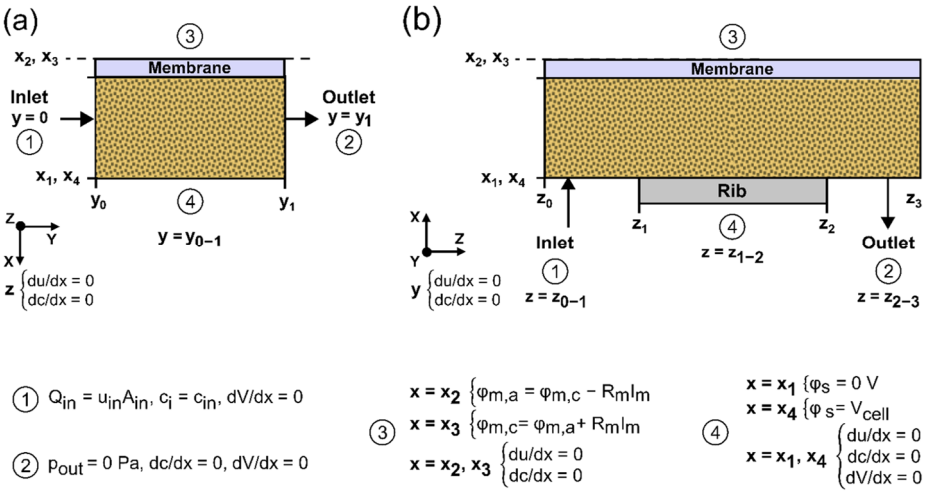

Figure 3.2: Schematic representation of the boundary conditions used in the electrochemical pore network model for one of the half cells in the single-electrolyte flow cell, with x_1-x_4 the x-coordinates, 0-y_1 the y-coordinates, and z_0-z_3 the z-coordinates of the different interfaces for the: **(a)** flow-through flow field, shown over the electrode length (y) and thickness (x), and **(b)** the interdigitated flow field, shown over the electrode width (z) and thickness (x). The flow field and current collector are located on the bottom side of the electrode and the membrane on the top, where the dashed line shows the symmetry condition over the membrane. The symbol list for this figure can be found in **Section A3.14**.

Table 3.1. Electrolyte and cell parameters used in the pore network model. [m] Experimentally measured parameter.

Parameter	Symbol	Value	Unit
Electrolyte conductivity	σ_L	30.84 [m]	S m^{-1}
Electrolyte density	ρ_L	1030 [75]	kg m^{-3}
Electrolyte viscosity	μ_L	1.143 × 10^{-3} [75]	Pa s
Diffusion coefficient of Fe^{2+}	$D_{Fe^{2+}}$	5.7 × 10^{-10} [76]	m^2 s^{-1}
Diffusion coefficient of Fe^{3+}	$D_{Fe^{3+}}$	4.8 × 10^{-10} [76]	m^2 s^{-1}
Equilibrium potential	E_{eq}	0.771 [6]	V
Anodic transfer coefficient	α_a	0.5 [77]	-
Cathodic transfer coefficient	α_c	0.5 [77]	-
Inlet Fe^{2+} concentration in both half-cells	$C_{Fe^{2+}}$	100	mol m^{-3}
Inlet Fe^{3+} concentration in both half-cells	$C_{Fe^{3+}}$	100	mol m^{-3}

The electrochemical PNM framework first solves the fluid transport and consecutively the coupled mass and charge transport within both compartments using an iterative approach. The pressure field was obtained using the Navier-Stokes equation, from which the velocity was back-calculated with the Hagen-Poiseuille equation. These equations can be solved independently from the mass and charge transport equations as a

result of the dilute electrolyte used in this study [35]. Subsequently, the obtained pressure field is fed in the iterative algorithm to solve the coupled mass and charge transport in the porous electrode using the advection-diffusion-reaction equation and the conservation of charge equation. The coupling of these two nonlinear systems of equations is done with the Butler-Volmer equation to obtain the species concentration and potential fields. The coupling of the half-cells is done at the membrane by only considering the overall macroscopic ionic resistance of the membrane using Ohm's law, resulting in the coupling of the charge transport in one half-cell with the electrolyte potential at the membrane boundary in the other half cell [67]. Using this approach, experimental contact resistances were not considered in the PNM, which impacts the model validation as described in more detail in **Section A3.10**.

To account for species depletion over the length of the electrode for the FTFF system, a network-in-series approach was used to match the length of the laboratory electrode (17 mm). In this approach, pore networks were stitched after one another in the length (y) direction, where each network was rotated to become a mirrored copy (in the flow (y) direction) of the previous network. The concentration at the end of one network was considered the inlet concentration of the next network. Because of the symmetry of the IDFF [67], the modeling domain was chosen to be half of an inlet channel, a full rib, and half of an outlet channel, resulting in a 1 x 2 mm^2 modeling domain for the IDFF simulations, see **Figure 3.2b**. For this flow field, species depletion occurs from the inlet channel over the rib to the outlet channel while species concentration along the channels can be assumed constant [78]. Thus, a network-in-series approach over the electrode length is not necessary. The computational time to run a 1-layer electrode with the FTFF using the network-in-series approach and applied potentials of -0.2 – 0 V with -0.02 V step intervals, was 90 min for a 1 x 17 mm^2 electrode using a single Intel® CoreTM i7-8750H CPU. For the IDFF, the same computation took 3 min for a 1 x 2 mm^2 electrode using a single Intel® Core™ i5-12500 CPU.

The PNM was solved for an applied potential with an initial guess for the concentration and overpotential. The initial guess of the concentration was set to the inlet concentration, whereas the initial guess of the overpotential was 0 V. After the convergence of one network and one applied potential, the initial guesses were updated based on the concentration and overpotential of the converged network. An under-relaxation scheme was imposed on the concentration and potential fields using a constant relaxation factor of 0.1 to counteract solution divergence because of the highly nonlinear nature of the system. Additionally, the charge transport source term was linearized as described in our previous work [35]. Numerical convergence was achieved when the relative (5×10^{-5}) and absolute (6×10^{-4} A cm^{-2}) tolerances were met for the total current, bound by a maximum of 50000 iterations.

The boundary conditions for the two flow fields are shown in **Figure 3.2**, where the boundary conditions of the IDFF were based on the work of Sadeghi *et al.* [67] and Shokri *et al.* [79]. The inlet pressure boundary condition is determined by setting a target inlet velocity from which the flow rate is calculated (see **equations A3.1 - A3.2** in **Section A3.4**). The inlet pressure at the boundary pores was determined so that the total flow rate entering the network matched the desired flow rate, the discharge pressure was set to zero, and no-flux boundary conditions were imposed at the current collector or rib and membrane regions. A constant inlet concentration of species is imposed at the inlet, and no-flux boundary conditions are applied at the other boundaries. The solid potential at the

current collector-electrode interface in the cathodic compartment is equal to the given cell voltage, whereas it is equal to zero in the anodic compartment because of the symmetry of the modeled domain. The electrolyte potential at the membrane is iteratively calculated from the electrolyte potential at the membrane in the other half-cell using Ohm's law, including the average voltage loss across the membrane interface. At the remaining boundaries, no-flux boundary conditions were imposed for the potential.

3.4. Results and discussion

3.4.1. Pressure drop analysis

To correlate the pumping losses of all flow cell configurations to the electrode thickness, associated with the constant supply of electrolyte into the electrode [58], we first quantify the pressure drop and obtain the apparent permeability from the Darcy-Forchheimer fittings (**equation (3.1)**). In **Figure 3.3**, the pressure drop per unit length is presented at different superficial velocities, alongside the apparent permeability and Forchheimer coefficient. To sustain the same velocity through the electrode in every electrode-flow field combination, the flow rate needs to increase linearly with the electrode thickness (**equation A3.1 - A3.2**). In flow cells utilizing IDFFs, the geometrical inlet area (i.e., electrode thickness multiplied by channel length) for the electrolyte is predefined by the constant area of the flow field channels. Thus, the pressure required for electrolyte ingress through the channel into the electrode is increased upon higher flow rates imposed by thicker electrodes. As a consequence, the results for the IDFF with both electrodes (**Figure 3.3a-b**) reveal a proportional increase in pressure drop when more electrode layers are added, evaluated at a constant electrolyte velocity. The increase in pressure drop at a constant electrolyte velocity is further supported by the assessment of the pressure drop at a constant flow rate in **Figure A3.6**. At a constant flow rate, no change in pressure losses is observed when increasing the number of electrode layers with the cloth electrode and only a small decrease is found for the paper electrode. In contrast, FTFF configurations show reverse trends (**Figure 3.3c-d**), featuring a substantial decrease in pressure losses, by almost a factor of two, per added electrode layer. In the FTFF configuration, the geometrical inlet area (i.e., channel width multiplied by electrode thickness) increases proportionally to the electrode thickness as the electrolyte flow is supplied from the base of the cell through the transversal cross-section area of the electrode. Simultaneously, to sustain a constant electrolyte velocity in the electrode, the flow rate increases linearly with the electrode thickness, expecting a constant pressure to flow the electrolyte through the porous electrode regardless of the electrode thickness. However, the pressure drop decreases with increased paper electrode thickness for FTFF configurations, which can be attributed to preferential channeling and subsequent hydraulic short-circuiting driven by the spacing between stacked layers [80]. The same trends were obtained using the PNM simulations for the FTFF combinations (**Table A3.3**); yet, the pressure drop was underestimated for all cases because of the inherent assumptions of PNMs (the flow resistance through the PNM is attributed to cylindrical throats with a constant circular cross-section, which is a simplification resulting in the underestimation of the pressure drop [81]) and simulating at uncompressed electrode conditions. Nevertheless, the PNM provides the same trends as observed experimentally, but with additional insights into the microstructural effects on cell operation.

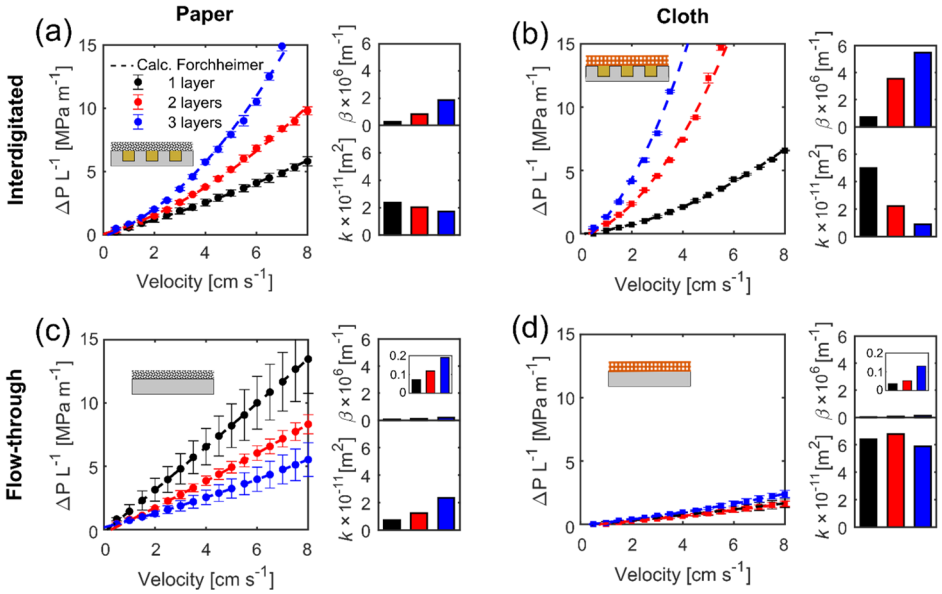

Figure 3.3: Pressure drop analysis of the four electrode-flow field configurations with 1, 2, and 3 electrode layers. The normalized pressure drop at different electrolyte velocities is presented on the left panel and the apparent permeability and Forchheimer coefficients from the Darcy-Forchheimer fittings on the bottom and top of the right panel, respectively. **(a)** Interdigitated flow field with the paper electrode, **(b)** interdigitated flow field with the cloth electrode, **(c)** flow-through flow field with the paper electrode, and **(d)** flow-through flow field with the cloth electrode.

IDFF configurations in combination with the paper electrode (**Figure 3.3a**) experience a lower pressure drop compared to the cloth electrode (**Figure 3.3b**), attributed to the evaluation at constant electrolyte velocity as the paper electrode is twice as thin. Hence, the higher pressure drop of one cloth electrode counterbalances the beneficial effect expected from the higher through-plane apparent permeability (i.e., perpendicular to the membrane, **Tables A3.3 - A3.4**) compared to one paper electrode, as observed in **Figure 3.3a-b**. Interestingly, the apparent permeability of the cloth-IDFF combinations undergoes a substantial decrease when stacking electrode layers. We hypothesize that this is a result of electrode compression and the interaction between the cloth microstructure and the flow induced by the IDFF, resulting in both in-plane and though-plane flow within the electrode. Stacking electrode layers can affect the through-plane microstructure because of resulting interfacial pores and pore misalignment. In **Figure 3.4**, we assess the fluid dynamics of every configuration using the PNM to shed light on the absolute velocity distribution through the throats in the electrode microstructures. When stacking cloth electrodes, the through-plane electrolyte pathways, defined by the large pore segments, are partially blocked because of electrode compression, and the fluid is forced to cross the small pores within the fiber bundles. Hence, low liquid permeability and electrode accessibility are attained as illustrated by the non-homogeneous electrolyte distribution in **Figure 3.4b**, where the fluid transport is predominantly through only a few large in-plane throats with high absolute electrolyte velocities. The apparent Forchheimer coefficient (**Figure 3.3b**) additionally evinces significant inertial effects [82] caused by the anisotropic microstructure of the cloth electrode, accentuated upon stacking electrodes. At the channel inlet and outlet regions

of the IDFF, high electrolyte velocities are sustained, increasing the Reynolds numbers in these regions as well as the inertial effects. The local high-velocity regions are predominantly observed for the cloth electrode, where upon stacking, most of the fluid transport takes place in the electrode layer closest to the current collector. Whereas for the paper electrode, which features a more uniform microstructure [26], the apparent permeability and Forchheimer coefficient are not as significantly affected by the addition of electrode layers when using an IDFF. The more homogeneous velocity profiles observed in **Figure 3.4a** explain this trend and reveal a better utilization of the paper electrode. In general, for both electrodes (**Figure 3.4a-b**), IDFFs induce under-the-rib convection which causes less electrode accessibility under channels [41]. In addition, in the region adjacent to the membrane, the simulations show lower electrolyte velocities which are expected to exacerbate local depletion, increasing the local mass transfer overpotential near the membrane when the electrode thickness is increased.

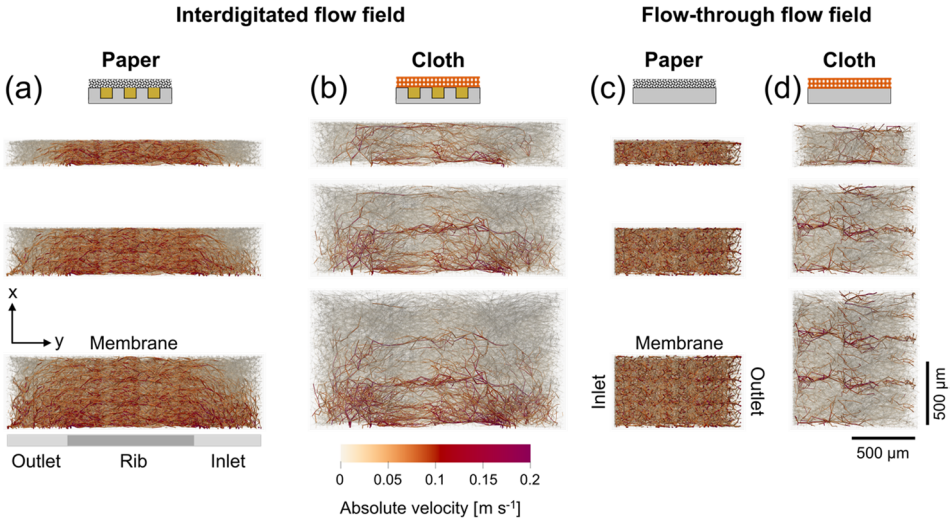

Figure 3.4: Absolute velocity profiles in the throats obtained with PNM simulations at 3.5 cm s^{-1} in the three-dimensional microstructure of paper and cloth electrodes for the four electrode-flow field combinations: **(a)** interdigitated flow field with the paper electrode, **(b)** interdigitated flow field with the cloth electrode, **(c)** flow-through flow field with the paper electrode, and **(d)** flow-through flow field with the cloth electrode. The visual representation of the throats does not include the actual throat diameter in the pore network to improve the visibility of the individual throat contributions to the absolute velocity.

By stacking electrodes with a near unimodal PSD (e.g., the paper electrode), voids can be created between the subsequential layers as a result of the mechanical behavior under compressive forces, enhancing the electrode permeability (**Figure 3.3c**) in the in-plane direction. When operating using an FTFF, the pressure drop in stacked paper electrodes (from 1 to 3 layers) is significantly decreased from 13.4 to 5.5 MPa m^{-1} at v_e = 8 cm s^{-1}. Despite the seemingly homogeneous velocity distribution in the porous media (**Figure 3.4c**), preferential pathways are formed sustaining higher local electrolyte velocities as a result of the inter-layer spacing, decreasing the pressure drop. In the cloth electrode (**Figure 3.3d**), no remarkable pressure drop alleviation is observed, which might be due to the obstruction and size reduction of the bimodal pore segments within the microstructure when stacking electrodes (**Figure 3.3d**) [24, 35, 77]. These characteristics

provide the cloth-FTFF combination with the lowest pressure losses (< 2.5 MPa m^{-1}) among all investigated cell configurations. In general, dominant in-plane convective flow induced with FTFFs leads to small inertial effects, quantified by ten times lower apparent Forchheimer coefficients compared to the hybrid in- and through-plane flow with IDFFs. For example, for the 1-layer case, the paper electrode with an FTFF features a $\beta = 0.2 \times 10^6$ m^{-1} whereas with an IDFF $\beta = 2 \times 10^6$ m^{-1}. These small inertial effects could result in less electrolyte mixing, causing a higher mass transfer resistance in flow-through designs [63, 78, 83].

3.4.2. Electrochemical performance

To evaluate the influence of stacking electrodes on the electrochemical performance, we perform polarization and electrochemical impedance spectroscopy measurements. For all flow cell configurations, the performance is improved when using stacked electrodes, as shown in **Figure 3.5a-d** in the cell polarization plots. However, their trends and magnitude depend on the specific flow field geometry and electrode microstructure, as well as the electrolyte velocity, which in **Figure 3.5** is kept constant at 3.5 cm s^{-1} (see **Figure A3.10** for other velocities). These differences can be explained by the ohmic, activation, and mass transfer overpotential losses in the reactor (**Figure 3.5e-h**), and the current distribution through the electrodes obtained with PNM simulations (**Figure 3.6**). It should be noted that the cell potential values in this work represent overpotential losses due to the single-electrolyte cell configuration employed; thus, a higher current density at a given cell potential indicates a better performance.

When stacking electrodes in flow cells, the internal surface area increases proportionally to the number of layers, attaining higher current densities by a decrease in both the activation and mass transfer overpotentials [76, 84, 85], as observed in **Figure 3.5**. The decrease in activation overpotential is however dependent on the redox chemistry used as sluggish kinetic electrolytes, such as vanadium (reaction rate constant $\approx 10^{-6}$ cm s^{-1} in H_2SO_4 [86]) benefit more of an increased internal surface area compared to kinetically facile electrolytes such as Fe^{2+}/Fe^{3+} electrolytes (reaction rate constant $\approx 10^{-3}$ cm s^{-1} in HCl and with thermally treated carbon electrodes [87]) because of the high exchange current density. Furthermore, the mass transfer overpotential is decreased upon electrode stacking as a result of evaluating at a constant electrolyte velocity, resulting in higher mass flow rates and thus enhanced reactant supply for thicker electrodes. On the other hand, the ohmic overpotential losses increase due to the larger contact (between stacked layers) and ionic resistances which disfavor the ionic transport across thicker electrodes [53]. Therefore, the reduction in activation and mass transfer resistances competes with the higher ohmic resistance, resulting in an optimum for the cell performance at a certain electrode thickness.

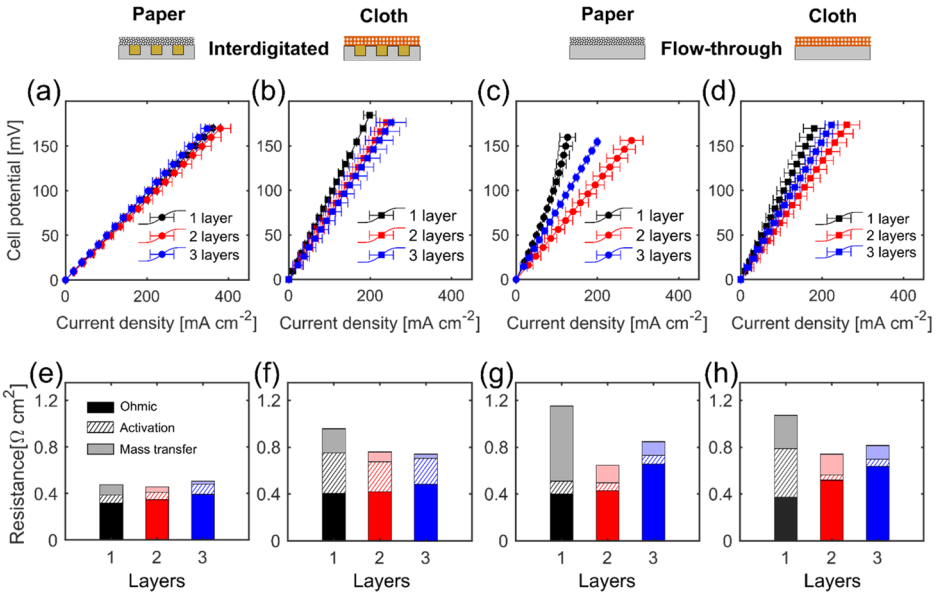

Figure 3.5: Electrochemical performance of the four electrode-flow field combinations with 1, 2, and 3 electrode layers at 3.5 cm s^{-1}. **(a-d)** Cell potential *vs*. current density curves, and **(e-h)** cumulative addition of ohmic, activation, and mass transfer resistances from impedance measurements, for the: **(a, e)** interdigitated flow field and paper electrode, **(b, f)** interdigitated flow field and cloth electrode, **(c, g)** flow-through flow field and paper electrode, and **(d, h)** flow-through flow field and cloth electrode. The impedance plots can be found in **Figure A3.9**.

In **Figure 3.6**, the current distribution profiles in one half-cell are plotted over the electrode thickness and length together with the normalized current values (normalized by the total current generated in the electrode). As observed for all cases, most of the current is generated near the membrane interface, driven by the high activation and mass transfer reaction overpotentials in that region as a result of greater species reaction rates [13, 35, 88, 89]. Additionally, the current distribution depends on the fluid dynamics of the system which is impacted by stacking electrodes and gives rise to different velocity profiles and species flux throughout the electrode volume. As a result, even though the addition of layers provides a larger reaction volume for the electrochemical reactions, the non-homogeneous distribution of the current and the low current magnitude obtained in the third layer does not further improve the electrochemical output of reactors with three electrode layers. As the electrolyte velocity is reduced, the species transport in the cell becomes more diffusion-driven, whereby the ions experience higher residence times to diffuse across the electrode thickness, benefiting less from the preferential pathways originating from high convection (**Figure 3.4**). Therefore, flatter current profiles are obtained at low electrolyte velocities (e.g., v_e = 0.5 cm s^{-1}) and a greater contribution of the total current is generated in the second and third layers (see **Figure A3.11**). Furthermore, follow-up studies should investigate the layer thickness of electrode-flow field configurations with various electrolyte solutions, as their kinetics and ionic conductivity will influence the ohmic, charge and mass transport potential losses on increasing electrode thickness. For instance, it is anticipated that for highly conductive electrolytes (e.g., aqueous electrolytes with high salt concentration [90]) the desired electrode layer thickness might be more than two layers, whereas for electrolytes with

low conductivity (e.g., organic electrolytes, diluted systems [74]) one layer might be more beneficial due to the large ohmic losses involved.

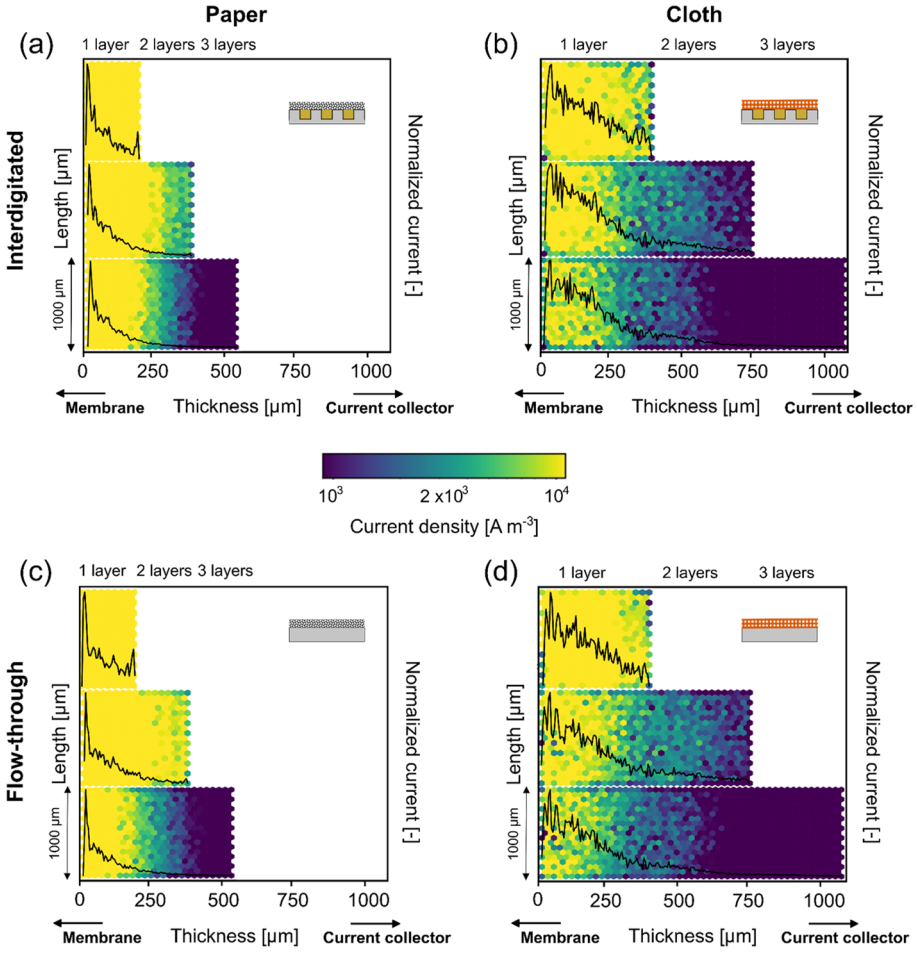

Figure 3.6: Current profiles in 2D with the current density per volume of electrode plotted over the thickness and length of the electrode, and in 1D with the normalized current (normalized by the total current generated in the electrode) plotted over the electrode thickness, with the membrane at 0 µm. The current profiles are shown for both flow fields and electrodes and for 1, 2, and 3 electrode layers at 3.5 cm s^{-1} and -0.2 V, obtained with pore network simulations, for: **(a)** the interdigitated flow field and paper electrode, **(b)** the interdigitated flow field and cloth electrode, **(c)** the flow-through flow field and paper electrode, and **(d)** the flow-through flow field and cloth electrode. The validation of the PNM can be found in **Section A3.10**.

3.4.2.1. Interdigitated flow field

For the IDFF, the benefit of adding more electrode layers strongly depends on the electrode type used. The ohmic, activation, and mass transfer resistances are significantly influenced by the electrode microstructure and internal surface area due to the complex

bidirectional velocity distribution with hybrid in-plane and through-plane flow induced by this flow field design [24]. As shown in **Figure 3.5e-f**, in the paper electrode-IDFF combination, the performance is not further enhanced upon the addition of more electrode layers, whereas for the cloth electrode, the performance is enhanced by stacking two electrodes. Although in **Figure 3.6** a greater current is generated in the second layer of the paper electrode compared to the cloth (i.e., for the paper-IDFF combination with two layers, 17 % of the current is generated in the second layer, whereas this is 6 % for the cloth-IDFF combination), the steep reduction in activation and mass transfer resistances (**Figure 3.5f**) results in a better performance output for two stacked cloth electrodes. The decrease in the activation (from 0.35 to 0.25 Ω cm^2) and mass transfer resistances (from 0.21 to 0.08 Ω cm^2) are partially related to the increase in internal surface area which counterbalances the negative effect of increased ohmic losses, resulting in a performance gain of 56 mA cm^{-2} at 150 mV for two cloth electrodes. In addition, from the 1D profiles in **Figure 3.6a-b**, it is shown that the configuration with one cloth electrode distributes the current more homogeneously over the entire electrode thickness, as a result of the large through-plane pores, compared to one paper electrode, despite that the cloth electrode is twice as thick.

Further understanding is supported by the concentration plots obtained with the PNM (**Figure 3.7**). In the IDFF configuration, the electrolyte is pushed from the inlet to the outlet channel over the rib. Thus, by stacking electrodes, the ionic species transport pathway becomes larger, increasing the ionic resistance. Due to the homogeneous PSD of the paper electrode (**Figure A3.5b**), the pore-to-pore reactant depletion exhibits a uniform profile. Yet, in the region close to the membrane, the high reaction rates (**Figure 3.6a**) lead to greater reactant depletion [79], which is exacerbated in the IDFF by the poor species supply driven by the lower local velocities near the membrane (**Figure 3.4b**) [59]. Similar phenomena occur in the electrode volume under the inlet and outlet channels, where the electrolyte convection is not as significant as under the ribs, resulting in stagnant zones due to preferential flow pathways. Consequently, stacking more carbon papers does not significantly improve the reactant distribution with IDFFs.

In the cloth electrode, the fluctuations in the normalized current distribution plot evince the heterogeneity of cloth materials [26, 33]. Their anisotropic microstructure with a bimodal PSD (**Figure A3.5d**) strongly affects the distribution of reactants [55], providing distinct concentration profiles in comparison to the paper electrode (**Figure 3.7**). A higher degree of local reactant depletion is found for the smaller pore segments with limited convective flow [35, 89], anticipated by the electrolyte velocity distribution (**Figure 3.4**). Higher velocities are reached in the large pores, which enhance species transport in the in-plane direction when adding a second layer. Hence, alleviating the overall mass transfer overpotential and simultaneously the activation overpotential (**Figure 3.5f**) due to the greater accessibility of the specific surface area for the redox reactions. However, when an additional third layer is added, the increase in ohmic resistance counteracts the decrease in the activation and mass transfer overpotentials, and the electrochemical response is no longer improved. We envision that modifying the through-plane microstructure of electrodes (i.e., gradients in porosity, pore size, and morphology through new synthesis techniques and materials [13, 60, 91]) enhances the electrolyte transport towards the membrane interface, increasing the reactant supply. Thereby, alleviating ohmic resistances and pressure losses in IDFF configurations, improving the electrolyte distribution, and enabling the use of thicker electrodes with a high surface area.

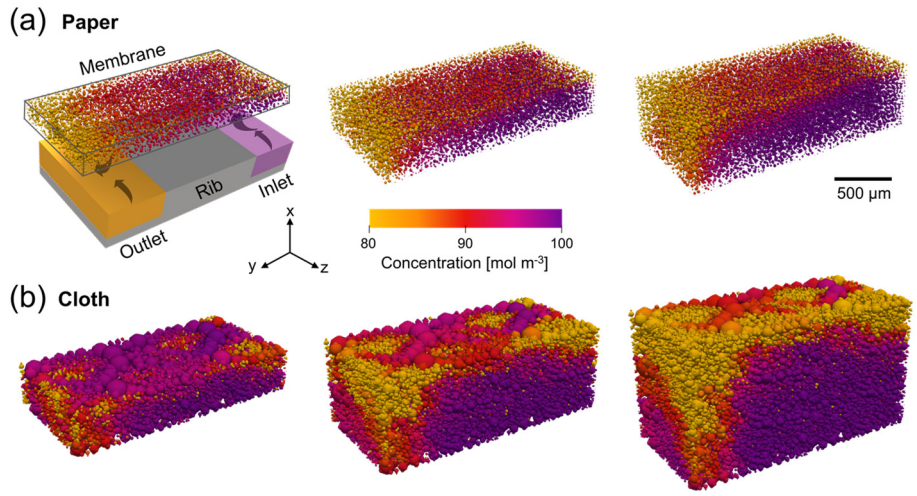

Figure 3.7: Concentration profiles of Fe^{3+} in the porous electrode using the interdigitated flow field (shown with a visual representation) obtained by pore network simulations at 3.5 cm s^{-1} and -0.2 V. The concentration profiles are shown for 1, 2, or 3 layers in thickness from left to right and for: **(a)** the paper electrode, and **(b)** the cloth electrode. The x-direction represents the thickness of the electrode from the flow field (bottom) to the membrane (top). The y-direction represents the length of the electrode and the z-direction the width.

3.4.2.2. Flow-through flow field

Flow reactors with FTFFs induce a near unidirectional in-plane flow throughout the electrode microstructure as shown in the velocity distribution analysis (**Figure 3.4c-d**), especially for the paper electrode. The addition of a second electrode layer for FTFF configurations enhances the performance of both investigated electrode materials at the analyzed electrolyte velocity (**Figure 3.5c-d**), resulting in a 145 mA cm^{-2} increase for the paper electrode and a 73 mA cm^{-2} increase for the cloth electrode. The analysis of ohmic, activation, and concentration overpotentials evidences a remarkable reduction in the activation and mass transfer resistances when adding a second layer, overcoming the negative impact of increased ohmic losses (**Figure 3.5g-h**). The main reasons for this reduction are the combination of the greater flow rate to maintain a constant electrolyte velocity, the increased internal surface area for the redox reactions, and the voids created between the stacked electrodes. However, further addition of a third layer no longer results in improved electrochemical performance, caused by no noticeable reduction in activation and mass transfer overpotentials. Further revealed by the current profiles in **Figure 3.6c-d**, where the reaction rate in the third layer is almost negligible compared to the first and second layers.

For the paper electrode, the performance gain with two layers is primarily defined by a decrease of 0.49 Ω cm^2 in the mass transfer resistance, ascribed to the greater flow rate resulting in higher non-reacted outlet concentrations and the increase in internal surface area. The high mass transfer overpotential in the paper-FTFF combination is caused by the lower mass transfer coefficient [63] as a result of the unimodal PSD and long electrolyte flow pathway, impacting the mass transfer resistance at low flow rates. In

contrast, for the cloth electrode, the performance improvement is dominated by a decrease of 0.37 Ω cm^2 in the activation overpotential as a result of the increased internal surface area when a second layer is added. Furthermore, the stacking of electrodes potentially enhances the electrode accessibility by better mixing across the large internal pores in the cloth electrode caused by the in-plane flow induced by the flow-through configuration (as shown in the velocity and concentration profiles of **Figure 3.4d** and **Figure A3.12b**, respectively).

3.4.3. Performance trade-off

The trade-off between the electrochemical performance and pressure losses should be evaluated to assess the influence of stacking electrodes on the overall flow cell performance. Therefore, in **Figure 3.8** we compare the current density at an applied cell potential of 75 mV with the pressure drop per unit length for the different flow cell configurations with one, two, and three electrode layers. It must be pointed out that we evaluate the trade-off for a single-electrolyte flow cell design to mitigate secondary effects such as membrane crossover or changes in the state-of-charge. Therefore, we applied a potential of 75 mV to a flow cell with an open-circuit voltage of 0 V, where the applied potential is equal to a voltage loss for full-cell operation. Thus, at a fixed applied potential in a single-electrolyte system, you want to maximize the current density for more efficient reactor operation. In **Figure 3.8**, each data point represents a distinct electrolyte velocity (0.5, 1.5, 3.5, and 5 cm s^{-1}) and the pumping requirements depend on the pressure drop and the electrolyte flow rate ($P_p = (Q\Delta P/\eta_p)$ with P_p the pumping power (W), Q the flow rate (m^3 s^{-1}), ΔP the pressure drop (Pa), and η_p the pumping efficiency (-)). Upon stacking electrode layers, higher electrolyte flow rates are necessary to ensure a constant electrolyte velocity, and therefore, thicker electrodes may negatively impact the performance trade-off.

For most flow cell configurations, an optimum trade-off is achieved by stacking two electrode layers, dominated by a significant increase in electrochemical performance. When stacking more layers, dominant ohmic losses and elevated pumping requirements negatively impact the performance trade-off. Stacking electrode layers for the paper-IDFF does not augment the electrochemical performance, as observed in **Figure 3.8a**, whereas for the cloth-IDFF combination, the electrochemical performance is improved but this comes at the cost of a significantly increased pressure drop. Hence, the best trade-off for both electrodes with the IDFF is obtained for a single electrode layer, as the expected material costs of stacking two electrode layers together with the high pumping power do not weigh against the increase in performance. For the FTFF, there is a significant performance gain in stacking two electrodes, as both the electrochemical performance and the associated pressure drop are improved (**Figure 3.8c**). Last, as anticipated, the cloth-FTFF combination features the lowest pressure drop, independent of the number of stacked layers, where the best trade-off is reached with two layers. Furthermore, we find that the optimum electrode layer thickness does not notably depend on the analyzed electrolyte velocity (each data point in **Figure 3.8**) for any of the flow cell designs.

When translating these findings to a broader context, we find that the optimal electrode thickness depends on the reactor design. For flow-through configurations, electrodes with an unimodal pore size distribution and high internal surface area feature

significant species depletion across the electrode length because of the long residence time in the electrode. Therefore, thicker electrodes with a bimodal PSD with large pores, such as the cloth electrode, should be used with this flow configuration as they facilitate a better electrolyte distribution at low pumping power. For the IDFF on the other hand, an increased internal surface area and a more uniform and smaller pore size distribution (e.g., the paper electrode) is beneficial as the residence time in the electrode is smaller. Combined with the hybrid in- and through-plane flow induced by this flow configuration, the best performance trade-off is found for thinner electrodes as the pressure drop decreases drastically. For carbon felts on the other hand, with unimodal PSDs with larger pores (60 µm) [69] we expect that thicker electrodes (>200 µm) are beneficial in combination with both the IDFF and FTFF. However, as commercial felt electrodes are much thicker (2 - 6 mm), stacking commercial felt electrodes is anticipated to have a detrimental impact on the pressure losses, electrolyte maldistribution, and ohmic losses associated with increased ionic resistance. Furthermore, the redox chemistry might also play a role in the selection of the electrode thickness where we anticipate that chemistries featuring sluggish kinetics will benefit from thicker electrodes due to the larger internal surface area, whereas electrolytes with facile redox kinetics will be less sensitive to an increase in electrode thickness as the high exchange current density and subsequent charge transfer rate will be high enough to not limit the cell performance.

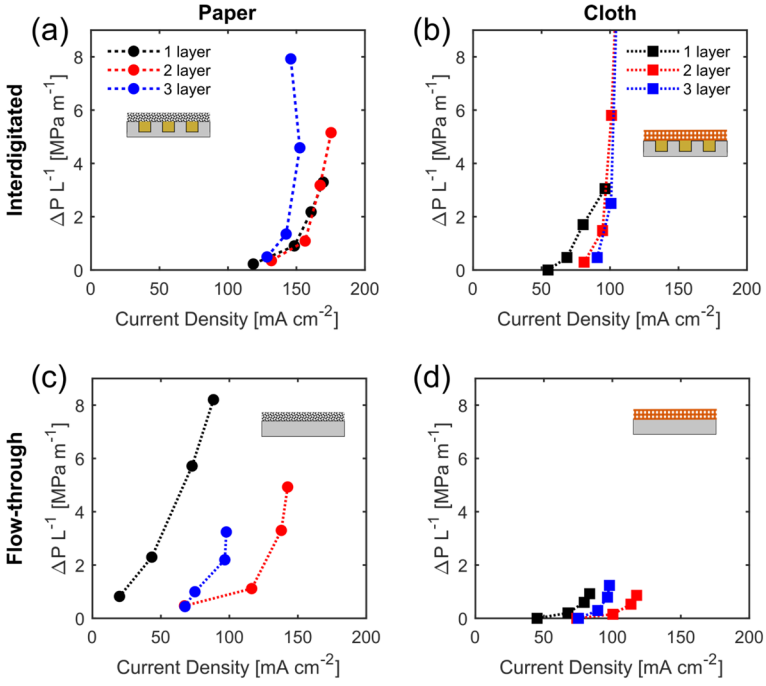

Figure 3.8: Balance between current density and pressure losses for the four electrode-flow field combinations with 1, 2, and 3 electrode layers, for the: **(a)** interdigitated flow field and paper electrode, **(b)** interdigitated flow field and cloth electrode, **(c)** flow-through flow field and paper electrode, and **(d)** flow-through flow field and cloth electrode. Each data point corresponds to a certain electrolyte velocity from 0.5 to 5 cm s^{-1} and the current densities are compared at 75 mV cell potential.

3.5. Conclusions

The electrode thickness determines the flow battery performance through the available reaction surface area, the electrolyte distribution, and the ohmic, activation, and mass transfer overpotentials. Increasing the electrode thickness by stacking commercial electrodes can be leveraged as a fast and inexpensive pathway to improve battery performance. While prior work investigated the influence of the electrode thickness in isolation from the type of flow field or electrode microstructure, here we systematically investigated the influence of the electrode thickness on the flow cell performance through electrode stacking of two commercial electrodes – Freudenberg paper and ELAT cloth – in combination with flow-through and interdigitated flow fields. We evaluated the electrochemical and fluid dynamic performance of the distinct flow cell designs using a series of polarization, electrochemical impedance spectroscopy, and pressure drop measurements in a single-electrolyte cell configuration with an aqueous electrolyte (Fe^{2+}/Fe^{3+} in HCl). Furthermore, we used pore network modeling to visualize the physicochemical phenomena occurring in the three-dimensional electrode microstructure and to understand local properties (e.g., concentration, current, pressure) besides the measurements performed in the analytical flow cell.

Using pressure drop measurements, we find that thicker electrodes in combination with flow-through flow fields decrease the pressure drop, which we attribute to hydraulic short-circuiting between the electrode layers. On the contrary, we find that for interdigitated flow fields, thinner electrodes are beneficial, which we hypothesize is because of the increase in pressure to push the electrolyte from the channel through the electrode at elevated flow rates. The electrochemical characterization shows the competing effects of reduced activation and mass transfer overpotentials with increased ohmic losses, which make the two-layer system (400 - 700 µm) the best configuration for almost all electrode-flow field combinations in terms of electrochemical performance. The paper-IDFF combination is however an exception to this trend, as no significant improvement is observed when more electrode layers are stacked. Furthermore, in the current distribution analysis from the PNM simulations, a negligible reaction rate was found in the third electrode layer, closest to the current collector, for all configurations. We find that the electrolyte velocity influences the electrode utilization, as under low electrolyte velocities (0.5 cm s^{-1}), more current is generated in the additional two and three layers because of increased reactant depletion as a result of low convection rates.

The narrow unimodal pore size distribution of the paper electrode adversely affects the benefits of increasing the electrode thickness in IDFF configurations, whereas the hierarchical anisotropic microstructure of the cloth electrode enhances the reactant replenishment. Consequently, the mass transfer resistance in the cloth electrode is reduced, allowing the electrolyte to access a greater electrode reaction volume through preferential pathways created by the larger pores. In the FTFF configuration, the impact of electrode thickness of specific electrode types on the electrochemical performance is more remarkable than in the IDFF. In particular, the combination with two stacked paper electrodes offers a two times higher current density compared to two stacked cloth electrodes, driven by the higher current generation in the second layer enabled by the better electrolyte distribution due to the uniform microstructure of the paper electrode.

In this study, even though we found similarities in the number of stacked electrode layers for different systems, we demonstrated the critical dependency between

the electrode-flow field interactions with the electrode thickness and their influence on different performance metrics (e.g., current distribution, pressure drop, electrolyte distribution) and corresponding system performance. When balancing the electrochemical performance with the associated pressure losses, thicker electrodes with an FTFF are leveraged as a promising strategy to enhance the overall efficiency of the flow cell at low pressure drop, whereas thinner electrodes are beneficial with IDFFs.

3.6. References

[1] A. A. Kebede, T. Kalogiannis, J. Van Mierlo, M. Berecibar, *Renewable and Sustainable Energy Reviews*. **159**, 112213 (2022).
[2] S. Chu, A. Majumdar, *Nature*. **488**, 294–303 (2012).
[3] S. Koohi-Fayegh, M. A. Rosen, *Journal of Energy Storage*. **27**, 101047 (2020).
[4] M. L. Perry, A. Z. Weber, *Journal of The Electrochemical Society*. **163**, A5064–A5067 (2016).
[5] P. Alotto, M. Guarnieri, F. Moro, A. Stella, *COMPEL*. **32**, 1459–1470 (2013).
[6] A. Z. Weber *et al.*, *Journal of Applied Electrochemistry*. **41**, 1137–1164 (2011).
[7] E. Sánchez-Díez *et al.*, *Journal of Power Sources*. **481**, 228804 (2021).
[8] L. F. Arenas, C. Ponce de León, F. C. Walsh, *Journal of Energy Storage*. **11**, 119–153 (2017).
[9] R. M. Darling, K. G. Gallagher, J. A. Kowalski, S. Ha, F. R. Brushett, *Energy Environ. Sci.* **7**, 3459–3477 (2014).
[10] S. Ha, K. G. Gallagher, *Journal of Power Sources*. **296**, 122–132 (2015).
[11] J. Luo, A. P. Wang, M. Hu, T. L. Liu, *MRS Energy & Sustainability*. **9**, 1–12 (2022).
[12] X. Zhou, X. Zhang, L. Mo, X. Zhou, Q. Wu, *Small*. **16**, 1907333 (2020).
[13] C. T. Wan *et al.*, *Adv. Mater.* **33**, 2006716 (2021).
[14] C. T. Wan *et al.*, *ACS Sustainable Chem. Eng.* **8**, 9472–9482 (2020).
[15] S. Wang, X. Zhao, T. Cochell, A. Manthiram, *J. Phys. Chem. Lett.* **3**, 2164–2167 (2012).
[16] K. Lee *et al.*, *ACS Appl. Mater. Interfaces*. **9**, 22502–22508 (2017).
[17] Y. Zeng *et al.*, *Applied Energy*. **238**, 435–441 (2019).
[18] B. Akuzum, Y. C. Alparslan, N. C. Robinson, E. Agar, E. C. Kumbur, *J Appl Electrochem*. **49**, 551–561 (2019).
[19] P. Geysens, Y. Li, I. Vankelecom, J. Fransaer, K. Binnemans, *ACS Sustainable Chem. Eng.* **8**, 3832–3843 (2020).
[20] K. Gong *et al.*, *ACS Energy Lett.* **1**, 89–93 (2016).
[21] D. Aaron, Z. Tang, A. B. Papandrew, T. A. Zawodzinski, *J Appl Electrochem*. **41**, 1175–1182 (2011).
[22] R. Schweiss, C. Meiser, D. Dan, *Batteries*. **4**, 55 (2018).
[23] Xiong Binyu, Zhao Jiyun, Li Jinbin, in *2013 IEEE Power & Energy Society General Meeting*, Vancouver, BC, Canada (2013).
[24] V. Muñoz-Perales *et al.*, *ChemRxiv* (2023), doi:10.26434/chemrxiv-2023-2zthc.
[25] W. Wang *et al.*, *Adv. Funct. Mater.* **23**, 970–986 (2013).
[26] A. Forner-Cuenca, E. E. Penn, A. M. Oliveira, F. R. Brushett, *J. Electrochem. Soc.* **166**, A2230–A2241 (2019).
[27] C. R. Dennison, E. Agar, B. Akuzum, E. C. Kumbur, *J. Electrochem. Soc.* **163**, A5163–A5169 (2016).
[28] N. Aguiló-Aguayo, T. Drozdzik, T. Bechtold, *Electrochemistry Communications*. **111**, 106650 (2020).
[29] M. D. R. Kok *et al.*, *Chemical Engineering Science*. **196**, 104–115 (2019).
[30] J. Sun *et al.*, *Energy Storage Materials*. **43**, 30–41 (2021).
[31] P. A. García-Salaberri *et al.*, *International Journal of Heat and Mass Transfer*. **127**, 687–703 (2018).
[32] P. A. García-Salaberri *et al.*, *Electrochimica Acta*. **295**, 861–874 (2019).
[33] K. M. Tenny, A. Forner-Cuenca, Y.-M. Chiang, F. R. Brushett, *Journal of Electrochemical Energy Conversion and Storage*. **17**, 041010 (2020).
[34] A. A. Wong, M. J. Aziz, *J. Electrochem. Soc.* **167**, 110542 (2020).
[35] M. van der Heijden, R. van Gorp, M. A. Sadeghi, J. Gostick, A. Forner-Cuenca, *J. Electrochem. Soc.* **169**, 040505 (2022).
[36] Y. Su *et al.*, *Ceramics International*. **49**, 7761–7767 (2023).
[37] R. Cervantes-Alcalá, M. Miranda-Hernández, *J Appl Electrochem*. **48**, 1243–1254 (2018).

[38] X. Ke *et al.*, *Chem. Soc. Rev.* **47**, 8721–8743 (2018).
[39] A. M. Pezeshki, R. L. Sacci, F. M. Delnick, D. S. Aaron, M. M. Mench, *Electrochimica Acta*. **229**, 261–270 (2017).
[40] S. Kumar, S. Jayanti, *Journal of Power Sources*. **307**, 782–787 (2016).
[41] M. Messaggi *et al.*, *Applied Energy*. **228**, 1057–1070 (2018).
[42] T. Jyothi Latha, S. Jayanti, *J Appl Electrochem*. **44**, 995–1006 (2014).
[43] Q. Xu, T. S. Zhao, C. Zhang, *Electrochimica Acta*. **142**, 61–67 (2014).
[44] R. M. Darling, M. L. Perry, *J. Electrochem. Soc.* **161**, A1381–A1387 (2014).
[45] Y. Wang, M. Li, L. Hao, *Journal of Electroanalytical Chemistry*. **918**, 116460 (2022).
[46] J. Sun, B. Liu, M. Zheng, Y. Luo, Z. Yu, *Journal of Energy Storage*. **49**, 104135 (2022).
[47] L. Wei *et al.*, *International Journal of Heat and Mass Transfer*. **179**, 121747 (2021).
[48] M. R. Gerhardt, A. A. Wong, M. J. Aziz, *Journal of The Electrochemical Society*. **165**, A2625–A2643 (2018).
[49] K.Q. Zhu *et al.*, *Energy Conversion and Management*. **267**, 115915 (2022).
[50] B. R. Chalamala *et al.*, *Proc. IEEE*. **102**, 976–999 (2014).
[51] K. L. Duncan, K.-T. Lee, E. D. Wachsman, *Journal of Power Sources*. **196**, 2445–2451 (2011).
[52] R. Banerjee, N. Bevilacqua, L. Eifert, R. Zeis, *Journal of Energy Storage*. **21**, 163–171 (2019).
[53] Q. H. Liu *et al.*, *J. Electrochem. Soc.* **159**, A1246–A1252 (2012).
[54] D. S. Aaron *et al.*, *Journal of Power Sources*. **206**, 450–453 (2012).
[55] H. Zhang *et al.*, *Energy Conversion and Management*. **241**, 114293 (2021).
[56] A. El-kharouf, T. J. Mason, D. J. L. Brett, B. G. Pollet, *Journal of Power Sources*. **218**, 393–404 (2012).
[57] Z. Wang *et al.*, *Journal of Power Sources*. **549**, 232094 (2022).
[58] E. Ali, H. Kwon, J. Kim, H. Park, *Journal of Energy Storage*. **32**, 101802 (2020).
[59] S. Tsushima, T. Suzuki, *J. Electrochem. Soc.* **167**, 020553 (2020).
[60] N. Misaghian, M. A. Sadeghi, K. M. Lee, E. P. L. Roberts, J. T. Gostick, *J. Electrochem. Soc.* **170**, 070520 (2023).
[61] J. Houser, J. Clement, A. Pezeshki, M. M. Mench, *Journal of Power Sources*. **302**, 369–377 (2016).
[62] A. Z. Weber *et al.*, *J Appl Electrochem*. **41**, 1137–1164 (2011).
[63] J. D. Milshtein *et al.*, *J. Electrochem. Soc.* **164**, E3265–E3275 (2017).
[64] K. V. Greco, A. Forner-Cuenca, A. Mularczyk, J. Eller, F. R. Brushett, *ACS Appl. Mater. Interfaces*. **10**, 44430–44442 (2018).
[65] P. K. Weissenborn, R. J. Pugh, *Journal of Colloid and Interface Science*. **184**, 550–563 (1996).
[66] A. Forner-Cuenca, E. E. Penn, A. M. Oliveira, F. R. Brushett, *J. Electrochem. Soc.* **166**, A2230 (2019).
[67] M. A. Sadeghi *et al.*, *J. Electrochem. Soc.* **166**, A2121–A2130 (2019).
[68] D. Zhang *et al.*, *Journal of Power Sources*. **447**, 227249 (2020).
[69] A. Forner-Cuenca, E. E. Penn, A. M. Oliveira, F. R. Brushett, *J. Electrochem. Soc.* **166**, A2230–A2241 (2019).
[70] I. Derr *et al.*, *Journal of Power Sources*. **325**, 351–359 (2016).
[71] N. Meddings *et al.*, *Journal of Power Sources*. **480**, 228742 (2020).
[72] G. Paasch, K. Micka, P. Gersdorf, *Electrochimica Acta*. **38**, 2653–2662 (1993).
[73] J.B. Jorcin, M. E. Orazem, N. Pébère, B. Tribollet, *Electrochimica Acta*. **51**, 1473–1479 (2006).
[74] J. D. Milshtein, J. L. Barton, R. M. Darling, F. R. Brushett, *Journal of Power Sources*. **327**, 151–159 (2016).
[75] J. T. Gostick, *Phys. Rev. E*. **96**, 023307 (2017).
[76] M. van der Heijden, A. Forner-Cuenca, in *Encyclopedia of Energy Storage* L. F. Cabeza, Ed. (Elsevier Inc., Oxford, ed. 2, 2022), pp. 480–499.

[77] A. Forner-Cuenca, F. R. Brushett, *Current Opinion in Electrochemistry*. **18**, 113–122 (2019).
[78] V. Muñoz-Perales, M. Van Der Heijden, P. A. García-Salaberri, M. Vera, A. Forner-Cuenca, *ACS Sustainable Chem. Eng.* **11**, 12243–12255 (2023).
[79] J. Shokri, D. Niblett, M. Babaei, V. Niasar, *J. Electrochem. Soc.* **169**, 120511 (2022).
[80] B. K. Chakrabarti *et al.*, *Sustainable Energy Fuels*. **4**, 5433–5468 (2020).
[81] A. Fathiganjehlou *et al.*, *Chemical Engineering Science*. **273**, 118626 (2023).
[82] A. Lenci, F. Zeighami, V. Di Federico, *Transp Porous Med*. **144**, 459–480 (2022).
[83] M. Van Der Heijden, M. Kroese, Z. Borneman, A. Forner-Cuenca, *Adv Materials Technologies*. **8**, 2300611 (2023).
[84] A. Tang, J. Bao, M. Skyllas-Kazacos, *Journal of Power Sources*. **248**, 154–162 (2014).
[85] N. M. Delgado *et al.*, *Journal of Power Sources*. **480**, 229142 (2020).
[86] B. Segel *et al.*, *J. Mater. Chem. A*. **10**, 13917–13927 (2022).
[87] E. B. Boz, P. Boillat, A. Forner-Cuenca, *ACS Appl. Mater. Interfaces*. **14**, 41883–41895 (2022).
[88] A. A. Shah, M. J. Watt-Smith, F. C. Walsh, *Electrochimica Acta*. **53**, 8087–8100 (2008).
[89] R. van Gorp, M. van der Heijden, M. Amin Sadeghi, J. Gostick, A. Forner-Cuenca, *Chemical Engineering Journal*, **455**, 139947 (2022).
[90] M. Skyllas-Kazacos, M. Kazacos, *Journal of Power Sources*. **196**, 8822–8827 (2011).
[91] L. F. Arenas, C. Ponce de León, F. C. Walsh, *Electrochemistry Communications*. **77**, 133–137 (2017).

3.7. Appendix 3

A3.1. Abbreviations

Symbol	Description
EIS	Electrochemical impedance spectroscopy
FTFF	Flow through flow field
IDFF	Interdigitated flow field
PNM	Pore network model
PSD	Pore size distribution
RFB	Redox flow battery

A3.2. List of symbols

Symbol	Description	Units
C	Inlet concentration	mol m^{-3}
$C_{i,s}$	Surface concentration of species i	mol m^{-3}
C_{ref}	Reference concentration	mol m^{-3}
D	Diffusion coefficient	m^2 s^{-1}
E_{eq}	Equilibrium potential	V
F	Faraday's constant, 96485 C mol^{-1}	C mol^{-1}
i	Current density	A m^{-2}
j_0	Exchange current density	A m^{-2}
k	Apparent permeability	m^2
L	Electrode length	m
η_p	Pumping efficiency	-
ΔP	Pressure drop	Pa
P_p	Pumping power	W
Q	Flow rate	m^3 s^{-1}
R	Universal gas constant, 8.314 J mol^{-1} K^{-1}	J mol^{-1} K^{-1}
T	Operating temperature	K
v_e	Electrolyte velocity	m s^{-1}
	Greek	
α	Reaction transfer coefficient	-
β	Apparent Forchheimer coefficient	m^{-1}
η_{act}	Activation overpotential	V
μ	Electrolyte viscosity	Pa s
ρ	Electrolyte density	kg m^{-3}
σ_L	Electrolyte conductivity	S m^{-1}
	Subscript	
a	Anodic	
c	Cathodic	
Fe^{2+}	Fe^{2+} species	
Fe^{3+}	Fe^{3+} species	
L	Electrolyte	

A3.3. Cell configuration for pressure drop measurements

A3.3.1. Cell configuration

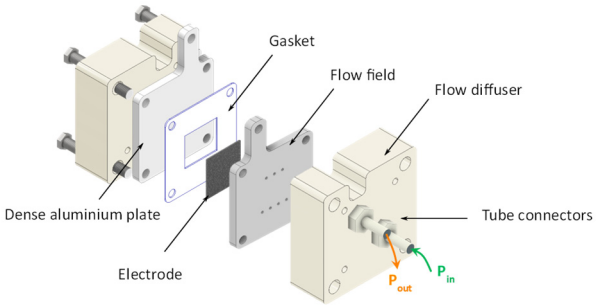

Figure A3.1: Custom flow cell setup for the pressure drop measurements, based on the original cell design of Milshtein *et al.* [1].

A3.3.2. Cell compression

The compression of the electrode was controlled by stacking incompressible polytetrafluoroethylene gaskets with different thicknesses (ERIKS, 210 µm, 105 µm and 55 µm in thickness) resulting in slightly different compression degrees depending on the electrode type and number of stacked electrode layers (all around 20 %, see **Table A3.1)**.

Table A3.1: The compression degree used depends on the electrode type and number of electrode layers.

Electrode type	Number of electrode layers	Compression [%]
Paper	1	23.8
	2	23.8
	3	19.8
Cloth	1	22.4
	2	19.3
	3	21.2

A3.4. Calculation of electrolyte velocity in the electrode

The superficial velocity of the electrolyte in the electrode (v_e) is correlated to the volumetric flow rate (Q), depending on the flow field geometry, which can be calculated according to the following formulas:

$$v_e{}^{FTFF} = \frac{Q}{t_e w_e} \tag{A3.1}$$

$$v_e{}^{IDFF} = \frac{Q}{(N-1) l_{ch} t_e}, \tag{A3.2}$$

where t_e and w_e are the electrode thickness and width (15 mm), respectively, l_{ch} is the channel length (16 mm), and N the total number of channels (7 channels). The flow rate to sustain an electrolyte velocity of 3.5 cm s^{-1} in the porous electrode for the evaluated reactor configurations is given in **Table A3.2**.

Table A3.2: Required flow rate to sustain an electrolyte velocity in the electrode of 3.5 cm s^{-1} in the four electrode-flow field configurations for 1, 2, and 3 electrode layers.

$v_e = 3.5\ \mathrm{cm\ s^{-1}}$	Flow rate (Q) [mL min^{-1}]		
	1 layer	**2 layers**	**3 layers**
FTFF + Freudenberg paper	5.04	10.08	15.91
FTFF + ELAT cloth	14.18	20.63	30.24
IDFF + Freudenberg paper	32.26	64.51	101.81
IDFF + ELAT cloth	63.50	132.05	193.54

A3.5. Electrochemical impedance spectroscopy: equivalent circuit model

The equivalent circuit model used in this work to fit the EIS data [2] consists of an inductor (L) in series with an ohmic resistor (R_Ω), as well as a constant-phase element (CPE) in parallel with a charge transfer resistor (R_{CT}), in series with a second constant-phase element (CPE), in parallel with a mass transfer resistor (R_{MT}), see **Figure A3.2**.

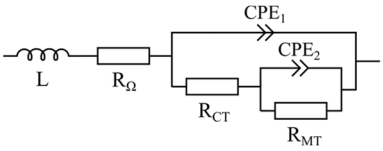

Figure A3.2: Equivalent circuit model for electrochemical impedance spectroscopy.

The Z fittings were made based on the average EIS data of the experimental data (every experiment was repeated twice (n=2)). An example of EIS data fitting in the form of a Nyquist plot is shown in **Figure A3.3**.

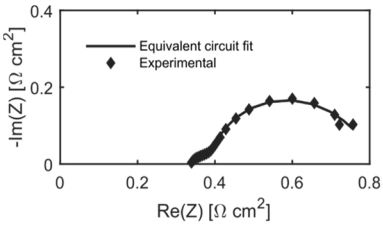

Figure A3.3: Experimental and equivalent circuit fit Nyquist plots for 1 layer of the paper electrode in combination with the interdigitated flow field.

A3.6. Pore network model description

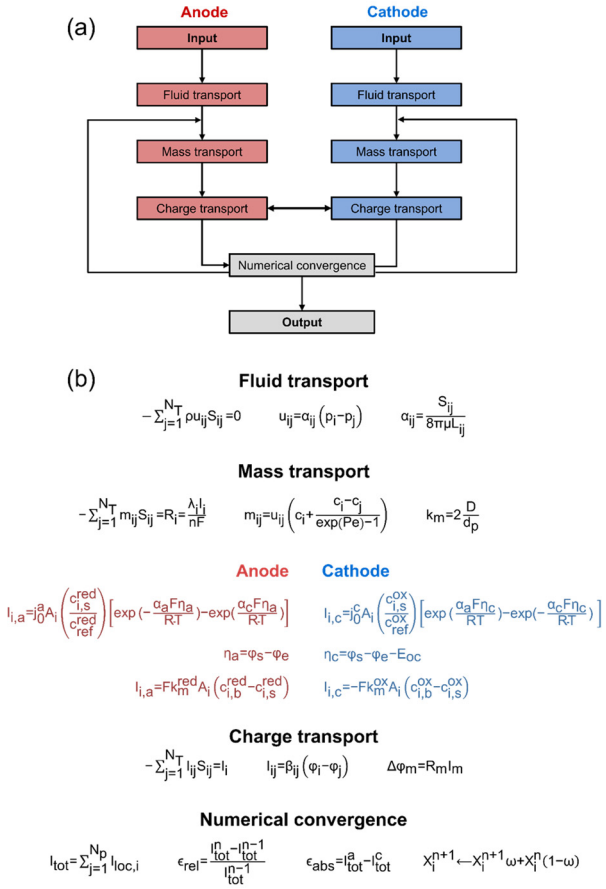

Figure A3.4: Pore network model description, including: **(a)** the flowchart of the iterative pore network modeling algorithm, showing the coupling of the anodic and cathodic half-cells and the iterative loop for achieving numerical convergence, and **(b)** the corresponding model equations.

A3.7. Pore network extraction

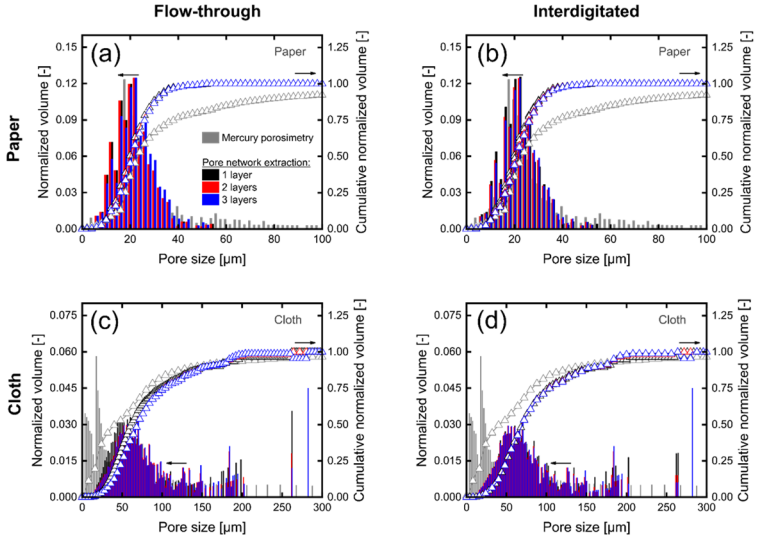

Figure A3.5: The pore size distributions of the electrodes for 1, 2, or 3 layers in thickness were obtained with mercury intrusion porosimetry [3] and the SNOW pore network extraction algorithm. The normalized pore size distributions and the cumulative normalized volumes are shown for: **(a)** the paper electrode used for the FTFF simulations, **(b)** the cloth electrode used for the FTFF simulations, **(c)** the paper electrode used for the IDFF simulations, and **(d)** the cloth electrode used for the IDFF simulations. The normalized volume is defined as the fraction of the total pore volume occupied by all pores within a 2 µm pore size range.

Table A3.3: Network properties of the extracted pore networks for 1, 2, or 3 layers in thickness for the paper and cloth electrodes, used for the FTFF simulations. The pressure drop was obtained at an electrolyte velocity of 3.5 cm s^{-1}.

Electrode	Parameter	1 layer	2 layers	3 layers
Freudenberg H23	In-plane permeability × 10^{-12} [m²]	2.6	2.7	2.7
	Through-plane permeability × 10^{-12} [m²]	1.0	1.4	1.7
	Anisotropy ratio [-]	2.5	1.9	1.6
	Internal surface area [m² m^{-3}]	1.6 × 10^5	1.4 × 10^5	1.4 × 10^5
	Porosity [-]	0.66	0.66	0.66
	Thickness [µm]	198	396	594
	Pressure drop [MPa m^{-1}]	0.91	0.87	0.85
ELAT Cloth	In-plane permeability × 10^{-12} [m²]	36	43	46
	Through-plane permeability × 10^{-12} [m²]	17	18	17
	Anisotropy ratio [-]	2.1	2.5	2.6
	Internal surface area [m² m^{-3}]	1.4 × 10^5	1.3 × 10^5	1.3 × 10^5
	Porosity [-]	0.73	0.73	0.73
	Thickness [µm]	375	750	1125
	Pressure drop [MPa m^{-1}]	0.074	0.053	0.050

Table A3.4: Network properties of the extracted pore networks for 1, 2, or 3 layers in thickness for the paper and cloth electrodes, used for the IDFF simulations. The pressure drop was obtained at an electrolyte velocity of 3.5 cm s^{-1}.

Electrode	Parameter	1 layer	2 layers	3 layers
Freudenberg H23	In-plane permeability × 10^{-12} [m²]	2.8	2.9	2.9
	Through-plane permeability × 10^{-12} [m²]	1.0	1.4	1.7
	Anisotropy ratio [-]	2.7	2.0	1.8
	Internal surface area [m² m^{-3}]	1.6 × 10^5	1.4 × 10^5	1.4 × 10^5
	Porosity [-]	0.66	0.66	0.66
	Thickness [µm]	198	396	594
	Pressure drop [MPa m^{-1}]	1.03	1.19	1.44
ELAT Cloth	In-plane permeability × 10^{-12} [m²]	37	44	47
	Through-plane permeability × 10^{-12} [m²]	19	18	18
	Anisotropy ratio [-]	2.1	1.0	3.4
	Internal surface area [m² m^{-3}]	1.3 × 10^5	1.3 × 10^5	1.3 × 10^5
	Porosity [-]	0.73	0.73	0.73
	Thickness [µm]	375	750	1125
	Pressure drop [MPa m^{-1}]	0.11	0.15	0.21

A3.8. Pressure drop vs. flow rate

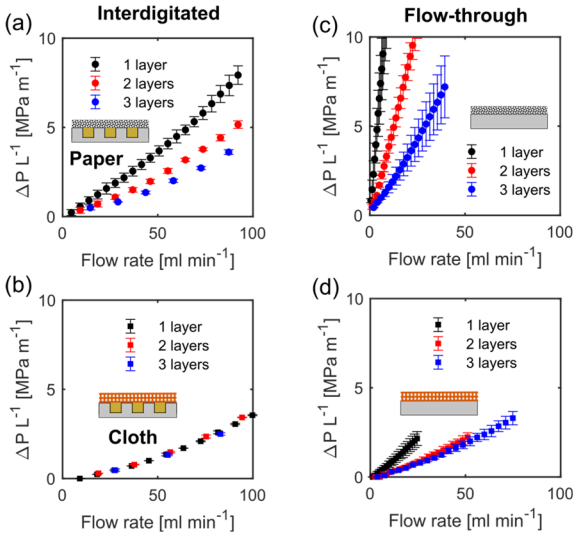

Figure A3.6: Hydraulic analysis of the four electrode-flow field configurations with 1, 2, and 3 electrode layers. The normalized pressure drop at different electrolyte flow rates is presented for: **(a)** the IDFF with the paper electrode, **(b)** the IDFF with the cloth electrode, **(c)** the FTFF with the paper electrode, and **(d)** the FTFF with the cloth electrode.

A3.9. Pore network model parameters

As reported in previous studies [4], the interactions between the distinct electrode microstructures and flow fields affect the accessibility of the internal surface area available in the electrode for the electrochemical reactions. As such, the kinetics and subsequent exchange current density (**Table A3.5**) experience significant variations among different electrode-flow field configurations. Interdigitated flow fields enable greater internal surface area accessibility in combination with the paper electrode, whereas flow-through flow fields with the cloth electrode.

Table A3.5: Exchange current density values for both electrodes and flow field geometries obtained from the experimental data.

Electrode	Flow field	Exchange current density [A m^{-2}]
Freudenberg H23	Flow-through	328
	Interdigitated	721
ELAT Cloth	Flow-through	305
	Interdigitated	222

Table A3.6: Membrane resistance values measured experimentally and fitted ohmic resistance obtained after a Non-Linear Least-Squares minimization of the experimental data.

Electrode	Flow field	Number of layers	Membrane resistance exp [Ω]	Fitted ohmic resistance [Ω]
Freudenberg H23	Flow-through	1	0.17	0.30
		2	-	0.08
		3	-	0.21
	Interdigitated	1	0.06	0.06
		2	-	0.05
		3	-	0.07
ELAT Cloth	Flow-through	1	0.19	0.21
		2	-	0.10
		3	-	0.15
	Interdigitated	1	0.16	0.20
		2	-	0.14
		3	-	0.13

A3.10. Pore network model validation

The pore network model was previously validated for an aqueous electrolyte (0.1 M Fe^{2+}/0.1 M Fe^{3+} in 1 M NaCl) for both one layer of Freudenberg H23 and one layer of ELAT Cloth [5] in combination with an FTFF. In this manuscript, the model is used to simulate various electrode thicknesses and is extended to capture the performance of the IDFF. Therefore, the model is again validated against experimental data by comparing the polarization curves obtained from the experiments with those obtained by the model, using the model parameters from **Tables 3.1** and **A3.3 - A3.5**. A discrepancy in the system resistance was observed for various cases, which was corrected with a Non-Linear Least-Squares Minimization of the ohmic resistance, see **Figure A3.7** (unfitted) and **A3.8** (fitted) and **Table A3.6**. The mismatch in ohmic resistance could have multiple causes, depending on experimental conditions, model assumptions, and system-to-system variations. Possible explanations include the following: **(1)** the averaged measured membrane resistance value can deviate from reality because of inherent flaws in the experimental method used. **Furthermore, the PNM does not consider additional resistances, such as contact and distributed resistances, which are present in the experiments**. These resistances can also vary for each system configuration and number of stacked layers, for example, the compression rate could affect this value, which slightly deviates for all experiments (**Table A3.1**). Moreover, the contact resistance is expected to have a significant influence on the ohmic resistance in the flow cell experiments and can be corrected by fitting the ohmic resistance. **(2)** The membrane resistance was used as a constant value in the model per configuration for all layers, while the ohmic resistance can vary depending on the flow field type, electrode thickness, and operation temperature [6] (the dependency is observed in **Table A3.6** as the ohmic resistance was different for the distinct configurations), and thus between different layers of stacked electrodes. **(3)** The conductivity of the electrolyte was measured in isolation from the electrochemical experiments and was assumed constant. The conductivity experiments were performed at room temperature instead of at elevated operation temperatures (generally 20-25 °C measured for similar cell configurations) as a result of heat production. Therefore, the conductivity value is lower in the model, and the temperature dependency with flow rate was not considered (i.e., using an IDFF, stacked electrodes, and operating at higher electrolyte velocities increases the temperature of the electrolyte) [4]. **(4)** The

PNM assumes complete electrode wetting, which is difficult to achieve in aqueous electrolyte systems. Last, **(5)** The PNM simulations were performed with uncompressed electrodes extracted from X-ray tomography images instead of taking into account the 20 % compression rate applied in the experiments. Furthermore, it must be noted that the PNM is an oversimplification of the pore space [5]. This includes the oversimplification of the fluid flow through the electrode and the mass transfer of the active species toward the electrode surface. It is therefore paramount that the PNM is primarily used qualitatively to assess profiles and trends, and is, therefore, a good tool to compare various reactor designs (e.g., electrode types, number of layers, electrolytes).

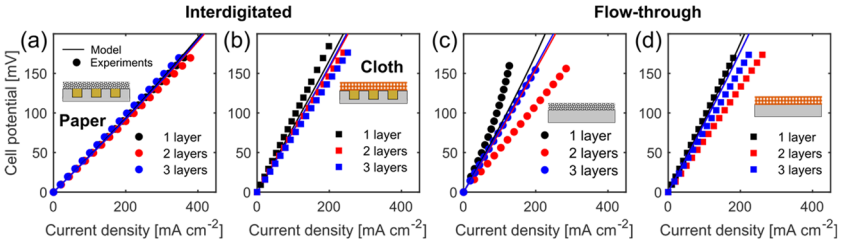

Figure A3.7: Comparison between unfitted model predictions with polarization experiments without fitted ohmic resistance values for the four electrode-flow field combinations with 1, 2, and 3 electrode layers at 3.5 cm s^{-1}: **(a)** interdigitated flow field and paper electrode, **(b)** interdigitated flow field and cloth electrode, **(c)** flow-through flow field and paper electrode, and **(d)** flow-through flow field and cloth electrode.

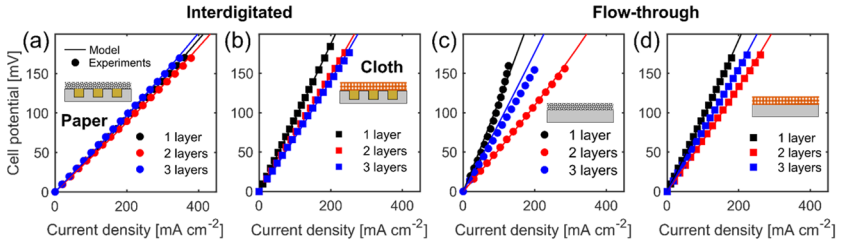

Figure A3.8: Comparison between model predictions with fitted ohmic resistance values (**Table A3.6**) and polarization experiments for the four electrode-flow field combinations with 1, 2, and 3 electrode layers at 3.5 cm s^{-1}: **(a)** interdigitated flow field and paper electrode, **(b)** interdigitated flow field and cloth electrode, **(c)** flow-through flow field and paper electrode, and **(d)** flow-through flow field and cloth electrode.

A3.11. Electrochemical Impedance Spectroscopy plots

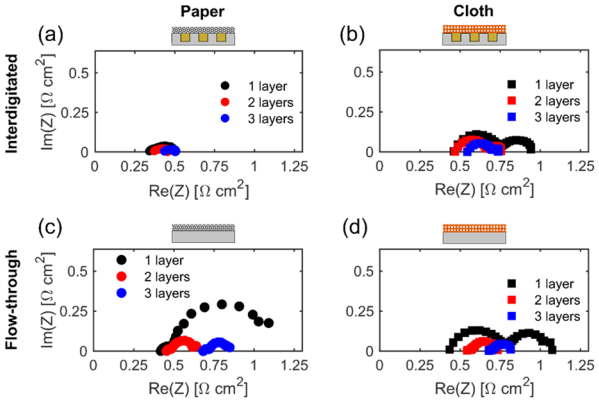

Figure A3.9: Electrochemical impedance data of the four electrode-flow field combinations with 1, 2, and 3 electrode layers at 3.5 cm s^{-1}: **(a)** interdigitated flow field and paper electrode, **(b)** interdigitated flow field and cloth, **(c)** flow-through flow field and paper, and **(d)** flow-through flow field and cloth electrode.

A3.12. Effect of the electrolyte velocity on the electrochemical performance

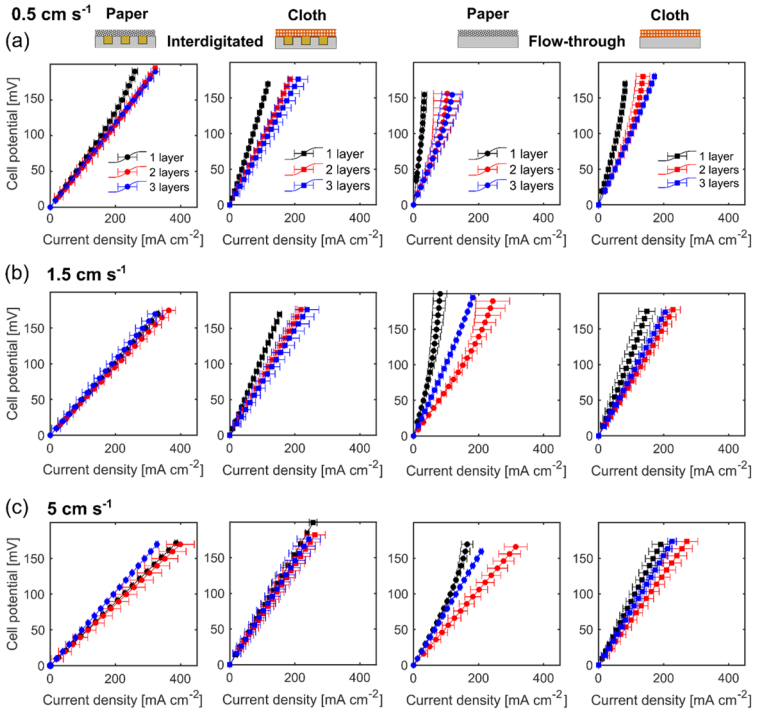

Figure A3.10: Cell potential *vs.* current density curves with error bars for the four electrode-flow field combinations (from left to right: paper with interdigitated flow field, cloth with interdigitated flow field, paper with flow-through flow field, and cloth with flow-through flow field) with 1, 2, and 3 electrode layers at **(a)** 0.5, **(b)** 1.5, and **(c)** 5 cm s^{-1}.

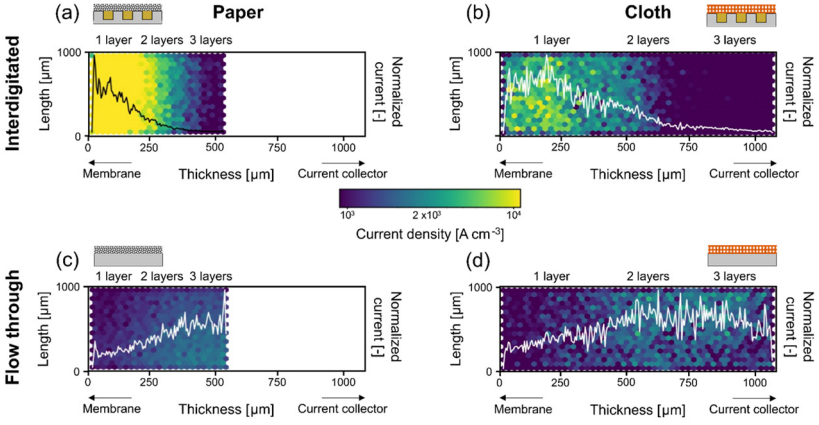

Figure A3.11: Current profiles in 2D with the current density per volume of electrode plotted over the thickness and length of the electrode, and in 1D with the normalized current (normalized by the total current generated in the electrode) plotted over the electrode thickness, with the membrane at 0 µm. The current profiles are shown for both flow fields and electrodes and for 3 electrode layers at 0.5 cm s^{-1} and -0.2 V, with: **(a)** the profiles for the interdigitated flow field and paper electrode, **(b)** the interdigitated flow field and cloth electrode, **(c)** the flow-through flow field and paper electrode, and **(d)** the flow-through flow field and cloth electrode.

A3.13. Concentration 3D plots for the flow-through flow field

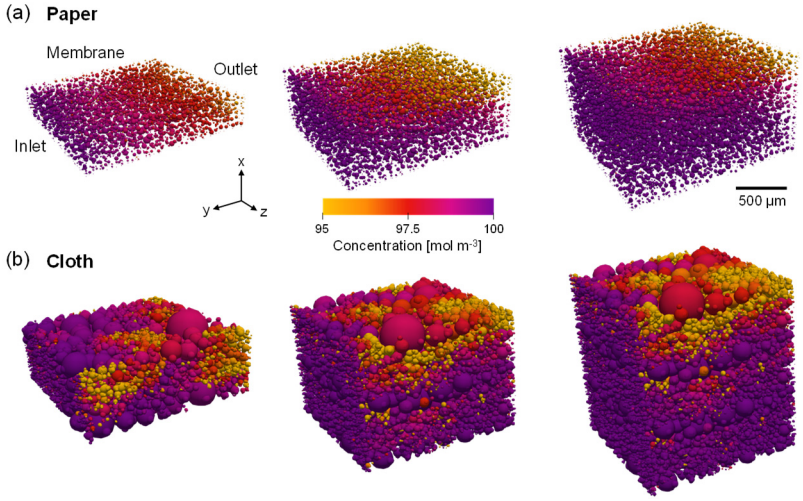

Figure A3.12. Concentration profiles of Fe^{3+} in the porous electrode using a flow-through flow field (shown with a visual representation) were obtained by pore network simulations at 3.5 cm s^{-1} and -0.2 V. The concentration profiles are shown for 1, 2, or 3 layers in thickness from left to right for the first network of the network in series and for: **(a)** the paper electrode, and **(b)** the cloth electrode. The x-direction represents the thickness of the electrode from the flow field (bottom) to the membrane (top). The y-direction represents the length of the electrode and the z-direction the width.

A3.14. List of Symbols

Symbol	Description	Units
A_i	Electrochemically active internal surface area of pore i	m^2
A_{in}	Geometrical inlet area of the electrode	m^2
c	Concentration	mol m^{-3}
D	Diffusion coefficient	m^2 s^{-1}
d_p	Pore diameter	m
E_{oc}	Open-circuit potential	V
F	Faradaic constant, 96,485 C mol^{-1}	C mol^{-1}
I	Current	A
I_{ij}	Charge flux	A m^{-2}
j_0	Exchange current density	A m^{-2}
k_m	Mass transfer coefficient	m s^{-1}
L	Conduit length, length of the medium	m
l_{ch}	Channel length	m
m	Mole flux	mol m^{-2} s^{-1}
n	Number of electrons, or iteration number	-
N	Number of channels	-
N_p	Number of pores	-
N_T	Number of throats	-
p	Pressure	Pa
Pe	Peclet number	-
Q	Flow rate	m^3 s^{-1}
R	(a) Molar gas constant, 8.314 J mol^{-1} K^{-1}	J mol^{-1} K^{-1}
	(b) Resistance	Ω
	(c) Net reaction rate	mol s^{-1}
S	Cross-sectional area	m^2
T	Operating temperature	K

t_e	Electrode thickness	m
u	Fluid velocity	m s^{-1}
V	Voltage	V
V_{cell}	Given cell potential	V
v_e	Superficial velocity of the electrolyte	m s^{-1}
w_e	Electrode width	m
X	Concentration or potential	mol m^{-3} or V
	Greek	
α	(a) Transfer coefficient	-
	(b) Hydraulic conductance of the throat	m Pa^{-1} s^{-1}
β	Electrical conductance	S m^{-2}
ϵ	Error value	-
η	Overpotential	V
λ	Stoichiometric coefficient	-
μ	Dynamic viscosity	Pa s
ρ	Electrolyte density	kg m^{-3}
φ	Potential	V
ω	Relaxation factor	-
	Superscripts	
a	Anode	
c	Cathode	
n	Iteration number	
ox	Oxidized form	
red	Reduced form	
	Subscripts	
a	Anode	
abs	Absolute	
b	Bulk	
c	Cathode	
e	Electrolyte, liquid phase	
i	Within pore i, species i	
ij	Pore i to pore j, throat ij	
in	Inlet	
j	Within pore j, species j	
loc	Local	
m	Membrane	
ref	Reference	
rel	Relative	
s	Solid phase, surface	
tot	Total	

A3.15. References

[1] J. D. Milshtein *et al.*, *J. Electrochem. Soc.* **164**, E3265–E3275 (2017).

[2] N. Meddings *et al.*, *Journal of Power Sources*. **480**, 228742 (2020).

[3] A. Forner-Cuenca, E. E. Penn, A. M. Oliveira, F. R. Brushett, *J. Electrochem. Soc.* **166**, A2230–A2241 (2019).

[4] V. Muñoz-Perales, S. E. Ibáñez, E. García-Quismondo, S. Berling, M. Vera, *J. Electrochem. Soc.,* **169**, 100522 (2022).

[5] M. van der Heijden, R. van Gorp, M. A. Sadeghi, J. Gostick, A. Forner-Cuenca, *J. Electrochem. Soc.* **169**, 040505 (2022).

[6] K. T. Cho *et al.*, *J. Electrochem. Soc.* **159**, A1806–A1815 (2012).

Chapter 4

Bottom-up design of porous electrodes by combining a genetic algorithm and a pore network model

Abstract

The microstructure of porous electrodes determines multiple performance-defining properties, such as the available reactive surface area, mass transfer rates, and hydraulic resistance. Thus, optimizing the electrode architecture is a powerful approach to enhance the performance and cost-competitiveness of electrochemical technologies. To expand our current arsenal of electrode materials, we need to build predictive frameworks that can screen a large geometrical design space while being physically representative. Here, we present a novel approach for the optimization of porous electrode microstructures from the bottom-up that couples a genetic algorithm with a previously validated electrochemical pore network model. In this first demonstration, we focus on optimizing redox flow battery electrodes. The genetic algorithm manipulates the pore and throat size distributions of an artificially generated microstructure with fixed pore positions by selecting the best-performing networks, based on the hydraulic and electrochemical performance computed by the model. For the studied VO^{2+}/VO_2^+ electrolyte, we find an increase in the fitness of 75 % compared to the initial configuration by minimizing the pumping power and maximizing the electrochemical power of the system. The algorithm generates structures with improved fluid distribution through the formation of a bimodal pore size distribution containing preferential longitudinal flow pathways, resulting in a decrease of 73 % for the required pumping power. Furthermore, the optimization yields a 47 % increase in surface area resulting in an electrochemical performance improvement of 42 %. Our results show the potential of using genetic algorithms combined with pore network models to optimize porous electrode microstructures for a wide range of electrolyte compositions and operation conditions.

This chapter is published as:

R. van Gorp*, M. van der Heijden*, M.A. Sadeghi, J. Gostick, and A. Forner-Cuenca, Bottom-up design of porous electrodes by combining a genetic algorithm and a pore network model, *Chemical Engineering Journal*, **455** (2023), pp. 139947, doi:10.1016/j.cej.2022.139947.

*Co-first authors

4.1. Introduction

Porous electrodes are performance-defining components in next-generation electrochemical technologies, such as batteries, fuel cells, and electrolyzers, where they are responsible for multiple key functions affecting thermodynamics, kinetics, and transport [1–7]. In redox flow batteries (RFBs), which are the focus of this study, the porous electrode provides the surface area for electrochemical reactions, facilitates mass, charge, and heat transport, and dictates the hydraulic requirements of the reactor [8–11]. Thus, the electrode microstructure determines the overall performance, durability, and operating cost of the system. However, the current arsenal of materials is limited to porous carbon fiber-based mats (e.g., papers, cloths, and felts) which have not been tailored to sustain liquid-phase electrochemistry. An effective means to improve the cost-competitiveness of RFBs and satisfy the stringent cost and performance requirements of emerging electrochemical systems is by designing tailored electrodes [12–14]. However, the design of porous electrodes in convection-enhanced electrochemical systems is particularly challenging as multiple contradictory requirements (e.g., facile mass transport, high electrochemical surface area, low pumping demands) must be satisfied simultaneously, motivating the development of advanced optimization strategies.

Porous electrode engineering has received notable attention in the past decade. Traditionally, the field was dominated by empirical design, where considerable research has been conducted on understanding the role of the electrode microstructure [5, 11, 15], increasing the active surface area and heteroatom content [16–18], and improving the flow distribution within porous electrodes [19–21]. However, the empirical design of electrodes is expensive, time- and labor-intensive, and limited to a narrow design space determined by existing manufacturing routes [12]. To support experimental design, multiscale modeling of porous electrodes has been deployed in recent years in a variety of forms. For example, macrohomogenous models were used to understand the influence of cell-averaged properties on the overall stack performance [10, 22, 23]. Moreover, geometrically resolved models, such as the Lattice Boltzmann method and computational fluid dynamic simulations, have been used to resolve reactive transport phenomena within porous electrode microstructures [24–26], which is needed to design advanced electrode architectures [26–31]. While these computational efforts have improved our understanding of reactive transport phenomena in porous electrodes, most of these studies have focused on modeling existing sets of materials but have not yet been deployed to realize the bottom-up design of electrodes.

To make these computational tools truly predictive and accelerate materials discovery, the community will need to build frameworks that enable the self-driven exploration of a broad geometrical design space. A promising approach to fill this research gap is to couple pore-scale simulations with machine learning and heuristic algorithms [32–35]. Facilitated by the rapid rise in computational power, the application of these methods has become an instrumental tool to optimize the topology of products for a wide-range of applications (e.g., aerospace, antennas, and heat exchangers), spurring interest to apply these methods for the optimization of porous electrode structures used in electrochemical devices [32]. The genetic algorithm (GA) is a widely used method that enables the heuristic optimization of a given design space and is based on the evolution of a population of candidate solutions, using operators based on diversity and selection [36]. The objective of the GA is to discover, emphasize, and recombine good building

blocks of solutions, which can be leveraged to generate increasingly better sets of candidate solutions for the given design case.

The integration of optimization tools within electrochemical numerical frameworks has been recently deployed to support the numerical identification of fitting parameters and find optimal operational conditions [33, 37–39], as well as to support the design of cell components [40–43]. Recently, Choi *et al.* utilized a GA in combination with a two-dimensional model of an all-vanadium flow battery to identify the fluid parameters using a fitness function involving the mean square error of the voltage between the experimental and simulated data. The simulated capacity-voltage curves showed good agreement with the experimentally obtained data, bringing the mean relative error between the model and experimental results down to ≤1.9 % (e.g., from 6.7 % to 0.62 % for 80 mA cm^{-2} and 60 mL min^{-1}) [37]. Moreover, Tenny *et al.* leveraged a GA with a neural network to identify optimal electrode properties (e.g., thickness, porosity, kinetic rate constant) using a macrohomogenous model that improves the power density in RFBs [33]. Further, Roy *et al.* showed the potential of applying topology optimization to design porous electrodes for different electrochemical applications, namely a flow battery and a supercapacitor. The algorithm optimized the current distribution which resulted in the formation of a porous material where the computed designs featured improved performance with respect to the baseline monolithic electrode [44]. Finally, Wan *et al.* developed a coupled machine learning and GA data-driven approach to design porous electrodes for RFBs, which resulted in electrodes with a larger specific surface area and high hydraulic permeability, but their design space was limited to fibrous structures [40]. Inspired by these previous efforts, we aim to develop a computational framework that affords large versatility of design, robust physical representativeness, and maintains a low computational cost.

To couple pore-scale simulations with genetic algorithms and optimize the electrode structure from the bottom-up, the modeling framework must resolve the relationship between the electrode microstructure and the battery performance in a computationally inexpensive manner. Geometrically-detailed modeling approaches (e.g., Lattice Boltzmann method, computational fluid dynamics) are difficult to couple with heuristic algorithms because of their high computational demands [45]. On the contrary, macrohomogenous models are computationally inexpensive, but are built on volume-averaged grids and thus fail to capture the electrode microstructure. Motivated by this challenge, here we explore the combination of pore network modeling (PNM), which is pore-scale but computationally light [27, 29], with a GA for microstructural optimization. The coupling of a GA and a PNM offers an excellent platform for the microstructural optimization of larger electrode fragments while remaining computationally feasible. The implementation of other approaches, such as the coupling of gradient-based optimization methods (e.g., topology optimization) with a finite element electrochemical model are promising [46], but their computational demands make them currently impractical for extensive screening of microstructures at a scale relevant for RFB operation. GAs utilizing PNMs have been used in other research fields, including the field of petroleum recovery [47–50]. One example is the work of Jamshidi *et al.*, who leveraged a genetic algorithm to extract a pore network with the static and hydraulic properties of a reservoir rock sample [48]. In another study, Xu *et al.* used a GA to reconstruct a PNM to approach the structure of a rock sample [49]. These previous studies have only focused on the application of GAs to extract networks of porous rock samples, whereas, to the best of

our knowledge, the use of genetic optimization coupled with PNMs has not yet been studied in the context of electrode microstructure design and optimization.

Here, we couple for the first time a pore network model with a genetic algorithm to optimize the three-dimensional microstructure of flow battery electrodes from the bottom-up. The model builds upon a previously developed PNM electrochemical framework. In our previous work, we validated this PNM for two different electrode microstructures (paper and cloth) and two redox electrolytes (aqueous and non-aqueous) [27]. In this first demonstration, the GA is used to manipulate the pore and throat size distribution and thus optimize the electrode microstructure for a given set of RFB operating conditions and chemistries, assuming perfect wetting of the generated electrode structure. The model is driven by the evaluation of a fitness function that minimizes the hydraulic power requirements and maximizes the electrochemical power output. First, we describe the modeling framework, including the coupling of the iterative electrochemical PNM with the GA. Second, we demonstrate the methodology for a VO^{2+}/VO_2^+ redox couple in a single electrolyte configuration building on artificially generated microstructures with fixed pore positions. Third, we evaluate the sensitivity of the microstructural evolutions towards variations in the electrolyte type and the flow cell operating conditions. Finally, we correlate the resulting performance with the microstructural evolutions originating from the optimization algorithm. Although the focus of this work is on the optimization of porous electrodes for flow batteries, this computational platform can be tailored to design porous materials for a wider variety of convection-enhanced electrochemical technologies such as hydrogen fuel cells, water electrolysis, and CO_2 electrolyzers.

4.2. Model development

The concept of a GA is based on the evolution of a population of candidate solutions to a given design case using operators based on natural diversity and selection. Recombination of good building blocks are leveraged to generate increasingly better sets of candidate solutions for a given design case. In this study, we utilized the geometrical functions available within OpenPNM, an open-source framework for pore network simulations [51], to generate cubic networks with a random distribution of pore sizes and fixed pore positions. The hydraulic and electrochemical performances of the generated cubic network structures were simulated by a model that solves for coupled electrochemical kinetics, mass transport, and momentum transport, validated and described in detail in our previous work [27]. Subsequently, a genetic optimization procedure is applied to evaluate the performance of each network based on a fitness function to combine the best-performing solutions and ultimately find optimal microstructural design characteristics (e.g., the pore size distribution) for a specific system and operating conditions.

The required computational time on a single Intel® Core™ i7-8700K CPU was ~48 hours for the evolution of 1000 generations for the reference system, using 50 individuals per generation and 10 parent networks (~3 seconds per network). It should be noted that the performance and fitness of all networks in a single generation can be computed concurrently if multiple computational cores were used.

4.2.1. Network generation

Cubic lattices were generated with the Cubic class algorithm in the OpenPNM Network module. This algorithm takes a network shape, spacing, and connectivity as inputs and produces a network with the pore and throat coordinates as an output. The shape of the cubic lattices determines the number of generated pores in each dimension, the spacing captures the center-to-center distance of adjacent pores in the cubic lattice, and the connectivity displays the total number of throat connections that a single pore within the cubic lattice embodies. The topological properties were subsequently attributed to the network's pores and throats using the OpenPNM Geometry module. Geometrical formulas of spheres and cylinders were employed together with a random seed value to create randomly distributed topologies. The most important topological properties are displayed in **Figure 4.1**.

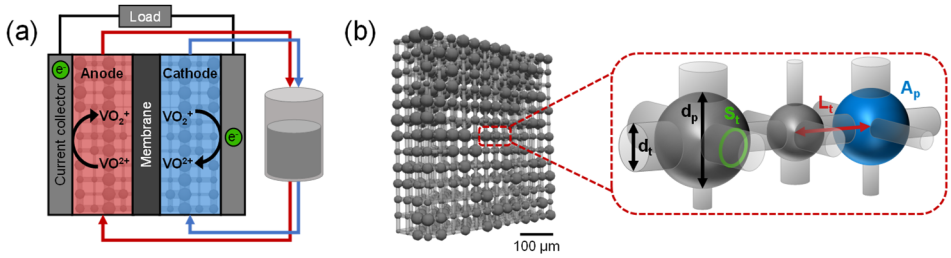

Figure 4.1: (a) Schematic overview of a single-electrolyte vanadium redox flow battery. **(b)** A magnification of the porous electrode microstructure and the pore-throat conduit listing the most important topological properties, namely the pore diameter (d_p), throat diameter (d_t), throat cross-sectional area (S_t), throat length (L_t), and pore internal surface area (A_p).

The pore diameter was assigned by a random process that depends on the maximum pore diameter and a modification factor, called the seed (S_p). This seed value is randomly generated for each pore and is confined between two boundary points, where in this work the boundary point values were arbitrarily chosen as 0.2 and 0.7 for the pore diameter, based on the standard option in the OpenPNM StickAndBall geometry class. The maximum pore size ($d_{p,max}$) was determined by finding the maximum pore diameter that can be placed in each location without overlapping any neighboring pore. The randomly generated seed value of each pore was multiplied by the maximum pore size to find the pore diameter, according to

$$d_p = S_p \, d_{p,max}. \tag{4.1}$$

To prevent the formation of connecting throats with a diameter larger than that of the smallest neighboring pore, each throat diameter was based on the smallest pore size of the two pores that the throat is connected to. This minimum pore size was subsequently multiplied by a throat factor of 0.8 to obtain the diameter of the throat (d_T). The throat factor is based on the ratio of the pore and throat diameters used by Sadeghi *et al.* to reasonably represent the porous structure of a commercial SGL 25AA electrode, which is a representative carbon fiber-based electrode used in flow batteries [29].

$$d_T = 0.8 \min (d_{p,1}, d_{p,2}) \tag{4.2}$$

The throat cross-sectional area (S_T) was determined from the throat diameter assuming that each throat is a perfect cylinder (**equation (4.3)**), whereas the throat's internal surface area (A_T) was calculated as the area of a cylinder mantel (**equation (4.4)**).

$$S_T = \frac{\pi}{4} d_T^2 \tag{4.3}$$

$$A_T = \pi \, d_T L_T \tag{4.4}$$

Where L_T is the throat length, calculated as the length between two throat end points. The throat conduit length on the other hand is defined as the summed length of two half-pores and the connected throat was used for calculating the hydraulic transport through the network. In cubic networks, the summed conduit length is equal to the network spacing.

The pore internal surface area (A_p) was calculated by subtracting the throat cross-sectional area of all neighboring throats of the pore, with N_T being the number of neighboring throats, from the surface area of a perfect sphere with diameter d_p.

$$A_p = \pi \, d_p^2 - \sum_{j=1}^{N_T} S_T \tag{4.5}$$

Equation (4.5) is an approximation of the pore internal surface area as the actual curvature of the intersection between the pore and throat was not taken into account. Note that the pore internal surface area is different from the pore cross-sectional area and that the pore and throat volumes were calculated using geometrical formulas of spheres and cylinders.

4.2.2. Iterative electrochemical algorithm

In this work, we elected to use single-electrolyte flow cells to ensure a constant state-of-charge of 50 %. This configuration enables studying electrode performance and overpotentials in isolation without competitive phenomena such as species crossover through the membrane or distinct redox kinetics in each half-cell [10, 12]. Thus, the modeled domain consists of two symmetric, mirrored porous electrodes in co-flow operation mode (**Figure 4.1a**). Therefore, the open circuit voltage is 0 V, and the opposite redox reactions take place in each of the half cells (i.e., the oxidation reaction in the anodic compartment and the reduction reaction in the cathodic compartment). In addition, a flow-through flow field design was employed since it provides near-unidirectional velocity distribution at the inlet channel, thereby simplifying the boundary conditions [52].

The electrochemical PNM framework, described and validated in our previous work, solves the fluid transport and successively the coupled mass and charge transport within the anodic and cathodic compartments using an iterative algorithm [27]. The model equations and boundary conditions can be found in **Section A4.3**. The iterative algorithm was integrated into the GA as visualized in **Figure 4.2**. First, the fluid transport was solved to obtain the pressure field described by the Navier-Stokes equation, from which the velocity is back-calculated using the Hagen-Poiseuille equation. Because of the assumption of dilute electrolyte, the fluid transport can be solved independently from the mass and charge transport of individual species [29]. The pressure field was subsequently fed in the iterative algorithm to solve the coupled mass and charge transport within the

electrode using two nonlinear systems of equations: the advection-diffusion-reaction and the conservation of charge. The two nonlinear systems of equations are coupled by the Butler-Volmer equation to obtain the species concentration and potential field. The coupling of both half-cells was done by treating the membrane as a macro continuum entity, allowing the protons to be transported between both half-cells. Thus, only the overall macroscopic ionic resistance of the membrane (Ohm's law) was considered, which coupled the charge transport within one half-cell with the electrolyte potential at the membrane boundary in the other half-cell [29].

The electrochemical model was solved for an arbitrarily applied potential with an initial guess for the overpotential and concentration. The initial guess of the overpotential was set to zero for the first network in the first generation, while the overpotential guess for the next networks was based on the previously modeled network results to speed up the iterative algorithm. The initial guess of the concentration was set to the inlet concentration for all modeled networks (100 mol m^{-3} for both vanadyl ion, VO^{2+}, and pervanadyl ion, VO_2^+, species).

The numerical convergence was achieved when the specified relative and absolute tolerances were met, defined by the total current generated or consumed, and bound by a maximum number of iterations. To counteract the divergence of the solution caused by the highly nonlinear nature of the system, an under-relaxation scheme was imposed on the concentration and potential fields using a constant relaxation factor (**Table 4.1**). In addition, a linearization of the charge transport source term was considered as explained in our previous work [27].

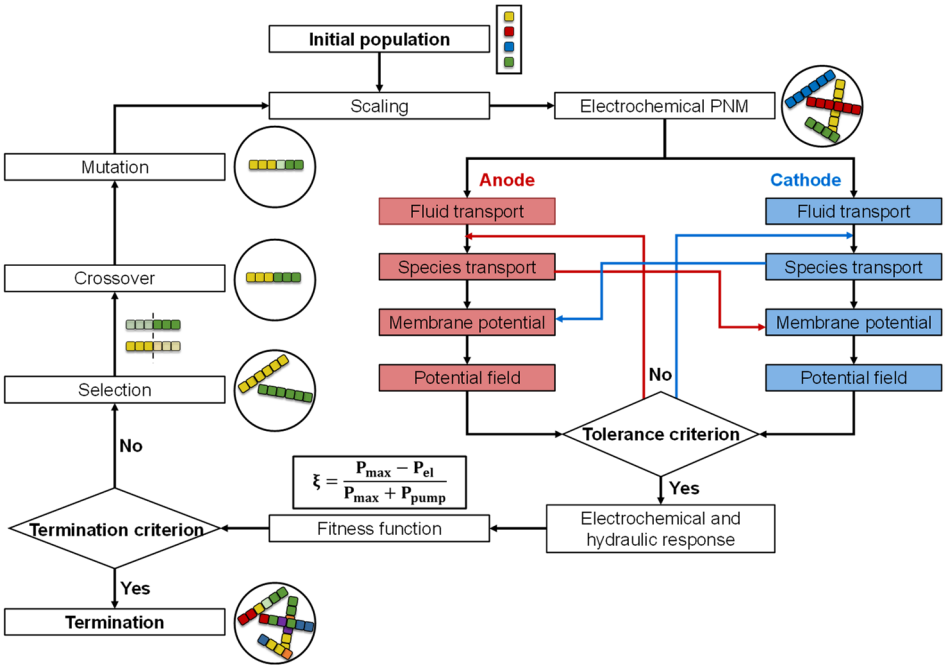

Figure 4.2: Schematic flowchart of the operations in the proposed genetic algorithm together with illustrations showing the changes in the network structure after each operation, where different colored squares represent different building blocks.

4.2.3. Genetic operations

Genetic optimization comprises five operations: initialization, selection, crossover, mutation, and termination. During initialization, a random set of candidate solutions is generated, called the population. This population evolves in successive generations where in each generation a fitness function is used to assess the adequacy of each candidate solution. Subsequently, the selection operator picks the fittest individuals in the population (i.e., the parents) for reproduction. These selected parents produce new individuals (i.e., the offspring) through a crossover and mutation operation. In the crossover operation, the offspring networks inherit their structure by mixing the information from both parent networks, and in the mutation operation stochastic changes are made in the offsprings' structure to broaden the search domain [53]. The genetic optimization is stopped when a specified termination criterion is reached, which can be based either on the desired fitness or the total number of generations. A schematic overview of the developed framework is presented in **Figure 4.2**, followed by a detailed description of each operation in the algorithm.

4.2.3.1. Initialization

The topologies of 50 cubic networks were randomly generated using the OpenPNM geometry functions. In this work, the optimization of a relatively small, cubic three-dimensional electrode structure (676 pores) was considered, see **Table 4.1**. Drawing inspiration from the microstructural properties of the commercially available electrode Freudenberg H23, which features a median pore size of ~ 22 µm and a measured thickness of 170 µm under 1 MPa compression, we generated an electrode with a thickness of 160 µm and a pore size range of 2 - 38 µm [11, 27, 54]. The electrode area was set to 580 x 580 μm^2. A comparison between the pore size range of a commercial Freudenberg H23 electrode and the artificially generated structures is presented in **Figure A4.3**. Each pore was connected to its direct neighbor, giving 6-faced connectivity. The boundary pores and throats required for the implementation of the transport algorithms were generated at each surface. The network porosity, network shape, number of pores, and number of throats are a direct result of the chosen input parameters. Finally, to study the influence of boundary effects on the simulation results, we performed a pore number sensitivity analysis. The results of this study are presented in **Section A4.5**.

The optimal value for the mutation range, mutation chance, number of offspring, and number of parent networks in the genetic optimization study is a balance between the size of the desired search domain and the required computational time. Parameter settings in current GAs are based on previously reported cases and are here inspired by the work of Grefenstette [55]. Additionally, the values for the evaluation criteria of the PNM algorithm (i.e., tolerance, number of iterations, relaxation factor) are described in our previous work [27].

To allow for a meaningful comparison between the pore networks generated in different generations, a network scaling step was taken after initialization. In this step, the total pore volume of each generated network was matched to the pore volume of a reference network by uniformly scaling all pore diameters. Thus, maintaining a constant network porosity during the evolution and simultaneously providing evolutionary freedom to optimize for the total pore surface area. The reference network consists of

pores with a diameter of 20 µm and throats with a diameter of 15.6 µm. The pore-to-throat diameter ratio was chosen to represent commercial porous electrodes using the data reported by Sadeghi *et al*. [29].

Table 4.1: Parameters used for the genetic optimization study.

Parameter	Value
Spacing	40 µm
Porosity	54 %
Network shape	[13, 13, 4]
Number of pores	676
Number of throats	1755
Network dimensions	580 x 580 x 160 μm^3
Connectivity	6
Number of generations	1000
Number of offspring	50
Number of parents	10
Mutation range	0.10
Mutation chance	0.05
Relative tolerance	10^{-4}
Absolute tolerance	10^{-4}
Maximum iterations	10000
Relaxation factor	0.1

4.2.3.2. Parent selection

The selection procedure of the GA follows the principle of survival of the fittest. The fitness of the networks was extracted from the developed electrochemical model which resolves the total generated current and pressure drop for each microstructure. The thermodynamic maximum electrochemical power (P_{max}) was determined by [56]

$$P_{max} = I\, E_{cell}, \tag{4.6}$$

where I is the total current and E_{cell} the open circuit cell potential of a full-vanadium battery system, which is assumed to be 1.26 V [57]. As we are fixing the overpotential (E_{losses}), we aim to increase the maximum electrochemical power by reaching higher total currents at a fixed overpotential. The electrochemical power loss (P_{el}), capturing the overpotentials in the cell, was defined as [56]

$$P_{el} = I\, E_{losses}, \tag{4.7}$$

where E_{losses} is the combined overpotential (activation, ohmic, and mass transfer) present in the single electrolyte cell. For the reference system, the overpotential losses were arbitrarily set to 0.5 V, which corresponds to 40 % of electrochemical losses as heat during cell discharge. Additionally, the pumping power (P_{pump}) required to pump the electrolyte through the electrode was determined by [58]

$$P_{pump} = \frac{Q\ \Delta \mathrm{P}}{\eta_p}, \tag{4.8}$$

where Q is the electrolyte flow rate (with an applied velocity of 1.5 cm s^{-1} for the reference system), ΔP the pressure drop, and η_p the pumping energy efficiency, which was assumed

to be 0.9 [58]. The fitness (ξ) of the pore network was subsequentially calculated by comparing the electrochemically generated power to the summation of the maximum electrochemically generated power and pumping power

$$\xi = \frac{P_{max} - P_{el}}{P_{max} + P_{pump}}, \tag{4.9}$$

The percentual increase in fitness after n generations can subsequently be determined by the following equation $(\xi_n - \xi_1)/\xi_1 \cdot 100\,\%$, where ξ_1 is the fitness of the best-performing network in the first generation of artificially-generated networks.

It must be noted that, in this work, we are optimizing the electrode structure for one specific redox couple (VO^{2+}/VO_2^+) in a single-electrolyte cell system. Therefore, we assume for this theoretical exercise that the overpotential resulting from the other redox pair (the V^{2+}/V^{3+} redox pair in a full-vanadium battery) is identical to be able to subtract P_{el} from P_{max}.

The maximum fitness is achieved when the pumping losses are zero, even though the overpotential losses are not (fully) optimized. The maximum fitness value is thus dependent on the fixed overpotential losses (0.5 V for the reference system). Finally, the ten networks with the highest fitness value ($\xi \rightarrow 0.603$ for the reference system) were selected as parents for the mating pool.

4.2.3.3. Crossover

The crossover operator randomly selects two parent networks from the mating pool to produce an offspring network. The pore size and throat size information of the produced offspring network was inherited from both parents via a two-step procedure. First, a random pore number was selected between the first (0) and the final index (n_P) of the pore diameter array. Subsequently, the geometry information (e.g., pore and throat diameters) before this pore number was obtained from the first parent, and the geometry information after the locus was inherited from the second parent, resulting in the offspring network.

4.2.3.4. Mutation

The mutation operator allows for random pore diameter changes in the generated offspring networks, which is critical for the exploration of the entire search domain. The degree of mutation was controlled by the mutation chance and the mutation range. The mutation chance describes the probability that a mutation occurs within each pore and the mutation range (σ_M) describes the severity of the mutation. If a pore was selected for mutation, a random mutation value (c_M) was stochastically chosen between $(1 - \sigma_M) \leq c_M \leq (1 + \sigma_M)$. The mutated pore diameter (d_p^M) was subsequently determined from the old pore diameter (d_p^o) by

$$d_p^M = c_M \, d_p^o. \tag{4.10}$$

To maintain a constant network porosity and thus a fair comparison between the network geometries in between different generations, the pore diameters of each newly generated

offspring network were uniformly scaled up or down until the total pore volume matches that of the specified reference network (**Section 4.2.3.1**).

4.2.3.5 Termination

The evolution of the network fitness follows a decaying upward growth. Thus, the improvement in network performance is diminishing with each consecutive optimization step. We observed that, for the reference system, the progression of the network fitness in the last 100 generations is only marginal (0.89 %) compared to the fitness increase over the first 100 generations (41 %). To enable the comparison of networks generated at different operating conditions and electrolyte properties, we terminate the genetic algorithm when a maximum number of generations (1000) is reached.

4.2.4. Operating parameters

In this study, we apply the numerical framework to optimize the electrode microstructure for the all-vanadium flow battery since this is the state-of-the-art system [59]. Specifically, here we considered a single-electrolyte cell design utilizing the VO^{2+}/VO_2^+ redox couple. This redox couple is kinetically-sluggish [10, 60], offering an interesting platform for optimizing the balance between electrochemical performance (i.e., mass transfer and available surface area) and parasitic pumping losses [61]. While quantitative modeling is challenging due to the use of single-electrolyte platforms, we aim to obtain overarching trends with the vanadium electrolyte that can guide the design of advanced electrodes. We hope that our findings will serve as a basis for future studies on tailored materials for specific redox chemistries. The physicochemical properties of the electrolyte and main operating conditions used as input in the electrochemical algorithm are shown in **Table 4.2**. These parameters were obtained from literature or have been experimentally determined as described in **Section A4.6**. To satisfy the dilute electrolyte assumption (i.e., migration is not considered in the iterative algorithm [62]), we operate the RFB cell at a relatively low vanadyl ion, VO^{2+}, and pervanadyl ion, VO_2^+, inlet concentration of 100 mol m^{-3} per species in an excess supporting electrolyte solution of 1000 mol m^{-3} H_2SO_4.

Table 4.2: Electrolyte and electro-kinetic properties for the VO^{2+}/VO_2^+ vanadium chemistry.

Parameter	Symbol	Value
Density of the electrolyte in both half-cells	ρ_l	992 kg m^{-3}
Viscosity of the electrolyte in both half-cells	μ	8.9 x 10^{-4} Pa s
VO^{2+} diffusion coefficient in the electrode [63]	D_{VO2+}	2.11 x 10^{-10} m^2 s^{-1}
VO_2^+ diffusion coefficient in the electrode [63]	D_{VO2+}	2.11 x 10^{-10} m^2 s^{-1}
Inlet VO^{2+} concentration in both half-cells	$c_{VO2+,in}$	100 mol m^{-3}
Inlet VO_2^+ concentration in both half-cells	$c_{VO2+,in}$	100 mol m^{-3}
Supporting electrolyte concentration		1.0 M H_2SO_4
Bulk electrolyte conductivity	σ_l	28 S m^{-1}
Cathodic transfer coefficient [19]	α_c	0.42
Anodic transfer coefficient [19]	α_a	0.42
Reference concentrations of active species	c_{ref}	100 mol m^{-3}
Exchange current density [19]	j_0	0.39 A m^{-2}
Electrolyte velocity	u	1.5 cm s^{-1}
Overpotential	E_{losses}	0.5 V

4.3. Results and discussion

4.3.1. Proof of concept

We first explore the application of the developed methodology to a model cubic architecture for the VO^{2+}/VO_2^+ electrolyte. In this step, we study the evolution of the fitness and the resulting electrode microstructure operating at the conditions listed in **Table 4.2**. The progression of the fitness value throughout 1000 generations of the best-performing microstructure in each generation is presented in **Figure 4.3a**, showing the remarkable improvement in network fitness of 75 % (0.27 to 0.48, with a maximum achievable fitness of 0.603). This improvement is the result of a decrease in the required pumping power of 73 % and an increase in the electrical performance of 42 % (**Figure 4.3b**), which shows the potential of a coupled GA and PNM framework as a method to discover improved electrode morphologies.

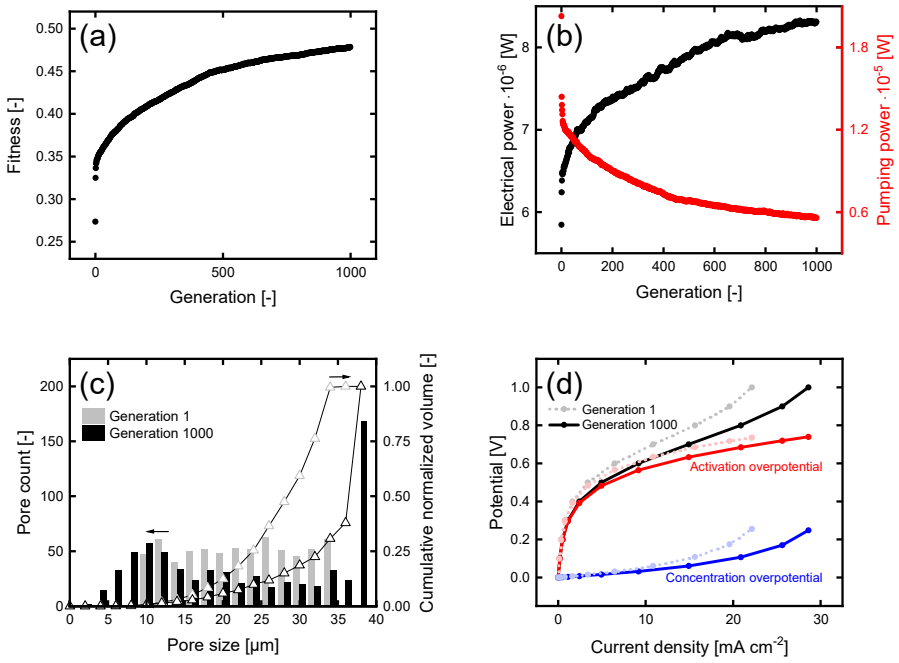

Figure 4.3: The results of the genetic algorithm for the VO^{2+}/VO_2^+ electrolyte, with: **(a)** the evolution of the algorithm over the number of generations by plotting the maximum fitness for each generation, **(b)** the maximum electrical performance and pumping power for each generation, **(c)** the pore size distributions of the first and final generation, showing the pore count and cumulative normalized volume distributions (divided in 2 µm pore sized bins), and **(d)** the polarization curve shown as the current density versus the potential, together with the activation and concentration overpotential contributions for the first and last generation.

For the studied system, the algorithm shows a higher tendency to optimize the pumping power than the electrochemical performance. The favored optimization of the pumping power is likely caused by three factors. First of all, the electrode microstructure is simulated using a flow-through configuration with a relatively low porosity of 54 % compared to the typical porosity values (66 - 90 %) in commercial electrodes [11, 15, 27, 64], which increases the pressure drop significantly compared to commercial electrodes with

flow-by configurations. Secondly, the pore coordinates, number of pores, and the maximum allowable pore size within the electrode microstructure are fixed, which restricts the ability of the algorithm to further enhance the electrochemical power. Finally, the fitness function has a quadratic dependency on the fluid velocity as $Q\ \Delta P \propto v^2$ (**equations (4.8) - (4.9)**, Hagen-Poiseuille), increasing the sensitivity of the algorithm towards achievable hydraulic performance.

The optimization procedure results in a final network with a bimodal pore and throat size distribution (**Figure 4.3c**) containing longitudinal flow pathways, composed of throats of the maximum allowable diameter, to effectively transport the electrolyte throughout the network (**Figure 4.4**). These flow pathways are distributed over the entire length of the network together with clusters of smaller pores. The alignment of the pores and corresponding throats highlights the importance of pore positioning, as the placement of interconnected larger pores facilitates the formation of low hydraulic resistance pathways while the diffusion-dominated regions of smaller pores provide additional electrochemical surface area to increase the power output of the system. As a result of the optimization, the average pore diameter of the network increased (from 13.3 to 13.8 µm) while the average throat diameter decreased (11.7 to 10.6 µm), which combined with the bimodality (isolated larger pores have an increased surface area (**Figure A4.5**, **equation (4.5)**) leads to a 47 % surface-to-volume ratio increase compared to the initial network (**Table A4.8**), despite the constant network volume scaling. These observations are in line with the high performance and low pumping requirements seen in recently developed materials such as the electrodes prepared using non-solvent induced phase separation manufactured by Wan & Jacquemond *et al.* that consists of bimodal porous microstructures with a large interconnected backbone of macrovoids alternated by segments of smaller pores [54, 65]. Furthermore, other authors observed that bimodal cloths have excellent transport properties while retaining high surface area [11, 66]. This result emphasizes the need to further develop manufacturing methodologies to prepare precisely engineered aligned structures to improve cell performance and reduce pumping power costs.

To gain insight into the absolute electrical performance of the generated structures, we performed a polarization sweep between 0 – 1 V with 0.1 V increments (**Figure 4.3d**). The computation reveals that, although the progression in the fitness function is significant, the absolute electrical performance (i.e., the electrochemical work that can be retrieved from the system ($P_{max} - P_{el}$)) of the generated networks is an order of magnitude lower in comparison to literature values [67, 68]. The low generated current can be explained by the lower internal surface area of the artificially generated electrode (0.8×10^4 m^2 m^{-3} for generation 1 and 1.2×10^4 m^2 m^{-3} for generation 1000) compared to commercial electrodes (~1×10^5 m^2 m^{-3}) [11, 69]. This effect is amplified by the sluggish kinetics of the vanadium electrolyte (k_0 = 6.8×10^{-7} m s^{-1} [58, 60]), resulting in large activation overpotential losses at 0.5 V. Operation at a higher overpotential (1 V) results in a higher relative contribution of the concentration overpotential on the overall system performance. Nonetheless, the generated structure, optimized at 0.5 V, also shows a significant reduction of the concentration overpotential at 1 V, increasing the current density by 29 % over 1000 generations. Consequently, after the evolution, the electrical performance at 1 V is 3.6 times greater than the required pumping power, instead of 1.4 times lower in magnitude than before the evolution. The ratio of pumping to electrical power is shown in **Figure 4.5**, with the demarcation of unity illustrating the trade-off between the electrochemical power ($P_{max} - P_{el}$) at a fixed overpotential and the pumping

power [11]. Although in practical systems the pumping power represents only a fraction of the generated electrical power (e.g., typically below 10 %), the model structures generated in the present study improve our fundamental understanding of the structure-performance relationships of electrodes in electrochemical devices. Future efforts should focus on initiating the optimization procedure with a more representative distribution of pores (i.e., non-cubic) within the porous network and more flexibility in the geometrical evolution. In addition, the theoretical design must consider manufacturability constrains to ensure that the computed structures can be realized in practice. In this context, emerging fabrication techniques (e.g., additive manufacturing, lithography) offer a promising platform to manufacture highly engineered microstructures, if the fabrication costs and manufacturing rates can be significantly reduced [70, 71]. An outlook on the manufacturability of the pore networks generated in this work is discussed in **Section A4.7.2**.

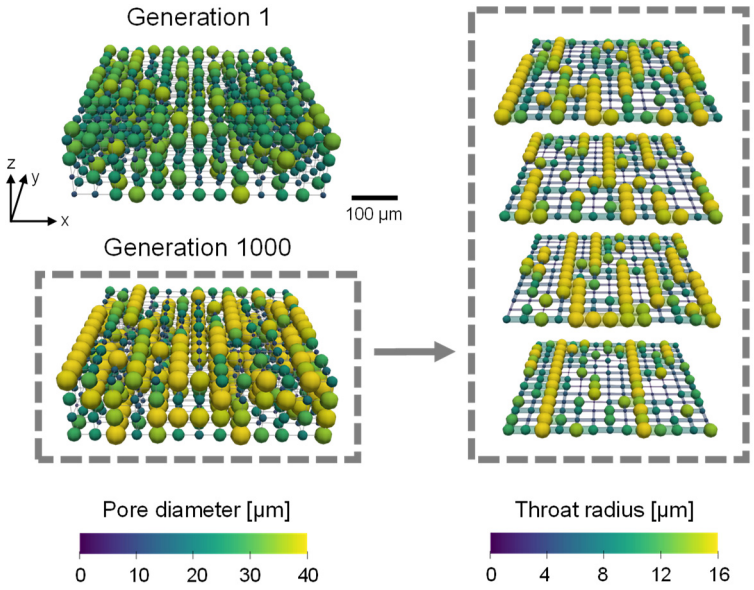

Figure 4.4: The results of the genetic algorithm optimized for the VO^{2+}/VO_2^+ electrolyte. The network structure of generation 1 and generation 1000 are shown together with the pore diameters with the flow in the y-direction and the thickness in the z-direction with the membrane facing to the top. In addition, the pore and throat diameters of generation 1000 are shown over each layer over the z-coordinate.

4.3.2. Parametric evaluation

In this section, we study the impact of variations in the operating conditions and electrolyte properties on the evolution of the electrode morphology and its performance. A systematic evaluation was conducted by modifying the electrolyte velocity (to 20 or 0.1 cm s^{-1}), exchange current density (to 1 x 10^4 or 1 x 10^{-4} A m^{-2}), or overpotential (to 1 or 0.1 V) as shown in **Figure 4.5**, to represent different fluid transport regimes, redox chemistries, or electrochemical operating conditions, respectively. We found that the variation of the tested parameters has two distinct effects on the network evolution: both

the exchange current density and overpotential directly influence the generated electrical power, while the electrolyte velocity impacts the pressure drop and thus the formation of longitudinal flow pathways.

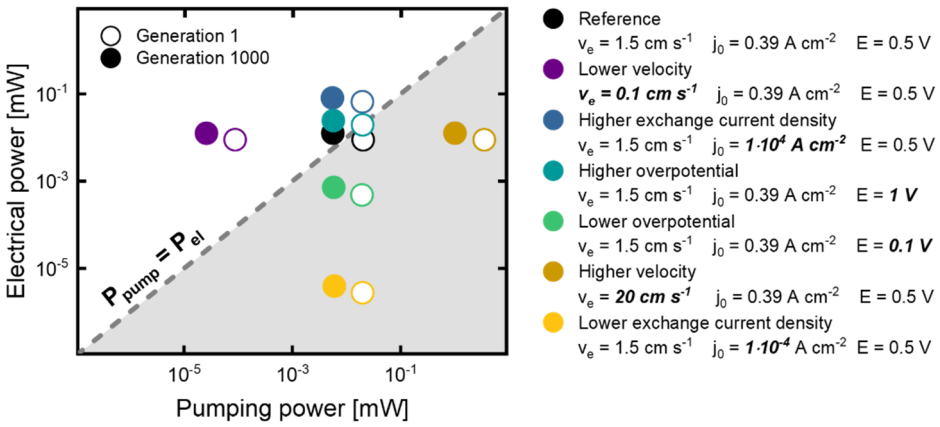

Figure 4.5: The pumping power versus electrical power ($P_{max} - P_{el}$) for the first and last generation of the seven different systems: the reference, lower velocity (to 0.1 cm s^{-1}), higher exchange current density (to 1 x 10^4 A m^{-2}), higher overpotential (to 1 V), lower overpotential (to 0.1 V), higher velocity (to 20 cm s^{-1}), and lower exchange current density (to 1 x 10^{-4} A m^{-2}) system. The dashed line and shaded region indicate a demarcation of unity.

In the following sections, we discuss the overarching trends that were extracted from the set of parameter runs. First, an evaluation of the trade-off between the pumping and electrochemical power for the initial and final networks is presented. Subsequently, the formation of longitudinal flow pathways is discussed. Finally, an analysis of the distribution of available surface area is described. A detailed overview of the individual results for all studied systems can be found in **Section A4.8**.

4.3.2.1. System performance

The trade-off between the required pumping power and the generated electrical power of the initial and final networks is shown in **Figure 4.5**. For all evaluated systems, the evolution over 1000 generations results in improved fitness, shifting the network performance towards a more efficient operational regime. An interesting result to emerge from this study is that the relative increases in electrical power and pumping power are relatively unaffected by the applied changes in the operating conditions and electrolyte properties. In all cases, we find that the reduction in pumping power (70 - 73 %) is the predominant factor for the improvement in the network fitness compared to the improvement in the electrochemical performance (22 - 48 %). Moreover, all studied systems feature a morphological shift towards a bimodal pore size distribution, resulting in improved fitness, electrical performance, pumping requirement, and surface area (41 - 49 %).

The results of the parametric evaluation show that the obtained relative increase (0.4 - 344 %) and the absolute values of the fitness function heavily depend on the operating conditions and electrolyte properties. Especially, the reduction in reaction

kinetics (decrease of the exchange current density from 0.39 to 1 x 10^{-4} A m^{-2}) affecting the electrochemical power of the system, and the increase in electrolyte velocity (from 1.5 to 20 cm s^{-1}) affecting the required pumping power, have a detrimental effect on the performance of the system. Although this observation is relevant in the search for optimized conditions for the most efficient system operation for specific applications (e.g., for vanadium RFBs) [33], this is beyond the scope of the current study, where we aim to demonstrate the potential of the optimization platform over a range of operating and electrolyte conditions. We envision that this methodology can serve as a basis to undertake further research that focuses on the optimization of electrode geometries for specific operational design cases (e.g., on distinct redox chemistries or other electrochemical technologies).

4.3.2.2. Longitudinal flow pathways

The inlet velocity of the electrolyte critically affects the trade-off between the system pressure drop (Hagen-Poiseuille) and reactant depletion effects, where *higher velocities* result in improved mass transfer at the cost of larger hydraulic requirements. However, a further increase in the operating velocity from 1.5 cm s^{-1} to 20 cm s^{-1} (**Figure A4.20**) does not result in a significant change in the number of longitudinal transport pathways. This can be explained by considering the ratio between the pumping and electrochemical power of the *reference* system. The pumping power required for the first generation is an order of magnitude higher than the electrochemical output of the system (**Figure 4.5**). Therefore, the algorithm puts a larger emphasis on reducing the pressure drop and, because longitudinal transport pathways comprising of throats with the maximum size are already formed at a velocity of 1.5 cm s^{-1}, there is limited opportunity to further optimize the pressure drop when changing the velocity to 20 cm s^{-1}. As a result, similar final morphologies are formed for both systems. Similarly, only a slight improvement in longitudinal flow paths was found for the *lower overpotential* case (0.1 V, **Table 4.3**, **Figure A4.17**).

Table 4.3: The number of longitudinal flow paths in the artificial electrode consisting of ≥ 6 and ≥ 10 connected pores of a pore diameter >30 µm with a maximum pore size of 38 µm. Together with the relative increase in surface area at the electrode-membrane interface over 1000 generations.

	Longitudinal flow paths [nr]		**Relative increase of surface area at the electrode-membrane interface [%]**
	≥ 6 (46 %)	≥ 10 (77 %)	
Reference	13	5	-18
Lower velocity	11	5	10
Higher exchange current density	12	9	6
Higher overpotential	8	6	10
Lower overpotential	11	9	5
Higher velocity	14	6	-8
Lower exchange current density	9	5	-4

The *exchange current density* dictates the intrinsic rate of the electrochemical reaction for a given electrolyte-electrode pair. Thus, decreasing this parameter to 1 x 10^{-4} A m^{-2} shifts the battery operation to a more kinetically limited regime (**Figure A4.22d**). Under these conditions (**Table 4.3, Figure A4.23**), we find that the optimization algorithm does not yield notable improvements, which we hypothesize is due to the very low starting performance (0.1 mA cm^{-2} at an overpotential of 1 V). In contrast, for the *higher exchange current density* system (1 x 10^{4} A m^{-2}), better-connected flow pathways emerge (**Table 4.3, Figure A4.11**) which we attribute to the higher drive of the algorithm to reduce mass transfer resistance under facile kinetics.

4.3.2.3. Distribution of available surface area

The redistribution of surface area is critical for the performance of systems that have a dominant electrochemical power over pumping power (**Figure 4.5**), such as the *lower velocity* and *higher exchange current density* systems. For these cases, we observe a redistribution of surface area towards the membrane-electrode interface. To quantify this trend, we compare the pore surface area of the electrode layer closest to the membrane with the total surface area increase in the electrode (**Table 4.3**, **Section A4.8.8**).

For the *lower velocity* (0.1 cm s^{-1}), the pumping power required is strongly reduced and the electrochemical power of the system governs the evolution of the fitness, which favors the optimization of the ohmic resistance and kinetic activity in the cell (**Figure 4.5**). The evolution of the network indeed stimulates the electrochemical performance of the cell, as we observed a 10 % increase in surface area at the electrode-membrane interface with respect to the baseline (**Table 4.3, Figure A4.9**). This finding is in agreement with our previous study, where we found that the pores in the region closest to the membrane surface are predominantly responsible for the current generated in the system [27], which is in line with the design principle of a zero-gap electrochemical cell [72]. Similarly, for the *higher exchange current density* system, the facile kinetics result in a dominant contribution of the electrochemical performance to the fitness evolution (**Figure 4.5**). The improved kinetics of the system results in the emergence of mass transfer limitations (**Figure A4.10d**) at an overpotential of 0.5 V, which is counteracted by an increase in, and improved distribution of, the surface area in the electrode (**Figure A4.12**). Interestingly, both the higher and lower overpotential systems also show a redistribution of accessible surface area towards the membrane (**Figure A4.15** and **A4.18**).

In summary, the developed computational framework efficiently optimizes electrode microstructures for a wide range of operating conditions relevant to redox flow batteries. In line with current experimental understanding, we find that the bottom-up design results in microstructures with bimodal pore size distributions, pore size gradients, and interconnected transport pathways. In this proof-of-concept study, we elect to leverage model-simplified geometries to elucidate fundamental microstructure-performance traits that can inspire new material concepts and inform more advanced computational platforms. Although beyond the scope of this work, future studies should consider more realistic electrode structures and manufacturability constrains as part of the evolution.

4.4. Conclusion

In this study, we developed a bottom-up computational approach to optimize the electrode microstructure of redox flow battery electrodes using a coupled genetic algorithm and electrochemical pore network model. We demonstrated that the framework offers a powerful tool to optimize the performance of flow battery electrode microstructures under a wide range of operating conditions. A proof-of-concept study was presented, applying the GA to randomly generated cubic networks using the VO^{2+}/VO_2^+ vanadium chemistry and a flow-through geometry, at a velocity of 1.5 cm s^{-1} and an overpotential of 0.5 V. The algorithm optimized the structures using a fitness function that enhances the electrical power output and reduces the hydraulic requirements, resulting in a fitness increase of 75 % (from 0.27 to 0.48 with a maximum fitness of 0.603). The improved performance was attributed to the formation of a bimodal porous structure with interconnected longitudinal pathways with larger pores, which decreased the pumping requirements (-73 %), and increased the electrode internal surface area (47 %), which enhanced the electrical power output (42 %). In addition, we performed a parametric evaluation that highlighted the response of the network evolution under a range of electrolyte and operating conditions. Based on the trade-off between the electrical power and the pumping power, the algorithm emphasizes either the optimization of the flow geometry or the distribution of the available surface area. Operation at a higher velocity, lower overpotential, or a higher exchange current density resulted in better-connected longitudinal flow paths compared to the reference system, reducing the hydraulic requirements. Operation at a lower inlet velocity or higher exchange current density resulted in a redistribution of the surface area close to the electrode-membrane interface, enhancing the electrochemical power output.

Looking forward, we propose to further improve the geometrical flexibility by integrating flexible placement of pores and starting the evolution from more complex microstructures. Furthermore, the implementation of code parallelization would greatly improve the algorithm's speed. Future efforts should incorporate manufacturability constrains into the optimization pipeline to ensure that the resulting structures can be synthesized. This study is the first step towards a computational design platform to accelerate the design and fabrication of porous architectures and we hope to inspire adjacent fields (e.g., computational scientists, mathematicians, mechanical engineers) to contribute to these developments. Although the methodology is applied to redox flow batteries here, the proposed framework can be tailored to any specific porous electrode in convection-enhanced electrochemical technologies (e.g., fuel cells, electrolysis, separations).

4.5. References

[1] S. P. S. Badwal, S. S. Giddey, C. Munnings, A. I. Bhatt, A. F. Hollenkamp, *Front. Chem.* **2**, 1–28 (2014).
[2] P. A. García-Salaberri *et al.*, *Electrochim. Acta*. **295**, 861–874 (2019).
[3] Z. Liu *et al.*, *NPG Asia Mater.* **11**, 12, 1-21 (2019).
[4] D. Qu, *AIP Conf. Proc.* **1597**, 14–25 (2014).
[5] N. Hedayat, Y. Du, H. Ilkhani, *Renew. Sustain. Energy Rev.* **77**, 1221–1239 (2017).
[6] J. J. Hwang, P. Y. Chen, *Int. J. Heat Mass Transf.* **49**, 2315–2327 (2006).
[7] G. Salitra, A. Soffer, L. Eliad, Y. Cohen, D. Aurbach, *J. Electrochem. Soc.* **147**, 2486 (2000).
[8] M. H. Chakrabarti *et al.*, *J. Power Sources*. **253**, 150–166 (2014).
[9] R. Schweiss, *Chem. Eng. Sci.* **226**, 115841 (2020).
[10] M. van der Heijden, A. Forner-cuenca, in *Encyclopedia of Energy Storage*, L. F. Cabeza, Ed. (Elsevier Inc., Oxford, ed. 2, 2022), pp. 480–499.
[11] A. Forner-Cuenca, E. E. Penn, A. M. Oliveira, F. R. Brushett, *J. Electrochem. Soc.* **166**, A2230–A2241 (2019).
[12] A. Forner-Cuenca, F. R. Brushett, *Curr. Opin. Electrochemistry*, **18**, 113-122 (2019).
[13] A. G. Lombardo, B. A. Simon, O. Taiwo, S. J. Neethling, N. P. Brandon, *J. Energy Storage*. **24**, 100736 (2019).
[14] J. H. Kim, T. J. Kang, *ACS Appl. Mater. Interfaces*. **11**, 28894–28899 (2019).
[15] B. A. Simon *et al.*, *Appl. Energy*. **306**, 117678 (2022).
[16] L. L. Zhang, Y. Gu, X. S. Zhao, *J. Mater. Chem. A*. **1**, 9395–9408 (2013).
[17] H. R. Jiang *et al.*, *J. Power Sources*. **440**, 227159 (2019).
[18] J. Melke *et al.*, *ACS Appl. Energy Mater.* **3**, 12, 11627-11640 (2020).
[19] K. V. Greco, A. Forner-Cuenca, A. Mularczyk, J. Eller, F. R. Brushett, *ACS Appl. Mater. Interfaces*. **10**, 44430–44442 (2018).
[20] A. Forner-Cuenca *et al.*, *Adv. Mater.* **27**, 6317–6322 (2015).
[21] J. Sun, H. R. Jiang, B. W. Zhang, C. Y. H. Chao, T. S. Zhao, *Appl. Energy*. **259**, 114198 (2020).
[22] J. Wlodarczyk, Master thesis, Zurich University of Applied Sciences (2019).
[23] J. L. Barton, F. R. Brushett, *Batteries*. **5**, 25 (2019).
[24] M. Espinoza-Andaluz, M. Andersson, B. Sundén, *Int. J. Hydrogen Energy*. **42**, 11689–11698 (2017).
[25] G. Qiu *et al.*, *Electrochim. Acta*. **64**, 46–64 (2012).
[26] D. Zhang *et al.*, *J. Power Sources*. **447**, 227249 (2020).
[27] M. van der Heijden, R. van Gorp, M. A. Sadeghi, J. Gostick, A. Forner-Cuenca, *J. Electrochem. Soc.* **169**, 040505 (2022).
[28] S. Gupta, T. M. Lim, S. H. Mushrif, *Electrochim. Acta*. **270**, 471–479 (2018).
[29] M. A. Sadeghi *et al.*, *J. Electrochem. Soc.* **166**, A2121–A2130 (2019).
[30] C. F. Chen, A. Verma, P. P. Mukherjee, *J. Electrochem. Soc.* **164**, E3146–E3158 (2017).
[31] M. Li *et al.*, *J. Energy Storage*. **32**, 101782 (2020).
[32] A. Mistry, A. A. Franco, S. J. Cooper, S. A. Roberts, V. Viswanathan, *ACS Energy Lett.* **6**, 1422–1431 (2021).
[33] K. Tenny, R. Braatz, Y.-M. Chiang, F. Brushett, *J. Electrochem. Soc.* **168**, 050547 (2021).
[34] J. Bao *et al.*, *Adv. Theory Simulations*. **3**, 1–13 (2020).
[35] Y. Yoon, M. J. Kim, J. J. Kim, *Electrochim. Acta*. **399**, 139424 (2021).
[36] M. Mitchell, *An introduction to genetic algorithms* (Massachusetts Institute of Technology, Cambridge, Massachusetts, fifth., 1999).
[37] Y. Y. Choi, S. Kim, S. Kim, J. Choi, *J. Power Sources*. **450**, 227684 (2020).
[38] Z. J. Mo, X. J. Zhu, L. Y. Wei, G. Y. Cao, *Int. J. Energy Res.* **30**, 585–597 (2006).
[39] L. Zhang *et al.*, *J. Power Sources*. **270**, 367–378 (2014).
[40] S. Wan *et al.*, *Appl. Energy*. **298**, 117177 (2021).

[41] X. Zeng *et al.*, *Int. J. Heat Mass Transf.* **105**, 81–89 (2017).
[42] S. Ebrahimi, B. Ghorbani, K. Vijayaraghavan, *Renew. Energy*. **113**, 846–854 (2017).
[43] V. A. Beck *et al.*, *J. Power Sources*. **512**, 230453 (2021).
[44] T. Roy, M. A. S. de Troya, M. A. Worsley, V. A. Beck, *Struct. Multidiscip. Optim.* **65**, 171 (2022).
[45] M. Agnaou, M. A. Sadeghi, T. G. Tranter, J. Gostick, *Comput. Geosci.* **140**, 104505 (2020).
[46] R. Behrou, A. Pizzolato, A. Forner-Cuenca, *Int. J. Heat Mass Transf.* **135**, 72–92 (2019).
[47] A. Nejad Ebrahimi, S. Jamshidi, S. Iglauer, R. Boozarjomehry, *Chem. Eng. Sci.* **92**, 157–166 (2013).
[48] S. Jamshidi, R. B. Boozarjomehry, M. R. Pishvaie, *Adv. Water Resour.* **32**, 1543–1553 (2009).
[49] L. Xu, X. Liu, L. Liang, *J. Nat. Gas Sci. Eng.* **21**, 907–914 (2014).
[50] A. Raoof, S. Majid Hassanizadeh, *Transp. Porous Media*. **81**, 391–407 (2010).
[51] J. Gostick *et al.*, *Comput. Sci. Eng.* **18**, 60–74 (2016).
[52] J. D. Milshtein *et al.*, *J. Electrochem. Soc.* **164**, E3265–E3275 (2017).
[53] K. Deb, *Sadhana - Acad. Proc. Eng. Sci.* **24**, 293–315 (1999).
[54] C. T. Wan *et al.*, *Adv. Mater.* **33**, 2006716 (2021).
[55] J. J. Grefenstette, *IEEE Trans. Syst.* **1**, 122–128 (1986).
[56] T. F. Fuller, J. N. Harb, *Electrochemical engineering* (2018).
[57] A. Z. Weber *et al.*, *J. Appl. Electrochem.* **41**, 1137–1164 (2011).
[58] Z. Cheng *et al.*, *Appl. Energy*. **279**, 115530 (2020).
[59] E. Sánchez-Díez *et al.*, *J. Power Sources*. **481**, 228804 (2021).
[60] T. Yamamura, N. Watanabe, T. Yano, Y. Shiokawa, *J. Electrochem. Soc.* **152**, A830 (2005).
[61] P. Leung *et al.*, *J. Power Sources*. **360**, 243–283 (2017).
[62] S. a Maier, *Fundamentals and Applications Plasmonics : Fundamentals and Applications* (2004), vol. 677.
[63] F. Chen *et al.*, *Int. J. Electrochem. Sci.* **10**, 725–736 (2015).
[64] K. M. Tenny *et al.*, *Energy Technol.* **10**, 2101162 (2022).
[65] R. R. Jacquemond *et al.*, *Cell Reports Phys. Sci.* **3**, 100943 (2022).
[66] X. L. Zhou, T. S. Zhao, Y. K. Zeng, L. An, L. Wei, *J. Power Sources*. **329**, 247–254 (2016).
[67] Q. H. Liu *et al.*, *J. Electrochem. Soc.* **159**, A1246–A1252 (2012).
[68] T. Davies, J. Tummino, *J. Carbon Res.* **4**, 8 (2018).
[69] K. M. Tenny, A. Forner-Cuenca, Y.-M. Chiang, F. R. Brushett, *J. Electrochem. Energy Convers. Storage*. **17**, 041010 (2020).
[70] M. P. Browne, E. Redondo, M. Pumera, *Chem. Rev.* **120**, 2783–2810 (2020).
[71] V. Egorov, U. Gulzar, Y. Zhang, S. Breen, C. O'Dwyer, *Adv. Mater.* **32**, 1–27 (2020).
[72] V. M. Palakkal *et al.*, *ACS Appl. Energy Mater.* **3**, 4787–4798 (2020).

4.6. Appendix 4

A4.1. Abbreviations

Symbol	Description
GA	Genetic algorithm
PNM	Pore network model
RFB	Redox flow battery

A4.2. List of symbols

Symbol	Description	Units
0	First index	-
ΔP	Pressure drop	Pa
A_p	Pore internal surface area	m^2
A_T	Throat internal surface area	m^2
c_M	Mutation value	-
d	Diameter	m
E	Overpotential	V
I	Generated total current	A
k_0	Kinetic rate constant	$m\ s^{-1}$
L_T	Throat length	m
n_p	Final index	-
N_T	Number of throats	-
P	Power	W
Q	Electrolyte flow rate	$m^3\ s^{-1}$
S_p	Pore seed	-
S_T	Throat cross-sectional area	m^2
	Greek	
η_p	Pumping energy efficiency	-
ξ	Fitness	-
σ_M	Mutation range	-
	Superscripts	
M	Mutated	
o	Old	
	Subscripts	
1	Generation 1	
1000	Generation 1000	
$losses$	Losses	
$cell$	Open circuit cell	
el	Electrochemical	
M	Mutated	
m	Membrane	
max	Thermodynamic maximum	
n	Generation number	
$pump$	Pumping	
SA	Surface area	

A4.3. Electrochemical model description

A4.3.1. Model equations

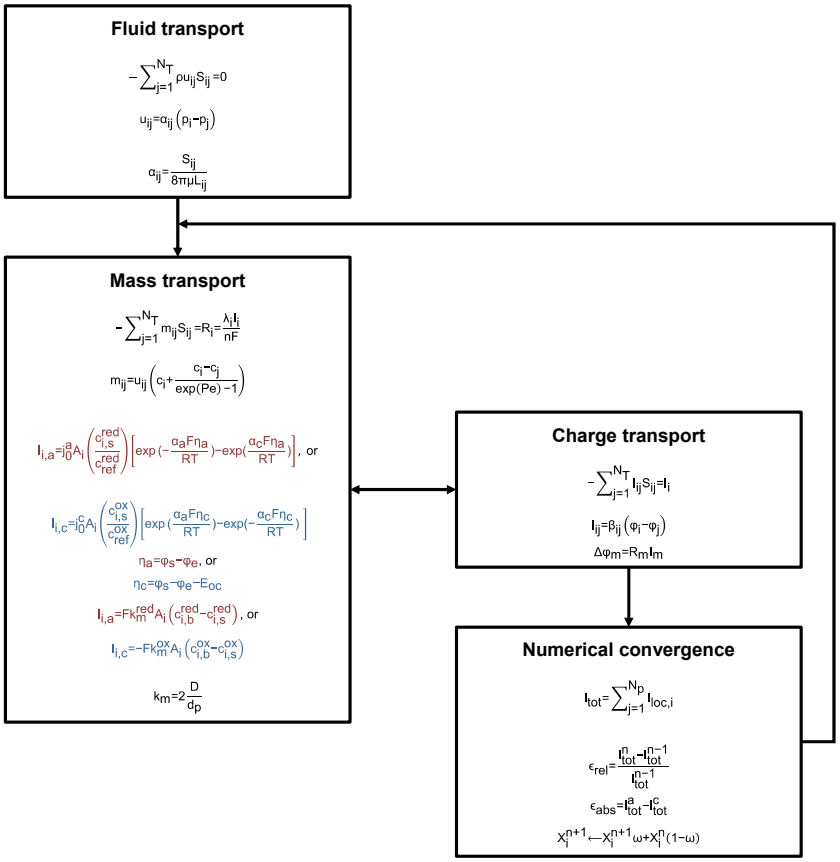

Figure A4.1: Flowchart of the iterative electrochemical algorithm showing the model equations. More details regarding the pore network model physics can be found in [1].

A4.3.2. Boundary conditions

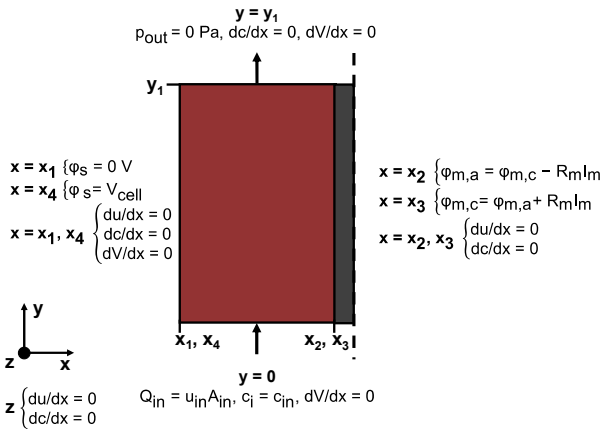

Figure A4.2: Schematic representation of the boundary conditions in the electrochemical model for one of the half cells in the single-electrolyte flow battery with x_1-x_4 the x-coordinates and 0-y_1 the y-coordinates of the different interfaces.

A4.3.3. List of symbols

Symbol	Description	Units
A_i	Electrochemically active internal surface area of pore i	m^2
A_{in}	Geometrical inlet area of the electrode	m^2
c	Concentration	mol m^{-3}
D	Diffusion coefficient	m^2 s^{-1}
d_p	Pore diameter	m
$E_{applied}$	Applied potential	V
E_{oc}	Open-circuit potential	V
F	Faradaic constant, 96,485 C mol^{-1}	C mol^{-1}
I	Current	A
I_{ij}	Charge flux	A m^{-2}
j_0	Exchange current density	A m^{-2}
k_m	Mass transfer coefficient	m s^{-1}
L	Conduit length, length of the medium	m
m	Mole flux	mol m^{-2} s^{-1}
n	Number of electrons, or iteration number	-
N_p	Number of pores	-
N_T	Number of throats	-
p	Pressure	Pa
Pe	Peclet number	-
Q	Flow rate	m^3 s^{-1}
R	(a) Molar gas constant, 8.314 J mol^{-1} K^{-1}	J mol^{-1} K^{-1}
	(b) Resistance	Ω
	(c) Net reaction rate	mol s^{-1}
S	Cross-sectional area	m^2
T	Operating temperature	K
u	Fluid velocity	m s^{-1}
V	Voltage	V
V_{cell}	Given cell potential	V
X	Concentration or potential	mol m^{-3} or V

	Greek	
α	(a) Transfer coefficient	-
	(b) Hydraulic conductance of the throat	m Pa^{-1} s^{-1}
β	Electrical conductance	S m^{-2}
ϵ	Error value	-
η	Overpotential	V
λ	Stoichiometric coefficient	-
μ	Dynamic viscosity	Pa s
ρ	Electrolyte density	kg m^{-3}
σ	Bulk electrolyte conductivity	S m^{-1}
φ	Potential	V
ω	Relaxation factor	-
	Superscripts	
a	Anode	
c	Cathode	
n	Iteration number	
ox	Oxidized form	
red	Reduced form	
	Subscripts	
a	Anode	
abs	Absolute	
b	Bulk	
c	Cathode	
e	Electrolyte, liquid phase	
i	Within pore i, species i	
ij	Pore i to pore j, throat ij	
in	Inlet	
j	Within pore j, species j	
l	Electrolyte	
loc	Local	
m	Membrane	
out	Outlet	
ref	Reference	
rel	Relative	
s	Solid phase, surface	
tot	Total	
$V1$	Vanadium species VO^{2+}	
$V2$	Vanadium species VO_2^+	

A4.4. Network comparison

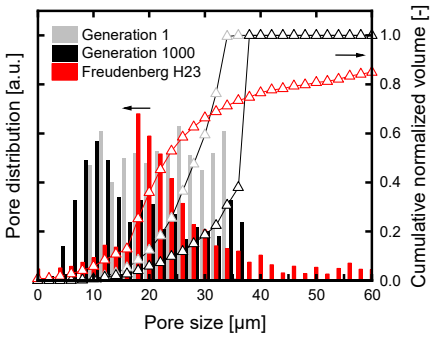

Figure A4.3: The pore size distribution and cumulative normalized volume of a commercial paper electrode (Freudenberg H23) and the first and final generation of this study (reference system). The normalized volume is defined as the fraction of the total pore volume occupied by all pores within a 2 µm pore size range. The data of the commercial paper electrode was obtained in a previous study [1].

A4.5. Pore sensitivity study

A pore number sensitivity analysis was performed to investigate the influence of the number of pores in the thickness direction (z-direction) on the simulation results. In this study, the number of pores in this direction varied between 2 – 20 pores, and in addition the effect of a smaller spacing was investigated. The absolute values of the performance metrics (i.e., fitness, electrical power, pumping power, and surface area) and relative improvements can be found in **Tables A4.1 - A4.3.** Additionally, the overarching trends extracted from the sensitivity study are visualized in **Figure A4.4**.

The total surface area of the electrode is correlated with its thickness. Thicker electrodes have a higher total surface area and thus a higher electrical power output. However, the thicker electrode structures experience a similar percentual increase in surface area and electrochemical power output as the thinner electrodes. On the other hand, the pumping power demands are higher for thicker electrodes, which is a result of the increased volumetric throughput at the constant inlet velocity. Interestingly, the percentual improvement in pumping power demand was lower for thicker electrodes (i.e., larger pore numbers). This lower efficiency gain observed for the thicker electrodes can be explained by the longer evolutionary time required to optimize the flow pathways of thicker electrodes. It is expected that similar pumping power reductions can be obtained when the number of generations is increased. Because of the higher pumping power improvement for thinner electrodes, the relative fitness increase after 100 generations is higher. If we look at the system with a smaller network spacing, we see a similar trend. The reduced spacing results in a restriction on the maximum throat size and thus limits the maximum pumping power improvement.

Apart from the variations in pumping power improvements, caused by the restriction on the maximum allowable throat size in the case of a smaller spacing and the slower formation of longitudinal pathways in the case of larger networks, the boundary effects on the system did not seem to significantly affect the simulation results. In addition, the results of the performed pore number sensitivity study show that the genetic algorithm can optimize the performance of a wide range of porous electrode configurations.

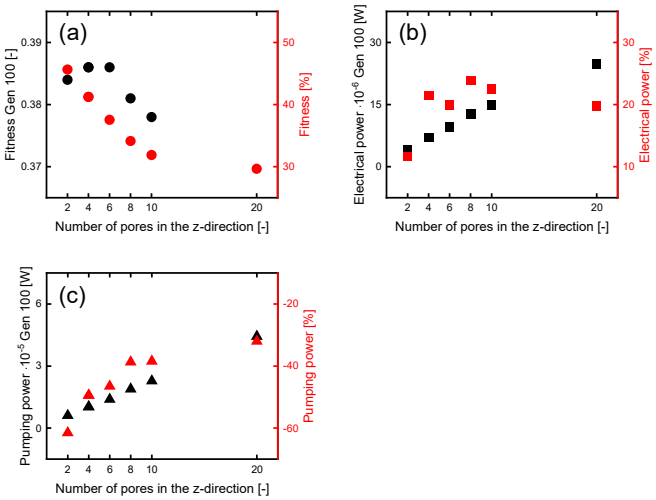

Figure A4.4: The results of the genetic algorithm pore sensitivity study optimized for the VO^{2+}/VO_2^+ electrolyte, where the results are shown for the different number of pores in the z-direction, with: **(a)** the fitness for the first generation and its improvement over 100 generations, **(b)** the electrical performance for the first generation and its improvement over 100 generations, and **(c)** the pumping power for the first generation and its improvement over 100 generations.

Table A4.1: Percentual increase in fitness, electrical power, and pumping power for all evaluated systems over the generations for the pore sensitivity study. *The spacing of this system is divided by two, the network size is multiplied by two in all directions to maintain the same network dimensions, and the pore and throat sizes of the reference network for volume scaling were also divided by two.

Percentual increase [%]	**Fitness**	**Electrical power**	**Pumping power**	**Surface area**
Number of pores in z-direction				
4	41	22	-49	23
2	46	12	-61	13
6	38	20	-46	22
8	34	24	-39	26
10	32	22	-38	25
20	30	20	-32	22
4, Spacing divided by 2*	38	20	-30	21

Table A4.2: The maximum absolute values of the fitness and surface area for the first and final generation for the pore sensitivity study. *The spacing of this system is divided by two, the network size is multiplied by two in all directions to maintain the same network dimensions, and the pore and throat sizes of the reference network for volume scaling were also divided by two.

	Fitness [-]		**Surface area [m²]**	
Number of pores in z-direction	Gen 1	Gen 100	Gen 1	Gen 100
4	0.27	0.39	5.9×10^{-7}	7.3×10^{-7}
2	0.26	0.38	3.8×10^{-7}	4.2×10^{-7}
6	0.28	0.39	8.2×10^{-7}	1.0×10^{-6}
8	0.28	0.38	1.1×10^{-6}	1.3×10^{-6}
10	0.29	0.38	1.3×10^{-6}	1.6×10^{-6}
20	0.28	0.36	2.4×10^{-6}	3.0×10^{-6}
4, Spacing divided by 2*	0.19	0.26	1.1×10^{-6}	1.4×10^{-6}

Table A4.3: The maximum absolute values of the electrical power and pumping power for the first and final generation for the pore sensitivity study. *The spacing of this system is divided by two, the network size is multiplied by two in all directions to maintain the same network dimensions, and the pore and throat sizes of the reference network for volume scaling were also divided by two.

	Electrical power [W]		**Pumping power [W]**	
Number of pores in z-direction	Gen 1	Gen 100	Gen 1	Gen 100
4	5.8×10^{-6}	7.1×10^{-6}	2.0×10^{-5}	1.0×10^{-5}
2	3.7×10^{-6}	4.2×10^{-6}	1.6×10^{-5}	6.1×10^{-6}
6	8.0×10^{-6}	9.6×10^{-6}	2.6×10^{-5}	1.4×10^{-5}
8	1.0×10^{-5}	1.3×10^{-5}	3.1×10^{-5}	1.9×10^{-5}
10	1.2×10^{-5}	1.5×10^{-5}	3.7×10^{-5}	2.3×10^{-5}
20	2.1×10^{-5}	2.5×10^{-5}	5.4×10^{-5}	4.4×10^{-5}
4, Spacing divided by 2*	1.2×10^{-5}	1.4×10^{-5}	6.7×10^{-5}	4.7×10^{-5}

A4.6. Operating parameters

A4.6.1. Electrolyte preparation

An electrolyte solution of 0.2 M vanadium (IV) sulfate oxide hydrate ($VOSO_4 \cdot xH_2O$, 99.9 %, Alfa Aesar) and 1.0 M sulfuric acid (H_2SO_4, 95.0 - 98.0 %, Sigma-Aldrich), dissolved in deionized water was prepared. The obtained stock solution was electrochemically converted to produce V(V). In this electrochemical oxidation step, 100 mL of the prepared electrolyte was equally divided over two reservoirs and subsequently pumped through the half-cells at a flow rate of 20 mL min^{-1} using a Masterflex L/S® Easy-Load® II pump and LS-14 tubing. Graphite current collectors with milled flow-through flow fields were used. One Freudenberg H23 (Fuel Cell Store, 210 µm thick, 80 % porosity) paper electrode with an external area of 2.55 cm^2 was placed on top of each current collector, using incompressible polytetrafluoroethylene gaskets with a total thickness of 165 µm, resulting in a 22 % compression. A cation-exchange Nafion 212 (Fuel Cell Store) membrane was used to separate the two half-cells. Subsequently, the cell was tightened to 2.2 N m using a torque-controlled screwdriver. Finally, a BioLogic VMP-300 potentiostat was used in potentiostatic mode to convert the V(IV) electrolyte to V(III) on the negative side and to V(V) on the positive side, by holding a potential of 2.0 V until a steady current of ~10 mA was measured. Humidified nitrogen was bubbled through both electrolyte tanks during the entire duration of the experiments to prevent oxidation of the redox couples from exposure to oxygen. A 50 % SOC V(IV)/V(V) solution was obtained by mixing the retrieved V(V) solution with the initial V(IV) solution in a 1:1 volumetric ratio.

A4.6.2. Electrolyte density, viscosity, and conductivity measurements

Electrolyte density measurements were performed *in triplo* with 10 mL electrolyte solutions using a Sartorius ED224S analytical balance. The viscosity of the solvent was used as the electrolyte viscosity. Finally, conductivity measurements were performed using a two-electrode custom conductivity cell, whose compartment was flooded with electrolyte and sealed shut, similar to the setup used in Milshtein et al.[2]. Electrochemical impedance spectroscopy, performed *in triplo* and repeated five times for each new assembly and new electrolyte solutions, was conducted at open-circuit voltage and room temperature (20 °C) using a Biologic VMP-300 potentiostat with an amplitude of 10 mV and a frequency range of 1 kHz - 100 kHz, 8 points per decade, 6 measurements per frequency, and a waiting time of 0.10 period before each frequency. The high-frequency intercept from the impedance measurement was identified as the total resistance, from which the electrolyte conductivity was obtained by correcting for combined cell and lead-resistances. These

resistances were obtained by constructing a calibration curve using aqueous conductivity standards (0.01 M, 0.1 M, and 1.0 M aqueous KCl) and by measuring an empty cell.

A4.7. Proof of principle

A4.7.1. Reference system

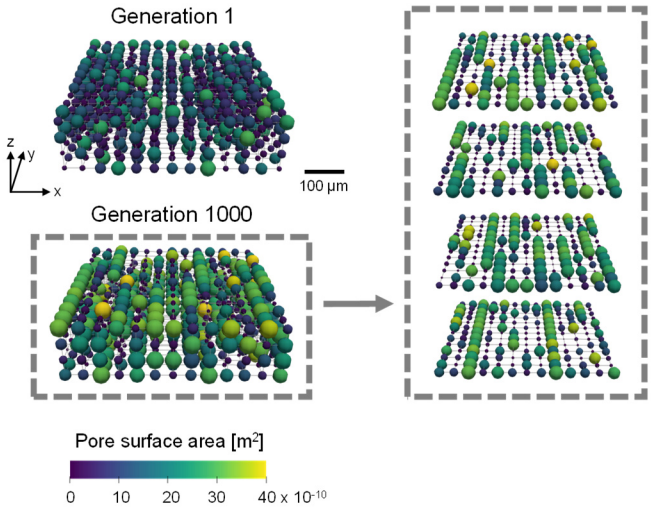

Figure A4.5: The results of the genetic algorithm optimized for the VO^{2+}/VO_2^+ electrolyte. The network structure of generation 1 and generation 1000 are shown together with the pore surface area with the flow in the y-direction and the thickness in the z-direction with the membrane facing to the top. In addition, the pore surface area of generation 1000 is shown over each layer over the z-coordinate.

Table A4.4: Total pore surface area values for each network layer for the first and final generation from the current collector to the membrane.

Pore surface area x 10^{-7} [m^2]	Generation 1	Generation 1000
Current collector	1.55	2.13
Internal 1	1.21	2.18
Internal 2	1.22	1.96
Membrane	1.77	2.43

A4.7.2. Manufacturability

We envision that the generated pore networks can serve as building blocks for the design and manufacturing of solid porous electrodes, following a three-step approach. In the first step, a solid porous structure is extracted from the pore and throat size information of the generated pore network. Here, we utilized the porous media generator recently published by Niblett *et al.* to generate a solid microstructure from the pore network that was proposed after 1000 generations [3]. A visual representation of this solid microstructure is presented in **Figure A4.6.** In the second step, the generated solid microstructure can be manufactured employing additive manufacturing techniques. Recently, Niblett *et al.* manufactured a gas diffusion layer for fuel cells utilizing stereolithography 3D printing [4]. However, the manufacturability of porous electrodes with this

method is currently impeded by the accuracy and precision of the stereolithography machines, limiting resolutions of the manufactured material to 50 µm. To overcome this limitation, more accurate but slower manufacturing methods, such as two-photon lithography, can be employed for electrode prototyping. We envision that, as the final step, the porous electrode can be altered by means of surface etching and surface chemistry modification steps to alter the nano-porosity and surface activity of the generated structure. By controlling the nano-structure of the manufactured electrode, several core electrode characteristics that influence RFB performance can be improved, such as the wettability and electrochemically active surface area [5, 6].

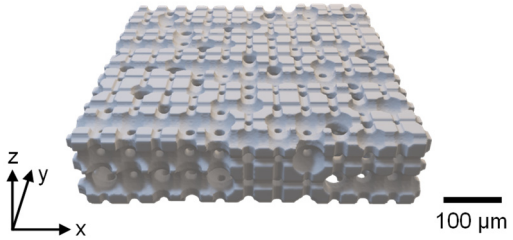

Figure A4.6: Solid-phase porous electrode microstructure extracted from the best-performing network in the proof-of-concept study after 1000 generations. To improve visibility, the pores and throats of the top and bottom layers are presented as half-pores and throats.

A4.8. Parametric evaluation

A4.8.1. Lower velocity system

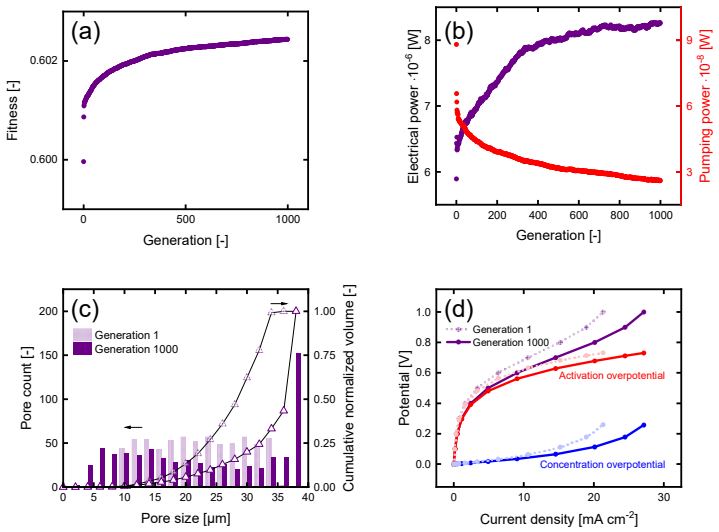

Figure A4.7: The results of the genetic algorithm optimized for the VO^{2+}/VO_2^+ electrolyte, evaluated at a velocity of 0.1 cm s^{-1}, with: **(a)** the evolution of the algorithm over the number of generations by plotting the maximum fitness for each generation, **(b)** the maximum electrical performance and pumping power for each generation, **(c)** the pore size distributions of the first and final generation, showing the pore count and cumulative normalized volume distributions (divided in 2 µm pore sized bins), and **(d)** the polarization curve shown as the current density versus the potential, together with the activation and concentration overpotential contributions for the first and last generation.

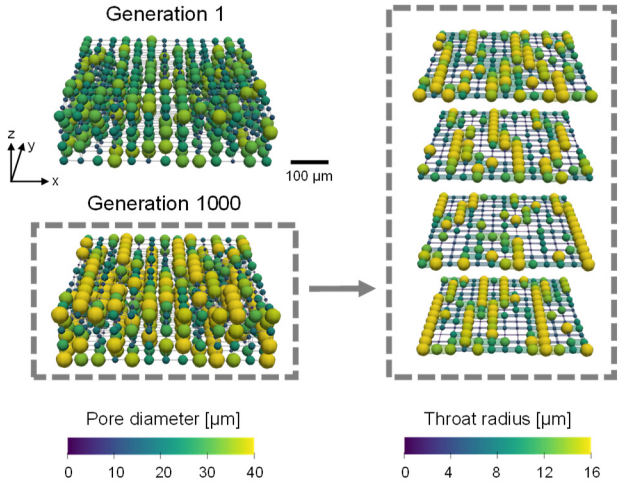

Figure A4.8: The results of the genetic algorithm optimized for the VO^{2+}/VO_2^+ electrolyte, evaluated at a velocity of 0.1 cm s^{-1}. The network structure of generation 1 and generation 1000 are shown together with the pore diameters with the flow in the y-direction and the thickness in the z-direction with the membrane facing to the top. In addition, the pore and throat diameters of generation 1000 are shown over each layer over the z-coordinate.

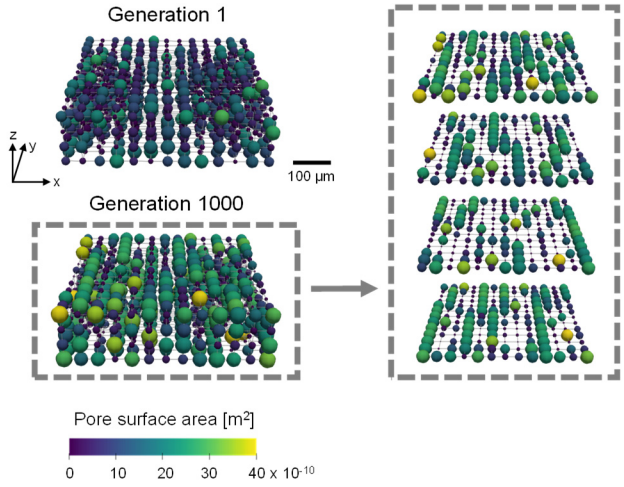

Figure A4.9: The results of the genetic algorithm optimized for the VO^{2+}/VO_2^+ electrolyte, evaluated at a velocity of 0.1 cm s^{-1}. The network structure of generation 1 and generation 1000 are shown together with the pore surface area with the flow in the y-direction and the thickness in the z-direction with the membrane facing to the top. In addition, the pore surface area of generation 1000 is shown over each layer over the z-coordinate.

A4.8.2. Higher exchange current density system

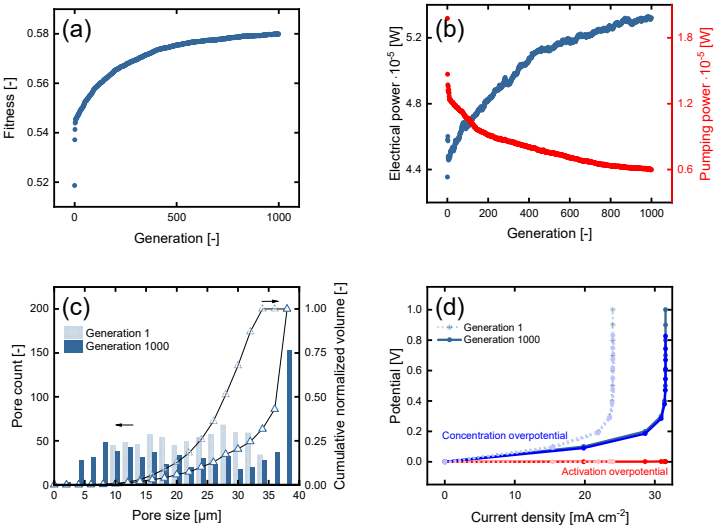

Figure A4.10: The results of the genetic algorithm optimized for the VO^{2+}/VO_2^+ electrolyte, but with a higher exchange current density of 1 x 10^4 A m^{-2}, with: **(a)** the evolution of the algorithm over the number of generations by plotting the maximum fitness for each generation, **(b)** the maximum electrical performance and pumping power for each generation, **(c)** the pore size distributions of the first and final generation, showing the pore count and cumulative normalized volume distributions (divided in 2 µm pore sized bins), and **(d)** the polarization curve shown as the current density versus the potential, together with the activation and concentration overpotential contributions for the first and last generation.

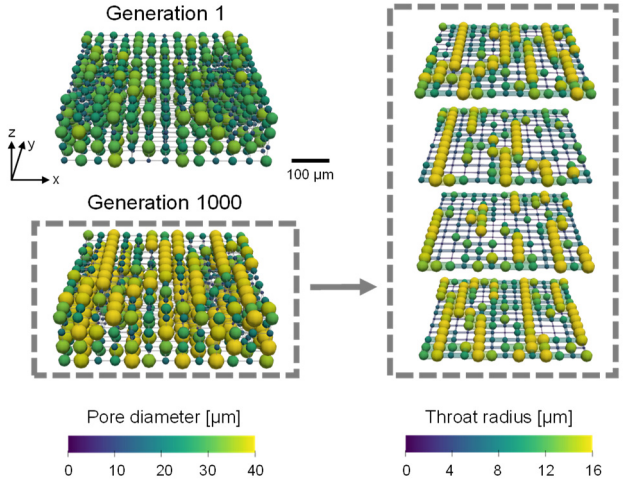

Figure A4.11: The results of the genetic algorithm optimized for the VO^{2+}/VO_2^+ electrolyte, but with a higher exchange current density of 1 x 10^4 A m^{-2}. The network structure of generation 1 and generation 1000 are shown together with the pore diameters with the flow in the y-direction and the thickness in the z-direction with the membrane facing to the top. In addition, the pore and throat diameters of generation 1000 are shown over each layer over the z-coordinate.

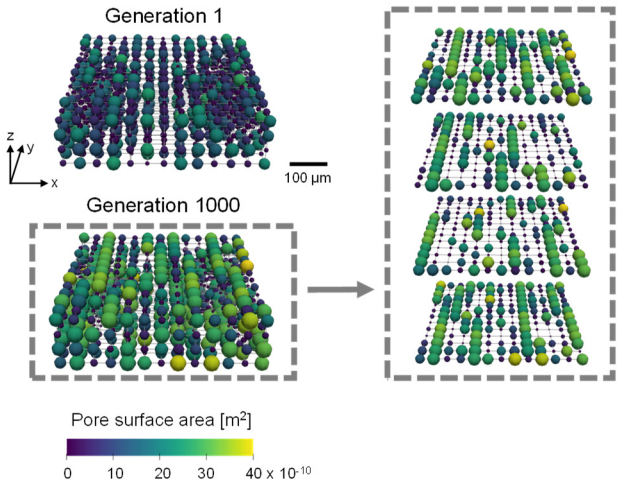

Figure A4.12: The results of the genetic algorithm optimized for the VO^{2+}/VO_2^+ electrolyte, but with a higher exchange current density of 1 x 10^4 A m^{-2}. The network structure of generation 1 and generation 1000 are shown together with the pore surface area with the flow in the y-direction and the thickness in the z-direction with the membrane facing to the top. In addition, the pore surface area of generation 1000 is shown over each layer over the z-coordinate.

A4.8.3. Higher overpotential system

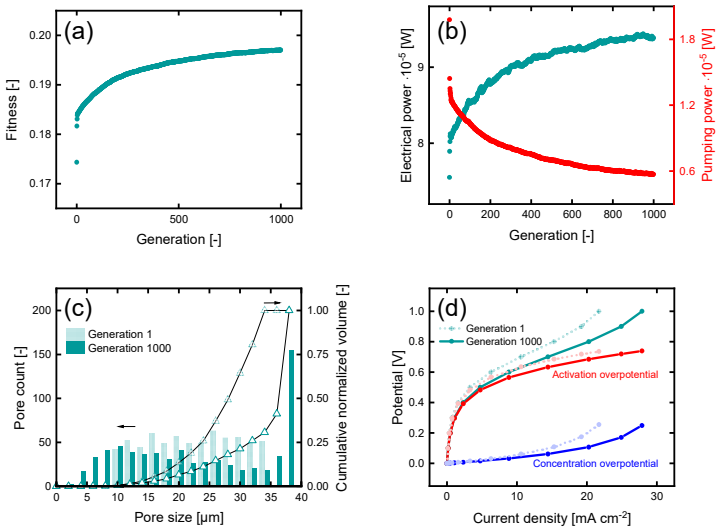

Figure A4.13: The results of the genetic algorithm optimized for the VO^{2+}/VO_2^+ electrolyte, evaluated at an overpotential of 1 V, with: **(a)** the evolution of the algorithm over the number of generations by plotting the maximum fitness for each generation, **(b)** the maximum electrical performance and pumping power for each generation, **(c)** the pore size distributions of the first and final generation, showing the pore count and cumulative normalized volume distributions (divided in 2 µm pore sized bins), and **(d)** the polarization curve shown as the current density versus the potential, together with the activation and concentration overpotential contributions for the first and last generation.

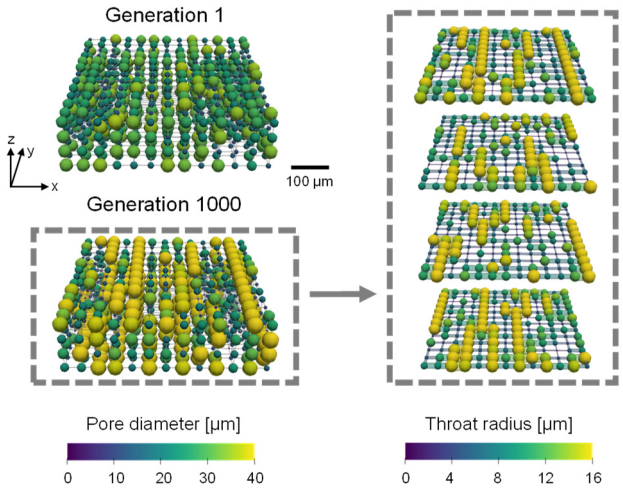

Figure A4.14: The results of the genetic algorithm optimized for the VO^{2+}/VO_2^+ electrolyte, evaluated at an overpotential of 1 V. The network structure of generation 1 and generation 1000 are shown together with the pore diameters with the flow in the y-direction and the thickness in the z-direction with the membrane facing to the top. In addition, the pore and throat diameters of generation 1000 are shown over each layer over the z-coordinate.

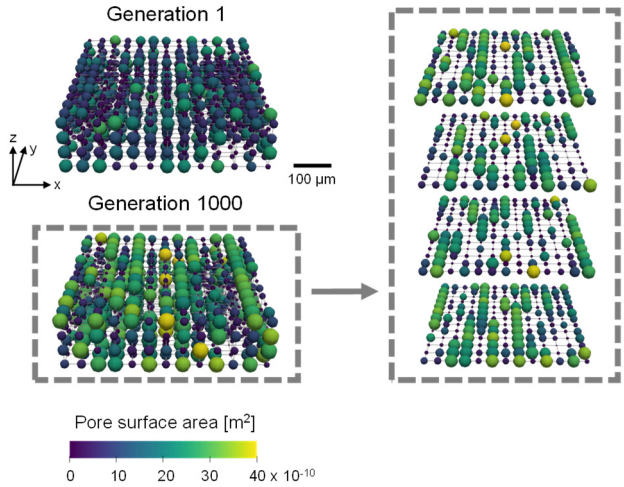

Figure A4.15: The results of the genetic algorithm optimized for the VO^{2+}/VO_2^+ electrolyte, evaluated at an overpotential of 1 V. The network structure of generation 1 and generation 1000 are shown together with the pore surface area with the flow in the y-direction and the thickness in the z-direction with the membrane facing to the top. In addition, the pore surface area of generation 1000 is shown over each layer over the z-coordinate.

A4.8.4. Lower overpotential system

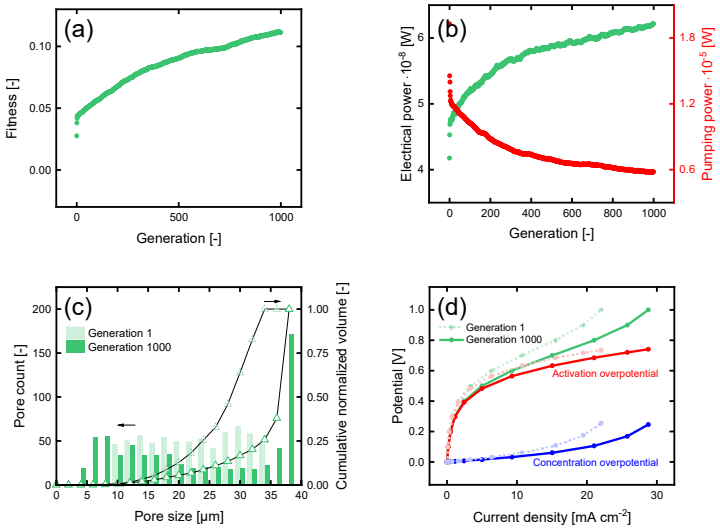

Figure A4.16: The results of the genetic algorithm optimized for the VO^{2+}/VO_2^+ electrolyte, evaluated at an overpotential of 0.1 V, with: **(a)** the evolution of the algorithm over the number of generations by plotting the maximum fitness for each generation, **(b)** the maximum electrical performance and pumping power for each generation, **(c)** the pore size distributions of the first and final generation, showing the pore count and cumulative normalized volume distributions (divided in 2 µm pore sized bins), and **(d)** the polarization curve shown as the current density versus the potential, together with the activation and concentration overpotential contributions for the first and last generation.

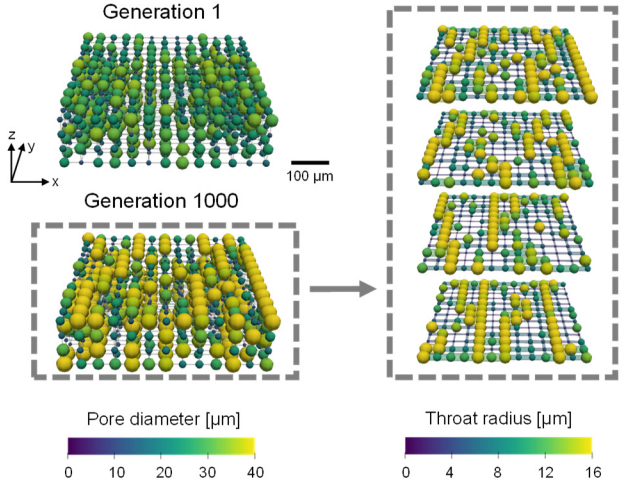

Figure A4.17: The results of the genetic algorithm optimized for the VO^{2+}/VO_2^+ electrolyte, evaluated at an overpotential of 0.1 V. The network structure of generation 1 and generation 1000 are shown together with the pore diameters with the flow in the y-direction and the thickness in the z-direction with the membrane facing to the top. In addition, the pore and throat diameters of generation 1000 are shown over each layer over the z-coordinate.

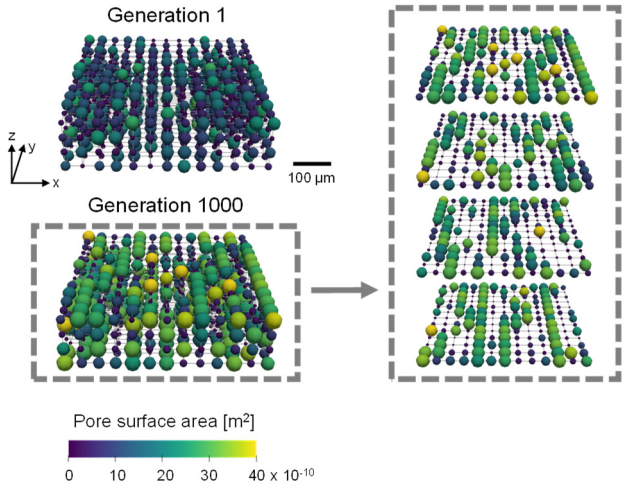

Figure A4.18: The results of the genetic algorithm optimized for the VO^{2+}/VO_2^+ electrolyte, evaluated at an overpotential of 0.1 V. The network structure of generation 1 and generation 1000 are shown together with the pore surface area with the flow in the y-direction and the thickness in the z-direction with the membrane facing to the top. In addition, the pore surface area of generation 1000 is shown over each layer over the z-coordinate.

A4.8.5. Higher velocity system

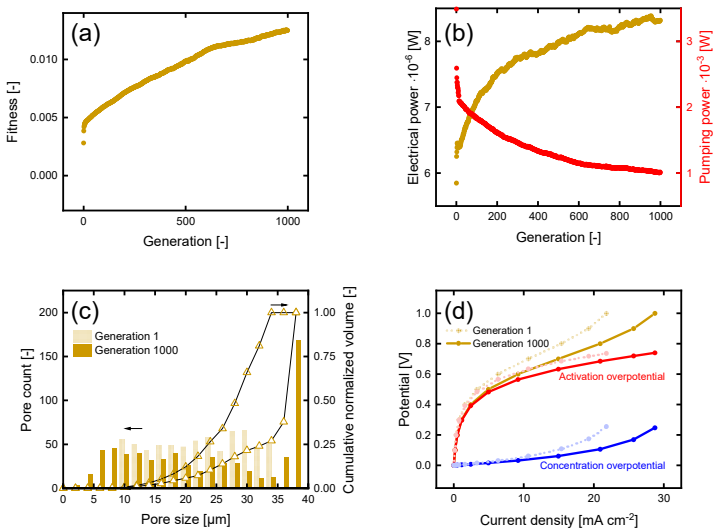

Figure A4.19: The results of the genetic algorithm optimized for the VO^{2+}/VO_2^+ electrolyte, evaluated at a velocity of 20 cm s^{-1}, with: **(a)** the evolution of the algorithm over the number of generations by plotting the maximum fitness for each generation, **(b)** the maximum electrical performance and pumping power for each generation, **(c)** the pore size distributions of the first and final generation, showing the pore count and cumulative normalized volume distributions (divided in 2 µm pore sized bins), and **(d)** the polarization curve shown as the current density versus the potential, together with the activation and concentration overpotential contributions for the first and last generation.

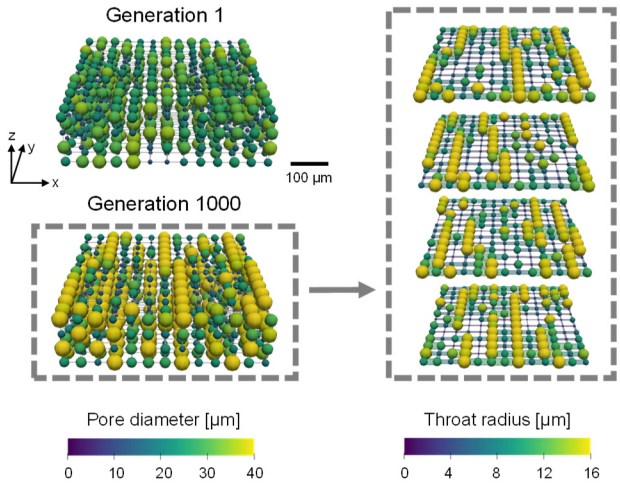

Figure A4.20: The results of the genetic algorithm optimized for the VO^{2+}/VO_2^+ electrolyte evaluated at a velocity of 20 cm s^{-1}. The network structure of generation 1 and generation 1000 are shown together with the pore diameters with the flow in the y-direction and the thickness in the z-direction with the membrane facing to the top. In addition, the pore and throat diameters of generation 1000 are shown over each layer over the z-coordinate.

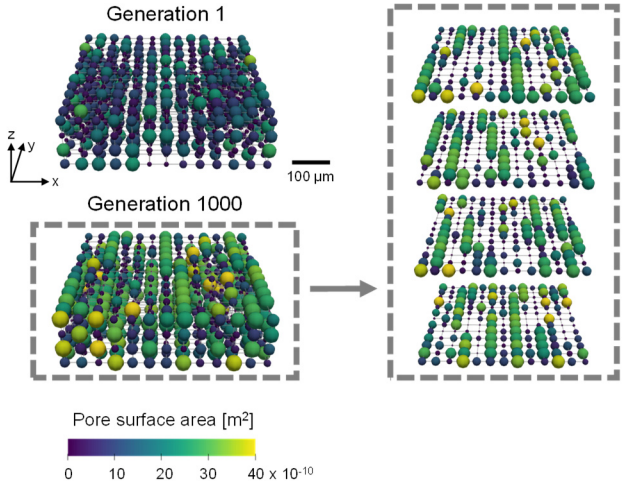

Figure A4.21: The results of the genetic algorithm optimized for the VO^{2+}/VO_2^+ electrolyte evaluated at a velocity of 20 cm s^{-1}. The network structure of generation 1 and generation 1000 are shown together with the pore surface area with the flow in the y-direction and the thickness in the z-direction with the membrane facing to the top. In addition, the pore surface area of generation 1000 is shown over each layer over the z-coordinate.

A4.8.6. Lower exchange current density system

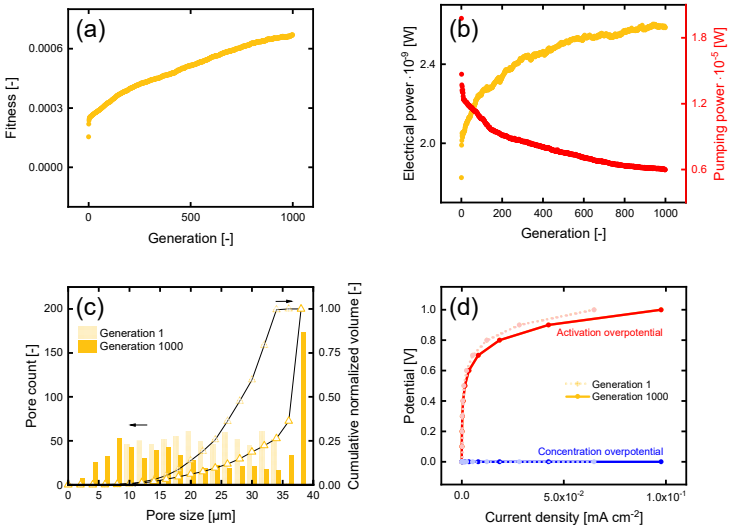

Figure A4.22: The results of the genetic algorithm optimized for the VO^{2+}/VO_2^+ electrolyte, but with a lower exchange current density of 1 x 10^{-4} A m^{-2}, with: **(a)** the evolution of the algorithm over the number of generations by plotting the maximum fitness for each generation, **(b)** the maximum electrical performance and pumping power for each generation, **(c)** the pore size distributions of the first and final generation, showing the pore count and cumulative normalized volume distributions (divided in 2 µm pore sized bins), and **(d)** the polarization curve shown as the current density versus the potential, together with the activation and concentration overpotential contributions for the first and last generation.

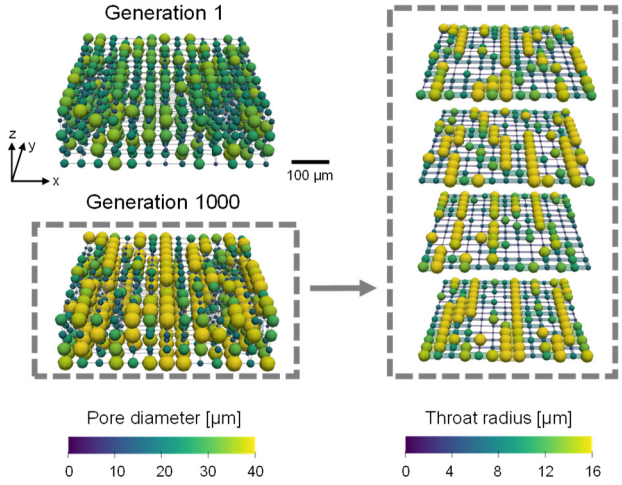

Figure A4.23: The results of the genetic algorithm optimized for the VO^{2+}/VO_2^+ electrolyte, but with a lower exchange current density of 1 x 10^{-4} A m^{-2}. The network structure of generation 1 and generation 1000 are shown together with the pore diameters with the flow in the y-direction and the thickness in the z-direction with the membrane facing to the top. In addition, the pore and throat diameters of generation 1000 are shown over each layer over the z-coordinate.

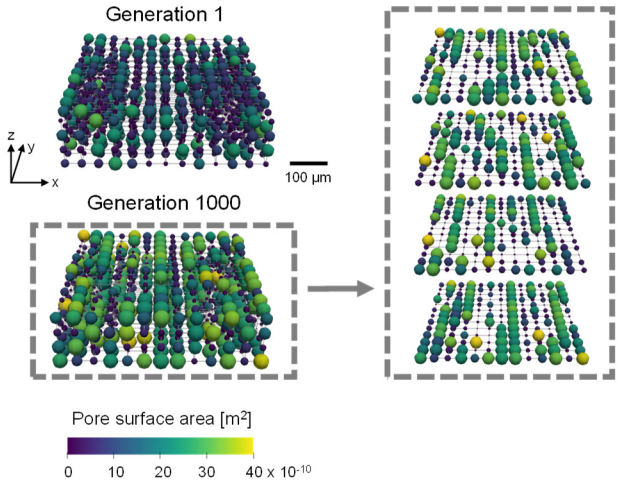

Figure A4.24: The results of the genetic algorithm optimized for the VO^{2+}/VO_2^+ electrolyte, but with a lower exchange current density of 1 x 10^{-4} A m^{-2}. The network structure of generation 1 and generation 1000 are shown together with the pore surface area with the flow in the y-direction and the thickness in the z-direction with the membrane facing to the top. In addition, the pore surface area of generation 1000 is shown over each layer over the z-coordinate.

A4.8.7. Parameter evolution

Table A4.5: The absolute values of the fitness and surface area for the best-performing network in the first and final generation.

	Fitness [-]		**Surface area [m^2]**	
	Gen 1	Gen 1000	Gen 1	Gen 1000
Reference	0.27	0.48	5.9 x 10^{-7}	8.7 x 10^{-7}
Lower velocity	0.60	0.60	6.0 x 10^{-7}	8.7 x 10^{-7}
Higher exchange current density	0.52	0.58	6.1 x 10^{-7}	8.6 x 10^{-7}
Higher overpotential	0.17	0.20	5.9 x 10^{-7}	8.3 x 10^{-7}
Lower overpotential	0.028	0.11	5.9 x 10^{-7}	8.8 x 10^{-7}
Higher velocity	0.0028	0.012	5.9 x 10^{-7}	8.7 x 10^{-7}
Lower exchange current density	0.00015	0.00067	6.0 x 10^{-7}	8.5 x 10^{-7}

Table A4.6: The absolute values of the electrical power and pumping power for the best-performing network in the first and final generation.

	Electrical power [W]		**Pumping power [W]**	
	Gen 1	Gen 1000	Gen 1	Gen 1000
Reference	5.8 x 10^{-6}	8.3 x 10^{-6}	2.0 x 10^{-5}	5.6 x 10^{-6}
Lower velocity	6.9 x 10^{-6}	8.3 x 10^{-6}	8.8 x 10^{-8}	2.6 x 10^{-8}
Higher exchange current density	4.4 x 10^{-5}	5.3 x 10^{-5}	2.0 x 10^{-5}	5.5 x 10^{-6}
Higher overpotential	7.6 x 10^{-5}	9.4 x 10^{-5}	2.0 x 10^{-5}	5.7 x 10^{-6}
Lower overpotential	4.2 x 10^{-8}	6.2 x 10^{-8}	1.9 x 10^{-5}	5.8 x 10^{-6}
Higher velocity	5.8 x 10^{-6}	8.3 x 10^{-6}	3.5 x 10^{-3}	1.0 x 10^{-3}
Lower exchange current density	1.8 x 10^{-9}	2.6 x 10^{-9}	2.0 x 10^{-5}	6.0 x 10^{-6}

Table A4.7: Percentual increase in fitness, electrical power, and pumping power over 1000 generations for the best-performing network in all evaluated systems.

Percentual increase [%]	Fitness	Electrical power	Pumping power	Surface area
Reference	75	42	-73	47
Lower velocity	0.41	40	-70	45
Higher exchange current density	12	22	-72	41
Higher overpotential	13	24	-71	41
Lower overpotential	303	49	-70	49
Higher velocity	344	42	-71	47
Lower exchange current density	335	42	-70	42

Table A4.8: Total pore surface area values for each network layer for the best-performing network in the first and final generation from the current collector to the membrane, evaluated for all systems.

System	Pore surface area x 10^{-7} [m^2]	Generation 1	Generation 1000
Reference	Current collector	1.55	2.13
	Internal 1	1.21	2.18
	Internal 2	1.22	1.96
	Membrane	1.77	2.43
Lower velocity	Current collector	1.69	2.49
	Internal 1	1.19	1.88
	Internal 2	1.36	1.87
	Membrane	1.49	2.49
Higher exchange current density	Current collector	1.57	2.56
	Internal 1	1.18	1.77
	Internal 2	1.22	1.74
	Membrane	1.53	2.55
Higher overpotential	Current collector	1.63	2.4
	Internal 1	1.21	1.79
	Internal 2	1.3	1.77
	Membrane	1.46	2.39
Lower overpotential	Current collector	1.53	2.35
	Internal 1	1.31	1.89
	Internal 2	1.22	1.96
	Membrane	1.62	2.63
Higher velocity	Current collector	1.58	2.35
	Internal 1	1.15	2.03
	Internal 2	1.29	2.01
	Membrane	1.59	2.32
Lower exchange current density	Current collector	1.5	2.42
	Internal 1	1.24	1.77
	Internal 2	1.33	2.05
	Membrane	1.56	2.23

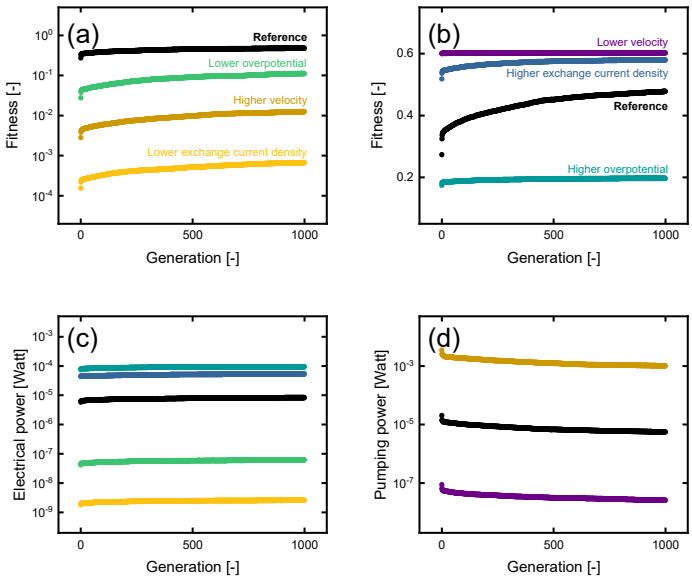

Figure A4.25: The results of the genetic algorithm optimized for the VO^{2+}/VO_2^+ electrolyte for the different systems, including a reference system and six systems with one parameter changed: a lower overpotential (to 0.1 V), a higher velocity (to 20 cm s^{-1}), a lower exchange current density (to 1 x 10^{-4} A m^{-2}), a lower velocity (to 0.1 cm s^{-1}), a higher exchange current density (to 1 x 10^4 A m^{-2}), and a higher overpotential (to 1 V). The evolution of the algorithm is shown over the number of generations, with: **(a-b)** the maximum fitness values, **(c)** the maximum electrical performance, and **(d)** the maximum pumping power.

A4.8.8. Relative increase of surface area at the electrode-membrane interface

The relative increase of surface area at the electrode-membrane interface was calculated from the total pore surface area increase over generations for the membrane layer and the total network, given in **Table A4.8**. The percentage was calculated using the increase in surface area in the membrane layer over the generations ($SA_{m,1000}/SA_{m,1}$) and the increase in surface area in the total network over the generations ($SA_{tot,1000}/SA_{tot,1}$). The lower connectivity of the pores at the current collector and the membrane (connectivity of 5 instead of 6) was considered in the calculation.

$$Percentual\ increase_{SA,m} = \left(1 - \frac{\frac{SA_{m,1000}}{SA_{m,1}}}{\frac{SA_{tot,1000}}{SA_{tot,1}}}\right) \cdot 100\% \qquad \text{(A4.1)}$$

A4.9. References

[1] M. van der Heijden, R. van Gorp, M. A. Sadeghi, J. Gostick, A. Forner-Cuenca, *J. Electrochem. Soc.* **169**, 040505 (2022).
[2] J. D. Milshtein, J. L. Barton, R. M. Darling, F. R. Brushett, *J. Power Sources*. **327**, 151–159 (2016).
[3] D. Niblett, M. Mamlouk, O. Emmanuel Godinez Brizuela, Porous Microstructure Generator (2022), , doi:https://doi.org/10.25405/data.ncl.20448471.v3.
[4] D. Niblett, Z. Guo, S. Holmes, V. Niasar, R. Prosser, *Int. J. Hydrogen Energy*. **47**, 23393–23410 (2022).
[5] C. T. Wan *et al.*, *Adv. Mater.* **33**, 2006716 (2021).
[6] A. Forner-Cuenca, E. E. Penn, A. M. Oliveira, F. R. Brushett, *J. Electrochem. Soc.* **166**, A2230–A2241 (2019).

Chapter 5

A versatile optimization framework for porous electrode design

Abstract

Porous electrodes are performance-defining components in electrochemical devices, such as redox flow batteries, as they govern the electrochemical performance and pumping demands of the reactor. Yet, conventional porous electrodes used in redox flow batteries are not tailored to sustain convective-enhanced electrochemical reactions. Thus, there is a need for electrode optimization to enhance the system performance. One approach was presented in our previous work, the coupling of a genetic algorithm with a pore network modeling framework. Here we present an extended optimization framework to carry out the bottom-up design of porous electrodes. We introduce additional geometrical versatility by adding a pore merging and splitting function, study the impact of various optimization parameters, geometrical definitions, and objective functions, and incorporate geometrically-detailed electrode structures and flow field geometries. Moreover, we show the need for optimizing electrodes for specific reactor architectures and operating conditions to design next-generation electrodes, by analyzing the genetic algorithm optimization for initial starting geometries with diverse morphologies (cubic, Voronoi, and an off-the-shelf extracted paper electrode), flow field designs (flow-through and interdigitated), and redox chemistries (VO^{2+}/VO_2^+ and TEMPO/TEMPO$^+$). For example, we found that for kinetically sluggish electrolytes with high ionic conductivity, electrodes with numerous small pores and high internal surface area provide enhanced performance, whereas for kinetically facile electrolytes with low ionic conductivity, low through-plane tortuosity and a high hydraulic conductance are required. The computational tool developed in this work can guide the design of high-performance electrode materials for a broad range of operating conditions, electrolyte chemistries, reactor designs, and electrochemical technologies.

This chapter is in preparation for submission as:

M. van der Heijden, G. Szendrei, V. de Haas, A. Forner-Cuenca, A versatile optimization framework for porous electrode design (2023).

5.1. Introduction

Porous electrodes are core reactor components in redox flow batteries (RFBs) and are integral to the battery performance, durability, and costs [1, 2]. The porous electrode provides the active surfaces for the electrochemical reactions, controls the distribution of the liquid electrolyte throughout the reaction zones, and conducts electrons and heat [3–6]. Off-the-shelf porous electrodes are carbon fiber-based mats that are generally repurposed from more mature electrochemical technologies such as low-temperature fuel cells and have not been tailored to sustain liquid-phase electrochemistry [1, 7]. Thus, for RFBs to become a cost-competitive energy storage technology, porous electrodes tailored to specific flow battery chemistries and flow reactors must be designed and manufactured [1, 8, 9]. However, because of the convection-enhanced nature of RFBs, the porous electrode design becomes challenging as contradictory requirements must be satisfied, including low pumping power, high electrochemical surface area, and facile mass transport [2, 5, 10]. Hence, to solve the complex design requirements, advanced optimization strategies could be applied to design porous electrodes from the bottom-up [2, 11–14].

Genetic algorithms (GAs) are promising for exploring a broad geometrical design space for the optimization of porous electrodes. GAs are probabilistic global optimization techniques inspired by the theory of evolution that enable heuristic optimization of a given design space based on a fitness function [15–18]. Therefore, GAs require only one objective function, can be parallelized, perform global optimization, and have a large solution space. These unique features have motivated the application of GAs to a wide variety of research fields, including the integration of electrochemical numerical frameworks for the optimization of RFB parameters and conditions [19, 20] and electrode structures [12–14]. For the optimization of the electrode geometry, a GA should be coupled to pore-scale simulations to capture the relationship between the battery performance and electrode microstructure in a computationally light manner. To this end, pore network models (PNMs) can be used as they capture microstructural effects at the mesoscale whilst being computationally light, owing to geometrical simplifications of the pore network [8, 21–24]. The coupling of PNMs and GAs has been used in other research fields including the extraction of pore networks of porous rock samples for petroleum recovery [12, 25–27]. However, the coupling of GAs with PNMs for the bottom-up design and optimization of electrode microstructures for RFBs remains largely unexplored.

The concept of combining a genetic algorithm with PNMs to optimize three-dimensional microstructures for flow battery electrodes was demonstrated in our previous work for cubic networks with fixed pore positions [14]. The performance of the individual networks was evaluated by a fitness function that maximizes the electrochemical power and minimizes the pumping power of the networks. Here, we extend the optimization framework to include more design flexibility by going beyond fixed pore positions through the integration of merging and splitting of pores (**Figure 5.1**). In addition, we evaluate the optimization algorithm for structures with diverse morphologies such as Voronoi networks and X-ray tomography-extracted networks of commercial electrodes. Furthermore, we investigate the effect of operation conditions by evaluating two chemistries, VO^{2+}/VO_2^+ and TEMPO/TEMPO$^+$, and two prevailing flow field geometries, a flow-through and an interdigitated flow fields.

In this work, we first describe the modeling framework including the network generation, the coupling of the GA with the electrochemical algorithm, the genetic

operations included in the GA, and the operation parameters investigated. Second, we analyze the influence of the optimization definitions (objective function, geometrical definitions including the surface area and throat factor, and network dimensions) on the optimization flexibility of the GA. Third, we show the geometrical evolution for the addition of pore merging and splitting as an additional mutation operation. Fourth, we deliberate on the influence of the network structure of the initial population on the fitness evolution. Fifth, we assess the impact of the flow field geometry on the optimized network structures. Sixth and last, we perform the optimization for two chemistries to investigate the importance of the selection of the starting network and the specific reactor architectures and operating conditions. This study, although applied to redox flow batteries here, shows the potential of optimization by genetic algorithms to design and optimize porous materials for a wide variety of convection-enhanced electrochemical applications. Furthermore, this work emphasizes the importance of co-designing electrodes and flow fields for specific reactor architectures and operating conditions.

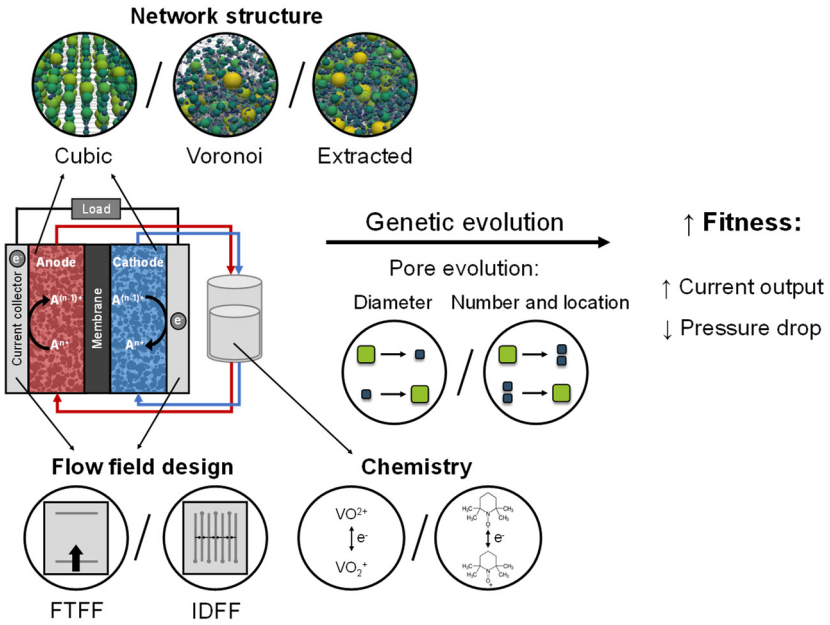

Figure 5.1: Schematic overview of the outline of this work, including a single-electrolyte flow cell, the starting networks used in the optimization (artificially generated cubic and Voronoi networks, and the X-ray tomography extracted paper electrode), the flow field designs (flow-through and interdigitated) used in this study, different chemistries (sluggish vanadium- and facile nitroxyl-based electrolytes), and pore evolution approaches (based on a pore diameter evolution and pore merging and splitting), to obtain an electrode with increased fitness by an enhanced current output and/or lower pressure drop.

5.2. Model development

Optimization by genetic algorithms can be applied to evolve a population of candidate solutions to increasingly better sets of solutions for the given design case. The principle is based on natural diversity and selection by the recombination of good building blocks. The concept of combining a genetic algorithm with pore network models is described in our previous work for cubic networks with fixed pore positions [14], and extended upon in the present study. The pumping and electrochemical power defining the selection criteria were solved using a developed and validated pore network model [21], that uses the open-source framework OpenPNM [24]. A PNM was employed because of the low computational cost required to simulate local transport within porous electrodes, where the void space is approximated by spherical pores and cylindrical throats. The PNM was developed for single-electrolyte flow cell designs in discharge mode with the co-flow operation of the anodic and cathodic half-cells and thus optimizes the electrode in only one half-cell, assuming perfect electrode wetting. The required computational time for the reference system on a single Intel® Core™ i7-8700K CPU was ~48 hours for 1000 generations based on 50 individuals and 10 parent networks (~2 seconds per network), which can be significantly reduced when using multiple computational cores. For example, after parallelizing the electrochemical part of the algorithm and running it on a cluster with 50 cores, the required computational time was reduced to ~27 hours for the reference system.

The presented genetic algorithm consists of nine steps: the network generation, initialization, volume scaling, the electrochemical PNM, parent selection, crossover, mutation, merging and splitting, and termination, see **Figure 5.2** for the schematic overview of the GA. In the network generation stage, the type of network was selected (cubic, Voronoi, or extracted), of which a random set was generated in the initialization step defining the first population. In the first step in the iterative GA, volume scaling was performed to ensure a meaningful comparison at constant electrode porosity between the different individuals in a population. Thereafter, the networks were evaluated based on the electrochemical PNM and a fitness function. Successively, the fittest individuals, i.e., parents, in the population were selected and defined as the next population by inheriting the information of two parent networks with a crossover step. Afterward, stochastic changes were made in the networks of the new population by pore mutation, after which the pores in the network had a chance to merge and split, resulting in the next generation. The iterative GA was repeated until the termination criterion was achieved based on the total number of generations. The population size, number of parents, mutation range and chance, and merging and splitting chance and ratio were initially chosen arbitrarily or inspired by the work of Grefenstette [28]. The number of generations and network size strongly impact the required computational time, which is kept to only 1000 generations and a small network size (~500 x 500 x 200 μm^3) to show the principle of the GA without being computationally intensive and requiring high computing resources. Finally, the parameters defining the evaluation criteria of the PNM were based on our previous works [14, 21]. All reference parameters used in this work for the GA can be found in **Table 5.1**.

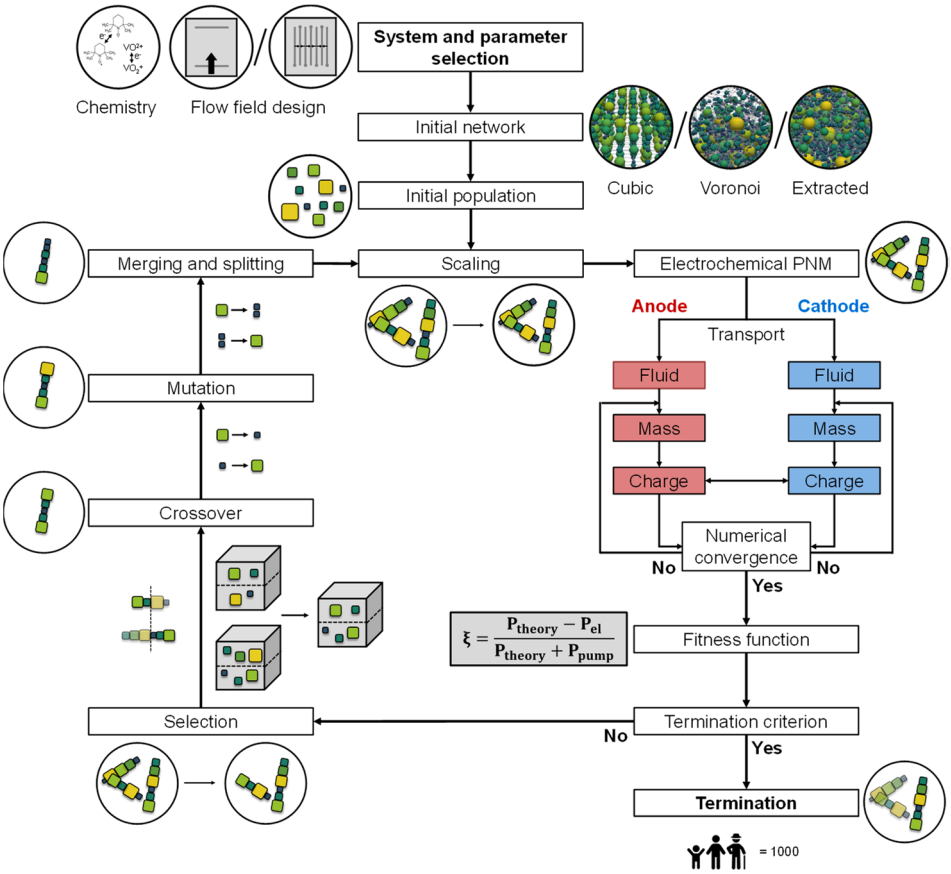

Figure 5.2: Schematic flowchart of the genetic algorithm used in this work, including a simplified flowchart of the integrated pore network model, together with illustrations of the chemistries, flow fields, initial networks, network structures after each operation, and the merging and splitting, crossover, and mutation operations. The colored building blocks represent the pores in the pore networks where each color represents a distinct pore diameter.

Table 5.1: Reference parameters used for the optimization study.

Parameter	Value
Number of generations	1000 or 200
Number of offspring	50
Number of parents	10
Mutation range	0.1
Mutation chance	0.05
Merging and splitting chance	0.1
Merging and splitting ratio	0.5
Relative tolerance	10^{-4}
Absolute tolerance	10^{-4}
Maximum iterations	10000
Relaxation factor	0.1

5.2.1. Network generation

Cubic ordered lattices can be used as a first step to evaluate the impact of topology optimization on the electrode performance and to help evaluate the influence of optimization parameters on genetic evolution. To induce randomization and complexity in the artificial networks, networks created by Voronoi tessellation of arbitrary base points could be used as starting geometries. Nevertheless, these simplified structures do not capture the permeability and electrochemical performance of fiber-based porous electrodes. To mimic the complex pore and throat locations, connections, and hydrodynamic properties of real porous electrodes, networks extracted from tomographic imaging should be investigated.

After the generation of the network structures with diverse morphologies, topological properties were attributed to the pores and throats in the network with geometry objects. The geometry objects are a subclass within OpenPNM that can be assigned to parts of the modeling domain. In this work, the geometric StickAndBall approach was applied to all networks, which handles pores as spheres and throats as cylinders in the generated networks for which geometrical properties can be calculated.

5.2.1.1. Artificial networks

The cubic and Voronoi networks were artificially generated with the Cubic and Voronoi class algorithms in the OpenPNM Network module, respectively. The cubic lattice networks were created using a network shape, spacing, and connectivity as input parameters, where the shape of the lattices defined the number of pores in each dimension, the spacing the center-to-center distance between neighboring pores, and the connectivity the number of throats that were connected to every single pore. Furthermore, for this network, boundary pores with insignificant pore diameters (0.8 µm) were added to the surface of the network. The Voronoi networks, on the other hand, take the network shape and number of points as input parameters, where the network shape represents the size of the network and the number of points the amount of pores present in the chosen network size. For each base point, a convex polyhedron was defined, where the points were closer to the base point compared to the other points. Accordingly, the vertices and edges of these polyhedrals defined the pores and throats in the network, where the structure is framed by a cuboid, required to apply the boundary conditions to this network. For both networks, the topological properties of the pores and throats were attributed using the OpenPNM Geometry module, considering the geometry of spheres and cylinders.

For the initial cubic network structures, the pore diameter (d_p) was assigned by a random process, depending on the maximum pore diameter ($d_{p,max}$) and a modification factor, the pore seed (S_p). The maximum pore diameter was determined by an iterative process by increasing the pore diameter until overlap with a neighboring pore was realized. The maximum pore diameter was subsequently multiplied with the pore seed, a value between 0.2 - 0.7, based on the standard option in the OpenPNM StickAndBall geometry class. The seed factor was randomly generated for each pore to obtain the pore diameter:

$$d_p = S_p \, d_{p,max}. \tag{5.1}$$

The pore diameter for the initial Voronoi network, on the other hand, was defined by the maximum pore diameter and uniformly scaled down with the volume-scaling step. Moreover, for both networks, the throat diameter (d_T) between two pores was determined based on the pore diameters of the two connecting pores and a scaling factor, the throat factor. The throat diameter was based on the smallest pore size of the two connecting pores to prevent the formation of throats with a larger diameter than the connecting pore diameters. The smallest pore diameter was multiplied with the throat factor, which was fixed at 0.8 in this work based on the ratio of pore and throat diameters used by Sadeghi *et al.* to mimic the commercial SGL 25AA electrode used in flow batteries [22], to obtain the throat diameter:

$$d_T = 0.8 \min (d_{p,1}, d_{p,2}). \tag{5.2}$$

As the throats are represented as cylinders, the throat cross-sectional area (S_T) was described by the throat diameter by **equation (5.3)** and the throat internal surface area (A_T) by the throat diameter and length (L_T), defined as the length between two throat endpoints, according to **equation (5.4)**. The throat conduit length, which is equal to the network spacing for cubic networks, was used for the hydraulic transport through the network and was described by the summation of the length of two half-pores and the length of the connected throat.

$$S_T = \frac{\pi}{4} d_T^2 \tag{5.3}$$

$$A_T = \pi \, d_T \, L_T \tag{5.4}$$

Finally, the initial definition of the pore internal surface area (A_p), described by the OpenPNM geometry functions, was defined by subtracting the throat cross-sectional area of N_T number of neighboring throats from the pore surface area. The definition is a simplification of the pore internal surface area as the curvature of the intersection between the pore and throat was not considered.

$$A_p = \pi \, d_p^2 - \sum_{j=1}^{N_T} S_T \qquad \text{Definition 1} \tag{5.5}$$

Because of the direct correlation between surface area and electrochemical performance, multiple surface area definitions were considered in this work, see **equations (5.5 - 5.8)**. All considered definitions are simplified descriptions of the surface area, identified to study the influence of geometrical definitions on the structure evolution.

$$A_p = \pi \, d_p^2 \qquad \text{Definition 2} \tag{5.6}$$

$$A_p = \pi \, d_p^2 - \sum_{j=1}^{N_T} (0.8 \, d_p)^2 \, \frac{\pi}{4} \qquad \text{Definition 3} \tag{5.7}$$

$$A_p = \pi \, d_p^2 - \sum_{j=1}^{N_T} S_T + \sum_{j=1}^{N_T} 0.5 \, A_T \qquad \text{Definition 4} \tag{5.8}$$

The network properties of the cubic and Voronoi structures are given in **Table 5.2**, where, in this work, small three-dimensional electrode structures were optimized with electrode geometrical areas of approximately 500 x 500 µm^2. To allow comparison between the three network structures, the network shape and spacing were based on the microstructural properties of the off-the-shelf Freudenberg H23 paper electrode (Fuel Cell Store, 80 % porosity) with a median pore size of 20 µm and a measured thickness of 210 µm [6, 10, 14, 21]. As the network porosity and the number of pores and throats are a

direct result of the chosen input parameters, to maintain a constant porosity between the three structures, the reference network of the Voronoi structure was chosen to have a diameter of 25 μm and 300 points as input parameters.

Table 5.2: Network properties used for the optimization study for the cubic, Voronoi, and extracted Freudenberg H23 electrode.

Parameter	Cubic	Voronoi	Extracted	Unit
Porosity	54	49	51	%
Network shape	[13, 13, 4]	-	-	-
Number of pores	676	1755	3348	-
Number of throats	1755	3506	10171	-
Network dimensions	580 x 580 x 220	500 x 500 x 220	500 x 500 x 198	μm^3
Pore seed	$0.2 < S_p < 0.7$	-	-	-
Spacing	40	-	-	μm
Connectivity	6	-	-	-

5.2.1.2. Extracted network

The extracted network used in this study was the Freudenberg H23 carbon paper electrode, imaged in a previous study [21] with X-ray computed tomography. After image processing including a two-dimensional median filter and a K-means cluster segmentation filter, the pore network was extracted using the SNOW algorithm that makes use of a marker-based watershed segmentation algorithm [29]. For this extraction, the inscribed pore diameter was used, and the network extraction was performed using a single Intel® Core™ i7-8750H CPU. During the extraction, the topological properties of the pores and throats within this network were automatically assigned considering the geometry of spheres and cylinders; however, to match with the geometrical definitions used in the GA, the network geometry was scaled to the definitions described above in **equations (5.2 - 5.4** and **5.5** or **5.6)**.

5.2.2. Initialization

The initial population was created based on the network properties (**Table 5.2**) and the number of offspring networks (**Table 5.1**). For the cubic and Voronoi networks, the diversity of the offspring comes from the randomization created by the pore seed or by the randomization in the generation of the networks, respectively, whereas for the extracted networks it is introduced by a mutation of the original extracted network, depending on a mutation factor and range, see **Section 5.2.7**.

5.2.3. Network scaling

To allow a meaningful comparison between individuals in each generation and between generations, a network scaling step was performed where the pore diameters were uniformly scaled to a reference network. The network scaling was based on the total pore volume, maintaining a constant network porosity during the evolution. The reference networks used for this scaling step depended on the network type. For cubic networks, the reference network was based on the pore-to-throat ratio described by Sadeghi *et al*.

where they translated a commercial porous electrode to a pore network consisting of pores with a diameter of 15.6 µm and throats with a diameter of 20 µm [22]. For the Voronoi network, only the pore diameter of the reference network was defined, which was kept constant at 25 µm. Finally, for the extracted networks, the initial extracted structure, scaled with the definitions described in **Section 5.2.1**, was used.

5.2.4. Electrochemical algorithm

The electrochemical algorithm developed and validated in our previous work [21] was integrated into the GA (**Figure 5.2**) to evaluate the performance of the individuals in every generation, with the electrochemical power and pumping power as outputs. The PNM was designed for single-electrolyte flow configurations with a constant state-of-charge of 50 % and an open circuit voltage of 0 V to study electrode overpotentials in isolation without secondary effects including membrane crossover and changing state-of-charge [1, 5]. The model solved the local fluid transport and the coupled mass and charge transport within both compartments using an iterative approach, where the locations of the flow field channels, ribs, current collectors, and membrane were defined by boundary conditions, see **Figure A5.2**. In this work, two flow field configurations were studied, a flow-through and an interdigitated flow field. The flow-through flow field was previously validated for two electrode structures and two electrolytes and showed a near-unidirectional velocity distribution from the inlet to the outlet channel over the entire electrode length [21]. The interdigitated flow field on the other hand was validated in another work and features a unique velocity profile from the inlet to the outlet channel through the electrode over a rib [30].

5.2.4.1. Iterative algorithm

In the PNM, the fluid transport can be independently solved from the mass and charge transport equations because of the dilute electrolyte assumption [22]. Hence, the fluid transport was first solved to obtain the pressure field with the Navier-Stokes equation. Using the Hagen-Poiseuille equation, the velocity field was subsequently back-calculated from the pressure field. The solved pressure field was then fed into the iterative algorithm to solve the coupled mass and charge transport equations with the advection-diffusion-reaction and the conservation of charge equations, coupled by the Butler-Volmer equation to obtain the species concentration and potential fields. Furthermore, the coupling between the anodic and cathodic compartments was made at the membrane by treating the membrane as a macro continuum entity by only considering the overall macroscopic ionic resistance of the membrane with Ohm's law. This allowed for the coupling of the charge transport within one compartment with the electrolyte potential at the membrane boundary in the other compartment.

The PNM was solved at a constant applied arbitrary overpotential of -0.5 V in discharge mode, with an initial guess for the concentration and overpotential fields. The initial guess for the concentration field was equal to the inlet concentration for all networks (100 mol m^{-3} for all redox species). The initial guess of the overpotential was updated after solving for each network to speed up the iterative approach, where the initial guess for the first network in the first generation was set to ±0.25 V. In the iterative approach, two numerical strategies were employed to counteract the solution divergence

as a result of the high nonlinear nature of the system. The first strategy was imposing an under-relaxation scheme on the concentration and potential fields with a constant relaxation factor, and the second strategy was the linearization of the charge transport source term [21]. Finally, numerical convergence was achieved when both the relative and absolute tolerances were met for the total current, bound by a maximum number of iterations. The parameters for numerical convergence are given in **Table 5.1**.

5.2.4.2. Flow field geometry

Because of symmetry along the width for the flow-through flow field, the modeled domain consisted of two symmetric, mirrored ~0.5 x 0.5 mm^2 electrodes. For the interdigitated flow field, the modeling domain was chosen to be half an inlet channel, a full rib, and half an outlet channel. We assumed the channel and rib dimensions to be 0.5 mm wide, resulting in ~1 x 0.5 mm^2 electrodes for the interdigitated flow field. The boundary conditions for the individual flow fields are shown in **Figure A5.2**.

5.2.5. Parent selection

The electrochemical performance and pressure drop of the individual network structures were analyzed in the GA with a fitness function (ξ) to select the best-performing networks for reproduction. The fitness function considers the maximum thermodynamical electrochemical power (P_{max}), electrochemical power loss (P_{el}), and pumping power (P_{pump}), where the maximum fitness is achieved when the pumping losses are zero. In this work, the electrochemical losses were evaluated at a fixed overpotential (E_{losses}) of 0.5 V, corresponding to 40 % of heat loss during cell discharge, and define the combined overpotential (activation, ohmic, and mass transfer) present in the single-electrolyte cell. By fixing the overpotential, we aim to increase the maximum electrochemical power by achieving a higher total current (I). Moreover, the open circuit cell potential (E_{cell}) of a full-vanadium battery system was considered 1.26 V [31] for the reference system. These chosen parameters resulted in a maximum achievable fitness value of 0.603 for the vanadium electrolyte. Further, as we optimized electrode structures for single-electrolyte cell designs, we assumed that the overpotentials resulting from the other redox pair were identical in this theoretical exercise. The pumping power required to pump the liquid electrolyte through the pore network depended on the electrolyte flow rate (Q), which was set at 1.5 cm s^{-1}, the pressure drop (ΔP), and a pumping efficiency (η_p), set to 0.9 [32]. Hence, the fitness function was defined by **equation (5.9)** by subtracting the electrochemically generated power by the summation of the maximum electrochemically generated power and pumping requirements [14, 32, 33].

$$\xi = \frac{P_{max} - P_{el}}{P_{max} + P_{pump}} = \frac{I(E_{cell} - E_{losses})}{I\,E_{cell} + \frac{Q\,\Delta P}{\eta_p}} \tag{5.9}$$

The individuals with the highest fitness value ($\xi \rightarrow 0.603$) were selected as parent networks and were subjected to crossover in the next step. Finally, the total percentual fitness increase over the generations can be calculated according to $(\xi_n - \xi_1)/\xi_1 \cdot 100\%$, with ξ_n the fitness of the best-performing network in the last evaluated generation, and ξ_1 the fitness of the best network of the first generation.

5.2.6. Crossover

The crossover operator was responsible for the recombination of the parent networks into new offspring networks, defining the next generation. These new offspring networks were stochastically generated as the parent networks were arbitrarily selected from the mating pool and the crossover point or coordinate was randomly selected. The crossover was performed by two different methods in this work: by single-point or coordinate-based crossover. The single-point crossover was used for networks with fixed pore coordinates by selecting a random pore between the first and final locus of the pore diameter array, defining the crossover point [34]. Thereafter, the new offspring networks were created by inheriting the geometrical information, including pore and throat diameters, of the first parent between the first pore and crossover point, and that of the second parent between the crossover point and final pore. Alternatively, the coordinate-based crossover was used to handle pore networks with a varying number of pores and pore coordinates and can thus be applied to networks that underwent pore merging and splitting. In this crossover approach, a plane at half the electrode width was selected as the crossover plane, which splits the left and right parts of two parent networks. Then, the left part of one parent and the right part of another parent were stitched together to form the new offspring networks. The old throats at the plane boundary were deleted and new throats were reestablished between the two parent networks at the plane boundary, where the nearest pores were connected and the number of original connections remained constant.

5.2.7. Mutation

The mutation operator is a fundamental instrument to ensure population diversity. In this work, the mutation was based on randomly changing the pore diameters of the offspring networks. To control the mutation, a mutation chance and range were introduced. The mutation chance defined the probability of mutation for each pore and the mutation range (σ_M) controlled the severity of the mutation. When a pore was selected for mutation, a random mutation value (c_M) was stochastically assigned to the pore within the boundaries defined by the mutation range: $(1 - \sigma_M) \leq c_M \leq (1 + \sigma_M)$. Thereafter, the pore diameter was mutated to a new value (d_p^M) by multiplying the mutation value with the old pore diameter (d_p^o):

$$d_p^M = c_M \, d_p^o. \tag{5.10}$$

5.2.8. Merging and splitting

In our previous work [14], the pore locations and the network connectivity were fixed, restricting the networks from evolving into more geometrically-detailed structures. Therefore, we incorporated merging and splitting of pores in the GA to broaden the design space for evolution by allowing pore mobility. The merging and splitting of pores were defined by a merging and splitting chance and ratio. When the ratio is 0.5, there is an equal chance for pore merging as for pore splitting, and the number of pores and throats is kept nearly constant over the evolution.

Pore merging was performed based on an in-built OpenPNM function with which two or more pores can be combined at the center of the selected pores. In this GA,

only two neighboring pores were allowed to merge, where the neighbor of the selected pore with the smallest pore diameter was chosen for merging. Furthermore, the pore volume was defined as the summation of the two pores, ensuring a constant total pore volume. Thereafter, the throat connections were reestablished between the neighbors of the merged pores and the new pore, decreasing the number of throats by one.

With pore splitting, on the other hand, the selected pore was split into two pores with equal pore volume. The new pore locations were stochastically determined within half a maximum pore diameter distance in each direction and a new throat was formed between the two new pores. The old throat connections with the neighboring pores of the split pore were reestablished to the closest of the two new pores, increasing the total number of throats in the network by one. Finally, it must be noted that for both pore merging and splitting, the new pore locations must be checked for pore overlap with nearby pores and if the new pores are within the specified network dimensions. In case of pore overlap, the pore locations were updated by stochastically altering their coordinates.

5.2.9. Termination

The iterative GA was repeated according to the scheme presented in **Figure 5.2** and was only terminated when the maximum number of generations was achieved. We elected this termination criterion to enable a meaningful comparison between networks generated at different operating conditions, evolutionary parameters, electrolyte properties, flow field architectures, and network geometries.

5.2.10. Operating parameters

In this study, two distinct redox chemistries were analyzed: the vanadium chemistry based on the vanadyl and pervanadyl ions (VO^{2+}/VO_2^{+}) and an organic electrolyte with the 2,2,6,6-tetramethylpiperidine-1-yl)oxyl radical and 2,2,6,6-tetramethyl-1-piperidinyloxy-oxo ion (TEMPO/$TEMPO^{+}$). The electrolyte and electro-kinetic properties of the electrolytes for a single-electrolyte cell design are given in **Table 5.3**, defined in our previous works [14, 21]. The open circuit cell potentials of the chemistries were based on full battery systems: the full vanadium [31], and the 4-hydroxy-2,2,6,6-tetramethylpiperidine-1-oxyl (TEMPO-OH) and methyl viologen system [35]. To comply with the dilute electrolyte assumption used in the PNM (i.e., migration was not considered [36]), we selected relatively low inlet concentrations of 100 mol m^{-3} per species in an excess supporting electrolyte solution of 1000 mol m^{-3} for the investigated electrolytes. We elected the vanadium electrolyte as our reference system which was used in the optimization unless stated otherwise. This system was selected as it is state-of-the-art [37] and features a kinetically-sluggish redox couple [5, 38], which allowed the optimization of both the electrochemical performance (i.e., available surface area and mass transfer) and parasitic pumping losses [39]. Even though single-electrolyte flow cell designs were used in this study, the overarching trends obtained can guide the design of next-generation porous electrode designs, depending on the system configuration (flow field design and operating conditions) and electrolyte properties.

Table 5.3: Electrolyte and electro-kinetic properties for the VO^{2+}/VO_2^+ and TEMPO/$TEMPO^+$ chemistries in both half-cells based on the data from [14, 21].

Parameter	Vanadium	TEMPO	Unit
Density of the electrolyte, ρ	992	852	kg m^{-3}
Viscosity of the electrolyte, μ	8.9 x 10^{-4}	3.4 x 10^{-4}	Pa s
Diffusion coefficient, D_1	2.11 x 10^{-10}	1.3 x 10^{-9}	m^2 s^{-1}
Diffusion coefficient, D_2	2.11 x 10^{-10}	1.3 x 10^{-9}	m^2 s^{-1}
Inlet concentration, $c_{1,in}$	100	100	mol m^{-3}
Inlet concentration, $c_{2,in}$	100	100	mol m^{-3}
Supporting electrolyte concentration	1.0 M H_2SO_4	1.0 M $TBAPF_6$	
Bulk electrolyte conductivity, σ	28	1.99	S m^{-1}
Cathodic transfer coefficient, α_c	0.42	0.5	-
Anodic transfer coefficient, α_a	0.42	0.5	-
Exchange current density, j_0	0.39	460	A m^{-2}
Electrolyte velocity, u	1.5	1.5	cm s^{-1}
Cell potential, E_{cell}	1.26	1.25	V
Overpotential, E_{losses}	0.5	0.5	V

5.3. Results and Discussion

5.3.1. Definitions of optimization functions

The objective of the GA is to optimize electrode structures based on a defined fitness function. Therefore, first, a suitable *fitness function* needs to be defined that considers the objective of the optimization. In this work, we use the definition of **equation (5.9)**, which is based on the pressure drop and current density of the networks having equal weight. **Equation (5.9)** optimizes to a maximum fitness of $\xi = 0.603$, which is achieved when the pumping power is zero. Thus, networks with a large starting fitness can only have a small relative fitness increase, though the percentual improvement in electrical and pumping power is absolute. In **Section A5.5.1** the effect of the fitness function on the optimization is investigated by performing optimization studies with only the pumping power or only the electrochemical power considered, according to:

$$\xi_{pump} = \frac{P_{max}}{P_{max}+P_{pump}} \tag{5.11}$$

$$\xi_{el} = P_{max} - P_{el}. \tag{5.12}$$

From this study, we find that when only optimizing for the *electrochemical power*, the pumping power remains unoptimized, even resulting in a stark increase of 721 % in the required pumping power. On the contrary, the electrochemical power improves significantly by 101 % because of the formation of large pores with a maximum pore diameter (38 - 40 µm) connected to small pores (<10 µm), increasing the internal surface area of the electrode according to **equation (5.5)**. The resulting network (**Figure A5.5**) is drastically different compared to the reference network (**Figure A5.3**) as no longitudinal transport pathways are formed in the flow direction but rather alternating large and small pores connected by throats with a small diameter (resulting in the increase in pumping power). Moreover, the resulting pore and throat size distributions are different, see **Figure A5.6**, where significantly more pores are formed of 40 µm (164 *vs.* 66), accompanied by more small throats of <10 µm (1290 *vs.* 800) compared to the reference fitness function. On the other hand, when optimizing for the *pumping power* alone, the optimization is

rather comparable to that of the reference network, additionally with an increase in electrochemical power (34 %). Hence, suggesting that the original fitness definition, with equal weight, steers towards the optimization of the pumping power over the electrochemical power. The presented study shows the importance of selecting a suitable fitness definition for the electrode optimization, where the weight of the fitness function components should be considered, e.g., by applying weight factors to guide the electrode optimization.

Moreover, the *geometrical definitions* used in the algorithm, e.g., the definitions of OpenPNM (**equations (5.1 - 5.5)**), strongly affect the optimization as they directly impact the electrochemical and pumping power. For example, the *throat factor* (**equation (5.2)**) chosen in this work of 0.8 [22], affects the pressure drop and internal surface area of the network, both by the throat cross-sectional area. The impact of the throat factor on the optimization is shown in **Section A5.5.2** where we adjusted the throat factor to 0.7 or 0.9, which affects the throat size relative to the pore size and thus directly alters the pressure drop. Additionally, the internal surface area and thus the electrochemical performance changed more drastically (8 % increase in electrochemical performance for a factor of 0.7 and 102 % for a factor of 0.9, compared to 30 % for the reference system). Moreover, by *scaling the extracted network* with the OpenPNM geometry definitions described in **Section 5.2.1**, the internal surface area is significantly impacted and decreased by ~30 x (from a total internal surface area of 6.0 x 10^5 m^{-1} to 1.9 x 10^4 m^{-1}), strongly decreasing the current output of the electrode (at 0.5 V: 15 mA cm^{-2} *vs.* 108 mA cm^{-2}, and at 1 V: 107 mA cm^{-2} *vs.* 726 mA cm^{-2}).

The *internal surface area* is complex to define as the translation of a macroporous electrode (e.g., fibrous mat) to a pore network based on spheres and cylinders is a simplification of the complex porous space and does not consider the surface roughness or electrochemical activity of the surface. Therefore, the simplified internal surface area definition used in the PNM should be based on the type of electrode structure and manufacturing technique. For example, OpenPNM defines the internal surface area by **equation (5.5)**, which results in that small pores have a relatively smaller surface area per unit volume, compared to larger pores, because of the larger relative penalty for the throat cross-sectional area subtraction. With this definition and the fixed lattice positions where each pore can occupy a fixed volume, large pores are beneficial as they both reduce the pressure drop and increase the surface area (larger surface area per constant volume), especially when connected to small pores (small subtraction of the throat cross-sectional areas, **equation (5.5)**). However, when not bound to fixed pore coordinates with a fixed volume, smaller pores should be beneficial for a high surface area per unit volume, whereas large interconnected pores mostly dictate the electrolyte transport [6, 10, 21, 30, 40]. To investigate the effect of the internal surface area definition on the structure evolution, four surface area definitions (**equations (5.5 - 5.8)**) were evaluated in **Section A5.5.4**. We observed that by changing this geometry parameter definition, the electrode optimization is affected, even for the cubic network with fixed pore coordinates. Nevertheless, we find that all surface area definitions result in optimized structures with a bimodal pore size distribution with longitudinal transport pathways in the flow direction that reduce the pumping power. In summary, this exercise shows the importance of selecting the appropriate geometry definitions for the optimization, as simplified descriptions can strongly over/underestimate the performance as well as alter the optimization. Thus, geometry definitions need to be identified that consider the

manufacturing method of the final electrodes, but this is beyond the scope of this work. In this manuscript, we chose to continue with the definitions set by OpenPNM unless stated otherwise.

Further factors that need to be selected before optimization are the parent-individual ratio and the mutation chance and range. These factors impact the optimization time required and the number of generations necessary for the optimization. Finally, an *electrode size* that provides a representative elementary volume of a manufacturable electrode must be utilized. In this study, we arbitrarily chose a ~500 x 500 x 200 μm^3 electrode for the flow-through flow field and a ~1000 x 500 x 200 μm^3 electrode for the interdigitated flow field. The optimization for an electrode that is twice as thick is shown in **Section A5.5.3**. Furthermore, the network scaling step could be reconsidered as constraining the porosity limits the internal surface area enhancement. The optimization freedom in a genetic algorithm with many variables and constraints has both advantages and disadvantages. If the constraints are well-understood and the variables are selected with care, this method can be very powerful for the optimization of electrode structures from the bottom-up. If appropriate optimization conditions can not be found, this approach is rather complex, and optimal solutions might not be obtained [41].

5.3.2. Beyond fixed lattice positions

In our previous work [14], the pore positions were fixed to a cubic lattice with a connectivity of 6, restricting the evolutionary freedom of the algorithm. To this end, we included *pore merging and splitting*, allowing for a change in the number of pores and their location. This additional network mutation step results in more evolutionary freedom but comes at the cost of an increased optimization complexity. As there is another randomization step involved, the algorithm requires more generations to achieve the same fitness increase but allows for more realistic network structures (i.e., closer to commercial fibrous electrodes employed in RFBs). The results of the optimization with merging and splitting are shown in **Section A5.6**. We compare the performance of the GA with only mutation, only merging and splitting, and a combination, showing the impact of both mutation operators on the optimization of the networks. Moreover, the GA was run without any mutation operator (i.e., no mutation and no merging and splitting), which resulted in minimal structure optimization (**Table A5.7**), proving that a mutation operator is key for structure optimization.

The results in **Section A5.6.1** show that the *mutation step* results in the main fitness improvement by allowing the formation of the electrolyte transport pathways in the flow direction consisting of large pores (36 - 40 μm), connected by large throats (29 - 32 μm, **Figure 5.3a**), enhancing both the electrical and pumping power. *Merging and splitting* alone, on the other hand, results in a fitness improvement (21 %), but the pores cannot form well-defined transport pathways because of the randomized locations of merging and splitting and due to the absence of mutation. When combined, transport pathways are formed, decreasing the pumping power and increasing the electrical performance. However, the total fitness improvement is lower (31 % *vs.* 42 %) compared to the case with only mutation. To this end, the effect of the *merging and splitting ratio* is investigated in **Section A5.6.2**. Simulations were performed with a 2:3 chance of merging over splitting (**Figure A5.15**) and a 1:3 chance (**Figure A5.16**), resulting in interesting trends. First, both cases show improved fitness, increased electrochemical

power, and decreased pumping power compared to the equal chance of merging and splitting, where the improvement in pumping power for both cases is even greater than for the reference system (i.e., the system with only mutation). Second, the 2:3 ratio results in a further enhancement of the pumping power because of the formation of more, and larger pores. Third, the 1:3 ratio enhances the electrochemical performance by an increase in the internal surface area. Furthermore, compared to all other systems with merging and splitting, the mass transfer overpotential is reduced after optimization for the 1:3 ratio at 1 V, increasing the current output of the system. These observations align well with previous studies in the literature [21, 42], where it is observed that many small pores enhance the electrochemical performance by providing more surface area and higher reaction rates. Moreover, the split pores are mainly formed near the membrane interface as most of the current is generated in this region [21, 42]. Thus, the ratio between merging and splitting is shown to be an important parameter that can steer the electrode optimization toward the formation of networks with more or fewer pores than the starting network.

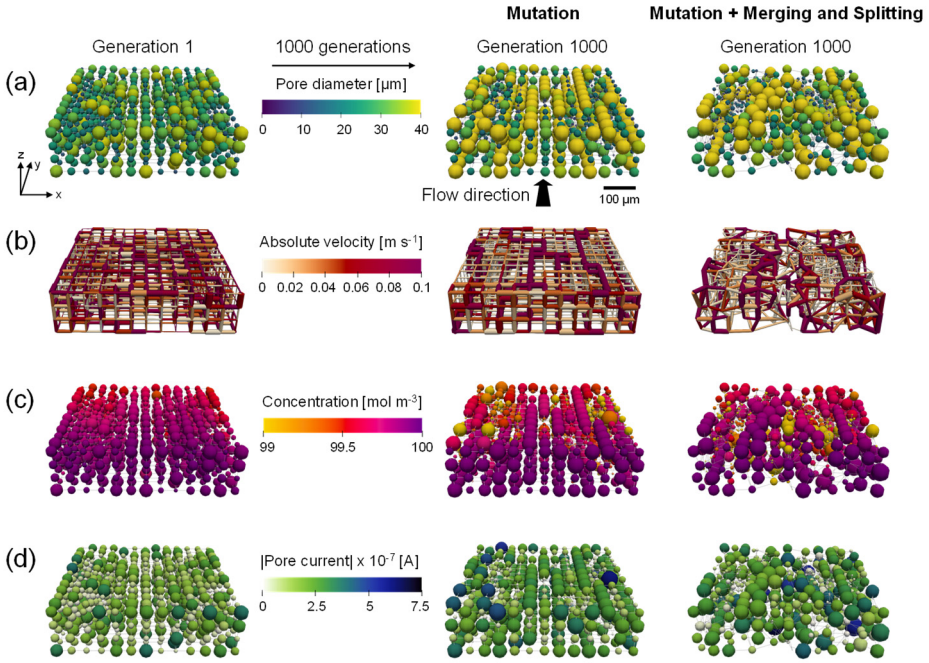

Figure 5.3: The geometrical evolution of cubic networks with only a mutation operator, and a combination of a mutation and a merging and splitting operator. The networks of the first and final (1000th) generations are shown, displaying the: **(a)** pore diameter evolution, **(b)** the throat absolute velocity, **(c)** the pore concentration, and **(d)** the absolute pore current. With the flow in the y-direction and the thickness in the z-direction with the membrane facing to the top.

Moreover, the network properties of the case with mutation and combined with merging and splitting are compared in **Figure 5.3**. In **Figure 5.3a** the pore diameter evolution is visualized, presenting the randomization of the merging and splitting operator and the formation of the longitudinal transport pathways for both cases. These transport paths consist of interconnected large pores, which, by geometrical definition, have throats with a large diameter connecting the pores. The large throats have a high absolute velocity (**Figure 5.3b**) and are thus driving the transport of the electrolyte through the electrode,

decreasing the pressure drop. Alongside the electrolyte transport pathways, isolated large pores are present with a large surface area (**equation (5.5)**), allowing more redox reactions to take place, decreasing the concentration locally (**Figure 5.3c**), and resulting in a high current output (**Figure 5.3d**). The outlet concentration in **Figure 5.3c** is high because of the small network sizes (~500 μm). If we run a network-in-series approach on the networks to simulate a laboratory-scale electrode size, the species outlet concentration is much lower, as discussed in our previous work [21]. When comparing **Figure 5.3a-d** for the two cases, the main difference is in the randomization of the structures as the overall optimization trends remain comparable, such as the formation of transport pathways and higher reaction rates near the membrane interface. To conclude from this comparison, mutation is necessary to speed up the optimization of the networks, whereas merging and splitting add an additional mode of randomization, allowing for more realistic networks to be formed, but at the cost of a slower fitness optimization.

5.3.3. Beyond cubic structures

Besides the addition of merging and splitting to allow for more realistic networks, we investigated the approach of starting the optimization from *morphologically distinct electrode structures*. To this end, we studied the artificially generated *Voronoi* network and the commercial *Freudenberg H23 carbon paper*, extracted using X-ray computed tomography and translated to a pore network [21]. The initial network structure strongly impacts the structure optimization in terms of the starting performance (fitness value and electrochemical and pumping power) and structure optimization flexibility (number of pores, pore locations, maximum pore diameter), especially when bound to fixed lattice positions. Therefore, here, we compare the networks without merging and splitting, to identify how distinct fixed lattice positions impact the electrode optimization. It must be noted that the internal surface area definition of **equation (5.5)** cannot be applied to the extracted electrode as a negative internal surface area is obtained (connectivity >6 resulting in a large throat cross-sectional area subtraction) resulting in the optimization of small pores (**Figure A5.17** and **Table A5.10**, with high absolute (negative) surface area to increase the absolute current). Hence, *surface area definition 2* (**equation (5.6)**) was used for the comparison of the three network structures.

The optimized structures, bound to a certain number of generations, are shown in **Figure 5.4** and the structure evolution is shown in **Section A5.7**. All networks show an improvement in fitness over generations, starting from different fitness values, where the fitness evolution is distinct for each optimization case. The *Voronoi* network shows a strong optimization in the first ~70 generations, after which a local maximum is obtained followed by a decrease in the fitness value. Therefore, the optimization was only performed for 200 generations. The decrease in fitness for the Voronoi shows one disadvantage of using GAs as, when appropriate optimization conditions can not be found, optimal solutions are not obtained [41]. On the other hand, for the extracted and cubic networks, we observe an increase in fitness with diminishing returns after 100 - 400 generations, respectively. Moreover, whereas the starting geometry of the Voronoi network featured a bimodal pore size distribution, both the unimodal cubic and extracted networks evolved towards a bimodal structure with large interconnected pores in addition to small pores (**Figures 5.4a** and **A5.20**). The bimodal structures consist of large connected pores in the flow direction, linked by throats of a large diameter and a high

absolute velocity (**Figure 5.4b**), responsible for the electrolyte transport and thus the decrease in pumping power (**Table A5.10**). The decrease in pumping power is the most prominent for the extracted network (65 % compared to 59 % for the cubic and 43 % for the Voronoi network) related to the higher absolute pumping power required because of the less ordered throats compared to the in-plane throats in the cubic network. Moreover, the extracted network has the highest increase in electrical power upon comparison using surface definition 2 (22 % *vs.* 3.6 % for the cubic network, and -19 % for the Voronoi network).

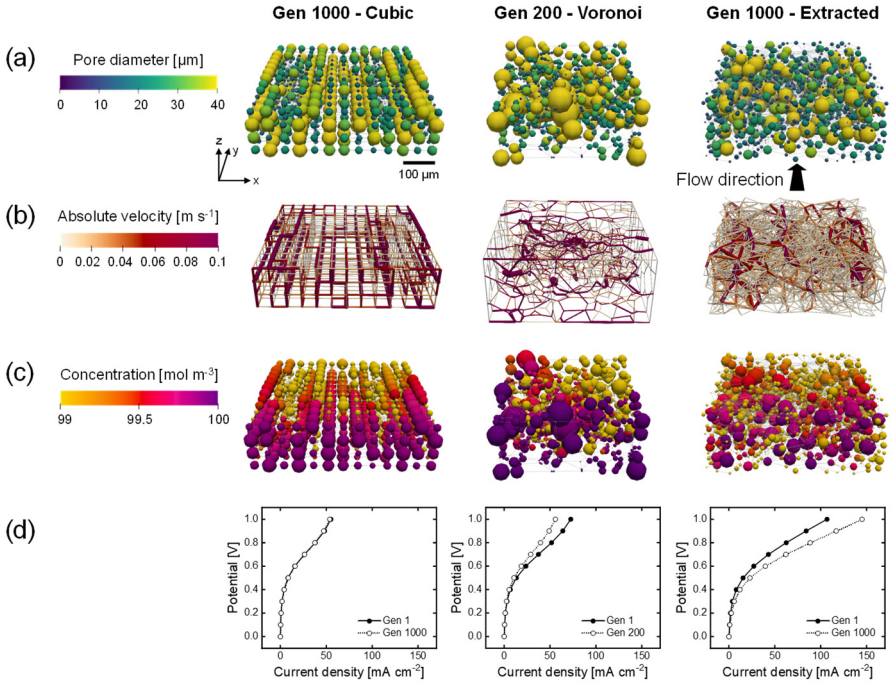

Figure 5.4: The geometrical evolution of a cubic, Voronoi, and extracted network with a mutation operator for the flow-through flow field and with internal surface area definition 2. The networks of the last (1000^{th} or 200^{th}) generation are shown, displaying the: **(a)** pore diameter, **(b)** the throat absolute velocity, **(c)** the pore concentration, and **(d)** the polarization curve of the first and last generation. With the flow in the y-direction and the thickness in the z-direction with the membrane facing to the top.

Furthermore, the *extracted network* shows a higher species conversion rate in the smaller pore segments (**Figure 5.4c**) compared to the other networks. Especially for the vanadium chemistry, with sluggish kinetics but high ionic conductivity, the large number of small pores in the extracted network is beneficial. In the electrochemical PNM used, the mass transfer coefficient is a function of the diffusion coefficient and the pore radius and is thus velocity-independent. Hence, small pores have a high mass transfer coefficient and thus a high species conversion per unit volume (**Figure 5.4c**). Even though small pores have a lower surface area, the extracted network has the same total surface area compared to the cubic network (1.4×10^{-6} m^2 *vs.* 1.5×10^{-6} m^2) because of the large number of small pores, resulting in enhanced mass transfer in the extracted network. Hence, the high number of small pores results in a significantly higher limiting current

density, as seen in **Figure 5.4d** at 1 V. Moreover, as a result of the structure optimization by the formation of a bimodal-like pore size distribution with small (2 - 20 µm) and large pores (40 - 60 µm) and large throats (20 - 40 µm), there is a strong reduction in the activation (7 % at ~60 mA cm^{-2}, due to the increase in internal surface area of 31 %), concentration (24 % at ~60 mA cm^{-2}), and ohmic overpotentials (41 % at ~60 mA cm^{-2}). For the *reference system* (cubic, flow-through, internal surface area definition 1), the increase in performance is caused by the reduction in the activation and concentration overpotentials (**Figure A5.3d**, at ~20 mA cm^{-2} a 4 % reduction in activation overpotential and a 41 % reduction in concentration overpotential) as a result of the increase in internal surface area (34 %), yet the ohmic overpotential is not significantly optimized for. The optimization of the ohmic overpotential in the *extracted network* is expected to come from an increased ionic flux towards the membrane due to the formation of large throat segments (20 - 40 µm) with higher electrolyte velocity in the through-plane direction (**Figure 5.4b**). The larger throats result in a greater penetration of the reaction front into the electrode for reactions, corroborated by the high hydraulic conductance of these larger throats through the network in the last generation, see **Figure A5.19**. Combined with the high conductivity of the electrolyte, provides the optimized extracted network with the largest current output at 1 V.

Hence, it is anticipated that due to a large number of pores and their random orientation, the *extracted network* has a greater optimization chance for both the electrical power and pumping power for the vanadium chemistry compared to the cubic network with fixed lattice positions. Moreover, all optimizations result in structures with a bimodal pore size distribution to decrease the pressure drop and increase the species conversion. Not only could these electrodes be manufactured with the optimized design by techniques such as 3D printing, but the learnings from the optimization (e.g., bimodal electrodes with electrolyte transport pathways in the in- and through-plane directions) could also guide conventional electrode manufacturing towards enhanced electrodes for specific reactor architectures and operating conditions.

5.3.4. Impact of the flow field design

To show the system dependency of the optimization framework and thus the need to engineer electrodes depending on their application requirements, we incorporated another flow field design into the framework, the interdigitated design. In our previous works [30, 43], as well as in other literature [44, 45], the interplay between the electrode and flow field was proven to be imperative to RFB performance. For example, Muñoz-Perales *et al.* found that for Fe^{2+}/Fe^{3+} single-electrolyte flow cells in combination with a flow-through flow field (FTFF), woven bimodal electrodes are favorable. Whereas when using interdigitated flow field (IDFF) designs, unimodal paper electrodes result in enhanced flow cell performance [44]. Hence, in this work, we elect to investigate the GA structure optimization with the FTFF and IDFF in combination with the cubic and extracted networks. The results of the *interdigitated design* are shown in **Figure 5.5** where the cubic network was optimized with the internal surface area definition 1 (**equation (5.5)**) and the extracted network with definition 2 (**equation (5.6)**). The optimization values are presented in **Tables A5.8 - A5.11**.

The fitness, electrical, and pumping power evolutions with the IDFFs portray a similar behavior compared to those of the FTFF, as well as the percentual increases over

the generations. When comparing the networks, the electrical power and surface area of the networks are about 2x greater with the *interdigitated flow field* because of the twice as wide network size. Moreover, noteworthy dissimilarities can be observed in the absolute pumping power required. For both the cubic and extracted networks, the pumping power increases when utilizing IDFFs because of the twice as wide electrode. When translating the required pumping power to lab-scale electrode sizes, it would result in a much higher pressure drop for the FTFF because of the longer electrolyte pathway through the electrode compared to that for the IDFF. Where the cubic structure has a lower pumping power compared to the extracted network combined with an FTFF (5.2 µW *vs.* 7.8 µW), the extracted structure shows a reduced pumping power after optimization with the interdigitated design (9.0 µW *vs.* 6.0 µW). In our previous works, we observed that the pressure drop through carbon paper electrodes is strongly reduced when using an IDFF [30], whereas the pressure drop was even increased through the 3D printed electrodes compared to FTFFs [43]. Hence, where the optimized cubic structure with in-plane high-velocity transport pathways is favorable with FTFFs, as are the 3D printed electrodes [43], the (optimized) paper electrode results in a lower pressure drop combined with IDFFs because of the combined in-plane and through-plane fluid flow over the rib.

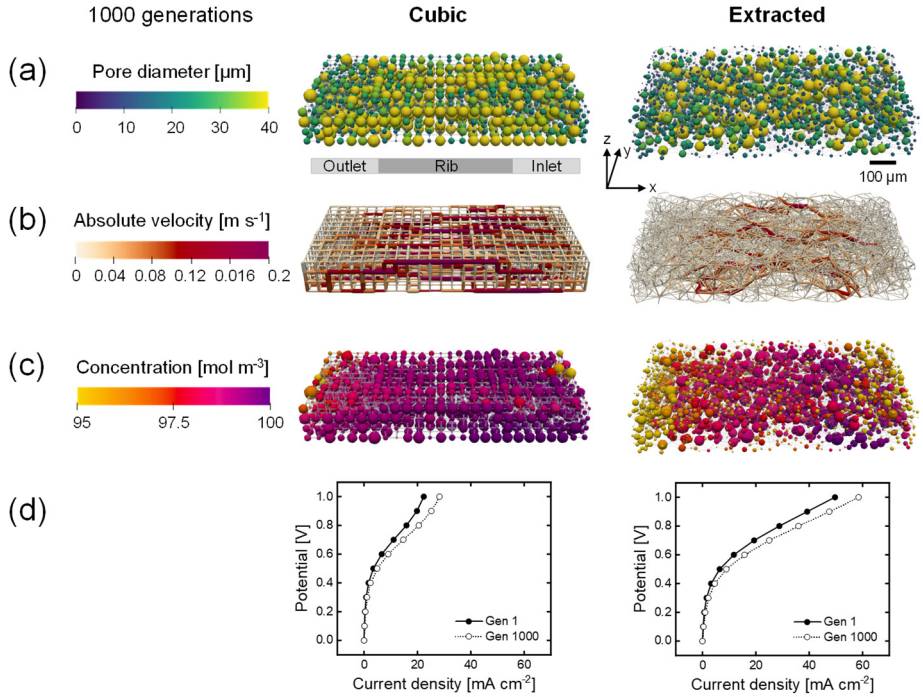

Figure 5.5: The geometrical evolution of a cubic (with internal surface area definition 1) and extracted (with internal surface area definition 2) network with a mutation operator and for the interdigitated flow field. The networks of the last (1000th) generation are shown, displaying the: **(a)** pore diameter, **(b)** the throat absolute velocity, **(c)** the pore concentration, and **(d)** the polarization curve of the first and last generation. With the flow in the x-direction and the thickness in the z-direction with the membrane facing to the top.

Furthermore, because of the distinct flow-distributions with these flow fields, the GA optimizes the electrodes to significantly different structures (**Figure 5.4a** and **Figure 5.5a**). For both the cubic and extracted networks, large pores connected by throats with a large diameter are formed in the flow direction (i.e., from the inlet to the outlet channel over a small rib). These electrolyte transport pathways result in throats with a high velocity from the inlet to the outlet (**Figure 5.5b**), decreasing the pressure drop. In addition to the electrolyte transport pathways, stagnant zones are formed near the membrane under the inlet and outlet channels with low electrolyte velocities (**Figure 5.5b**) and high species conversion (**Figure 5.5c**) [30]. It must be noted that the species conversion is higher for the IDFF compared to the FTFF because of the electrode width and electrolyte pathway, and because the results are shown without the network-in-series approach for the FTFF [21]. Moreover, as shown in the polarization curves (**Figures 5.4d** and **5.5d**), the ohmic overpotential is again reduced for the extracted network as the hydraulic conductance in the flow direction is improved for the optimized structure (**Figure A5.25**) because of the formation of large throats (**Figure A5.26)**, enhancing the ionic flux towards the membrane. When comparing the polarization curves in **Figures 5.4d** and **5.5d**, we find that the cubic structure shows similar performance in terms of the current output with both flow fields (54 mA cm^{-2} at 1 V with internal surface area definition 2), whereas the extracted structure shows a 2.5 times lower performance with the interdigitated design (~58 mA cm^{-2} *vs.* ~145 mA cm^{-2} at 1 V). The formation of the stagnant zones under the inlet and outlet channels with high species conversion, for both the initial and final networks, is anticipated to cause increased activation overpotential compared to the FTFF. These regions occupy a significant part of the internal surface area but feature a low electrolyte velocity (**Figure 5.5b**) which could lead to inferior electrolyte replenishment.

In conclusion, when comparing the electrode optimization for FTFFs and IDFFs, similar trends can be observed. The optimization with both flow fields results in structures with a bimodal pore size distribution with large pores connected by throats with a large diameter responsible for the electrolyte transport causing a reduction in the pumping requirements of 55 - 77 % for all investigated systems. Moreover, the electrical power is improved by 22 - 39 % caused by an increase in the internal surface area and improved hydraulic conductance. Utilizing *interdigitated flow fields* reduces the pressure drop through lab-scale electrodes, especially for structures with small pores, but results in a lower current output for such electrodes compared to flow-through flow designs with the vanadium electrolyte. Moreover, the distinct flow fields feature unique electrolyte flow profiles through the electrode with an in-plane flow in the length direction for the FTFF and combined in- and through-plane flow in the width and thickness direction for the IDFF. Hence, the coupling of electrode design with specific flow field architectures is crucial and should be considered in future RFB electrode design. We recommend the optimization on larger electrode sizes as now only half and inlet, a full rib, and half an outlet channel were considered, and to optimize the electrode and flow field designs in tandem, by for example including the flow field design optimization into the GA framework.

5.3.5. Chemistry-dependent optimization

The electrolyte chemistry dictates the electrochemical performance by, among others, the kinetic rate constant and ionic conductivity. The vanadium VO^{2+}/VO_2^+ electrolyte features sluggish kinetics, with a low exchange current density of 0.39 A m^{-2}, and a high ionic conductivity of 28 S m^{-1} [14]. Therefore, as shown in **Sections 5.3.3** and **5.3.4**, the vanadium electrolyte prioritizes the electrode structure optimization for a high internal surface area to decrease the activation overpotential over the enhancement of the through-plane hydraulic conductance to decrease the ohmic overpotential, especially for the cubic structure. Thus, we expect that the electrolyte chemistry can considerably influence the structure optimization and we therefore investigate the optimization of the non-aqueous TEMPO/$TEMPO^+$ electrolyte [21] with facile kinetics (exchange current density of 460 A m^{-2}) and a low ionic conductivity (2.0 S m^{-1}). The impact of the electrolyte on the structure evolution was assessed for both the cubic and extracted networks for the FTFF (**Figure 5.6**) using internal surface area definition 1 for the cubic network and definition 2 for the extracted network. The fitness, electrical power, and pumping power evolution values can be found in **Figures A5.27** and **A5.28** and **Tables A5.12** - **A5.15**.

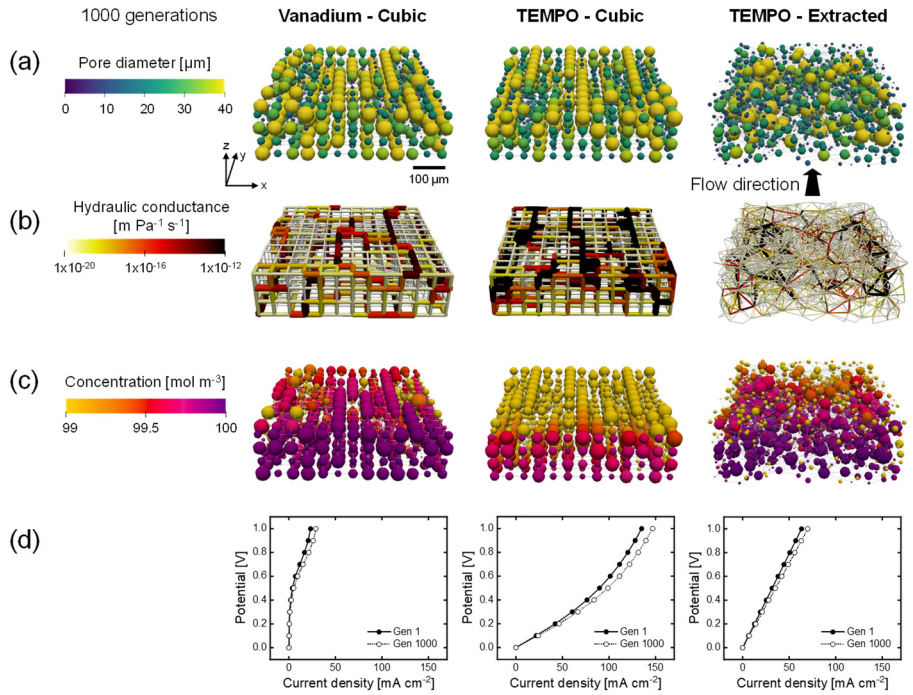

Figure 5.6: The geometrical evolution for the vanadium and TEMPO-electrolytes for a cubic and extracted network with a mutation operator and for the flow-through flow field. The networks of the last (1000^{th}) generation are shown, displaying the: **(a)** pore diameter, **(b)** the throat hydraulic conductance, **(c)** the pore concentration, and **(d)** the polarization curve of the first and last generation. With the flow in the y-direction and the thickness in the z-direction with the membrane facing to the top.

First, the fitness of the networks with the *TEMPO electrolyte* is close to the theoretical maximum ($\xi \rightarrow 0.603$) as both the pumping power and electrical power are improved. The pumping power is lower than for the vanadium electrolyte because of the lower electrolyte viscosity (3.4 x 10^{-4} *vs.* 8.9 x 10^{-4} Pa s), yet the same percentual decrease in pumping power is obtained for both electrolytes (54 % for the cubic structures and 65 - 66 % for the extracted networks). The electrical power is enhanced with the TEMPO electrolyte at 0.5 V applied potential (100 mA cm^{-2} *vs.* 5 mA cm^{-2} for the cubic network and 35 mA cm^{-2} *vs.* 23 mA cm^{-2} for the extracted network) because of the negligible activation overpotential due to the facile kinetics (**Figure 5.6d**). To this end, the percentual increase in the internal surface area is lower for the TEMPO electrolyte (18 % *vs.* 34 % for the cubic and 25 % *vs.* 31 % for the extracted network), which translates to a lower percentual increase in the electrical power for the cubic (7.5 % *vs.* 30 %) and extracted networks (11 *vs.* 22 %). Furthermore, facile kinetics give rise to a higher species conversion as can be seen from the concentration profiles in **Figure 5.6c**.

When evaluating the performance at 1 V applied potential in **Figures 5.4d** and **5.6d**, it is found that the *cubic network* has a considerably higher current output with the *TEMPO electrolyte* (140 mA cm^{-2} *vs.* 29 mA cm^{-2}) compared to the vanadium electrolyte because of the strong decrease in activation overpotential. Whereas the extracted network has a lower performance with the TEMPO electrolyte at 1 V (70 mA cm^{-2} *vs.* 145 mA cm^{-2}) due to an increased ohmic overpotential. These results support our claim on the importance of the operating conditions, reactor design, and electrolyte chemistry on the electrode selection and optimization, as the cubic network that performed significantly worse with the vanadium chemistry, outperforms the extracted network with the TEMPO chemistry. Even though the internal surface area is 1.6 x lower for the cubic network, the activation (0.04 V *vs.* 0.009 V at ~70 mA cm^{-2}) and concentration overpotentials (0.04 *vs.* 0.006 V at ~70 mA cm^{-2}) are larger, and the membrane resistance and ionic conductivity are the same for both networks, the ohmic overpotential is notably higher for the extracted network at a fixed current density (0.09 V *vs.* 0.85 V at ~70 mA cm^{-2}, not considering the membrane overpotential which is 0.13 V for both networks). The stark difference can be explained by the hydraulic transport through the networks. As the ionic conductivity is low for the TEMPO electrolyte, the hydraulic conductance of the networks becomes imperative to the network performance as it dictates the penetration of the reaction front from the membrane towards the current collector and is thus optimized for during the structure evolution (**Figure 5.6b**). Due to the cubic structure with large pores and throats in the flow direction, but additionally in the through-plane direction, causing a low resistance to flow, the ionic flux towards the membrane is high compared to the extracted network. The random orientation of the throats in the *extracted network* in combination with their small diameter, results in a low hydraulic conductance in the through-plane direction, and thus a high ohmic overpotential, resulting in lower species conversion compared to the cubic network (**Figure 5.6c**, species conversion takes place predominantly near the membrane). The GA optimizes for the hydraulic conductance towards the membrane over the generations for both networks as is shown in **Figures A5.6b** and **A5.29**, resulting in a decrease in the ohmic overpotential of 13 % (evaluated at ~55 mA cm^{-2} for the extracted network and at ~120 mA cm^{-2} for the cubic network). To this end the internal surface area near the membrane is increased in the cubic network (**Table A5.15**) to form throats with a large diameter, increasing the higher hydraulic conductance near the membrane to counterbalance the low ionic conductivity of the TEMPO electrolyte. The 3x greater

current output obtained with the cubic network compared to the extracted electrode at 0.5 V for the TEMPO electrolyte, even with internal surface area definition 1 for the cubic network (underestimation compared to definition 2), is substantial and should guide researchers for the design of next-generation electrodes for organic electrolytes where the ionic conductivity is generally the performance-limiting factor. However, a note must be made that the electrode dimensions and fluid flow rate most likely impact these results.

Finally, in **Figures A5.30 - A5.32** we evaluate the performance of the *TEMPO electrolyte* combined with IDFFs resulting in interesting trends. Whereas longitudinal transport pathways are formed and similar percentual enhancements in the fitness, electrical, and pumping power are experienced, the current output with both the cubic and extracted networks is lower compared to with the FTFF as well as with the vanadium electrolyte. The performance of the IDFF with the TEMPO electrolyte is dictated by the ohmic resistance in the system responsible for the hydraulic conductance. Because in the IDFF, the electrolyte flow path is more tortuous and both in- and through-plane, this results in an unfavorable flow path for the TEMPO electrolyte, exacerbated with the cubic electrode.

To conclude the chemistry-dependent optimization, we propose some manufacturing guidelines for the fabrication of next-generation electrodes, depending on the electrolyte chemistry. For electrolytes with *sluggish kinetics*, we advise electrodes with a high surface area to decrease the activation overpotential. Where, especially for electrolytes with sluggish kinetics and high ionic conductivity, electrodes with numerous small pores and throats are beneficial, yet such structures have a high pressure drop. Hence, combined with some in-plane electrolyte transport pathways in the flow direction would result in the best performance trade-off. Whereas for electrolytes with *low ionic conductivity*, we advise the manufacturing of electrodes with large throats in the through-plane direction (low through-plane tortuosity) for increased performance. Especially for electrolytes with fast kinetics and low ionic conductivity, electrodes with large in- and through-plane electrolyte transport pathways result in an increased current output and decreased pressure drop. However, the internal surface area of the electrodes should not be too low to be able to sustain a low activation overpotential [43]. Furthermore, the presented guidelines for electrode design should go together with the selection of a suitable *fabrication method* and approach to translate the pore network to the solid structure as is often required for manufacturing purposes. Where 3D printing is promising for optimized structures for electrolytes with low ionic conductivity and/or facile kinetics due to the high geometrical order that can be achieved, fabrication methods such as electrospinning might be more beneficial for sluggish kinetics systems as greater internal surface areas can be realized. Moreover, this work shows that the current GA framework can only optimize the performance of the electrodes to a certain degree. Hence, with the current optimization approach, the selection of the starting network for the optimization is crucial. To diminish the importance of the starting network, mutation operators such as merging and splitting, or pore migration to induce freedom in the location of pores, should go together with the option to change the number of pores, which could be investigated in depth in future work.

This work is the first step for the bottom-up optimization of electrode structures for electrochemical devices. By extending the presented tool, electrode optimization can be further improved and coupled to electrode manufacturing techniques. Possible extensions could include the incorporation of manufacturing constraints depending on the

manufacturing technique of choice (e.g., mechanical stability, shrinkage upon carbonization, converting to the solid structure), redefining the fitness function, including more mutation parameters such as pore migration and changing the number of pores, incorporating various pore and throat geometries (beyond spheres and cylinders, depending on the manufacturing technique) or refined geometrical definitions (e.g., a better representation of the internal surface area), the translation to other electrochemical technologies, the coupling of the framework to computational fluid dynamic models (for higher detailed optimization or the simulation of advanced flow field geometries), and the full parallelization of the algorithm.

5.4. Conclusions

In this work, we present a bottom-up tool for electrode optimization for tailored reactor architectures and operating conditions using the coupling of a genetic algorithm with a pore network model. The bottom-up approach was validated in our previous work whereas here we focus on the addition of pore merging and splitting, the ability to start the optimization from pore networks with a diverse morphology, and the addition of the interdigitated flow field design. In addition, we elaborate on the possible choices in the optimization definitions including the selection of the objective function, geometrical definitions (internal surface area, throat factor), network dimensions, and mutation and merging and splitting parameters. The genetic algorithm provides numerous optimization variables and constraints that must be well-understood and selected with care for successful optimization.

We found that mutation is the key operation driving the optimization, whereas pore merging and splitting can act as an additional mutation operation by inducing randomization and optimization beyond fixed pore coordinates. Moreover, the influence of system parameters, including the choice of electrolyte and flow field design, on the electrode optimization and performance is shown. For all analyzed systems, the genetic algorithm enhances the fitness by a strong reduction in pumping power of ~51 - 77 % and an improvement in electrical power of ~8 - 39 % by the formation of longitudinal flow pathways in the flow direction of large pores and throats with high hydraulic conductance, connected to regions with higher species conversion. We found that for the vanadium electrolyte, extracted paper electrodes as starting structures speed up the electrode optimization, opening a path for the optimization of commercially available electrodes. Moreover, the structure evolution is strongly impacted by the flow field design because of the induced fluid path through the electrode. Specifically, we found that interdigitated flow fields alleviate the pressure losses but result in a lower electrical output for vanadium electrolyte systems when combined with structures with numerous small pores. Furthermore, the electrode optimization was analyzed for two redox chemistries (VO^{2+}/VO_2^+ and TEMPO/$TEMPO^+$) for which substantial differences were observed in the current output with the cubic and extracted networks. For the vanadium chemistry with sluggish kinetics and high ionic conductivity, the extracted network results in the highest current output due to the presence of small pores with high mass transfer rates per unit volume, increasing the species conversion and thus the resulting current output. For the TEMPO electrolyte with fast kinetics and low ionic conductivity, electrodes with large in- and through-plane electrolyte transport pathways with low through-plane tortuosity have a higher current output because of the enhanced hydraulic conductance.

Accordingly, we strongly advise that next-generation electrodes are optimized and manufactured depending on the required reactor architectures and operating conditions. For example, for kinetically sluggish electrolytes with high ionic conductivity, an electrode with numerous small pores, and thus high internal surface area, and some electrolyte transport pathways in the flow direction result in high system performance. Whereas for kinetically facile electrolytes with low ionic conductivity, electrodes with large in- and through-plane throats with low through-plane tortuosity and a high hydraulic conductance would provide enhanced RFB performance.

In this study, we show the successful application of the genetic algorithm and that the obtained results can have a significant impact on the design of electrode structures for redox flow batteries. Hence, the tool provided in this work can guide the design of next-generation electrodes for a broad range of operating conditions, electrolyte chemistries, reactor designs, and electrochemical technologies. Nevertheless, we encourage researchers to further extend the optimization framework by for example coupling the algorithm to suitable manufacturing techniques to further increase the impact and potential of this framework.

5.5. References

[1] A. Forner-Cuenca, F. R. Brushett, *Curr. Opin. Electrochem.*, **18**, 113-122 (2019).
[2] V. A. Beck *et al.*, *J. Power Sources*. **512**, 230453 (2021).
[3] M. H. Chakrabarti *et al.*, *J. Power Sources*. **253**, 150–166 (2014).
[4] R. Schweiss, *Chem. Eng. Sci.* **226**, 115841 (2020).
[5] M. van der Heijden, A. Forner-cuenca, in *Encyclopedia of Energy Storage*, L. F. Cabeza, Ed. (Elsevier Inc., Oxford, ed. 2, 2022), pp. 480–499.
[6] A. Forner-Cuenca, E. E. Penn, A. M. Oliveira, F. R. Brushett, *J. Electrochem. Soc.* **166**, A2230–A2241 (2019).
[7] C. Minke, U. Kunz, T. Turek, *J. Power Sources*. **342**, 116–124 (2017).
[8] A. G. Lombardo, B. A. Simon, O. Taiwo, S. J. Neethling, N. P. Brandon, *J. Energy Storage*. **24**, 100736 (2019).
[9] J. H. Kim, T. J. Kang, *ACS Appl. Mater. Interfaces*. **11**, 28894–28899 (2019).
[10] C. T. Wan *et al.*, *Adv. Mater.* **33**, 2006716 (2021).
[11] T. Roy, M. A. S. de Troya, M. A. Worsley, V. A. Beck, *Struct. Multidiscip. Optim.* **65**, 171 (2022).
[12] A. Raoof, S. Majid Hassanizadeh, *Transp. Porous Media*. **81**, 391–407 (2010).
[13] S. Wan *et al.*, *Appl. Energy*. **298**, 117177 (2021).
[14] R. van Gorp, M. van der Heijden, M. A. Sadeghi, J. Gostick, A. Forner-Cuenca, *Chem. Eng. J.* **455**, 139947 (2023).
[15] Z. J. Mo, X. J. Zhu, L. Y. Wei, G. Y. Cao, *Int. J. Energy Res.* **30**, 585–597 (2006).
[16] M. Mitchell, *An introduction to genetic algorithms* (Massachusetts Institute of Technology, Cambridge, Massachusetts, fifth., 1999).
[17] C. B. Lucasius, G. Kateman, *Chemom. Intell. Lab. Syst.* **19**, 1–33 (1993).
[18] D. B. Hibbert, *Chemom. Intell. Lab. Syst.* **19**, 277–293 (1993).
[19] Y. Y. Choi, S. Kim, S. Kim, J. Choi, *J. Power Sources*. **450**, 227684 (2020).
[20] K. Tenny, R. Braatz, Y.-M. Chiang, F. Brushett, *J. Electrochem. Soc.* **168**, 050547 (2021).
[21] M. van der Heijden, R. van Gorp, M. A. Sadeghi, J. Gostick, A. Forner-Cuenca, *J. Electrochem. Soc.* **169**, 040505 (2022).
[22] M. A. Sadeghi *et al.*, *J. Electrochem. Soc.* **166**, A2121–A2130 (2019).
[23] M. A. Sadeghi *et al.*, *J. Electrochem. Soc.* **166**, A2121–A2130 (2019).
[24] J. Gostick *et al.*, *Comput. Sci. Eng.* **18**, 60–74 (2016).
[25] A. Nejad Ebrahimi, S. Jamshidi, S. Iglauer, R. Boozarjomehry, *Chem. Eng. Sci.* **92**, 157–166 (2013).
[26] S. Jamshidi, R. B. Boozarjomehry, M. R. Pishvaie, *Adv. Water Resour.* **32**, 1543–1553 (2009).
[27] L. Xu, X. Liu, L. Liang, *J. Nat. Gas Sci. Eng.* **21**, 907–914 (2014).
[28] J. J. Grefenstette, *IEEE Trans. Syst.* **1**, 122–128 (1986).
[29] J. T. Gostick, *Phys. Rev. E*. **96**, 1–15 (2017).
[30] V. Muñoz-Perales *et al.*, *ChemRxiv* (2023), doi:10.26434/chemrxiv-2023-n2mmd.
[31] A. Z. Weber *et al.*, *J. Appl. Electrochem.* **41**, 1137–1164 (2011).
[32] Z. Cheng *et al.*, *Appl. Energy*. **279**, 115530 (2020).
[33] T. F. Fuller, J. N. Harb, *Electrochemical engineering* (2018).
[34] D. E. Goldberg, *NN Schraudolph J.*. (1989).
[35] T. Liu, X. Wei, Z. Nie, V. Sprenkle, W. Wang, *Adv. Energy Mater.* **6**, 1501449 (2016).
[36] A. J. Bard, L. R. Faulkner, *Electrochemical methods* (John Wiley & Sons, New York, Second., 2001).
[37] E. Sánchez-Díez *et al.*, *J. Power Sources*. **481**, 228804 (2021).
[38] T. Yamamura, N. Watanabe, T. Yano, Y. Shiokawa, *J. Electrochem. Soc.* **152**, A830 (2005).
[39] P. Leung *et al.*, *J. Power Sources*. **360**, 243–283 (2017).
[40] R. R. Jacquemond *et al.*, *Cell Reports Phys. Sci.* **3**, 100943 (2022).

[41] K. Thoiba Meetei, *Int. J. Sci. Res.* **3**, 231–235 (2014).
[42] C. T. C. Wan, R. R. Jacquemond, Y. M. Chiang, A. Forner-Cuenca, F. R. Brushett, *Energy Technol.* **11**, 2300137 (2023).
[43] M. van der Heijden, M. Kroese, Z. Borneman, A. Forner-Cuenca, *Adv. Mater. Technol.*, **8** (18), 2300611 (2023).
[44] V. Muñoz-Perales *et al.*, *ChemRxiv* (2023), doi:10.26434/chemrxiv-2023-2zthc.
[45] R. M. Darling, M. L. Perry, *J. Electrochem. Soc.* **161**, A1381–A1387 (2014).

5.6. Appendix 5

A5.1. Abbreviations

Symbol	Description
FTFF	Flow-through flow field
GA	Genetic algorithm
IDFF	Interdigitated flow field
PNM	Pore network model
RFB	Redox flow battery

A5.2. List of symbols

Symbol	Description	Units
ΔP	Pressure drop	Pa
A_p	Pore internal surface area	m^2
A_T	Throat internal surface area	m^2
c	Concentration	mol m^{-3}
c_M	Mutation value	-
d	Diameter	m
D	Diffusion coefficient	m s^{-1}
E	Potential	V
I	Generated total current	A
j_0	Exchange current density	A m^{-2}
L_T	Throat length	m
N_T	Number of throats	-
P	Power	W
Q	Electrolyte flow rate	m^3 s^{-1}
S_p	Pore seed	-
S_T	Throat cross-sectional area	m^2
u	Electrolyte velocity	m s^{-1}
	Greek	
α	Transfer coefficient	-
η_p	Pumping energy efficiency	-
μ	Viscosity	Pa s
ξ	Fitness	-
ρ	Density	kg m^{-3}
σ	Conductivity	S m^{-1}
σ_M	Mutation range	-
	Superscripts	
M	Mutated	
o	Old	
	Subscripts	
1	Generation 1	
1,2	Pore number, active species	
a	Anodic	
c	Cathodic	
$cell$	Open circuit cell	
el	Electrochemical	

in	Inlet
losses	Losses
max	Thermodynamic maximum, maximum
n	Last generation
p	Pore
pump	Pumping
T	Throat

A5.3. Electrochemical algorithm

A5.3.1. Model equations

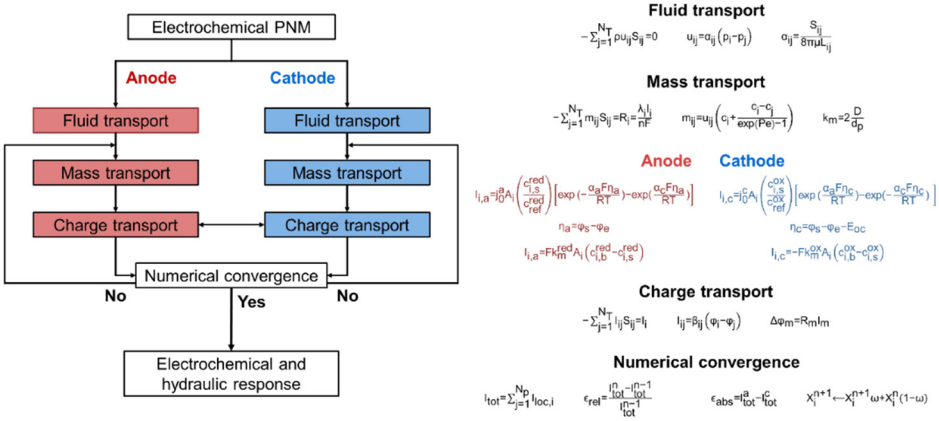

Figure A5.1: Flowchart and model equations of the pore network model incorporated into the genetic algorithm. More information regarding the pore network model physics can be found in [1].

A5.3.2. Boundary conditions

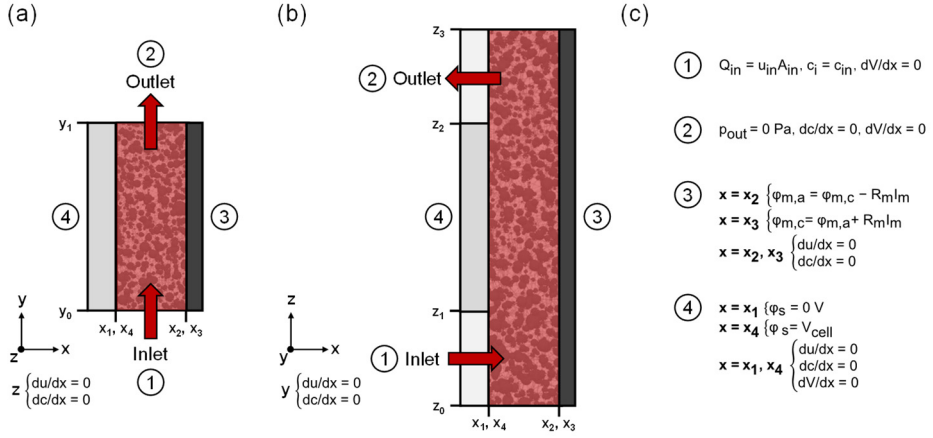

Figure A5.2: Schematic representation of the boundary conditions applied in the electrochemical pore network model for one representative model element and one half cell of the symmetric flow battery. x_1-x_4 represents the electrode thickness, 0-y_1 the length, and 0-z_3 the width coordinates of the different interfaces, with (1) the flow field inlet, (2) flow field outlet, (3) membrane, and (4) current collector, shown for: **(a)** the flow-through flow field, and **(b)** the interdigitated flow field. **(c)** The boundary conditions applied for the different interfaces.

A5.3.3. List of symbols

Symbol	Description	Units
A_i	Electrochemically active internal surface area of pore i	m^2
A_{in}	Geometrical inlet area of the electrode	m^2
c	Concentration	mol m^{-3}
D	Diffusion coefficient	m^2 s^{-1}
d_p	Pore diameter	m
E_{oc}	Open-circuit potential	V
F	Faradaic constant, 96,485 C mol^{-1}	C mol^{-1}
I	Current	A
I_{ij}	Charge flux	A m^{-2}
j_0	Exchange current density	A m^{-2}
k_m	Mass transfer coefficient	m s^{-1}
L	Conduit length, length of the medium	m
m	Mole flux	mol m^{-2} s^{-1}
n	Number of electrons, or iteration number	-
N_p	Number of pores	-
N_T	Number of throats	-
p	Pressure	Pa
Pe	Peclet number	-
Q	Flow rate	m^3 s^{-1}
R	(a) Molar gas constant, 8.314 J mol^{-1} K^{-1}	J mol^{-1} K^{-1}
	(b) Resistance	Ω
	(c) Net reaction rate	mol s^{-1}
S	Cross-sectional area	m^2
T	Operating temperature	K
u	Fluid velocity	m s^{-1}
V	Voltage	V
V_{cell}	Given cell potential	V
X	Concentration or potential	mol m^{-3} or V
	Greek	
α	(a) Transfer coefficient	-
	(b) Hydraulic conductance of the throat	m Pa^{-1} s^{-1}
β	Electrical conductance	S m^{-2}
ϵ	Error value	-
η	Overpotential	V
λ	Stoichiometric coefficient	-
μ	Dynamic viscosity	Pa s
ρ	Electrolyte density	kg m^{-3}
φ	Potential	V
ω	Relaxation factor	-
	Superscripts	
a	Anode	
c	Cathode	
n	Iteration number	
ox	Oxidized form	
red	Reduced form	
	Subscripts	
a	Anode	

abs	Absolute
b	Bulk
c	Cathode
e	Electrolyte, liquid phase
i	Within pore i, species i
ij	Pore i to pore j, throat ij
in	Inlet
j	Within pore j, species j
loc	Local
m	Membrane
ref	Reference
rel	Relative
s	Solid phase, surface
tot	Total

A5.4. Reference system

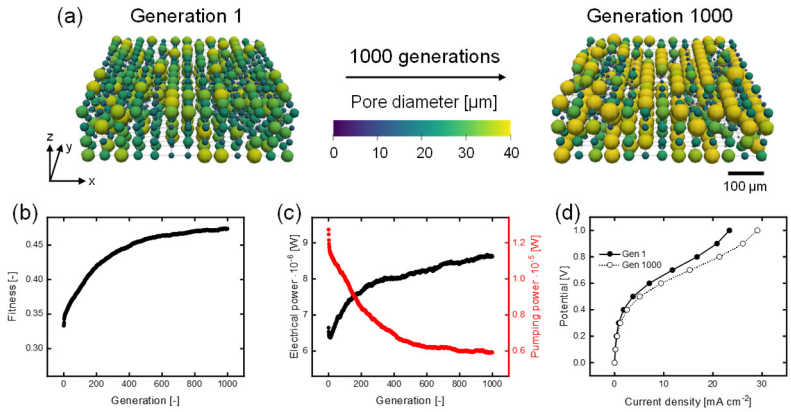

Figure A5.3: The results of the genetic algorithm optimized for the VO^{2+}/VO_2^+ electrolyte, evaluated for the **reference** system (cubic network with mutation and a flow-through flow field), with: **(a)** the structure evolution over 1000 generations with the flow in the y-direction and the thickness in the z-direction with the membrane facing to the top, **(b)** the maximum fitness evolution, **(c)** the maximum electrical power and pumping power evolution, and **(d)** the polarization curve for the first and last generation.

A5.5. Definitions of optimization functions

A5.5.1. Fitness function definition

Two other fitness function definitions were investigated, one which only considers the pumping power, **equation (A5.1)**, and one that only takes into account the electrochemical performance, **equation (A5.2)**.

$$\xi_{pump} = \frac{P_{max}}{P_{max}+P_{pump}} \tag{A5.1}$$

$$\xi_{el} = P_{max} - P_{el} \tag{A5.2}$$

With ξ the fitness function, P_{max} the thermodynamic maximum electrochemical power, P_{pump} the pumping power, and P_{el} the electrochemical power loss.

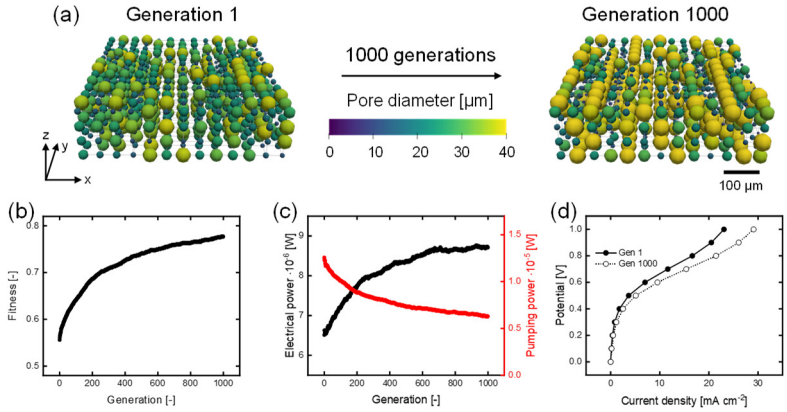

Figure A5.4: The results of the genetic algorithm optimized for the VO^{2+}/VO_2^+ electrolyte, evaluated for the reference system (cubic network with mutation and a flow-through flow field), and optimized for only the **pumping power**, with: **(a)** the structure evolution over 1000 generations with the flow in the y-direction and the thickness in the z-direction with the membrane facing to the top, **(b)** the maximum fitness evolution, **(c)** the maximum electrical power and pumping power evolution, and **(d)** the polarization curve for the first and last generation.

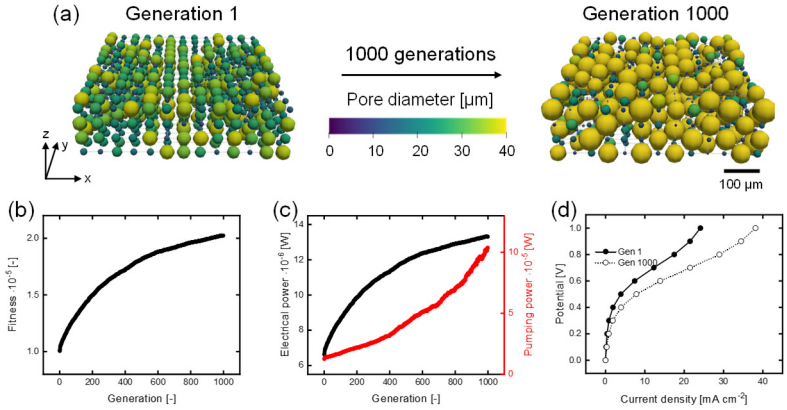

Figure A5.5: The results of the genetic algorithm optimized for the VO^{2+}/VO_2^+ electrolyte, evaluated for the reference system (cubic network with mutation and a flow-through flow field), and optimized for only the **electrochemical power**, with: **(a)** the structure evolution over 1000 generations with the flow in the y-direction and the thickness in the z-direction with the membrane facing to the top, **(b)** the maximum fitness evolution, **(c)** the maximum electrical power and pumping power evolution, and **(d)** the polarization curve for the first and last generation.

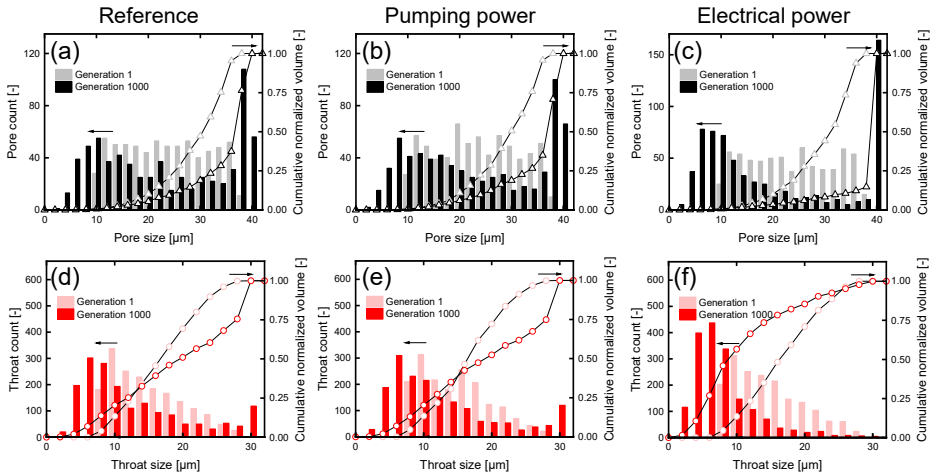

Figure A5.6: The **(a-c)** pore and **(d-f)** throat size distributions of the first and final generation, showing the pore or throat count and cumulative normalized volume distributions (divided in 2 µm pore or throat sized bins) for **(a)** the reference system, **(b)** optimized for only the pumping power, and **(c)** optimized for only the electrical power.

A5.5.2. Throat factor

The impact of the throat diameter on the structure evolution was analyzed by adjusting the throat factor of 0.8 to 0.7 and 0.9:

$$d_T = 0.7 \min\left(d_{p,1}, d_{p,2}\right) \tag{A5.3}$$

$$d_T = 0.9 \min\left(d_{p,1}, d_{p,2}\right), \tag{A5.4}$$

with d_T the throat diameter and d_p the pore diameter of the connecting pores.

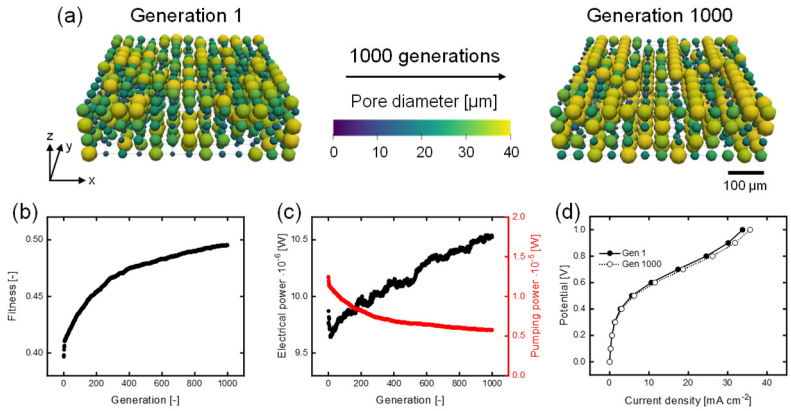

Figure A5.7: The results of the genetic algorithm optimized for the VO^{2+}/VO_2^+ electrolyte, evaluated for the reference system (cubic network with mutation and a flow-through flow field), with a **throat factor of 0.7**, with: **(a)** the structure evolution over 1000 generations with the flow in the y-direction and the thickness in the z-direction with the membrane facing to the top, **(b)** the maximum fitness evolution, **(c)** the maximum electrical power and pumping power evolution, and **(d)** the polarization curve for the first and last generation.

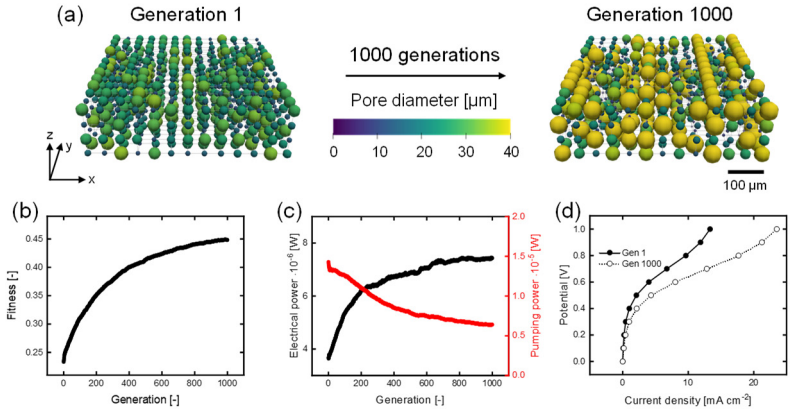

Figure A5.8: The results of the genetic algorithm optimized for the VO^{2+}/VO_2^+ electrolyte, evaluated for the reference system (cubic network with mutation and a flow-through flow field), with a **throat factor of 0.9**, with: **(a)** the structure evolution over 1000 generations with the flow in the y-direction and the thickness in the z-direction with the membrane facing to the top, **(b)** the maximum fitness evolution, **(c)** the maximum electrical power and pumping power evolution, and **(d)** the polarization curve for the first and last generation.

A5.5.3. Electrode thickness

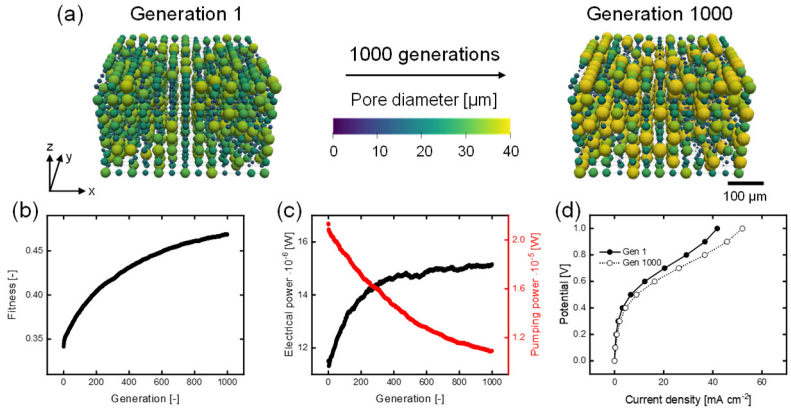

Figure A5.9: The results of the genetic algorithm optimized for the VO^{2+}/VO_2^+ electrolyte, evaluated for the reference system with an electrode **thickness of 400 µm**, with: **(a)** the structure evolution over 1000 generations with the flow in the y-direction and the thickness in the z-direction with the membrane facing to the top, **(b)** the maximum fitness evolution, **(c)** the maximum electrical power and pumping power evolution, and **(d)** the polarization curve for the first and last generation.

A5.5.4. Surface area definition

The pore internal surface area (A_p) definitions, described in **Section 5.2.1.1.**, are the following:

$$A_p = \pi\, d_p^2 - \sum_{j=1}^{N_T} S_T \qquad \text{Definition 1} \qquad \text{(A5.5)}$$

$$A_p = \pi\, d_p^2 \qquad \text{Definition 2} \qquad \text{(A5.6)}$$

$$A_p = \pi\, d_p^2 - \sum_{j=1}^{N_T} (0.8\, d_p)^2\, \frac{\pi}{4} \qquad \text{Definition 3} \qquad \text{(A5.7)}$$

$$A_p = \pi\, d_p^2 - \sum_{j=1}^{N_T} S_T + \sum_{j=1}^{N_T} 0.5\, A_T, \qquad \text{Definition 4} \qquad \text{(A5.8)}$$

with d_p the pore diameter, S_T the throat cross-sectional area of N_T number of neighboring throats, and A_T the throat internal surface area. First, the internal surface area of the electrodes is altered, impacting the electrochemical power directly and thus the fitness value of the first generation. The surface area increase is significantly higher when using definition 1, while it is even decreased when using definition 4. For definitions 1 - 3, the surface area is enhanced when the transport pathways consisting of large pores are formed, as the throat cross-sectional area subtraction is small in definitions 1 and 3, and large pores have a high surface area in definition 2, whereas the formation of these pathways is unfavorable with definition 4. The effect on the electrical power can also be seen in the surface area distribution of the individual electrode layers (no significant increase near the membrane for definitions 2 - 4) and the pumping power decrease (more significant for definitions 2 - 4), shifting the optimization towards pumping power optimization for definitions 2 - 4.

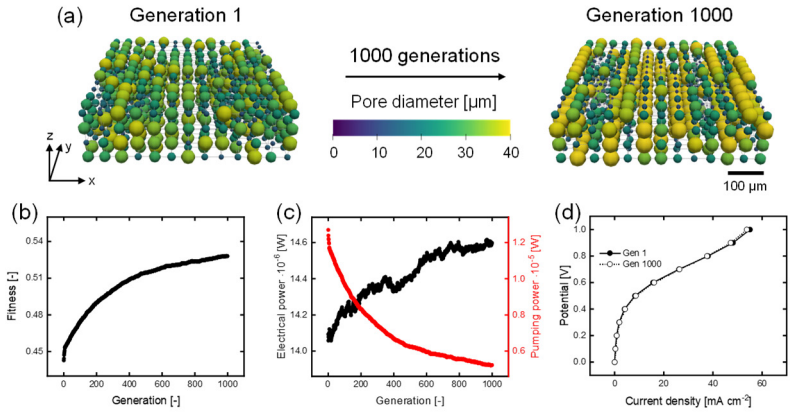

Figure A5.10: The results of the genetic algorithm optimized for the VO^{2+}/VO_2^+ electrolyte, evaluated for the reference network with surface area **definition 2**, with: **(a)** the structure evolution over 1000 generations with the flow in the y-direction and the thickness in the z-direction with the membrane facing to the top, **(b)** the maximum fitness evolution, **(c)** the maximum electrical power and pumping power evolution, and **(d)** the polarization curve for the first and last generation.

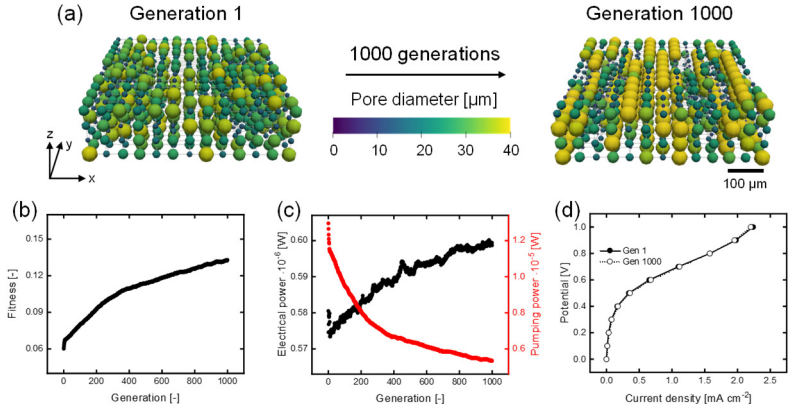

Figure A5.11: The results of the genetic algorithm optimized for the VO^{2+}/VO_2^+ electrolyte, evaluated for the reference network with surface area **definition 3**, with: **(a)** the structure evolution over 1000 generations with the flow in the y-direction and the thickness in the z-direction with the membrane facing to the top, **(b)** the maximum fitness evolution, **(c)** the maximum electrical power and pumping power evolution, and **(d)** the polarization curve for the first and last generation.

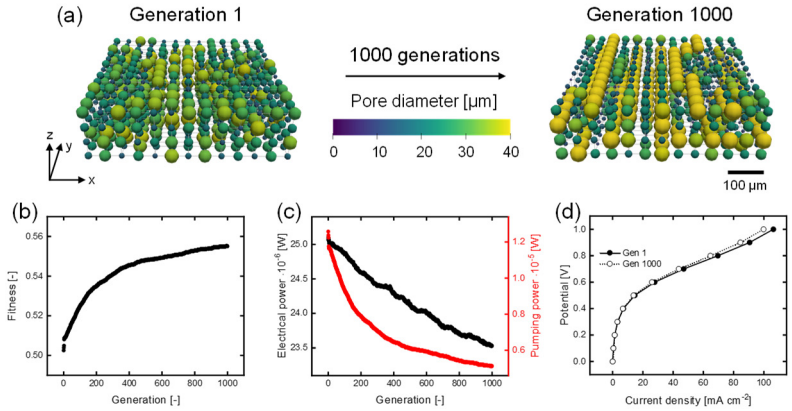

Figure A5.12: The results of the genetic algorithm optimized for the VO^{2+}/VO_2^+ electrolyte, evaluated for the reference network with surface area **definition 4**, with: **(a)** the structure evolution over 1000 generations with the flow in the y-direction and the thickness in the z-direction with the membrane facing to the top, **(b)** the maximum fitness evolution, **(c)** the maximum electrical power and pumping power evolution, and **(d)** the polarization curve for the first and last generation.

Table A5.1: The absolute values of the fitness and surface area for the best-performing network in the first and final generation for the definitions of optimization functions comparisons.

	Fitness [-]		**Surface area [m²]**	
	Gen 1	Gen 1000	Gen 1	Gen 1000
Reference (Definition 1)	0.33	0.47	6.8×10^{-7}	9.0×10^{-7}
Pumping power only	0.56	0.78	6.6×10^{-7}	9.1×10^{-7}
Electrochemical power only	1.0×10^{-5}	2.0×10^{-5}	6.7×10^{-7}	1.5×10^{-6}
Throat factor 0.7	0.40	0.50	1.0×10^{-6}	1.1×10^{-6}
Throat factor 0.9	0.23	0.45	3.7×10^{-7}	7.9×10^{-7}
400 µm in thickness	0.34	0.47	1.2×10^{-6}	1.6×10^{-6}
Definition 2	0.44	0.53	1.4×10^{-6}	1.5×10^{-6}
Definition 3	0.06	0.13	5.8×10^{-8}	6.1×10^{-8}
Definition 4	0.50	0.56	2.6×10^{-6}	2.4×10^{-6}

Table A5.2: The absolute values of the electrical power and pumping power for the best-performing network in the first and final generation for the definitions of optimization functions comparisons.

	Electrical power [W]		**Pumping power [W]**	
	Gen 1	Gen 1000	Gen 1	Gen 1000
Reference (Definition 1)	6.5×10^{-6}	8.5×10^{-6}	1.2×10^{-5}	5.9×10^{-6}
Pumping power only	6.5×10^{-6}	8.5×10^{-6}	1.2×10^{-5}	6.3×10^{-6}
Electrochemical power only	6.5×10^{-6}	1.4×10^{-5}	1.2×10^{-5}	1.0×10^{-4}
Throat factor 0.7	1.0×10^{-5}	1.1×10^{-5}	1.2×10^{-5}	5.8×10^{-6}
Throat factor 0.9	3.7×10^{-6}	7.5×10^{-6}	1.4×10^{-5}	6.4×10^{-6}
400 µm in thickness	1.2×10^{-5}	1.5×10^{-5}	2.1×10^{-5}	1.1×10^{-5}
Definition 2	1.4×10^{-5}	1.5×10^{-5}	1.2×10^{-5}	5.2×10^{-6}
Definition 3	6.0×10^{-7}	6.0×10^{-7}	1.3×10^{-5}	5.3×10^{-6}
Definition 4	2.5×10^{-5}	2.4×10^{-5}	1.2×10^{-5}	5.1×10^{-6}

Table A5.3: Percentual increase in fitness, electrical power, and pumping power over 1000 generations for the best-performing network in all evaluated systems for the definitions of optimization functions comparisons.

Percentual increase [%]	Fitness	Electrical power	Pumping power	Surface area
Reference (Definition 1)	42	30	-54	34
Pumping power only	40	34	-50	38
Electrochemical power only	101	101	721	119
Throat factor 0.7	25	7.8	-54	9.2
Throat factor 0.9	92	102	-55	115
400 μm in thickness	37	32	-49	38
Definition 2	19	3.6	-59	5.6
Definition 3	121	3.1	-59	6.3
Definition 4	10	-6.1	-59	-5.4

Table A5.4: Total pore surface area values for each network layer for the best-performing network in the first and final generation from the current collector to the membrane, evaluated for the definitions of optimization functions comparisons.

Pore surface area x 10^{-7} [m^2]	Generation	Current collector	Internal 1	Internal 2	Membrane
Reference (Definition 1)	1	1.9	1.5	1.3	1.8
	1000	2.5	1.8	2.2	2.4
Pumping power only	1	1.8	1.3	1.5	1.7
	1000	2.7	1.7	2.2	2.5
Electrochemical power only	1	1.9	1.5	1.5	1.9
	1000	3.8	3.2	3.6	4.2
Throat factor 0.7	1	2.4	2.3	2.4	2.7
	1000	2.8	2.5	2.7	2.9
Throat factor 0.9	1	1.1	0.73	0.74	1.0
	1000	2.2	1.7	1.8	2.2
Definition 2	1	3.4	3.5	3.6	3.7
	1000	3.4	3.8	4.4	3.5
Definition 3	1	1.5	1.4	1.4	1.4
	1000	1.7	1.3	1.7	1.5
Definition 4	1	6.2	6.7	6.6	5.9
	1000	6.2	5.9	6.3	5.7

A5.6. Beyond fixed lattice positions

A5.6.1. The effect of mutation

The effect of mutation was investigated by running the GA with merging and splitting (0.1 % chance per pore per generation) with and without mutation. Moreover, the genetic algorithm without any form of mutation (no mutation or merging and splitting) was analyzed and the results are shown in **Tables A5.5 - A5.7**.

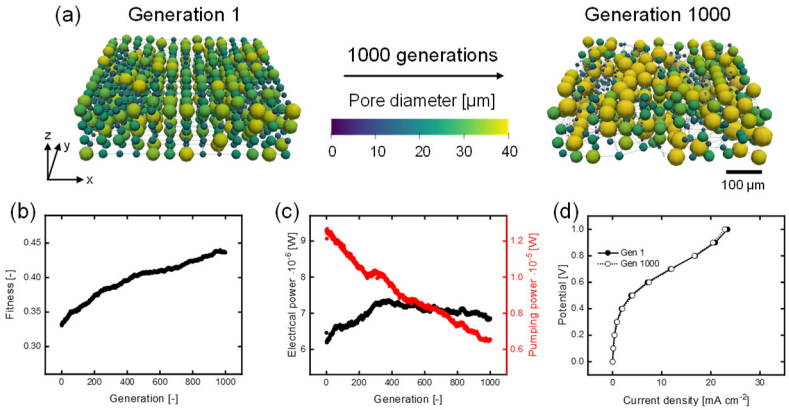

Figure A5.13: The results of the genetic algorithm optimized for the VO^{2+}/VO_2^+ electrolyte, evaluated for the reference network with mutation **combined with merging and splitting**, with: **(a)** the structure evolution over 1000 generations with the flow in the y-direction and the thickness in the z-direction with the membrane facing to the top, **(b)** the maximum fitness evolution, **(c)** the maximum electrical power and pumping power evolution, and **(d)** the polarization curve for the first and last generation.

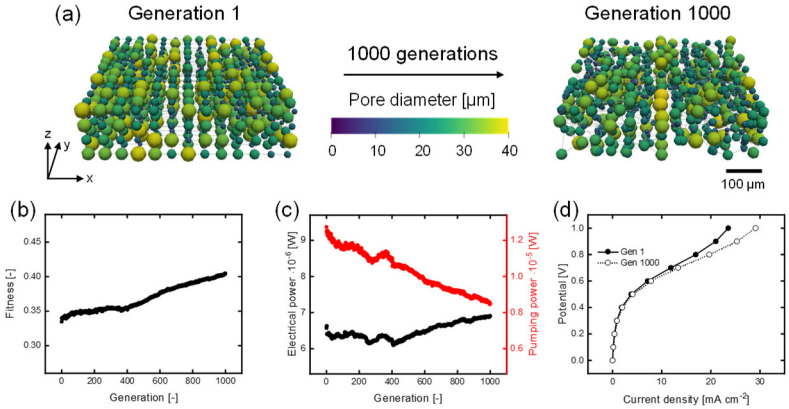

Figure A5.14: The results of the genetic algorithm optimized for the VO^{2+}/VO_2^+ electrolyte, evaluated for the reference network with **only merging and splitting**, with: **(a)** the structure evolution over 1000 generations with the flow in the y-direction and the thickness in the z-direction with the membrane facing to the top, **(b)** the maximum fitness evolution, **(c)** the maximum electrical power and pumping power evolution, and **(d)** the polarization curve for the first and last generation.

A5.6.2. The effect of merging and splitting

The effect of merging and splitting was investigated by running the GA with different merging and splitting ratios (1:3 and 2:3, *vs.* 1:1).

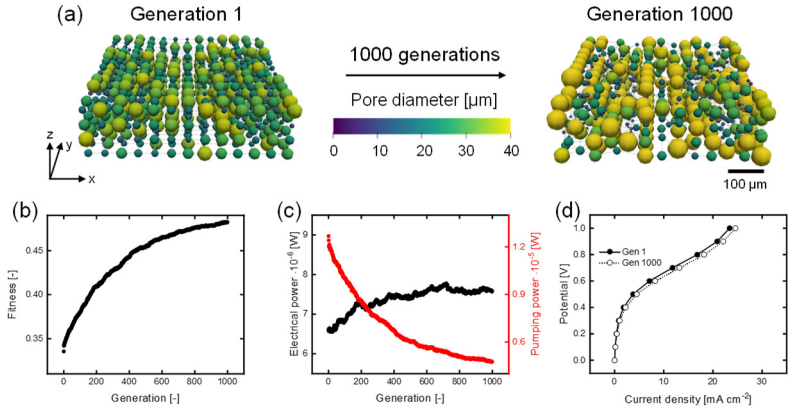

Figure A5.15: The results of the genetic algorithm optimized for the VO^{2+}/VO_2^+ electrolyte, evaluated for the reference network with mutation and merging and splitting with the **2:3 ratio**, with: **(a)** the structure evolution over 1000 generations with the flow in the y-direction and the thickness in the z-direction with the membrane facing to the top, **(b)** the maximum fitness evolution, **(c)** the maximum electrical power and pumping power evolution, and **(d)** the polarization curve for the first and last generation.

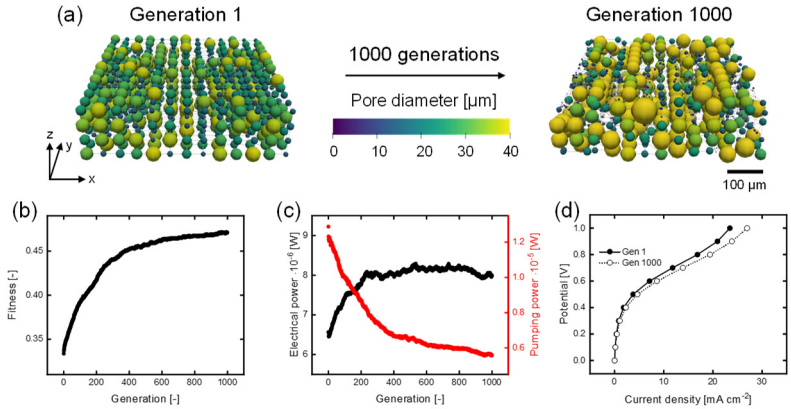

Figure A5.16: The results of the genetic algorithm optimized for the VO^{2+}/VO_2^+ electrolyte, evaluated for the reference network with mutation and merging and splitting with the **1:3 ratio**, with: **(a)** the structure evolution over 1000 generations with the flow in the y-direction and the thickness in the z-direction with the membrane facing to the top, **(b)** the maximum fitness evolution, **(c)** the maximum electrical power and pumping power evolution, and **(d)** the polarization curve for the first and last generation.

Table A5.5: The absolute values of the fitness and surface area for the best-performing network in the first and final generation for the mutation and merging and splitting evaluation.

	Fitness [-]		**Surface area [m²]**	
	Gen 1	Gen 1000	Gen 1	Gen 1000
Mutation	0.33	0.47	6.8×10^{-7}	9.0×10^{-7}
Mutation + Merging and Splitting	0.33	0.44	6.6×10^{-7}	7.2×10^{-7}
Only Merging and Splitting	0.33	0.40	6.7×10^{-7}	7.0×10^{-7}
No mutation	0.33	0.34	6.7×10^{-7}	6.5×10^{-7}
Mutation + dominated Merging (2:3)	0.34	0.48	6.8×10^{-7}	8.0×10^{-7}
Mutation + dominated Splitting (1:3)	0.33	0.47	6.7×10^{-7}	8.5×10^{-7}

Table A5.6: The absolute values of the electrical power and pumping power for the best-performing network in the first and final generation for the mutation and merging and splitting evaluation.

	Electrical power [W]		**Pumping power [W]**	
	Gen 1	Gen 1000	Gen 1	Gen 1000
Mutation	6.5×10^{-6}	8.5×10^{-6}	1.2×10^{-5}	5.9×10^{-6}
Mutation + Merging and Splitting	6.5×10^{-6}	7.0×10^{-6}	1.2×10^{-5}	6.6×10^{-6}
Only Merging and Splitting	6.5×10^{-6}	7.0×10^{-6}	1.3×10^{-5}	8.6×10^{-6}
No mutation	6.5×10^{-6}	6.5×10^{-6}	1.3×10^{-5}	1.2×10^{-5}
Mutation + dominated Merging (2:3)	6.5×10^{-6}	7.5×10^{-6}	1.2×10^{-5}	4.8×10^{-6}
Mutation + dominated Splitting (1:3)	6.5×10^{-6}	8.0×10^{-6}	1.3×10^{-5}	5.9×10^{-6}

Table A5.7: Percentual increase in fitness, electrical power, and pumping power over 1000 generations for the best-performing network in all evaluated systems for the mutation and merging and splitting evaluation.

Percentual increase [%]	**Fitness**	**Electrical power**	**Pumping power**	**Surface area**
Mutation	42	30	-54	34
Mutation + Merging and Splitting	31	6	-48	10
Only Merging and Splitting	21	5	-33	4
No mutation	4.3	-1.7	-5.0	-1.9
Mutation + dominated Merging (2:3)	44	15	-62	19
Mutation + dominated Splitting (1:3)	41	22	-57	27

A5.7. Network evolution

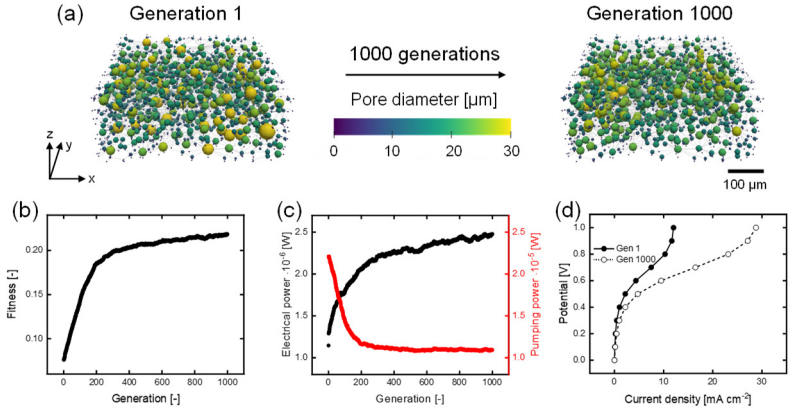

Figure A5.17: The results of the genetic algorithm optimized for the VO^{2+}/VO_2^+ electrolyte, evaluated for the **extracted Freudenberg H23 electrode** (with mutation and a flow-through flow field), with: **(a)** the structure evolution over 1000 generations with the flow in the y-direction and the thickness in the z-direction with the membrane facing to the top, **(b)** the maximum fitness evolution, **(c)** the maximum electrical power and pumping power evolution, and **(d)** the polarization curve for the first and last generation.

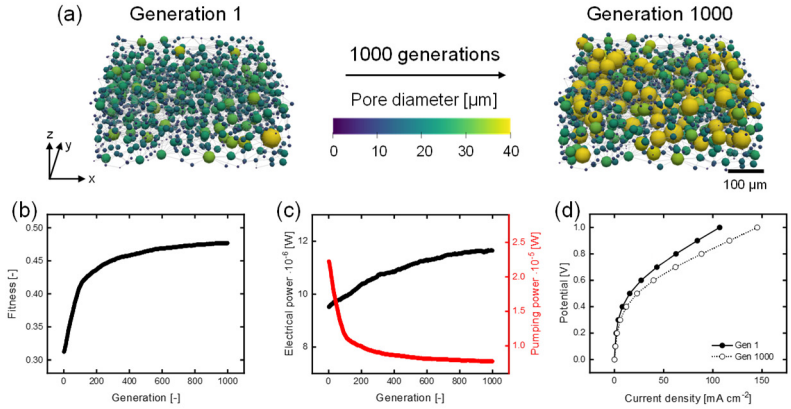

Figure A5.18: The results of the genetic algorithm optimized for the VO^{2+}/VO_2^+ electrolyte, evaluated for the extracted Freudenberg H23 electrode (with mutation and a flow-through flow field) with surface area **definition 2**, with: **(a)** the structure evolution over 1000 generations with the flow in the y-direction and the thickness in the z-direction with the membrane facing to the top, **(b)** the maximum fitness evolution, **(c)** the maximum electrical power and pumping power evolution, and **(d)** the polarization curve for the first and last generation.

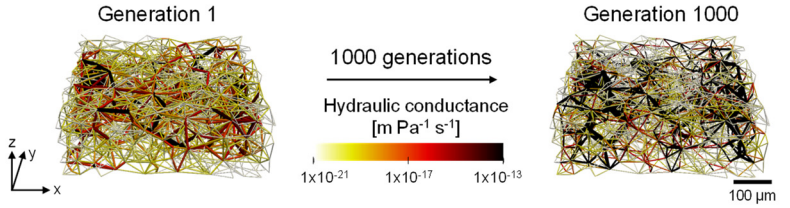

Figure A5.19: The hydraulic conductance of the throats for the first and last generation optimized for the VO^{2+}/VO_2^+ electrolyte, evaluated for the extracted Freudenberg H23 electrode (with mutation and a flow-through flow field) with surface area definition 2, with the flow in the y-direction and the thickness in the z-direction with the membrane facing to the top.

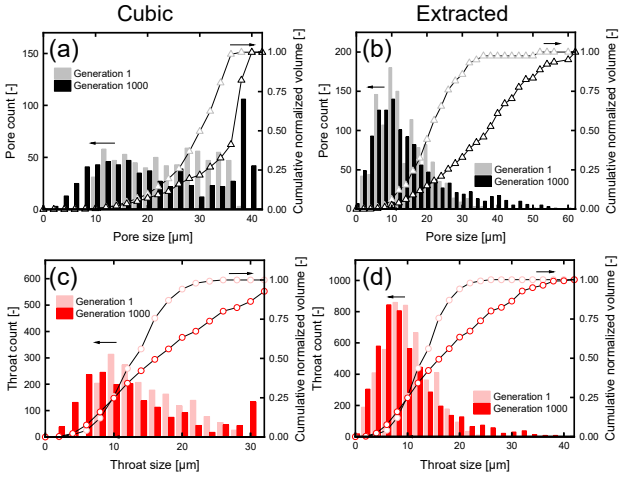

Figure A5.20: The **(a-b)** pore and **(c-d)** throat size distributions of the first and final generation, showing the pore or throat count and cumulative normalized volume distributions (divided in 2 µm pore or throat sized bins) for **(a)** the cubic network, and **(b)** the extracted network.

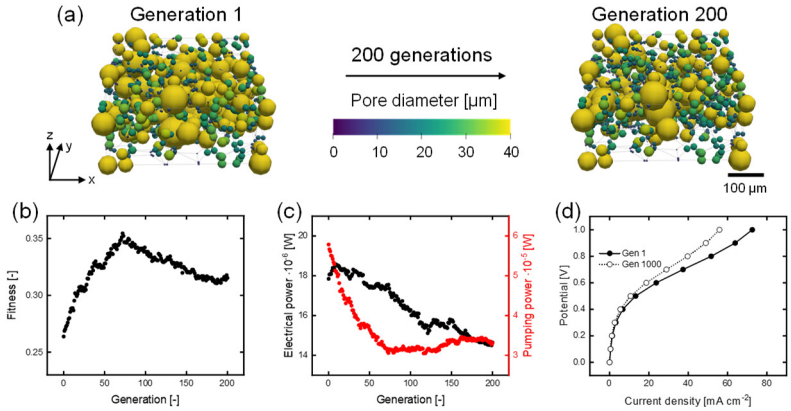

Figure A5.21: The results of the genetic algorithm optimized for the VO^{2+}/VO_2^+ electrolyte, evaluated for the **Voronoi network** (with mutation and a flow-through flow field) with surface area definition 2, with: **(a)** the structure evolution over 1000 generations with the flow in the y-direction and the thickness in the z-direction with the membrane facing to the top, **(b)** the maximum fitness evolution, **(c)** the maximum electrical power and pumping power evolution, and **(d)** the polarization curve for the first and last generation.

A5.8. Impact of the flow field design

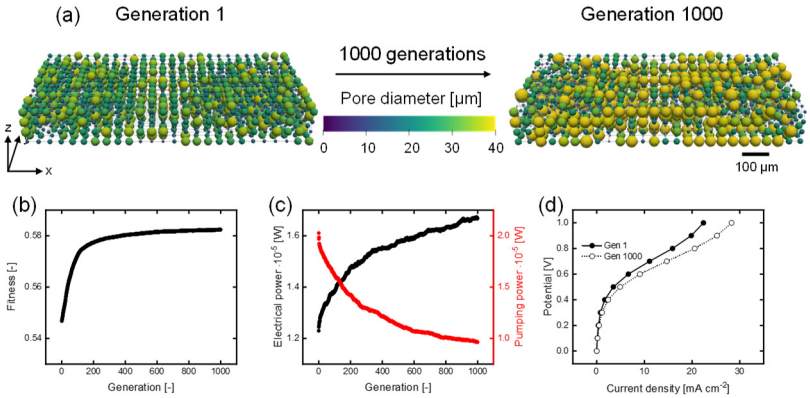

Figure A5.22: The results of the genetic algorithm optimized for the VO^{2+}/VO_2^+ electrolyte, evaluated for the reference network with the **interdigitated flow field**, with: **(a)** the structure evolution over 1000 generations with the flow in the y-direction and the thickness in the z-direction with the membrane facing to the top, **(b)** the maximum fitness evolution, **(c)** the maximum electrical power and pumping power evolution, and **(d)** the polarization curve for the first and last generation.

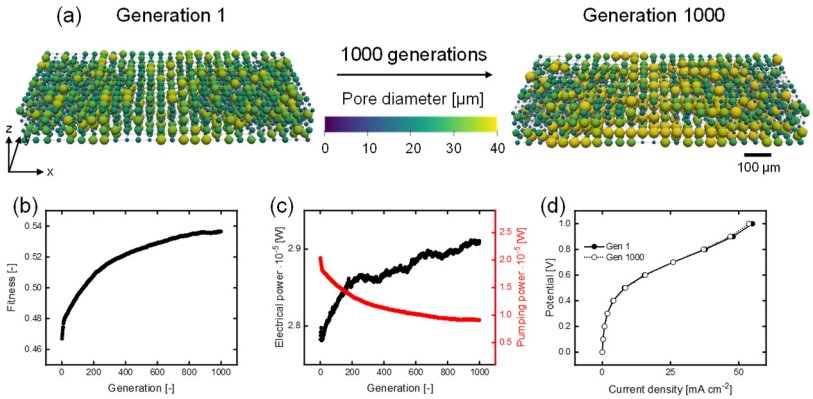

Figure A5.23: The results of the genetic algorithm optimized for the VO^{2+}/VO_2^+ electrolyte, evaluated for the reference network with the interdigitated flow field and with surface area **definition 2**, with: **(a)** the structure evolution over 1000 generations with the flow in the y-direction and the thickness in the z-direction with the membrane facing to the top, **(b)** the maximum fitness evolution, **(c)** the maximum electrical power and pumping power evolution, and **(d)** the polarization curve for the first and last generation.

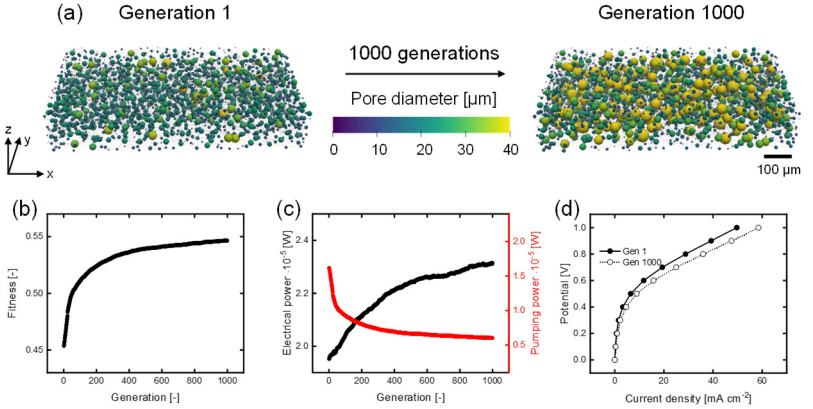

Figure A5.24: The results of the genetic algorithm optimized for the VO^{2+}/VO_2^+ electrolyte, evaluated for the **extracted Freudenberg H23 electrode** with the interdigitated flow field and with surface area definition 2, with: **(a)** the structure evolution over 1000 generations with the flow in the y-direction and the thickness in the z-direction with the membrane facing to the top, **(b)** the maximum fitness evolution, **(c)** the maximum electrical power and pumping power evolution, and **(d)** the polarization curve for the first and last generation.

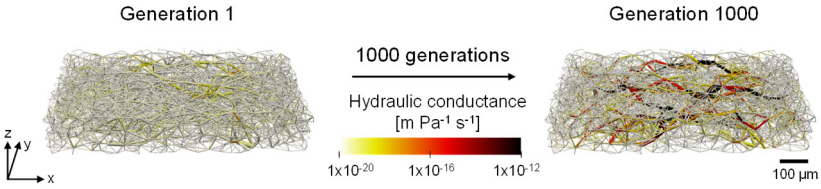

Figure A5.25: The hydraulic conductance of the throats for the first and last generation optimized for the VO^{2+}/VO_2^+ electrolyte, evaluated for the extracted Freudenberg H23 electrode and the interdigitated flow field (with mutation) with surface area definition 2, with the flow in the y-direction and the thickness in the z-direction with the membrane facing to the top.

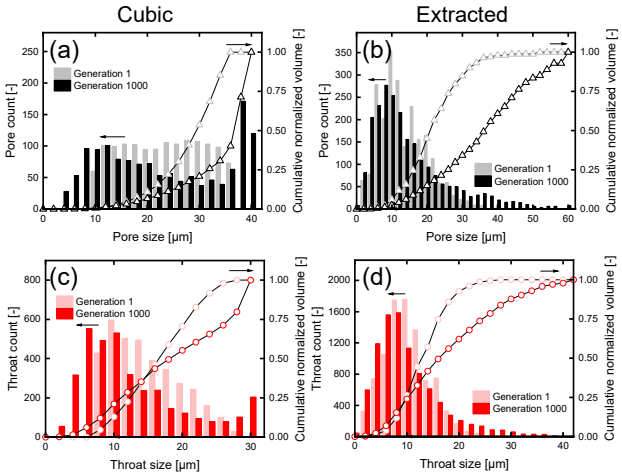

Figure A5.26: The **(a-b)** pore and **(c-d)** throat size distributions of the first and final generation, showing the pore or throat count and cumulative normalized volume distributions (divided in 2 µm pore or throat sized bins) for **(a)** the cubic network, and **(b)** the extracted network, both with the interdigitated flow field.

Table A5.8: The absolute values of the fitness and surface area for the best-performing network in the first and final generation for the initial structure and flow field design comparison. *All simulations were performed for 1000 generations with the exception of the Voronoi network (200 generations).

	Fitness [-]		**Surface area [m²]**	
	Gen 1	Gen 1000 */200	Gen 1	Gen 1000 */200
Surface area definition 1				
Flow-through flow field Cubic	0.33	0.47	6.8×10^{-7}	9.0×10^{-7}
Flow-through flow field Extracted	0.05	0.22	-1.1×10^{-7}	-2.3×10^{-7}
Interdigitated flow field Cubic	0.36	0.49	1.3×10^{-6}	1.7×10^{-6}
Surface area definition 2				
Flow-through flow field Cubic	0.44	0.53	1.4×10^{-6}	1.5×10^{-6}
Interdigitated flow field Cubic	0.47	0.54	2.8×10^{-6}	3.0×10^{-6}
Flow-through flow field Extracted	0.31	0.48	1.1×10^{-6}	1.4×10^{-6}
Interdigitated flow field Extracted	0.37	0.54	1.8×10^{-6}	2.7×10^{-6}
Flow-through flow field Voronoi	0.26	0.32	2.0×10^{-6}	1.6×10^{-6}

Table A5.9: The absolute values of the electrical power and pumping power for the best-performing network in the first and final generation for the initial structure and flow field design comparison. *All simulations were performed for 1000 generations with the exception of the Voronoi network (200 generations).

	Electrical power [W]		**Pumping power [W]**	
	Gen 1	Gen 1000 */200	Gen 1	Gen 1000 */200
Surface area definition 1				
Flow-through flow field Cubic	6.5×10^{-6}	8.5×10^{-6}	1.2×10^{-5}	5.8×10^{-6}
Flow-through flow field Extracted	1.2×10^{-6}	2.5×10^{-6}	3.2×10^{-5}	1.1×10^{-5}
Interdigitated flow field Cubic	1.2×10^{-5}	1.7×10^{-5}	2.0×10^{-5}	9.6×10^{-6}
Surface area definition 2				
Flow-through flow field Cubic	1.4×10^{-5}	1.5×10^{-5}	1.2×10^{-5}	5.2×10^{-6}
Interdigitated flow field Cubic	2.8×10^{-5}	2.9×10^{-5}	2.0×10^{-5}	9.0×10^{-6}
Flow-through flow field Extracted	1.0×10^{-5}	1.2×10^{-5}	2.2×10^{-5}	7.8×10^{-6}
Interdigitated flow field Extracted	1.7×10^{-5}	2.3×10^{-5}	2.6×10^{-5}	6.0×10^{-6}
Flow-through flow field Voronoi	1.8×10^{-5}	1.5×10^{-5}	5.8×10^{-5}	3.3×10^{-5}

Table A5.10: Percentual increase in fitness, electrical power, and pumping power over 1000/200 generations for the best-performing network in all evaluated systems for the initial structure and flow field design comparison. *All simulations were performed for 1000 generations with the exception of the Voronoi network (200 generations).

Percentual increase [%]	Fitness	Electrical power	Pumping power	Surface area
Surface area definition 1				
Flow-through flow field Cubic	42	30	-54	34
Flow-through flow field Extracted	346	116	-67	119
Interdigitated flow field Cubic	37	36	-52	39
Surface area definition 2				
Flow-through flow field Cubic	19	3.6	-59	5.6
Interdigitated flow field Cubic	15	4.6	-55	6.4
Flow-through flow field Extracted	53	22	-65	31
Interdigitated flow field Extracted	48	39	-77	48
Flow-through flow field Voronoi	20	-19	-43	-16

Table A5.11: Total pore surface area values for each network layer for the best-performing network in the first and final generation from the current collector to the membrane, evaluated for the flow field design comparison.

Pore surface area x 10^{-7} [m^2]	Generation	Current collector	Internal 1	Internal 2	Membrane
Flow-through flow field Cubic	1	1.9	1.5	1.3	1.8
	1000	2.5	1.8	2.2	2.4
Interdigitated flow field Cubic	1	3.5	2.6	2.8	3.1
	1000	5.1	4.0	3.6	4.6

A5.9. The effect of the electrolyte chemistry

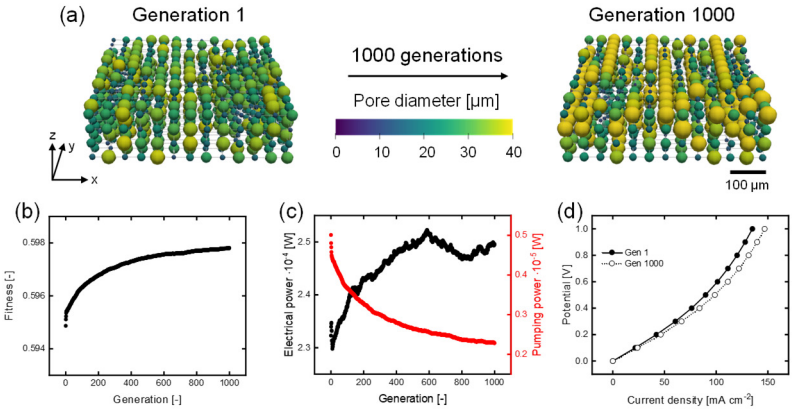

Figure A5.27: The results of the genetic algorithm optimized for the **TEMPO/TEMPO$^+$ electrolyte**, evaluated for the reference system (cubic network with mutation and a flow-through flow field), with: **(a)** the structure evolution over 1000 generations with the flow in the y-direction and the thickness in the z-direction with the membrane facing to the top, **(b)** the maximum fitness evolution, **(c)** the maximum electrical power and pumping power evolution, and **(d)** the polarization curve for the first and last generation.

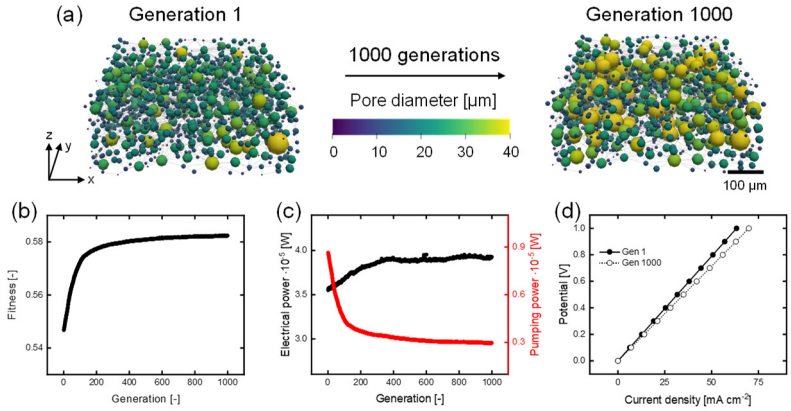

Figure A5.28: The results of the genetic algorithm optimized for the TEMPO/TEMPO$^+$ electrolyte, evaluated for the **extracted Freudenberg H23 electrode** (with mutation and a flow-through flow field) with surface area definition 2, with: **(a)** the structure evolution over 1000 generations with the flow in the y-direction and the thickness in the z-direction with the membrane facing to the top, **(b)** the maximum fitness evolution, **(c)** the maximum electrical power and pumping power evolution, and **(d)** the polarization curve for the first and last generation.

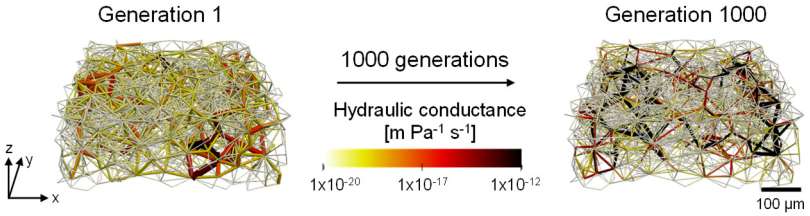

Figure A5.29: The hydraulic conductance of the throats for the first and last generation optimized for the TEMPO/TEMPO$^+$ electrolyte, evaluated for the extracted Freudenberg H23 electrode (with mutation and a flow-through flow field) with surface area definition 2, with the flow in the y-direction and the thickness in the z-direction with the membrane facing to the top.

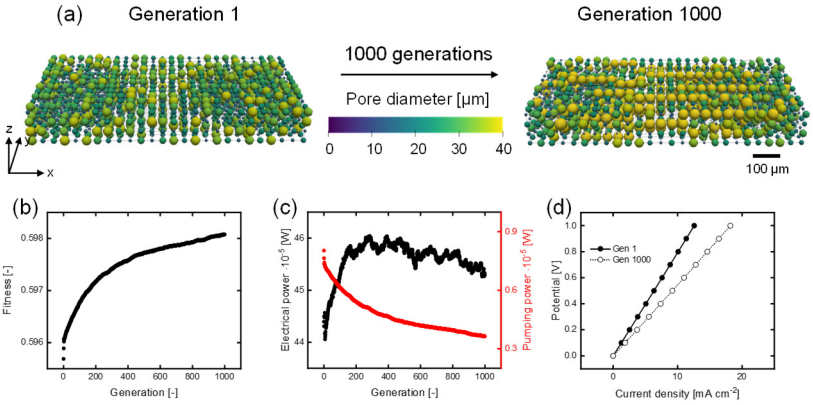

Figure A5.30: The results of the genetic algorithm optimized for the TEMPO/TEMPO$^+$ electrolyte, evaluated for the cubic network (with mutation) and an **interdigitated flow field**, with: **(a)** the structure evolution over 1000 generations with the flow in the y-direction and the thickness in the z-direction with the membrane facing to the top, **(b)** the maximum fitness evolution, **(c)** the maximum electrical power and pumping power evolution, and **(d)** the polarization curve for the first and last generation.

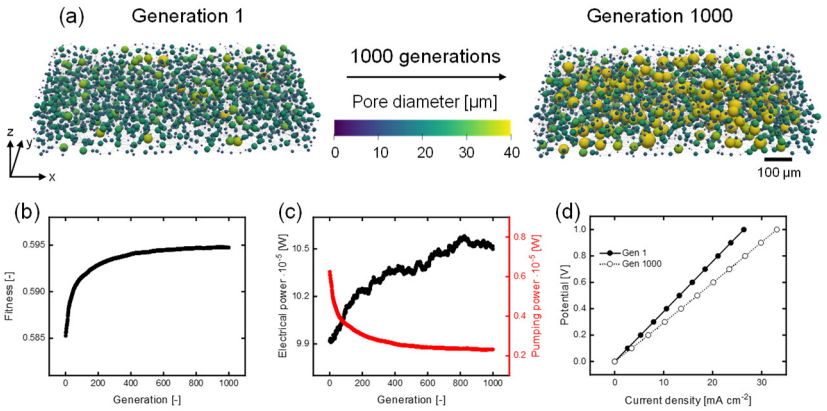

Figure A5.31: The results of the genetic algorithm optimized for the TEMPO/TEMPO$^+$ electrolyte evaluated for the **extracted Freudenberg H23 electrode** (with mutation) and an interdigitated flow field with surface area definition 2, with: **(a)** the structure evolution over 1000 generations with the flow in the y-direction and the thickness in the z-direction with the membrane facing to the top, **(b)** the maximum fitness evolution, **(c)** the maximum electrical power and pumping power evolution, and **(d)** the polarization curve for the first and last generation.

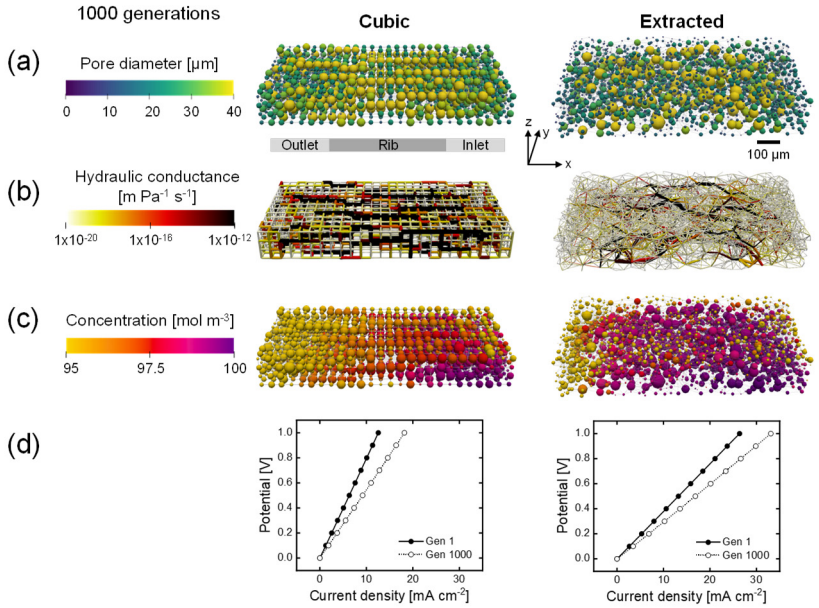

Figure A5.32: The geometrical evolution of a cubic (with internal surface area definition 1) and extracted (with internal surface area definition 2) network for the TEMPO/TEMPO$^+$ electrolyte with a mutation operator and for the interdigitated flow field. The networks of the last (1000th) generation are shown, displaying the: **(a)** pore diameter, **(b)** the throat hydraulic conductance, **(c)** the pore concentration, and **(d)** the polarization curve of the first and last generation. With the flow in the x-direction and the thickness in the z-direction with the membrane facing to the top.

Table A5.12: The absolute values of the fitness and surface area for the best-performing network in the first and final generation for the chemistry comparison.

	Fitness [-]		**Surface area [m^2]**	
	Gen 1	Gen 1000	Gen 1	Gen 1000
Surface area definition 1				
Vanadium Flow-through Cubic	0.33	0.47	6.8×10^{-7}	9.0×10^{-7}
Vanadium Interdigitated Cubic	0.36	0.49	1.3×10^{-6}	1.7×10^{-6}
TEMPO Flow-through Cubic	0.59	0.60	6.7×10^{-7}	7.8×10^{-7}
TEMPO Interdigitated Cubic	0.60	0.60	1.3×10^{-6}	1.5×10^{-6}
Surface area definition 2				
Vanadium Flow-through Extracted	0.31	0.48	1.1×10^{-6}	1.4×10^{-6}
TEMPO Flow-through Extracted	0.55	0.58	1.1×10^{-6}	1.4×10^{-6}
Vanadium Interdigitated Extracted	0.37	0.54	1.8×10^{-6}	2.7×10^{-6}
TEMPO Interdigitated Extracted	0.57	0.59	1.8×10^{-6}	2.6×10^{-6}

Table A5.13: The absolute values of the electrical power and pumping power for the best-performing network in the first and final generation for the chemistry comparison.

	Electrical power [W]		**Pumping power [W]**	
	Gen 1	Gen 1000	Gen 1	Gen 1000
Surface area definition 1				
Vanadium Flow-through Cubic	6.5×10^{-6}	8.5×10^{-6}	1.2×10^{-5}	5.8×10^{-6}
Vanadium Interdigitated Cubic	1.2×10^{-5}	1.7×10^{-5}	2.0×10^{-5}	9.6×10^{-6}
TEMPO Flow-through Cubic	2.3×10^{-4}	2.5×10^{-4}	5.0×10^{-6}	2.3×10^{-6}
TEMPO Interdigitated Cubic	4.4×10^{-4}	4.5×10^{-4}	8.0×10^{-6}	3.6×10^{-6}
Surface area definition 2				
Vanadium Flow-through Extracted	1.0×10^{-5}	1.2×10^{-5}	2.2×10^{-5}	7.8×10^{-6}
TEMPO Flow-through Extracted	3.6×10^{-5}	3.9×10^{-5}	8.6×10^{-6}	3.0×10^{-7}
Vanadium Interdigitated Extracted	1.7×10^{-5}	2.3×10^{-5}	2.6×10^{-5}	6.0×10^{-6}
TEMPO Interdigitated Extracted	7.6×10^{-5}	1.1×10^{-4}	1.0×10^{-5}	2.3×10^{-6}

Table A5.14: Percentual increase in fitness, electrical power, and pumping power over 1000 generations for the best-performing network in all evaluated systems for the chemistry comparison.

Percentual increase [%]	**Fitness**	**Electrical power**	**Pumping power**	**Surface area**
Surface area definition 1				
Vanadium Flow-through Cubic	42	30	-54	34
Vanadium Interdigitated Cubic	37	36	-52	39
TEMPO Flow-through Cubic	0.50	7.5	-54	18
TEMPO Interdigitated Cubic	0.40	2.0	-55	18
Surface area definition 2				
Vanadium Flow-through Extracted	53	22	-65	31
TEMPO Flow-through Extracted	6.5	11	-66	25
Vanadium Interdigitated Extracted	48	39	-77	48
TEMPO Interdigitated Extracted	4.5	39	-77	40

Table A5.15: Total pore surface area values for each network layer for the best-performing network in the first and final generation from the current collector to the membrane, evaluated for the chemistry comparison.

Pore surface area x 10^{-7} [m^2]	**Generation**	**Current collector**	**Internal 1**	**Internal 2**	**Membrane**
Vanadium Flow-through Cubic	1	1.9	1.5	1.3	1.8
	1000	2.5	1.8	2.2	2.4
TEMPO Flow-through Cubic	1	1.8	1.3	1.4	1.8
	1000	1.6	1.7	2.2	2.4

A5.10. References

[1] M. van der Heijden, R. van Gorp, M. A. Sadeghi, J. Gostick, A. Forner-Cuenca, *J. Electrochem. Soc.* **169**, 040505 (2022)

Chapter 6
Quantifying concentration distributions in redox flow batteries with neutron radiography

Abstract

The continued advancement of electrochemical technologies requires an increasingly detailed understanding of the microscopic processes that control their performance, inspiring the development of new multi-modal diagnostic techniques. Here, we introduce a neutron imaging approach to enable the quantification of spatial and temporal variations in species concentrations within an operating redox flow cell. Specifically, we leverage the high attenuation of redox-active organic materials (high hydrogen content) and supporting electrolytes (boron-containing) in solution and perform subtractive neutron imaging of active species and supporting electrolyte. To resolve the concentration profiles across the electrodes, we employ the in-plane imaging configuration and correlate the concentration profiles to cell performance with polarization measurements under different operating conditions. Finally, we use time-of-flight neutron imaging to deconvolute concentrations of active species and supporting electrolyte during operation. Using this approach, we evaluate the influence of cell polarity, voltage bias, and flow rate on the concentration distribution within the flow cell and correlate these with the macroscopic performance, thus obtaining an unprecedented level of insight into reactive mass transport. Ultimately, this diagnostic technique can be applied to a range of (electro)chemical technologies and may accelerate the development of new materials and reactor designs.

This chapter is submitted for publication and posted online as preprint:

R.R. Jacquemond*, M. der Heijden*, E.B. Boz*, E.R.C. Ruiz, K.V. Greco, J.A. Kowalski, V. Muñoz-Perales, F.R. Brushett, D.C. Nijmeijer, P. Boillat, A. Forner-Cuenca, Quantifying Concentration Distributions in Redox Flow Batteries with Neutron Radiography, *ChemRxiv* (2023), doi:10.26434/chemrxiv-2023-8xjv5.

*Co-first authors

6.1. Introduction

Contemporary energy storage technologies do not fulfill the stringent performance and cost requirements of the current and future electrical grid [1–3]. Developing cost-effective and high-performance storage platforms is paramount to integrate intermittent renewable energy technologies into the energy network [4]. Among the existing battery technologies, redox flow batteries (RFBs) have emerged as a promising candidate for large-scale energy storage. Intrinsic to their design, RFBs offer opportunities for economic scaling as the electrolyte reservoirs and the reactor size can be independently scaled, decoupling the power rating and energy capacity [5]. Furthermore, flow batteries are easy to manufacture, can utilize various electrolyte chemistries, and are recyclable [5, 6]. Common RFB architectures consist of an electrochemical stack with alternating electrodes, separators, and bipolar plates where the electrical power is generated, and external storage tanks containing the electrolyte solutions where energy is stored. The electrolyte is pumped through the reactor and is composed of dissolved redox active materials that can be reversibly converted between different oxidation states. The redox reactions are sustained at the surface of the porous electrodes through which the electrolyte continuously flows, and an ionic current is carried through the separator to maintain the electroneutrality in each half-cell [7]. However, electrochemical losses (ohmic, charge transfer, and mass transfer overpotentials) impact the overall efficiency and cost of the battery, which challenges their economic competitiveness [8]. Thus, materials research for RFBs is focused on advancing the component properties to improve the overall performance and durability of the system [9–11].

The stack performance and lifetime are governed by multiple properties of the individual cell components and their complex interplay, which gives rise to phenomena such as reactive mass transport. The physicochemical properties of the electrolyte and the main components (porous electrodes and separator), together with the reactor design (flow field geometry, transport lengths) determine the available surface area for reactions and control the transport of mass and charge. The electrode microstructure dictates the trade-off between the pressure drop and the accessible surface area [12], whereas the separator type, chemical composition, and nanostructure [13] impact the RFB performance by regulating the transport of species between the positive and negative compartments. Conventionally, the cell performance is assessed using electrochemical diagnostic tools (e.g., polarization curves, charge-discharge capacity, electrochemical impedance spectroscopy) together with *ex-situ* characterization methods (e.g., scanning electron microscopy with energy dispersive X-ray analysis) where novel materials are macroscopically evaluated by empirical comparison (internal surface area, porosity, tortuosity) with the current state-of-the-art [14]. Although this is a valid approach to screen promising material candidates, valuable information is lost due to the complexity of identifying local performance-limiting factors related to electrode utilization, and mass transport within the reactor area. From the perspective of an electrochemical diagnostic technique, the cell is a homogenous system, a so-called “black box”, with inputs and outputs in the form of current or voltage. Electrochemical cells, however, are anisotropic systems with an inhomogeneous distribution of reaction rate, current, and species concentration within the reactor volume. This gives rise to a myriad of limiting phenomena in the cell that cannot be observed with conventional electrochemical techniques, including gas evolution, improper electrode wetting, local depletion in species concentration, membrane crossover, and precipitation. Thus, to properly correlate

the material properties to the device performance, the development of locally resolved characterization methods is essential [15–17].

The most straightforward route to access information at a microscopic level is employing *operando* imaging of electrochemical systems in tandem with complementary electrochemical diagnostics, which has been instrumental in the rapid development of polymer electrolyte fuel cells [18, 19] and lithium-ion batteries [20, 21]. Over the last years, several groups have developed imaging and spectroscopic approaches that enable *operando* characterization of RFBs. In the following, we describe a set of representative examples, and not an exhaustive list of advances, on *operando* imaging characterization of redox flow cells. Wong *et al.* applied fluorescence microscopy and particle velocimetry to a quinone-based flow battery to quantitively image active species and velocity distributions near the electrode-flow field interface and highlight inhomogeneous flow profiles within the porous electrodes [22]. This technique holds promise to image flow velocity profiles and to resolve the electrochemical activity at the electrode-electrolyte interface. However, fluorescent species are necessary for operation, the electrochemical cell must be modified with transparent windows, and the technique is restricted to a limited penetration depth through porous carbon or metallic electrodes. Moreover, Jervis *et al.,* Tariq *et al.,* Eifert *et al.,* and Köble *et al.* employed X-ray tomographic microscopy to visualize gas pockets within the liquid electrolyte [23–26]. The authors successfully separated the carbon electrode phase from the liquid electrolyte and the gas pockets present in the porous electrodes, showing incomplete wetting of carbon fiber electrodes. X-ray imaging can yield 3D reconstructions of electrode microstructures and can uncover wetting dynamics in porous media. However, despite being considered non-destructive, high X-ray doses are generally needed to obtain high temporal and spatial resolutions, while low doses are necessary to stay under the X-ray induced degradation threshold of the materials under investigation, causing a trade-off between resolution and exposure time [27–29]. Zhao *et al.* employed coupled *in-situ* nuclear magnetic resonance and electron paramagnetic resonance to track reaction mechanisms occurring within the electrolyte [30, 31]. It is an effective technique to monitor the state-of-charge of the electrolyte within the tanks and to track chemical transformations. However, nuclear magnetic resonance-based techniques suffer from challenging cell-design modifications to probe the concentration within the reactor volume. While these techniques have provided important insights into flow distributions, electrode wetting, electrolyte state-of-charge, and degradation, a technique that enables *operando*, reactor-level, and non-invasive imaging of the electrochemical cell is necessary to understand how the microscopic properties of materials impact the cell performance.

Neutron radiography is an alternative technique to fulfill these requirements and has been applied to electrochemical devices for more than two decades [32]. Neutron imaging is a non-invasive technique that is suitable to study systems during extended operation. Neutrons are electrically neutral particles and therefore offer a high penetration depth even through high atomic weight elements, as neutrons only interact with the nuclei and not with the electron cloud, resulting in no or minimal modification of the electrochemical cell design for imaging [33]. One of the first studies was reported by Mosdale *et al*. who calculated the water content within the membrane of a proton exchange membrane fuel cell *in operando* [34]. Due to the through-plane configuration of their setup, the authors designed a cell with neutron-transparent components, enabling selective investigation of the membrane hydration. Following this work, neutron radiography was mainly applied to develop the understanding of proton exchange

membrane fuel cells [18, 32, 35–38]. The interest of using neutron imaging to study fuel cells resides in the high attenuation of hydrogen atoms in liquid water and low attenuation of gases (O_2, air, H_2), alongside the high neutron penetration through the materials constituting the cell. Therefore, the use of neutron imaging improved the fundamental understanding of water management in fuel cells under various operating conditions [39-42]. Additionally, neutron imaging studies cover other electrochemical technologies such as lithium-ion batteries [20, 43–46], electrolyzers [47, 48], and alkaline batteries [46, 49]. More recently, Clement *et al.* used neutron radiography to study the gas evolution and correlated it to the properties of the electrode material during the charging process of a vanadium RFB [50]. We hypothesize that imaging with neutrons can achieve further than contrast between liquid, gas, and solid phases, and allows imaging of the dissolved species within the electrode pore space [51,52]. Unlike X-rays, neutrons have no marked trend in the distribution of mass attenuation coefficients across the periodic table, so contrast between elements does not follow a predictable trajectory. However, several elements (e.g., H, Li, B), which are central to redox flow batteries, feature high attenuation of hydrogen atoms, making neutrons highly suited to study organic redox molecules [53, 54], which are of interest for various electrochemical technologies such as RFBs and CO_2-electrolyzers. These features make it possible to perform neutron radiography of non-aqueous electrochemical systems and to obtain contrast between the redox active molecules and the supporting salts, opening an avenue to study *in-situ* or *operando* motion of species in performance-defining materials such as separators and porous electrodes.

Here we explore, for the first time, the use of neutron imaging to reveal reactive transport phenomena and concentration distributions in non-aqueous redox flow batteries (NAqRFBs) as a model system to demonstrate this approach. NAqRFBs are an attractive option for energy storage because of their larger electrochemical stability windows and their use of organic molecules made from earth-abundant elements. In this work, neutron radiography is used to extract concentration profiles of redox-active species or supporting salts within the reactor of an *operando* NAqRFB. Resolving the concentration profiles locally in the reactor area (the performance-defining region of the RFB including the flow fields, electrodes, and separator) is a powerful complementary approach to the contemporary macroscopic characterization techniques and can be used to elucidate the coupled mass transport phenomena (convection, diffusion, migration, reaction). In this work, we perform in-plane transmission neutron imaging of NAqRFBs in two beamlines offering distinct capabilities in terms of resolution and species identification. Compared to conventional through-plane imaging, in-plane imaging can reveal the concentration gradients emanating from the flow field channels towards the separator, provided appropriate spatial resolution is achievable. The NEUTRA beamline operates with thermal neutrons (white-beam) allowing cumulative concentration profiles of the active materials and the supporting salts with a high spatial resolution over the region of interest. The ICON beamline operates with cold neutrons and utilizes the time-of-flight neutron imaging (ToF-NI) as a spectral technique to image the reactor via energy-resolved neutron radiography, but the use of this technique results in a drop in temporal resolution caused by switching to a pulsed source. However, ToF-NI enables the deconvolution of concentration profiles of several species in the electrolyte (i.e., active species and supporting ion), thus by adding the time dimension we can resolve the movement of species between half cells under a voltage bias, giving insight into the coupled transport phenomena within the reactor area.

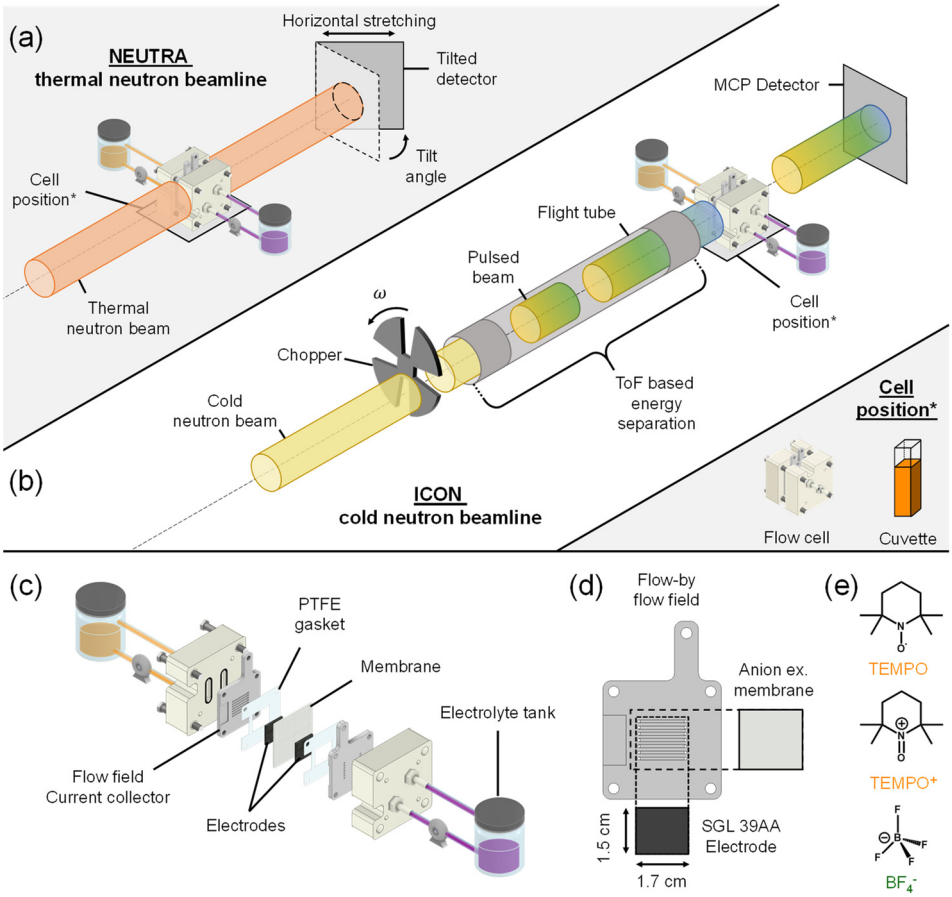

Figure 6.1: Schematic representations of **(a-b)** the neutron imaging set-ups, and **(c-e)** the flow battery cell design and components, utilizing non-aqueous electrolytes. **(a)** Neutron imaging using the NEUTRA beamline, where a cumulative concentration profile of TEMPO, $TEMPO^+$, and BF_4^- species is obtained. **(b)** Neutron imaging using the ICON beamline, where the moderation of the neutron velocities enables to select the energy of the neutrons by means of a mechanical chopper disk, a flight tube, and a microchannel plate detector, where deconvoluted concentration profiles of active species (TEMPO and $TEMPO^+$) and supporting electrolyte anions (BF_4^-) are obtained. The cell positions in **(a-b)** were used for both flow cell and cuvette imaging. **(c)** Exploded view of the flow cell components and the connected electrolyte tanks. **(d)** Representation of the cell components (parallel flow field, anion exchange membrane, and SGL 39AA porous electrode) with their dimensions. **(e)** Chemical structures of the attenuating active species TEMPO and $TEMPO^+$, and the attenuating supporting species BF_4^-.

In the first part of this work (**Figure 6.1a**) the experiments performed at the NEUTRA beamline are described during flow cell polarization to extract concentration profiles of 2,2,6,6-tetramethylpiperidin-1-yl)oxyl (TEMPO) in its neutral and oxidized form, dissolved in solution together with a low neutron attenuating supporting salt, potassium hexafluorophosphate (KPF_6), or with a highly attenuating counter-ion (BF_4^-). To this end, calibration curves are obtained for all species used in this work, after which the cells are imaged during operation and concentration profiles of dissolved species in

the reactor volume are extracted. In the second part of this work (**Figure 6.1b**), polarization experiments are performed using TEMPO with BF_4^- as the counter-ion at the ICON beamline. First, the neutron attenuation of the electrolyte solutions is calibrated at different neutron energies prior to *operando* imaging. By utilizing the principle of energy-dependency of their neutron cross-sections, we quantify the concentration change of active species and supporting salt separately during operation and reveal the dominant transport mechanisms within the electrodes and between half cells under voltage stimuli. This approach pushes the limits of neutron imaging by probing concentration profiles and species movement evolving in an operating flow cell and we hope it will serve as a guide for researchers intending to perform species-sensitive *operando* neutron imaging.

6.2. Materials and methods

6.2.1. Chemicals

2,2,6,6-Tetramethylpiperidin-1-yl)oxyl (TEMPO, Sigma Aldrich, 98 %), nitrosonium tetrafluoroborate ($NOBF_4$, Thermo Scientific, 98 %), nitrosonium hexafluorophosphate ($NOPF_6$, Thermo Scientific, 95%), acetonitrile-d3 (CD_3CN, Zeochem AG, 99.8 %D), acetonitrile (CH_3CN, Sigma Aldrich, ≥ 99.9 %), and potassium hexafluorophosphate (KPF_6, Thermo Scientific, 99 %) were used without further purification.

6.2.2. Electrolyte preparation

TEMPO was converted to its cation form 2,2,6,6-Tetramethyl-1-piperidinyloxy-oxo ($TEMPO^+$) via chemical oxidation with nitrosonium salts in a nitrogen-filled glove box (MBraun, LABstar, O_2 < 1 ppm, H_2O < 1 ppm). TEMPO (12.52 g) was dissolved in acetonitrile, where 1.1 molar equivalents of nitrosonium hexafluorophosphate ($NOPF_6$, 15.42 g) or nitrosonium tetrafluoroborate ($NOBF_4$, 10.29 g) dissolved in CH_3CN were slowly added during 2 hours to prevent NO_x build-up [12]. Then, a rotary evaporator (40 °C, gradual decrease from atmospheric pressure to vacuum) was used to remove the solvent, and $TEMPO^+PF_6^-$ or $TEMPO^+BF_4^-$ salts were recovered. The electrolytes were prepared by weighting the solid fractions (TEMPO, $TEMPO^+PF_6^-$, and KPF_6 or TEMPO and $TEMPO^+BF_4$) prior to adding CD_3CN until full dissolution. Finally, the volume was adjusted in a graduated flask to reach 20 mL of total volume. For the experiments using KPF_6 as supporting salt, a 50 % state-of-charge (SoC) solution was prepared for each side with two different total concentrations of TEMPO species (0.5 M at the working electrode (WE) side and 0.2 M at the counter electrode (CE) side) in 0.1 M KPF_6. For the experiments using BF_4^- ions, 0.5 M of TEMPO was used at the CE against 0.5 M of $TEMPO^+BF_4^-$ at the WE without additional added supporting salt to achieve high BF_4^- concentrations without compromising the imaging process. For all imaging experiments, CD_3CN is used as the solvent to reduce its contribution to the overall transmission as deuterium has a 10-fold lower total cross-section than hydrogen (at a neutron velocity of 2200 m s^{-1}) [55].

6.2.3. Calibration experiments

To quantify the concentration of the species within the electrochemical cells, the attenuation coefficients were determined with cuvette calibration measurements to correlate neutron transmission with solution concentration. The attenuation of the beam by the sample was calculated using the Lambert-Beer law [51], described as

$$T = e^{-\sigma_i n_i \delta}, \tag{6.1}$$

where T is the transmitted intensity after correction for the attenuation of an empty cuvette [-], σ_i the conventional microscopic cross-section [m^2], n_i the number density of species i [m^{-3}], which is related to the concentration of species i by $C_i = n_i/N_A$ [mol m^{-3}], and δ is the thickness of the cuvette [m].

For the NEUTRA and ICON beamline measurements, cuvettes (1 cm optical path) were filled with different electrolyte solutions to calibrate the attenuation of the neutron beam. For the NEUTRA beamline experiments, the reference cuvettes were filled with CD_3CN (solvent) or 0.2 M KPF_6 in CD_3CN (supporting electrolyte). To verify the linearity between concentration and neutron attenuation, solutions of TEMPO, $TEMPO^+PF_6^-$, and $TEMPO^+BF_4^-$ in CD_3CN were measured at molarities of 0.1, 0.2, 0.3, 0.4, and 0.5 M. For the ICON beamline measurements, a single concentration point method was used as the linearity of the neutron attenuation as a function of the electrolyte concentration was obtained at the NEUTRA beamline. The reference cuvette was filled with CD_3CN (solvent) and the single concentration points were measured for the solutions of interest of 0.5 M TEMPO and 0.5 M $TEMPO^+BF_4^-$ in CD_3CN.

6.2.4. Flow cell parts

Neutron imaging was performed using a laboratory-scale redox flow cell with minimal modifications for imaging. The flow diffusers were machined from polypropylene (McMaster-Carr) and the graphite parallel flow-by flow fields, also functioning as current collectors, featuring seven 1.6 cm long flow channels (0.5 mm depth and 1 mm width), were milled from 3.18 mm thick resin-impregnated graphite plates (G347B graphite, MWI, Inc.) [12]. All flow cells employed a Fumasep FAB-PK-130 (Fuel Cell Store, dry thickness 130 µm) anion exchange membrane. The electrodes had a geometric area of 2.55 cm^2 enclosed within incompressible polytetrafluorethylene gaskets (ERIKS) and/or compressible expanded polytetrafluorethylene (ePTFE, Gore®, 520 µm nominal) gaskets to improve the sealing of the flow cell (**Figure 6.1c**). For the experiments with the NEUTRA beamline, the flow cells contained three Sigracet 39AA electrodes (Fuel Cell Store, 280 µm nominal thickness, 89 % porosity) per anode and cathode sides (six electrodes in total), sandwiching the membrane. The electrodes were compressed at 25 % compression by selecting an incompressible gasket thickness of 630 µm. For the experiments at the ICON beamline, one AvCarb G100 felt electrode (Fuel Cell Store, 3200 µm nominal thickness, 95 % porosity) per side was used. Each side was sealed with two incompressible 1 mm gaskets and three compressible gaskets to reach a stack thickness of 3200 µm (measured from the neutron images). The reactor design was slightly modified, without impacting the transport phenomena within the cell, by grooving the current collectors and the gaskets around the active area (**Figure 6.1d**) to minimize the attenuation from cell parts with the neutron beam and thereby enhance the

sensitivity. After assembly, the cells were tightened with a torque-controlled wrench to 2 N m and the cell was mounted 1 - 3 mm in front of the neutron detector on a robotized platform. Peristaltic pumps (Cole-Parmer) were used to pump the electrolyte to the cells with rubber tubes (Masterflex LS-14 tubing) connected to two separate 20 mL electrolyte tanks. Two flow rates were employed, 15.1 mL min^{-1} and 5.6 mL min^{-1} for the NEURA experiments and 21.1 mL min^{-1} and 6.7 mL min^{-1} for the ICON experiments, corresponding to superficial velocities within the flow field channels of 7.19 cm s^{-1} and 2.67 cm s^{-1}, and 10.0 cm s^{-1} and 3.19 cm s^{-1}, respectively, as calculated using **equation (6.2).**

$$u = \frac{Q}{N_{ch} W_{ch} D_{ch}} \tag{6.2}$$

Where u is the fluid velocity [m s^{-1}], Q is the electrolyte flow rate [m^3 s^{-1}], N_{ch} is the number of inlet channels in the flow field configuration (7 channels) [-], W_{ch} is the width of the channel (1 x 10^{-3} m) [m], and D_{ch} is the depth of the channel (5 x 10^{-4} m) [m].

6.2.5. Electrochemical protocols

Electrochemical measurements were conducted with a Biologic VSP-3e potentiostat. For the experiments in the NEUTRA beamline, the open circuit voltage (OCV) of the cells was measured for 1 hour (for the experiments with the KPF_6 supporting salt) or 2 hours (for the experiments with the BF_4^- supporting ion) at 15.1 mL min^{-1} after the cell was filled with the electrolyte to monitor the diffusion of species between the WE and CE. Thereafter, the cell was successively held at -0.3 V, +0.3 V, -0.6 V, and +0.6 V for 20 min at each potential step. Then the flow rate was decreased to 5.6 mL min^{-1} and the same potential protocol was applied. The entire electrochemical protocol was *ca*. 220 min and neutron radiographs were collected during the entire duration of the experiment. All measurements were performed in the same cell by filling and emptying the cell with the different solutions with a rinsing step in between with 0.5 M TEMPO dissolved in CD_3CN.

For the experiments at the ICON beamline, the OCV of the cells was measured for 10 min at 21.1 mL min^{-1} after which the cell was successively held at -0.6 V and +0.6 V for 1 hour at each potential step. Then the flow rate was decreased to 1.7 mL min^{-1} and the same potential protocol was applied. Then the flow rate was increased to 6.7 mL min^{-1} and the cell was successively held at -0.6 V, +0.6 V, -0.3 V, and +0.3 V for 1 hour at each potential step. Finally, the flow rate was switched to 96 mL min^{-1} and the cell was held at -0.6 V and +0.6 V for 1 hour at each potential step. The entire electrochemical protocol took around 720 min to complete. For this study, only two flow rates (21.1 mL min^{-1} and 6.7 mL min^{-1}) were analyzed in detail. The electrolyte was not refreshed during the entire experiment.

6.2.6. Neutron radiography

Neutron radiography experiments were performed at the NEUTRA thermal neutron and ICON cold neutron imaging beamlines at the Spallation Neutron Source (SINQ) facility of the Paul Scherrer Institute, Switzerland. In the SINQ facility, the neutrons were ejected

from a lead spallation target that was hit with a proton beam at 590 MeV energy with 1.5 mA proton current. The ejected neutrons were moderated by heavy water and reached thermal velocities (with a mean energy of 25 meV) [56]. For the NEUTRA beamline, attenuated neutrons were captured by a scintillator screen (10 µm thick, Gd_2O_2S:Tb) and converted to visible light, which is subsequently captured by the charge-coupled device camera detector (Andor) at an exposure time of 30 s. A tilted detector setup was used at the NEUTRA beamline that enables stretching in the horizontal transverse direction (with respect to the beam trajectory), see **Figure 6.1a**, meaning that the membrane-electrode assembly can be imaged with higher spatial resolution [57]. The resulting pixel size in the direction across the membrane was 6 µm and the effective resolution, considering the blurring intrinsic to the detector and due to the beam divergence, was approximately 20 µm.

For the ICON beamline, neutrons were further moderated with a liquid deuterium (D_2) tank held at 25 K, decreasing the velocity of neutrons to the cold spectrum (mean energy of 8.53 meV) [58]. Similarly, the neutron beam passes through a series of collimators, beam limiters, and shutters, but before interacting with the sample, the neutron beam passes through a mechanical chopper allowing ToF-NI. The chopper creates a pulsed neutron beam whereas the traveled length of the neutrons through the flight tubes allows dispersion of the pulse based on the velocity of the constituent neutrons. The chopper rotated at a speed of 22 Hz with 4 regularly spaced openings, resulting in a pulse repetition frequency of 88 Hz. The angle of each opening was 18°, resulting in a 20 % duty cycle. The path length between the chopper and the detector was 5.5 m. Finally, the neutrons were detected (exposure time 120 s per acquisition) at a microchannel plate detector having a fixed pixel size of 55 µm, an effective resolution of approximately 150 µm, and a field of view of 28 x 28 mm^2 (512 x 512 $pixel^2$ images). In this way, the ToF-NI spectral technique in the ICON beamline allows spectral imaging of the sample, adding a new mode of contrast to conventional neutron radiography [51, 59]. Per single ToF cycle of 11.36 ms (88 Hz of chopper disk rotation), 109 raw transmission images were taken. In total, 10560 cycles were completed over a total acquisition time of 2 min from high to low neutron energies, and the resulting images are binned over 109 images. Each of the recorded images represents the sum of the corresponding 10560 images acquired at one point of the cycle. Because of the relatively broad width of the neutron pulse (2.73 ms), each frame represents a blend of several neutron energies. This is not detrimental to the distinction of hydrogen and boron atoms, as the variation of neutron attenuation as a function of energy does not exhibit any stark feature. Frames were averaged from frames 16 - 30 to construct high-energy (HE) images and from frames 31 - 50 to construct low-energy (LE) images. The HE neutron energy ranges from 77.3 - 17.0 meV with a mean at 28.3 meV, and the LE neutron energy ranges from 16.0 - 5.7 meV with a mean at 8.5 meV. Since the image acquisition time is short compared to the experimental time (360 min), it can be assumed that HE and LE images are taken at the same cell conditions. It was not possible to utilize the lower energy neutron spectra (frames 50 - 109) due to significant beam scattering and diffraction caused by the compression gaskets at their interface.

6.2.7. Image processing

Image processing by mathematical calculations was performed to extract the sample information as described in the image processing pipeline (**Figure 6.2**). Neutron radiography was performed in a subtractive manner, meaning that the transmission data from the samples are corrected for undesirable contributions, such as scattering and absorption of the cell components, detector background effects, and beam instabilities. The image processing sequence for NEUTRA is shown in detail in **Figure A6.1** and a description of the individual steps is given below:

1 *Dark current correction:* Dark current images were taken with closed beam shutters and optical shutters of the camera to correct for the electronic bias within the camera circuitry.
2 *White spot filtering:* White spots, resulting from gamma rays or other types of radiation hitting the camera chip, were filtered from the images by an outlier filtering approach, where pixels that deviate largely from their surroundings are replaced by a median value of these surroundings.
3 *Gaussian filtering:* This filtering step reduces the statistical noise that is caused by high-frequency photons hitting the camera.
4 *Open beam correction:* Open beam images were taken without the electrochemical cell in the beamline to account for the spatial variation in beam intensity by dividing the images by the averaged open beam image.
5 *Registration:* This step accounts for the physical movement of the cell during the experiments due to thermal dilation or relaxation of the cell body. All images were registered to a "reference" (the electrochemical cell filled with a 0.2 M KPF_6 in CD_3CN solution) by applying a correlation algorithm on certain cell regions to find the optimum geometrical transformation.
6 *Intensity correction:* This step corrects for beam intensity variations throughout the experiment duration by defining a non-changing area in the cell that corresponds to an area with no known changes (e.g., a part in the cell body). Gain and offset were applied to the images to match the intensity within the non-changing area region to that of the reference image.
7 *Scattered background correction:* To account for the scattered background resulting from neutrons that are scattered by the cell and the detector, a scattered background image was obtained by interpolating the intensity values between so-called "black bodies". These "black bodies" are boron rods located in a grid fashion on a steel plate and are placed in front of the sample. The black body images were processed with all the processing steps described above, but the averaging on the images was performed before registration and intensity correction steps to reduce the amount of noise. The final image was subtracted from the images to account for the scattered background.
8 *Referencing:* In this step, the images were divided pixel-wise by the reference image, which underwent all the processing steps above except registration and intensity correction as these steps are based on the position and average intensity of the non-changing area in the reference image.
9 *Positioning:* Images were rotated so that the flow channels are vertically aligned.

10 *Cell mask:* A cell mask was used to remove all the other parts of the image to obtain an image with only the region of interest, i.e., the membrane, electrode, and flow channels.

11 *Concentration calculation:* The final transmission values obtained per pixel were correlated to the species concentration via the Lambert-Beer law (**equation (6.1)**) as described in **Section 6.2.3**, where the microscopic cross-sections were obtained from the cuvette measurements and with δ_{cell} the electrolyte thickness within the cell [m] which is a function of the cell geometry, electrode porosity, and compression according to:

$$\delta_{cell} = L_e \varepsilon_e, \tag{6.3}$$

where L_e is the electrode width (1.7×10^{-2} m) [m] and ε_e the electrode porosity at the applied compression (which is 85.3 % for three stacked SGL 39AA paper electrodes) [-].

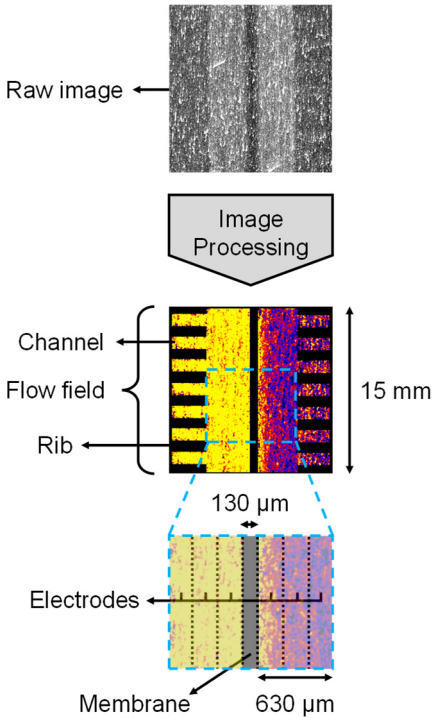

Figure 6.2: Schematic representation of the image processing for the NEUTRA beamline experiments including the raw and final image. The final image shows the flow fields, electrodes, and membrane together with their dimensions.

Due to the nature of the microchannel plate detector and the ToF-NI method used at the ICON beamline, the image processing sequence is slightly different than for NEUTRA. Overlap correction was performed on all images before the image processing steps due to the characteristics of the microchannel plate detector [60]. The image processing sequence to obtain transmission images is listed below:

1 *Outlier removal:* Dead pixels (or zero pixels) were removed from the images by averaging pixels around them and setting the new value to it.
2 *Scrubbing correction:* To avoid bias due to the detector efficiency over time, open beam images were used to correct for any change of contrast not related to the experiment but to the detector. The function interpolates between open beam images and sets a weight to correct them.
3 *Scattered background correction:* Although microchannel plate detectors have less contribution of scattered background due to the transmission of neutrons parallel to the beam axis, we still performed scattered background correction to improve accuracy [61]. For ICON, the black bodies were strips of Boral (2.5 mm width) in a steel plate.
4 *Registration*
5 *Binning:* Selection and merging of the HE and LE images based on the energy-dependent calibration curves of the neutron attenuation of the different species of interest and accounting for the edge scattering effects.
6 *Intensity correction*
7 *Referencing*
8 *Positioning*
9 *Cell mask*
10 *Concentration calculation:* The concentration of each species was obtained by solving a system of equations for the transmission of each region of interest (see **Figure 6.6b**), where the LE and HE microscopic cross-sections of the species can be correlated to the concentration distribution of the *operando* images via the following operation

$$\begin{bmatrix} -ln(T_{LE}) \\ -ln(T_{HE}) \end{bmatrix} = \delta_{cell} \cdot \begin{bmatrix} \sigma_{BF4,LE} & \sigma_{TEMPO,LE} \\ \sigma_{BF4,HE} & \sigma_{TEMPO,HE} \end{bmatrix} \cdot \begin{bmatrix} C_{BF4} \\ C_{TEMPO} \end{bmatrix} \cdot N_A, \tag{6.4}$$

where T_{LE} and T_{HE} are the low-energy and high-energy transmission values per pixel of the *operando* experiment images [-], $\sigma_{i,LE}$ and $\sigma_{i,HE}$ are the low-energy and high-energy microscopic cross-sections [m^2], and C_i is the pixel-wise concentrations of the species i [mol m^{-3}], which are TEMPO or BF_4^-. The electrolyte thickness, δ_{cell}, is defined according to **equation (6.3)**, which for the felt electrode used in the ICON experiments is around 1.62 cm.

6.3. Results and discussion

First, we discuss the results of the white-beam imaging obtained at the NEUTRA beamline, followed by the ToF-NI performed at the ICON beamline. Each section describes the *ex-situ* calibrations used to correlate the concentrations of species in the electrolyte with neutron attenuations, and the characterization of concentration profiles in the *operando* flow cells under various potential and flow configurations. In the NEUTRA section, two sets of experiments are performed, one with a low attenuating supporting salt (KPF_6) and one with a highly attenuating counter-ion (BF_4^-), to differentiate between the redox active species and the supporting ions.

6.3.1. White-beam neutron imaging (NEUTRA)

6.3.1.1. Attenuation of electrolyte species

Achieving contrast between the electrolyte constituents (solvent, redox-active species, and supporting ions) is critical to identifying and quantifying their dynamics within the electrochemical cell. We capitalize on the flexibility in the choice of solvent, supporting electrolytes, and redox-active molecules for NAqRFBs, and measure attenuation coefficients for a set of electrolyte types and components using cuvettes (**Figure 6.3a**). The attenuation difference between the neat deuterated solvent (CD_3CN) and 0.2 M supporting salt solution (KPF_6, in CD_3CN) is sufficiently small to be neglected, confirming the negligible attenuation of KPF_6 at this neutron energy and concentration. On the other hand, the addition of 0.5 M TEMPO in this electrolyte solution results in a larger attenuation coefficient as it has four methyl groups rich in hydrogen atoms attached to a piperidine ring (molecular formula $C_9H_{18}NO$). The large number of hydrogen atoms results in a stark contrast between the supporting salt (KPF_6) and the active species (TEMPO/$TEMPO^+$). For the concentration range investigated in this study (0 - 0.5 M), TEMPO and $TEMPO^+PF_6^-$ dissolved in CD_3CN show similar neutron attenuations (**Figures 6.3a**). The similar cross sections of TEMPO and $TEMPO^+$ are expected given their identical chemical composition (only one electron difference), resulting in almost identical interaction with neutrons, and further confirming the low attenuation of PF_6^- ions. Finally, when the counter-ion PF_6^- of $TEMPO^+$ is replaced with BF_4^-, the attenuation at the same concentration is nearly doubled (**Figure 6.3a**), which indicates that TEMPO species and BF_4^- ions have similar microscopic cross-sections. Although the counter ion contains no hydrogen atoms, BF_4^- contains boron which features a large neutron absorption cross-section for thermal neutrons [62]. **Figure 6.3b** shows a linear correlation between neutron attenuation *vs.* concentration for the different species employed in this study, which confirms the validity of the chosen operating range (0 – 0.5 M) where the Lambert-Beer law (**equation (6.1)**) holds. The microscopic cross-sections obtained here are then applied to obtain local concentrations in the electrochemical reactor volume during operation.

6.3.1.2. Transport of the active species

We then perform neutron imaging on an operating redox flow cell to visualize concentration profiles of TEMPO/$TEMPO^+$ (**Figure 6.4**). The cell is connected to tanks with 50 % SoC TEMPO/$TEMPO^+$ at 0.5 M concentration on the CE side and 0.2 M on the WE side, both with 0.2 M KPF_6 to provide ionic conductivity and to minimize supporting salt impact on neutron attenuation (**Figure 6.4a**). Because the WE and CE compartments are separated by an anion exchange membrane, the transport of cations such as $TEMPO^+$ and K^+ is significantly hindered, whereas the anions and neutral molecules such as PF_6^- and TEMPO can more easily pass through. Using this cell architecture, we can track the movement of TEMPO between the electrodes. The cell is discharged (negative potential applied at the WE) and charged (positive potential applied at the WE) alternately, such that the state-of-charge after each complete cycle does not significantly deviate from the initial condition. Two voltage magnitudes were tested to understand their impact on the electrochemically-driven transport processes. The electrochemical sequence goes through OCV, -0.3, +0.3, -0.6, and +0.6 V steps, each for 20 min at the highest tested inlet flow rate of 15.1 mL min^{-1} (**Figure 6.4b**). We also

studied the impact of flow rate by performing the same electrochemical sequence (without the OCV step) but at 5.6 mL min^{-1} (**Figure A6.2**). The current-time and voltage-time curves of the entire experiment can be found in **Figure A6.3**. *Operando* imaging of the cell during the electrochemical protocol results in transmission images where the attenuation at each location represents the integral of neutron-matter interactions along the neutron path (**Figure 6.1a**). These images are then averaged for the duration of a voltage step (20 min) and result in concentration maps for a given condition at steady-state (**Figure 6.4c-d**). The color scale represents the cumulative concentration of TEMPO and $TEMPO^+$ and ranges from 0 - 0.5 M, resulting in a 2D map of the species concentration in the reactor area. The membrane area is omitted as the quantification of concentrations is not reliable in this region due to the high hydrogen content of the polymer membrane material (perfluorinated with a polyketone reinforcement) and the membrane thickness (130 µm). Finally, we calculate the concentration profiles across the thickness of the electrodes and compute these between the flow field-electrode interfaces of both half cells. Using this approach, one-dimensional concentration profiles, parallel with the electrical field, are obtained.

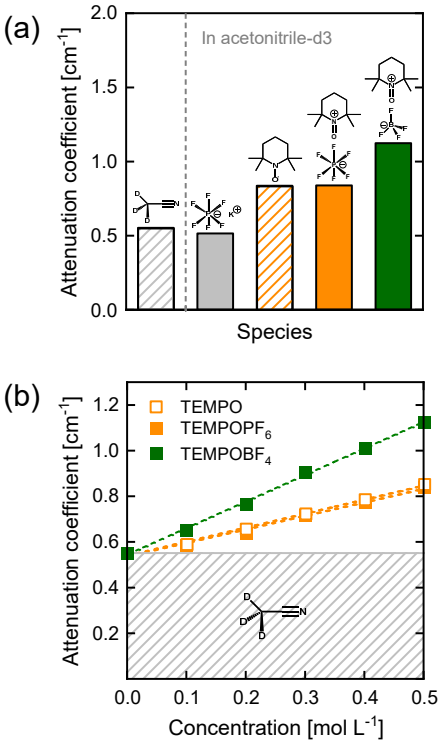

Figure 6.3: Determination of the attenuation coefficient for the chemicals used in this study obtained at the NEUTRA beamline. **(a)** The attenuation coefficients of the different species in CD_3CN: the solvent only, supporting electrolyte (0.2 M), and species TEMPO, $TEMPO^+PF_6^-$, and $TEMPO^+BF_4^-$ (all 0.5 M). **(b)** The linear dependence of the macroscopic neutron cross-section of the TEMPO, $TEMPO^+PF_6^-$, and $TEMPO^+BF_4^-$ species to the concentration (0.1, 0.2, 0.3, 0.4, and 0.5 M), where the shaded area represents the attenuation of the solvent.

The experiment begins with an OCV step where no current is drawn from the cell. The brighter color of the CE side in the OCV radiograph represents a higher concentration compared to the WE side, as expected by the concentrations of the electrolyte fed (0.5 M and 0.2 M TEMPO/$TEMPO^+$). Moreover, the concentration on both sides does not show dark regions (**Figure 6.4c-d**), suggesting full wetting, at least to the spatial resolution of the measurement. Overall, the concentration profiles under cell polarization do not strongly deviate from the initial OCV state, except at positive potentials near the membrane area on the WE, which can be explained, in part, by the reactor configuration (i.e., anion exchange membrane, stacked carbon paper electrodes, and parallel flow fields) and the low ionic conductivity of non-aqueous electrolytes [8], resulting in low current densities and charge consumption. In this experiment, the concentration gradient is from left to right due to the higher cumulative TEMPO/$TEMPO^+$ concentration on the CE side. Under negative potentials (-0.3 V and -0.6 V), TEMPO is converted to $TEMPO^+$ in the CE side, resulting in a build-up of $TEMPO^+$, while the opposite reaction takes place in the WE, resulting in $TEMPO^+$ depletion. To compensate for the charge, PF_6^- crosses through the membrane towards the CE side, which is not visible in the images due to its low attenuation. Although favorable to sustain the electrochemical reaction, we do not expect TEMPO to cross to the CE side as this would be against its concentration gradient, thus the images and profiles for negative potentials are nearly identical to the OCV conditions (**Figure 6.4c-d**).

On the contrary, when positive potentials are applied (+0.3 V), the TEMPO concentration in the CE side increases, amplifying its existing concentration gradient towards the WE. This results in a stronger diffusive flux towards the WE side at positive potentials, supported by the bright concentration front in the corresponding radiographs, together with the steep concentration profiles near the membrane. Increasing the potential to +0.6 V amplifies this trend and the concentration front extends deeper within the WE (**Figure 6.4d**). Decreasing the flow rate to 5.6 mL min^{-1} further intensifies the concentration front in the WE (**Figure A6.2**) for both the positive and negative potentials. The concentration front reveals mass transfer limitations, determined by the applied potential, electrolyte velocity, species concentration, and electrolyte and electrode properties [8]. To visualize such limiting phenomena, we utilized a flow-by flow field design that induces limited convection within the porous electrode. Thus, we anticipate that a convection-enhanced flow field (such as interdigitated or flow-through) would reduce the concentration gradients [63]. In this first set of experiments, the low neutron cross-section of the KPF_6 salt was utilized to maximize the contrast of TEMPO and $TEMPO^+$ compared to other electrolyte components. To visualize the motion of anions, we employ a strongly attenuating counter-ion (BF_4^- instead of PF_6^-) without any additional supporting salt to amplify the contrast between all species in the electrolyte.

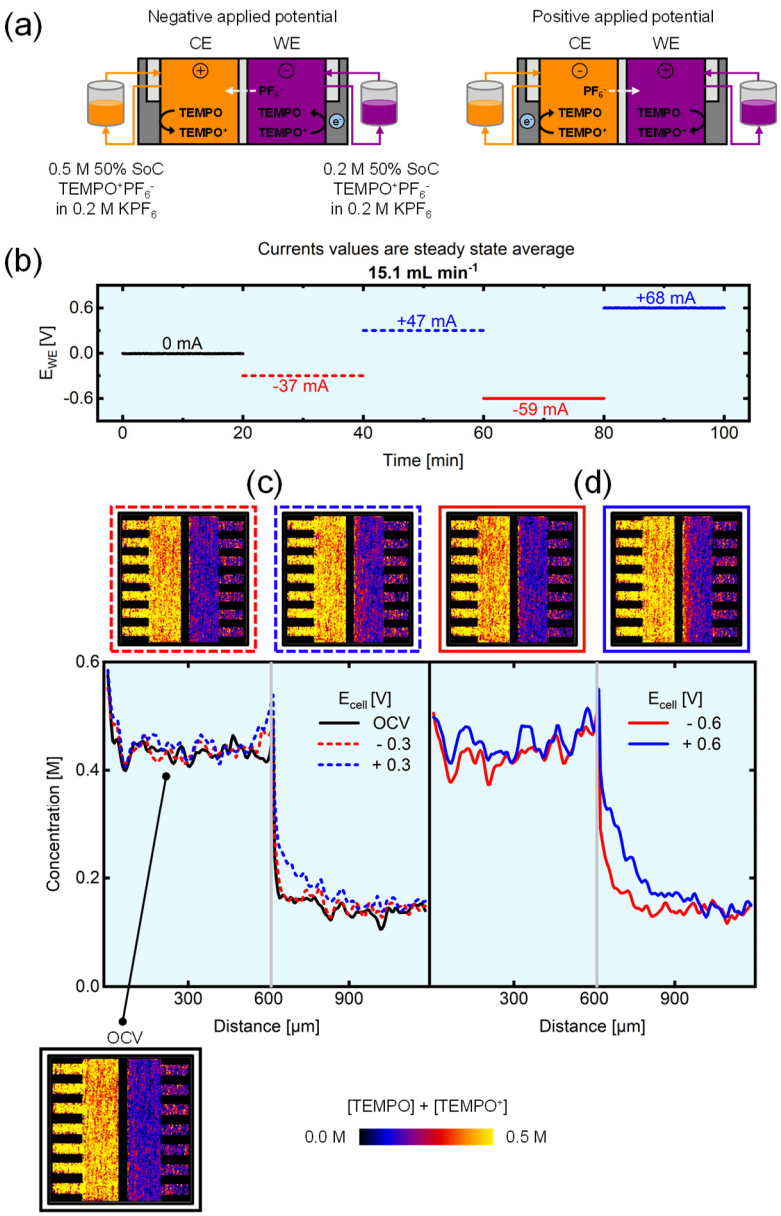

Figure 6.4: *Operando* imaging of the active species transport in the NEUTRA beamline with the low attenuating KPF_6 supporting salt. **(a)** Schematic representation of the non-aqueous cell designs during charge and discharge mode, where the counter electrode (CE) corresponds to 0.5 M TEMPO/$TEMPO^+PF_6^-$ at 50% state-of-charge in 0.2 M KPF_6 and the working electrode (WE) to 0.2 M TEMPO/$TEMPO^+PF_6^-$ at 50% state-of-charge in 0.2 M KPF_6. **(b)** Electrochemical sequence over time showing the applied potential steps and measured averaged current output at an inlet flow rate of 15.1 mL min^{-1}. **(c-d)** Cumulative active species (TEMPO/$TEMPO^+$) concentration profiles over the electrode thickness at an inlet flow rate of 15.1 mL min^{-1}. The averaged snapshots of the cell after image processing and the concentration profiles are shown for various applied potential steps: **(c)** OCV, -0.3 V, and +0.3 V, and **(d)** -0.6 V and +0.6 V.

6.3.1.3. Transport of the counter-ion

Supporting ions are essential in RFBs to provide ionic conductivity [64, 65], where here we leverage BF_4^- as counterion due to its high neutron attenuation (see **Section 6.3.1.1**) [55]. To quantify the influence of migration on the charged species transport (i.e., stoichiometric operation), we do not add a supporting salt in the electrolyte (**Figure 6.5a**), which negatively impacts the obtained current density (**Figure A6.5**) but enables visualization of the counterion. Furthermore, the use of an anion-exchange membrane significantly restricts $TEMPO^+$ movement between compartments, which leaves BF_4^- as the main charge carrier. As we perform subtractive neutron imaging, the isolation of [TEMPO], [$TEMPO^+$], and [BF_4^-] is not possible with white-beam neutron imaging, resulting in cumulative concentration maps (see the combined color scale in **Figure 6.5**). Although the concentration information is cumulative, by tuning experimental parameters (type of ion-exchange membrane and tank concentrations) we hypothesize that the observed changes can be attributed to the motion of certain species, which is predominantly BF_4^- in this configuration. A novel approach to isolate the concentration of species in solution with neutron imaging is discussed in **Section 6.3.2**.

In the first hour of the experiment, the system is kept at OCV conditions to track diffusional crossover through the membrane (**Figure 6.5b**). Although we track a change in OCV over time, indicating crossover and concentration equilibration, the slight concentration variations in this short period are not quantitatively captured by the radiographs (OCV radiograph in **Figure 6.5c**). Although BF_4^- has a strong concentration gradient towards the CE side, the OCV profile does not show significant deviation from the initial concentrations, which is attributed to the Donnan exclusion of $TEMPO^+$ coupled with the barrier properties of the dense anion exchange membrane [66]. Furthermore, the concentrations in the reactor volume are homogeneous and no local fluctuations are observed. We conclude that the timeframe of the OCV period is shorter than the time needed for diffusional crossover of species at this configuration.

After the OCV period, alternating potential steps are applied to the electrochemical cell, and the current response is recorded in time (**Figure A6.5**). At negative potentials, $TEMPO^+$ is converted to TEMPO in the WE, and BF_4^- migrates to the CE compartment (**Figure 6.5a**). We can observe a local accumulation of attenuating species in the vicinity of the membrane on the CE side, while the opposite trend is observed in the WE compartment (**Figure 6.5c**), attributed to the migration of the BF_4^- anion from the WE to the CE to maintain electroneutrality. This effect is more pronounced at a higher potential (-0.6 V *vs.* -0.3 V, **Figure 6.5c**), which illustrates the influence of migration. Starker concentration gradients are obtained at lower flow rates (5.6 mL min^{-1}, **Figure 6.5d**), as the convective mass transfer is lower. At the WE, we find higher concentrations in the areas near the flow field inlets in comparison with the area under the ribs. We hypothesize that velocity distributions within the porous electrodes, induced by the flow-by flow field design and the relatively thick, porous electrode stack, explain these variations in concentration throughout the electrode volume. This phenomenon is more visible at the highest flow rate as the convective forces pushing the electrolyte in the porous electrode are higher (**Figure 6.5d**). In summary, at negative potentials, the profiles show an increasing species concentration in the CE occurring synchronously with a decrease in the WE (**Figure 6.5c**).

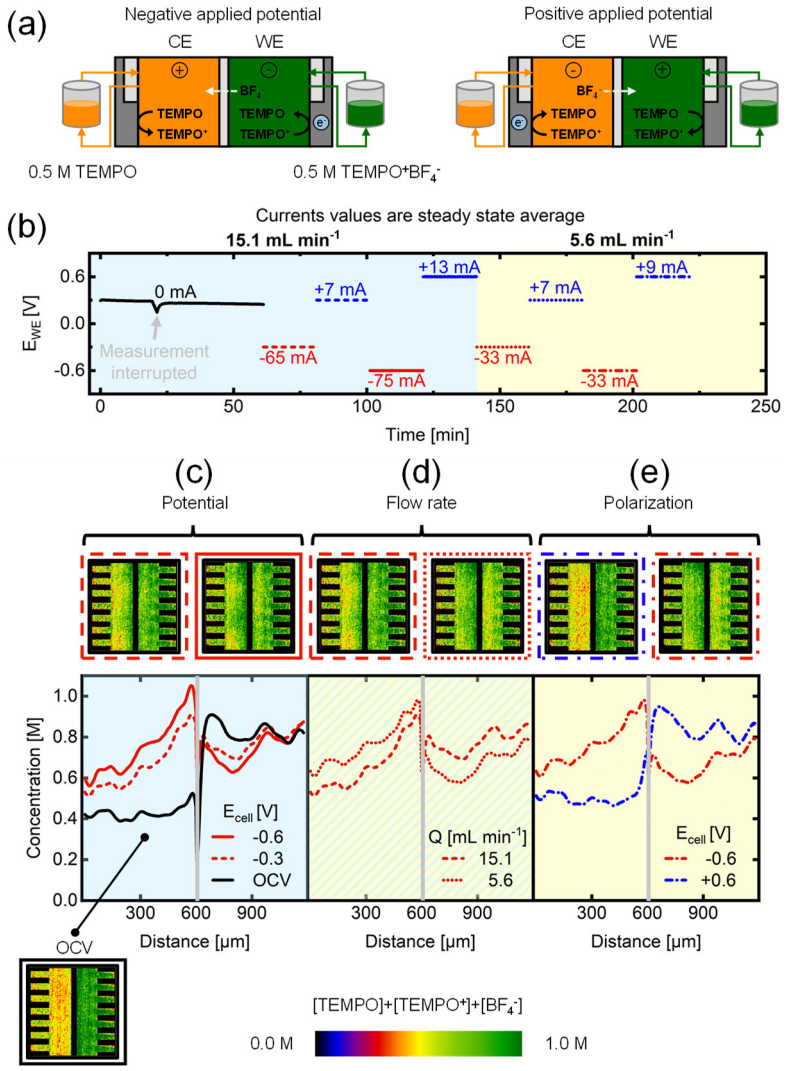

Figure 6.5: *Operando* imaging of the active species transport in the NEUTRA beamline with the neutron attenuating BF_4^- supporting ion. **(a)** Schematic representation of the non-aqueous cell designs during charge and discharge mode, where the counter electrode (CE) corresponds to 0.5 M TEMPO and the working electrode (WE) to 0.5 M $TEMPO^+BF_4^-$. **(b)** Electrochemical sequence over time showing the applied potential steps and measured averaged current output at two inlet flow rates of 15.1 mL min^{-1} and 5.6 mL min^{-1}. **(c-e)** Cumulative active species (TEMPO/$TEMPO^+$) and BF_4^- supporting ion concentration profiles over the reactor area. The concentration profiles and averaged snapshots of the cell over the whole period of each individual potential step after image processing are shown for various applied potential steps and show the influence of various operation parameters: **(c)** applied potential magnitude (OCV, -0.3 V, and -0.6 V at 15.1 mL min^{-1}), **(d)** flow rate (-0.3 V at 15.1 mL min^{-1} and 5.6 mL min^{-1}), and **(e)** polarization sign (-0.6 V and +0.6 V at 5.6 mL min^{-1}).

When a positive potential is applied to the WE, the cumulative concentration rapidly returns to its initial value, and the resulting radiographs and the concentration profiles (**Figure 6.5e**) resemble the OCV conditions. This is attributed to the relatively low change in cell capacity at negative potentials, consuming only ~8% of the total capacity (**Figure A6.6**). The small capacity consumption in the NEUTRA experiments is caused by the reactor architecture used (stacked paper electrodes and a flow-by flow field) in combination with the low ionic conductivity of the electrolyte, resulting in relatively low current densities. Therefore, at positive potentials, only a small amount of TEMPO is present in the WE compartment to be converted back to $TEMPO^+$. As a result, large overpotentials are generated throughout the cell due to the low concentration of reactants to sustain the current. This explains the asymmetry in the current magnitudes when the polarity of the cell is reversed (i.e., +7 mA *vs.* -65 mA at 15.1 mL min^{-1} and +/-0.3 V, **Figure 6.5b**). Using white-beam neutron imaging, we have obtained cumulative concentration maps of active species and supporting electrolytes. Using this approach, we have coupled macroscopic electrochemical cell performance with microscopic concentration distributions, revealing mass transfer modes under different cell potentials, flow rates, and cell polarities. However, we are not able to isolate concentrations of active species and supporting ions with this incident beam. Acknowledging these limitations, we then utilize time-of-flight imaging to obtain quantitative insights into reactive transport phenomena of both the active species and counter-ion, under similar experimental conditions (**Figure 6.5a** and **6.7a**).

6.3.2. Energy-resolved neutron imaging (ICON)

In pursuit of deconvoluting the concentrations of different species in the electrolyte, we investigate the use of energy-resolved neutron radiography at the ICON beamline. This beamline utilizes a colder neutron spectrum by secondary moderation of the neutron beam, and slower neutrons undergo inelastic scattering events with a higher probability than thermal neutrons, allowing more variations in species cross-sections to be observed. It is also possible to perform spectral neutron imaging with a time-of-flight based technique at ICON, which is currently not possible at the NEUTRA beamline due to space limitations. Since the time-of-flight of neutrons in the flight tube is inversely proportional to the square root of their energy, the ToF-NI technique can add a fourth dimension to conventional radiography. This can provide an additional mode of contrast as neutron attenuation is a function of its energy. We anticipate that if the neutron attenuation of active species and the supporting ions have distinct energy dependency profiles, we can separate the contribution of each species from the final radiograph.

6.3.2.1. Correlating attenuation with neutron energy

The difference in relative neutron attenuation of materials enables tuning of the contrast between different species. To this end, we first performed calibration experiments with cuvettes, filled with 0.5 M solutions of TEMPO and $TEMPO^+BF_4^-$ in CD_3CN. **Figure 6.6a** shows attenuation coefficients as a function of the time of flight, where the BF_4^- attenuation coefficient is determined by subtracting the coefficient of TEMPO from $TEMPO^+BF_4^-$. Here, an increasing time-of-flight indicates a decreasing neutron energy. $TEMPO^+BF_4^-$ reaches nearly twice the cross-section of TEMPO at higher energies,

corroborating the previous observations made at the NEUTRA beamline (**Figure 6.3**) that TEMPO and BF_4^- have similar microscopic cross-sections. The linearity of the concentration with neutron attenuation was already demonstrated in the NEUTRA beamline, thus we selected only one concentration (0.5 M) corresponding to the starting concentration in the flow cell experiments.

Using the matrix operation shown in **equation (6.4)** and **Figure 6.6b**, the respective contributions of TEMPO and BF_4^- from the total neutron attenuation can be separated. For this purpose, we need to define two regions within the spectrum, the HE and LE regions. The difference in attenuation coefficients between TEMPO and BF_4^- varies as a function of neutron energy, this means that the slope of the graph in **Figure 6.6a** should be different between species, or in mathematical terms, the determinant of the microscopic cross-section matrix should not be zero. The neutron cross-sections of the solvent and the species of interest are reported for HE and LE regions in **Figure 6.6b**. The values reported here correspond to the microscopic cross-section averaged over LE and HE ranges, described in **Section 6.2.6**. Although maximum contrast is achieved around 8 ms ToF, the LE region was moved towards higher energies to prevent the excessive neutron edge effects/scattering at interfaces between gaskets observed at lower energies. Finally, the matrix operation is applied pixel-wise to the greyscale transmission image to calculate the contribution of species and a color map is applied to designate the concentrations (**Figure 6.6b**). Achieving contrast between TEMPO and $TEMPO^+$ is still not possible, but because the movement of $TEMPO^+$ between compartments is blocked by the anion exchange membrane, we can track the movement of BF_4^- and TEMPO separately during battery operation.

6.3.2.2. Deconvoluting concentrations in a flow cell

To demonstrate the potential of energy-selective and *operando* neutron imaging, a flow cell with asymmetric concentrations (0.5 M TEMPO on the CE and 0.5 M $TEMPO^+BF_4^-$ on the WE side, **Figure 6.7a**) was imaged. The electrolyte compositions are identical to the previous experiment that utilized BF_4^- as the counter-ion but we increased the electrode thickness to accommodate for the lower spatial resolution. Previous experiments carried out on the NEUTRA beamline were set up with a tilted detector to increase the spatial resolution of the images [67], resulting in a pixel size of ~6 µm to study a 630 µm thick electrode. In the ICON experiments, the ToF detection system resulted in a larger pixel size (~55 µm). Thus, to compensate for the discrepancies in spatial resolution, a thicker felt electrode (3200 µm) was employed. The cell features stacked gaskets (incompressible PTFE and compressible ePTFE) to enclose the thick felt electrode, where the interface around the ePTFE gaskets shows up in the LE image as low transmission regions (dark vertical lines in the grayscale image in **Figure 6.6b**) due to higher neutron edge effect or scattering. Nevertheless, the central regions of the incompressible gaskets (~1 mm) were large enough to define four regions of interest where the concentrations can be determined (**Figure 6.6b**), and the reported concentrations are averaged over this volume for both compartments. To track the movement of species during the operation sequence, we opted for plotting the averaged concentrations over time (**Figure 6.7c**).

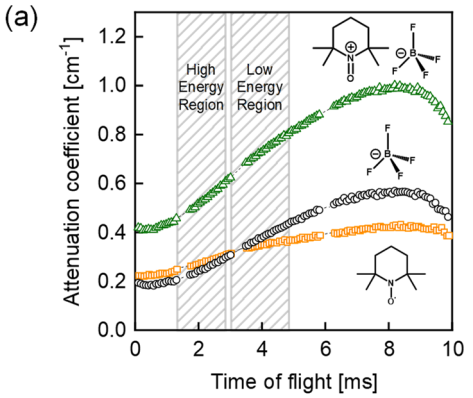

(b)

Microscopic cross sections [cm²]			C_i
Species (i)	$\sigma_{i,LE}$	$\sigma_{i,HE}$	i
TEMPO	0.34	0.28	0.5
$TEMPO^+BF_4^-$	0.72	0.53	0.5
BF_4^-	0.37	0.25	0.5

$$\begin{bmatrix} -ln(T_{LE}) \\ -ln(T_{HE}) \end{bmatrix} = \delta_{cell} \cdot \begin{bmatrix} \sigma_{BF_4^-,LE} & \sigma_{TEMPO,LE} \\ \sigma_{BF_4^-,HE} & \sigma_{TEMPO,HE} \end{bmatrix} \cdot \begin{bmatrix} C_{BF_4} \\ C_{TEMPO} \end{bmatrix} \cdot N_A$$

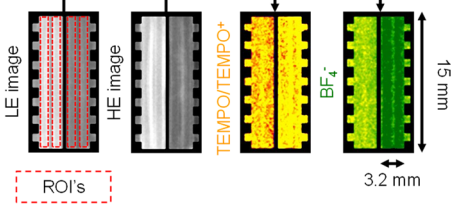

Figure 6.6: Energy selective imaging at the ICON beamline. **(a)** Energy dependency of the attenuation coefficient of TEMPO, $TEMPO^+BF_4^-$, and BF_4^- obtained from the cuvette experiments (all 0.5 M), where the time-of-flight is a function of the neutron energy. **(b)** Schematic representation of the main components in the image processing sequence for the ICON beamline experiments including the table of microscopic cross-sections, the low- and high-energy transmission images (grayscale), and deconvoluted active species and supporting ion images of the flow cell, showing the flow fields, electrodes, and membrane together with their dimensions. The transmission images are processed using the given equation to extract the concentration maps (colored images) of $TEMPO/TEMPO^+$ and BF_4^-.

The experiment starts with an OCV period of 10 min, after which the cell was polarized at an electrolyte flow rate of 21.1 mL min^{-1} followed by a reduced flow rate of 6.7 mL min^{-1} (**Figures 6.7b** and **A6.6**). From the deconvoluted concentration maps (**Figure 6.7c**), we confirm that BF_4^- is the main charge carrier and that the membrane blocks the transport of TEMPO/TEMPO, as their concentration remains relatively stable in both compartments throughout the entire electrochemical sequence. We map BF_4^- motion which is driven by the applied potential – BF_4^- migrates to the CE at negative applied potentials and to the WE at positive applied potentials (**Figure 6.7c**). When a negative potential is applied, $TEMPO^+$ reduces to TEMPO in the WE compartment while the reverse reaction occurs in the CE. Simultaneously, the concentration maps and

averaged concentrations show that BF_4^- moves through the membrane towards the CE to balance the positive charge of the generated $TEMPO^+$ species. On the other hand, applying a positive potential to the WE reverses the direction of the migration flux of the BF_4^- ions and concentrations close to the initial state of the battery (i.e., OCV) can be recovered. Moreover, the concentrations of the active species within the reactor area show larger variations for the highest flow rate (**Figure 6.7c**), induced by faster species conversion (i.e., higher current densities, **Figure 6.7b**), and greater convective electrolyte replenishing in the porous electrode. This brings the concentrations to extreme values due to the fast depletion of reactants in the electrolyte and promotes larger ionic currents.

From the capacity curves (**Figure A6.7**), we observe that after the first potential step (-0.6 V at 21.1 mL min^{-1}), 60 % of the total capacity is consumed. In the next step, after an applied potential of +0.6 V, only 45 % of the total capacity is recovered (due to the lower current at set time), which results in 15 % underutilized capacity after a full polarization cycle. At the lower flow rate (6.7 mL min^{-1}), the capacity consumed at negative applied potentials is almost fully recovered at positive applied potentials, resulting in near symmetric current magnitudes. Interestingly, we find comparatively higher currents with this reactor architecture in comparison with the reactor architecture used in the NEUTRA beamline (**Figure 6.5**). We attribute these differences to the use of a different electrode architecture (a thick felt vs. a stack of thin carbon papers) and lower compressive forces. The higher porosity, apparent permeability, and internal surface area of the felt electrode can explain the higher current densities observed in this reactor configuration.

Here, we demonstrate the potential of the ToF-NI spectral technique to isolate and visualize concentration distributions of active and supporting species in redox flow cells. Compared to the use of conventional neutron radiography, the ToF method required larger acquisition times and provided lower spatial resolution but enabled the detection of neutron energies necessary to deconvolute species concentrations. Future studies will explore the use of neutron radiography to investigate the influence of reactor components (membranes, electrodes, and flow fields) on ion transport phenomena in the battery and study the wetting behavior of the porous carbon fiber electrodes as a function of the electrode properties and fluid dynamic conditions. Future work could also explore the use of molecularly engineered redox active materials that enable deconvolution between their oxidized and reduced pairs.

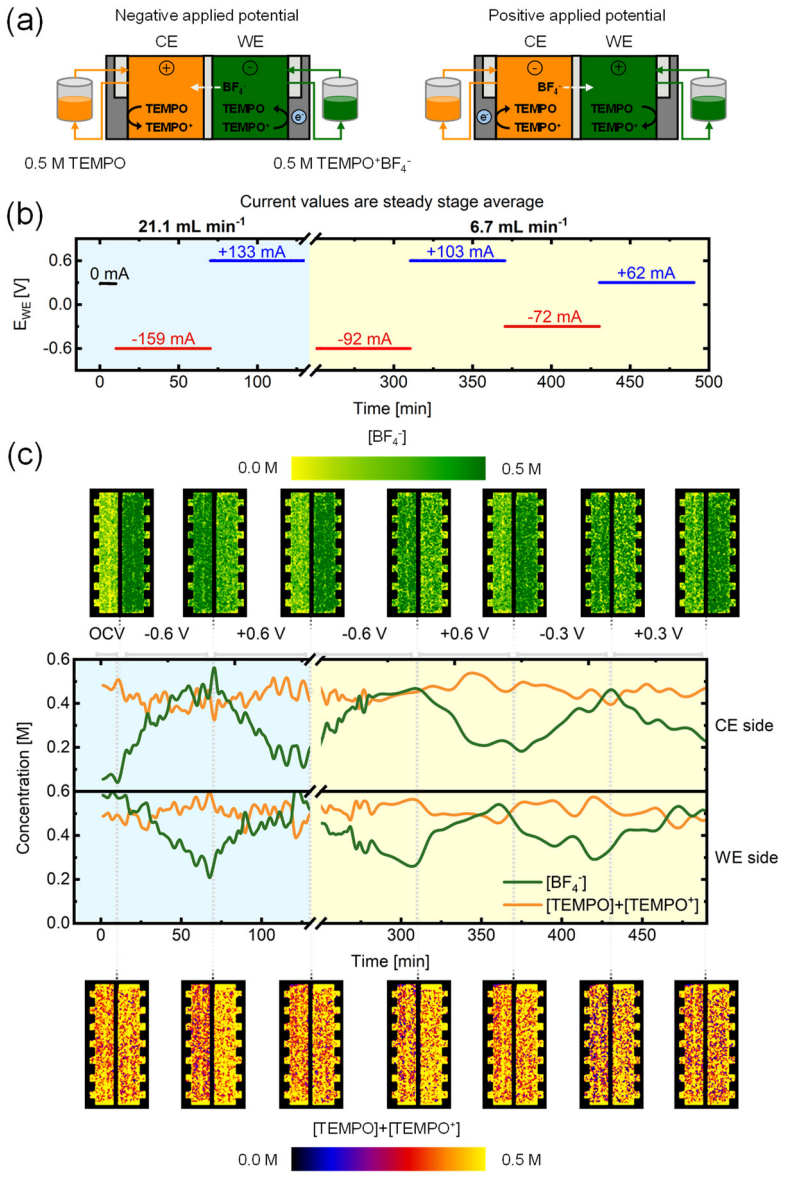

Figure 6.7: *Operando* imaging of the active species transport in the ICON beamline with the neutron attenuating BF_4^- supporting ion. **(a)** Schematic representation of the non-aqueous cell designs during charge and discharge mode, where the counter electrode (CE) corresponds to 0.5 M TEMPO and the working electrode (WE) to 0.5 M $TEMPO^+BF_4^-$. **(b)** Electrochemical sequence over time showing the applied potential steps and measured averaged current output at two inlet flow rates of 21.1 mL min^{-1} and 6.7 mL min^{-1}. **(c)** Deconvoluted active species (TEMPO/$TEMPO^+$) and BF_4^- supporting ion concentration profiles. The averaged snapshots of the cell after image processing and the concentration profiles over time are shown for various applied potential steps and flow rates: OCV, -0.6 V, and +0.6 V at 21.1 mL min^{-1} and -0.6 V, -0.6 V, -0.3 V, and +0.3 V at 6.7 mL min^{-1}, from left to right, where the OCV images are averaged over 5 images and the applied potentials averaged over 4 images.

6.4. Conclusions

We have developed a novel neutron radiography approach to quantify the concentration of species in solution during electrochemical operation in redox flow cells. Redox-active organic molecules with high hydrogen content and boron-containing supporting species were utilized as imaging probes, enabling the visualization of the different species in the electrolyte. Using a low attenuating supporting salt (KPF_6), we selectively image the motion of redox-active species (TEMPO/$TEMPO^+$) within the reactor area, while the motion of supporting ions is investigated with highly attenuating supporting species (BF_4^-). We used a tilted detector setup to achieve high spatial resolution in-plane, and successfully revealed the spatial distribution of the cumulative species concentration across the reactor thickness (i.e., perpendicular to the membrane plane) under various operating conditions. Through a series of systematic experiments, we visualized mass transport at various cell polarities – showing the selective transport of anions through a charge-selective membrane; flow rates – revealing the influence of convection on concentration profiles; and cell voltage – tracking the impact of migration in driving supporting electrolyte. To isolate the concentration of redox-active species and supporting anions, we performed energy-resolved neutron imaging with the time-of-flight technique. Taking advantage of the energy-dependency of the neutron attenuation of TEMPO/$TEMPO^+$ and BF_4^-, we obtained concentration maps of redox-active species and supporting anions. With this approach, we unambiguously tracked the motion of BF_4^- across the membrane driven by the applied voltage and found minimal transport of TEMPO/$TEMPO^+$ through the separator.

In summary, we demonstrate for the first time the use of neutron radiography to image concentrations of redox-active species and supporting salts in *operando* electrochemical flow cells. By combining macroscopic electrochemical response with microscopic concentration distributions, neutron radiography can provide valuable insights into species motion within the reactor area, and this can be used to quantify mass transport mechanisms (migration, diffusion, convection) and phenomena affecting the performance of the battery in operation (e.g., electrolyte depletion, precipitation, physical failure in RFB stacks). These insights can directly be used to compare and select optimal cell components and to aid computational efforts. We anticipate that the use of molecular engineering to design redox molecular probes with controlled molecular structure, diffusivity, and redox potential, can enable deconvolution of different oxidation states and degradation products. Although we focus on nonaqueous redox flow cells as a case study, the approach presented here can be applied to a broad range of fields involving reactive transport phenomena such as flow chemistry, organic synthesis, electrochemical separations, and electrolyzers.

6.5. References

[1] P. Albertus, J. S. Manser, S. Litzelman, *Joule*. **4**, 21–32 (2020).
[2] C. A. Hunter *et al.*, *Joule*. **5**, 2077–2101 (2021).
[3] O. J. Guerra, *Nat Energy*. **6**, 460–461 (2021).
[4] Y. Yao, J. Lei, Y. Shi, F. Ai, Y.-C. Lu, *Nat Energy*. **6**, 582–588 (2021).
[5] E. Sánchez-Díez *et al.*, *Journal of Power Sources*. **481**, 228804 (2021).
[6] P. Leung *et al.*, *RSC Adv.* **2**, 10125–10156 (2012).
[7] A. Z. Weber *et al.*, *J Appl Electrochem*. **41**, 1137–1164 (2011).
[8] M. van der Heijden, A. Forner-Cuenca, in *Encyclopedia of Energy Storage,* L.F. Cabeza, Ed. (Elsevier Inc., Oxford, ed. 2, 2022), pp. 480–499.
[9] A. Forner-Cuenca, F. R. Brushett, *Current Opinion in Electrochemistry*. **18**, 113–122 (2019).
[10] Z. Li, Y.-C. Lu, *Advanced Materials*. **32**, 2002132 (2020).
[11] C. A. Machado *et al.*, *ACS Energy Lett.* **6**, 158–176 (2021).
[12] A. Forner-Cuenca, E. E. Penn, A. M. Oliveira, F. R. Brushett, *J. Electrochem. Soc.* **166**, A2230 (2019).
[13] R. S. Kingsbury, S. Zhu, S. Flotron, O. Coronell, *ACS Appl. Mater. Interfaces*. **10**, 39745–39756 (2018).
[14] Y. Yao, J. Lei, Y. Shi, F. Ai, Y.-C. Lu, *Nat Energy*. **6**, 582–588 (2021).
[15] J. Houser, J. Clement, A. Pezeshki, M. M. Mench, *Journal of Power Sources*. **302**, 369–377 (2016).
[16] M. Messaggi *et al.*, *Applied Energy*. **228**, 1057–1070 (2018).
[17] H. R. Jiang *et al.*, *Journal of Power Sources*. **440**, 227159 (2019).
[18] P. Boillat, E. H. Lehmann, P. Trtik, M. Cochet, *Current Opinion in Electrochemistry*. **5**, 3–10 (2017).
[19] J. Eller *et al.*, *J. Electrochem. Soc.* **158**, B963–B970 (2011).
[20] B. Michalak *et al.*, *Sci Rep*. **5**, 15627 (2015).
[21] D. P. Finegan *et al.*, *Nat Commun*. **6**, 6924 (2015).
[22] A. A. Wong, M. J. Aziz, S. Rubinstein, *ECS Trans.* **77**, 153–161 (2017).
[23] R. Jervis *et al.*, *J. Phys. D: Appl. Phys.* **49**, 434002 (2016).
[24] F. Tariq *et al.*, *Sustainable Energy Fuels*. **2**, 2068–2080 (2018).
[25] K. Köble *et al.*, *Journal of Power Sources*. **492**, 229660 (2021).
[26] L. Eifert *et al.*, *ChemSusChem*. **13**, 3154–3165 (2020).
[27] Y. A. Gandomi *et al.*, *J. Electrochem. Soc.* **165**, A970–A1010 (2018).
[28] P. J. Withers *et al.*, *Nat Rev Methods Primers*. **1**, 18 (2021).
[29] J. Roth, J. Eller, F. N. Büchi, *J. Electrochem. Soc.* **159**, F449–F455 (2012).
[30] E. W. Zhao *et al.*, *Nature*. **579**, 224–228 (2020).
[31] E. W. Zhao *et al.*, *J. Am. Chem. Soc.* **143**, 1885–1895 (2021).
[32] R. J. Bellows, M. Y. Lin, M. Arif, A. K. Thompson, D. Jacobson, *J. Electrochem. Soc.* **146**, 1099–1103 (1999).
[33] P. Boillat, E. H. Lehmann, P. Trtik, M. Cochet, *Current Opinion in Electrochemistry*. **5**, 3–10 (2017).
[34] R. Mosdale, G. Gebel, M. Pineri, *Journal of Membrane Science*. **118**, 269–277 (1996).
[35] A. Forner-Cuenca *et al.*, *Adv. Mater.* **27**, 6317–6322 (2015).
[36] V. Manzi-Orezzoli *et al.*, *J. Electrochem. Soc.* **167**, 064516 (2020).
[37] P. P. Mukherjee *et al.*, *ECS Trans.* **25**, 505–512 (2009).
[38] M. A. Hickner *et al.*, *J. Electrochem. Soc.* **155**, B427 (2008).
[39] A. Forner-Cuenca *et al.*, *J. Electrochem. Soc.* **163**, F1389–F1398 (2016).
[40] J. I. S. Cho *et al.*, *Energy*. **170**, 14–21 (2019).
[41] J. Zhang *et al.*, *Electrochimica Acta*. **51**, 2715–2727 (2006).
[42] M. Siegwart *et al.*, *J. Electrochem. Soc.* **167**, 064510 (2020).
[43] D. X. Liu *et al.*, *Angew. Chem. Int. Ed.* **53**, 9498–9502 (2014).

[44] M. Lanz, E. Lehmann, R. Imhof, I. Exnar, P. Novák, *Journal of Power Sources*. **101**, 177–181 (2001).
[45] D. Goers *et al.*, *Journal of Power Sources*. **130**, 221–226 (2004).
[46] G. V. Riley, D. S. Hussey, D. Jacobson, *ECS Trans.* **25**, 75–83 (2010).
[47] C. Lee *et al.*, *Electrochimica Acta*. **279**, 91–98 (2018).
[48] O. F. Selamet *et al.*, *International Journal of Hydrogen Energy*. **38**, 5823–5835 (2013).
[49] I. Manke *et al.*, *Appl. Phys. Lett.* **90**, 214102 (2007).
[50] J. T. Clement, PhD thesis, University of Tennessee, Knoxville, TN, USA (2016).
[51] E. R. C. Ruiz *et al.*, *Materials Today Advances*, **19**, 100405 (2023).
[52] M. Strobl *et al.*, *J. Phys. D: Appl. Phys.* **42**, 243001 (2009).
[53] J. I. Wood, Pergamon Press, Oxford ; New York, 1st ed., (1982).
[54] P. Rinard, US Nuclear Regulatory Commission, Washington, D. C., (1991), pp. 357–377.
[55] Sears, V. F., *Neutron News*. **3:3**, 26–37.
[56] E. H. Lehmann, P. Vontobel, L. Wiezel, *Nondestructive Testing and Evaluation*. **16**, 191–202 (2001).
[57] P. Boillat, G. Frei, E. H. Lehmann, G. G. Scherer, A. Wokaun, *Electrochem. Solid-State Lett.* **13**, B25 (2010).
[58] A. P. Kaestner *et al.*, *Nuclear Instruments and Methods in Physics Research Section A: Accelerators, Spectrometers, Detectors and Associated Equipment*. **659**, 387–393 (2011).
[59] A. S. Tremsin, J. V. Vallerga, *Radiation Measurements*. **130**, 106228 (2020).
[60] A. S. Tremsin, J. V. Vallerga, J. B. McPhate, O. H. W. Siegmund, *J. Inst.* **9**, C05026 (2014).
[61] P. Boillat *et al.*, *Opt. Express, OE*. **26**, 15769–15784 (2018).
[62] R. S. Carter, H. Palevsky, V. W. Myers, D. J. Hughes, *Phys. Rev.* **92**, 716–721 (1953).
[63] J. D. Milshtein *et al.*, *J. Electrochem. Soc.* **164**, E3265–E3275 (2017).
[64] N. Elgrishi *et al.*, *J. Chem. Educ.* **95**, 197–206 (2018).
[65] H. Zhang, X. Li, J. Zhang, Eds., *Redox Flow Batteries: Fundamentals and Applications* (CRC Press, Boca Raton, 2017).
[66] L. Gubler, *Current Opinion in Electrochemistry*. **18**, 31–36 (2019).
[67] P. Boillat, PhD thesis, ETH Zurich (2009).

6.6. Appendix 6

A6.1. Image processing

A6.1.1. NEUTRA

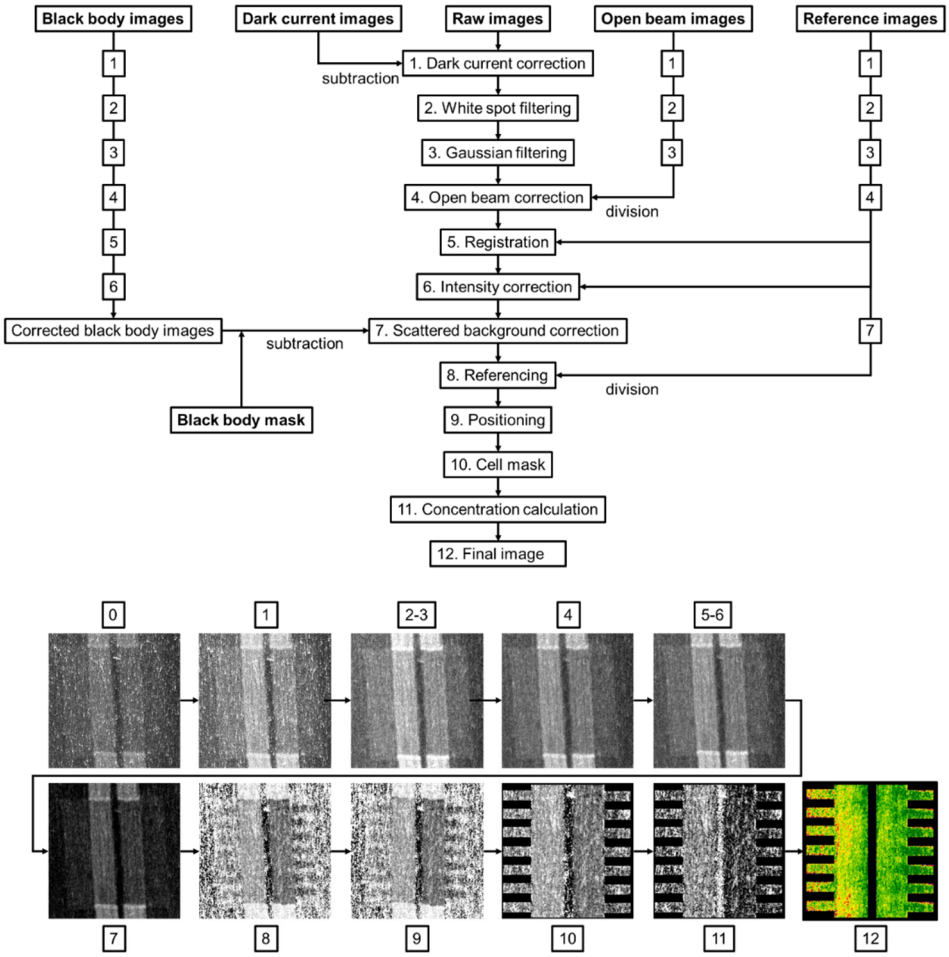

Figure A6.1: Image processing sequence for the experiments conducted at the NEUTRA beamline and the resulting images after each processing step.

A6.2. Concentration profiles at a lower flow rate

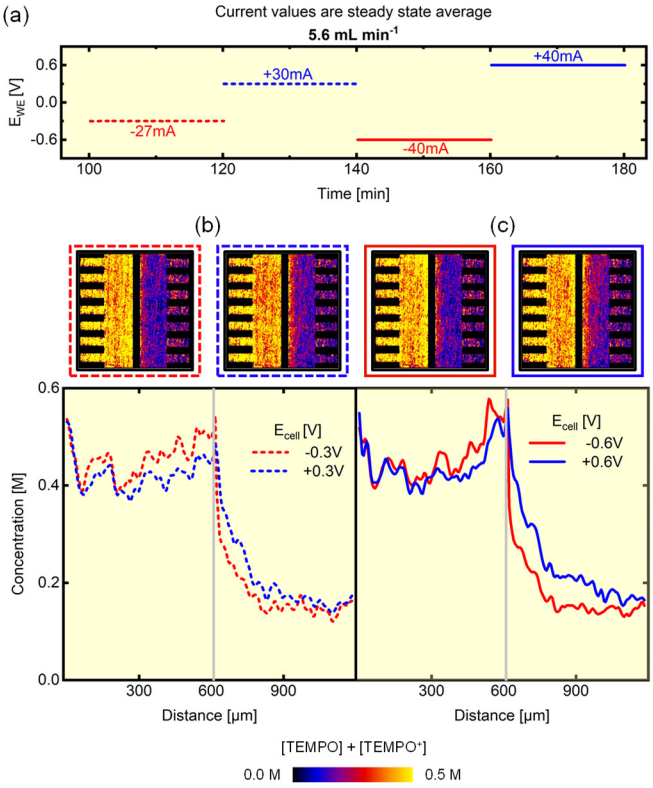

Figure A6.2: *Operando* imaging of the active species transport in the NEUTRA beamline with the low attenuating KPF_6 supporting salt at a lower flow rate. **(a)** Electrochemical sequence over time showing the applied potential steps and measured averaged current output at an inlet flow rate of 5.6 mL min^{-1}. **(b-c)** Cumulative active species (TEMPO/$TEMPO^+$) concentration profiles over the electrode thickness at an inlet flow rate of 5.6 mL min^{-1}. The averaged snapshots of the cell after image processing and the concentration profiles are shown for various applied potential steps: **(b)** -0.3 V and +0.3 V, and **(c)** -0.6 V and +0.6 V.

A6.3. Electrochemical performance

A6.3.1. NEUTRA - PF_6^- experiment

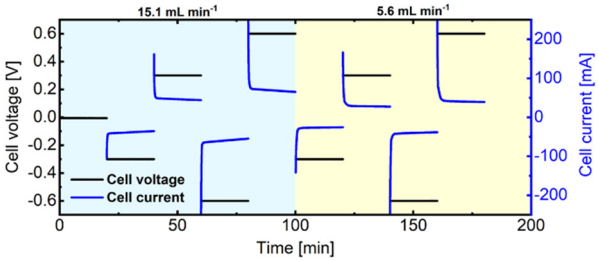

Figure A6.3: Electrochemical sequence over time showing the applied potential steps and measured current output at two inlet flow rates of 15.1 mL min^{-1} and 5.6 mL min^{-1} with the low attenuating KPF_6 supporting salt in the NEUTRA beamline.

A6.3.2. NEUTRA - BF_4^- experiment

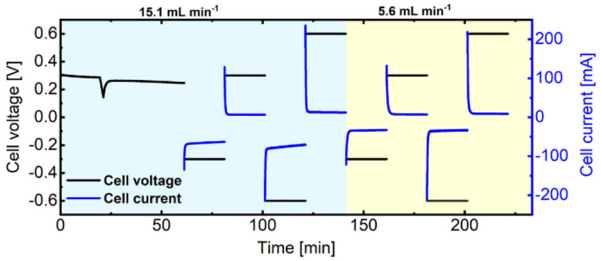

Figure A6.4: Electrochemical sequence over time showing the applied potential steps and measured current output at two inlet flow rates of 15.1 mL min^{-1} and 5.6 mL min^{-1} with the neutron attenuating BF_4^- supporting ion in the NEUTRA beamline.

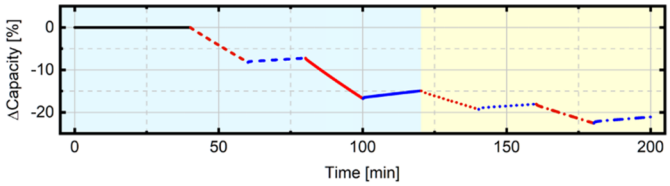

Figure A6.5: Capacity change over time for various applied potential steps and two inlet flow rates of 15.1 mL min^{-1} and 5.6 mL min^{-1} with the neutron attenuating BF_4^- supporting ion in the NEUTRA beamline.

A6.3.3. ICON - BF_4^- experiment

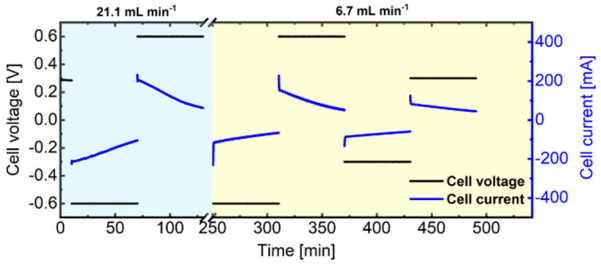

Figure A6.6: Electrochemical sequence over time showing the applied potential steps and measured current output at two inlet flow rates of 15.1 mL min^{-1} and 5.6 mL min^{-1} with the neutron attenuating BF_4^- supporting ion in the ICON beamline.

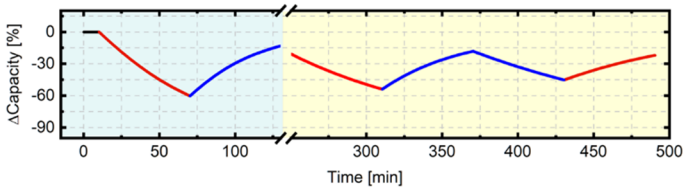

Figure A6.7: Capacity change over time for various applied potential steps and two inlet flow rates of 15.1 mL min^{-1} and 5.6 mL min^{-1} with the neutron attenuating BF_4^- supporting ion in the ICON beamline.

Chapter 7

Neutron imaging to study the influence of porous electrodes and flow fields on concentration distributions in redox flow cells

Abstract

Understanding the reactive mass transport through redox flow cells is key to enhanced reactor performance. Conventional flow cell characterization techniques rely on electrochemical diagnostics that macroscopically assess the material properties and performance but fail to resolve local performance metrics. To this end, *operando* imaging in tandem with electrochemical diagnostics can be used to provide a deeper understanding of the influence of reactor components on the coupled mass and charge transport. In this work, *operando* neutron radiography is utilized to study concentration distributions in porous electrodes for two non-aqueous electrolyte configurations. Symmetric flow cell experiments were performed to investigate the reactive mass transport in three electrodes – a carbon paper (SGL 39AA), a carbon cloth (1186 HCB AvCarb), and an in-house manufactured non-solvent induced phase-separated electrode – and with two flow field designs – parallel and interdigitated. We found that for a kinetically facile electrolyte with low ionic conductivity and with parallel flow fields, electrodes with a bimodal pore size distribution with large voids in the though-plane direction augment the current output by a higher capacity use. Moreover, a greater current output is sustained by the convective transport with interdigitated flow fields at a fixed applied potential and flow rate compared to parallel designs. Finally, we show that secondary phenomena, including salt precipitation and underutilization of the flow field channels, can be tracked with neutron radiography. Hence, neutron radiography is a promising approach to investigate the role of the individual reactor components by studying the concentration distributions during operation.

This chapter is in preparation for submission as:

M. van der Heijden, R.R. Jacquemond, E.B. Boz, P. Boillat, A. Forner-Cuenca, Neutron imaging to study the influence of porous electrodes and flow fields on concentration distributions in redox flow cells (2023).

7.1. Introduction

Redox flow batteries (RFBs) are rechargeable electrochemical systems with the potential for large-scale stationary energy storage due to their design flexibility which enables scaling the power and energy independently, simplicity in manufacturability, and system adaptability (i.e., different electrolytes and operating conditions) [1–5]. However, power losses (overpotentials) in the battery limit the system efficiency and increase the costs, hampering market penetration [6, 7]. One strategy to increase power density is to design reactors and materials, as well as to select operating conditions, that improve reactive mass transport in the electrochemical cell [5]. The electrolyte distribution through the reactor is mainly governed by the flow fields and electrodes [8, 9], where the porous electrodes dictate the electrolyte distribution through their structure, provide active surfaces for the electrochemical reactions, cushion mechanical compression, and facilitate mass, charge, and heat transport [10, 11]; whereas the flow fields distribute the electrolyte to the porous electrodes, and thus define the pressure drop and electrode utilization [11–14]. Conventional porous electrodes used in RFBs are fibrous mats assembled in coherent structures such as cloths, papers, and felts, designed as gas diffusion electrodes for polymer electrolyte fuel cells [3, 9, 10], but remain unoptimized for all-liquid transport. Hence, research is conducted to design porous electrodes tailored for application in RFBs [9, 15–25]. In parallel, to design tailored electrodes, the structure-function-performance relationships, i.e., the interplay between transport and reactions, must be investigated and well-understood. To this end, there is a growing interest in investigating the performance of conventional porous electrodes depending on their application [3, 8, 13, 26–32] as the flow field design, electrolyte chemistry, and operating conditions can strongly impact the electrode performance. For example, in literature, it was found that the cloth electrode shows improved performance compared to paper or felt electrodes for a kinetically facile redox couple and a flow-through flow configuration [3]. Muñoz *et al.* supported this claim; however, they also observed that the paper electrode is more beneficial in combination with interdigitated flow fields compared to the cloth electrode [12], showing the need for electrode design depending on the specific reactor architecture. Hence, understanding the flow field-electrode interplay is crucial in designing cost-competitive RFBs by augmenting performance and efficiency.

Conventional techniques to evaluate the performance of the electrochemical cell and its components rely on electrochemical diagnostic tools, such as polarization curves and electrochemical impedance spectroscopy, and *ex-situ* characterization methods, e.g., scanning electron microscopy and X-ray photoelectron spectroscopy [11]. Despite being effective in investigating material properties and performance, local *operando* performance metrics, such as concentration distributions through the reactor, are complex to resolve, obfuscating the deeper understanding of the influence of the reactor components on the coupled mass and charge transport. Hence, locally resolved characterization methods are essential to correlate the material and reactor component properties to the battery performance. One promising route is the combination of *operando* imaging diagnostics, such as X-ray tomographic microscopy [33–36], fluorescence/confocal imaging [37], magnetic resonance imaging [38, 39], nuclear magnetic resonance imaging [40, 41], and neutron imaging [42, 43], with conventional electrochemical tools. Neutron imaging is of special interest as it enables reactor-level, long-duration, and non-invasive imaging of the electrochemical cell with no or minimal reactor modifications [42]. Utilizing the advantage of neutrons that only interact with the nuclei

(not with the electron cloud), a high penetration depth can be reached even through high atomic weight elements. Even though the distribution of mass attenuation coefficients of neutrons across the periodic table does not follow a predictable trajectory, the relatively high attenuation of hydrogen atoms [44, 45] makes neutron imaging a suitable technique for numerous electrochemical technologies. Combined with the high attenuation of boron, which is frequently used in supporting salts in the BF_4^- form, this technique is suitable to study non-aqueous RFBs (NAqRFBs) with organic redox molecules. Moreover, neutron radiography allows *operando* imaging of dissolved species within porous electrodes and flow fields as contrast can be achieved between liquid, gas, and solid phases [46]. The main drawback is however that the attenuation of the cell components needs to be minimized (i.e., low hydrogen content materials) and more expensive deuterated solvents should be used to study the active species in the reactor. Nevertheless, neutron imaging on NAqRFBs allows the study of porous electrodes, membranes, and flow fields by utilizing the contrast between redox-active molecules, supporting ions/salts, solvent, gas, and reactor components [43].

Although neutron imaging has been applied to the field of electrochemistry by imaging *operando* fuel cells [47–55], lithium-ion batteries [56–59], electrolyzers [60, 61], and alkaline batteries [62], the application to RFBs is limited. Research efforts on neutron imaging for RFBs include the work of Clement *et al.,* who used neutron radiography to study unwanted side reactions in an operating vanadium RFB. They correlated the gas formation to the operating conditions and electrode material properties and observed that by using an elevated charging voltage sweep, the electrodes can be electrochemically treated to decrease the gas formation rates [42]. Furthermore, in our previous works on neutron radiography for RFBs [43, 63], we revealed concentration distributions and reactive transport phenomena in NAqRFBs [43], we correlated electrolyte infiltration to accessible surface area in porous electrodes, and we studied the influence of membrane types on transport phenomena in NAqRFBs [63]. Yet, the *operando* visualization of transport phenomena and concentration distributions through microstructurally-diverse porous electrodes and flow field geometries with minimal cell modifications remains underexplored; yet can aid in the optimization of these cell components for efficient battery operation.

In this work, we study reactive mass transport in redox flow cells by imaging concentration profiles across the cell during operation. We investigate the role of three porous electrode types, a paper (SGL 39AA), woven (1186 HCB AvCarb Cloth), and an in-house manufactured non-solvent induced phase-separated (NIPS) electrode, and two flow field geometries, a parallel (PFF) and an interdigitated flow field (IDFF), using neutron radiography in *operando* NAqRFBs (**Figures 7.1a** and **d**). Non-aqueous electrolytes allow good contrast with neutron imaging and have well-defined properties (low surface tension and facile kinetics [2, 7, 64–66]). Additionally, they offer an interesting option for RFBs because of their earth-abundant elements and larger electrochemical stability windows (as compared to aqueous electrolytes); however, they have a low ionic conductivity [32]. In this work, two non-aqueous electrolyte combinations are studied, one with a low attenuating supporting salt (**Figure 7.1b**) and one with a highly attenuating supporting ion (**Figure 7.1c**), to track the transport of redox molecules and that of the combined transport of redox molecules and supporting ions, respectively, through the porous electrodes. Moreover, we simultaneously perform polarization experiments to probe the effect of the potential and electrolyte flow rate on the concentration distribution and reactor performance for the distinct electrode structures and flow field designs. This

work shows the potential of advanced imaging techniques to gain a deeper understanding of individual reactor components during operation, such as porous electrodes and flow fields, which could speed up the optimization of these components to make electrochemical technologies, such as NAqRFBs, more efficient and cost-competitive.

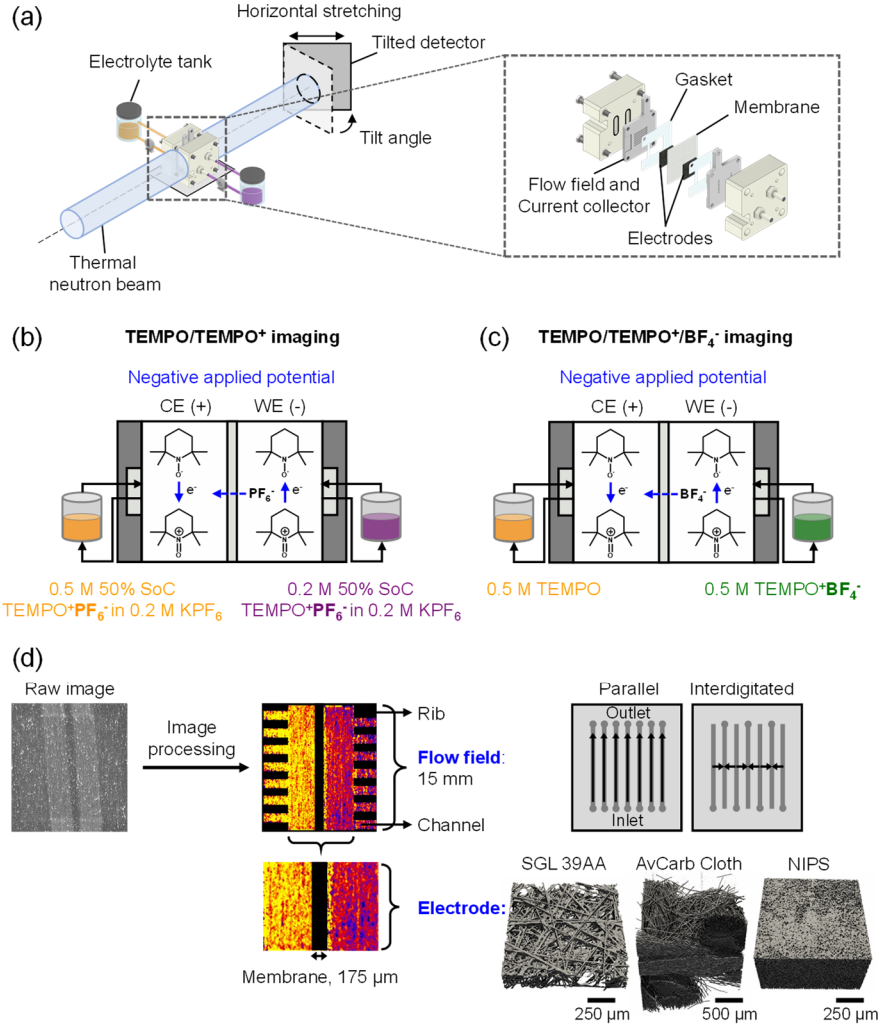

Figure 7.1: Schematic representations of **(a)** the neutron imaging set-up to obtain a cumulative concentration profile of the active species and supporting ions, together with the flow cell design and cell components, and **(b-c)** the non-aqueous cell design with the chemical structures of the active species (TEMPO/TEMPO$^+$), shown for a negative applied potential, with the different electrolyte tank compositions used in this study: **(b)** with on the counter electrode 0.5 M TEMPO/TEMPO$^+$PF$_6^-$ at 50% state-of-charge in 0.2 M KPF$_6$ and at the working electrode 0.2 M TEMPO/TEMPO$^+$PF$_6^-$ at 50% state-of-charge in 0.2 M KPF$_6$, and **(c)** with on the counter electrode 0.5 M TEMPO and at the working electrode 0.5 M TEMPO$^+$BF$_4^-$. **(d)** Simplified representation of the image processing steps from raw to processed image, where the final image shows the flow fields, electrodes, and porous separator (Daramic 175), together with the flow field types used in this study: parallel and interdigitated, and the X-ray tomographic images of the electrode types used: SGL 39AA, AvCarb Cloth, and an in-house manufactured NIPS electrode.

7.2. Materials and methods

7.2.1. Electrode structure and material properties

Two commercial carbon fiber-based porous electrodes were investigated in this study: the randomly-organized paper electrode with binder Sigracet 39AA (SGL 39AA, Fuel Cell Store, 280 µm, 630 µm compressed thickness, 89 % porosity, and 85 % compressed porosity), and the highly ordered woven electrode 1186 HCB Cloth (AvCarb, 1200 µm, 630 µm compressed thickness, 82 % porosity [27], and 66 % compressed porosity) with a 2 x 2 basket wave. Furthermore, an in-house manufactured NIPS electrode (600 µm, 530 µm compressed thickness, 87 % porosity, and 85 % compressed porosity) was additionally studied. NIPS electrodes are non-fibrous porous electrodes with interconnected pore networks that feature good performance in convection-driven flow cells. They offer a wide variety of microstructures, with a controlled bimodal pore size distribution (PSD) with macrovoids or with a porosity gradient, depending on manufacturing conditions, and are fabricated using a facile manufacturing process [15, 24, 25].

The porous electrodes were scanned using a laboratory micro-CT (Scanco Medical µCT 100 cabinet microCT scanner, holder type U50822 with a diameter of 9 mm and a height of 78 mm) at an isotropic resolution of 3.3 µm/voxel. The scans were conducted with a peak potential of 55 kVp, a current of 72 µA, 4 W, and a 0.1 mm aluminum filter. Between 433 - 1234 projection images were taken of the electrodes over 360 degrees. Thereafter, the gray-scale X-ray tomographic microscopy images were processed using ImageJ by applying a two-dimensional median filter with a radius of 2.0 pixels to reduce the noise in the images, and a K-means cluster segmentation filter to assign each voxel to either the solid or void phase.

7.2.2. Electrolyte preparation

2,2,6,6-Tetramethylpiperidin-1-yl)oxyl (TEMPO, Sigma Aldrich, 98 %) was converted to the oxidized form by chemical oxidation with nitrosonium salts: nitrosonium hexafluorophosphate ($NOPF_6$, Thermo Scientific, 95 %) or nitrosonium tetrafluoroborate ($NOBF_4$, Thermo Scientific, 98 %), inside a nitrogen-filled glove box (MBraun, LABstar, $O_2 < 1$ ppm, $H_2O < 1$ ppm). 1.1 molar equivalents of the nitrosonium salt (15.42 g $NOPF_6$ or 10.29 g $NOBF_4$) were slowly added over 2 hours to TEMPO (12.52 g), all dissolved in acetonitrile (CH_3CN, Sigma Aldrich, ≥ 99.9 %), to prevent NO_x build-up [67]. The acetonitrile was subsequently evaporated using a rotary evaporator (40 °C, gradual decrease from atmospheric pressure to vacuum) to obtain the $TEMPO^+PF_6^-$ or $TEMPO^+BF_4^-$ salts. Solutions of 20 mL were prepared for the two experimental configurations (**Figures 7.1b** and **c**). For the experiments with the potassium hexafluorophosphate salt (KPF_6, Thermo Scientific, 99 %), 50 % state-of-charge (SoC) solutions were prepared with different concentrations of TEMPO species (0.5 M and 0.2 M TEMPO/$TEMPO^+PF_6^-$) in 0.2 M KPF_6 dissolved in deuterated acetonitrile-d_3 (CD_3CN, Zeochem AG, 99.8 %D), to minimize the attenuation of the solvent on the overall transmission as deuterium has a 10 times lower cross-section compared to hydrogen (at 2200 m s^{-1} neutron velocity) [68]. For the experiments using the BF_4^- supporting ions, solutions of 0.5 M TEMPO and 0.5 M $TEMPO^+BF_4^-$ dissolved in acetonitrile-d_3 were prepared.

7.2.3. Neutron radiography

The neutron radiography experiments were conducted at the NEUTRA beamline at the Spallation Neutron Source facility of the Paul Scherrer Institute in Switzerland. The NEUTRA beamline operates with thermal neutrons that were emitted from a lead spallation target upon interaction with a proton beam (590 MeV energy, 1.5 mA proton current) and subsequently moderated by heavy water to reach thermal velocities (25 meV) [69]. The NEUTRA beamline was equipped with an in-plane imaging set-up with a tilted CCD detector to produce a stretched image in the horizontal transverse direction with respect to the incident beam (**Figure 7.1a**), allowing a higher spatial resolution across the flow field-electrode-separator domain [70]. This resulted in a pixel size of 6 µm in this domain, translating to an effective resolution of 20 µm by considering the beam divergence and blurring of the detector. The attenuated neutrons were captured by a scintillator screen (10 µm thick, Gd_2O_2S:Tb), converted to visible light, and confined by the charge-coupled device camera detector (Andor, 30 s exposure time). The imaging configuration allows us to resolve the concentration distribution locally through the electrode thickness (**Figure 7.1d**) and provides a deeper understanding of the coupled mass transport phenomena (reaction, convection, diffusion, and migration) which is unattainable using conventional characterization methods.

7.2.4. Calibration experiments

Ex-situ cuvette calibration measurements were performed to obtain the attenuation coefficients of various electrolyte solutions to quantify the total concentration in the electrochemical cells. The attenuation coefficients, i.e., the attenuation of the neutron beam by the sample, were obtained with the Lambert-Beer law [46]:

$$T = e^{-\sigma_i n_i \delta} \tag{7.1}$$

where T is the transmitted intensity [-] corrected for the attenuation of an empty cuvette, σ_i the conventional microscopic cross-section [m^2], n_i the number density of species i [m^{-3}] which is a function of the concentration of species i (C_i) [mol m^{-3}] and Avogadro's number [mol^{-1}] (N_A, 6.02 x 10^{23} mol^{-1}) by $C_i = n_i/N_A$, and δ the sample thickness [m] which was 1 cm for the cuvettes and $\delta = L_e \varepsilon_e$ for the flow cell experiments, with L_e being the electrode width (17 mm) [m] and ε_e the electrode porosity at the applied compression [-]. The cuvette calibration measurements were performed to obtain the microscopic cross-sections for solutions of CD_3CN (solvent reference), 0.2 M KPF_6 (supporting electrolyte), and solutions of varying molarities (0.1, 0.2, 0.3, 0.4, and 0.5 M) of TEMPO, $TEMPO^+PF_6^-$, and $TEMPO^+BF_4^-$ to additionally verify the linearity between the concentration and neutron attenuation, all dissolved in CD_3CN. An extensive discussion of the calibration experiments is provided in our previous work [43]. Where we showed that the macroscopic cross-sections of TEMPO and $TEMPO^+PF_6^-$ in acetonitrile-d_3 are similar, that KPF_6 has a negligible neutron attenuation compared to acetonitrile-d_3, and that the macroscopic cross-section of $TEMPO^+BF_4^-$ is roughly double that of TEMPO.

7.2.5. Flow cell configuration

The flow cell experiments were performed using a laboratory-scale flow cell platform [3, 71, 72], and the cell was mounted on a robotized platform 1-3 mm in front of the neutron detector. The flow cell was slightly modified without impacting the electrolyte transport through the cell (grooved flow fields and gaskets around the active area, see **Figure 7.1a**) to enhance the sensitivity by minimizing the cell part attenuation with the neutron beam. The electrolyte solutions were pumped through the flow cell using a Masterflex L/S® Easy-Load® II peristaltic pump and LS-14 tubing, where the cell in- and outlets were connected to two separate solution reservoirs of 20 mL. The flow cells were custom-made with machined polypropylene (McMaster-Carr) flow diffusers and graphite current collectors (G347B graphite, 3.18 mm thick, MWI, Inc.), milled with the desired flow field design: parallel (seven 16 x 1 x 0.5 mm^3 channels parallel to the electrolyte flow that all function as inlet- and outlet channel) or interdigitated (seven 16 x 1 x 0.5 mm^3 channels parallel to the electrolyte flow, of which four inlet- and three outlet channels) to supply the electrolyte solutions to the porous electrode (**Figure 7.1d**). To compare the three electrodes in the neutron imaging set-up, a trade-off between the electrode thicknesses and compression rate was made, resulting in the stacking of three paper electrodes, one highly compressed cloth electrode resulting in a lower porosity, and thinner gaskets for the NIPS electrode. The electrodes with a geometric area of 2.55 cm^2 were confined within incompressible polytetrafluorethylene gaskets (ERIKS, 210 µm and 110 µm). To separate both half-cells, a Daramic 175 (SLI Flatsheet Membrane, 175 µm) porous separator was used and the cell was tightened to 2 N m with a torque-controlled wrench.

To compare the flow cell performance between the different electrodes, the electrolyte flow rate was controlled and kept fairly constant. The evaluated flow rates were 15.3 and 5.1 mL min^{-1} for the paper, 15.3, 5.1, 45.9, and 1.7 mL min^{-1} for the cloth, and 12.8 and 4.5 mL min^{-1} for the NIPS electrode, performed in the given order (from high to low flow rate to remove residual gas bubbles and to enhance electrode wetting). Furthermore, the two flow field designs, PFF and IDFF, were investigated at a constant electrolyte flow rate (15.3 and 5.1 mL min^{-1}) instead of at a constant electrolyte velocity, where the electrolyte velocity can be obtained with **equation (7.2)** for the PFF (7.3, 2.4, 21.9, and 0.8 cm s^{-1} in the channels) and with **equation (7.3)** for the IDFF (0.42 and 0.14 cm s^{-1} in the electrode), shown for both the electrolyte velocity in the channel and in the electrode [26, 28].

$$v_{PFF,ch} = \frac{Q}{N_{ch} W_{ch} D_{ch}}, v_{PFF,e} \approx 0 \tag{7.2}$$

$$v_{IDFF,ch} = \frac{Q}{N_{ch,in} W_{ch} D_{ch}}, v_{IDFF,e} = \frac{Q}{(N_{ch}-1) L_{ch} L_e} \tag{7.3}$$

With v being the electrolyte velocity [m s^{-1}] with the PFF or IDFF in the flow channel or the electrode, Q the electrolyte flow rate [m^3 s^{-1}], N_{ch} the total number of channels in the flow field configuration (7 channels for the PFF and IDFF) [-], $N_{ch,in}$ the number of inlet channels (4 channels for the IDFF) [-], W_{ch} the channel width (1 x 10^{-3} m) [m], D_{ch} the channel depth (5 x 10^{-4} m) [m], L_{ch} the channel length (1.6 x 10^{-2} m) [m], and L_e the compressed electrode thickness (6.3 x 10^{-4} m or 5.3 x 10^{-4} m) [m].

7.2.6. Electrochemical performance

The electrochemical measurements were performed with a Biologic VSP-3e potentiostat. To obtain the final concentration distributions through the reactor, subtractive imaging was used to correct e.g., background effects. To this end, three sets of flow cell images were required: an empty cell without electrolyte solution, a "solvent-only" reference cell where the cell was filled with a 0.2 M KPF_6 in acetonitrile-d_3 solution, and a cell with the electrolyte solution of interest containing either the electrolyte with the low attenuating salt or the highly attenuating supporting ion. All measurements were performed in the same cell by filling and emptying the cell with different solutions.

For the electrochemical cells with the electrolyte of interest, the experimental procedure started with measuring the open circuit voltage (OCV) to monitor species diffusion between the half-cells for 20 min for the KPF_6 supporting salt experiments or for 1 hour for the BF_4^- supporting ion experiments. The OCV experiments were performed at 15.1 mL min^{-1} for all experiments with an exception for the NIPS electrode (12.8 mL min^{-1}). Then, the electrochemical sequence was performed by successively applying -0.3 V, +0.3 V, -0.6 V, and +0.6 V for 20 min at each potential step for each investigated flow rate, resulting in a total electrochemical protocol of 180 - 220 min for the paper electrode for both the PFF and IDFF (**Figure A7.6** and **Figure A7.9**, respectively). The NIPS electrode was subject to the same electrochemical protocol; however, due to beam shutdown during the BF_4^- supporting ion experiment at ~90 minutes, the -0.3 V and +0.3 V images are missing at 4.5 mL min^{-1}, as only the -0.6 V and +0.6 V sequences for both flow rates were repeated (**Figure A7.1c** and **Figure A7.3c**). Additionally, there was a beam shutdown for the IDFF, resulting in a time jump of 40 min between minutes 100 - 140 in the KPF_6 experiment (**Figure A7.6b**). Finally, the cloth electrode (**Figure A7.1b** and **Figure A7.3b**) was investigated for two additional flow rates for which the electrochemical sequence was held at -0.6 V and +0.6 V for 20 min, resulting in an electrochemical sequence of 260 - 300 min, though they were not evaluated in this work. Neutron radiographs were collected during the entire duration of the experiments and the supporting salt and supporting ion experiments were performed on the same cell with a rinsing step in between with 0.5 M TEMPO dissolved in acetonitrile-d_3 in both half-cells (with an exception for the paper – PFF configuration).

7.2.7. Image processing

The image processing steps to obtain the final concentration distribution color maps (**Figure 7.1d**) were performed using a Jupyter Notebook script, where the transmission data of the samples was corrected for detector background effects, beam variations, changes in the sample position, interactions of the beam with other cell components, and camera noise, in a subtractive manner. To this end, five image sets were obtained (raw, black body, open beam, dark current, and reference images), where the raw images were processed in the following order: **(1)** a dark current correction with dark current images (with closed beam and optical shutters of the camera) to eliminate the electronic bias within the camera circuity. **(2)** Filtering steps, consisting of a white spot filter that corrects for white spots as a result of radiation hitting the camera using an outlier filtering approach, and a Gaussian filter that reduces the statistical noise from high-frequency photons that hit the camera. **(3)** An open beam correction using the open beam images (no sample in the beamline, which underwent image processing steps 1-2) to correct for

spatial variations in the beam intensity. **(4)** A registration step using the reference images (the electrochemical cell filled with a 0.2 M KPF_6 in acetonitrile-d_3 solution, which underwent processing steps 1-3) to account for cell movements as a result of relaxation or thermal dilation of the electrochemical cell. **(5)** Intensity correction because of beam intensity variations using the reference images. **(6)** A scattered background correction to correct for neutrons scattered by the detector and cell using the "black body" images (reference images with a steel plate with a boron-dotted grid in front of the cell, which underwent processing steps 1-5) by interpolating the intensity values between the "black bodies". **(7)** A referencing step using the reference images (that underwent image processing steps 1-3 and 6) to obtain the transmission values of only the species of interest. **(8)** Image rotation step to align the cells horizontally. **(9)** The application of a cell mask to show the region of interest (flow fields and electrodes). **(10)** Finally, a concentration calculation step was performed to obtain the concentration images of the species of interest from the final transmission values using the Lambert-Beer law (**equation (7.1)**). An extensive description of the image processing steps is provided in our previous work [43].

7.3. Results and discussion

7.3.1. Influence of the electrode structure

7.3.1.1. TEMPO/TEMPO$^+$ imaging

As described in our previous work [43], imaging of the active species, TEMPO/TEMPO$^+$, can be achieved when using the low attenuating supporting salt KPF_6. The active species movement as a result of a concentration gradient, velocity field, and voltage bias can be visualized by tracking the concentration distribution through the reactor owing to the large neutron attenuation of the hydrogen-containing TEMPO species. The cell configuration has tanks with 50 % SoC TEMPO/TEMPO$^+$ at 0.5 M concentration on the counter electrode (CE) side and 0.2 M on the working electrode (WE) side, both with 0.2 M KPF_6 for ionic conductivity and a minimal supporting salt impact on the neutron attenuation (**Figure 7.1b**). **Figure 7.2** shows the *operando* electrochemical data and concentration profiles for the three electrodes at OCV, -0.6 V, and +0.6 V for a flow rate of 5 mL min^{-1}. The images and profiles are averaged over 20 minutes for each potential point and represent a pixel average (over the electrode length and width) in the direction of the neutron beam. We plot the average concentration over the electrode thickness, from the CE to the WE. The concentration profiles were obtained using a "concentration factor" ($-\sigma_i\, n_i\, \delta$) to translate the neutron transmission to the concentration in the cell (**Section 7.2.4**). After taking the natural logarithm of the images, the images were divided by the following factors to obtain the concentration profiles through the cell: -0.891 L mol^{-1} for the paper and NIPS electrodes, and -0.686 L mol^{-1} for the cloth electrode with a lower porosity (**equation (7.1)**). Moreover, the flow fields are shown by alternating channels and ribs (black areas), and a mask was applied over the porous separator as the concentration of active species cannot be accurately determined because of the low thickness and neutron attenuation of the separator itself. Furthermore, after image processing there is still a certain degree of dynamic noise present in the images (presumably neutrons reaching the camera) and thus in the concentration profiles, as a result of imaging artifacts that are hard to correct even after the averaging step. The

electrochemical sequence and the concentration profiles at the higher flow rate and lower potentials are shown in **Section A7.1.1**.

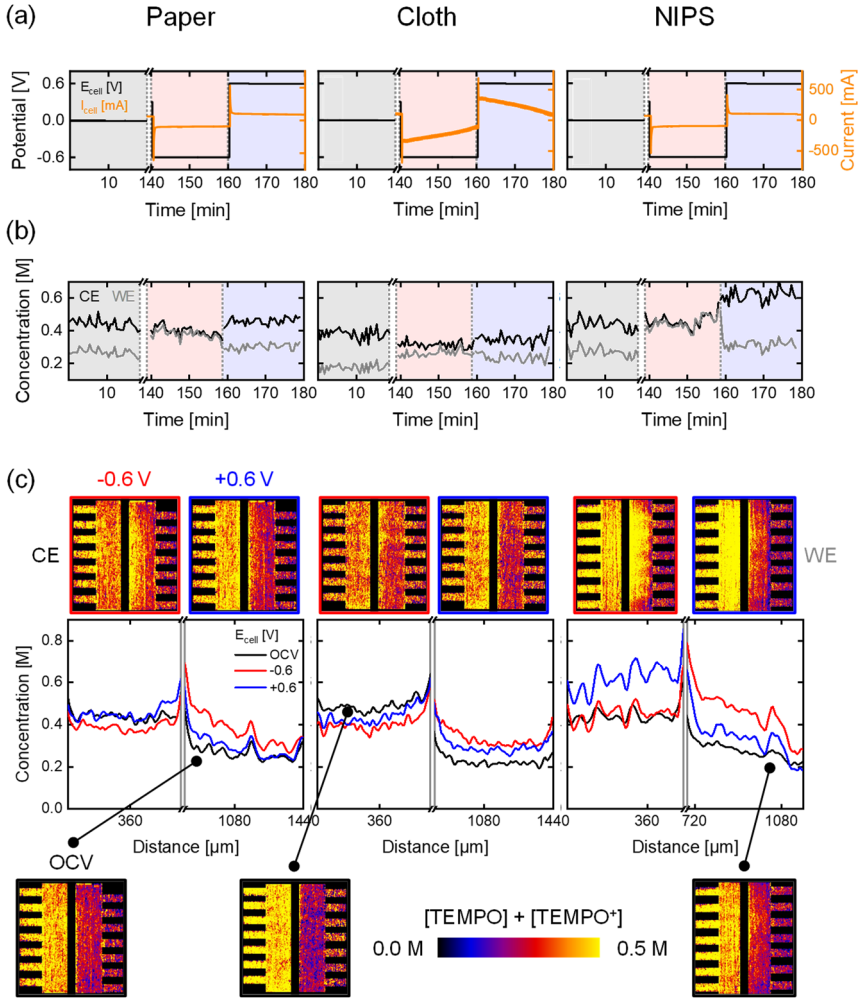

Figure 7.2: *Operando* neutron imaging of the active species transport with the low attenuating KPF_6 supporting salt for three electrode types: paper, cloth, and an in-house manufactured NIPS electrode, at an inlet flow rate of 5 mL min^{-1} and evaluated at OCV, -0.6 V, and +0.6 V. **(a)** The potential applied and current output of the electrochemical cells. **(b)** The averaged concentration profiles over time in the counter electrode (CE) and the working electrode (WE). **(c)** The cumulative active species (TEMPO/$TEMPO^+$) concentration profiles over the electrode thickness with the averaged snapshots of the cell after image processing, with on the counter electrode 0.5 M TEMPO/$TEMPO^+PF_6^-$ at 50% state-of-charge in 0.2 M KPF_6 and at the working electrode 0.2 M TEMPO/$TEMPO^+PF_6^-$ at 50% state-of-charge in 0.2 M KPF_6.

The concentration distribution or electrochemical data are notably different for the distinct electrode types (**Figure 7.2**) under similar cell conditions (flow rate, voltage bias, and electrolyte composition). The concentration distribution of the active species in the reactor is affected by a complex interplay between coupled phenomena including the

mass transport from the electrolyte tanks to the cell, from the flow channels to the electrode, and through the porous electrode and separator, together with the interconversion of TEMPO/TEMPO$^+$ species on the electrode surface. To decouple the mass transport from the redox reactions, the cells were first analyzed at OCV. At OCV, the concentrations in the electrodes are fairly constant over time and uniform over the thickness in each half-cell with concentrations equal to the tank concentrations (**Figure 7.2b**), indicating that the 20 min timeframe is too short for species diffusion through the porous separator to balance the concentration gradient [73]. After the OCV period, an alternating negative and positive voltage bias is applied, and the current output is recorded over time (**Figure 7.2a**). When a negative potential is applied at the WE, the concentration distribution through the reactor changes caused by species movement because of the electric field [74]. For all electrode systems at a negative potential, an increase in the species concentration can be observed in the WE, accompanied by a decrease in the CE. At the CE, TEMPO is oxidized to TEMPO$^+$ and as a response to the electric field migrates towards the WE. This transport is accompanied by species diffusion of the CE to the WE because of the concentration gradient [74]. When the potential is reversed, the opposite behavior is shown and the concentration profiles more or less return to their OCV profiles.

Although the electrode structures of the paper and NIPS electrodes are microscopically inherently different, the macroscopic electrochemical response with this system configuration (parallel flow field, electrolyte solution, and operating conditions) is similar as they both have a constant current output of approximately -100 mA at an applied potential of -0.6 V and +100 mA at + 0.6 V, at steady-state. Yet, the electrodes feature nuanced differences in the concentration distributions (**Figure A7.2b**). The NIPS electrode portrays starker changes in the concentration profiles with the electric field sign, and the concentration profile in the WE for the NIPS electrode shows a more pronounced slope in the thickness direction featuring a higher concentration near the separator, especially at negative potentials and low flow rates. These findings are a result of the migration of TEMPO$^+$ species as a response to the electric field [43, 63], the diffusion of TEMPO species from the concentrated to the dilute side [74], an increased reaction rate near the separator [13, 32], the low ionic conductivity and facile kinetics of the electrolyte [32], the distinct electrode microstructure, and low convection (parallel flow field) [28]. The NIPS electrode has small pores (pore size gradient in the thickness direction with the smaller pores (~1 - 5 μm in size) facing the separator for high electrochemical activity [13, 15, 24, 32] *vs.* the paper electrode with a unimodal PSD with an average pore size of 63 μm [3]) resulting in a high tortuosity, low apparent permeability (1.0 x 10^{-11} m^2 [27] *vs.* 7.4 x 10^{-11} m^2 for the paper electrode [3]), and a low effective diffusivity compared to the other electrodes. Moreover, the low ionic conductivity of the TEMPO electrolyte combined with the low hydraulic conductance in the through-plane direction because of the small pores and low electrolyte velocity, presumably result in a low penetration depth of the reaction front from the separator towards the flow field. Hence, the reactions take place closer to the separator (facile kinetics) increasing the concentration locally, causing a sloped concentration profile. Thus, even though the ECSA of the NIPS electrode (between 0.84 – 2.9 $m^2\ g^{-1}$ [25]) is greater compared to the other electrodes (0.50 $m^2\ g^{-1}$ for the paper electrode [3] and 0.028 – 0.81 $m^2\ g^{-1}$ for the cloth electrode [27]), because of the facile kinetics and low ionic conductivity of the TEMPO electrolyte, the low effective diffusivity, high tortuosity, and low hydraulic conductance of the NIPS electrode compared to the other electrodes result in the same current output as for the paper electrode.

The electrochemical performance of the cloth electrode is considerably different compared to the other two electrodes. The current output with the cloth electrode is significantly higher (an average of ±240 mA for the cloth electrode *vs.* ±100 mA for the paper electrode, at an applied potential of ±0.6 V) and decreases over time, revealing a higher species conversion. As the SoC changes over time because of the high conversion per pass in this electrode, the concentration of the to-be-converted species (TEMPO or $TEMPO^+$) decreases over time in the reactor, impacting the reaction rate and thus resulting in a reduction in current over time (following the Butler-Volmer equation [11]) [73]. The higher reaction rate results in that the cloth electrode has a superior performance compared to the other two investigated electrodes for the specific system configuration (electrolyte with fast kinetics, low ionic conductivity, and with the PFF). The weave structure of the cloth electrode ensures a bimodal PSD (pore diameters centered at *ca.* 20 µm and 100 µm with pores spanning 5 - 500 µm [27]) with large voids in the through-plane direction (high through-plane permeability, low tortuosity (1.15 – 1.35), and low apparent Forchheimer coefficient (1.2×10^3 m^{-1}) [27]) between the fiber bundles, which enhances the hydraulic conductance. Whereas the small pores between the individual fibers ensure small diffusion lengths to the electrode surface compared to paper electrodes [3, 27]. Furthermore, when analyzing the concentration profiles through the reactor, small differences can be observed when comparing the cloth and the paper electrode as the cloth electrode features more uniform profiles in the thickness direction (i.e., with an insignificant slope **Figure A7.2a**). Furthermore, the concentration changes in the CE and WE are smaller for the cloth electrode over time for all flow rates and applied potentials (**Figure A7.1b**). Hence, this suggests a deeper penetration depth of the reaction front from the separator towards the flow field in the cloth electrode due to the large through-plane void segments (high effective diffusivity and high hydraulic conductance) [75, 76]. Thus, the presumed enhanced through-plane hydraulic conductance of the cloth electrode compared to the other electrodes could cause the high current output for the TEMPO electrolyte with low ionic conductivity.

The concentration variations between the cloth and paper electrodes are minor in comparison with the significant differences in the macroscopic electrochemical output of the cells. Thus, whereas for the NIPS electrode the macroscopic trends are comparable to those of the paper electrode while the electrodes portray distinct behavior based on their concentration distributions, the opposite is observed when comparing the paper and cloth electrodes. Hence, local imaging diagnostics (e.g., fluorescence/confocal microscopy [37]) are of interest to study local microstructural effects (diffusion boundary layers, local reaction rates, local electrolyte velocities) in depth to explain the significant differences at the reactor level that cannot solely be explained by the concentration distributions obtained in this work. By combining the *operando* electrochemical performance with *operando* neutron radiography, the current output can be linked to local concentration distributions in the reactor area depending on the operation conditions. In this work, we show that by tracking the cumulative TEMPO/$TEMPO^+$ movement, a bimodal PSD with large through-plane voids with a low tortuosity (and thus a high effective diffusivity) is beneficial for PFF configurations as the large voids improve through-plane electrolyte transport and thus warrant high current densities with a kinetically facile electrolyte with low ionic conductivity.

7.3.1.2. TEMPO/TEMPO$^+$/BF_4^- imaging

In this section, the cumulative imaging of TEMPO/TEMPO$^+BF_4^-$ using the highly attenuating supporting ion BF_4^- is discussed. With the electrolyte configuration consisting of 0.5 M TEMPO at the CE and 0.5 M TEMPO$^+BF_4^-$ at the WE (**Figure 7.1c**), the movement of the counter-ion BF_4^- can also be studied. In our previous work [43], this configuration made it possible to track the counter-ion movement through the anion exchange membrane; however, in this work a porous separator was used, permitting the transport of all species between the half-cells to a certain extent. The *operando* electrochemical data and concentration profiles for the three electrodes at OCV, -0.6 V, and +0.6 V for a flow rate of 5 mL min^{-1} are visualized in **Figure 7.3** and the electrochemical sequence and concentration profiles at the higher flow rate and lower potentials are shown in **Section A7.1.2**, together with the capacity data.

At the start of the OCV, there is a potential difference between both half-cells because of the 0 % and 100 % SoCs of the tanks (different tank configurations were used for the low-attenuating supporting salt experiments). Over time, the OCV decreases because of electrolyte mixing between the compartments as a result of species diffusion through the separator [73], yet the time frame is not long enough to balance the concentration gradients. When a negative potential is applied, TEMPO is oxidized to TEMPO$^+$ and as a response to the electric field migrates towards the WE, creating a concentration gradient for the TEMPO species, upon which TEMPO is expected to diffuse towards the CE through the porous separator. The BF_4^- on the other hand, migrates towards the CE because of the electric field and to support the TEMPO oxidation reaction, resulting in an overall increase in attenuation in the CE and a decrease in the WE [74]. When a positive potential is applied, the opposite behavior is revealed, and the concentration profiles roughly return to their OCV profiles. Before analyzing the differences between the three electrodes it must be mentioned that the CE in the configuration with the paper electrode cannot be analyzed quantitatively because of significant salt precipitation, affecting the neutron attenuation with the electrolyte. The salt precipitation is a result of not rinsing the cells between the KPF_6 supporting salt and BF_4^- counter ion experiments, as the BF_4^- ions precipitate when in contact with K^+ ions due to the low solubility of KBF_4 in acetonitrile [77]. Therefore, the other experiments were performed with a rinsing step in between (with a 0.5 M TEMPO solution).

The electrochemical output for the paper and NIPS electrodes is again similar (~±75 mA at ±0.6 V). Yet, nuanced differences can be observed in the concentration distributions where the NIPS electrode shows a greater concentration slope in the thickness direction towards the separator (**Figure A7.4b**). The similarities in the macroscopic response are supported by the capacity curves (**Figure A7.5**), showing that for both electrodes only ~10 % is converted at 5 mL min^{-1} and -0.6 V in 20 min. The capacity for the cloth electrode is however different with a 35 % conversion rate. An average current output of -244 mA at -0.6 V translates to 3 mmol reacted in the time-frame of 20 min of the total 5 mmol available per half-cell, explaining the drop in current over time at a constant applied potential [73] as shown in **Figures 7.2a** and **7.3a**. Furthermore, the capacity is not fully restored in the cloth electrode when the electric field is reversed, this can also be remarked from the concentration profiles in the CE and WE as they are not returning to the OCV profiles for the cloth electrode. As we fix the potential and time, but not the current, the capacity cannot fully be restored because of the asymmetry in the tanks (with 0 % and 100 % SoC starting concentrations). The current

study shows that using neutron radiography the capacity curves can be correlated to the concentration profiles, species cross-over can be tracked, and secondary phenomena can be detected.

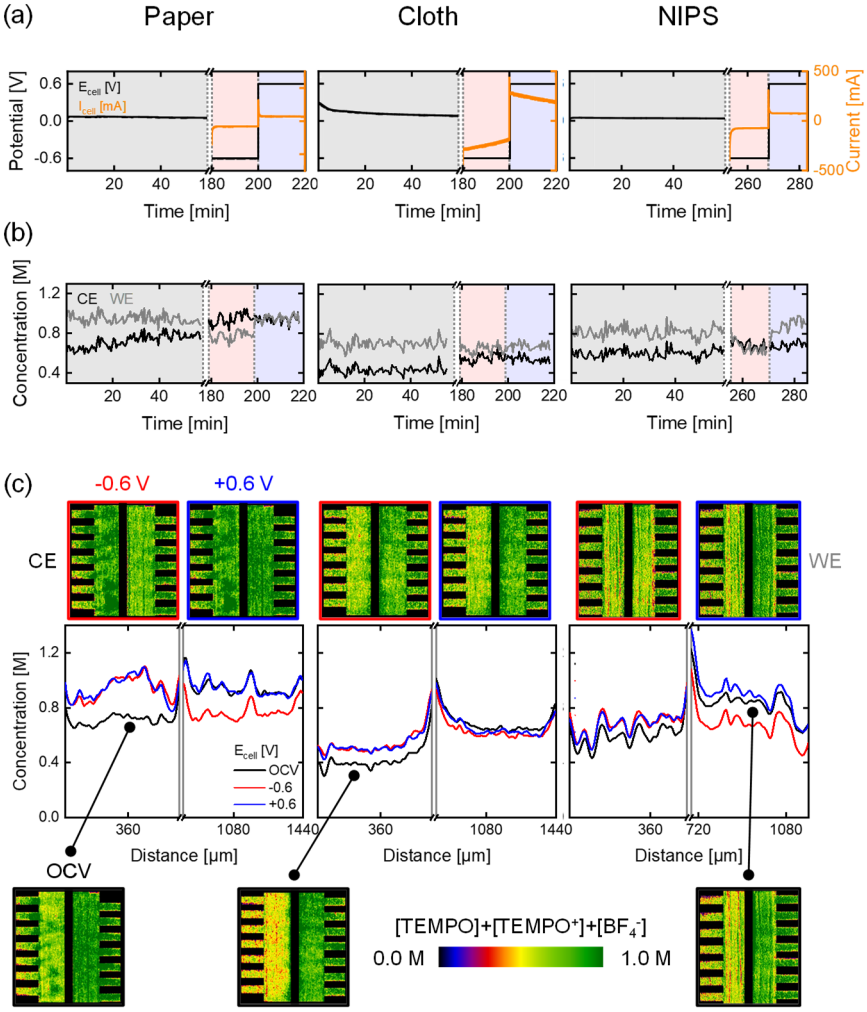

Figure 7.3: *Operando* neutron imaging of the active species transport with the attenuating $BF4^-$ supporting ion for three electrode types: paper, cloth, and an in-house manufactured NIPS electrode, at an inlet flow rate of 5 mL min^{-1} and evaluated at OCV, -0.6 V, and +0.6 V. **(a)** The potential applied and current output of the electrochemical cells. **(b)** The averaged concentration profiles over time in the counter electrode (CE) and the working electrode (WE). **(c)** The cumulative active species (TEMPO/$TEMPO^+$) and BF_4^- supporting ion concentration profiles over the electrode thickness with the averaged snapshots of the cell after image processing, with on the counter electrode 0.5 M TEMPO and at the working electrode 0.5 M $TEMPO^+BF_4^-$.

7.3.2. Impact of the flow field design

The flow field largely determines the electrolyte distribution through the electrode and the pressure drop of the system [8, 11, 13]. Several flow field designs are known in the literature but are commonly divided into flow-through and flow-by designs, where the differences lie in the main transport mechanisms to and through the porous electrode: in flow-through flow fields the electrolyte transported is convection-driven, whereas in flow-by designs the electrolyte transport is dominated by diffusion [78]. Therefore, in this work, we investigate two well-known flow field designs, the PFF – a flow-by flow field – and the IDFF – a flow-through flow field – both with distinct flow distributions through the electrode. For the comparison, the paper electrode was chosen, to study the effect of the flow field design on the reactor performance with an electrode with a unimodal PSD.

In this section, the imaging of the active species and the cumulative imaging of TEMPO/TEMPO$^+$BF$_4^-$ are discussed simultaneously. The *operando* electrochemical data and concentration profiles for the two flow fields at OCV, -0.6 V, and +0.6 V for a flow rate of 5 mL min^{-1} are visualized in **Figures 7.4** and **Figure A7.8,** and the electrochemical sequence and the concentration profiles at the higher flow rate and lower potentials are shown in **Section A7.2**, together with the capacity data. Notable differences are observed between the two flow fields, where for both electrolyte solutions the most prominent difference between the flow fields is the current output of the systems. The current output is significantly greater with the IDFF (average of -295 mA at -0.6 V (KPF_6), +295 mA at +0.6 V (KPF_6), -217 mA at -0.6 V (BF_4^-), and +235 mA at +0.6 V (BF_4^-) in a 20 min time frame with the IDFF compared to an average of -98 mA at -0.6 V (KPF_6), +98 mA at +0.6 V (KPF_6), -84 mA at -0.6 V (BF_4^-), and +74 mA at +0.6 V (BF_4^-) with the PFF), which is caused by forced-convection [8, 9, 13, 28]. Moreover, the current in the IDFF decreases over time as a result of the changing SoC because of the high conversion per pass decreasing the concentration of the to-be-converted species over time in the reactor. This finding is in line with the literature [8, 9, 13, 26, 28, 79] as the presence of forced convection in the IDFF results in a higher reaction rate and subsequent current output because of enhanced mass transport by a higher electrolyte velocity through the electrode and thus an increased hydraulic conductance to obtain a deeper penetration of the reaction front through the electrode [28]. The higher reaction rates are further supported by the capacity curves (**Figure A7.11**) as 30 % of the species is converted with the IDFF in 20 min at -0.6 V. We observed in the previous section that the PFF performance can be enhanced when using electrodes with a bimodal PSD (with large through-plane voids), as the cloth electrode attained a 2.5 x higher current output under the same operating conditions. Hence, we believe that the ideal flow field configuration is system (i.e., electrode, electrolyte) dependent and needs to be subjected to further studies.

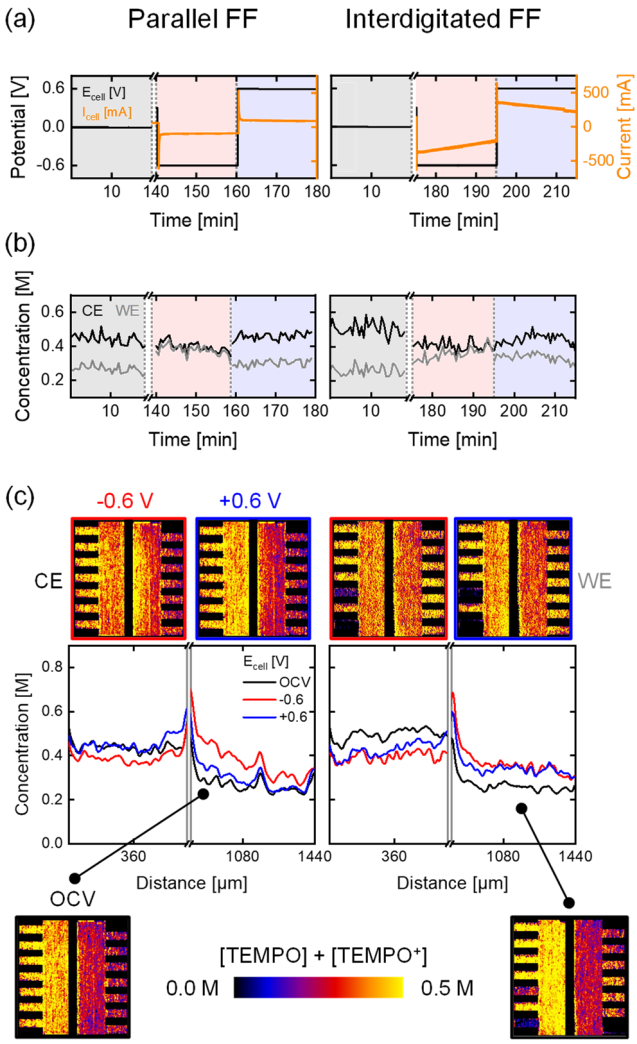

Figure 7.4: *Operando* neutron imaging of the active species transport with the low attenuating KPF_6 supporting salt for two flow field designs: parallel and interdigitated, at an inlet flow rate of 5 mL min^{-1} and evaluated at OCV, -0.6 V, and +0.6 V. **(a)** The potential applied and current output of the electrochemical cells. **(b)** The averaged concentration profiles over time in the counter electrode (CE) and the working electrode (WE). **(c)** The cumulative active species ($TEMPO/TEMPO^+$) concentration profiles over the electrode thickness with the averaged snapshots of the cell after image processing, with on the counter electrode 0.5 M $TEMPO/TEMPO^+PF_6^-$ at 50% state-of-charge in 0.2 M KPF_6 and at the working electrode 0.2 M $TEMPO/TEMPO^+PF_6^-$ at 50% state-of-charge in 0.2 M KPF_6.

When analyzing the concentration profiles through the reactor in **Figure 7.4**, minor differences can be observed in comparison to the PFF, as more uniform profiles over the electrode thickness are detected because of the convective-dominated transport with the IDFF (**Figure A7.7**). Yet, the flow fields are compared at a fixed flow rate through the reactor, resulting in significantly different electrolyte velocities to, but especially through, the porous electrodes, resulting in a higher electrolyte velocity to the

electrode with the IDFF according to **equations (7.2 - 7.3)** [26, 28]. Moreover, as the IDFF is convection-driven, the electrolyte velocity through the electrode is even higher compared to the PFF, for which calculating the electrolyte velocity through the electrode is challenging, and often a negligible electrolyte velocity is assumed [26, 28]. Thus, care must be taken when comparing various flow field designs as both comparing at constant electrolyte flow rate and at constant flow velocity has their advantages and disadvantages. Yet, the electrolyte flow does impact the reactor performance with the different flow field designs directly, as can be seen in the concentration images. The bottom channels in the IDFF are not properly filled in the low attenuating supporting salt experiments (**Figure 7.4c**), though they are filled in the highly attenuating supporting ion experiments (**Figure A7.8c**). The filling of the channels impacts the electrolyte distribution through the reactor and thus the reactive transport. Underutilization of the channels is therefore associated with a loss in performance which could be overcome by proper operation (i.e., channel filling) or advancing the flow field design by e.g., improved manifold design. Hence, neutron imaging is not only a powerful tool to investigate concentration distributions through the reactor area, but it also allows the detection of system secondary phenomena including salt precipitation and underutilization of the flow channels.

7.4. Conclusion

In this work, we study the cell-level reactive mass transport in redox flow cells with *operando* neutron radiography in tandem with electrochemical diagnostics. The influence of various reactor components on the cell performance is investigated by analyzing the electrochemical performance and in-plane local concentration distributions of three electrodes – the SGL 39AA carbon paper, 1186 HCB AvCarb carbon cloth, and an in-house manufactured non-solvent induced phase-separated electrode – and two flow field designs – parallel and interdigitated. The in-plane concentration distribution is resolved for symmetric cell configurations with model redox couples with well-defined properties. Two non-aqueous electrolyte configurations were analyzed, one with the attenuating active species TEMPO/$TEMPO^+$ and one with the attenuation of both the active species and the supporting ion BF_4^-. We found that the distinct electrode structures have unique current and concentration profiles with parallel flow fields, motivating in-depth analysis of both the macroscopic and microscopic electrode performance. The NIPS electrode has a similar macroscopic electrochemical behavior as the paper electrode despite the significantly higher electrochemically active surface area, but features starker concentration fluctuations upon different applied potential signs and a more pronounced concentration slope in the thickness direction. Whereas the cloth electrode features a significantly higher current output by an increased capacity utilization and more uniform concentration profiles over the reactor area. Moreover, we found that interdigitated flow field designs with forced convection have a greater current output at a fixed applied potential and flow rate due to higher capacity utilization as a result of the enhanced through-plane electrolyte transport. Thus, proving the importance of the selection of the electrode structure, flow field geometry, and electrolyte chemistry in tandem.

With this work, we provide the community the visualization of concentration distributions through the electrochemical flow reactor during battery operation to better understand the underlying transport principles of various electrode structures and flow fields, which could potentially guide advancements in reactor design. Though, local

concentration variations (<10 μm e.g., near boundary layers) require local imaging diagnostics such as fluorescence microscopy to study local microstructural effects (diffusion boundary layers, local reaction rates, local electrolyte velocities) [37]. Nevertheless, we believe that neutron radiography is a powerful tool to investigate concentration distributions through the electrochemical cell area, and in addition, provides information regarding system operation including the presence of salt precipitation or the underutilization of the flow channels.

7.5. References

[1] A. Z. Weber *et al.*, *J. Appl. Electrochem.* **41**, 1137–1164 (2011).
[2] P. Leung *et al.*, *J. Power Sources*. **360**, 243–283 (2017).
[3] A. Forner-Cuenca, E. E. Penn, A. M. Oliveira, F. R. Brushett, *J. Electrochem. Soc.* **166**, A2230–A2241 (2019).
[4] M. Skyllas-Kazacos, M. H. Chakrabarti, S. A. Hajimolana, F. S. Mjalli, M. Saleem, *J. Electrochem. Soc.* **158**, R55 (2011).
[5] E. Sánchez-Díez *et al.*, *J. Power Sources*. **481**, 228804 (2021).
[6] A. Forner-Cuenca, F. R. Brushett, *Curr. Opin. Electrochem.* **18**, 113–122 (2019).
[7] R. M. Darling, K. G. Gallagher, J. A. Kowalski, S. Ha, F. R. Brushett, *Energy Environ. Sci.* **7**, 3459–3477 (2014).
[8] V. Muñoz-Perales *et al.*, *ChemRxiv* (2023), doi:10.26434/chemrxiv-2023-n2mmd.
[9] M. van der Heijden, M. Kroese, Z. Borneman, A. Forner-Cuenca, *Adv. Mater. Technol.*, **8**, 18, 2300611 (2023).
[10] M. H. Chakrabarti *et al.*, *J. Power Sources*. **253**, 150–166 (2014).
[11] M. van der Heijden, A. Forner-cuenca, in *Encyclopedia of Energy Storage*, L. F. Cabeza, Ed. (Elsevier Inc., Oxford, ed. 2, 2022), pp. 480–499.
[12] V. Muñoz-Perales *et al.*, *ChemRxiv* (2023), doi:10.26434/chemrxiv-2023-2zthc.
[13] V. Muñoz-Perales *et al.*, *ChemRxiv* (2023), doi:10.26434/chemrxiv-2023-n2mmd.
[14] V. Muñoz-Perales, M. van der Heijden, P. Á. García-Salaberri, M. Vera, A. Forner-Cuenca, *ACS Sustain. Chem. Eng.*, **11**, 33, 11243-12255 (2023).
[15] C. T. Wan *et al.*, *Adv. Mater.* **33**, 2006716 (2021).
[16] T. Roy, M. A. S. de Troya, M. A. Worsley, V. A. Beck, *Struct. Multidiscip. Optim.* **65**, 171 (2022).
[17] R. van Gorp, M. van der Heijden, M. A. Sadeghi, J. Gostick, A. Forner-Cuenca, *Chem. Eng. J.* **455**, 139947 (2023).
[18] V. A. Beck *et al.*, *Proc. Natl. Acad. Sci. U. S. A.* **118**, 1–10 (2021).
[19] L. F. Arenas, C. Ponce de León, F. C. Walsh, *Electrochem. commun.* **77**, 133–137 (2017).
[20] A. Forner-Cuenca, F. R. Brushett, *Curr. Opin. Electrochemistry*, 10 (2019).
[21] P. Wang *et al.*, *Adv. Mater. Technol.* **5**, 1901030 (2020).
[22] S. Wan *et al.*, *Appl. Energy*. **298**, 117177 (2021).
[23] V. A. Beck *et al.*, *J. Power Sources*. **512**, 230453 (2021).
[24] R. R. Jacquemond *et al.*, *Cell Reports Phys. Sci.* **3**, 100943 (2022).
[25] C. T. C. Wan, R. R. Jacquemond, Y. M. Chiang, A. Forner-Cuenca, F. R. Brushett, *Energy Technol.* **11**, 2300137 (2023).
[26] J. D. Milshtein *et al.*, *J. Electrochem. Soc.* **164**, E3265–E3275 (2017).
[27] K. M. Tenny, A. Forner-Cuenca, Y.-M. Chiang, F. R. Brushett, *J. Electrochem. Energy Convers. Storage*. **17**, 041010 (2020).
[28] R. M. Darling, M. L. Perry, *J. Electrochem. Soc.* **161**, A1381–A1387 (2014).
[29] M. Macdonald, R. M. Darling, *AIChE J.* **65**, 1–11 (2019).
[30] C. R. Dennison, E. Agar, B. Akuzum, E. C. Kumbur, *J. Electrochem. Soc.* **163**, A5163–A5169 (2016).
[31] A. A. Wong, M. J. Aziz, *J. Electrochem. Soc.* **167**, 110542 (2020).
[32] M. van der Heijden, R. van Gorp, M. A. Sadeghi, J. Gostick, A. Forner-Cuenca, *J. Electrochem. Soc.* **169**, 040505 (2022).
[33] K. Köble *et al.*, *J. Power Sources*. **492**, 229660 (2021).
[34] L. Eifert *et al.*, *ChemSusChem*. **13**, 3154–3165 (2020).
[35] F. Tariq *et al.*, *Sustain. Energy Fuels*. **2**, 2068–2080 (2018).
[36] R. Jervis *et al.*, *J. Phys. D. Appl. Phys.* **49**, 434002 (2016).
[37] A. A. Wong, S. M. Rubinstein, M. J. Aziz, *Cell Reports Phys. Sci.* **2**, 100388 (2021).
[38] K. R. Minard, V. V. Viswanathan, P. D. Majors, L. Q. Wang, P. C. Rieke, *J. Power Sources*. **161**, 856–863 (2006).

[39] Z. Dunbar, R. I. Masel, *J. Power Sources*. **171**, 678–687 (2007).
[40] E. W. Zhao *et al.*, *J. Am. Chem. Soc.* **143**, 1885–1895 (2021).
[41] E. W. Zhao *et al.*, *Nature*. **579**, 224–228 (2020).
[42] J. T. Clement, PhD thesis, University of Tennessee (2016).
[43] R. R. Jacquemond *et al.*, *ChemRxiv* (2023), doi:10.26434/chemrxiv-2023-8xjv5.
[44] J. Wood, *Computational Methods in Reactor Shielding* (Elsevier Ltd, UK, 1982).
[45] P. Rinard, (1997), pp. 357–377.
[46] E. R. C. Ruiz *et al.*, *Materials Today Advances*, **19**, 100405 (2023).
[47] P. Boillat, E. H. Lehmann, P. Trtik, M. Cochet, *Curr. Opin. Electrochem.* **5**, 3–10 (2017).
[48] A. Forner-Cuenca *et al.*, *Adv. Mater.* **27**, 6317–6322 (2015).
[49] V. Manzi-Orezzoli *et al.*, *J. Electrochem. Soc.* **167**, 064516 (2020).
[50] M. A. Hickner *et al.*, *J. Electrochem. Soc.* **155**, B427 (2008).
[51] R. J. Bellows, M. Y. Lin, M. Arif, A. K. Thompson, D. Jacobson, *J. Electrochem. Soc.* **146**, 1099–1103 (1999).
[52] A. Forner-Cuenca *et al.*, *J. Electrochem. Soc.* **163**, F1389–F1398 (2016).
[53] J. I. S. Cho *et al.*, *Energy*. **170**, 14–21 (2019).
[54] J. Zhang *et al.*, *Electrochim. Acta*. **51**, 2715–2727 (2006).
[55] M. Siegwart *et al.*, *J. Electrochem. Soc.* **167**, 064510 (2020).
[56] B. Michalak *et al.*, *Sci. Rep.* **5**, 1–9 (2015).
[57] D. X. Liu *et al.*, *Angew. Chemie - Int. Ed.* **53**, 9498–9502 (2014).
[58] M. Lanz, E. Lehmann, R. Imhof, I. Exnar, P. Novák, *J. Power Sources*. **101**, 177–181 (2001).
[59] D. Goers *et al.*, *J. Power Sources*. **130**, 221–226 (2004).
[60] C. H. Lee *et al.*, *Electrochim. Acta*. **279**, 91–98 (2018).
[61] O. F. Selamet *et al.*, *Int. J. Hydrogen Energy*. **38**, 5823–5835 (2013).
[62] I. Manke *et al.*, *Appl. Phys. Lett.* **90**, 1–4 (2007).
[63] R. R. Jacquemond, PhD thesis, Eindhoven University of Technology (2023).
[64] R. Dmello, J. D. Milshtein, F. R. Brushett, K. C. Smith, *J. Power Sources*. **330**, 261–272 (2016).
[65] J. D. Milshtein, R. M. Darling, J. Drake, M. L. Perry, F. R. Brushett, *J. Electrochem. Soc.* **164**, A3883–A3895 (2017).
[66] J. A. Kowalski, L. Su, J. D. Milshtein, F. R. Brushett, *Curr. Opin. Chem. Eng.* **13**, 45–52 (2016).
[67] A. Forner-Cuenca, E. E. Penn, A. M. Oliveira, F. R. Brushett, *J. Electrochem. Soc.* **166**, A2230–A2241 (2019).
[68] V. F. Sears, *Neutron News*. **3**, 26–37 (1992).
[69] E. H. Lehmann, P. Vontobel, L. Wiezel, *Nondestruct. Test. Eval.* **16**, 191–202 (2001).
[70] P. Boillat, G. Frei, E. H. Lehmann, G. G. Scherer, A. Wokaun, *Electrochem. Solid-State Lett.* **13**, 68–71 (2010).
[71] J. D. Milshtein, J. L. Barton, R. M. Darling, F. R. Brushett, *J. Power Sources*. **327**, 151–159 (2016).
[72] J. L. Barton, J. D. Milshtein, J. J. Hinricher, F. R. Brushett, *J. Power Sources*. **399**, 133–143 (2018).
[73] R. R. Jacquemond, R. Geveling, A. Forner-Cuenca, K. Nijmeijer, *J. Electrochem. Soc.* **169**, 080528 (2022).
[74] X. G. Yang, Q. Ye, P. Cheng, T. S. Zhao, *Appl. Energy*. **145**, 306–319 (2015).
[75] R. Omrani, in *PEM Fuel Cells*, G. Kaur, Ed. (Elsevier, Burnaby, Canada, 2021), pp. 91–122.
[76] L. M. Baumgartner, C. I. Koopman, A. Forner-Cuenca, D. A. Vermaas, *ACS Sustain. Chem. Eng.* **10**, 4683–4693 (2022).
[77] P. Kurzweil, M. Chwistek, *J. Power Sources*. **176**, 555–567 (2008).
[78] X. Ke *et al.*, *Chem. Soc. Rev.* **47**, 8721–8743 (2018).
[79] B. K. Chakrabarti *et al.*, *Sustain. Energy Fuels*. **4**, 5433–5468 (2020).

7.6. Appendix 7

A7.1. Influence of the electrode structure

A7.1.1. TEMPO/TEMPO$^+$ imaging

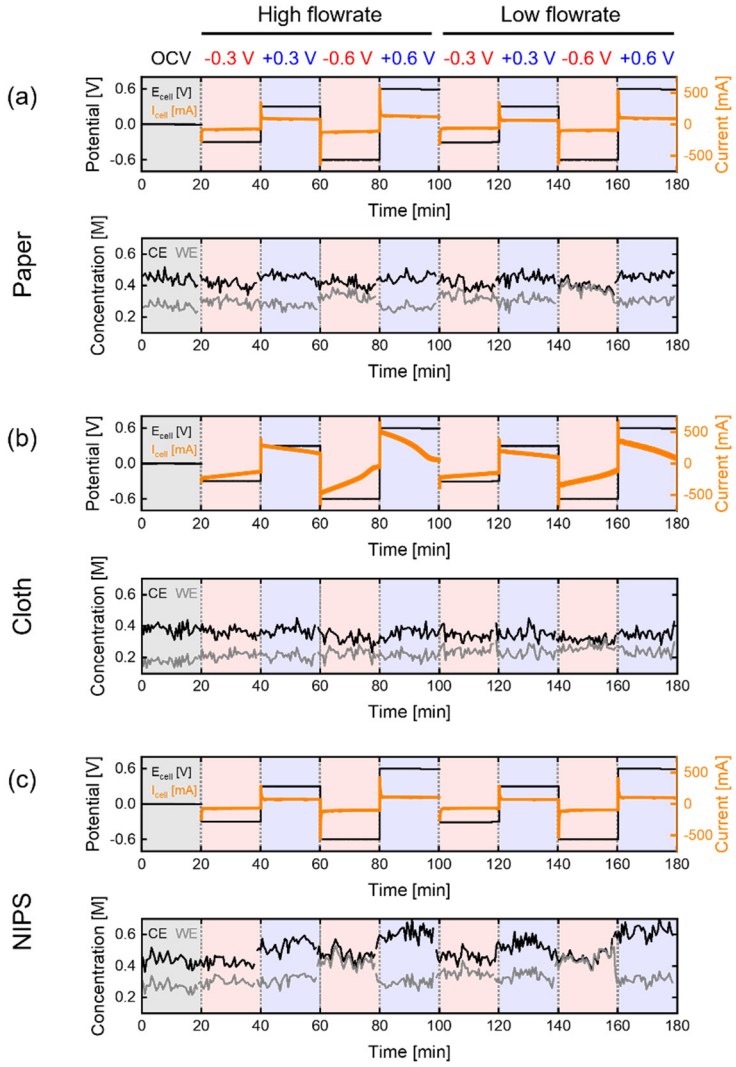

Figure A7.1: *Operando* neutron imaging of the active species transport with the low attenuating KPF_6 supporting salt for three electrode types: **(a)** SGL 39AA, **(b)** AvCarb Cloth, and **(c)** an in-house manufactured NIPS electrode, at an inlet flow rate of 13 - 15 mL min^{-1} and 5 mL min^{-1} and evaluated at OCV, -0.3 V, +0.3 V, -0.6 V, and +0.6 V. Where the potential applied and current output of the electrochemical cells are plotted over time, as well as the concentration profiles over time in the counter electrode (CE) and the working electrode (WE).

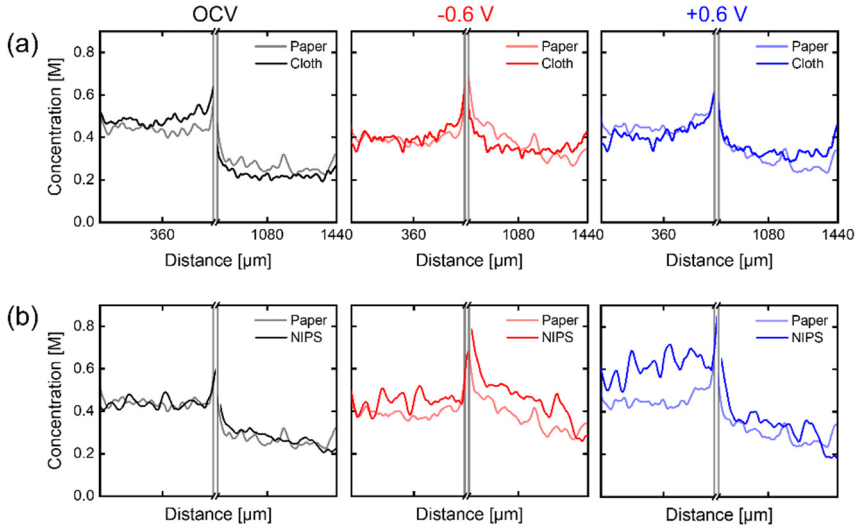

Figure A7.2: The cumulative active species (TEMPO/TEMPO$^+$) concentration profiles over the electrode thickness with the low attenuating KPF_6 supporting salt for three electrode types: **(a)** the SGL 39AA and the AvCarb Cloth, and **(b)** the SGL 39AA and an in-house manufactured NIPS electrode, at an inlet flow rate of 5 mL min^{-1} and evaluated at OCV, -0.6 V, and +0.6 V.

A7.1.2. TEMPO/TEMPO$^+$/BF_4^- imaging

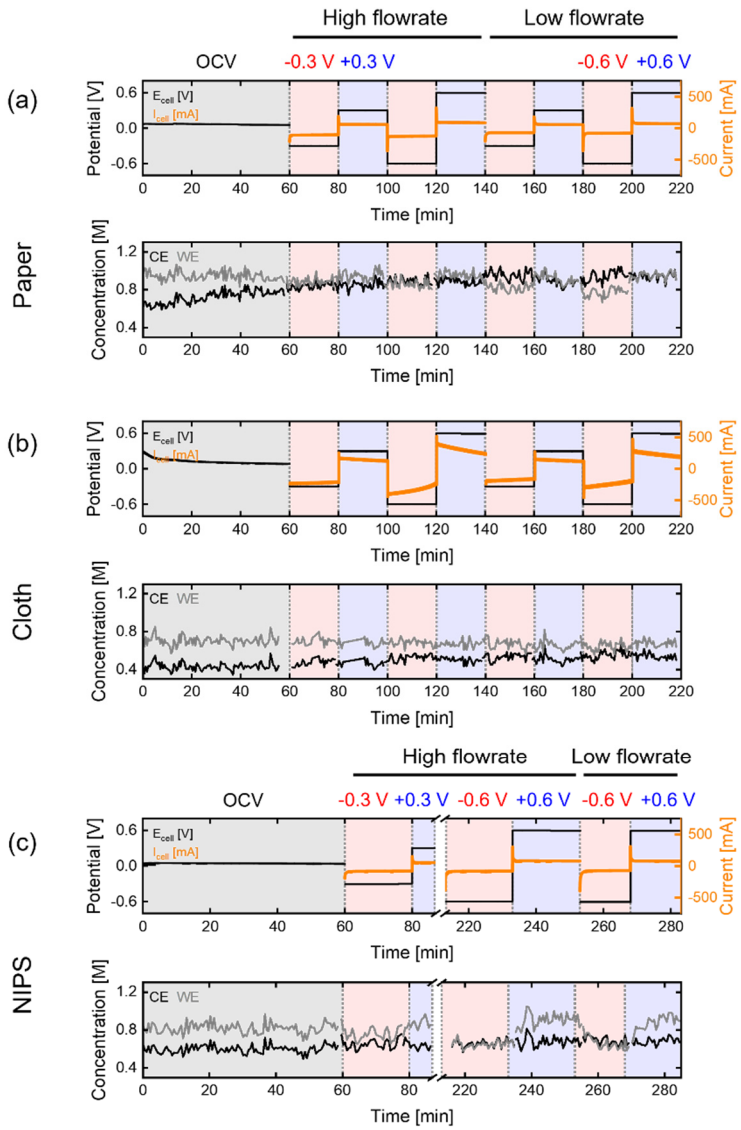

Figure A7.3: *Operando* neutron imaging of the active species transport with the attenuating BF4$^-$ supporting ion for three electrode types: **(a)** SGL 39AA, **(b)** AvCarb Cloth, and **(c)** an in-house manufactured NIPS electrode, at an inlet flow rate of 13 - 15 mL min^{-1} and 5 mL min^{-1} and evaluated at OCV, -0.3 V, +0.3 V, -0.6 V, and +0.6 V. Where the potential applied and current output of the electrochemical cells are plotted over time, as well as the concentration profiles over time in the counter electrode (CE) and the working electrode (WE).

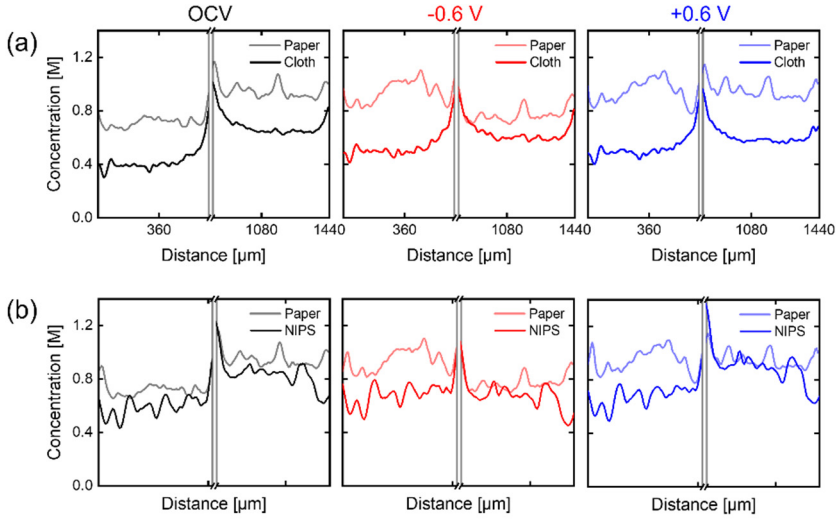

Figure A7.4: The cumulative active species (TEMPO/TEMPO$^+$) and BF_4^- supporting ion concentration profiles over the electrode thickness for three electrode types: **(a)** the SGL 39AA and the AvCarb Cloth, and **(b)** the SGL 39AA and an in-house manufactured NIPS electrode, at an inlet flow rate of 5 mL min^{-1} and evaluated at OCV, -0.6 V, and +0.6 V.

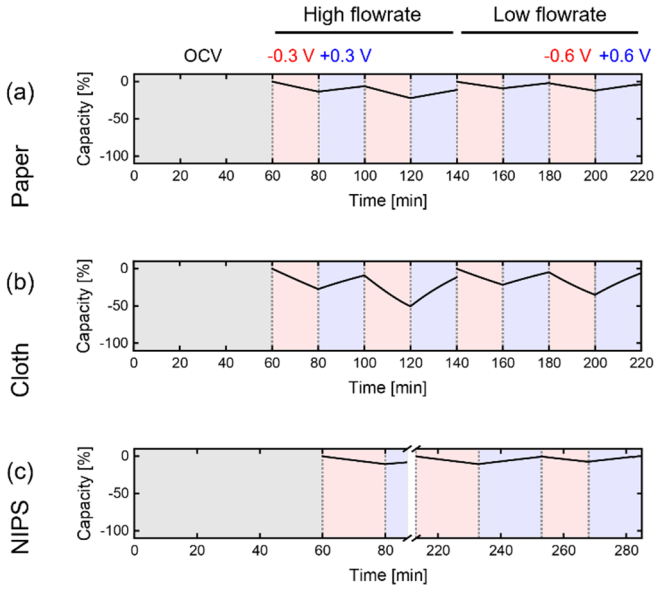

Figure A7.5: *Operando* neutron imaging of the active species transport with the attenuating $BF4^-$ supporting ion for three electrode types: **(a)** SGL 39AA, **(b)** AvCarb Cloth, and **(c)** an in-house manufactured NIPS electrode, at an inlet flow rate of 13 - 15 mL min^{-1} and 5 mL min^{-1} and evaluated at OCV, -0.3 V, +0.3 V, -0.6 V, and +0.6 V. Where the capacity of the electrochemical cells is plotted over time.

A7.2. Impact of the flow field design

A7.2.1. TEMPO/TEMPO$^+$ imaging

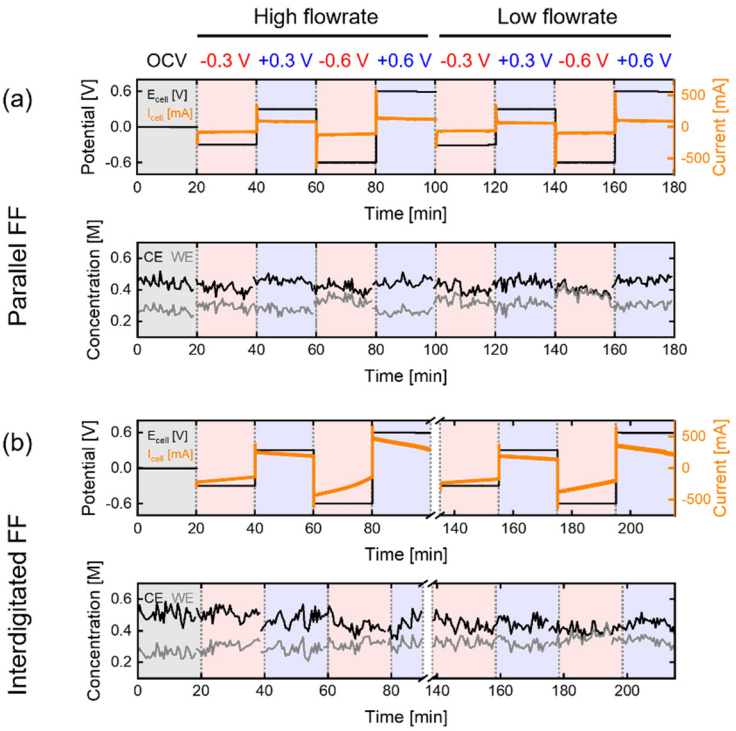

Figure A7.6: *Operando* neutron imaging of the active species transport with the low attenuating KPF_6 supporting salt for two flow field designs: **(a)** parallel, and **(b)** interdigitated, at an inlet flow rate of 15 mL min^{-1} and 5 mL min^{-1} and evaluated at OCV, -0.3 V, +0.3 V, -0.6 V, and +0.6 V. Where the potential applied and current output of the electrochemical cells are plotted over time, as well as the concentration profiles over time in the counter electrode (CE) and the working electrode (WE).

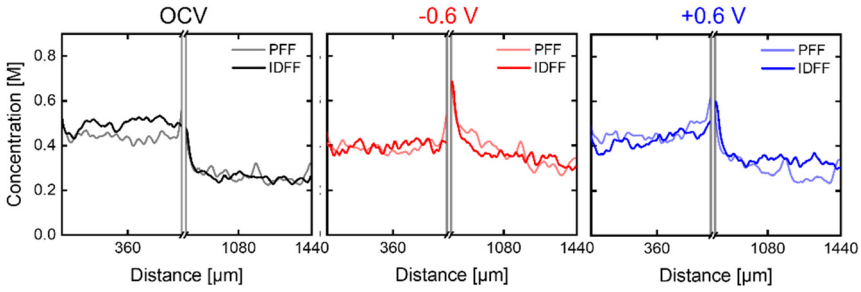

Figure A7.7: The cumulative active species (TEMPO/TEMPO$^+$) concentration profiles over the electrode thickness with the low attenuating KPF_6 supporting salt for the parallel and interdigitated flow fields, at an inlet flow rate of 5 mL min^{-1} and evaluated at OCV, -0.6 V, and +0.6 V.

A7.2.2. TEMPO/TEMPO$^+$/BF$_4^-$ imaging

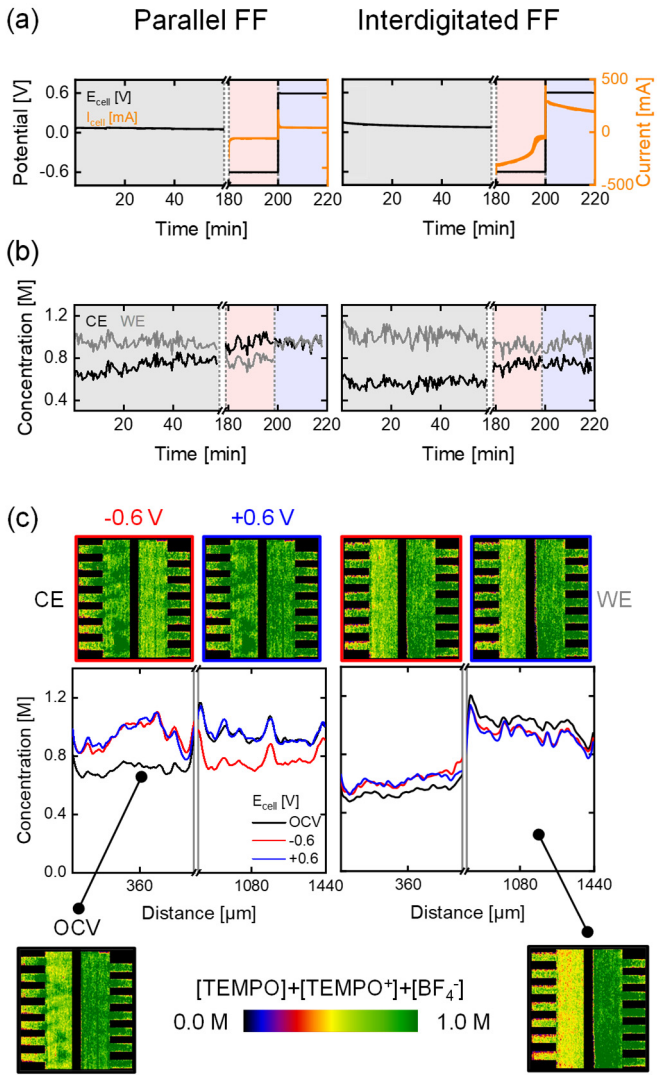

Figure A7.8: *Operando* neutron imaging of the active species transport with the attenuating BF4$^-$ supporting ion for two flow field designs: parallel and interdigitated, at an inlet flow rate of 5 mL min^{-1} and evaluated at OCV, -0.6 V, and +0.6 V. **(a)** The potential applied and current output of the electrochemical cells. **(b)** The averaged concentration profiles over time in the counter electrode (CE) and the working electrode (WE). **(c)** The cumulative active species (TEMPO/TEMPO$^+$) and BF$_4^-$ supporting ion concentration profiles over the electrode thickness with the averaged snapshots of the cell after image processing, with on the counter electrode 0.5 M TEMPO and at the working electrode 0.5 M TEMPO$^+$BF$_4^-$.

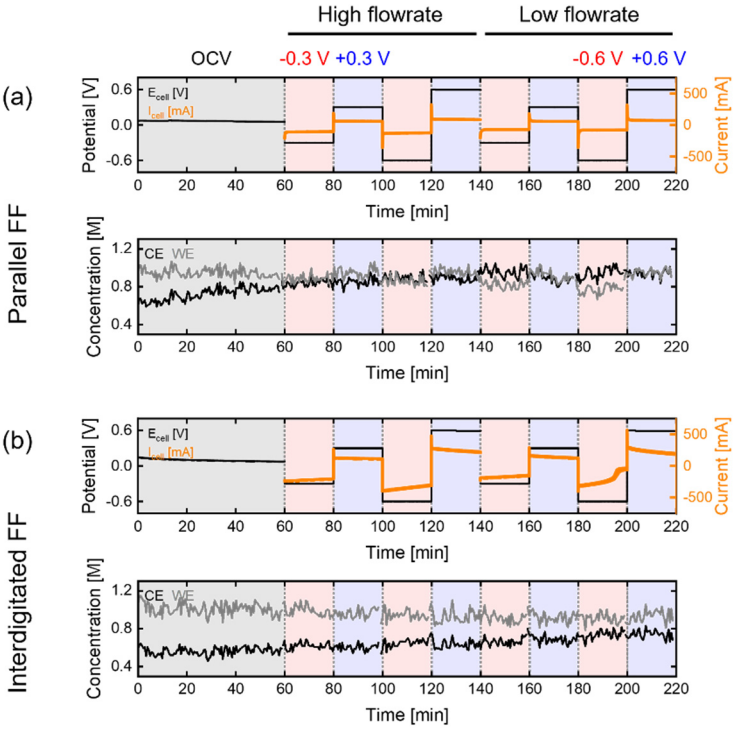

Figure A7.9: *Operando* neutron imaging of the active species transport with the attenuating $BF4^-$ supporting ion for two flow field designs: **(a)** parallel, and **(b)** interdigitated, at an inlet flow rate of 15 mL min^{-1} and 5 mL min^{-1} and evaluated at OCV, -0.3 V, +0.3 V, -0.6 V, and +0.6 V. Where the potential applied and current output of the electrochemical cells are plotted over time, as well as the concentration profiles over time in the counter electrode (CE) and the working electrode (WE).

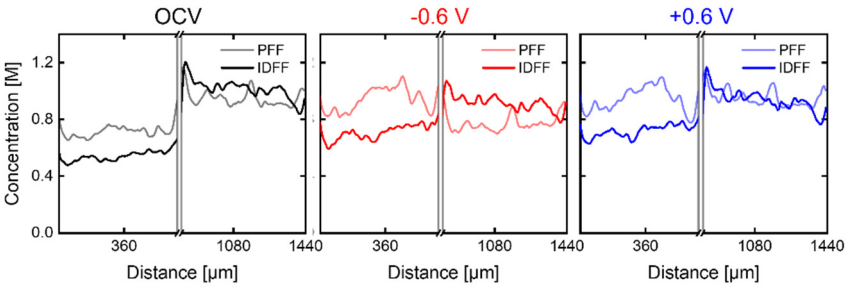

Figure A7.10: The cumulative active species (TEMPO/$TEMPO^+$) and BF_4^- supporting ion concentration profiles over the electrode thickness for the parallel and interdigitated flow fields, at an inlet flow rate of 5 mL min^{-1} and evaluated at OCV, -0.6 V, and +0.6 V.

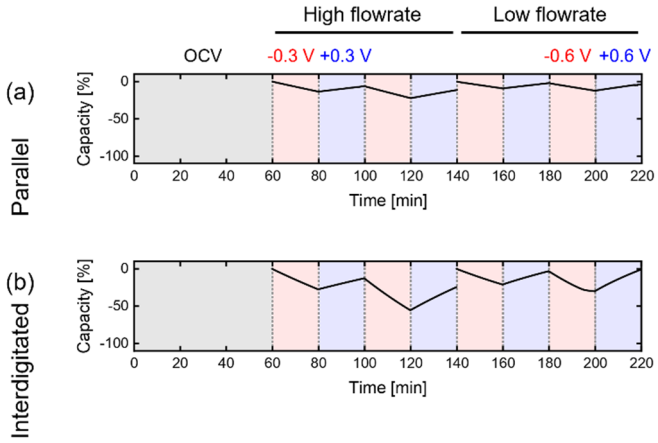

Figure A7.11: *Operando* neutron imaging of the active species transport with the attenuating $BF4^-$ supporting ion for two flow field designs: **(a)** parallel, and **(b)** interdigitated, at an inlet flow rate of 15 mL min^{-1} and 5 mL min^{-1} and evaluated at OCV, -0.3 V, +0.3 V, -0.6 V, and +0.6 V. Where the capacity of the electrochemical cells is plotted over time.

Chapter 8

Investigating mass transfer relationships in stereolithography 3D printed electrodes for redox flow batteries

Abstract

Porous electrodes govern the electrochemical performance and pumping requirements in redox flow batteries, yet conventional carbon-fiber-based porous electrodes have not been tailored to sustain the requirements of liquid-phase electrochemistry. 3D printing is an effective approach to manufacturing deterministic architectures, enabling the tuning of electrochemical performance and pressure drop. In this work, model grid structures are manufactured with stereolithography 3D printing followed by carbonization and tested as flow battery electrode materials. Microscopy, tomography, spectroscopy, fluid dynamics, and electrochemical diagnostics are employed to investigate the resulting electrode properties, mass transport, and pressure drop of ordered lattice structures. The influence of the printing direction, pillar geometry, and flow field type on the cell performance is investigated and mass transfer *vs.* electrode structure correlations are elucidated. It is found that the printing direction impacts the electrode performance through a change in morphology, resulting in enhanced performance for diagonally printed electrodes. Furthermore, mass transfer rates within the electrode are improved by helical or triangular pillar shapes or by using interdigitated flow field designs. This study shows the potential of stereolithography 3D printing to manufacture customized electrode scaffolds, which could enable multiscale structures with superior electrochemical performance and low pumping losses.

This chapter is published as:

M. van der Heijden, M. Kroese, Z. Borneman, and A. Forner-Cuenca, Investigating mass transfer relationships in stereolithography 3D printed electrodes for redox flow batteries, *Advanced Materials Technologies*, **8**, 18 (2023), pp. 2300611, doi:10.1002/admt.202300611.

8.1. Introduction

Electrochemical energy storage systems have emerged as key technologies to accommodate the intermittent nature of sustainable energy sources (e.g., solar and wind) by bridging temporal and geographical gaps between energy demand and supply [1–5]. Redox flow batteries (RFBs) are a promising option for large-scale energy storage due to their ability to independently scale the power and energy and their long operation lifetimes [6–9]. In RFBs, the energy is stored in an electrolyte solution containing dissolved active species, stored in external tanks, which are pumped through the electrochemical stack where the active species undergo electrochemical reactions [10]. The electrochemical stack defines the power density of the system, which is governed by the flow fields, electrodes, and membranes employed. However, current RFBs are unoptimized and remain too costly for widespread deployment [4, 11]. One approach to increase their cost competitiveness is to enhance the power density and efficiency of the electrochemical cell, for example, by engineering porous electrodes tailored for application in RFBs. Porous electrodes are performance- and cost-defining components that provide the electrochemically active surfaces for the electrochemical reactions, the porous structure for the electrolyte distribution, and facilitate mass, charge, and heat transport [10, 12]. These properties are influenced by the choice of material, electrode structure, and manufacturing technique.

Conventional porous electrodes used in RFBs are fibrous mats, fabricated by the carbonization of polymer precursors, and assembled in coherent structures such as papers, cloths, and felts. The electrode structure and thickness are controlled by the manufacturing process, such as weaving, compacting, hydroentangling, and electrospinning, and thus by the arrangement of the micrometric fibers [4, 13]. Their performance has extensively been investigated and depends highly on the macrostructure (cell-level, e.g., type of electrode and alignment) and microstructure (submicrometer-scale, e.g., carbon fiber engineering) [8, 14–19]. We and others investigated the influence of the electrode structure on the electrochemical performance and pressure drop. We showed that the woven cloth electrode utilizes the highest current density and lowest pressure drop, which we assigned to the bimodal pore size distribution (PSD) and well-defined electrode structure [8]. Additionally, Simon *et al*. investigated the performance of two cloth and two paper electrodes and suggested that the permeability of fibrous materials strongly correlates to the electrochemical cell behavior under forced convective conditions. Hence, they found that the cloth electrodes with higher permeability, inter-pore connectivity, and mass-transfer coefficients display enhanced RFB performance [19]. Furthermore, Tenny *et al*. investigated the nuanced relationships between the morphology of various cloth electrodes and their electrochemical performance and pumping requirements and suggested that the 1071 HCB plain weave pattern offers the best performance trade-off [14]. Although these studies gained insights into the requirements of electrodes for RFB application (i.e., well-defined structure, bimodal PSD), the investigated commercial electrodes are repurposed fuel cell gas diffusion electrodes and are not optimized for their use in all-liquid RFBs [4, 20]. In addition, the conventional manufacturing and functionalization methods mainly focus on the optimization of the microstructure, but the electrolyte distribution, electrode-electrolyte interface, and electrode conductivity remain unidentified [13, 21, 22]. Incomplete understanding of the structure-function-performance relationships and the interplay between the electrode and other RFB components (including the flow field and electrolyte chemistry) challenge the

deterministic design of electrode materials. Furthermore, conventional electrodes have limited morphological diversity, constricting the physicochemical properties of the electrode (e.g., low structural control, confined PSD), and thus limit the electrode permeability. Hence, these constrictions motivate the development of new synthesis and manufacturing techniques with large control over the materials properties, macro-, and microstructure.

Recently, additive manufacturing, or 3D printing, has been employed to fabricate customized electrodes, enabling the fine-tuning of the fluid transport and electrochemically active surface area [13, 23]. In addition, additive manufacturing has great potential for upscaling as the manufacturing can be parallelized and combined with the electrochemical reactor design by e.g., multi-material 3D printing [23, 24]. Several additive manufacturing techniques have been employed to fabricate electrodes for electrochemical devices [5, 24, 25] including material jetting [26], material extrusion [13, 27–32], powder bed fusion [33, 34], VAT photopolymerization (i.e., stereolithography (SLA) [22, 35, 36], digital light processing [37, 38]), and two-photon polymerization [39]. The choice of precursor (e.g., metals, plastics, composites, inorganics [24]) and the manufacturing method control the structural properties of the electrode comprising the feature size, geometry, porosity, size, surface roughness, and mechanical stability, as well as the manufacturing time [25]. Various studies have been conducted on using metals like stainless steel and nickel as electrodes for electrochemical energy storage applications [28, 29, 33, 34]; however, metal-based electrodes are generally not as viable compared to carbon-based electrodes due to elevated costs and corrosion resistance in relevant electrochemical environments. Moreover, carbonaceous materials have high electrical conductivity and stability and are inexpensive. In addition, their electrical, thermal, and mechanical properties can be altered based on their crystallinity, hybridization, and functional groups, which makes them the uttermost flexible and suitable electrode material for RFBs [4, 40–42]. Therefore, several research groups have shown interest in using polymer precursors [36] followed by carbonization to manufacture carbon-based electrodes [35], also recently for the fabrication of RFB electrodes [13, 22]. Wang *et al*. presented a novel hybrid method to fabricate porous carbon electrodes with pores spanning the millimeter to nanometer scale by combining SLA, carbonization, and chemical activation. They showed that by tuning the pore diameter and overlap ratio, electrode characteristics such as porosity, thickness, specific surface area, and electrical resistance can be engineered. They additionally tested their 3D printed designs in a supercapacitor and a vanadium RFB and observed that for the RFB a large specific surface area was found to be crucial in achieving enhanced electrochemical performance [22]. Moreover, Beck & Ivanovskaya *et al*. designed 3D printed carbon-based graphene aerogel electrodes with simple cubic and face-centered cubic lattice structures using the material extrusion method. They revealed that structures with engineered flow enhance mass transfer in flow-through electrodes as the mass transport properties strongly depend on the flow when operating in the inertial regime [13]. These studies showed the potential of utilizing 3D printing to manufacture electrodes for RFBs, where the printing resolution, time, and dimensions are the main hurdles in commercially exploiting additive manufacturing for porous electrodes. Furthermore, advances in understanding the role of the electrode structure on both the electrochemical performance and pressure drop should be made to optimize or engineer next-generation porous electrodes [4, 43, 44]. Nonetheless, utilizing additive manufacturing techniques enables the electrode structures to be manufactured in a rigorous and parametric manner,

allowing reactor design-dependent (i.e., flow field geometry, electrolyte chemistry) optimization.

In this work, we focus on understanding the impact of the electrode structure on the mass transport properties of ordered lattice structures in flow cells. Thereby contributing to the understanding of the structure-function-performance relationships in RFBs by exploring novel in-house manufactured electrode architectures. We investigate the influence of the printing direction, pillar geometry, and flow field design on the mass transport in the electrode, and provide insight into the design flexibility [22] and orientation (printing direction) of SLA 3D printing to examine the challenging trade-off between electrochemical performance and pumping requirements. We utilize SLA in combination with carbonization to obtain conductive carbon electrodes which are studied in single electrolyte flow cells containing an organic redox couple with an acetonitrile-based electrolyte, a model electrolyte because of its low surface tension and fast kinetics [7, 11, 45-47], and compared the printed structures to commonly used commercial electrodes.

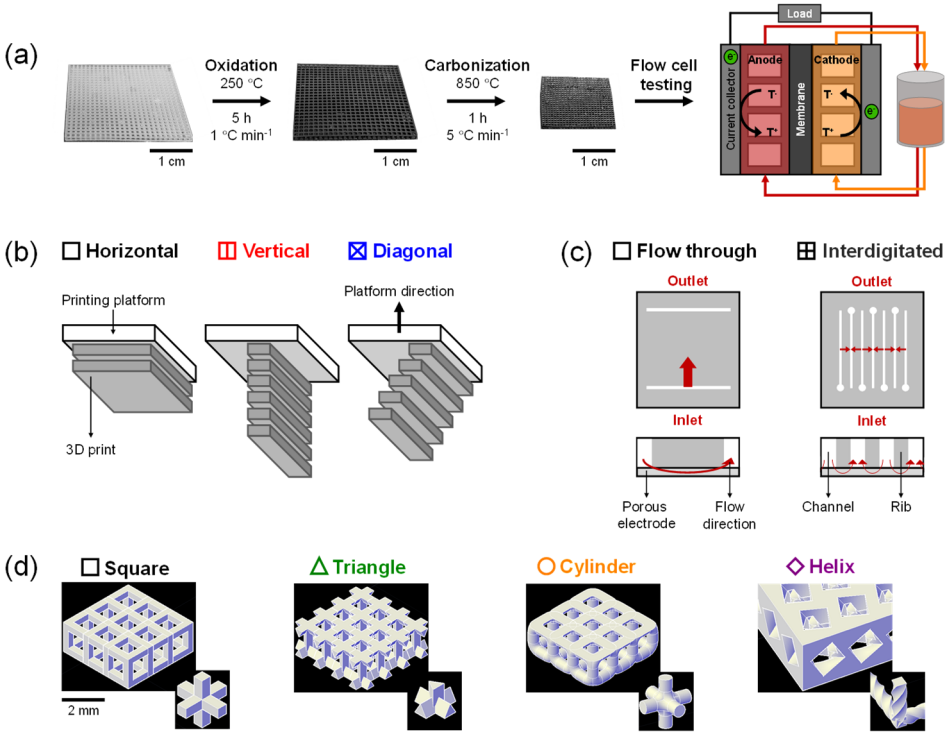

Figure 8.1: Schematic representation of the outline of this manuscript, with: **(a)** the process workflow to obtain a conductive electrode from a nonconductive 3D print to be tested in a flow cell, and **(b-d)** the different systems tested for their performance in a flow cell consisting of studies on: **(b)** the printing direction, **(c)** the flow field, and **(d)** the pillar shape.

In this study, we first discuss the manufacturing of the 3D printed electrodes (**Figure 8.1a**), comprising the thermal treatment steps and structure evaluation. Second, we analyze the physicochemical properties of the 3D printed electrodes including the carbon content, conductivity, and surface area. Third, we examine the pressure drop of the printed electrodes. Fourth, we describe the effect of a horizontal, vertical, and diagonal

printing direction on the structure performance (**Figure 8.1b**), followed by the influence of distinct flow fields (flow through and interdigitated, **Figure 8.1c**), and pillar shapes (square, triangle, cylinder, and helix, **Figure 8.1d**). Lastly, we analyze the influence of the printing direction, flow field, and pillar shape on the dimensionless mass transport within the electrode, where we make a comparison between the 3D printed electrodes and two commercial porous electrodes to evaluate their potential for RFB applications. This study shows the capability of 3D printing to manufacture customized structures, enabling the fine-tuning of the electrochemical performance and pressure drop of porous electrodes. We hypothesize that a combination of additive manufacturing with emerging computational approaches in topology optimization [21] could enable the bottom-up design and manufacturing of advanced electrode materials.

8.2. Materials and methods

8.2.1. 3D printing

The four 3D printed electrode designs (30 x 30 x 1.5 mm^3, **Figure 8.1d**) were drawn using the AUTOCAD (LT 2023) software. The void space of one repeating unit of the square and helical designs, hereafter referred to as pores, was 0.9 x 0.9 x 0.9 mm^3 in size with a pillar thickness of 0.3 mm, the triangular design pores of 0.81 x 0.81 x 0.81 mm^3 with pillars of 0.48 mm, and the cylindrical design pores of 0.72 x 0.72 x 0.72 mm^3 with pillars of 0.48 mm, resulting in a calculated porosity of approximately 77 % for all designs. The AUTOCAD designs were loaded into the 3D printing software PreForm (Formlabs) where the 3D designs were translated to printable structures by adding a baseplate and support pillars using the auto-generate option (density of 1.00 and a touchpoint size of 0.50 mm), connecting the baseplate to the 3D design (**Figure A8.1**). The designs were orientated parallel to the printing platform for the horizontal printing direction, whereas for the vertical and diagonal printing directions, the designs were orientated with a 90° and 45° angle to the printing platform, respectively (**Figure 8.1b**, **Figure A8.1**). The stereolithography 3D printer Form 3 (Formlabs) was used with the clear acrylate-based UV-curing High Temp V2 (Formlabs) resin. The 3D printer was equipped with a 405 nm laser, a power of 120 mW, a laser spot size of 85 µm, an XY motor resolution of 25 - 300 µm (based on the printer settings), and a Z motor resolution of 25 µm, provided by Formlabs, where the X/Y/Z resolution refers to the laser step size in the specified direction. The total printing time was approximately 1 hour per structure. Finally, the 3D prints were washed using the Form Wash (Formlabs) for 5 minutes in isopropanol to rinse off the excess resin.

8.2.2. Thermal treatment

To understand the thermal response of the resin in terms of its thermal stability and degradation, we performed thermogravimetric analysis (PerkinElmer TGA 4000 apparatus). The thermogravimetric analysis was performed from room temperature to 1000 °C using a ramp rate of 10 °C min^{-1} and an oxygen or nitrogen gas flow of 20 mL min^{-1}.

After printing the structures, the polymeric scaffolds were thermally treated to form conductive electrodes. First, the 3D printed material was oxidized in a muffle oven

(Naberthem model P300) under atmospheric air at 250 °C for 5 hours at the peak temperature with a ramp rate of 1 °C min^{-1} which functioned as a stabilization step in obtaining the 3D structure with minimal deformation [48]. Subsequently, the material was carbonized in a tubular oven (Carbolite so. 3/96/782, TZF 12/75/700) under a nitrogen atmosphere (0.2 mPa) for 1 hour at a peak temperature of 850 °C with a ramp rate of 5 °C min^{-1} for all structures, except for the cylindrical pillar design. The cylindrical pillar design was carbonized with a ramp rate of 1 °C min^{-1} to prevent structure deformation because of the slightly reduced porosity. Volume shrinkage and thickness decrease occur during carbonization because of the out-gassing of gaseous products, which could lead to structure deformation, including curling due to compressive forces during volume shrinkage (**Figure A8.3c**) [40]. Therefore, we placed the structures (six at once) in a perforated metal framework consisting of stainless-steel plates separated by 2 mm bolts (**Figure A8.2**) to constrict the samples whilst allowing gas release.

8.2.3. Microscopy, spectroscopy, and tomography

The 3D printed surfaces and cross-sections after printing, oxidation, and/or carbonization were examined with a scanning electron microscope (SEM, JEOL JSM-IT100) using a secondary electron imaging (SEI) detector with a 10 kV acceleration voltage. The elemental composition, carbon, oxygen, and nitrogen content of the 3D printed structures were examined with the energy-dispersive X-ray spectroscopy (EDS) detector. To eject more electrons out of the sample, the acceleration voltage was increased to 16 kV. The non-carbonized samples were sputter coated in an argon environment with platinum at 40 mA for 60 seconds before imaging, using a Jeol JFC-2300HR high-resolution fine coater. The equivalent pore diameter was obtained from the SEM images by measuring the pore area using the median filter, threshold, and measuring tools of ImageJ. The pore area was used to calculate the equivalent pore diameter assuming the pore is a perfect circle with the measured pore area, see the inset of **Figure 8.2b** for a visual representation. The electrode thickness was measured using a micrometer at five different locations on the electrodes for all manufactured electrodes (six electrodes per investigated system, n=6).

The elemental analysis of the samples was additionally performed using X-ray Photoelectron Spectroscopy (XPS) using a Thermo Scientific K-alpha X-ray photo-electron spectrometer equipped with a monochromatic small-spot X-ray source and a 180° double-focusing hemispherical analyzer with a 128-channel detector. The spectra were obtained using an aluminum anode (Al Kα = 1486.6 eV) source operating at 72 W with a spot size of 400 µm. Survey scans were measured at a constant energy pass of 200 eV, whereas the region scans for carbon, oxygen, and nitrogen were measured at 50 eV. The background pressure was set to 2×10^{-8} mbar argon and rose to 4×10^{-7} mbar argon during the measurement because of the charge compensation.

The 3D printed electrodes were scanned using a laboratory micro-CT (Scanco Medical µCT 100 cabinet microCT scanner, holder type U50822 with a diameter of 9 mm and a height of 78 mm) at an isotropic resolution of 3.3 µm/voxel. The scans were carried out using a peak potential of 55 kVp, a current of 72 µA, 4 W, and a 0.1 mm aluminum filter to acquire 580 projection images over 360 degrees. The gray-scale X-ray tomographic microscopy (XTM) images were subsequently processed using ImageJ by

applying a two-dimensional median filter with a radius of 2.0 pixels to reduce the noise in the images. Thereafter, each voxel was assigned to either the solid or void phase using a K-means cluster segmentation filter. A 3.3 x 3.3 mm^2 selection was made and imported in Paraview to extract the internal surface area, limited by the imported image size, XTM sample size, resolution, imaging time, and by the selection of an area without defects and curvature. For the visual representation of the samples in 3D, a smaller 1.7 x 1.7 mm^2 area selection was used.

8.2.4. Flow cell configuration

Symmetric flow cell experiments were conducted in a laboratory-scale flow cell platform [8, 49, 50] inside a nitrogen-filled glovebox (MBraun, LABstar, O_2 <1 ppm, H_2O <1 ppm). The electrolyte solution was pumped through the flow cell using a Masterflex L/S® Easy-Load® II pump and LS-14 tubing, where the cell in- and outlets were connected to a single solution reservoir with separate tubing to ensure a constant state of charge at the cell inlets. Custom-made flow cells were used with machined polypropylene (McMaster-Carr) flow diffusers. Graphite current collectors (G347B graphite, 3.18 mm thick, MWI, Inc.) were used and milled with the desired flow field design: flow-through (two 13 x 1 x 0.5 mm^3 flow channels perpendicular to the electrolyte flow) or interdigitated (seven 16 x 1 x 0.5 mm^3 channels parallel to the electrolyte flow, of which four inlet and three outlet channels), to distribute the electrolyte to and through the porous electrode (**Figure 8.1c**). On each half cell, one 3D printed electrode with a geometric area of 2.55 cm^2 (1.7 cm x 1.5 cm) was confined within a 1 mm incompressible polytetrafluoroethylene gasket (ERIKS). The commercial electrodes, Freudenberg H23 and ELAT Cloth, with the same geometrical area, were confined within 165 µm or 375 µm thickness gaskets, respectively. One electrode was used per half-cell. A Daramic 175 (SLI Flatsheet Membrane, 175 µm) porous separator was used to separate both half-cells, and the cell was tightened to 2.2 N m. To account for differences in electrode thickness, the performance was compared at similar inlet velocities, where the 3D printed electrodes with a flow-through flow field (FTFF) were measured at 10, 5.0, 1.5, and 0.5 cm s^{-1} for the polarization experiments (based on previous work [15]) and at 10, 5.0, 2.5, 1, and 0.5 cm s^{-1} for the limiting current density experiments, the 3D printed electrode with the interdigitated flow field (IDFF) at 4, 2.3, 1.5, and 0.5 cm s^{-1} for both experiments (limited by the upper limit of the peristaltic pump and tubes used), and the Freudenberg H23 and ELAT Cloth at 20, 10, 5, and 1.5 cm s^{-1} for the polarization experiments and at 20, 10, 5, 2.5, and 1 cm s^{-1} for the limiting current density experiments (limited by the lower limit of the peristaltic pump and tubes used). All experiments were performed with electrolyte velocities in descending order to enhance electrode wetting by the removal of residual gas bubbles in the cell. The volumetric flow rate, Q, was calculated for the flow-through flow field by multiplying the electrolyte velocity, v, by the geometrical inlet area of the electrode, A_{geo} (thickness multiplied by the width of the electrode), see **equation (8.1)**. Whereas the flow rate of the interdigitated flow field was calculated by multiplying the electrolyte velocity by the number of inlet channels, n_c (4 channels), the length of the channel, L_c (16 mm), and the incompressible gasket thickness, L (1 mm for the 3D printed electrodes), see **equation (8.2)**

$$Q_{FTFF} = vA_{geo} \tag{8.1}$$

$$Q_{IDFF} = vn_cL_cL, \tag{8.2}$$

where Q_{FTFF} and Q_{IDFF} are the volumetric flow rate for the flow-through flow field and interdigitated flow field, respectively.

8.2.5. Electrical conductivity

The electrical conductivity of the carbonized 3D printed electrode was obtained by measuring the electrical resistance of the electrode in a flow cell configuration without flow, where one electrode (with a 1 mm gasket) was located between the two current collectors. The electrical resistance was measured using the Biologic VMP-300 potentiostat with electrochemical impedance spectroscopy at open circuit voltage with an amplitude of 10 mV and a frequency range of 10 kHz - 50 Hz, 8 points per decade, 8 measurements per frequency, and a waiting time of 0.10 period before each frequency, where the high-frequency intercept was identified as the value of the electrode resistance, corrected for the high-frequency intercept of a cell without electrodes (i.e., only flow fields). The measurements were repeated two times for new assemblies (n=2). The electrical conductivity, σ_e, can be obtained from the electrode resistance according to

$$\sigma_e = \frac{L}{A_e R_e}, \tag{8.3}$$

where A_e is the electrode area (2.55 cm^2), and R_e the electrode resistance. The electrical conductivity of commercial electrodes was measured with the appropriate gasket thickness (165 µm for the Freudenberg H23 and 375 µm for the ELAT Cloth) as characteristic length. Because of the nature of this measurement, the electrical conductivity is likely underestimated as contact resistances are not corrected for but could play a significant role.

8.2.6. Pressure drop measurements

The pressure drop measurements were performed with acetonitrile (MeCN, Acros Organics 99.9+ %) as it has similar density, viscosity, and surface tension as the organic electrolyte due to the low species concentration used in this work. The difference between inlet and outlet pressures was measured when stabilized using pressure sensors (Stauff SPG-DIGI-USB, -1 - 16 bar) over a range of flow rates depending on the pressure drop (3D printed electrode between 239.4 - 89.8 mL min^{-1}, carbonized 3D printed electrodes between 180 - 67.5 mL min^{-1}, Freudenberg H23 between 29.7 - 1.5 mL min^{-1}, and the ELAT Cloth between 67.5 - 16.9 mL min^{-1}). For the pressure drop measurement, an altered cell design was used consisting of only one flow field, electrode, and gasket. The membrane in this configuration was replaced with a 3D printed backing plate (High Temp V2, Formlabs) and only one side of the cell was connected to the solution reservoir. The pressure drop of the cells with the electrode was corrected for a cell without an electrode to isolate the pressure drop through the electrode without piping and cell elements. All measurements were repeated twice for new cell assemblies (n=2), and the pump was calibrated for different gasket thicknesses and flow fields used. The Darcy-Forchheimer equation was used to fit the pressure drop data to extract the permeability, κ, of the electrodes according to the following equation:

$$\frac{\Delta P}{L_e} = \frac{\mu v}{\kappa} + \beta \rho v^2, \tag{8.4}$$

with ΔP the pressure drop, L_e the electrode length (17 mm), μ the electrolyte viscosity (3.4 x 10^{-4} Pa s [15]), β the non-Darcy or Forchheimer coefficient, and ρ the electrolyte density (852 kg m^{-3} [15]). The Forchheimer coefficient accounts for inertial effects in the fluid flow [8]. The permeability and Forchheimer coefficients were extracted using a secondary polynomial fit of **equation (8.4)**.

8.2.7. Electrolyte preparation

The oxidized form of the redox couple 2,2,6,6-tetramethyl-1-piperidinyloxy-oxo hexafluorophosphate ($TEMPO^+PF_6^-$) was synthesized inside a nitrogen-filled glove box (MBraun, LABstar, O_2 <1 ppm, H_2O <1 ppm) by chemical oxidation of 2,2,6,6-tetramethylpiperidin-1-yl)oxyl (TEMPO, Sigma Aldrich 98 %, 20.52 g) dissolved in acetonitrile by slowly adding 1.1 molar equivalents of nitrosonium hexafluorophosphate ($NOPF_6$, Thermo Scientific, 95 %, 25.28 g) during 3 hours to prevent NO_x build-up [8]. Afterward, a rotary evaporator (40 °C, gradual decrease from atmospheric pressure to vacuum) was used to recover the $TEMPO^+PF_6^-$. Stock solutions of 750 mL were prepared and stored inside the glovebox for both the polarization and limiting current density experiments. The stock solution for the polarization experiments consisted of 0.1 M TEMPO, 0.1 M $TEMPO^+PF_6^-$, and 1 M tetrabutylammonium hexafluorophosphate ($TBAPF_6$, Sigma Aldrich >99 %) dissolved in MeCN. For the limiting current density experiments, the concentration was lower and asymmetric where the concentration of the reduced species was five times higher, hence the limiting current was determined by the oxidation reaction. This solution consisted of 28.9 mM TEMPO, 5.78 mM $TEMPO^+PF_6^-$, and 1 M $TBAPF_6$ dissolved in MeCN. For each experiment, 20 mL of the stock solutions were used per cell.

8.2.8. Electrochemical performance

All electrochemical measurements, performed with a Biologic VMP-300 potentiostat, were repeated three times for new cell assemblies (n=3) and new electrolyte solutions for each flowrate in descending order. Polarization and limiting current density measurements were performed by employing constant voltage steps of 0.05 V for 1 minute and measuring the steady-state current over a voltage range of 0 - 1 V. Electrochemical impedance spectroscopy measurements were performed at open circuit voltage with an amplitude of 10 mV and a frequency range of 2 Hz – 200 kHz or 20 mHz - 200 kHz, 8 points per decade, 6 measurements per frequency, and a waiting time of 0.10 period before each frequency, where the high-frequency intercept was identified as the value of the total cell resistance and was used to obtain the iR_Ω-corrected potential data. Each cell was first stabilized by flowing the solution for the limiting current density experiments through the cell at the highest flow rate for approximately 10 minutes. Thereafter, the limiting current density experiment was performed (impedance measurement to evaluate the resistance of the cell (2 Hz - 200 kHz), polarization, and impedance (20 mHz - 200 kHz)), after which the electrolyte was replaced, and the regular polarization experiment was performed (impedance, polarization, and impedance).

8.2.9. Limiting current measurements

The limiting current can be obtained by diminishing the active species concentration such that at an applied potential the surface concentration can be assumed zero. The limiting current was defined as [10, 14, 29, 51]:

$$i_{lim} = naFC_{i,b}k_m, \tag{8.5}$$

where i_{lim} is the limiting current per electrode volume, n the number of electrons transferred (n=1 for the TEMPO/TEMPO$^+$PF$_6^-$ system), a the internal surface area of the electrode, F Faraday's constant, $C_{i,b}$ the bulk concentration of the oxidized species i, and k_m the mass transfer coefficient. From the limiting current density, the volume-specific surface area mass transfer coefficient ($a\ k_m$) can be estimated as follows

$$a\ k_m = \frac{I_{lim}}{nFC_{i,b}V}, \tag{8.6}$$

with I_{lim} the current measured by the polarization experiment with fixed potential steps and V the electrode volume. Using **equation (8.6)**, the resulting $a\ k_m$ values for the different electrodes at a range of superficial velocities can be found and plotted on a double-log scale. The slope represents a power law relationship in the following form:

$$a\ k_m = C1v^{C2}, \tag{8.7}$$

where $C1$ represents the dimensionless prefactor and $C2$ the dimensionless exponent.

8.2.10. Commercial electrode materials

To compare the 3D printed electrodes with commercial electrodes, two carbon fiber-based, binder-free electrodes were selected with distinct microstructural properties and good performance in non-aqueous RFBs [8, 51]: a non-woven Freudenberg H23 (Fuel Cell Store, 210 µm uncompressed thickness and 80 % porosity) paper electrode with curved fibers and a narrow PSD in the range of 2 - 40 µm [8, 15], and a highly ordered woven ELAT Cloth (Fuel Cell Store, 380 µm uncompressed thickness and 82 % porosity) electrode with a plane weave pattern and a bimodal PSD of about 2 - 300 µm (approximately 2 - 40 µm and 40 - 300 µm) [8, 15].

8.2.11. Surface area determinations

The internal surface area of the 3D printed electrode was determined by three different methods. **(1)** The first method was by algebraic calculations of the internal geometrical surface area by the set pillar and pore sizes for the 3D print (AUTOCAD), and by the measured pillar and pore sizes using SEM and ImageJ for the resulting carbonized structure, considering the geometry of spheres, cuboids, cylinders, and triangular prisms. **(2)** The second method was by measuring the ratio in exchange current densities between the 3D printed electrodes and the commercial Freudenberg H23 with known internal surface area (7.2 x 10^4 m^{-2} m^{-3} [8]), as the exchange current density can be defined as:

$$j_0 = aFk_0C_i^{\alpha}C_j^{\alpha}, \tag{8.8}$$

where j_0 is the exchange current density per electrode volume, k_0 the standard rate constant that was assumed comparable for the different electrodes for the estimation of the surface area, $C_{i/j}$ the concentration of the reduced and oxidized species (100 mol m^{-3}), and α the charge transfer coefficient of the reduced or oxidized species (we assumed 0.5 for both TEMPO and $TEMPO^{+}PF_6^{-}$ [52]). The exchange current density was obtained from the polarization data by fitting the low current density region (< 100 mA cm^{-2}) to the Butler-Volmer equation [15]:

$$i = j_0 \left(\frac{C_{i,s}}{C_{i,b}}\right)\left[\exp(-\frac{\alpha F \eta_{act}}{RT}) - \exp(\frac{\alpha F \eta_{act}}{RT})\right], \quad (8.9)$$

where i is the current density per volume obtained from the polarization curve, $C_{i,s}$ the surface concentration of species i, $C_{i,b}$ the bulk concentration of species i, and η_{act} the activation overpotential obtained after iR_Ω-correction of the experimental data and assuming the mass transfer overpotential to be negligible, thus the surface concentration being equal to the bulk concentration. **(3)** The third method used the XTM images, where a 3.3 x 3.3 mm^2 selection was made from the center of the processed image to prevent boundary effects from sample cutting. This image was imported in Paraview to extract the internal surface area by applying the threshold (0.5 - 255), contour, extract surface, and integrate variables (cell data) filters.

The algebraic approach (method **(1)**) was also used to obtain the porosity of the electrode by dividing the void volume by the total volume of the electrode, based on the pore and pillar dimensions set by AUTOCAD, or obtained from the equivalent diameter using the SEM images in combination with ImageJ (as described in **Section 8.2.3**).

8.3. Results and discussion

8.3.1. Thermal sequence and manufacturing fidelity

Designed ordered lattice structures were manufactured by 3D printing of a resin, consisting of acrylate monomers, urethane dimethacrylate, and a photoinitiator, with an SLA printer. To obtain a well-defined conductive electrode that can be used in flow batteries, the 3D printed structures need to be carbonized (**Figure 8.1a**). We find that, to carbonize acrylic structures without large structural deformation, the 3D prints should have a porosity of at least 70 % after printing (determined experimentally), and should be placed in a perforated metal framework (**Figure A8.2** and **A8.3a,c**). In addition, the curing of the resin must be investigated depending on the type of resin and 3D printer used [53]. In this study, it was found that for the High Temp V2 resin, the printing resolution was impacted by significant resin spreading and curing of excess resin into the pores, resulting in a 150 ± 50 µm smaller pore diameter than the input geometry (**Figure A8.4**). Therefore, it was chosen, considering the porosity of the print, to manufacture square pillar designs with pores of 0.9 x 0.9 x 0.9 mm^3 and a pillar thickness of 0.3 mm.

First, a thermographic analysis must be performed (**Figure 8.2a**) to investigate if the material can withstand carbonization. Then, the appropriate thermal sequence must be selected, which is material-dependent (i.e., resin formulation and material geometry) [42]. The carbonization temperature impacts the carbon content, carbon structure (amorphous to crystalline carbon), carbonization phase (polyaddition, pyrolysis,

dehydrogenation, or annealing), and thus the conductivity of the material. The ramp rate impacts the gas release rate which can drastically influence the resulting structure by impacting the carbon atom rearrangement, carbon content, and surface area [40, 42, 54, 55]. Carbonization sequences used in the literature [22, 35] resulted in significant structure deformation and were thus not suited for the resin used in this work (**Figure A8.3b**). Therefore, the thermal sequence was selected based on the thermogravimetric analysis performed (**Figure 8.2a**), which showed that the main mass loss for this material, due to dehydrogenation, polymer degradation, and the out-gassing of gaseous products [40, 42], is between 300 - 450 °C in a nitrogen atmosphere and thus the oxidation step should be <300 °C and the carbonization step >450 °C. It was found that oxidation at 250 °C for 5 hours with a ramp rate of 1 °C min^{-1} before carbonization at 850 °C for 1 hour with a ramp rate of 5 °C min^{-1} resulted in a stable carbonized 3D printed structure. The oxidation step before carbonization acts as a stabilization step and involves chemical reactions such as crosslinking [48, 56], which is crucial in obtaining 3D structures with minimal deformation. Literature studies have shown that the carbonization temperature should be >1100 °C to obtain highly conductive structures [55–57]; yet, in this work, the structures were carbonized at 850 °C because of the upper limit of the carbonization oven used, which resulted in conductive electrodes (**Table 8.1**, 85 S m^{-1} for the 3D printed electrode compared to 82 S m^{-1} for the Freudenberg H23 and 122 S m^{-1} for the ELAT Cloth).

SEM was used to visualize the structures after printing, oxidation, and carbonization (**Figure 8.2c-d**), for which ImageJ was used to extract the equivalent diameters (**Figure 8.2b**) to assess the pore shrinkage due to dehydrogenation, polymer degradation, and the out-gassing of gaseous products after thermal treatment [40, 42]. To quantify the shrinkage of the horizontally printed structure, we elect to visualize the pores from the top (top layer after printing), bottom, and side. Upon oxidation, the pore sizes shrunk by 11 % in an isotropic manner as shown in **Figure 8.2b**, whereas after carbonization the total pore shrinkage was 45 % and anisotropic, as the pores at the top shrunk more (52 %) than the pores at the side (40 %). We hypothesize that this anisotropic shrinkage is a result of the printing line direction, as these printing lines are in the through-plane direction (perpendicular to the flow with an FTFF, **Figure 8.2c**), and partially retain their features after carbonization. Interestingly, for the vertical printing direction, the pores at the side shrunk more (45 %) than the top and bottom pores (39 %) because of the printing lines in the in-plane direction. The diagonal case lies in between, where an isotropic shrinkage of 50 % is observed in all directions. The pore diameters of all systems are shown in **Tables A8.1** and **A8.2**. Furthermore, the shrinkage caused a porosity decrease for all tested electrodes (from 77 % to 59 % for the horizontally printed electrode, see **Table 8.1**, based on the pillar and pore geometry, assuming a smooth electrode surface).

When comparing the 3D printed carbonized structures to the SEM images before carbonization (**Figures 8.2**, **8.4a**, and **A8.6 - A8.7**) and the input geometry (**Figure 8.1d**), it is observed that the distinct pillar shapes remain mainly present upon carbonization, especially for the square and triangular designs. The cylinder and helical structures however show deviations from the input geometry which is partially a result of the 3D printing accompanied by resin spreading and curing into the pores. Although the SEM images before and after carbonization show similar structural properties (**Figure A8.7**), both electrodes expanded on the highest density regions (pillar connections) after carbonization, altering the surface curvature at the top side for both designs, as well as

the pore shape of the cylindrical design. Overall, these results show the versatility of SLA 3D printing in combination with carbonization to obtain porous electrodes with geometrical (electrode design) and orientational (printing direction) flexibility.

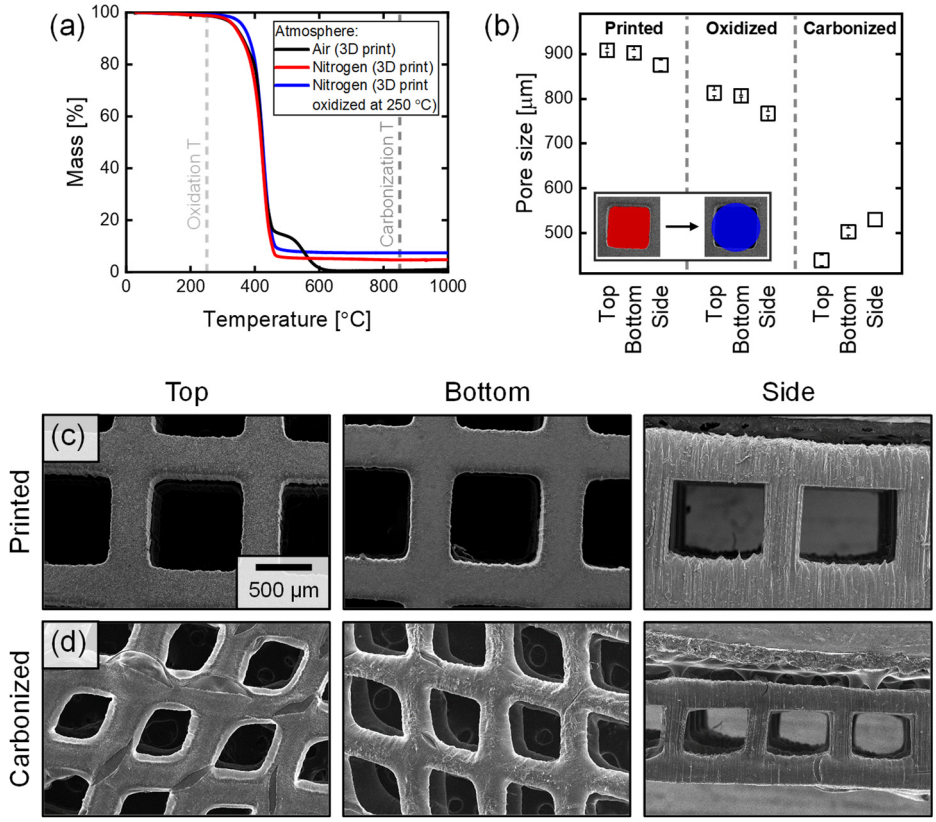

Figure 8.2: (a) The mass loss with temperature of the 3D print in air or nitrogen atmosphere, and that of the oxidized 3D print in a nitrogen atmosphere, extracted from thermogravimetric analysis. The dashed lines display the chosen oxidation and carbonization temperatures of 250 °C and 850 °C, respectively. **(b-d)** To quantify the pore shrinkage, we elect to visualize the pores from the top, bottom, and side. **(b)** The pore sizes of the top, bottom, and side view of the horizontal 3D print after printing, oxidation, and carbonization (n=6), where the pore size was extracted using ImageJ by assuming the pore to be a perfect circle with the pore size being the equivalent pore diameter, visualized by the figure inset. **(c-d)** Scanning electron microscope images of the 3D prints of the top, bottom, and side view (from left to right) at 50 x magnification for the horizontal 3D structure after **(c)** printing, and **(d)** carbonization.

8.3.2. Physicochemical analysis

Following the manufacturing of the 3D printed electrodes, the carbon content, conductivity, and surface area should be analyzed. The carbon content was obtained with EDS and XPS (the carbon, oxygen, and nitrogen contents are shown in **Table A8.3**) and increased upon carbonization (from 71 to 94 atom% measured by EDS and from 77 to 82 atom% measured by XPS) accompanied by a decrease in oxygen content (from 27 to

5.0 atom% measured by EDS and from 20 to 12 atom% measured by XPS). Deconvoluted carbon signals obtained by XPS show the increase in carbon sp2/sp3 bonds relative to the carbon-oxygen bonds upon carbonization and can be found in **Section A8.4.2**. Moreover, the material is moderately conductive after carbonization, **Table 8.1** (85 S m^{-1} for the 3D printed electrode compared to 82 S m^{-1} for the Freudenberg H23 and 122 S m^{-1} for the ELAT Cloth). The conductivity is however lower compared to the 3D printed electrode of Niblett *et al.* [35], who obtained a conductivity of 150 S m^{-1} after carbonization at 900 °C. This is because the electrical conductivity in this work is underestimated as a result of contact resistances (the electrical conductivity of commercial electrodes is ~300 S m^{-1} [51]). Nevertheless, carbonization at higher temperatures (e.g., >1100 °C) enables the formation of highly conductive graphitic structures [55–57], which should be the focus of future work.

Table 8.1: Material characteristics of the 3D print with a square pillar shape and horizontal printing direction after printing and carbonization, where the internal surface area was obtained with three different methods: *1 by algebraic calculations of the pillar and pore sizes, *2 by the exchange current density ratio between the 3D printed electrode and a commercial (paper) electrode with known internal surface area, and *3 by extracting the internal surface area from the XTM images using Paraview. ‡ The 3D printed material swells and partially dissolves upon contact with acetonitrile, thus a reliable permeability value could not be obtained.

	Printed	**Carbonized**
Porosity [%]	77*1	59*1
Internal surface area [m^2 m^{-3}]	2671*1	4697*1/ 6581*2 / 6471*3
Conductivity [S m^{-1}]	0	85
In-plane permeability x 10^{-10} [m^{-2}]	5.7‡	47
Forchheimer coefficient x 10^4 [m^{-1}]	0.87‡	0.32
Minimum pore size [µm]	902 ± 8	439 ± 12
Thickness [µm]	1500	1210 ± 123

The available surface area and the surface density of electroactive sites of the electrode dictate the number of reaction sites present for the electrochemical reactions. Yet, in this work the available surface area was estimated based on the geometry defined by the input structure before carbonization and by three different methods after carbonization (by geometrical calculations, by the ratio between exchange current densities, and by using XTM images), see **Table 8.1**. It was found that the internal surface area per volume increases by a factor of two after carbonization. Moreover, the internal surface area is further increased for the vertical and diagonal designs as a result of the printing lines that induce surface roughness (**Table 8.2**), where the diagonal orientation has the highest internal surface area. Regarding the pillar structure analysis, the internal surface area was slightly impacted by the design choice of evaluating at constant porosity, affecting the pillar and pore dimensions and thus the internal surface area (**Table A8.4 - A8.5**). Consequently, the helical design has the highest internal surface area, and the triangular design has the lowest. Nonetheless, the final porosity and surface area remain notably low for the 3D printed electrodes compared to commercially available electrodes with a porosity of 66 - 90 % [8, 15, 19, 58], and an internal surface area of 7.2 x 10^4 m^2 m^{-3} [8] for the paper electrode and 1.4 x 10^4 m^2 m^{-3} for the cloth electrode [4, 15]. This is a result of the big pores and narrow PSD (490 - 530 µm), resulting from the printer resolution, compared to the PSD of commercial electrodes with significantly smaller pores.

Table 8.2: The internal surface area of the different 3D printed electrodes after carbonization, where the internal surface area was obtained with two methods: *2 by the exchange current density ratio between the 3D printed electrode and a commercial electrode with known internal surface area, and *3 by extracting the internal surface area from the XTM images using Paraview. Together with the constants ($C1$ and $C2$) of the volume-specific surface area mass transfer coefficient ($a\ k_m$) as a function of the electrolyte velocity, and the constants ($C3$ and $C4$) of the Sherwood number as a function of the Peclet number, where the exponential factors ($C2$ and $C4$) are the same for both mass transfer expressions.

Printing direction – pillar shape – flow field	Internal surface area [$m^2\ m^{-3}$]	$C1$ [-]	$C2 = C4$ [-]	$C3^{*3}$ [-]
Horizontal – square – FTFF	6581*2 / 6471*3	0.131	0.701	0.010
Vertical – square – FTFF	8663*2 / 7006*3	0.124	0.621	0.016
Diagonal – square – FTFF	10463*2 / 7040*3	0.123	0.585	0.019
Horizontal – triangle – FTFF	5794*2 / 5046*3	0.131	0.740	0.013
Horizontal – cylinder – FTFF	5850*2 / 5735*3	0.149	0.645	0.023
Horizontal – helix – FTFF	7650*2 / 6560*3	0.179	0.700	0.013
Horizontal – square – IDFF	6581*2 / 6471*3	0.276	0.651	0.030

Moreover, care must be taken with the interpretation of the internal surface area values where in the first and third calculation methods the surface roughness was not considered (not considered in the geometrical calculations and not considered in the extracted images as a result of the XTM imaging resolution), although present as a result of the printing lines (**Figure 8.2c-d**), increasing the internal surface area of the designs [35]. Furthermore, in the second method, the kinetic rate constant of the 3D printed electrode systems was assumed constant to use the ratio between the exchange current densities of the commercial paper electrode, with known internal surface area, and the 3D printed electrodes. Based on the cyclic voltammetry measurements (**Section A8.4.4**), this second method can only be used to compare the 3D printed designs amongst themselves, as the redox reactions on the 3D printed electrode surface are not fully reversible, potentially related to the limited electronic conductivity of the 3D printed electrodes [42]. This was observed by the correlation between the peak current and scan rate, where electrochemical quasi-reversibility is observed for the 3D printed electrode by the shift in peak-to-peak separation with scan rate, showing a different correlation compared to that of the commercial electrode (**Figure A8.12**) [59]. Rezaei *et al*. found that the carbonization conditions of the High Temp V1 resin (Formlabs, an older version of the High Temp V2 used in this study) affect the reversibility of the redox reactions, supporting the need to carbonize 3D printed materials at elevated temperatures [42]. Besides the crude assumptions made in determining the internal surface area of the 3D printed electrodes, the obtained values are in a small range of 4600 - 6600 $m^2\ m^{-3}$ and are significantly lower than that of the commercial electrodes.

8.3.3. Pressure drop

To assess the pumping losses through the electrochemical cell, pressure drop measurements were performed. The permeability, acquired from the Darcy-Forchheimer equation (**equation (8.4)**), and pressure drop before and after carbonization of the 3D printed electrodes can be compared to two commercial electrodes with distinct electrode geometries: the binder-free randomly organized Freudenberg H23 paper electrode with a narrow PSD and the highly ordered ELAT Cloth woven electrode with a bimodal PSD.

It was found that the pressure drop of the 3D printed electrodes is reduced by a factor of ~14 compared to the cloth electrode and by a factor of ~65 compared to the paper electrode at a constant electrolyte velocity (at 10 cm s^{-1}, **Figure 8.3a**). Hence, resulting in a higher permeability (47 x 10^{-10} m^2 for the 3D printed electrode compared to 0.16 x 10^{-10} m^2 and 0.89 x 10^{-10} m^2 for the paper and cloth electrodes, respectively), which is a remnant of the big pore sizes in the 3D printed electrode ordered as highly connected transport pathways in both the in-plane and through-plane directions [21]. The large pores in the 3D printed electrode additionally affect the inertial effects in the electrodes, captured by the Forchheimer coefficient that describes the deviation of the pressure drop from Darcy's law, which is significantly lower than for the commercial electrodes (0.32 x 10^4 m^{-1} for the 3D printed electrode compared to 2.8 x 10^4 m^{-1} and 1.4 x 10^4 m^{-1} for the paper and cloth electrodes, respectively).

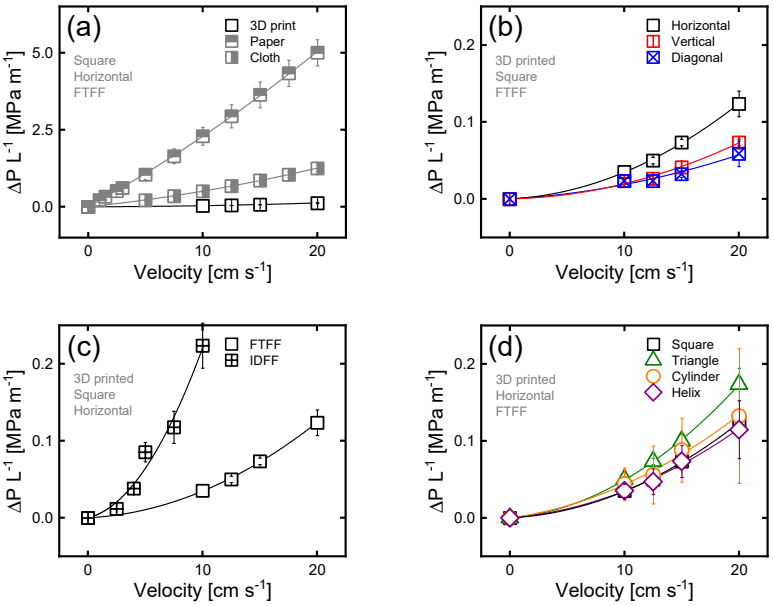

Figure 8.3: The pressure drop values (n=2) over a range of electrolyte velocities for: **(a)** the 3D printed, paper, and cloth electrode, **(b)** the horizontal, vertical, and diagonal printing directions, **(c)** the flow through and interdigitated flow fields, and **(d)** the square, triangular, cylindrical, and helical pillar shapes. The horizontal, FTFF, square, and 3D printed refer to the same 3D printed electrode. The permeability and Forchheimer coefficients were obtained with a secondary polynomial fit of **equation (8.4)**.

Compared to the horizontal orientation, the pressure drop is lower for both the vertical and diagonal printed systems (**Figure 8.3b**). Furthermore, the inertial effects in the vertical and diagonal printed systems were reduced compared to the horizontal system (**Table A8.5**) which is a remnant of the through-plane surface roughness in this system, that enhances electrolyte mixing by inertial effects. Moreover, the flow field impacts the pressure drop in the system [60]. Compared to the FTFF, the IDFF electrolyte pathway through the electrode is reduced (over a 1 mm rib instead of over the 17 mm electrode length from the inlet to the outlet channel(s)). Therefore, for fibrous paper electrodes with a small and narrow PSD (e.g., Freudenberg H23), the pressure drop is greatly decreased when using an IDFF; however, for structures with large pores in the in-plane direction

(e.g., 3D printed electrodes or cloth electrodes) the pressure drop can be higher [60]. This is observed for the 3D printed electrode, where the pressure drop is larger because of the fluid pathway in this flow field (**Figure 8.1c**), which is both in the in-plane and through-plane directions from the inlet channel, over the rib, to the outlet channel. Thus, the electrolyte is forced through the structure and cannot follow a straight fluid pathway from the inlet to the outlet channel as is the case for the FTFF. Furthermore, the pillars partially block the inlet and outlet channels of the IDFF, increasing the pressure drop, resulting in a higher inertial contribution (2.4×10^4 m^{-1}) and a lower permeability (24×10^{-10} m^2). Lastly, the pressure drop through the electrode is affected by the pillar shape. Utilizing a triangular design increases the pressure drop, whereas the pressure drop could be slightly reduced by using a helical pillar shape. Nonetheless, the permeabilities follow a diverse trend as a result of the inertial contributions, where the highest permeability can be achieved by using a square pillar design (**Table A8.5**).

8.3.4. Influence of printing direction

To evaluate the potential of using 3D printed electrodes for RFB applications, the electrochemical performance in a symmetric flow cell is analyzed by performing polarization and electrochemical impedance spectroscopy measurements. The electrochemical performance is analyzed using iR_Ω-corrected polarization curves to investigate the effect of the internal surface area and mass transfer in the 3D printed electrode designs. In this study, a non-aqueous electrolyte was used to ensure complete wetting of the carbonaceous structure [8]. Hence, pretreatment or functionalization of the electrode to improve wetting can be omitted because of the low surface tension of the solvent. To employ the 3D prints in aqueous systems, the hydrophilicity should be improved through modifications of the carbon electrode surfaces by, for example, post-thermal treatment of the carbonized structure [61], but this is beyond the scope of this work.

First, the influence of the printing direction on the electrode performance was investigated. SLA is a point-based, layer-by-layer technique resulting in high geometrical and orientational (printing direction) design flexibility. The orientation of the designs impacts the electrode performance because of resin curing of individual layers, affecting the internal surface area, conductivity, shrinkage upon carbonization, and the resin spreading that is additionally affected by gravity. The printing orientation regarding the printing platform is therefore of interest to optimize the performance of 3D printed electrodes in future work. In this work, the 3D prints were orientated with a 0°, 90°, and 45° angle regarding the printing platform to manufacture designs with a horizontal, vertical, and diagonal printing direction, respectively (**Figures 8.1b**, **8.4a-b**, and **A8.9**).

Enhanced performance is observed for the vertical and diagonal systems in **Figure 8.4c**. The increase in surface area can directly be connected to an increase in electrochemical performance, as the attainable current density linearly correlates to the internal surface area by the charge transfer overpotential [10]. In addition, the convoluted charge and mass transfer resistances are lower for these systems (**Figure 8.4d**) because of the increased surface area. Unfortunately, these resistances are convoluted in the impedance plots, most likely due to distributed ohmic on account of electronic resistances [62, 63] caused by the carbonization at a relatively low temperature and lack of sufficient solid phase conductivity [40, 55]. Nevertheless, the differences between the impedance spectra of the three systems are velocity-dependent, highlighting that the printing

direction additionally impacts the mass transfer overpotential. A note must be made on the high-frequency intercept of the three different systems, as this value, which includes the membrane resistance and contact resistances, is 1.4 times higher for the diagonal system (**Figure A8.17**) as a result of higher contact resistances because of a reduced electrode thickness (**Table A8.5**).

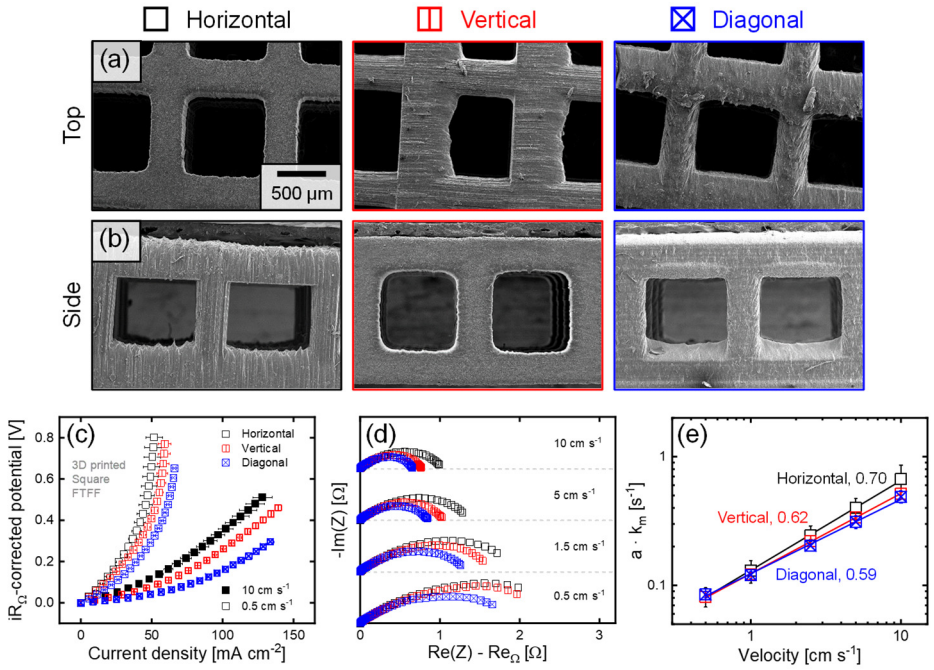

Figure 8.4: (a-b) Scanning electron microscope images of the 3D prints of the horizontal, vertical, and diagonal printing direction (from left to right) at 50 x magnification, for the 3D structure after printing **(a)** from the top, and **(b)** from the side. **(c-e)** Electrochemical data (n=3) of the horizontal, vertical, and diagonal printing directions, with: **(c)** the iRΩ-corrected polarization curves at 10 and 0.5 cm s^{-1}, **(d)** the electrochemical impedance spectroscopy data corrected for the high-frequency intercept at 10, 5, 1.5, and 0.5 cm s^{-1}, and **(e)** the $a\ k_m$ values for different superficial velocities with the best-fit lines (solid lines) and the slope of the fit (next to the system label), plotted on a double-log scale.

The impact of the printing direction on the mass transport in the electrode can be assessed by measuring the limiting current over a range of superficial velocities (**Figure 8.4e**). The prefactors and exponents of the different systems can be found in **Table 8.2**. At increased electrolyte velocities, the mass transfer is enhanced in the horizontal system compared to the vertical and diagonal systems. This is a result of the stronger dependency on the electrolyte velocity by a higher exponent (**Table 8.2**) potentially caused by the through-plane surface roughness (**Figure 8.4a-b**) leading to increased turbulence and thus mixing, as was observed by the higher inertial contribution to the pressure drop (**Table A8.5**). Thus, whereas the diagonal system has a higher electrochemical performance, the mass transfer can be enhanced with horizontal systems.

8.3.5. Influence of the flow field type

The interplay between the flow field design and electrode structure has proven to be crucial in the selection of electrode types for RFBs [60]. Therefore, we investigate two commonly used flow field designs, the FTFF (used throughout this study as a reference flow field) and the IDFF, both with distinct flow distributions through the electrode. Compared to the FTFF, the IDFF electrolyte pathway length through the electrode is reduced, impacting the mass transfer and thus the electrochemical performance (**Figure 8.5a**). The flow distribution in the IDFF reduces the mass transfer overpotential [50, 51] at all measured electrolyte velocities (**Figure 8.5b, Figure A8.14b**) by providing a shorter electrolyte transport path, potentially by an improved active species mass transfer of the bulk to the electrode surface, and by increased inertial effects and mixing (**Section 8.3.3**).

The mass transfer coefficient through the electrode is greatly enhanced when utilizing an IDFF compared to an FTFF (**Figure 8.5c**) [50, 51], resulting in a twice as high prefactor (**Table 8.2**). Although the prefactor is significantly higher for the IDFF, the dependency on the electrolyte velocity is reduced. This is because the effect on the exponent in **equation (8.7)** depends on the electrode-flow field combination. IDFFs are anticipated to reduce this exponent significantly compared to flow-through designs for electrodes with a uniformly narrow PSD of pores in the sub-micrometer range (e.g., paper electrodes [51]), and only slightly impact the exponent for electrodes with a bimodal PSD (e.g., woven electrodes [58]) spanning a larger pore size range, as also observed in this work (**Table 8.2**).

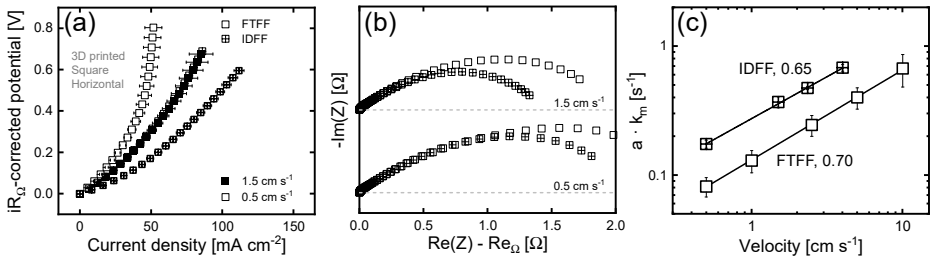

Figure 8.5: Electrochemical data (n=3) of the 3D printed electrode with a flow through and interdigitated flow field, with: **(a)** the iRΩ-corrected polarization curves at 1.5 and 0.5 cm s^{-1}, **(b)** the electrochemical impedance spectroscopy data corrected for the high-frequency intercept at 1.5 and 0.5 cm s^{-1}, and **(c)** the $a\ k_m$ values for different superficial velocities with the best-fit lines (solid lines) and the slope of the fit (next to the system label), plotted on a double-log scale.

8.3.6. Influence of pillar geometry

Turbulence promotors or electrode mixers are used in many research fields to enhance mass transfer by inducing turbulence or mixing in the system [13, 28, 29, 64, 65]. Consequently, the mass transfer at the electrode surface is enhanced resulting in an increased limiting current density (**Figure A8.18**). The importance of the electrode microstructure (e.g., pillar shape or mixer unit cell) on the mass transport was shown by Hereijgers *et al*. in their structured 3D electrodes derived from static mixer unit cell designs. They showed that similar mass transfer coefficients and electrochemical output can be obtained whilst

reducing the pressure drop substantially [29]. Furthermore, de Rop *et al.*, showed with computational fluid dynamics simulations that, by changing the pillar shape in electrochemical reactors from cylindrical to diamond, the mass transfer coefficient can be increased by a factor of two as a result of significant mixing effects [66]. Hence, in this work we investigate the influence of the electrode pillar shape on the electrochemical performance, focusing on mass transport. To this end, our ordered cubic lattice structures with distinct pillar geometries (square, triangular, cylindrical, and helical, **Figure 8.6a**) were investigated. To compare the different structures, the porosity was kept constant, impacting the pillar and pore dimensions slightly for the different structures (**Section 8.2.1**).

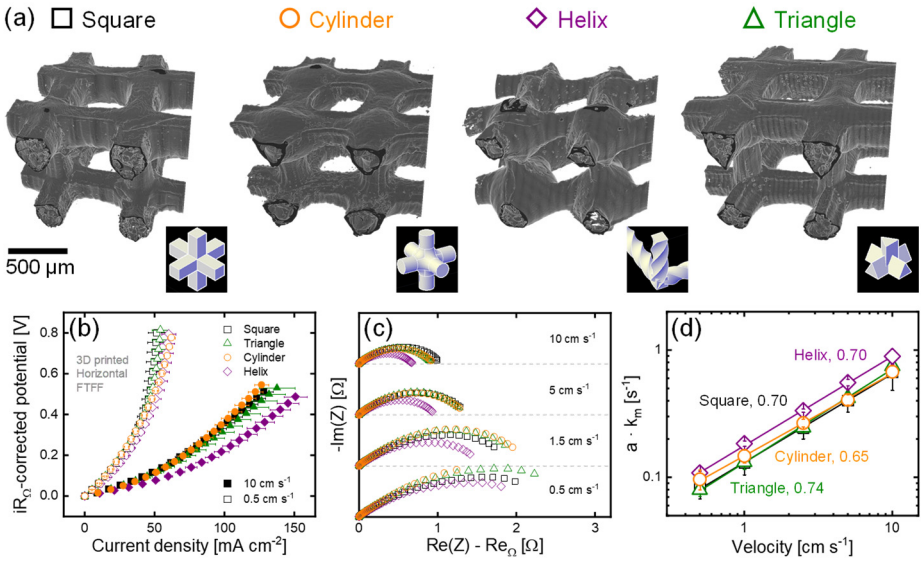

Figure 8.6: (a) Subsection of the X-ray tomographic images of the 3D prints after carbonization with a square, triangular, cylindrical, and helical pillar structure. **(b-d)** Electrochemical data (n=3) of the square, triangular, cylindrical, and helical pillar shapes, with: **(b)** the iR_Ω-corrected polarization curves at 10 and 0.5 cm s^{-1}, **(c)** the electrochemical impedance spectroscopy data corrected for the high-frequency intercept at 10, 5, 1.5, and 0.5 cm s^{-1}, and **(d)** the $a\ k_m$ values for different superficial velocities with the best-fit lines (solid lines) and the slope of the fit (next to the system label), plotted on a double-log scale.

We found that the triangular and cylindrical pillar shapes do not significantly affect the electrochemical performance (**Figure 8.6b**) compared to the square pillar shape. The combined charge and mass transfer resistances in these structures are similar to that of the square system but slightly lower at enhanced electrolyte velocities and higher at reduced electrolyte velocities (**Figure 8.6c**). This is a result of the lower internal surface area of the triangular and cylindrical systems (**Table 8.2**), increasing the charge transfer overpotential, in combination with the distinct mass transfer relationships for these electrodes (**Figure 8.6d**), impacting the dependency of the mass transfer overpotential on the electrolyte velocity. The helical pillar shape, however, especially impacts the current density and resistance compared to the other designs (**Figure 8.6b-c**). This is hypothesized to be related to the higher internal surface area and improved mass transfer through the electrode (**Figure 8.6d**), which indicates a relationship between the pillar

geometry and the mass transfer through the electrode. Based on the literature [66], it is anticipated that the pillar geometry presented in this work influences the mass transport through the electrode by affecting the electrolyte distribution around the pillars. The helical pillar shape shows an increased mass transfer coefficient with a 1.4 times higher prefactor compared to the square pillar shape (**Figure 8.6d** and **Table 8.2**) where the helical twist in the pillar structure (**Figure 8.6a**) is expected to induce local mixing of the electrolyte, improving the active species mass transfer of the bulk to the electrode surface [28, 29, 33, 66]. Future work could focus on visualizing the concentration distribution around the pillars in ordered structures, for example using fluorescence [67] or confocal microscopy, to better understand the mixing phenomenon in porous electrodes.

8.3.7. Mass transfer correlations

Typically, the mass transfer relation is extended to compute non-dimensional numbers such as the Sherwood (Sh) and the Peclet (Pe) numbers to correct for the differences in internal surface area and porosity between electrode structures. Using this approach, the manufactured structures can be compared to commercial electrodes in terms of their mass transfer coefficient, corrected for differences in porosity and internal surface area. The Sherwood number describes the correlation between the convective and diffusive mass transport, defined as

$$Sh = \frac{\varepsilon a k_m}{D_i a^2}, \tag{8.10}$$

with ε being the electrode porosity, a the internal surface area of the electrode, k_m the mass transfer coefficient, and D_i the electrolyte diffusion coefficient (1.3 x 10^{-9} m^2 s^{-1} for the TEMPO/$TEMPO^+PF_6^-$ couple [14, 68]). The Peclet number relates the convective velocity to the diffusive velocity as follows:

$$Pe = \frac{v}{aD_i}. \tag{8.11}$$

By plotting the Sherwood number over the Peclet number, a power law relationship can be determined in the following form

$$Sh = C3Pe^{C4}, \tag{8.12}$$

where $C3$ is the prefactor and $C4$ the exponent. By fitting the experimental data to this relationship, the mass transfer can be analyzed by dimensionless numbers, where a larger exponent results in a stronger velocity dependency of the mass transfer coefficient [13]. **Figure 8.7** shows this relation and the prefactors and exponents are listed in **Table 8.2**.

For the printing direction study (**Figure 8.7a**) no noticeable differences were observed compared to **Figure 8.4e** as only the contrast between the distinct printing directions becomes more pronounced at higher Peclet numbers. Furthermore, as the IDFF is investigated with the same electrode design (identical porosity and surface area), the differences between the flow fields remain the same, where the IDFF outperforms the FTFF with a significantly higher prefactor but a reduced velocity dependency (**Figure 8.7b)**. For the various pillar shapes when corrected for the internal surface area and porosity (**Figure 8.7c**), we find that the square design features the lowest prefactor compared to the other structures, showing the dependency of different morphologies on

the mass transfer rates. Furthermore, the triangular design has a greater dependency on the electrolyte velocity, and the cylindrical design a smaller, resulting in differences in mass transfer at larger Peclet numbers. The corrected mass transfer relations confirm the higher activation overpotential contribution to the polarization and impedance curves for the cylindrical and triangular designs (**Figure 8.6b-c**) and hint that these structures, like the helical structure, could enhance the mass transfer around the pillars compared to the square design [66]. This study shows that by slightly affecting the electrode geometry by altering the pillar shape or printing direction, the mass transfer in the electrode can be enhanced. Hence, future work should focus on diverse pillar or fiber shapes and their orientation [16] to enhance the mass transport in porous electrodes for RFBs.

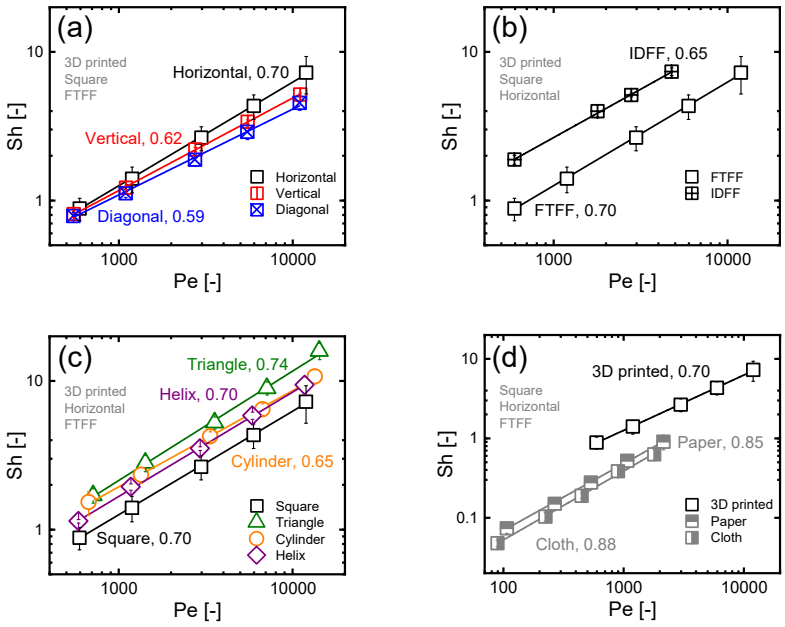

Figure 8.7: The mass transfer relations for different superficial velocities (n=3) represented by the Sherwood over the Peclet number with the best-fit lines (solid lines) and the slope of the fit (next to the system label), plotted on a double-log scale for: **(a)** the horizontal, vertical, and diagonal printing direction, **(b)** the flow through and interdigitated flow field, **(c)** the square, triangular, cylindrical, and helical pillar shapes, and **(d)** the 3D print and commercial paper and cloth electrodes. The horizontal, FTFF, square, and 3D print refer to the same 3D printed electrode.

Even though the printing resolution was limited and therefore the electrode feature sizes, which strongly impact the internal surface area, SLA 3D printed carbonized electrodes can be promising for flow cell applications. To investigate their potential, a comparison is made with a paper and a cloth electrode, which have been shown to be among the best performing electrodes in non-aqueous redox flow batteries [8]. These electrodes are well studied [8, 14, 15], but remain unoptimized for all-liquid RFBs. The main advantage of these commercial electrodes over 3D printed electrodes is their superior internal surface area, resulting in a better volume-specific surface area mass transfer coefficient ($a \cdot k_m$) as a function of the electrolyte velocity (**Figure A8.19**). However, when corrected for the internal surface area, **Figure A8.20d**, their mass transfer coefficients appear lower than that of the 3D printed electrode, particularly at low

electrolyte velocities. Although the prefactor is significantly lower for the commercial electrodes, also for the Sherwood over Peclet number plots (**Figure 8.7d**), the sensitivity of the mass transfer relation to the electrolyte velocity as defined by the exponent is larger as a result of forced convection through the dense fiber structure [14, 51]. As a result of the superior internal surface area of the commercial electrodes, their electrochemical power output outperforms the 3D printed designs, see **Figure A8.15**. The 3D printed designs, however, outperform the commercial electrodes in terms of pumping requirements (**Figure 3a**). When evaluating the trade-off between electrochemical performance and pumping requirements in terms of flow cell efficiency, the cloth electrode performs best in terms of both electrochemical and pumping power requirements [8, 15, 60].

For the 3D printed electrodes to compete with commercial electrodes for application in RFBs, their design must be optimized. First and foremost, their internal surface area needs to be increased by designing electrodes with smaller feature sizes by using advanced 3D printing technologies (e.g., two-photon lithography), combined with highly porous surfaces obtained through e.g., etching, thermal treatments, coatings, or addition of porogens in the printing resin [69]. A higher internal surface area enhances the electrochemical current density but generally results in structures with a smaller and narrower PSD, reducing the electrode permeability. Thus, high electrolyte permeabilities should be attained by considering the flow field-electrode interplay in the designs to maintain a low-pressure drop in the reactor. To this end, a bimodal PSD could be beneficial for the design of next-generation RFB electrodes [15, 21]. Furthermore, tailored resins should be investigated where the resin formulation (i.e., monomers and photoinitiator) should be optimized to reduce resin spreading and control shrinkage during carbonization. Lastly, mass transport within porous electrodes needs to be optimized on all length scales to enhance the electrolyte distribution, internal mixing, and mass transport toward the electrode surface, for which the electrode thickness is an important optimization parameter. After implementing the above-mentioned properties, the 3D printed electrodes should be compared to state-of-the-art electrodes where their mechanical stability, cycling performance, and cost of manufacturing should additionally be considered to investigate the practical applicability of 3D printed electrodes for RFB applications.

8.4. Conclusion

In this study, we manufactured electrode structures using SLA 3D printing followed by carbonization to investigate the impact of the electrode structure on mass transport properties and pressure drop in electrochemical flow cells. The goal of this study is to contribute to the understanding of structure-function-performance relationships applicable to redox flow batteries by exploring novel in-house manufactured electrode structures with diverse three-dimensional features. Using single electrolyte flow cells as diagnostic platforms, we employed a reversible and facile redox couple ($TEMPO/TEMPO^+PF_6^-$) in a non-aqueous electrolyte as a method to deconvolute the influence of the mass transfer overpotentials on the flow cell performance. With this systematic methodology, we studied the influence of the printing direction, pillar geometry, and flow field on the mass transfer rates in ordered lattice structures.

The investigated electrodes impact cell performance through variations in internal surface area, pressure drop, and mass transport. It was found that the printing

orientation (with respect to the printing platform) impacts the electrode performance through a change in electrode microstructure, affecting the shrinking direction upon carbonization, internal surface area, and thus the charge transfer resistance, mass transfer resistance, and pressure drop. A horizontal printing direction shows low in-plane surface roughness but enhanced mass transfer, whereas a diagonal printing direction features a higher internal surface area and lower pressure drop, but a reduced mass transfer coefficient. Furthermore, we find that the mass transfer in the electrode can be enhanced by improving the electrolyte mixing by altering the pillar shape to a helical or triangular design, and by using an interdigitated flow field. By comparing the printed structures to commercial electrodes, we show the potential of using 3D printing as a viable manufacturing method to enhance mass transport in RFBs. However, for the 3D printed electrodes to compete with commercial electrodes, their design must be optimized by increasing the internal surface area, which could be achieved by printing electrode structures with smaller feature sizes with advanced 3D printing technologies or by incorporating high surface area materials onto the electrode surfaces. We hypothesize that the combination of a macroporous electrode architecture with finer, nanoscale porosity, surface roughness, and mixing elements can provide the seemingly contradictory requirements of high permeability, mass transfer rates, and electrochemically available surface area.

This study shows the potential of 3D printing to manufacture customized electrodes with high geometrical and orientational (printing direction) flexibility, which have a measurable impact on the electrochemical performance and pressure drop. Furthermore, manufacturing guidelines to enhance the mass transport in porous electrodes are provided and can be translated to other advanced manufacturing techniques. Looking forward, we propose to fine-tune the resin formulation and carbonization steps (e.g., carbonization at elevated temperatures >1100 °C), and explore additional thermal treatment steps or coatings aiming to obtain porous electrodes with higher carbon content, conductivity, and internal surface area. Additionally, future work should focus on alternative pillar or fiber geometries and their orientation to enhance the mass transport in porous electrodes. Owing to the design flexibility, 3D printing can be combined with topology optimization of the porous electrode to realize the manufacturing of computationally optimized structures.

8.5. References

[1] S. P. S. Badwal, S. S. Giddey, C. Munnings, A. I. Bhatt, A. F. Hollenkamp, *Front. Chem.* **2**, 1–28 (2014).
[2] Z. Liu *et al.*, *NPG Asia Mater.* **11**, 1–21 (2019).
[3] D. Qu, *AIP Conf. Proc.* **1597**, 14–25 (2014).
[4] A. Forner-Cuenca, F. R. Brushett, *Curr. Opin. Electrochem.* **18**, 113–122 (2019).
[5] C. Zhu *et al.*, *Nano Today*. **15**, 107–120 (2017).
[6] A. Z. Weber *et al.*, *J. Appl. Electrochem.* **41**, 1137–1164 (2011).
[7] P. Leung *et al.*, *J. Power Sources*. **360**, 243–283 (2017).
[8] A. Forner-Cuenca, E. E. Penn, A. M. Oliveira, F. R. Brushett, *J. Electrochem. Soc.* **166**, A2230–A2241 (2019).
[9] M. Skyllas-Kazacos, M. H. Chakrabarti, S. A. Hajimolana, F. S. Mjalli, M. Saleem, *J. Electrochem. Soc.* **158**, R55 (2011).
[10] M. van der Heijden, A. Forner-cuenca, in *Encyclopedia of Energy Storage*, L. F. Cabeza, Ed. (Elsevier Inc., Oxford, ed. 2, 2022), pp. 480–499.
[11] R. M. Darling, K. G. Gallagher, J. A. Kowalski, S. Ha, F. R. Brushett, *Energy Environ. Sci.* **7**, 3459–3477 (2014).
[12] M. H. Chakrabarti *et al.*, *J. Power Sources*. **253**, 150–166 (2014).
[13] V. A. Beck *et al.*, *Proc. Natl. Acad. Sci. U. S. A.* **118**, 1–10 (2021).
[14] K. M. Tenny, A. Forner-Cuenca, Y.-M. Chiang, F. R. Brushett, *J. Electrochem. Energy Convers. Storage*. **17**, 041010 (2020).
[15] M. van der Heijden, R. van Gorp, M. A. Sadeghi, J. Gostick, A. Forner-Cuenca, *J. Electrochem. Soc.* **169**, 040505 (2022).
[16] S. Dussi, C. H. Rycroft, *Phys. Fluids*. **34**, 043111 (2022).
[17] D. Zhang *et al.*, *J. Power Sources*. **447**, 227249 (2020).
[18] M. A. Sadeghi *et al.*, *J. Electrochem. Soc.* **166**, A2121–A2130 (2019).
[19] B. A. Simon *et al.*, *Appl. Energy*. **306**, 117678 (2022).
[20] C. T. Wan *et al.*, *Adv. Mater.* **33**, 2006716 (2021).
[21] R. van Gorp, M. van der Heijden, M. A. Sadeghi, J. Gostick, A. Forner-Cuenca, *Chem. Eng. J.* **455**, 139947 (2023).
[22] P. Wang *et al.*, *Adv. Mater. Technol.* **5**, 1901030 (2020).
[23] X. Tian *et al.*, *Adv. Energy Mater.* **7**, 1–17 (2017).
[24] V. Egorov, U. Gulzar, Y. Zhang, S. Breen, C. O'Dwyer, *Adv. Mater.* **32**, 1–27 (2020).
[25] M. P. Browne, E. Redondo, M. Pumera, *Chem. Rev.* **120**, 2783–2810 (2020).
[26] A. Azhari, E. Marzbanrad, D. Yilman, E. Toyserkani, M. A. Pope, *Carbon N. Y.* **119**, 257–266 (2017).
[27] X. Wei *et al.*, *Sci. Rep.* **5**, 1–7 (2015).
[28] J. Hereijgers, J. Schalck, J. Lölsberg, M. Wessling, T. Breugelmans, *ChemElectroChem*. **6**, 378–382 (2019).
[29] J. Hereijgers, J. Schalck, T. Breugelmans, *Chem. Eng. J.* **384**, 123283 (2020).
[30] C. Zhu *et al.*, *Nano Lett.* **16**, 3448–3456 (2016).
[31] M. Wirth, K. Shea, T. Chen, *Mater. Des.* **225**, 111449 (2023).
[32] Q. Li *et al.*, *J. Power Sources*. **542**, 231810 (2022).
[33] J. Lölsberg *et al.*, *ChemElectroChem*. **4**, 3309–3313 (2017).
[34] L. F. Arenas, C. Ponce de León, F. C. Walsh, *Electrochem. commun.* **77**, 133–137 (2017).
[35] D. Niblett, Z. Guo, S. Holmes, V. Niasar, R. Prosser, *Int. J. Hydrogen Energy*. **47**, 23393–23410 (2022).
[36] J. Wicks *et al.*, *Adv. Mater.*, **33**, 7, 2003855 (2021).
[37] B. Bian *et al.*, *Nano Energy*. **44**, 174–180 (2018).
[38] M. A. Saccone, R. A. Gallivan, K. Narita, D. W. Yee, J. R. Greer, *Nature*. **612**, 685–690 (2022).
[39] J. Bauer, A. Schroer, R. Schwaiger, O. Kraft, *Nat. Mater.* **15**, 438–443 (2016).

[40] J. A. Lee, S. W. Lee, K. C. Lee, S. Il Park, S. S. Lee, *J. Micromechanics Microengineering*. **18**, 035012 (2008).
[41] R. L. McCreery, *Chem. Rev.* **108**, 2646–2687 (2008).
[42] B. Rezaei, J. Y. Pan, C. Gundlach, S. S. Keller, *Mater. Des.* **193**, 108834 (2020).
[43] A. G. Lombardo, B. A. Simon, O. Taiwo, S. J. Neethling, N. P. Brandon, *J. Energy Storage*. **24**, 100736 (2019).
[44] J. H. Kim, T. J. Kang, *ACS Appl. Mater. Interfaces*. **11**, 28894–28899 (2019).
[45] R. Dmello, J. D. Milshtein, F. R. Brushett, K. C. Smith, *J. Power Sources*. **330**, 261–272 (2016).
[46] J. D. Milshtein, R. M. Darling, J. Drake, M. L. Perry, F. R. Brushett, *J. Electrochem. Soc.* **164**, A3883–A3895 (2017).
[47] J. A. Kowalski, L. Su, J. D. Milshtein, F. R. Brushett, *Curr. Opin. Chem. Eng.* **13**, 45–52 (2016).
[48] H. Steldinger, A. Esposito, K. Brunnengräber, J. Gläsel, B. J. M. Etzold, *Adv. Sci.* **6**, 1–9 (2019).
[49] J. D. Milshtein, J. L. Barton, R. M. Darling, F. R. Brushett, *J. Power Sources*. **327**, 151–159 (2016).
[50] J. L. Barton, J. D. Milshtein, J. J. Hinricher, F. R. Brushett, *J. Power Sources*. **399**, 133–143 (2018).
[51] J. D. Milshtein *et al.*, *J. Electrochem. Soc.* **164**, E3265–E3275 (2017).
[52] J. Wallauer, M. Drüschler, B. Huber, "Electrochemical Kinetics of a classical redox couple - A combined approach by EIS and CV" (Darmstadt).
[53] B. Msallem, S. Neha, C. Shuaishuai, F. S. Halbeisen, F. M. T. Hans-Florian Zeilhofer, *J. Clin. Med.* **9**, 1–18 (2020).
[54] J. Schulte-fischedick, W. Krenkel, in *12Int. Conf. on Composite Materials-ICCM12* (1999).
[55] Y. M. Hassan *et al.*, *J. Anal. Appl. Pyrolysis*. **125**, 91–99 (2017).
[56] M. S. A. Rahaman, A. F. Ismail, A. Mustafa, *Polym. Degrad. Stab.* **92**, 1421–1432 (2007).
[57] M. Gehring *et al.*, *RSC Adv.* **9**, 27231–27241 (2019).
[58] K. M. Tenny *et al.*, *Energy Technol.* **10**, 2101162 (2022).
[59] N. Elgrishi *et al.*, *J. Chem. Educ.* **95**, 197–206 (2018).
[60] V. Muñoz-Perales *et al.*, *ChemRxiv* (2023), doi:10.26434/chemrxiv-2023-2zthc.
[61] K. V. Greco, A. Forner-Cuenca, A. Mularczyk, J. Eller, F. R. Brushett, *ACS Appl. Mater. Interfaces*. **10**, 44430–44442 (2018).
[62] A. M. Pezeshki, R. L. Sacci, F. M. Delnick, D. S. Aaron, M. M. Mench, *Electrochim. Acta*. **229**, 261–270 (2017).
[63] J. Landesfeind, J. Hattendorff, A. Ehrl, W. A. Wall, H. A. Gasteiger, *J. Electrochem. Soc.* **163**, A1373–A1387 (2016).
[64] S. J.-M. C. Weusten, PhD thesis, Eindhoven University of Technology (2022).
[65] F. B. Leitz, L. Marinčić, *J. Appl. Electrochem.* **7**, 473–484 (1977).
[66] M. De Rop, J. Hereijgers, T. Breugelmans, Beyond the limits of mass transfer: How pillar electrodes influence electrochemical reactors (2022).
[67] A. A. Wong, S. M. Rubinstein, M. J. Aziz, *Cell Reports Phys. Sci.* **2**, 100388 (2021).
[68] T. Suga, Y. J. Pu, K. Oyaizu, H. Nishide, *Bull. Chem. Soc. Jpn.* **77**, 2203–2204 (2004).
[69] Z. Dong *et al.*, *Nat. Commun.* **12**, 247 (2021).

8.6. Appendix 8

A8.1. Abbreviations

Symbol	Description
EDS	Energy dispersive X-ray spectroscopy
FTFF	Flow through flow field
IDFF	Interdigitated flow field
PSD	Pore size distribution
RFB	Redox flow battery
SEM	Scanning electron microscope
SLA	Stereolithography
XPS	X-ray photoelectron spectroscopy
XTM	X-ray tomographic microscopy

A8.2. List of symbols

Symbol	Description	Units
ΔP	Pressure drop	Pa m
a	Electrode internal surface area	$m^2\ m^{-3}$
A_e	Electrode area	m^2
A_{geo}	Geometrical inlet area	m^2
C	Concentration	$mol\ m^{-3}$
$C1, C3$	Prefactor	-
$C2, C4$	Exponent	-
D	Diffusion coefficient	$m^2\ s^{-1}$
F	Faradaic constant, 96,485 C mol $^{-1}$	$C\ mol^{-1}$
i	Current density	$A\ m^{-3}$
i_{lim}	Limiting current density	$A\ m^{-3}$
I_{lim}	Limiting current	A
j_0	Exchange current density	$A\ m^{-3}$
k_0	Standard rate constant	$m\ s^{-1}$
k_m	Mass transfer coefficient	$m\ s^{-1}$
L	Gasket thickness	m
L_c	Length of the channel	m
L_e	Electrode length	m
n	Number of electrons transferred	-
n_c	Number of inlet channels	-
Pe	Peclet number	-
Q	Volumetric flow rate	$m^3\ s^{-1}$
R	Molar gas constant, 8.314 J $mol^{-1}\ K^{-1}$	$J\ mol^{-1}\ K^{-1}$
R_e	Electrode resistance	Ω
Sh	Sherwood number	-
T	Operating temperature	K
v	Electrolyte velocity	$m\ s^{-1}$
V	Electrode volume	m^3
	Greek	
α	Charge transfer coefficient	-
β	Forchheimer coefficient	m^{-1}
ε	Porosity	-
η_{act}	Activation overpotential	V
κ	Permeability	m^2

μ	Electrolyte viscosity	Pa s
ρ	Electrolyte density	kg m^{-3}
σ_e	Electrical conductivity	S m^{-1}

Subscript

$3D$	3D printed electrode
b	Bulk
$FTFF$	Flow through
i	Species i
$IDFF$	Interdigitated
j	Species j
$paper$	Paper electrode
s	Surface

A8.3. Manufacturing of 3D printed electrodes

A8.3.1. PreForm supports

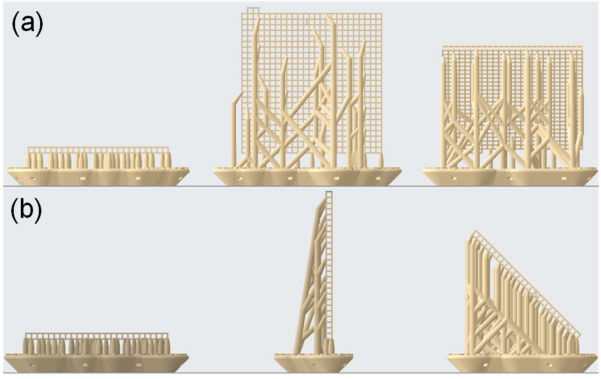

Figure A8.1: A visualization of the supports (pillars and baseplate) generated with the PreForm software to translate 3D designs to printable objects, shown for the horizontal, vertical, and diagonal orientations from left to right and from two different viewpoints in **(a)** and **(b)** with a 90° rotation.

A8.3.2. Structure deformation

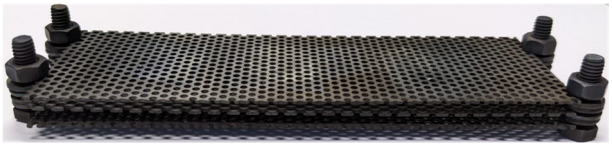

Figure A8.2: The perforated metal framework used in the tubular oven to hold the 3D printed structures to prevent structure deformation during carbonization, in which six samples can be carbonized at the same time.

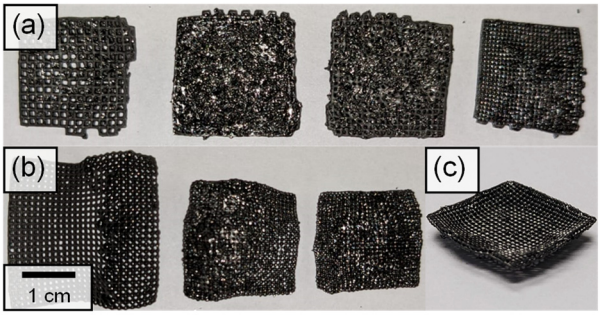

Figure A8.3: Examples of structure deformation during carbonization, showing the effect of: **(a)** porosities lower than 70%, **(b)** a thermal sequence without first an oxidation step, as used in Niblett *et al.* [1] of carbonization to 300 °C with 3 °C min^{-1} with a 1 h hold, to 500 °C with 1 °C min^{-1} with a 1 h hold, to 850 °C with 3 °C min^{-1} with a 1 h hold, and to RT with 10 °C min^{-1}, and **(c)** carbonization without the perforated metal framework (**Figure A8.2**) to hold the samples.

A8.3.3. Resin spreading

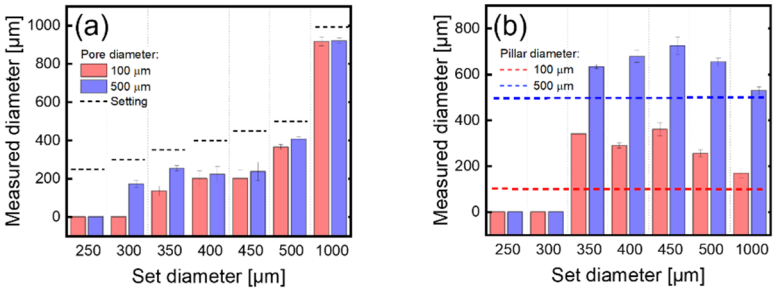

Figure A8.4: (a) The pore diameter measured versus set by the input geometry (n=6), showing the spreading of the resin from the pillar into the pore, decreasing the pore size, and **(b)** the pillar diameter measured over the set diameter of the pores, where the diameter set by the input geometry is shown with the dashed lines, showing the spreading of the resin into the pores.

A8.3.4. Pore size

Table A8.1: The equivalent pore diameters, d_p, of the 3D printed designs before carbonization (n=6), extracted from the SEM images with ImageJ.

Equivalent pore diameter [µm]	d_p top	d_p bottom	d_p side
Horizontal – square	908 ± 4	902 ± 8	875 ± 12
Vertical – square	808 ± 9	803 ± 9	901 ± 11
Diagonal - square	871 ± 6	864 ± 10	845 ± 7
Horizontal - triangle	854 ± 1	880 ± 1	827 ± 25
Horizontal - cylinder	687 ± 1	699 ± 3	692 ± 9
Horizontal - helix	786 ± 7	754 ± 28	657 ± 11

Table A8.2: The equivalent pore diameters, d_p, of the 3D printed designs after carbonization (n=6), extracted from the SEM images with ImageJ.

Equivalent pore diameter [µm]	d_p top	d_p bottom	d_p side
Horizontal – square	439 ± 12	503 ± 8	530 ± 14
Vertical – square	486 ± 12	486 ± 12	500 ± 21
Diagonal - square	429 ± 14	429 ± 14	431 ± 17
Horizontal - triangle	536 ± 12	482 ± 19	519 ± 19
Horizontal - cylinder	420 ± 5	399 ± 6	399 ± 12
Horizontal - helix	524 ± 17	478 ± 11	505 ± 32

A8.3.5. Scanning electron microscopy images

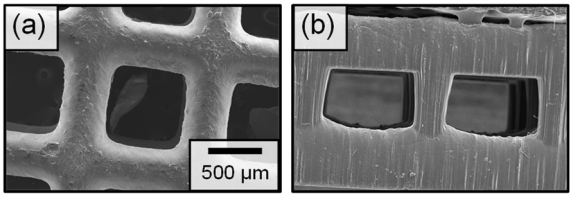

Figure A8.5: Scanning electron microscope images of the 3D print after oxidation at 50 x magnification of **(a)** the top, and **(b)** the side view.

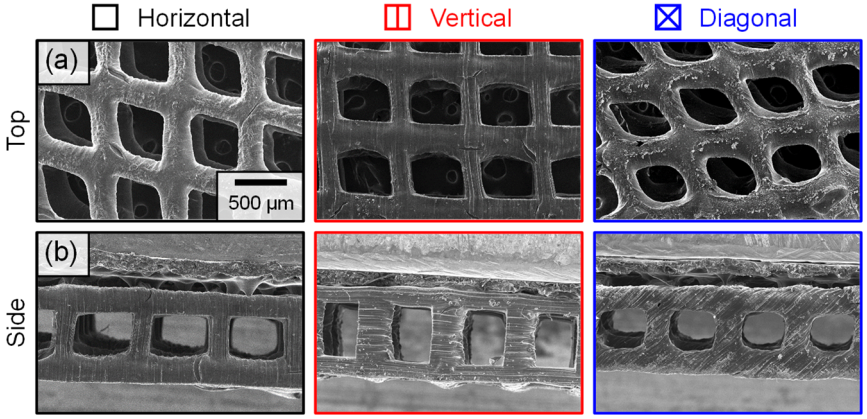

Figure A8.6: Scanning electron microscope images of the 3D prints of the horizontal, vertical, and diagonal printing direction (from left to right) at 50 x magnification, for the 3D structure after carbonization **(a)** from the top, and **(b)** from the side view.

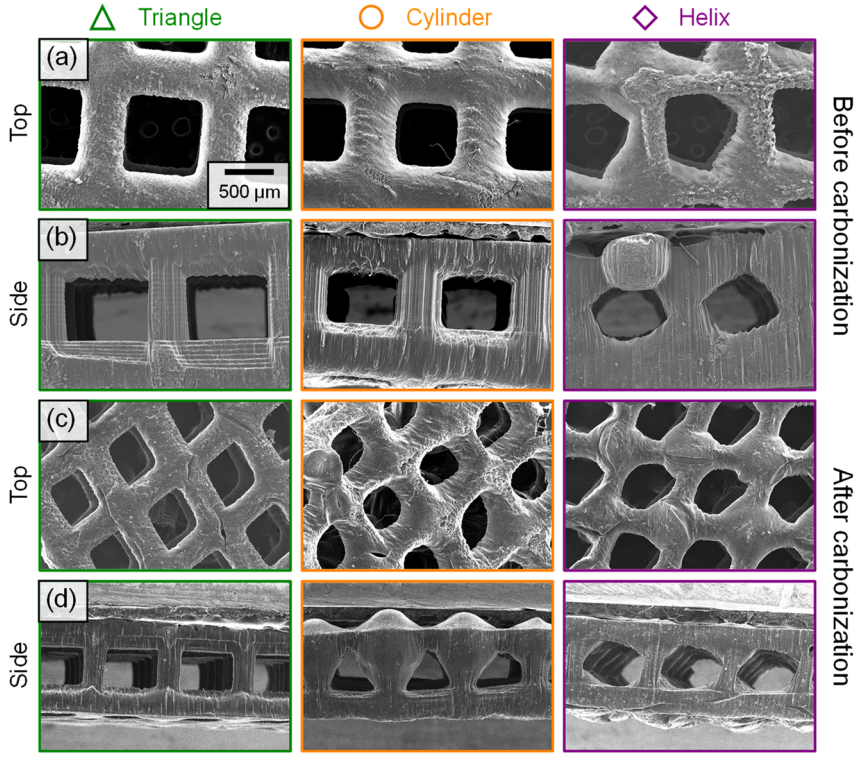

Figure A8.7: Scanning electron microscope images of the 3D prints of the triangle, cylinder, and helical pillar shapes (from left to right) at 50 x magnification, for the 3D structure before carbonization: **(a)** from the top, and **(b)** from the side, and after carbonization **(c)** from the top, and **(d)** from the side.

A8.3.6. X-ray tomographic microscopy images

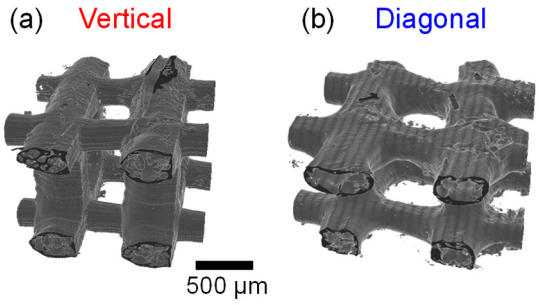

Figure A8.8: X-ray tomographic images of the 3D prints after carbonization with: **(a)** a vertical, and **(b)** a diagonal printing direction.

A8.3.7. Printing direction

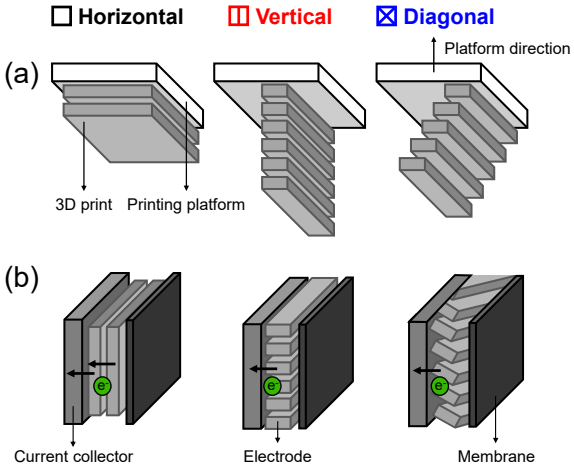

Figure A8.9: Visualization of the printing direction: **(a)** with respect to the printing platform, and **(b)** in the flow cell configuration.

A8.4. Physicochemical analysis

A8.4.1. Elemental analysis

Table A8.3: Carbon, nitrogen, and oxygen content of the 3D printed structure with a square pillar shape and horizontal printing direction after printing, oxidation, and carbonization obtained by EDS and XPS. The EDS values are an average over six experiments (n=6), whereas the XPS was performed on only one sample (n=1). In the XPS data small traces of contaminations in the form of silicon were found.

	EDS			XPS			
[atom%]	**Carbon**	**Nitrogen**	**Oxygen**	**Carbon**	**Nitrogen**	**Oxygen**	**Silicon**
Printed	71 ± 0.9	1.9 ± 0.1	27 ± 0.8	77	2.5	20	1.1
Oxidized	69 ± 1.5	2.0 ± 0.2	29 ± 1.3	73	4.1	22	0.48
Carbonized	94 ± 0.5	1.2 ± 0.1	5.0 ± 0.5	82	1.1	12	4.9

A8.4.2. X-ray photoelectron spectroscopy

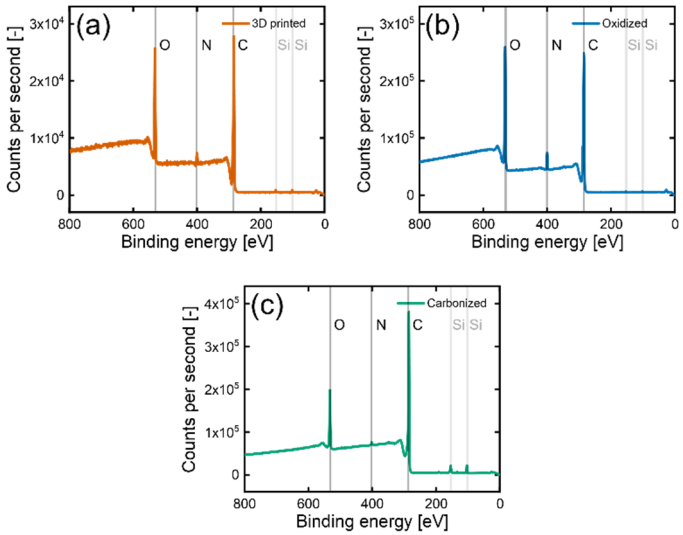

Figure A8.10: XPS spectra of the survey analysis displaying the oxygen, nitrogen, and carbon signals, for: **(a)** after printing, **(b)** after oxidation, and **(c)** after carbonization. Small traces of contaminations in the form of silicon were found in the XPS surveys.

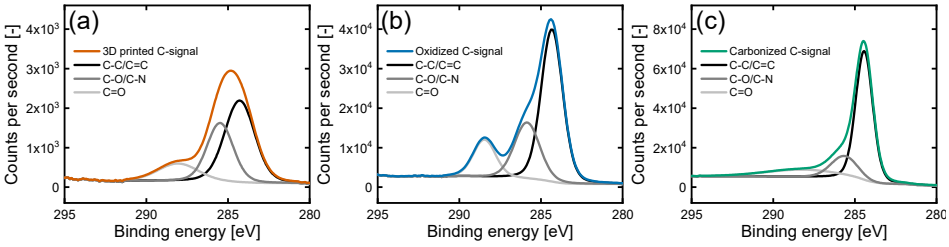

Figure A8.11: XPS spectra of the C-peaks displaying the C-C/C=C signal at 284 eV, the C-O/C-N signal at 286 eV, and the C=O signal at 289 eV [2–4], for: **(a)** after printing, **(b)** after oxidation, and **(c)** after carbonization.

A8.4.3. Material characteristics

Table A8.4: Material characteristics of the 3D print before carbonization, where the internal surface area was obtained by algebraic calculations of the pillar and pore sizes obtained by SEM and ImageJ. ‡ The porosity and internal surface area of the helical structure were not calculated but assumed similar to the other structures.

	Square Vertical	**Square Diagonal**	**Triangle**	**Cylinder**	**Helix**
Porosity [%]	76	76	77	75	‡
Internal surface area [m^2 m^{-3}]	2846	2810	2323	2178	‡
Thickness [µm]	1500	1500	1770	1680	1500

Table A8.5: Material characteristics of the 3D print after carbonization, where the internal surface area was obtained by algebraic calculations of the pillar and pore sizes obtained by SEM and ImageJ. ‡ The porosity and internal surface area of the helical structure were not calculated with the algebraic method but were assumed similar to the other structures. The permeability and Forchheimer coefficients were obtained with a second polynomial fit of **equation (8.4)**.

	Square Vertical	**Square Diagonal**	**Triangle**	**Cylinder**	**Helix**
Porosity [%]	64	60	81	68	‡
Internal surface area [m^2 m^{-3}]	4892	5443	3586	4106	‡
In-plane permeability x 10^{-10} [m^{-2}]	110	40	29	17	29
Forchheimer coefficient x 10^4 [m^{-1}]	0.20	0.12	0.44	0.28	0.27
Thickness [µm]	1078 ± 104	971 ± 144	1214 ± 98	1137 ± 181	1304 ± 99

A8.4.4. Cyclic voltammetry

To evaluate the reversibility of the electrochemical reactions on the 3D printed electrode, cyclic voltammetry was performed. The cyclic voltammetry curves were obtained by measuring the carbonized 3D printed electrode and the Freudenberg H23 paper electrode (both were clamped with golden crocodile clips) in cyclic voltammetry mode of the Biologic VMP-300 in a 0.2 M TEMPO, 1 M $TBAPF_6$ in MeCN solution in a three-electrode setup with a platinum mesh as counter electrode and a Ag/AgCl (3 M) reference electrode, without stirring. The cyclic voltammetry was performed by cycling the potential from -0.7 to 1.3 V (*vs.* Ag/AgCl) at varying scan rates (225, 144, 64, 25, and 9 mV s^{-1}) for two cycles. All measurements were corrected for the solution resistance by automatic iR$_\Omega$-compensation (solution resistance extracted at 100 kHz and 20 mV sinus amplitude, 85 % compensation applied).

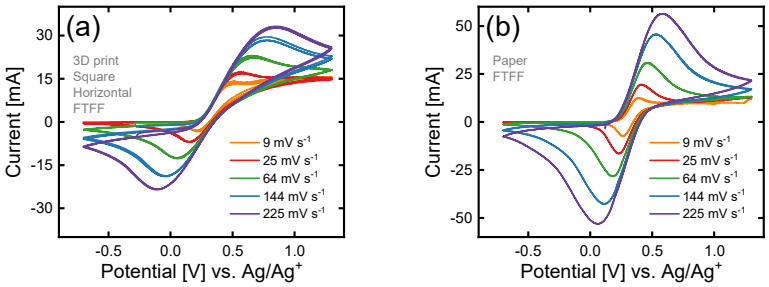

Figure A8.12: Cyclic voltammetry at various scan rates (9, 25, 64, 144, and 225 mV s^{-1}) for: **(a)** the 3D printed electrode, and **(b)** the Freudenberg H23 paper electrode. The active species concentration was 0.2 M TEMPO in 1 M $TBAPF_6$ in MeCN.

A8.4.5. Mechanical stability

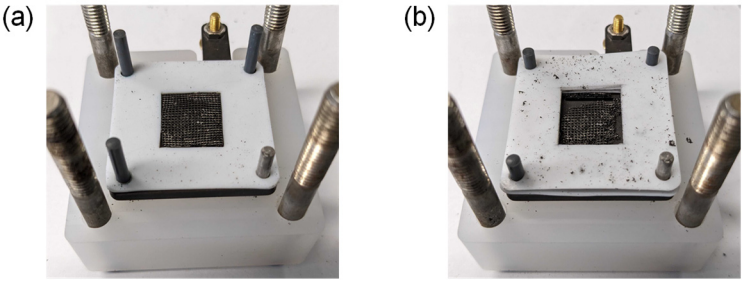

Figure A8.13: Mechanical stability test of the 3D printed electrodes after different applied compression rates. The 3D printed electrodes can withstand up to approximately 28 % compression before they break. **(a)** The 3D printed electrode after the electrochemical experiments (compression of 21 %). **(b)** The broken 3D printed electrode after 45 % compression applied.

A8.5. Electrochemical performance

A8.5.1. Polarization curves

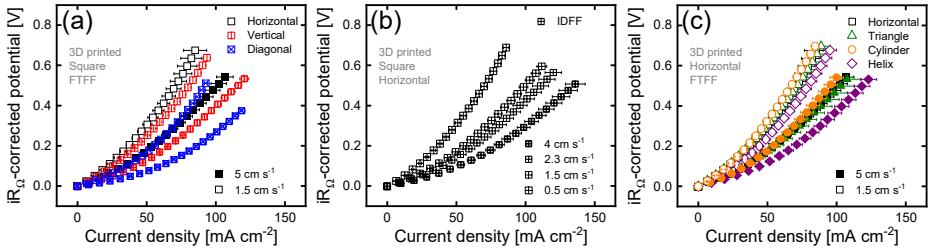

Figure A8.14: iR_Ω corrected polarization curves (n=3) for: **(a)** the different printing directions at 5 and 1.5 cm s^{-1}, **(b)** the interdigitated flow field at 4, 2.3, 1.5, and 0.5 cm s^{-1}, and **(c)** the different pillar shapes at 5 and 1.5 cm s^{-1}.

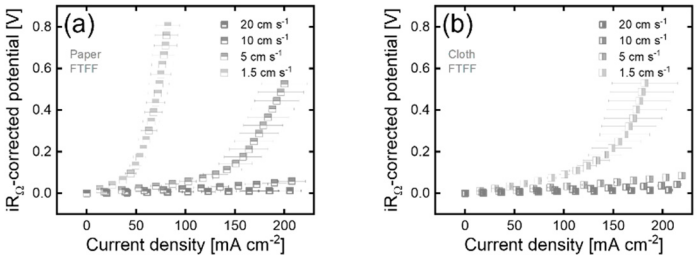

Figure A8.15: iR_Ω corrected polarization curves (n=3) at 20, 10, 5, and 1.5 cm s^{-1} for: **(a)** the paper electrode, and **(b)** the cloth electrode.

A8.5.2. Impedance spectroscopy

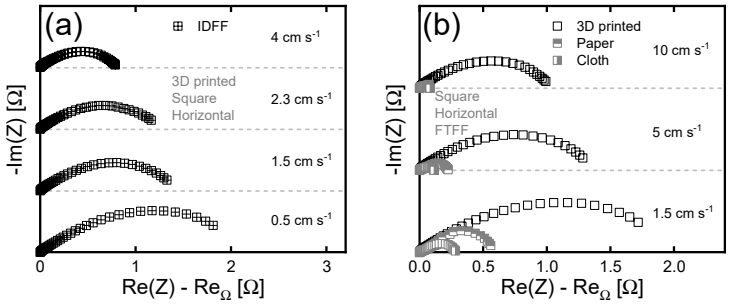

Figure A8.16: The electrochemical impedance spectroscopy data (n=3) corrected for the high-frequency intercept for: **(a)** the interdigitated flow field at 4, 2.3, 1.5, and 0.5, cm s^{-1}, and **(b)** the 3D printed and commercial paper and cloth electrode at 10, 5, and 1.5, cm s^{-1}.

A8.5.3. Ohmic resistance

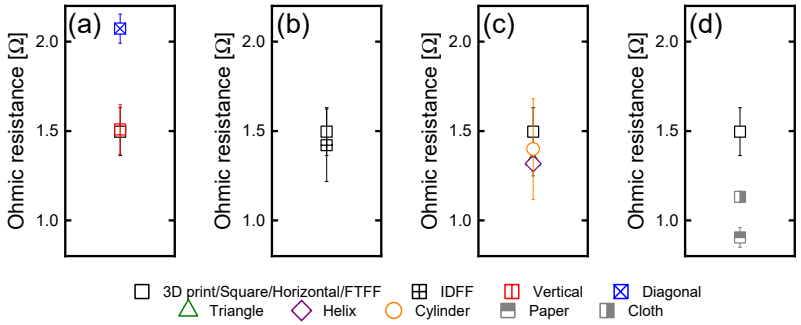

Figure A8.17: Ohmic resistance values (n=3) obtained from the high frequency intercept of the electrochemical impedance spectroscopy data, corrected for in the iR_{Ω}-corrected polarization curves, for: **(a)** the horizontal, vertical, and diagonal printing direction, **(b)** the flow through and interdigitated flow field, **(c)** the square, triangular, cylindrical, and helical pillar shapes, and **(d)** the 3D printed and commercial paper and cloth electrodes.

A8.5.4. Limiting current plot

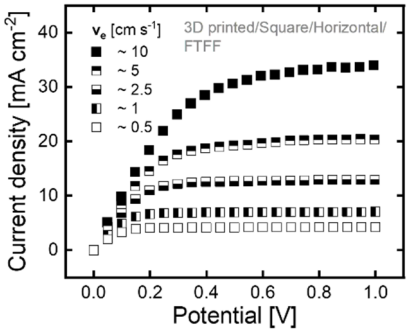

Figure A8.18: Limiting current density plots (n=3) of the current density over the potential for five different electrolyte velocities, shown for the 3D printed electrode.

A8.5.5. Volume-specific surface area mass transfer coefficient

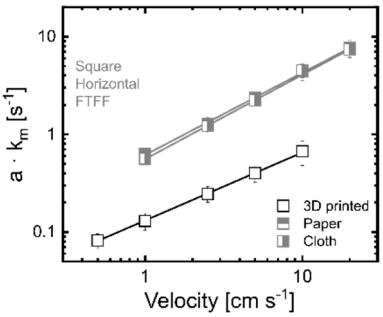

Figure A8.19: The $a\ k_m$ values (n=3) for different electrolyte velocities plotted on a double-log scale for the 3D printed and commercial paper and cloth electrodes.

A8.5.6. Mass transfer correlations

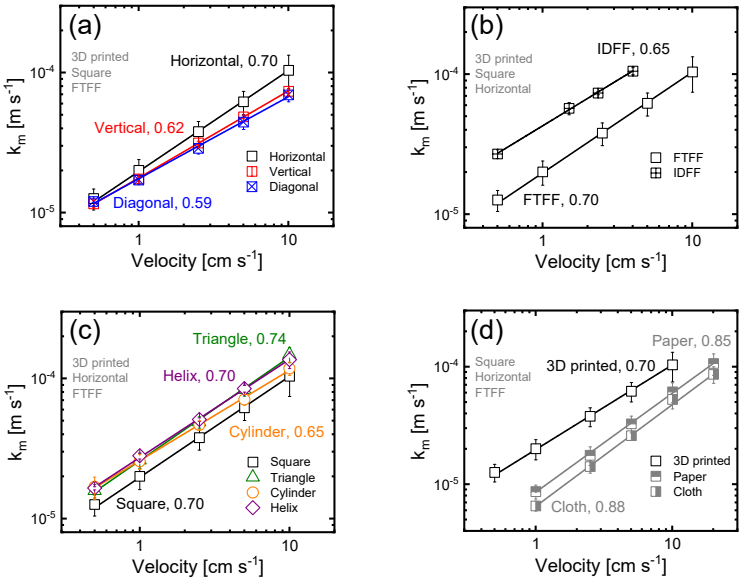

Figure A8.20: The mass transfer values (n=3) for different electrolyte velocities plotted on a double-log scale for: **(a)** the horizontal, vertical, and diagonal printing direction, **(b)** the flow through and interdigitated flow field, **(c)** the square, triangular, cylindrical, and helical pillar shapes, and **(d)** the 3D printed and commercial paper and cloth electrodes.

A8.6. References

[1] D. Niblett, Z. Guo, S. Holmes, V. Niasar, R. Prosser, *Int. J. Hydrogen Energy*. **47**, 23393–23410 (2022).
[2] P. Parikh *et al.*, *Chem. Mater.* **31**, 2535–2544 (2019).
[3] B. Rezaei, J. Y. Pan, C. Gundlach, S. S. Keller, *Mater. Des.* **193**, 108834 (2020).
[4] P. Trogadas *et al.*, *Electrochem. commun.* **48**, 155–159 (2014).

Chapter 9
Conclusions and outlook

Abstract

In this final chapter, the main conclusions and key learnings of each chapter are discussed. Then, an outlook for each of the research objectives is provided, including ongoing research directions that are currently being explored by the candidate as well as future directions of interest.

9.1. Conclusions

This dissertation focused on uncovering the role of the electrode microstructure on redox flow cell performance to guide electrode design for enhanced performance in redox flow batteries (RFBs). By combining a computational modeling framework, advanced imaging diagnostics, topology optimization, and additive manufacturing, fundamental structure-function-performance relationships were uncovered. A pore network modeling platform was developed, experimentally validated, and used to assess the performance of porous electrodes in redox flow cells. The pore network model was subsequently applied to gain insight into the role of the electrode thickness on flow cell performance. Moreover, the computational model was integrated into a genetic algorithm approach for the bottom-up design of hierarchically organized porous electrodes, which was subsequently extended to the optimization of randomly organized structures. Furthermore, a novel neutron radiography approach was introduced to study the concentration distribution in *operando* redox flow cells and was shown to be valuable in uncovering the influence of individual reactor components on RFB performance. Finally, additive manufacturing was employed to fabricate model grid electrodes for RFBs and was shown to have potential as a highly controlled manufacturing technique for advanced electrode designs. An overview of the conclusions of this dissertation, divided per chapter, is presented below.

In **Chapter 2**, an electrolyte agnostic, microstructure-informed, and computationally inexpensive pore network modeling platform was developed to improve the fundamental understanding of the relationship between electrode microstructure and flow battery performance. The pore network model was built using the open-access platform OpenPNM and solves the electrochemical kinetics, fluid flow, mass transport, and charge conservation. Moreover, the model utilizes a network-in-series approach to account for species depletion over the electrode length, enabling the simulation of large electrode sizes. Single-electrolyte flow cell experiments were performed to validate the robustness of the modeling framework for two distinct electrolytes – an aqueous Fe^{2+}/Fe^{3+} and a non-aqueous TEMPO/$TEMPO^{+}$ electrolyte – and two types of porous electrodes – a Freudenberg carbon paper and an ELAT carbon cloth, extracted by X-ray tomographic microscopy and converted into a pore network. The electrochemical model solves the electrolyte fluid transport and couples both half-cells by iteratively solving the species and charge transport at a low computational cost. The electrochemical performance of the non-aqueous electrolyte was well captured by the model without fitting parameters, allowing rapid benchmarking of porous electrode microstructures. For the aqueous electrolyte, it was found that incomplete wetting of the electrode results in an overprediction of the electrochemical performance. To account for incomplete wetting, the near-surface mass transfer coefficient was fitted successfully. Moreover, the electrode structures and electrolytes were studied through their overpotentials, current distribution, concentration profile, pressure drop, and overall performance trade-off, providing useful structure-performance relationships for improved electrode design. Finally, a parametric sweep was performed where the correlation between electrical power and pumping power was studied to identify operation envelopes for efficient flow cell operation. In summary, the systematic and rigorous analysis revealed scenarios where the current modeling framework lacks accuracy (e.g., aqueous electrolytes with woven electrodes) which motivates further research on three-dimensional modeling of multi-scale microstructures and multiphase flows. Regardless, the developed chemistry and microstructure agnostic model showed to accurately describe the electrochemical performance under a broad

range of operating conditions and redox chemistries at low computational cost and provides a robust platform to analyze the structural properties from first principles. Coupled with machine learning approaches, the pore network model can be used as a predictive framework to accelerate porous electrode engineering.

In **Chapter 3**, the developed pore network model of **Chapter 2** was used to systematically study the influence of the electrode thickness, by electrode stacking, on the flow cell performance for two types of porous electrodes – a Freudenberg carbon paper and an ELAT carbon cloth – combined with flow through and interdigitated flow fields. The electrochemical and fluid dynamic performance of the systems was evaluated by using polarization, electrochemical impedance spectroscopy, and pressure drop measurements, combined with pore network simulations for single-electrolyte cell configurations with the aqueous Fe^{2+}/Fe^{3+} electrolyte. It is shown that flow field-electrode interactions impact the influence of the electrode thickness on different performance metrics (pressure drop, current density, overpotentials, electrolyte distribution) and thus system performance. Yet, the competing effects of a reduction in the activation and mass transfer overpotentials and an increase in ohmic overpotential make the two-layer configuration (400 - 700 μm) the best performing in terms of the current output, with an exception for the paper-interdigitated flow field configuration. When balancing the electrochemical performance with the associated pressure losses, thicker electrodes with a bimodal pore size distribution with large pores, such as the cloth electrode, combined with flow-through flow fields enhance the system performance by facilitating high surface area and a low pressure drop. On the other hand, thinner electrodes with a uniform and small pore size distribution and a high surface area, e.g., the paper electrode, are favorably combined with interdigitated flow fields because of their reduced residence time and pressure drop in the electrode. This study showed the importance of co-designing the electrode (i.e., thickness and microstructure) and the flow field geometry to obtain efficient system operation.

In **Chapter 4**, a bottom-up computational approach was developed to optimize electrode structures using a genetic algorithm coupled to the pore network model developed in **Chapter 2**. The algorithm was proven to be powerful in the optimization of flow battery electrode performance by increasing both the electrochemical and the pumping power output, under a wide range of operating conditions. The proof-of-concept study applied the algorithm to a randomly generated cubic structure with fixed pore coordinates, optimized for the VO^{2+}/VO_2^{+} vanadium chemistry with a flow-through flow field, investigated at 1.5 cm s^{-1} and an overpotential of 0.5 V. The structure was optimized employing a fitness function that resulted in a 75 % enhancement of the fitness attributed to a strong decrease in pumping power of 73 % and an increase in electrochemical performance of 42 %. The improved performance was ascribed to the bimodal pore size distribution with interconnected longitudinal pathways with larger pores and the increase in internal surface area. Moreover, the performed parametric evaluation highlighted that there is a trade-off between the electrical power and pumping power where the algorithm emphasizes either the optimization of the flow geometry or the distribution of the available surface area, depending on the electrolyte and operating conditions. This work is the first step to constructing a computational platform that can accelerate the design and fabrication of porous electrodes. Although the computational approach was applied to redox flow batteries, the methodology can be tailored to all convection-enhanced electrochemical technologies with porous electrodes.

In **Chapter 5**, the genetic algorithm developed in **Chapter 4** was extended. First, the evolutionary freedom was broadened by the integration of pore merging and splitting into the algorithm, allowing for pore evolution beyond fixed lattice positions. Second, the electrode optimization was performed on Voronoi and off-the-shelf electrodes, extracted using X-ray tomography, allowing the optimization of commercially used electrodes. Third, the interdependency of the electrode structure and the flow field designs was shown by analyzing electrodes optimized for two distinct flow configurations – flow-through and interdigitated, highlighting the importance of coupled electrode-flow field optimization. Fourth, the significance of optimizing the electrode for specific reactor architectures and operating conditions was shown by optimizing electrodes for two distinct chemistries – the aqueous Fe^{2+}/Fe^{3+} and the non-aqueous TEMPO/$TEMPO^{+}$ electrolytes. Furthermore, the optimization definitions were elaborated upon to inform the reader of the optimization flexibility of the algorithm and the importance of the selection of the fitness function and the geometrical definitions dictating the electrode structure and performance. This work presents a tool for electrode optimization and shows the possibilities and design rules of electrode optimization with genetic algorithms.

In **Chapter 6**, a novel neutron radiography approach was introduced to investigate the species concentration distribution in *operando* redox flow cells. By utilizing organic redox molecules with high hydrogen content and supporting ions containing boron, contrast was achieved, allowing the visualization and tracking of the active species and supporting ions through the reactor. By tuning the attenuation of the supporting salt or ion, the active species movement was decoupled from the background electrolyte. The spatial distribution of the attenuating species in the flow field, electrode, and membrane domain, thus perpendicular to the membrane, was resolved by utilizing a tilted detector and investigated for a range of operating conditions (applied potential magnitude and sign, and flow rates). Furthermore, energy-resolved neutron imaging was performed using the time-of-flight neutron imaging technique, which allowed to separate the contribution of the active species from the supporting ions during battery operation. The novel approach allowed the imaging of spatial active species and supporting ion concentrations in *operando* electrochemical flow cells for the first time, enabling the coupling of the electrical and chemical response. Neutron radiography can provide valuable insight into flow cell operation, including the species distribution and transport mechanisms, which is useful in the selection of optimal cell configurations, electrolyte compositions, and operating conditions toward enhanced RFB operation.

In **Chapter 7**, the neutron radiography approach of **Chapter 6** was used to study the local transport properties in three electrode structures – the SGL 39AA carbon paper, 1186 HCB AvCarb carbon cloth, and an in-house manufactured non-solvent induced phase-separated (NIPS) electrode – and with two flow field designs – parallel and interdigitated. By performing *operando* neutron imaging on symmetric flow cells, the concentration distribution through the reactor of non-aqueous electrolytes was tracked, allowing the study of structure-performance relationships that can guide enhanced electrode design. Combined with parallel flow fields, with diffusion-dominated transport, it was found that electrodes with a bimodal pore size distribution with large pores in the though-plane direction enhance the flow cell performance by better electrolyte distribution and electrode utilization resulting in a higher current output. Additionally, the convective nature of interdigitated flow fields enhances the flow cell performance compared to parallel designs by allowing higher reaction rates. Yet, despite the large differences in the current output for the investigated configurations, similar concentration

profiles at the reactor level were observed. Finally, it was shown that neutron radiography can also be employed to investigate system secondary phenomena such as salt precipitation and underutilization of the flow field channels during operation.

In **Chapter 8**, model grid electrode structures were manufactured by stereolithography 3D printing followed by carbonization to investigate the effect of structural properties on the mass transport and pressure drop in redox flow cells. Structure-function-performance relationships were elucidated by exploring novel in-house manufactured electrodes with distinct features. The influence of the printing direction, pillar geometry, and flow field design was studied systematically using single-electrolyte flow cell configurations using a reversible and facile redox couple in a non-aqueous electrolyte. Hence, the mass transfer overpotentials could be decoupled from the flow cell performance. In addition, the cell polarization performance, internal surface area, pressure drop, mass transfer coefficients, and physicochemical electrode properties were studied. The printing orientation concerning the printing platform was found to influence the electrode performance by a change in the electrode roughness that impacted the internal surface area, pressure drop, and charge and mass transport resistances. The pillar geometry, on the other hand, impacts the mass transport in the electrode by affecting electrolyte mixing through the electrode. Helical or triangular pillar designs were found to be superior over square and cylindrical designs, as well as employing interdigitated flow fields over flow-through flow fields. Moreover, the performance of the 3D printed electrodes was compared to commercial electrodes and was found to have an enhanced mass transfer coefficient and a decreased pressure drop. However, the significantly lower internal surface area of the 3D printed electrodes prevents direct competition with off-the-shelf electrodes. Nevertheless, the potential of 3D printing to manufacture customized electrodes with a high geometrical and orientational flexibility was shown, together with manufacturing guidelines to speed up the research towards optimized novel electrode structures for electrochemical devices.

9.2. Future directions

9.2.1. Objective 1 - Pore network modeling: towards predictive models

The pore network model (PNM) developed in **Objective 1** is an effective computational model for simulating the performance of porous electrodes for a wide variety of operating conditions. As the real electrode can be translated to a pore network, the electrode microstructure can be correlated to the performance, and structure-performance relationships can be elucidated to guide the design of novel porous electrodes for electrochemical applications. Although effective, the PNM can be further improved to better capture the electrode performance. In this section, possible extensions of the model are provided, of which some are currently being explored and therefore discussed in more detail. In this objective, by developing a computational modeling framework, we aim to speed up the understanding and design of electrodes for electrochemical applications, with a focus on redox flow batteries. Hence, by collaborating and sharing our research we can make a greater impact on society. Therefore, the pore network model with several extensions is available on GitHub (***github.com/MaximevdHeijden/PNM-RFB-electrode***).

Possible research directions for extending the modeling framework include:

(1) ***The extension of the PNM to model a full non-symmetric redox flow battery to simulate charge-discharge cycles.*** To this end, multiple extensions must be made to the model including the addition of species migration, species crossover, and charged membranes. The first step is the extension of the advection-diffusion-reaction equation to the full Nernst-Planck equation to include species migration. In the current model, the low species concentration and high background electrolyte concentration make the assumption of negligible migration applicable [1]. Combined with the single-electrolyte configuration and without the simulation of a charged membrane, the performance of the flow cells can be well-described. However, for systems operating at higher species concentration, with full-cell configurations, and/or with charged membranes, species migration must be considered. A good starting point for the proposed extension is the publication of Agnaou *et al.* where they added the Nernst-Planck equation in OpenPNM [2]. Furthermore, the model could be extended to include charged membranes. The current framework accounts for the membrane by considering the membrane resistance using Ohm's law. Whilst being a reasonable assumption for single-electrolyte configurations, it cannot be translated to full-cell designs as species crossover should be considered. Furthermore, for charged membranes, the charged groups, electro-osmosis, and species migration should be taken into account. A starting point is the paper of Aghighi *et al.* where they simulated a full fuel cell membrane-electrode-assembly using a PNM [3].

(2) ***Incorporating temperature effects in the modeling framework.*** We observed that, during flow cell operation, the temperature increase in the electrolyte tanks for our single-electrolyte 2.55 cm^2 flow cells could be as high as 5 °C, indicating an even higher temperature increase in the reactor. With electrolyte conductivity experiments it was found that the conductivity of the non-aqueous TEMPO-based electrolyte strongly changed with temperature, significantly impacting the battery performance as the conductivity is a performance-limiting parameter for TEMPO electrolytes. The increase in ionic conductivity with temperature was studied by Zhang *et al.* for NaCl and $CaCl_2$ in propylene carbonate and water for which they derived an equation relating the ionic conductivity to the temperature and electrolyte concentration, originating from the correlations between the conductivity and mobility, and mobility and ionic strength [4]. To incorporate such a relation between temperature and ionic conductivity, the PNM should take into account reactor (overpotential losses) and pump heating. Several thermal models exist and could be used for inspiration, including the work of Ren *et al.* [5].

(3) ***A more accurate computation of the pressure drop in the pore network.*** The fluid transport dictates the mass transport characteristics and pressure drop and should be properly defined. The developed PNM describes the pore pressure by the Hagen-Poiseuille equation, where the pressure drop over the throats is defined by the hydraulic conductance of the cylindrical throat connecting pore i and j, and the pressure drop over the pores is defined using shape factors. However, besides the throat constriction factor, throat expansion and contraction should be considered [6, 7]. To this end, we extended the PNM to include throat expansion and contraction in the pressure drop definition, see **Figure 9.1a**, as described below.

When the fluid flows from pore i to pore j, a pressure drop is induced by the contraction of the flow cross-sectional area, followed by a pressure drop from the flow from throat ij to pore j by expansion. The overall fluid head loss over the pore-throat-pore element in a pore network can subsequently be obtained by solving the mechanical energy

balances combined with the pressure drop, based on the work of Larachi *et al.* [7], according to:

$$p_i - p_j = T_{ij}L_{ij} + C_{ij} + E_{ij}, \tag{9.1}$$

with $p_{i/j}$ the fluid total head of pore i or j, T_{ij} the constriction dissipation loss factor, L_{ij} the conduit length of the connecting throat, C_{ij} the contraction dissipation loss factor, and E_{ij} the expansion dissipation loss factor. The total head is assumed to consist only of the static pore pressure due to the low Reynolds operation in the electrode [7] but could be expanded in future work to include the velocity and gravitational head. The constriction, contraction, and expansion terms are given in **equations (9.2) - (9.4)**.

$$C_{ij} = \frac{\rho q_{ij}^2}{2\pi^2 r_{ij}^4}\left[\left(\frac{C_0}{Re_{ij}}\right)^N + \frac{1}{2^N}\left(1 - \frac{r_{ij}^2}{r_i^2}\right)^N\right] \tag{9.2}$$

$$E_{ij} = \frac{\rho q_{ij}^2}{2\pi^2 r_{ij}^4}\left[\left(\frac{E_0}{Re_{ij}}\right)^M + \left(1 - \frac{r_{ij}^2}{r_j^2}\right)^{2M}\right] \tag{9.3}$$

$$T_{ij} = \frac{8\mu q_{ij}}{\pi r_{ij}^4} \tag{9.4}$$

With ρ the mass density of the electrolyte, q_{ij} the throat ij volumetric flux, r_i the radius of pore i, r_{ij} the radius of throat ij, μ the dynamic viscosity of the electrolyte, Re_{ij} the Reynolds number in throat ij is defined as $Re_{ij} = \frac{2\rho q_{ij}}{\pi\mu r_{ij}}$, C_0 and E_0 laminar constants that describe viscous laminar contributions from contraction and expansion and correspond to 26 and 27 for a wide range of Reynolds numbers, respectively (though derived for pores that are ~2 orders of magnitude greater in size [6, 7]), and N and M the contraction and expansion curvature parameters that act as the fitting parameters in the PNM. The final mass balance for the electrolyte around pore i in the network is:

$$-\sum_{j=1}^{N_i} q_{ij} = \alpha_{ij}(P_i - P_j) = 0, \tag{9.5}$$

where N_i is the number of pore connections of pore i and α_{ij} is the factor matrix entry of the throat-pore-throat element ij, which can be defined by combining **equations (9.1) - (9.5)** and solved iteratively by a direct substitution procedure.

Moreover, the oversimplification of throats as perfect cylinders is tackled by the addition of a global correction factor, the throat effective aspect ratio F, which is employed as a fitting parameter for the pore radii: $r_{ij}^{eff} = Fr_{ij}$ [6, 7], with r_{ij}^{eff} the effective radius of throat ij.

The fitting parameters N, M, and F are obtained by fitting the PNM with experimental pressure drop data. These experiments were performed the same way as described in **Chapter 8** of this dissertation. The pressure drop was measured (n=2) for electrolyte velocities between 1.5 - 25 cm s^{-1} for single-electrolyte flow cells with the Freudenberg H23 electrode and both the flow-through and the interdigitated flow field designs. The experimental data can be found in **Figure 9.1b-c** together with the 1D Darcy-Forcheimer fittings. Furthermore, the PNM fittings are shown, where the overall pressure drop for all superficial velocities was fitted by modifying the N and M curvature parameters and the throat effective aspect ratio F. For the fitting, throats with a diameter exceeding that of the connecting pore are assigned the minimum pore diameter of the

connection pores. This fitting procedure resulted in fitting parameters of F = 1.26, N = 0.677, and M = 1.36 for the flow-through flow field, with a relative root mean squared error of 1.7 %. The anisotropic nature of the Freudenberg H23 electrode (**Chapter 2**), combined with the induced in- and through-plane flow direction for the interdigitated flow field configuration, necessitated refitting F, resulting in F = 1.11 with a relative root mean squared error of 0.4 %.

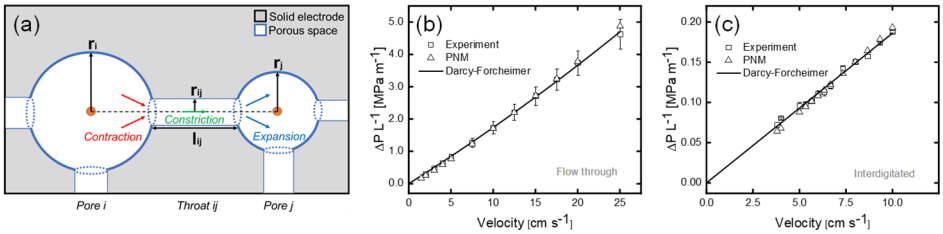

Figure 9.1: **(a)** Schematic representation of the spheres and cylinders representing the pores and throats in the pore network model, together with the pore and throat radius, throat length, and the visualization of throat contraction, constriction, and expansion. **(b-c)** Pressure drop per electrode length over a range of superficial velocities showing the experimental data, Darcy-Forchheimer fits, and pore network model fitting results for the: **(b)** flow-through flow field, and **(c)** interdigitated flow field.

(4) ***The addition of a velocity-dependent mass transfer coefficient.*** The current mass transfer coefficient definition relies on the film theory in which the film layer is assumed equal to the pore radius in every pore. Hence, the mass transfer coefficient only varies with the diffusion coefficient and pore diameter and is thus velocity independent. The relation can be improved by applying a velocity-dependent mass transfer coefficient correlation defined by dimensionless parameters [8], which we, therefore, included in the model as described below.

The mass transport in the porous electrode in the developed PNM is described by the advection-diffusion-reaction equation. The rate of the electrochemical reaction at the pore liquid-solid interface depends on the mass transport of reactive species from the pore bulk to the pore surface, where the active species conservation equation of the consumed active species around pore i is defined as

$$R_i = \frac{\lambda_i I_i}{nF}, \tag{9.6}$$

with R_i the active species net reaction rate, λ_i the dimensionless stoichiometric coefficient in the half-reactions, I_i the current in pore i, n the number of electrons in the half-reaction, and F Faraday's constant. The net reaction rate depends on the species mass transport by

$$R_i = \frac{\lambda_i}{n} k_m A_i \left(c_{b,i} - c_{s,i}\right), \tag{9.7}$$

where k_m is the mass transfer coefficient of the active species, A_i the electrochemically active internal surface area, $c_{b,i}$ the bulk concentration of the active species, and $c_{s,i}$ the surface concentration of the active species. In the PNM described in **Chapter 2**, the mass transfer coefficient was estimated by neglecting inertia effects and applying the film theory, resulting in the following relation:

$$k_m = 2\frac{D}{d_p}, \tag{9.8}$$

where D is the diffusion coefficient of the active species and d_p the pore diameter. By using **equation (9.8)**, a velocity-independent mass transport relation is implemented in the model, which is an oversimplification of the mass transport in porous electrodes. Therefore, the mass transport relationship was improved to include the electrolyte velocity dependency, based on the work by Misaghian *et al.* [8], commonly expressed in the form of a power law equation:

$$k_m{}^{global} = C_1\, v_e{}^{C_2}, \tag{9.9}$$

with $k_m{}^{global}$ the global mass transfer coefficient, v_e the superficial electrolyte inlet velocity, and C_1 and C_2 dimensionless factors that depend on the electrode structure [9]. **Equation (9.9)** uses a global mass transfer coefficient correlation and can be applied at the continuum scale; however, the PNM is a pore-scale method that necessitates a local mass transfer coefficient correlation that applies to the individual pores [8]. The local correlation, in terms of the pore velocity v_{PNM}, is defined as follows:

$$k_m{}^{local} = C_1\, v_{PNM}{}^{C_2}. \tag{9.10}$$

The direct local output variables acquired after solving the fluid field (**proposed research direction (3)**) are the static pore pressures, throat volumetric fluxes, and velocity vectors. The pore velocity vector is not a direct local output variable but can be calculated using appropriate assumptions: the fluid velocity field is assumed to be a continuous function close to the pore center and the pore velocity of pore i, $v_{i,PNM}$, can be calculated from the downstream throats leaving the pore in the x, y, and z-directions according to **equation (9.11)** [7]. The pore velocity is then equal to the summation of the flowrate of the downstream throats leaving pore i, N_{out}.

$$v_{i,PNM} = \sqrt{\left(v_{x,i}^{PNM}\right)^2 + \left(v_{y,i}^{PNM}\right)^2 + \left(v_{z,i}^{PNM}\right)^2} = \frac{\sum_{i=1}^{N_{out}} q_{ij}}{\pi r_i^2} \tag{9.11}$$

To implement the mass transport relationship of **equation (9.10)** in the PNM, the prefactor and exponent need to be derived from experiments. At limiting current density conditions, the concentration of the active species at the electrode surface can be assumed negligible. Therefore, limiting current experiments were performed the same way as described in **Chapter 8** of this dissertation, with an electrolyte solution containing 5 mM TEMPO, 25 mM $TEMPO^+$, and 1 M $TBAPF_6$ in acetonitrile. The limiting current was extracted from the polarization curves (n=3) in the range of 0.7 - 0.9 V for electrolyte velocities between 0.5 - 10 cm s^{-1} and 0.33 - 6.67 cm s^{-1} in single-electrolyte flow cells with the Freudenberg H23 electrode for the flow-through and the interdigitated flow field designs, respectively.

The $k_m{}^{global}$ can be extracted from limiting current density experiments following two methods. The first method, which assumes the bulk concentration to remain constant, can be derived from **equations (9.6)** and **(9.7)** and is represented by **equation (9.12)**, with I_{lim} the limiting current, V the electrode volume, and a being the specific surface area of the electrode. The second approach accounts for species depletion, given by **equation (9.13)**, and is obtained by assuming plug-flow behavior and by integrating the 1D mass conservation equation over the flow path [10, 11], with L_{fp} the

length of the flow path, c_{in} the inlet concentration, and H and W the height and width of the electrode, respectively. The second method assumes a unidirectional flow path and is thus only applicable to the flow-through flow field (FTFF) configuration. Because the length of the flow path with the FTFF greatly exceeds that of with the interdigitated flow field (IDFF), the second method (i.e., accounting for species depletion) is employed for the FTFF configuration, whereas the first method (i.e., assuming no species depletion) is used for the IDFF configuration. It was found that the application of the first method in computing ${k_m}^{global}$ for the FTFF configuration indeed resulted in a significant underestimation, additionally shown by Kok *et al.* [12].

$${k_m}^{global} = \frac{I_{lim}}{nFac_{in}V} \tag{9.12}$$

$${k_m}^{global} = \frac{v_e}{a\,L_{fp}} \ln\left(1 - \frac{I_{lim}}{nFHWc_{in}v_e}\right) \tag{9.13}$$

The resulting power-law relationships with the FTFF and IDFF, corresponding to literature trends [9, 13, 14], see **Figure 9.2a**, are:

$${k_{m,FTFF}}^{global} = 7.43 \cdot 10^{-4}\, {v_e}^{0.79} \tag{9.14}$$

$${k_{m,IDFF}}^{global} = 2.26 \cdot 10^{-3}\, {v_e}^{0.85}. \tag{9.15}$$

The ${k_m}^{local}$ correlation can be derived numerically by mimicking the limiting current density experiments used for the global correlations. Over a range of superficial inlet velocities, the ${k_m}^{global}$ is computed with **equation (9.16)** with N_{tot} the total number of reactive pores, and by assuming the bulk concentration equal to the inlet concentration. The subsequent reaction rate can be obtained with **equation (9.17)** with the local mass transfer coefficient in pore i, computed with the local pore velocities.

$${k_m}^{global} = \frac{\sum_{i=1}^{N_{tot}} R_i}{\sum_{i=1}^{N_{tot}} A_i c_{b,i}} \tag{9.16}$$

$$\sum_{i=1}^{N_{tot}} R_i = \sum_{i=1}^{N_{tot}} {k_{m,i}}^{local} A_i c_{b,i} \tag{9.17}$$

The PNM addresses the practical constraint of the experimental method (i.e., assuming a constant bulk concentration) by only activating a reaction term in certain portions of the electrode, referred to as "reactive pockets" [12]. These reactive pockets are randomly selected non-overlapping regions of the electrode that account for roughly 11 - 14 % of the entire reactive network volume. The reported k_m^{global} value per applied inlet velocity is then computed through an averaging procedure of a series of iterations (e.g., 500) for newly assigned random reactive pockets in each iteration.

The local mass transport relations are subsequently obtained through varying C_1 and C_2 such that the numerically determined ${k_m}^{global}$ matches the experimentally obtained ${k_m}^{global}$. The resulting PNM fits can be found in **Figure 9.2a** with the following relations:

$${k_{m,FTFF}}^{local} = 1.43 \cdot 10^{-4}\, {v_e}^{0.80} \tag{9.18}$$

$${k_{m,IDFF}}^{local} = 5.0 \cdot 10^{-4}\, {v_e}^{0.86}. \tag{9.19}$$

The fitting is successful with a relative root mean squared error of 0.50 % for the FTFF and 2.0 % for the IDFF. Furthermore, a comparison is made between the

velocity-independent and dependent correlations in **Figure 9.2b-c**, showing the significant overestimation of the mass transfer coefficient by the velocity-independent definition at low electrolyte velocities [8].

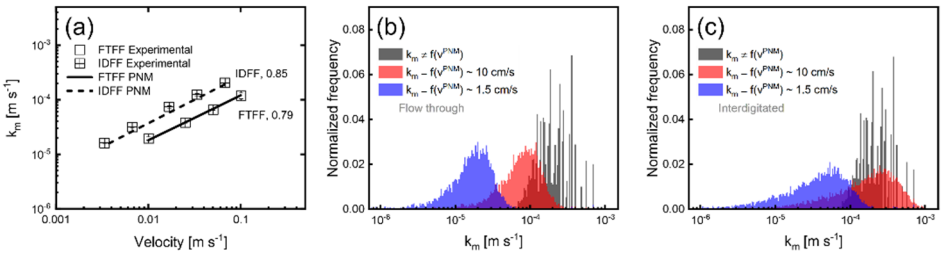

Figure 9.2: **(a)** The global mass transfer coefficient relationship obtained experimentally and by fitting the pore network model to the experimental results over a range of superficial inlet velocities, for the flow-through and interdigitated flow fields, plotted on a double-log scale. **(b-c)** Histograms with the normalized frequency of the velocity-independent and dependent local mass transfer coefficients at the pores of the pore network model for inlet velocities of 10 and 1.5 cm s^{-1} for **(b)** the flow-through flow field, and **(c)** the interdigitated flow field.

(5) ***Extending the PNM to simulate multiphase flow to account for hydrogen evolution and incomplete wetting of the porous structure.*** The current model only relies on all-liquid transport and thus omits gas transport. Therefore, the model could overpredict the flow cell performance as, for certain chemistries and operating conditions, incomplete wetting and hydrogen evolution can impact the performance in experimental conditions. Pore network models for multiphase flow exist in great amounts in the literature and include the work of Aghighi *et al.* on fuel cells [15, 16].

(6) ***Simulating a wide variety of flow field designs, including flow-by and hybrid flow field geometries.*** To date, the RFB performance with flow-by and hybrid flow geometries is generally simulated with volume-averaged computational fluid dynamic simulations [14, 17–21], without considering the electrode pore structure. Complex flow field designs should be incorporated into pore-scale simulations, for example into PNMs as they are computationally light, to investigate the effect of the fluid flow induced by the flow field on the local performance in the electrode. In the current PNM, the boundary conditions determine the flow field, which is inaccurate or impractical for flow-by or hybrid designs. Therefore, we propose the coupling of pore network models with computational fluid dynamic simulations to simulate the flow field channels, intending to extend the knowledge on flow field-electrode interactions [22]. Therefore, to model a variety of flow field designs, we started the coupling of the PNM to a continuum model that accurately describes the fluid flow in flow field channels. We started with the computation of a parallel flow field design, inspired by the work of Weishaupt *et al.* [22], which is briefly described below.

First, a 2D continuum model was built using a mathematical model and discretization schemes that describes steady, incompressible, and laminar fluid flow in flow channels. The Navier-Stokes equation depicting the fluid flow was solved using the SIMPLER algorithm. The model was developed using the book of Versteeg *et al.* [23], and will not be discussed in detail here. Yet, the 2D continuum model was validated in isolation through a grid refinement study for flow between two flat plates with the

analytical solution of the parabolic flow profile. The modeling domain consisted of a rectangular channel with the same dimensions as a single parallel flow field flow channel. The Navier-Stokes equations were solved on an equally spaced cartesian grid with the inlet velocity imposed as a Dirichlet boundary and the outlet as a Neumann outlet boundary. A good match between the model and analytical solution was found for various grid points (n = 10, 50, 100, 500, and 1000) and the order of convergence matches that of the discretization scheme used, verifying the continuum model.

Second, the developed continuum model was coupled to the PNM, with a 2D-ordered grid structure, see **Figure 9.3a**. The coupling is inspired by the work of Weishaupt *et al.* [22] and will not be discussed in detail here. The coupling conditions used are valid for single-phase, incompressible, creeping laminar flow at the intersecting surfaces (connecting points between both models, i.e., pore intersection with the boundary of the continuum model) and are formulated for mechanical equilibrium at the intersecting surfaces and mass conservation over the intersecting surfaces. Each surface pore in the pore network has a connectivity of one, has a pore diameter equal to the projected cross-sectional area of the connected throat on the interface, and is split in half by the interface. For the definition of the mass and momentum coupling balances, we refer to Weishaupt *et al.* [22], and we included a mass conservation coupling condition, continuity of pressure across the coupling interface for the normal momentum component, and the conservation of the tangential momentum component (**Figure 9.3a**). The coupling conditions were applied using a Dirichlet-type coupling scheme, employing Dirichlet pressure boundary conditions to the surface pores of the PNM, and Dirichlet normal and tangential velocity component boundary conditions of the continuum model at the control volumes associated with the coupling interface. The continuum model and PNM are coupled in an iterative procedure by first solving the fluid flow of the continuum model followed by that of the PNM. The continuum model is initialized by assigning guessed normal and tangential velocity components at the coupling interface, and updated throughout the iterative scheme through relaxation with the solution of the previous iteration.

The coupling of the continuum model with the PNM in 2D was verified according to the reference solution used by Weishaupt *et al.* [22]. The coupling was validated for model grid structures in 2D with a connectivity of 4, for 21 surface pores, and with three different porous structures having distinct throat width-to-length ratios [22]. Furthermore, two distinct laminar channel flow regimes were studied, channel flow in the Stokes regime with a maximum Reynolds number of <0.01 and with a Reynolds number of ~400, of which the latter is closer to an operation regime of an RFB with parallel flow fields. Moreover, the model was investigated for 1 and 5 control volumes per throat width using an equidistant grid. The model was successfully validated using the reference in Weishaupt *et al.* [22], in accordance with their model validation, and can thus resolve the fluid field over regular porous structures for steady, isothermal, single-phase laminar flow operating at high and low Reynolds numbers. The model validation for one of the simulated cases is shown in **Figure 9.3b-e**. Subsequently, the model was successfully extended to random 2D structures by using a Voronoi tessellation as a pore network. Finally, the model was extended to include component mass transport by continuity of component concentration at the interface and by conservation of the component's mole flux across the coupling interface, though this part is not validated yet.

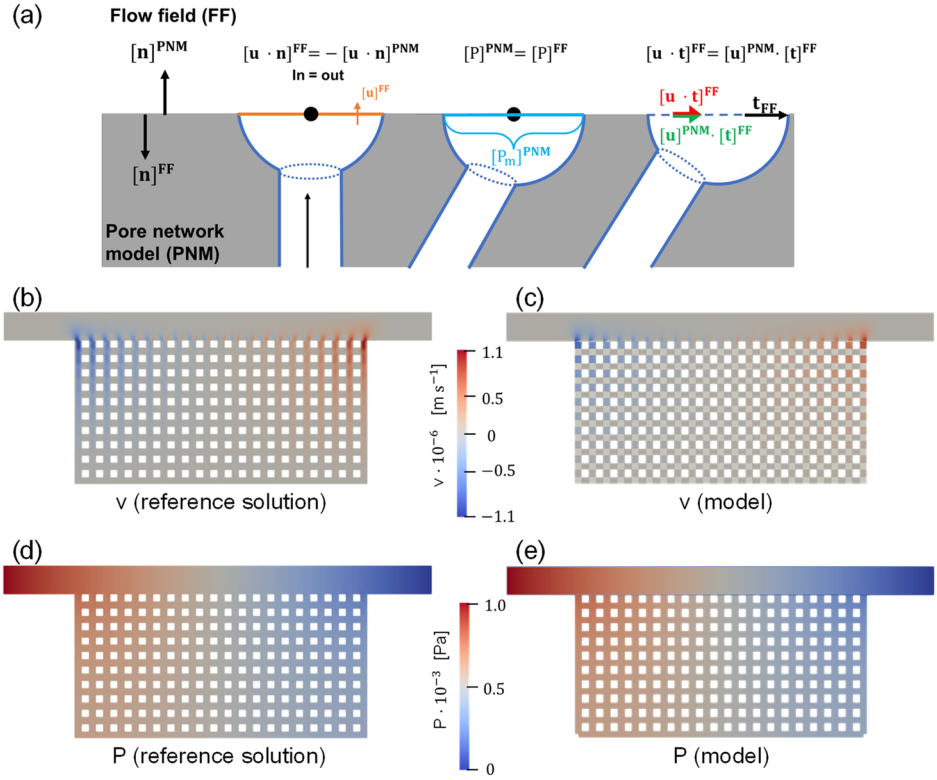

Figure 9.3: **(a)** Schematic of the continuum model and pore network model coupling conditions. The left pore represents the mass conservation coupling condition, the middle pore the continuity of pressure across the coupling interface for the normal momentum component, and the right pore the conservation of the tangential momentum component. **(b-e)** Qualitative comparison of the continuum model and pore network model coupling with the reference solution from [22] **(b,c)** for the normal velocity component **(d,e)** and pressure.

Nevertheless, the coupling of the continuum model and PNM should be extended to capture the fluid and mass transport of a parallel flow field in combination with a tomography-extracted pore network in 3D. For the implemented coupling scheme only the tangential velocity coupling condition needs to be expanded in the third dimension, while all other coupling conditions remain unchanged. Further, to maintain computational feasibility in 3D, the possibility of local grid refinement should be investigated. Moreover, completely different coupling conditions could be applied. A prominent example would be the mortar scheme introduced by Mehmani and Balhoff [24], as it is based on an averaging method and therefore would enable the utilization of a coarser grid. Finally, the continuum model can be applied to the iterative PNM framework, in which first the fluid field is solved, followed by the coupled mass and charge transfer.

(7) ***The coupling of the PNM with other modeling frameworks to increase the model accuracy.*** The benefit of coupling modeling frameworks is that the advantages of both could be combined to obtain a modeling framework with a low computational cost and high accuracy. For example, the PNM could be coupled to pore-level models that can

simulate surface roughness and incomplete pore wetting of individual pores, or to computational fluid dynamic models that can better capture the fluid flow through the electrode. By combining pore-level models with the PNM, the trends at the pore-level could be translated to the overall pore structure to decrease the computational cost of the modeling framework, compared to simulating the entire electrode using detailed pore-level models, which is computationally expensive [25].

(8) ***The use of the PNM to aid in the design of advanced electrode structures.*** The PNM is useful for investigating the transport properties in porous electrodes, which could aid in assessing the electrode performance for a range of operating conditions, electrolyte solutions, and flow field geometries. To this end, with the model developed in **Chapter 2** and extended in **Chapter 3**, two novel non-solved induced phase-separated electrodes were analyzed with the PNM (**Figure 9.4**), a NIPS with macrovoids (the DMF - 0.20g/mL - 21 °C developed by Jacquemond *et al.* [26]) and a porosity gradient NIPS (developed by Wan *et al.* [27]). The performances of both electrodes were evaluated with the TEMPO/TEMPO$^+$ electrolyte with low electrolyte conductivity and facile kinetics, and with the VO^{2+}/VO_2^+ electrolyte with high conductivity but sluggish kinetics. Furthermore, the flow-through and interdigitated flow fields were analyzed and the resulting polarization curves can be found in **Figure 9.4c**.

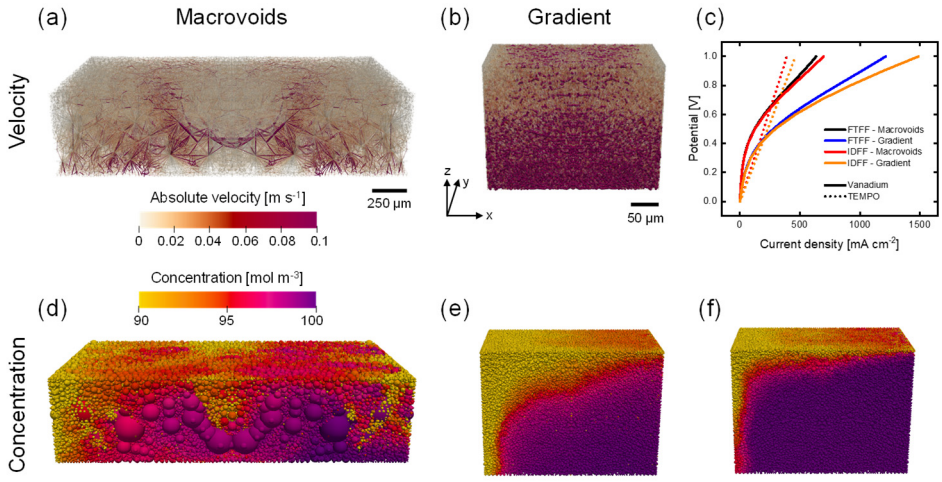

Figure 9.4: Preliminary results of pore network model simulations of novel non-solvent induced phase-separated electrodes: **(a,d)** with macrovoids [26], and **(b,e-f)** with a porosity gradient [27]. **(a-b)** The absolute velocity profiles through the throats in the electrode for the vanadium chemistry, with an interdigitated flow field, and evaluated at 8 cm s^{-1}. **(c)** Polarization curves for all tested systems: 2 electrode types (with macrovoids and a porosity gradient), 2 flow field designs (flow-through and interdigitated), and 2 chemistries (vanadium and TEMPO). **(d-f)** Concentration profiles through the electrode with the interdigitated flow field, evaluated at 8 cm s^{-1} and 1 V overpotential, for: **(d-e)** the vanadium chemistry, and **(f)** the TEMPO chemistry. The electrodes have different scale bars because of the difference in electrode size (due to network extraction RAM issues for the porosity gradient (a large number of pores)), hence, both electrodes have a different channel and rib distance.

Several performance trends can be obtained from the PNM simulations, including: **(1)** the porosity gradient electrode outperforms the electrode with macrovoids in terms of the electrochemical performance for all configurations. The effect is most prominent for the vanadium electrolyte with sluggish kinetics because of the significant decrease in the activation overpotential with the porosity gradient electrode due to the high internal surface area. **(2)** The porosity gradient electrode features a significantly higher pressure drop compared to the electrode with macrovoids, resulting in a higher pumping power requirement, which is especially detrimental for flow-through flow configurations. **(3)** The electrode with macrovoids features electrolyte transport pathways as a result of the macrovoids (**Figure 9.4a**), leading to convection and diffusion transport-dominated domains. These domains dictate the electrochemical performance by the formation of local reaction zones besides convective electrolyte transport domains, see **Figure 9.4d**. **(4)** The porosity gradient electrode has a uniform in-plane electrolyte distribution with the flow-through flow field and follows the path-of-least-resistance with the interdigitated design, resulting in high convection over the rib and local reaction zones above the channels, near the membrane (**Figure 9.4b,e**). **(5)** The vanadium electrolyte results in a higher current output at elevated potentials due to the greater utilization of the available internal surface area at the investigated electrolyte velocity, because of the higher electrolyte conductivity compared to the TEMPO electrolyte (**Figure 9.4e-f**).

Based on the presented study, I advise using the porosity gradient electrode in combination with interdigitated flow designs and with electrolytes with high ionic conductivity. On the contrary, the electrode with macrovoids could be used in combination with flow-through flow fields and kinetically facile electrolytes. A PNM assessment, such as the brief analysis presented here, can guide electrode and system design, which could save valuable time and experimental resources.

(9) ***A better geometrical representation of the porous structure.*** One possible extension would be to include compressed electrode structures by obtaining the X-ray tomograms under compression using a similar set-up as used by Tenny *et al.* [28]. By including compressed electrodes in the PNM, the experiments can be conducted under compression, as is desired for industrial applications, resulting in minimal contact resistances and thus minimal ohmic corrections during model validation [29]. Furthermore, pore and throat geometrical definitions beyond spheres and cylinders could be integrated to better translate the electrode structure to a pore network. Although spheres and cylinders are a reasonable assumption for the pore space in many commercial fibrous electrodes, it is an oversimplification and could be inaccurate for more complex electrode structures such as woven electrodes [30]. To this end, it is worth investigating various geometrical definitions of the pore space. OpenPNM has several built-in geometrical definitions including cones and cylinders, pyramids and cuboids, and cubes and cuboids. For example, Misaghian *et al.* used pyramids to represent the pore space of a randomly organized fibrous material with a binder [8]. Yet, such geometrical definitions could still underestimate the complex space in porous electrodes as surface roughness is complex to include, for which additional correction factors must be considered.

(10) ***Finally, the extension of the PNM to model other electrochemical technologies*** by adopting multiphase flow and by adjusting the reaction terms in the model. Various PNMs already exist for fuel cells, but pore network models for complex hybrid batteries (e.g., iron plating, iron-air) or CO_2-electrolysis could be viable options to explore.

9.2.2. Objective 2 - Genetic algorithm to guide the manufacturing of bottom-up designed electrodes

The genetic algorithm (GA), utilizing the pore network model of **Objective 1**, was developed in **Objective 2**. In the GA, optimized porous electrodes are computed from the bottom-up by natural selection of the fittest structures driven by the theory of evolution. A GA has a high degree of evolutionary freedom and can easily be adapted and expanded depending on the operating conditions (potential, flow rate), network properties (artificial, extracted), system configuration (flow field, electrolyte), and desired optimization functions (mutation, migration). The framework was built to speed up and guide the design of electrodes for electrochemical applications, with a focus on redox flow batteries. As a greater scientific impact can be made by sharing research, the modeling framework with all added extensions is made available on GitHub (***github.com/MaximevdHeijden/GA-RFB-electrode***) as the presented GA is a proof-of-concept and should be further developed in future work. Possible extensions or improvements of the modeling framework include:

(1) ***The selection of an appropriate fitness function and geometrical definitions.*** In the presented model, both the pumping power and electrical power are optimized to an equal degree. The current fitness function must be analyzed in depth and a suitable definition should be used depending on the desired electrode optimization. Moreover, the geometrical definitions of OpenPNM are currently employed, which significantly oversimplify and underestimate the electrode performance, affecting the optimization of the electrodes by e.g., an inaccurate internal surface area definition. Moreover, with the manufacturing technique of choice in mind, other geometrical shapes beyond spheres and cylinders could be incorporated to better represent the to-be-manufactured optimized electrode structure. For example, Misaghian *et al.* used pyramids to represent the pore space, which they claimed is a better representation of fibrous materials with binder [8].

(2) ***The implementation of manufacturing constraints.*** During the structure evolution, the electrodes could be screened for dead-end pores, interconnection of the solid phase, and a minimum size/length of the void- and solid phases. Moreover, additional manufacturing constraints, concerning the manufacturing technique of choice, could be incorporated. For example, when using 3D printing as a manufacturing technique, the printing resolution and layer thickness could be implemented in the GA, together with a shrinkage factor when a carbonization step is required. Moreover, the void space should be converted into a solid structure as is generally necessary for electrode fabrication. One possible method could be the manufacturing of the inverted void space, as was presented in **Section A4.7.2**, which could be used in combination with 3D printing. Another option would be to develop an "inverse" SNOW algorithm [31] that can translate the void space back into a fibrous material.

(3) ***The extension of the evolutionary freedom of the GA.*** Examples include the addition of pore migration and the coupled optimization of the electrode structure with the flow field design. Furthermore, the optimization could be performed for ***full-cell designs*** for which both the cathode and anode can be independently optimized, considering e.g., species crossover. In addition, the ***full parallelization*** of the GA should be investigated. In the current GA version, as described in **Chapter 5**, only the performance evaluation of the structures is parallelized to the number of individuals. The

mutation, crossover, volume scaling, and merging and splitting steps could also be parallelized to further reduce the computational time and enable the optimization of larger electrode structures.

(4) ***The adaptation of the GA approach for the optimization of other electrochemical technologies*** such as hydrogen fuel cells, water electrolyzers, and CO_2 electrolyzers. Moreover, the PNM implemented in the GA could be replaced by ***another pore-scale model***, and/or can be ***coupled*** to additional modeling frameworks to increase the accuracy of the optimization and/or decrease the computational costs.

9.2.3. Objective 3 - Advanced imaging techniques: locally resolved diagnostics

Throughout this dissertation, advanced imaging techniques were employed, including X-ray tomographic microscopy (XTM) in **Chapters 2**, **3**, **5**, **7**, and **8**, and neutron imaging in **Chapters 6** and **7**. Locally resolved diagnostics enable a deeper understanding of local properties within the reactor, providing key information regarding the *operando* transport processes in the electrochemical cell. Advanced imaging is thus crucial in flow battery research and should be developed further. Possible research directions include:

(1) ***Further investigation of redox flow batteries with the neutron radiography approach.*** First and foremost, full cell performance should be probed with energy-selective neutron imaging. By engineering an anolyte and a catholyte with distinct neutron attenuations, the concentration distribution during operation in both half-cells can be resolved. Moreover, neutron radiography can be used to gain a deeper understanding of the reactive transport processes in the porous electrode, as investigated in **Chapter 7**, which is of special interest for novel electrode structures to investigate their potential, design flaws, and points of improvement. Furthermore, the electrode-flow field interplay could be studied further, of which the significance was provided in **Chapter 7**, including studies on the electrolyte transport from the flow field channel to the porous electrode, flow channel utilization, and novel flow channel configurations. In addition, neutron radiography could be used to investigate electrolyte crossover with neutron-attenuating active species to study the impact of distinct membrane types, cell configurations, and electrode structures. Jacquemond *et al.* [32] recently studied electrolyte crossover through different membranes utilizing symmetric cell configurations. Their research could be extended to full cell designs and more membrane types (various charge densities and thicknesses), and can be combined with diverse reactor configurations to study the magnitude and effect of electrolyte crossover on the cell performance. Finally, cell malfunction studies could be performed including the investigation of channel utilization and salt precipitation (**Chapter 7**), but also on hydrogen evolution [33] and electrode wetting. Such studies are not only interesting from a fundamental point of view but additionally for industrial use to optimize the stack configuration and design, and operating conditions.

(2) ***Utilizing operando and ex-situ XTM for porous electrode characterization.*** *Operando* X-ray computed tomography can be used to study gas formation through the reactor with high spatial resolution [34–37]. Whereas *ex-situ* XTM can be used to investigate the electrode structure and structural integrity, for example upon compression [28]. Particularly the structural comparison of novel electrodes, e.g., 3D printed electrodes or

NIPS electrodes, before and after extensive electrochemical cycling with XTM is expected to be powerful and can gain insight into the local mechanical stability of novel electrodes.

(3) ***Developing additional operando locally resolved imaging techniques.*** Promising approaches [38] include nuclear magnetic resonance to track the state-of-charge [39], magnetic resonance imaging to analyze the electrolyte and temperature distributions [40, 41], CCD camera studies with colorimetric analysis to probe electrochemical reactions [42], and fluorescence/confocal imaging to visualize electrolyte reactions and transport behavior [43]. The latter, confocal imaging, is currently being explored by us. Inspired by the work of Wong *et al.* [43] we aim to study mass and reactive transport in model grid structures by combining confocal microscopy with 3D printing. Using our transparent flow cell (**Figure 9.5a**) we elect to study the reduction reaction of anthraquinone-2,6-disulfonate (AQDS) to H_2AQDS (**Figure 9.5b**) [44] by making use of the change in fluorescence signal upon AQDS reduction. Combined with model grid structures with varying pillar designs, orientations, and locations, and distinct flow field designs, the mass transport through the reactor area can be studied.

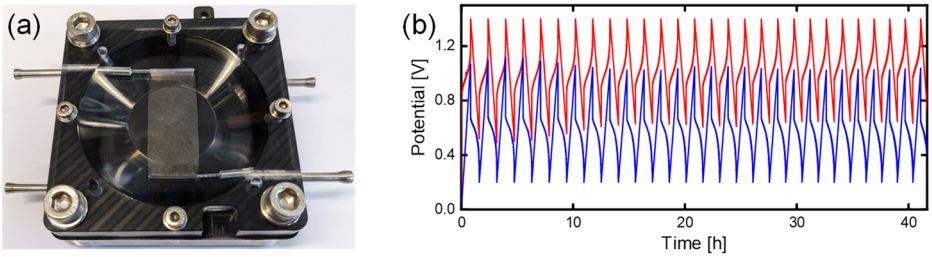

Figure 9.5: **(a)** In-house designed confocal imaging cell, and **(b)** a test run providing the cycling ability of the chemistry of interest for the confocal measurements: 100% state-of-charge 0.1 M AQDS in 1 M KCl and 100% state-of-charge 0.3 M ferrocyanide in 1 M KCl (with argon purging of the tanks). The cycling performance of the full-cel was obtained with the regular RFB cell configuration with a 2.55 cm^2 geometrical area, with two stacked thermally treated SGL 39AA electrodes, an interdigitated flow field, a Nafion 212 membrane, and evaluated at 5 cm s^{-1} and 100 mA applied current.

9.2.4. Objective 4 - Advanced manufacturing: towards higher performance

In **Objective 4** the potential of 3D printing as a manufacturing technique for RFB electrodes was investigated. Even though the studied model grid structures were produced using a low-resolution stereolithography 3D printer (0.9 x 0.9 x 0.9 mm^3 pores with a pillar thickness of 0.3 mm) resulting in a low internal surface area, we showed that the mass transport and pressure drop can be improved compared to off-the-shelf electrodes. To become competitive with commercially used electrodes, alternative 3D printing techniques must be investigated in combination with optimized electrode designs. To this end, we propose to explore the following:

(1) ***Enhancing the internal surface area of the 3D printed electrodes to improve their electrochemical output.*** By utilizing a 3D printer with higher resolution, e.g., by using two-photon polymerization, smaller features down to the submicrometer scale can

be printed [45–47], increasing the internal surface area of the structures. Moreover, the internal surface area can be enlarged by obtaining 3D structures with porous surfaces. Possible methods to obtain a porous surface include etching, thermal treatments, coatings, or the addition of a porogen into the printing resin (if a liquid resin is used, for example with photopolymerization-based additive manufacturing techniques). We investigated the option of altering the resin formulation to induce surface porosity by the addition of a porogen into the resin formulation, inspired by the work of Dong *et al.* [48]. To this end, we studied various resin formulations (monomer type, porogen type, and porogen concentration, combined with a photoinitiator) and extraction methods (different solvents, heat treatments, and pressures) and performed the experiments on single resin droplets that were photopolymerized with UV-light (405 nm). The success of the porogen extraction was subsequently analyzed by thermographic analysis and scanning electron microscopy (**Figure 9.6**). We managed to obtain a certain degree of porosity on the electrode surface, see **Figure 9.6**, but further optimization is required. It is believed that CO_2 supercritical drying as a porogen extraction method, as was applied by Dong *et al.* [48], could increase surface porosity and can result in enhanced electrode performance for RFB application.

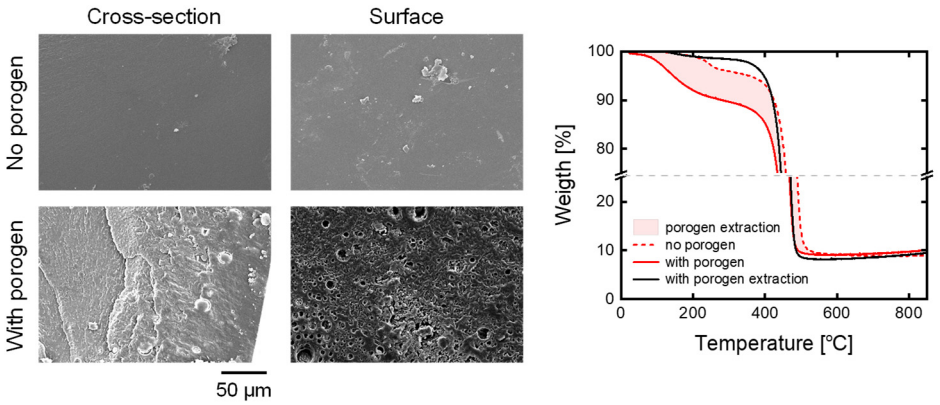

Figure 9.6: Scanning electron microscopy images at 500 x magnification of the surface and cross-section of cured resins with and without porogen. The cured resin samples with porogen underwent a porogen extraction method of 24 hours in a solvent. Furthermore, the thermographic analysis is shown for this specific cured resin formulation and extraction method where the red line represents a sample with porogen that is not extracted, the red dotted line without porogen, and the black line with porogen extracted with the 24-hour wash in a solvent method.

(2) ***The increase in internal surface area must go hand-in-hand with attaining a high electrolyte permeability.*** Hence, the trade-off between a high internal surface area and thus small pores, and a high electrolyte permeability and thus an open structure, must be optimized. We believe that a bimodal pore size distribution is key in providing a high current output and additionally a low pressure drop in the reactor. Yet, the electrode-flow field interactions must be considered in the design of such electrode structures as the flow induced by the flow field impacts the optimized orientation of the large and small pores.

(3) ***Investigating advanced electrode designs.*** Potential research directions include optimized pillar or fiber geometries and shapes, their orientation, location, and layer thickness, but additionally designs beyond pillar or fiber structures. Moreover, the

electrode thickness and mechanical stability should be optimized. Advanced electrode designs are required to enhance the mass transport in porous electrodes on all length scales by improving the electrolyte distribution, internal mixing, and diffusion layer thickness. To this end, 3D printing can be combined with topology optimization methods to realize the manufacturing of computationally optimized electrode structures, as was suggested in **Objective 2**.

(4) ***Fine-tuning the resin formulation and thermal sequence.*** By refining the resin formulation, the degree of resin spreading and thus the printing resolution could be controlled, together with the surface roughness and porosity, the shrinkage degree upon carbonization, the mechanical and chemical stability, and potentially the conductivity by electing conductive resins. Whereas, the thermal sequence can be optimized by e.g., carbonization at elevated temperatures (>1100 °C) to improve the conductivity. The ideal carbonization sequence and oxidation stabilization step could vary for different resins and electrode structures and should be investigated in detail to produce conductive, mechanically stable electrodes with high surface porosity.

(5) ***The potential of 3D printed electrodes for RFB applications compared to current state-of-the-art electrodes.*** The electrochemical performance, pumping requirements, mechanical and chemical stability, cycling performance, and cost of manufacturing should all be considered to evaluate whether additive manufacturing could become a competing electrode manufacturing strategy.

9.3. References

[1] A. J. Bard, L. R. Faulkner, *Electrochemical methods* (John Wiley & Sons, New York, Second., 2001).
[2] M. Agnaou, M. A. Sadeghi, T. G. Tranter, J. Gostick, *Comput. Geosci.* **140**, 104505 (2020).
[3] M. Aghighi, M. A. Hoeh, W. Lehnert, G. Merle, J. Gostick, *J. Electrochem. Soc.* **163**, F384–F392 (2016).
[4] W. Zhang, X. Chen, Y. Wang, L. Wu, Y. Hu, *ACS Omega*. **5**, 22465–22474 (2020).
[5] J. Ren *et al.*, *Int. J. Heat Mass Transf.* **192**, 122926 (2022).
[6] A. Fathiganjehlou *et al.*, *Chem. Eng. Sci.* **273**, 118626 (2023).
[7] F. Larachi *et al.*, *Chem. Eng. J.* **240**, 290–306 (2014).
[8] N. Misaghian, M. A. Sadeghi, K. Lee, E. Roberts, J. Gostick, *J. Electrochem. Soc.* **170**, 070520 (2023).
[9] M. van der Heijden, M. Kroese, Z. Borneman, A. Forner-Cuenca, *Adv. Mater. Technol.*, 2300611 (2023).
[10] X. You, Q. Ye, P. Cheng, *J. Electrochem. Soc.* **164**, E3386–E3394 (2017).
[11] D. Schmal, J. Van Erkel, P. J. Van Duin, *J. Appl. Electrochem.* **16**, 422–430 (1986).
[12] M. D. R. Kok *et al.*, *Chem. Eng. Sci.* **196**, 104–115 (2019).
[13] B. A. Simon *et al.*, *Appl. Energy*. **306**, 117678 (2022).
[14] J. D. Milshtein *et al.*, *J. Electrochem. Soc.* **164**, E3265–E3275 (2017).
[15] M. Aghighi, J. Gostick, *J. Appl. Electrochem.* **47**, 1323–1338 (2017).
[16] M. Aghighi, M. A. Hoeh, W. Lehnert, G. Merle, J. Gostick, *J. Electrochem. Soc.* **163**, F384–F392 (2016).
[17] V. Muñoz-Perales, M. van der Heijden, P. Á. García-Salaberri, M. Vera, A. Forner-Cuenca, *ACS Sustain. Chem. Eng.*, **11** (33), 12243-12255 (2023).
[18] M. Messaggi *et al.*, *Appl. Energy*. **228**, 1057–1070 (2018).
[19] M. Macdonald, R. M. Darling, *AIChE J.* **65**, 1–11 (2019).
[20] C. H. Chen, K. Yaji, S. Yamasaki, S. Tsushima, K. Fujita, *J. Energy Storage*. **26**, 100990 (2019).
[21] Q. Xu, T. S. Zhao, P. K. Leung, *Appl. Energy*. **105**, 47–56 (2013).
[22] K. Weishaupt, V. Joekar-Niasar, R. Helmig, *J. Comput. Phys. X*. **1**, 100011 (2019).
[23] H. Versteeg, W. Malalasekera, *Introduction to Computational Fluid Dynamics, An: The Finite Volume Method* (Pearson, Loughborough University, second., 2007).
[24] Y. Mehmani, M. T. Balhoff, *Multiscale Model. Simul.* **12**, 667–693 (2014).
[25] J. Zhao, F. Qin, D. Derome, Q. Kang, J. Carmeliet, *Adv. Water Resour.* **145**, 103738 (2020).
[26] R. R. Jacquemond *et al.*, *Cell Reports Phys. Sci.* **3**, 100943 (2022).
[27] C. T. C. Wan, R. R. Jacquemond, Y. M. Chiang, A. Forner-Cuenca, F. R. Brushett, *Energy Technol.* **11**, 2300137 (2023).
[28] K. M. Tenny *et al.*, *Energy Technol.* **10**, 2101162 (2022).
[29] V. Muñoz-Perales *et al.*, *ChemRxiv* (2023), doi:10.26434/chemrxiv-2023-n2mmd.
[30] M. van der Heijden, R. van Gorp, M. A. Sadeghi, J. Gostick, A. Forner-Cuenca, *J. Electrochem. Soc.* **169**, 040505 (2022).
[31] J. T. Gostick, *Phys. Rev. E*. **96**, 1–15 (2017).
[32] R. R. Jacquemond, PhD thesis, Eindhoven University of Technology (2023).
[33] J. T. Clement, PhD thesis, University of Tennessee (2016).
[34] R. Jervis *et al.*, *J. Phys. D. Appl. Phys.* **49**, 434002 (2016).
[35] F. Tariq *et al.*, *Sustain. Energy Fuels*. **2**, 2068–2080 (2018).
[36] K. Köble *et al.*, *J. Power Sources*. **492**, 229660 (2021).
[37] L. Eifert *et al.*, *ChemSusChem*. **13**, 3154–3165 (2020).
[38] Y. A. Gandomi *et al.*, *J. Electrochem. Soc.* **165**, A970–A1010 (2018).
[39] E. W. Zhao *et al.*, *Nature*. **579**, 224–228 (2020).
[40] Z. Dunbar, R. I. Masel, *J. Power Sources*. **171**, 678–687 (2007).

[41] I. E. Gunathilaka, J. M. Pringle, L. A. O'Dell, *Nat. Commun.* **12**, 1–9 (2021).
[42] H. Park *et al.*, *Proc. Natl. Acad. Sci. U. S. A.* **119**, 1–9 (2022).
[43] A. A. Wong, S. M. Rubinstein, M. J. Aziz, *Cell Reports Phys. Sci.* **2**, 100388 (2021).
[44] W. Lee, A. Permatasari, Y. Kwon, *J. Mater. Chem. C.* **8**, 5727–5731 (2020).
[45] S. Chandrasekaran *et al.*, *Carbon N. Y.* **179**, 125–132 (2021).
[46] A. Vyatskikh *et al.*, *Nat. Commun.* **9**, 593 (2018).
[47] Y. C. Saraswat *et al.*, *J. Colloid Interface Sci.* **564**, 43–51 (2020).
[48] Z. Dong *et al.*, *Nat. Commun.* **12**, 1–12 (2021).

9.4. Appendix 9

A9.1. Abbreviations

Symbol	Description
FTFF	Flow-through flow field
GA	Genetic algorithm
IDFF	Interdigitated flow field
NIPS	Non-solvent induced phase separation
PNM	Pore network model
RFB	Redox flow battery
XTM	X-ray tomographic microscopy

A9.2. List of symbols

Symbol	Description	Units
a	Specific surface area of the electrode	$m^2\ m^{-3}$
A_i	Electrochemically active internal surface area	$m^2\ m^{-3}$
$c_{b,i}$	Bulk concentration of the active species	$mol\ m^{-3}$
C_1, C_2	Dimensionless factors	-
C_0	Laminar constant for viscous laminar contributions from contraction	-
C_{ij}	Contraction dissipation loss factor	Pa
c_{in}	Inlet concentration	$mol\ m^{-3}$
$c_{s,i}$	Surface concentration of active species	$mol\ m^{-3}$
D	Diffusion coefficient of the active species	$m^2\ s^{-1}$
d_p	Pore diameter	m
E_0	Laminar constant for viscous laminar contributions from expansion	-
E_{ij}	Expansion dissipation loss factor	Pa
F	(a) Throat effective aspect ratio	Pa
	(b) Faraday's constant, 96,485 C mol^{-1}	$C\ mol^{-1}$
H	Height of the electrode	m
I_i	Current in pore i	A
I_{lim}	Limiting current	A
k_m	Mass transfer coefficient of the active species	$m\ s^{-1}$
L_{fp}	Length of the flow path	m
L_{ij}	Conduit length of the connecting throat	m
M	Expansion curvature parameter	-
N	Contraction curvature parameter	-
n	Number of electrons in the half-reaction	-
N_i	Number of pore connections of pore i	-
N_{out}	Number of downstream throats leaving pore i	-
N_{tot}	Total number of reactive pores	-
$p_{i/j}$	Fluid total head of pore i or j	Pa
q_{ij}	Throat ij volumetric flux	$m^3\ s^{-1}$
r	Radius	m
Re	Reynolds number	-
R_i	Active species net reaction rate	$mol\ s^{-1}$
T_{ij}	Constriction dissipation loss factor	$Pa\ m^{-1}$
V	Electrode volume	m^{-3}
v_e	Electrolyte velocity	$m\ s^{-1}$

W	Width of the electrode	m
	Greek	
α_{ij}	Factor matrix entry of the throat-pore-throat element ij	-
λ_i	Stoichiometric coefficient in the half-reactions	-
μ	Dynamic viscosity of the electrolyte	Pa m
ρ	Mass density of the electrolyte	kg m^{-3}
	Superscripts	
eff	Effective	
pnm	Pore network model	
	Subscripts	
$FTFF$	Flow-through flow field	
$global$	Global	
i	Pore i	
ij	Throat ij	
$idff$	Interdigitated flow field	
j	Pore j	
$local$	Local	
pnm	Pore network model	

Authorship statement

Chapter 1: Introduction

The PhD candidate and promotor conceptualized the content of the book chapter based on the invited topic on overpotentials and transport phenomena in redox flow batteries. The PhD candidate performed the literature research, wrote the manuscript, and created the figures. The promotor gave feedback on the book chapter and the PhD candidate revised the book chapter based on the feedback. To better cover the complete scope of this PhD thesis, the published book chapter was extended as the introduction chapter of this dissertation, for which the PhD student conceptualized the content of the chapter, created the figures, and wrote the text. The promotor gave general directions on improving the content and the PhD student revised the introduction accordingly.

Chapter 2: Assessing the versatility and robustness of pore network modeling to simulate redox flow battery electrode performance

The PhD candidate supervised a master student (co-first author) with whom the publication was conceptualized and written in collaboration. The master student took the initial lead in the development of the model, under the supervision of the PhD candidate and the promotor, after which the PhD candidate further improved the model. All the simulations and experiments presented in this publication were conducted by the PhD candidate as well as the visualization of the results. The data analysis and interpretation were a joint effort with the master student. The promotor provided feedback on the manuscript, which was implemented by the PhD candidate and the master student.

Chapter 3: Understanding the role of the electrode thickness on redox flow cell performance

The PhD candidate collaborated with another PhD student (co-first author) and together they conceptualized the publication, analyzed and interpreted the data, created the figures, and wrote the manuscript. The other PhD student performed the initial experiments (pressure drop, polarization, and impedance), of which several were repeated by the PhD candidate with a master student she supervised (co-author). The PhD candidate additionally performed the membrane and electrolyte conductivity measurements and the exchange current density extractions. The model from **Chapter 2** was extended by the PhD candidate and another master student she supervised (co-author), and the PhD candidate performed all the simulations. The promotor provided feedback on the manuscript, which was implemented by the PhD candidate and the other PhD student.

Chapter 4: Bottom-up design of porous electrodes by combining a genetic algorithm and a pore network model

The PhD candidate supervised a master student (co-first author) with whom the publication was conceptualized and written in collaboration. The master student took the initial lead in the development of the model, under the supervision of the PhD candidate and the promotor, after which the PhD candidate further improved the model. The simulations and experiments presented in this publication were conducted by the PhD candidate as well as the visualization of the results. The data analysis and interpretation were a joint effort with the master student. The promotor provided feedback on the manuscript, which was implemented by the PhD candidate and the master student.

Chapter 5: A versatile optimization framework for porous electrode design

The PhD candidate conceptualized the work and together with two master students she supervised (co-authors), developed, and extended the modeling framework. The PhD candidate proposed the research question, wrote the chapter, performed the simulations, analyzed and interpreted the data, and made the figures. The promotor gave general directions on improving the content and the PhD student revised the chapter accordingly.

Chapter 6: Quantifying concentration distributions in redox flow batteries with neutron radiography

The PhD candidate collaborated with two other PhD students (co-first authors), and together they conceptualized the work, performed the experiments, analyzed and interpreted the data, created the figures, and wrote the manuscript. The image processing of the NEUTRA beamline experiments was performed by the PhD candidate and the image processing of the ICON beamline experiments was performed by another co-author. The promotor provided feedback on the manuscript, which was implemented by the PhD candidate and the other PhD students.

Chapter 7: Neutron imaging to study the influence of porous electrodes and flow fields on concentration distributions in redox flow cells

The PhD candidate conceptualized the work and together with two other PhD students (co-authors) performed the experiments. The PhD candidate proposed the research question, processed the data, performed the image analysis, analyzed and interpreted the data, made the figures, and wrote the chapter. The promotor gave general directions on improving the content and the PhD student revised the chapter accordingly.

Chapter 8: Investigating mass transfer relationships in stereolithography 3D printed electrodes for redox flow batteries

The PhD candidate proposed the research question, conceptualized the work, performed the experiments, analyzed and interpreted the data, made the figures, and wrote the chapter. The promotor and copromotor provided feedback on the manuscript, which was implemented by the PhD candidate.

Chapter 9: Conclusions and outlook

The PhD student conceptualized the content of the chapter, created the figures, and wrote the text. Part of the content of this chapter is based on ongoing work by the PhD candidate of which some in collaborations with master students she supervised. The promotor gave general directions on improving the content and the PhD student revised the chapter accordingly.

Acknowledgments

I would like to use this opportunity to thank everyone who contributed, both scientifically and socially (/mentally), to my PhD journey. In these four years, I learned a lot, not only about electrochemistry or modeling (which were both completely new to me) but also about myself and my career ambitions. This would not have been possible without the great people I had the honor to work with and supported me.

First of all, **Toni**, without you my thesis would not look the same. You were a real mentor, you taught me so much, you were very patience, inspiring, sometimes a bit chaotic, kind, thoughtful, and even made me a little less Dutch (direct). Your evergoing enthusiasm for science is very inspiring, which infected me to continue the academic path (as far as it takes me at least). I cannot thank you enough for everything I learned in the past four years and for all the freedom you gave me to carry out my research. I wish you and your lovely family all the best and I really hope we stay in touch! **Kitty**, bedankt voor je steun de afgelopen vier jaar in goede en slechte tijden. Van jou heb ik geleerd meer in mijzelf te geloven en dat ik moet gaan voor de kansen die ik krijg, iets wat als academica zeer van pas komt. Ik ben blij dat jij de voorzitter kan zijn tijdens mijn verdediging, zijn jullie toch alle drie aanwezig in mijn commissie! En tot slot, heel erg bedankt dat je me in contact hebt gebracht met Toni voor een PhD, anders was ik nooit gaan werken aan elektrochemie! **Zandrie**, bedankt dat je mijn copromotor bent, ook al ligt mijn onderzoeksonderwerp niet binnen jouw directe expertise, je gaf altijd een ander inzicht in mijn onderzoek waar ik anders zelf nooit aan had gedacht! **Caroline**, bedankt dat je altijd voor iedereen klaar staat en dat we alles aan jou kunnen vragen!

I also would like to thank all members of my **thesis committee** prof.dr.ir. J.A.M. Kuipers, prof.dr.ir. M. van Sint Annaland, prof.dr.ing. T. Breugelmans, and dr. Y. Gonzalez Garcia for being part of my doctoral committee. I really appreciate your time and effort in reading and assessing this extremely long thesis and for attending my ceremony.

I also would like to thank all my **collaborators** from the past four years, and I hope we will work together again in the near future! Vignesh and Merit, thank you for your nice suggestions and input during the project meetings, and the visits to Elestor and Nedstack! Thank you Fikile, Kevin, Katharine, and Charles from MIT for your insights and knowledge on flow batteries, and for having the opportunity to see your labs. Pierre and Ricardo from PSI, thank you both for your help during and after our intense neutron campaign. Especially for all your efforts on the image processing, which is still a bit of a black box to me. You both brought our manuscripts/working papers to the next level! And last but definitely not least, thank you Jeff and Amin from the University of Waterloo

for all your help and insights on pore network modeling. Your open-source software (OpenPNM) is truly great, and I love that you are actively helping everyone who wants to use the code, it is really inspiring.

Vanesa, when I talk about collaborators, I of course cannot forget you, but you simply need a separate paragraph. Even though you were only at the TU/e for six months, I had the honor to work with you for much longer and got to know you more on a personal level. You are not only a hard-working excellent researcher, but you are also an amazing person! I loved our collaborations and I hope we can continue to work together (hopefully when we are both in the US! Fingers crossed!). I wish you all the best in the future and I am excited that you can make it to my defense!

Daniëlle and Emre, my paranymphs, where do I start… **Daniëlle**, jij was echt DE persoon die ik wilde spreken in mijn stress-dagen vóór het inleveren van mijn thesis. Het is altijd fijn om met je te praten en om even te kunnen ventileren. Ook al hebben we pas laat meer contact met elkaar gekregen, ik zou nu niet meer zonder je kunnen. Je bent echt geweldig, lief, down-to-earth (haha ik zie het al voor me hoe je reageert als je dit leest) en realistisch (wat ik soms nodig heb). Ik hoop dat we goed contact houden, waar we ook zijn! **Emre**, you're amazing! I think that, when I think back over many years, one of the things I will remember of my PhD times will be you. We basically went through everything together for four years, all the fun things (parties), sad things (Covid), dramas, and good times (US, Switzerland, Vienna). You know, just talking to you can make me happy again. You are really fun to be around, and I can tell you anything. Thanks for being there for me and for being a great friend! Both, thank you so much for being there for me during my PhD and for having my back as paranymphs! Love you both!

#**Adrian**myconferencehusband! We are always talking about postdocs that help the PhD students during their journey, well I think you also helped me a lot. Perhaps not so much with the science, but with allowing me to disturb you with whatever question I had, I really appreciate it! I loved going to conferences with you, going for crazy runs or hikes during the conferences with Dan, and of course, drinking some liters of cocktails afterwards. I hope we can continue this nice trend in the future (although that depends on what my future holds, as I am not worried about your academic path 'they better hire you!'), but until then let's plan a cheese fondue again soon! En bij Adrian hoort natuurlijk ook Bassie, ownee das de mijne, ik bedoel mijn favo-fries **Marrit**! Meid, je bent een topper! Ik hoop dat we weer snel in het voorjaar een rondje kunnen gaan fietsen en dat Sagan en Teske nog eens letter kunnen ravotten samen!

Rèmy, wijfie! I think you are one of the strangest but kindest guys I know. You are always willing to help anyone at any time, I really appreciate that of you! It was great to see you in your element during our trip to PSI, to see the real unfiltered strange, hard-working, messy person that you are. Also, thanks again for being willing to help me in my running goals in the US, perhaps we should start again, and this time really do the 21 km with you, me, and #Adrian. **Anna**, oh you, you bully. How can a person be so mean but also so nice, kind, caring, and full of initiative, I love it! You always kept me sharp as you never knew when you would scare the hell out of me again. I always love to hang

out with you, it's never boring and you always know fun things to do, I really hope we can do this for many more years. But let's start with our Bachelorettes and Weddings ;).

Joey, mijn eerste SepTech maatje, het was toch een stuk gezelliger om samen alle examens en opdrachten na te kijken. Ook al hadden we met werk niks met elkaar te maken, kon ik wel altijd even ventileren bij je en jij lekker klagen tijdens een koffietje of biertje, topper! En met een Joey daar kwam een Menno, **Menno** ik wens je echt al het goede toe. We moeten dit voorjaar niet vergeten samen nog een rondje te fietsen! **Moji**, although we basically just met, I already know you are an amazing guy! I hope we can finally start working together after my busy pre-Dr. period. Thanks for all your help and that I could basically always disturb you with any question. Soon-to-be baby daddy **Jeroen**, bedankt dat je altijd klaar staat om te helpen, om te luisteren naar mijn geklaag, voor het delen van je geheimen en voor het leren delegeren haha. Ik ga je harde aanstekelijke lach zeker missen! Sweet, sweet (and addicted to sweet Monster) **Inma**, thank you for everything you do for us and for the strictness you bring to the group ;). You should know that I have full faith in you, you are incredibly smart and full of random knowledge, you will do great, and I can't wait to see what you will do in the future.

Furthermore, I would like to thank the entire **MMP-EMS crew**! You are all lovely people that I will definitely miss a lot when I am gone. Thank you office-mate-that-is-always-in-the-lab Senan, party-girl Irene, meme-master Winnie, Rens-de-bouwer, Mert the coffee addict, my beloved replacement Marina (please don't forget her anymore), Nadia, Jadwiga, Simona, Ameya, Aylin, Woutje, Cees, Renate, Pelin, Niek, and Sarthak. Also, a big thanks to the old MMP-EMS members that I gladly met during my PhD: Niki, Gemma, Machiel, Jesse, Baichen, Sjoukje, Kiran, and Anna.

To all my wonderful students, thank you for your great efforts and hard work, you are all a true addition to my PhD thesis and personal development! De persoon die ik zeker niet mag vergeten, de perfecte student **Rik**! Rik, jij hebt mijn PhD gekick-start, daar wil ik je echt voor bedanken. Ook al hadden we ups en downs in de samenwerking, it was a good one! Met als resultaat twee papers waar we heel trots op mogen zijn. Jij bent een doorzetter, aanpakker, suuuuper slim en ook nog eens een goeie gast! Ga zo door en ik weet zeker dat jij het ontzettend ver gaat schoppen. **Victor**, nog zo'n perfecte student en een top kerel! Bedankt voor alles, vooral voor het goed documenteren van je werk zodat ik dat niet meer hoef te doen haha. Hopelijk kan Toni je alsnog overhalen om een PhD te doen in onze groep, want als er iemand perfect in de groep past en een PhD tot een succes kan brengen ben jij het! **Marit**, na al het gestruggle op het lab met de printer en oven hebben we toch echt een mooi project afgerond, wat hopelijk de basis is voor mijn toekomstige carrière, daarvoor wil ik je bedanken! Je was prettig mee samen te werken, heel gestructureerd en ik wens je het allerbeste toe! **Gabor**, thanks a lot for all your hard work during Covid, not being allowed to come to the university, you still managed to do it! I wish you all the best and I hope to see you again one day! **Nard**, mijn introkiddo/student, wat een topkerel ben je toch! Je bracht altijd veel positiviteit met je mee wat iedereen meteen liet lachen, we hebben meer mensen nodig zoals jij! **Jacky**, helaas is het project vroegtijdig gestopt, maar ik vond het fijn om met je te werken, je was altijd zo gemotiveerd en enthousiast. Hopelijk gaat het snel beter met je en wie weet kan je dan altijd nog je project oppakken. Ik wens je veel gezondheid en succes toe!

Natuurlijk is werk niet alles en daarom wil ik graag mijn **familie en vrienden** bedanken dat jullie er altijd voor mij zijn, ook tijdens mijn PhD reis de afgelopen vier jaar! Ik wil vooral mijn lieftallige ouders, opa en oma's, broertje (hehe dat blijf je, ookal ben je oneindig lang), zusje (lieftallige getuige) en schoonouders bedanken! Bedankt dat jullie altijd voor ons (ik, Bas en onze kleine doerak Sagan) klaar staan! Ik hou van jullie, jullie betekenen heel veel voor me! Pap en mam, jullie vooral, bedankt voor alles de afgelopen 27.5 jaar! Jullie hebben me altijd gesteund, uitgedaagd en liefgehad. Ik zou niet weten wat ik zonder jullie zou moeten <3.

En dan mijn grootste schatten van allenmaal, Bas en Sagan! **Sagan** – ja ik bedank mijn hond – je bent een schatje, zo fijn om altijd blij onthaalt te worden als ik thuiskom! Je bent ook echt de grootste draak die ik ken met al je streken, die zul je vast van je andere ba(a)s hebben ;). **Bas**, mijn soon-to-be husband, bedankt voor alles de afgelopen jaren! Op jou kan ik echt altijd rekenen en je staat altijd voor me klaar. Vooral bedankt voor je geduld, steun, positieve insteek, nuchterheid en liefde, vooral het laatste half jaar, die was toch wel zwaarder. Ik kan je ook niet genoeg bedanken voor het feit dat je volledig achter mij staat wat betreft onze toekomst en bereid bent om met mij naar de andere kant van de wereld te verhuizen! Ik hou heel veel van je en ik kijk er nu al naar uit om je binnenkort mijn man te noemen! Ik heb zin in onze toekomst, die kan niet anders dan perfect zijn zolang we samen zijn! <3

About the author

Maxime van der Heijden was born on April 11, 1996, in Valkenswaard, The Netherlands. She obtained her Bachelor's and Master's degrees in Chemical Engineering and Chemistry at Eindhoven University of Technology, The Netherlands, in 2017 and 2019, respectively. For her Masters, she received the VNCI Topsector Chemistry Scholarship, sponsored by DSM. During her Masters, she specialized in Molecular Systems and Materials Chemistry and performed her Master thesis on multi-dye coordination in layered smectics for light guiding purposes in the group Stimuli-responsive Functional materials and Devices. To finalize her Master studies, she completed an internship at DSM Coating Resins BV. (Waalwijk) on receptive coatings for inkjet printing. In November 2019, she joined the Electrochemical Materials and Systems group at Eindhoven University of Technology as a PhD Candidate under the supervision of Dr. Antoni Forner-Cuenca. During her research, she worked on the engineering of porous electrodes for redox flow batteries by combining modeling approaches, imaging diagnostics, and advanced manufacturing. The most important results of her work are presented in this thesis. After her PhD, she will continue in the group of Dr. Antoni Forner-Cuenca as a postdoctoral researcher.

List of publications

Publications related to this thesis

Publications:

V. Muñoz-Perales[*], **M. van der Heijden**[*], V. de Haas, J. Olinga, M. Vera, and A. Forner-Cuenca, Understanding the role of electrode thickness on redox flow cell performance, (2023), *ChemElectroChem,* Accepted Manuscript, doi:10.1002/celc.202300380.

M. van der Heijden, M. Kroese, Z. Borneman, and A. Forner-Cuenca, Investigating mass transfer relationships in stereolithography 3D printed electrodes for redox flow batteries, *Advanced Materials Technologies*, **8**, 18 (2023), pp. 2300611.

R. van Gorp[*], **M. van der Heijden**[*], M.A. Sadeghi, J. Gostick, and A. Forner-Cuenca, Bottom-up design of porous electrodes by combining a genetic algorithm and a pore network model, *Chemical Engineering Journal*, **455** (2023), pp. 139947.

M. van der Heijden[*], R. van Gorp[*], M.A. Sadeghi, J. Gostick, and A. Forner-Cuenca, Assessing the versatility and robustness of pore network modeling to simulate redox flow battery electrode performance, *Journal of the Electrochemical Society*, **169** (2022), pp. 040505.

M. van der Heijden, and A. Forner-Cuenca, Transport Phenomena and Cell Overpotentials in Redox Flow Batteries, *in Encyclopedia of Energy Storage*, L. F. Cabeza, Ed. (Elsevier Inc., Oxford, ed. 2, 2022), pp. 480–499.

Preprints:

R.R. Jacquemond[*], **M. van der Heijden**[*], E.B. Boz[*], E.R.C. Ruiz, K.V. Greco, J.A. Kowalski, V. Muñoz Perales, F.R. Brushett, D.C. Nijmeijer, P. Boillat, and A. Forner-Cuenca, Unravelling Concentration Profiles in Redox Flow Batteries Using Neutron Radiography, *ChemRxiv* (2023), doi:10.26434/chemrxiv-2023-8xjv5.

In preparation:

M. van der Heijden, G. Szendrei, V. de Haas, and A. Forner-Cuenca, A versatile optimization framework for porous electrode design (2023).

M. van der Heijden, R.R. Jacquemond, E.B. Boz, P. Boillat, and A. Forner-Cuenca, Neutron imaging to study the influence of porous electrodes and flow fields on concentration distributions in redox flow cells (2023).

Other publications

Publications:

V. Muñoz-Perales, **M. van der Heijden**, P.A. Garcia-Salaberri, M.V. Coello, and A. Forner-Cuenca, Engineering Lung-inspired Flow Field Geometries for Redox Flow Batteries with Stereolithography 3D Printing, *ACS Sustainable Chemistry and Engineering*, **11**, 33 (2023), pp. 12243–12255.

K.M. Tenny, K.V. Greco, **M. van der Heijden**, T. Pini, A. Mularczyk, A. Vasile, J. Eller, A. Forner-Cuenca, Y. Chiang, and F.R. Brushett, A Comparative Study of Compressive Effects on the Morphology and Performance of Carbon Paper and Cloth Electrodes in Redox Flow Batteries, *Energy Technology*, **10** (2022), pp. 2101162.

G. Timmermans, **M. van der Heijden**, B.M. Oosterlaken, S.C.J. Meskers, A.P.H.J. Schenning, and M.G. Debije, Flexible Nanoporous Liquid Crystal Networks as Matrixes for Förster Resonance Energy Transfer (FRET), *ACS Applied Nano Materials*, **3**, 4 (2020), pp. 3904–3909.

J. ter Schiphorst, M.L.M.K.H.Y.K. Cheng, **M. van der Heijden**, R.L. Hageman, E.L. Bugg, T.J.L. Wagenaar, and M.G. Debije, Printed luminescent solar concentrators: Artistic renewable energy, *Energy and Buildings*, **207** (2020), pp. 109625.

In preparation

E.B. Boz, **M. van der Heijden**, R.R. Jacquemond, P. Boillat, and A. Forner-Cuenca, Correlating electrolyte infiltration with accessible surface area in microporous electrodes using neutron radiography (2023).

R.R. Jacquemond, **M. van der Heijden**, E.B. Boz, E.R.C. Ruiz, D.C. Nijmeijer, P. Boillat, and A. Forner-Cuenca, Understanding the Influence of Membrane Type on Transport Phenomena in Non-Aqueous Redox Flow Batteries with Neutron Radiography (2023).

*Co-first authors

List of conference abstracts

Conference and symposium oral presentations (first-author)

M. van der Heijden, Marit Kroese, Jacky Olinga, Zandrie Borneman, Antoni Forner-Cuenca, Stereolithography 3D Printing As a Versatile Tool to Manufacture Porous Electrodes for Redox Flow Batteries, *244th Electrochemical Society Meeting*, Gothenburg, Sweden, 2023.

M. van der Heijden, R. van Gorp, G. Szendrei, V. de Haas, M.A. Sadeghi, J. Gostick, A. Forner-Cuenca, Starting from the Bottom: Coupling a Genetic Algorithm and a Pore Network Model for Porous Electrode Design, *243rd Electrochemical Society Meeting*, Boston, US, 2023.
Travel grant Battery Division

M. van der Heijden, R. van Gorp, G. Szendrei, V. de Haas, M.A. Sadeghi, J. Gostick, A. Forner-Cuenca, Starting from the bottom: Coupling a genetic algorithm and a pore network model for porous electrode optimization, *15th Annual InterPore Meeting*, Edinburgh, Scotland, 2023.

M. van der Heijden, R. van Gorp, G. Szendrei, V. de Haas, M.A. Sadeghi, J. Gostick, A. Forner-Cuenca, Coupling a genetic algorithm and a pore network model for redox flow battery porous electrode optimization, *19th ModVal Symposium*, Duisburg, Germany, 2023.

M. van der Heijden, R. van Gorp, G. Szendrei, M.A. Sadeghi, J. Gostick, A. Forner-Cuenca, Towards bottom-up design of porous electrode microstructures – An approach coupling evolutionary algorithms and pore network modeling, *241st Electrochemical Society Meeting*, Vancouver, Canada, 2022.

M. van der Heijden, R. van Gorp, G. Szendrei, M.A. Sadeghi, J. Gostick, A. Forner-Cuenca, Towards bottom-up design of porous electrode microstructures – coupling evolutionary algorithms and pore network modeling, *17th Netherlands Process technology Symposium*, Delft, The Netherlands, 2022.

M. van der Heijden, R. van Gorp, G. Szendrei, A. Borneman, A. Forner-Cuenca, Towards bottom-up design of porous electrode microstructures for redox flow batteries, *Porous Media Tea Time Talks*, Online, Session 20, YouTube, 2021.

Conference and symposium poster presentations (first-author)

M. van der Heijden, M. Kroese, Z. Borneman, A. Forner-Cuenca, Investigating Mass Transfer Relationships in Stereolithography-Based 3D Printed Electrodes for Redox Flow Batteries, *243rd Electrochemical Society Meeting*, Boston, US, 2023.

M. van der Heijden, M. Kroese, Z. Borneman, A. Forner-Cuenca, Investigating mass transfer relationships in stereolithography 3D printed electrodes for redox flow batteries, *15th Annual InterPore Meeting*, Edinburgh, Scotland, 2023.

M. van der Heijden, R. van Gorp, G. Szendrei, M.A. Sadeghi, J. Gostick, Z. Borneman, A. Forner-Cuenca, Towards bottom-up design of porous electrode microstructures – coupling genetic algorithms with pore network modeling of redox flow battery electrodes, *13th Annual InterPore Meeting*, Online, 2021.
Student Poster Award

M. van der Heijden, R. van Gorp, G. Szendrei, Z. Borneman, A. Forner-Cuenca, Optimizing the 3D Microstructure of Redox Flow Battery Electrodes, *CHAINS 2020*, Online, 2020.

M. van der Heijden, Z. Borneman, A. Forner-Cuenca, Optimizing the 3D microstructure of redox flow battery electrodes, *2020 Membrane Symposium*, Essen, 2020.

R.R. Jacquemond*, **M. van der Heijden***, Z. Borneman, D.C. Nijmeijer, A. Forner-Cuenca, Towards Bottom-up Engineered Electrodes for Redox Flow Batteries, *1st ECCM graduate school*, Eerbeek, 2019.